TAMPEREEN TEKNILLINEN YLIOPISTO
TAMPERE UNIVERSITY OF TECHNOLOGY

Anssi Laaksonen

Structural Behaviour of Long Concrete Integral Bridges

Julkaisu 978 • Publication 978

Tampere 2011

Tampereen teknillinen yliopisto. Julkaisu 978
Tampere University of Technology. Publication 978

Anssi Laaksonen

Structural Behaviour of Long Concrete Integral Bridges

Thesis for the degree of Doctor of Science in Technology to be presented with due permission for public examination and criticism in Rakennustalo Building, Auditorium RG202, at Tampere University of Technology, on the 2nd of September 2011, at 12 noon.

Tampereen teknillinen yliopisto - Tampere University of Technology
Tampere 2011

Supervisor and Custos: Prof. Dr. Ing. Tim Länsivaara
Tampere University of Technology
Faculty of Built Environment
Department of Civil Engineering
Unit of Earth and Foundation Structures
Tampere, Finland

Supervisor: Prof. Dr. Tech. Ralf Lindberg
Tampere University of Technology
Faculty of Built Environment
Department of Civil Engineering
Tampere, Finland

Preliminary Assessors: Prof. Dr. Tech. Karl Õiger
Tallinn Technical University
Faculty of Civil Engineering
Department of Structural Design
Tallinn, Estonia

Prof. Dr. Ing. Steinar Nordal
Norwegian University of Science and Technology
Faculty of Engineering Science and Technology
Department of Civil and Transport Engineering
Trondheim, Norway

Opponent: Prof. Dr. Tech. Matti Ollila
Helsinki, Finland

ISBN 978-952-15-2615-2 (printed)
ISBN 978-952-15-2618-3 (PDF)
ISSN 1459-2045

To Mira

- Ilman ylämäkiä ei olisi alamäkiä

- There are no downhills without uphills

ABSTRACT

Anssi Laaksonen: Structural Behaviour of Long Concrete Integral Bridges 204 p. + 61 p. app.

There are more than 20,000 bridges in Finland, of which about 2000 with a sum of span lengths over 20m are actual integral abutment road bridges. The lower building and maintenance costs of integral abutment bridges compared to conventional abutment bridges have increased interest for the former.

This study deals with the structural behaviour of long concrete integral abutment bridges. The bridge subtype was limited to fully integral abutment bridges without any bearings or expansion joints. This study examines structural behaviour from the viewpoint of a bridge designer taking into consideration the effects of soil-structure interaction. It is a part of larger research project called “Soil-Bridge Structure Interaction”.

The main goal was to determine the effects of different soil properties at opposite bridge ends on the structural behaviour of fully integral bridges Another important goal was to determine the maximum allowable total thermal expansion length of a fully integral concrete bridge in terms of structural behaviour of piles at the bridge ends at the climatic conditions of monitored bridges. A further goal was to give suggestions for constructing integral bridges together with the whole research team.

Three bridges, Haavistonjoki Bridge, Myllypuro Overpass and Tekemäjärvenoja Bridge, were monitored during this study. The main focus of the monitoring was the Haavistonjoki Bridge. The instrumentation of Haavistonjoki Bridge on the Tampere-Jyväskylä highway was completed in autumn 2003. Monitoring data have been collected by a total of 191 gauges, of which 98 are still working seven years after the monitoring started. The instrumentation is used to measure longitudinal abutment movements, abutment rotations, earth pressure behind abutments, superstructure displacements, frost depth, air temperature, and temperature differences in superstructure and approach embankment.

The method for calculating uniform bridge superstructure temperature based on ambient temperature was developed on the basis of monitoring results from the Haavistonjoki Bridge. The temperature was calculated backwards until 1959 with this method. Obtained results correlate very well with the temperature loads of Eurocode EN 1991-1-5.

Structural analyses were run on single laterally loaded composite piles and a whole bridge structure using software based on the finite element method. The analyses on single com-

posite piles used the following variables: pile size and number, corrosion or no corrosion, three different soil properties, hinged or rigid pile top connection. A total of 192 composite FE models including composite piles were analysed. Hyperbolic soil behaviour with hysteresis loops was defined. The lateral displacement capacity of the head of a pile based on the yield strength of structural steel was obtained from these analyses.

Four and six span fully integral bridges with or without a cantilever span and with different pile diameters at the abutments were analysed with whole bridge FE models. They were non-linear quasi-static FE analyses. Reinforced slab, reinforced beam-and-slab and post-tensioned beam-and-slab structures were analysed. A total of 168 bridge models were analysed with various loads according to Finnish guidelines. Soil behaviour was found to be hyperbolic with hysteresis loops in the case of both the laterally loaded pile and the end screen based on literature and monitoring results. The modulus of lateral subgrade reaction was carefully studied in both model types (pile and bridge) to take into account the effect of pile diameter.

The thermal expansion of Haavistonjoki Bridge was not symmetrical. A behaviour model that explains this phenomenon was discovered during the study. The difference in the lateral strength and stiffness of hyperbolic soil behaviour at the integral bridge ends causes eccentric displacements during thermal expansion around the centre of thermal expansion. The phenomenon is taken into account in FE analyses and in suggestions for integral bridge design and construction. The suggestion for the maximum total thermal expansion length of a fully integral bridge was determined on the basis of piles of different size resulting in different maximum lengths. The obtained maximum limit was approximately 120m, and it is based on the structural behaviour of the piles and the integral bridge superstructure. However, there are many factors influencing integral bridge behaviour, which places limitations on research not to mention bridge design and construction. Hence, the suggested 100m limit for the allowable thermal expansion length of this study for bridge design is somewhat less than the ultimate limit defined in this study.

KEYWORDS: Integral abutment bridge, soil-structure interaction, laterally loaded pile, modulus of lateral subgrade reaction, thermal expansion length, bridge monitoring

TIIVISTELMÄ

Anssi Laaksonen: Pitkän betonisen liikuntasaumattoman sillan rakenteellinen käyttäytyminen
204 s. + 61 liites.

Suomessa on yli 20 000 siltaa, joista 2000 yli 20 m jännemittojen summan omaavista laatta- ja laattapalkkisilloista ovat liikuntasaumattomia. Alhaisemmat rakentamis- ja ylläpitokustannukset ovat lisänneet kiinnostusta liikuntasaumattomiin siltoihin tavanomaisiin maatuellisiin siltoihin verrattuna.

Tämä työ käsittelee pitkän betonisen ja liikuntasaumattoman sillan rakenteellista käyttäytymistä. Tarkasteltava sillan alatyyppi on rajoitettu täysin liikuntasaumattomaan siltatyyppiin missä ei ole lainkaan laakereita tai liikuntasaumalaitteita. Tämä työ tarkastelee sillansuunnittelijan kaltaisesti liikuntasaumattoman sillan rakenteellista käyttäytymistä rakenteen ja maan yhteistoiminnan vaikutukset huomioiden. Tämä työ on osa laajempaa tutkimusohjelmaa: ”Sillan ja maan yhteistoiminta”.

Päätavoitteena oli tuoda esiin täysin liikuntasaumattoman sillan eri päätytuilla olevien erilaisten maan ominaisuuksien vaikutus sillan rakenteelliseen käyttäytymiseen. Suurimman sallitun lämpölaajenevan pituuden määrittäminen täysin liikuntasaumattomalle sillalle päätytukien paalujen rakenteellisen käyttäytymisen kannalta monitoroitujen siltakohteiden ilmasto-olosuhteissa oli myös tärkeä tavoite. Edelleen tavoitteena oli antaa suosituksia yhdessä koko tutkimusprojektin kanssa liikuntasaumattomien siltojen rakentamiseen.

Kolmea siltaa, Haavistonjoen silta, Myllypuron risteyssilta ja Tekemäjärvenojan ratasilta, monitorointiin tämä työn aikana. Tämä työ keskittyy monitorointien osalta pääasiassa Haavistonjoen siltaan. Haavistonjoen sillan instrumentointi Tampere-Jyväskylä valtatiellä valmistui keväällä 2003. Mittausdataa on kerätty monitoroimalla yhteensä 191 anturilla joista 98 on yhä toimintakuntoisia 7 vuotta monitoroinnin alkamisesta. Instrumentointia on käytetty mittaamaan päätytukien pituussuuntaisia siirtymiä, päätytuen kiertymiä, maanpaineita päätytuen takana, sillan päällysrakenteen siirtymiä, routaantumissyvyyttä, ulkoilman lämpötilaa ja lämpötilaeroja sillan päällysrakenteesta ja päätypenkereestä.

Työssä kehitettiin analyysimenetelmä sillan keskimääräisen lämpötilan määrittämiseksi ulkoilman lämpötilasta Haavistonjoen sillan monitorointitulosten perusteella. Keskimääräinen lämpötila laskettiin tällä menetelmällä vuodesta 1959 eteenpäin. Saavutetut tulokset vastaavat todella hyvin lämpötilakuormia eurokoodin standardissa EN 1991-1-5.

Rakenteelliset analyysit tehtiin elementtimenetelmään perustuvalla ohjelmistolla yksittäiselle vaakakuormitetulle paalulle ja koko sillan rakenteelle. Yksittäisten liittorakenteisten paalujen analyysit sisälsivät seuraavia muuttujia: paalujen koko, korroosio huomioiden tai ilman, kolme erilaista kitkamaamateriaalia ja jäykästi tai momenttijäykästi tuetun paalun yläpään. Yhteensä 192 FE-mallia analysointiin näillä liittorakenteisilla paaluilla. Työssä käytettiin hyperbolista ja hystereesiloopin muodostavaa maamateriaalin käyttäytymistä. Vaakasuuntainen paalun yläpään siirtymäkapasiteetti rakenneteräksen myötörajan perusteella määritettiin näiden analyysien perusteella.

Neljä- ja kuusiaukkoisia täysin liikuntasaumattomia siltoja ulokkeella tai ilman ja eri halkaisijan omaavilla paaluilla päätytuilla analysoitiin koko sillan FE-malleilla. Analyysit tehtiin kvasistaattisina epälineaarisina FE-analyyseina. Teräsbetonisia laatta-, teräsbetonisia laattapalkki- ja jälkijännitettyjä laattapalkkirakenteita analysoitiin. Maamateriaalin käyttäytyminen määritettiin hyperboliseksi yhdessä hysteerisen käyttäytymisen kanssa sekä vaakakuormitetun paalun että päätypalkin osalta perustuen kirjallisuuteen ja monitorointituloksiin. Alustalukua tarkasteltiin varovaisesti molemmissa malleissa (paalu- ja siltamalli) jotta paalun halkaisijan vaikutus tuli huomioon otetuksi.

Lämpölaajeneminen ei tapahtunut symmetrisesti Haavistonjoen sillalla. Tähän esitettiin työssä käyttäytymismalli. Hyperbolisesti käyttäytyvän maamateriaalin erilainen lujuus ja jäykkyys päätytukien kesken aiheuttaa epäkeskeisiä liikkeitä lämpölaajenemisesta liikuntakeskiöön verrattuna. Tämä ilmiö on otettu huomioon FE-analyyseissa ja liikuntasaumattoman sillan suunnittelun ja rakentamisen suosituksissa. Suositus täysin liikuntasaumattoman sillan suurimmaksi lämpölaajenevaksi pituudeksi saavutettiin eri paalujen halkaisijoilla. Saavutettu raja on noin 120 m ja se perustuu paalujen ja täysin liikuntasaumattoman sillan päällysrakenteen rakenteelliseen käyttäytymiseen. Kuitenkin monet tekijät vaikuttavat liikuntasaumattoman sillan käyttäytymiseen, jotka aiheuttavat useita rajauksia tutkimukseen, puhumattakaan sillansuunnittelusta ja rakentamisesta. Täten suositeltu 100 m raja liikuntasaumattoman sillan sallituksi lämpölaajenevaksi pituudeksi on hieman vähemmän kuin tässä työssä määritetty äärimmäinen raja.

HAKUSANAT: Liikuntasaumaton silta, rakenteen ja maan yhteistoiminta, vaakakuormitettu paalu, alustaluku, lämpölaajeneva pituus, sillan monitorointi

FOREWORD

The seven years of conducting this research were a busy period that was educational to the doctoral candidate and expanded his perspectives. I hope that this study reflects his persistent character.

This study was conducted at the Unit of Earth and Foundation Structures of Tampere University of Technology (TUT) in 2004-2011.

I extend my thanks to the supervisor of my research, Prof. Tim Länsivaara (TUT), who was willing to listen even to my most peculiar ideas during the work.

I also acknowledge my debt to my advisor and supervisor Prof. Ralf Lindberg (TUT), who encouraged me and engaged in fruitful discussions with me.

I am deeply grateful to the preliminary assessors, Prof. Steinar Nordal and Prof. Karl Õiger, whose advice and comments on my study were highly valuable.

I am also greatly indebted to the Unit of Engineering Structures and the Unit of Structural Engineering (until 1.1.2011 Road and Bridge Engineering Division) of the Finnish Transport Agency (FTA) for financing most of this study and the related research project (from 1.1.2010 the Finnish Road Administration has been part of FTA).

Heartfelt thanks go also to the members of the project supervisory group. The members of the supervisory group changed during this project and I acknowledge my debt to all of them. The current make-up of the group is: Lic.Tech. Timo Tirkkonen (FTA), M.Sc. Juha Noeskoski (FTA), Pentti Tiensuu (Teknikum Oy), Lic.Tech. Antti Niemi (Teknikum Oy) and Prof. Tim Länsivaara (TUT).

This study has also received funding from A-Insinöörit Suunnittelu Oy, the Finnish Foundation for Technology Promotion (TES), the Finnish Cultural Foundation (SKR), the Association of Finnish Civil Engineers (RIL), the City of Tampere and the Finnish Association of Consulting Firms (SKOL), Maanrakennusalan Neuvottelukunta (MANK) and the Kerttu and Jukka Vuorinen Foundation c/o Concrete Association of Finland to whom I express my gratitude for giving me more time to concentrate on this study.

In addition to FTA, the Finnish Railway Administration (from 1.1.2010 also part of FTA), Teknikum Oy and Ruukki Oyj have funded research and studies closely related to this study, for which I am very grateful.

I also express my thanks to the entire staff of the Unit of Earth and Foundation Structures for their unselfish help with many problems. I want to bring out especially M.Sc. Kauko Sahi and thank him for the irreplaceable help with numerous measuring arrangements and his endless interest in the technology related to my work.

Warm thanks also to my colleagues of the Unit of Bridge and Specific Structures at A-Insinöörit Suunnittelu Oy. We had several constructive discussions about my study.

Finally, I want to thank Mira, who cared for me during the long hours spent on this study regardless of the time of day. Without her support, this study could never have been completed.

Tampere, June 2011
Anssi Laaksonen

TABLE OF CONTENTS

NOTATIONS

Symbols

a	acceleration [m/s^2]
A	loaded area [m^2]
$A_{+/-}$	step constant of uniform temperature calculation [1/h]
A_c	cross sectional area of concrete [m^2]
$A_{c,ss}$	cross sectional area of concrete superstructure [m^2]
A_{cc}	considered area in determination of spring properties [m^2]
A_s	cross sectional area of structural steel section [m^2]
A_y	cross sectional area of reinforcement [m^2]
B	width of end screen [m]
C_0	curvature of cross section at stage D_0 [-]
$C_{0,y}$	curvature of cross section when structural steel yields at stage D_0 [-]
cc	centre-to-centre spacing of piles [m]
cc_b	spring division along end screen width [m]
cc_h	spring division along end screen height [m]
cc_s	spring division along pile length [m]
D	pile diameter [m]
D*t	circular pile cross section, diameter*steel wall thickness [mm*mm]
d_m	distance between measuring points [m]
d_T	rate of uniform bridge superstructure temperature change [°C/h]
D_X	displacement in global X-direction in bridge model [m]
$D_{X,des}$	displacement of bridge end from uniform temperature change when the bridge model is symmetrical [m]
$D_{X,end1}$	displacement of bridge end 1, see Figure 6.59 [m]
$D_{X,end2}$	displacement of bridge end 2, see Figure 6.59 [m]
E	elastic modulus of continuum [MN/m^2]
E_{50l}	lateral soil modulus [MN/m^2]
E_{50v}	vertical soil modulus [MN/m^2]
EA_0	short-term tension stiffness of composite cross section [MN]
$EA_{0->00}$	change in tension stiffness of composite cross section [MN]
EA_{00}	long-term tension stiffness of composite cross section [MN]
e_c	concrete force resultant distance from centre axis of composite cross section [m]
E_c	secant modulus of concrete at 28 days, obtained from formula $E_c = \sigma_c / \varepsilon_c$ [MN/m^2]
E_{cc}	secant modulus of concrete with creep effect [MN/m2]
E_{ce}	elastic modulus of concrete [35] [MN/m^2]
E_{cl}	soil modulus for clays [MN/m^2]
EI_0	bending stiffness of composite cross section at stage D_0 [MNm^2]
EI_1	bending stiffness of structure without creep effect [MNm^2]
EI_2	bending stiffness of structure with creep effect [MNm^2] [45]
EI_p	bending stiffness of pile cross section [MNm^2]
E_p	modulus of elasticity of pile [MN/m^2]

E_s	elastic modulus of structural steel [MN/m^2]
E_sI_s	bending stiffness of steel part of composite cross section [MNm^2]
E_y	elastic modulus of reinforcement [MN/m^2]
F	force [MN]
F_{brake}	longitudinal force exerted on the superstructure due to braking of loading vehicle [MN]
f_{ck}	characteristic compressive cylinder strength of concrete at 28 days [MN/m^2]
$f_{ck,cube}$	characteristic compressive cubic strength of concrete at 28 days [MN/m^2]
F_f	total failure loads of embankment behind end screens [MN]
F_{pt}	average post-tensioning force immediately after post-tensioning work [MN]
$F_{pt,h}$	longitudinal component of average post-tensioning force immediately after post-tensioning work [MN]
f_s	yield strength of structural steel [MN/m^2]
F_{top}	lateral force at top of pile [MN]
F_X	normal force on pile [MN]
G_{ce}	elastic shear modulus of concrete [MN/m^2]
H	height of end screen [m]
h_d	average structural height along superstructure [m]
h_j	height of post-tendon profile [m]
HP	H-shaped pile cross section, for example HP250x85 or HP310x125
I_0	moment of inertia of composite cross section if all parts are of structural steel [m^4]
I_p	moment of inertia for pile [m^4]
k	soil stiffness per unit length (Winkler type) [MN/m^2]
k_{50}	modulus of lateral subgrade reaction at stage when $0.5*q_f$ is reached [MN/m^2]
$k_{50,tot}$	total modulus of lateral subgrade reaction of piles at bridge end at stage when $0.5*q_f$ is reached [MN/m^2]
k_a	modulus of lateral subgrade reaction when modulus of subgrade reaction is linearly distributed along pile length [MN/m^2]
$k_{a,cyclic}$	cyclic modulus of lateral subgrade reaction when modulus of subgrade reaction is linearly distributed along pile length [MN/m^2]
$k_{a,staat}$	static modulus of lateral subgrade reaction when modulus of subgrade reaction is linearly distributed along pile length [MN/m^2]
k_b	modulus of lateral subgrade reaction when modulus of subgrade reaction is constant along pile length [MN/m^3]
k_{eq}	equivalent linearly distributed modulus of lateral subgrade reaction when modulus of lateral subgrade reaction is linearly distributed along pile length, see Figure 6.18a [MN/m^2]
k_f	secant modulus of lateral subgrade reaction at failure point [MN/m^2]
k_h	coefficient of modulus of lateral subgrade reaction [MN/m^3]
$k_{h,emb}$	coefficient of modulus of lateral subgrade reaction against end screen [MN/m^3]
$k_{h,L}$	coefficient of modulus of lateral subgrade reaction at location of earth pressure cell L [MN/m^3]

k_{h50}	coefficient of modulus of lateral subgrade reaction at stage when $0.5*q_f$ is reached [MN/m^3]
k_i	initial modulus of lateral subgrade reaction [MN/m^2]
K_p	passive earth pressure coefficient [-]
k_s	spring stiffness [MN/m]
k_{s50}	spring stiffness k_{s50} at stage when $0.5*q_f$ is reached is [MN/m]
k_{ss}	axial stiffness of bridge superstructure [MN/m]
L	thermal expansion length of bridge superstructure [m]
L_{exp}	total thermal expansion length of bridge superstructure [m]
L_{inf}	average length of influence zone at embankment [m]
L_k	length of middle span [m]
L_m	uniform span length [m]
L_{out}	length in outputting of results, see Figure 6.59 and Part 6.4.10.6 [m]
L_p	length of pile, see Figure 6.18 [m]
L_{pt}	length of post-tensioned span [m]
L_r	length of side span [m]
m	mass of loading vehicle [kg]
m_{50}	modulus number depending of soil type at stage when $0.5*q_f$ is reached [-]
M_{50}	odometer soil modulus [MN/m^2]
m_{cc}	multiplier for stiffness and strength of soil from normalised pile spacing [-]
$m_{cc,av}$	average multiplier for stiffness and the strength of soil from normalised pile spacing [-]
$m_{cc,mid}$	multiplier for stiffness and the strength of soil from normalised pile spacing at location of middle pile [-]
m_d	multiplier for bridge models' loads: temperature drop at curing time of concrete, shrinkage and creep in post-tensioned structures [-]
m_G	multiplier for soil stiffness and strength [-]
$m_{h,emb}$	modified constant of modulus of lateral subgrade reaction against end screen [MN/m^3]
m_{heq}	equivalent modified constant of lateral subgrade reaction in case modulus of lateral subgrade reaction k_h is linearly distributed along pile length, see Figure 6.18a [MN/m^3]
$M_{min,a}$	minimum bending moment of pile when modulus of lateral subgrade reaction is linearly distributed along pile length [MNm]
$M_{min,a}$	minimum bending moment of pile when modulus of lateral subgrade reaction is constant along pile length [MNm]
m_{nh}	modified constant of lateral subgrade reaction [MN/m^3]
M_R	resultant bending moment of cross section [MNm]
m_s	shape factor depending on shape of loaded area [-]
M_{top}	bending moment at top of pile [MNm]
$M_{top,a}$	bending moment at top of pile when modulus of lateral subgrade reaction is linearly distributed along pile length [MNm]
$M_{top,a,1}$	bending moment at top of pile when modulus of lateral subgrade reaction is linearly distributed along pile length with full soil stiffness and non-creep concrete (as in bridge FE model) and reduced pile top displacement [MNm]

$M_{top,a,2}$	bending moment at top of pile when modulus of lateral subgrade reaction is linearly distributed along pile length with reduced soil stiffness and concrete with creep and full pile top displacement [MNm]
$M_{top,b}$	bending moment at top of pile when modulus of lateral subgrade reaction is constant along pile length [MNm]
M_y	bending moment around local Y-axis [MNm]
$M_{y,end,tot}$	superstructure total bending moment at end of bridge, see Figure 6.58
$M_{y,intermed,tot}$	superstructure total bending moment at first intermediate support, see Figure 6.58.
$M_{y,mid,tot}$	superstructure total bending moment at span L_r, see Figure 6.58.
$M_{y,tot}$	superstructure total bending moment (main direction in superstructure) [MNm]
M_z	bending moment around local Z-axis (main direction in piles), see Figure 6.51 and 6.54 [MNm]
n_h	constant of modulus of lateral subgrade reaction [MN/m^3]
$n_{h,a}$	constant of modulus of lateral subgrade reaction when modulus of lateral subgrade reaction is linearly distributed along pile length [MN/m^3]
n_{h50}	constant of modulus of lateral subgrade reaction at stage when $0.5*q_f$ is reached [MN/m^3]
p	earth pressure [MN/m^2]
P	vertical loading [MN]
q	load per unit length [MN/m]
q_f	lateral soil failure resistance [MN/m]
q_r	lateral soil reaction at beginning of reloading [MN/m]
q_{ult}	lateral soil resistance, asymptote of hyperbolic behaviour [MN/m]
R	relation of traffic load earth pressure to rigid wall and integral bridge end screen [-]
r_{end}	rotation of end screen [rad]
R_f	scaling parameter [-]
s	length of pile above ground level, see Figure 6.18 [m]
s_U	undrained shear strength of cohesive soil [MN/m^2]
t	time of braking test and loading time in quasi-static analyses [s]
T1-T4	names of bridge abutments and intermediate supports [-]
T_a	relative stiffness factor when coefficient of lateral subgrade reaction is linearly distributed [-]
T_{amb}	ambient shade air temperature [°C]
$T_{e.max}$	maximum uniform bridge temperature component [°C]
$T_{e.min}$	minimum uniform bridge temperature component [°C]
T_{max}	maximum shade air temperature with a 0.02 annual probability of being exceeded (equivalent to a mean return period of 50 years) [°C]
T_{min}	minimum shade air temperature with a 0.02 annual probability of being exceeded (equivalent to a mean return period of 50 years) [°C]
$T_{u,0}$	initial uniform temperature of bridge superstructure [°C]
v	speed of loading vehicle [m/s]
w	balanced load [MN/m]

W_0	section modulus of composite cross section if all parts are of structural steel [m3]
W_s	elastic section modulus of structural steel [m3]
X	longitudinal co-ordinate at bridge centre, at bridge end 1 X = $-L_{exp}/2$ and at bridge end 2 X = $L_{exp}/2$ [m]
y	lateral displacement of pile [m]
y_{50}	lateral displacement of pile at stage when $0.5*q_f$ is reached [m]
$y_{50,end}$	lateral displacement of end screen at stage when $0.5*p_p$ is reached [m]
y_f	lateral displacement at failure point [m]
y_r	lateral displacement at beginning of reloading [m]
y_{top}	pile top lateral displacement [m]
$y_{top,all}$	pile top lateral displacement capacity [m]
z	depth from ground and/or road surface [m]
z_{ref}	reference depth, see Figure 6.18b [m]
Δ	displacement [m]
Δ_{bottom}	measured displacement change at bottom measuring point [m]
Δ_L	change in bridge length [m]
ΔT_E	non-linear part of the temperature difference component [°C]
ΔT_{eq}	equivalent modelled temperature drop [°C]
$\Delta T_{eq,cc}$	equivalent temperature drop from creep of concrete [°C]
$\Delta T_{eq,shr}$	equivalent temperature drop from shrinkage of concrete [°C]
ΔT_M	linear temperature difference component [°C]
ΔT_{mod}	modelled temperature drop in bridge models [°C]
ΔT_N	overall range of uniform bridge temperature component [°C]
Δ_{top}	measured displacement change at top measuring point [m]
ΔT_U	change of uniform temperature component [°C]
$\Delta T_{u,\ d12h}$	offset of uniform temperature in 12h stepped uniform temperature analyses [°C]
$\Delta T_{u,solar}$	offset of uniform temperature caused by solar radiation [°C]
$\Delta\varepsilon_{tot}$	increase in compressive strain of composite cross section [-]
$\Delta\sigma_c$	decrease in concrete stress [MN/m^2]
$\Delta\sigma_s$	increase in structural steel compression stress [MN/m^2]
α_{cT}	coefficient of thermal expansion for concrete structures [1/°C]
β	positive constant between small and large strain cycle amplitudes [-]
β_{50}	stress exponent depending on soil type at stage when $0.5*q_f$ is reached [-]
ε_0	initial strain on composite cross section from force F_X [-]
ε_a	amplitude of strain cycle, see Figure 2.23 [-]
ε_{an}	amplitude of negative strain cycle, see Figure 2.23 [-]
ε_{ap}	amplitude of positive strain cycle, see Figure 2.23 [-]
ε_c	strain on concrete [-]
$\varepsilon_{c,shr}$	shrinkage strain on concrete [-]
ε_{c0}	initial strain on concrete [-]
ε_{c1}	final strain at $t = \infty$ with stress σ_{c1} [-]
ε_{cc}	strain on concrete at time $t = \infty$ with constant stress σ_0 [-]
$\varepsilon_{s,b}$	strain on structural steel at bottom of composite cross section [-]
$\varepsilon_{s,t}$	strain on structural steel at top of composite cross section [-]

ε_y	yield strain of structural steel [-]
ϕ	creep coefficient of concrete at time t = ∞ with constant stress σ_c [-]
ϕ_{av}	average creep factor of pile and superstructure [-]
ϕ_{mod}	modified creep coefficient of concrete at time t = ∞ with stress σ_{c1}[-]
ϕ_s	soil internal friction angle [º]
γ'	effective unit weight of soil [MN/m^3]
γ_c	partial safety factor for structural concrete [-]
γ_s	partial safety factor for structural steel [-]
γ_y	partial safety factor for structural reinforcement [-]
λ_1	characteristic value when coefficient of lateral subgrade reaction is constant [1/m]
λ_2	characteristic value when coefficient of lateral subgrade reaction is linearly distributed [1/m]
ν	Poisson's ratio of soil [-]
ν_c	Poisson's ratio of concrete [-]
ρ	ageing coefficient of concrete [-]
ρ_c	density of concrete [t/m^3]
σ_0	reference stress, 0.1 used in this study [MN/m^2]
σ_c	compressive stress of concrete [MN/m^2]
σ_{c1}	final compressive stress of composite cross section at t = ∞ [MN/m^2]
σ_{pt}	Average post-tensioning stress immediately after post-tensioning work distributed across entire cross-sectional area $A_{c,ss}$ [MN/m^2]
$\sigma_{s,b}$	stress of structural steel at bottom of composite cross section [MN/m^2]
$\sigma_{s,t}$	stress of structural steel at top of composite cross section [MN/m^2]
σ_v	effective vertical stress [MN/m^3]
ξ_1	dimensionless variable in differential equation where coefficient of lateral subgrade reaction is constant [-]
ξ_2	dimensionless variable in differential equation where coefficient of lateral subgrade reaction is linearly distributed [-]
ξ_{50}	factor between y_{50} and y_f [-]
ψ	relaxation coefficient of concrete [-]
ζ	factor for correcting units [m]

Dimensioning stages of pile composite cross section, subscripts for pile diameter D are:

D_0 = capacity in SLS

D_{0c} = capacity in SLS with corrosion

D_1 = capacity in SLS with $\phi = 1$

D_{1c} = capacity in SLS with $\phi = 1$ and corrosion

D_{00} = capacity in SLS with $\phi = \infty$

D_{00c} = capacity in SLS with $\phi = \infty$ and corrosion

D_d = capacity in ULS

D_{dc} = capacity in ULS with corrosion

Capacities of composite pile cross sections:

$M_{0,max}$ = maximum moment capacity in stage D_0

$M_{0,max2}$ = maximum moment capacity in stage D_0 with simplified formulas

$M_{0,max3}$ = maximum moment capacity in stage D_0 with accurate analysis

$N_{0,opt}$ = normal force with $M_{0,max}$

$N_{0,opt2}$ = normal force with $M_{0,max}$ with simplified formulas

$M_{0,s}$ = moment capacity of structural steel in stage D_0

$M_{0,c}$ = moment capacity of concrete in stage D_0

$M_{1c,max}$ = maximum moment capacity in stage D_{1c}

$N_{1c,opt}$ = normal force with $M_{1c,max}$

Bridge and pile models:

SHR = model for bridge shrinkage (contraction) stage, see Figure 6.19

EXP = model for bridge expansion stage, see Figure 6.19

WS = soil properties 1, see Table 6.4

NS = soil properties 2, see Table 6.4

HS = soil properties 3, see Table 6.4

SS = subsoil properties, see Table 6.4

R = rigid pile top connection

F = hinged pile top connection

T1 = model for bridge without cantilever span, see Figure 6.19

T2 = model for bridge with cantilever span, see Figure 6.19

B1, B2, B3, B4 and B5 = main bridge types, see Figure 6.37, B4 and B5 are not analysed in this study

L1, L2 and L3 = total thermal expansion lengths, see Paragraph 6.4.2

S1 and S2 = side span ratio, see Figure 6.37 and Paragraph 6.4.2

These notations are used both together and separately, for example B1_L1_S1 or T2_SHR

Element types of finite element models, LUSAS (14.3-2 kit242) [93]:

BTS3 = thick non-linear beam element: “A straight beam element in 3D which includes shear deformations. The geometric properties are constant along the length. Three nodes with end release conditions. The third node is used to define the local xy plane.” [93]

JSH4 = joint element: “3D joint elements which connect two nodes by six springs in the local x, y and z directions. The 3rd and 4th nodes are used to define the local x-axis and local xy plane, respectively.” [93]

QTS4 = thick shell element: “The element formulation takes into account membrane, shear and flexural deformations.” Four nodes numbered anticlockwise. [93]

Global co-ordinates of bridge models:

X = longitudinal global co-ordinate of bridge models, see Figure 6.44, 6.44 and 6.51
Y = transverse global co-ordinate of bridge models, see Figure 6.44, 6.44 and 6.51
Z = vertical global co-ordinate of bridge models, see Figure 6.44, 6.44 and 6.51

Global/local axes of LUSAS:

X/x = marked on axle with double arrow, see Figure 6.44, 6.44 and 6.51
Y/y = marked on axle with one arrow, see Figure 6.44, 6.44 and 6.51
Z/z = marked with axle without an arrow, see Figure 6.44, 6.44 and 6.51

Abbreviations

A500HW	Steel grade of reinforcing bar
AASHTO	American Association of State Highway and Transportation Officials
ASCE	American Society of Civil Engineers
BF1	Behaviour type 1 of soil backfill in bridge analyses
BF1	Behaviour type 2 of soil backfill in bridge analyses
Bmo	Railway gravel carriage
DOT	Department of Transportation (state)
EBT	Effective bridge temperature
Ek1	Vertical specific traffic load pattern [42]
EN	European Standard
ENV	European Prestandard
EPC	Earth pressure cell
FEM	Finite Element Method
FHWA	Federal Highway Agency
Finnra	Finnish Road Administration (Finnish Transport Agency from 1.1.2010)
FMI	Finnish Meteorological Institute
FTA	Finnish Transport Agency
IABSE	International Association for Bridge and Structural Engineering
IAJB	Integral Abutment and Jointless Bridges
ISSI	Intelligence soil-structure interaction
LIN	Linear
Lk1	Vertical traffic load pattern [42]
LTM	Lift and travel type machine
NA	National Appendix of European Standard
NL	Non-linear
PC Beam	Post-tensioned beam-and-slab structure
RakMK	Finnish Building Code
RC Beam	Reinforced concrete beam-and-slab structure
RC Slab	Reinforced concrete slab structure
RHK	Finnish Rail Administration (Finnish Transport Agency from 1.1.2010)
S355J2H	Steel grade of structural steel
SFS	Finnish Standards Association
SLS	Serviceability limit state
SSI	Soil-structure interaction
Tka	Railway engine
TLEP	Traffic load earth pressure
TUT	Tampere University of Technology
ULS	Ultimate limit state
US	United States
UTC	Universal co-ordinated time

1 INTRODUCTION

1.1 Definition of an integral bridge

An integral abutment bridge is a bridge type where the superstructure is either partly or monolithically connected to the substructures and surrounding soil. For the purposes of this study, an integral bridge is defined as a bridge where the bridge end interacts with embankment soil. In [2] an integral bridge means a bridge without deck joints. A new aspect in the classification is that the integral bridge can have a joint. Conventional bridges act longitudinally against embankment soil too, but the significance of the soil-structure interaction is minor because the created cyclic forces are minor compared to those affecting integral bridges. The longitudinal rigidity of an integral bridge depends on the type of the structure. Figure 1.1 describes the proposed classification of bridges that move horizontally against embankment soil.

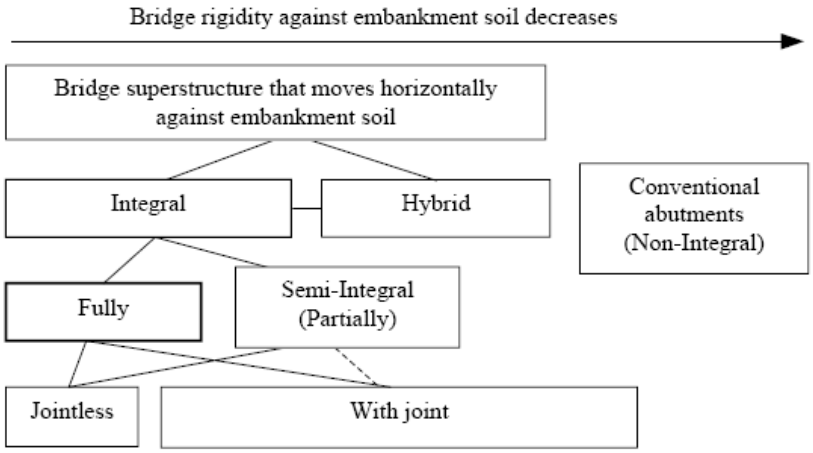

Figure 1.1. Proposed classification on the basis of abutment type of bridge moving horizontally against embankment soil. In this figure, a joint refers to a joint at the road surface.

Bridges can be classified in several ways. The proposed classification was developed based on the structural behaviour of the integral bridge. The structure types of Figure 1.1 are presented in Figure 1.2. Bearings and joints offset part of the longitudinal stiffness of the bridge superstructure compared to fully integral ones.

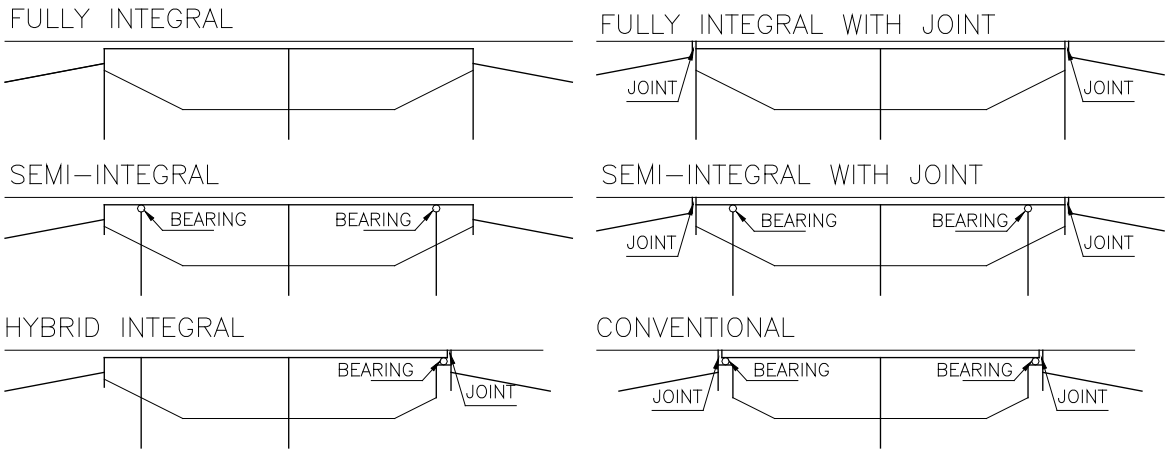

Figure 1.2. Bridge types of different longitudinal stiffness.

Integral bridge abutment configurations according to [137] are presented in Figure 1.2. This study focusses mainly on the stub-type abutment (f) of Figure 1.3 touching also on type (e). Types (a) to (c) are used mainly with shorter integral bridges in Finland and are not discussed here.

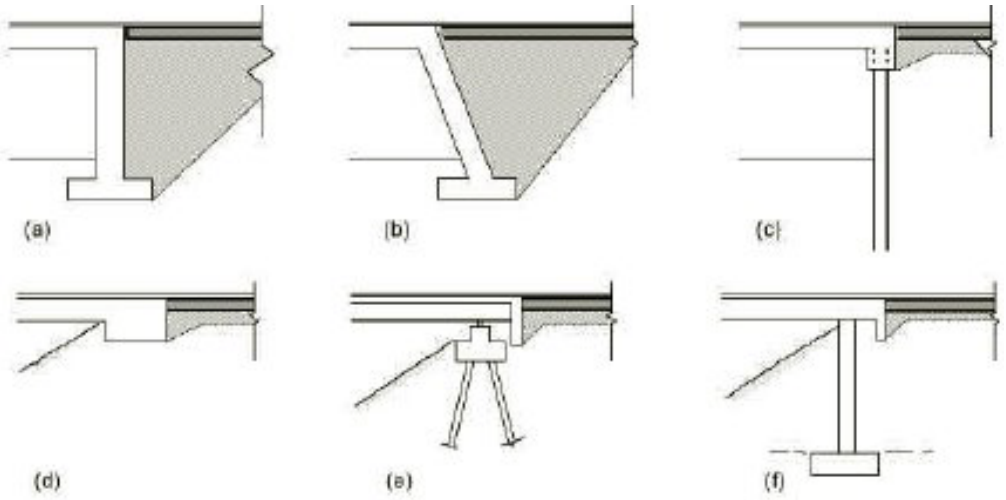

Figure 1.3. (a) & (b) frame abutments, (c) embedded abutment, (d) bank pad abutment, (e) & (f) end screen abutments. Integral bridge abutment types according to [137].

The reasonable and possible structural solution for an integral bridge depends strongly on:

- Climate
- Bridge length
- Requirements of road
- Bridge site

It is obvious that the structural solution is important when deciding maximum integral bridge length. Building practise also has its significance. The point is to pay attention to how long an integral bridge would be in Finnish conditions based on structural behaviour and which important phenomena are involved. The main terms used in this study concerning integral bridges are presented in Figure 1.4.

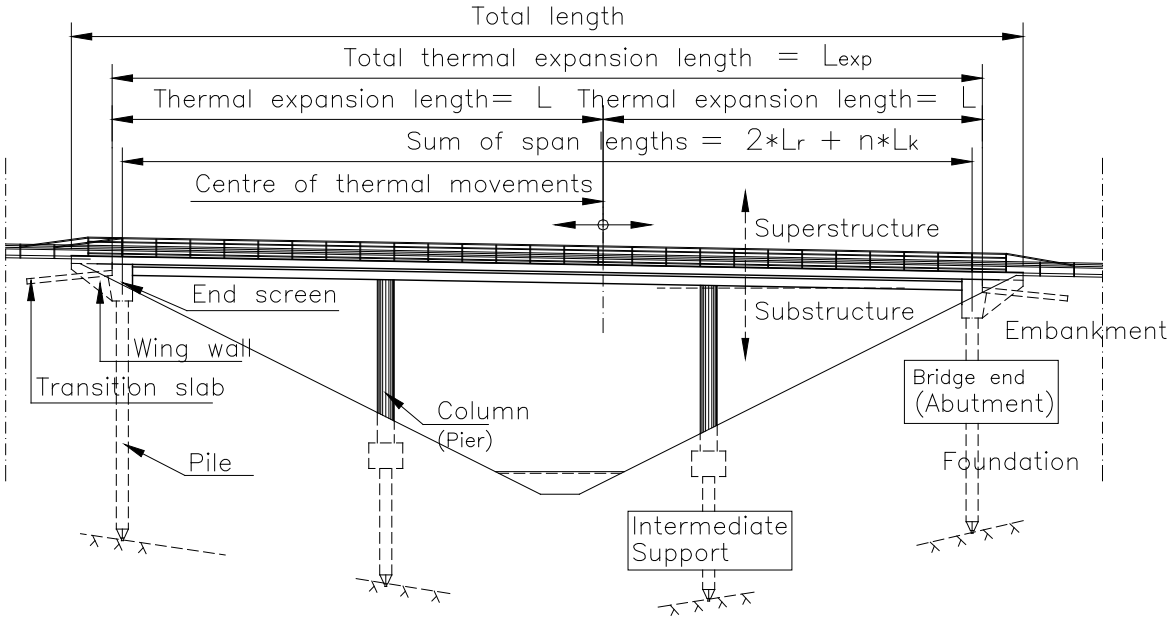

Figure 1.4. The main terms of this study, L_r and L_k, are presented in Paragraph 6.4.2.

Total thermal expansion length, L_{exp}, is the distance between the outer surfaces of end screens. Thermal expansion length, L, is the distance from the centre of thermal movements to the outer surface of an end screen. There are two different thermal expansion lengths if the centre of thermal movement is not at the centre of the bridge superstructure. The total length of the bridge is the distance between superstructure ends along the centre line of the bridge. In this study bridge abutments are called bridge ends.

1.2 Motivation

An integral bridge is an economical structure both as to building and maintenance costs [43].

The amount of construction materials needed is smaller than in the case of a conventional bridge. One main reason for that is that earth pressure forces act against each other through the superstructure from one abutment to another. Hence, the forces that cause abutment tilting are minor compared to a conventional bridge. Furthermore, part of the live load of an integral bridge is carried by the bending moments of abutment piles. A negative feature are the high interaction forces against the embankment soil. Mainly changes in bridge superstructure temperature also cause significant interaction forces against the bridge abutments.The presented negative effects verifiably supersede the benefits of the live load carrying effect.

Especially the maintenance costs of an integral bridge are smaller than those of a conventional bridge because the former usually have no expansions joints or bearings that are

costly to maintain during the bridge's life span. In other types of integral bridges maintenance costs depend on whether there are bearings or joints. The embankment soil may require more maintenance with integral than conventional bridges.

When building integral bridges, it is vital to know the important phenomena affecting them and what the allowable total thermal expansion length limitation may be.

1.3 Related research projects

The main subjects of an integral bridges research project are presented in Figure 1.4. The project covers both railway and road bridges. This study focusses on road bridges, but some results from railway bridge monitoring are also used. The project consists of many important studies and research methods, which are used in technical research. Extensive bridge monitoring projects form the core of this comprehensive research.

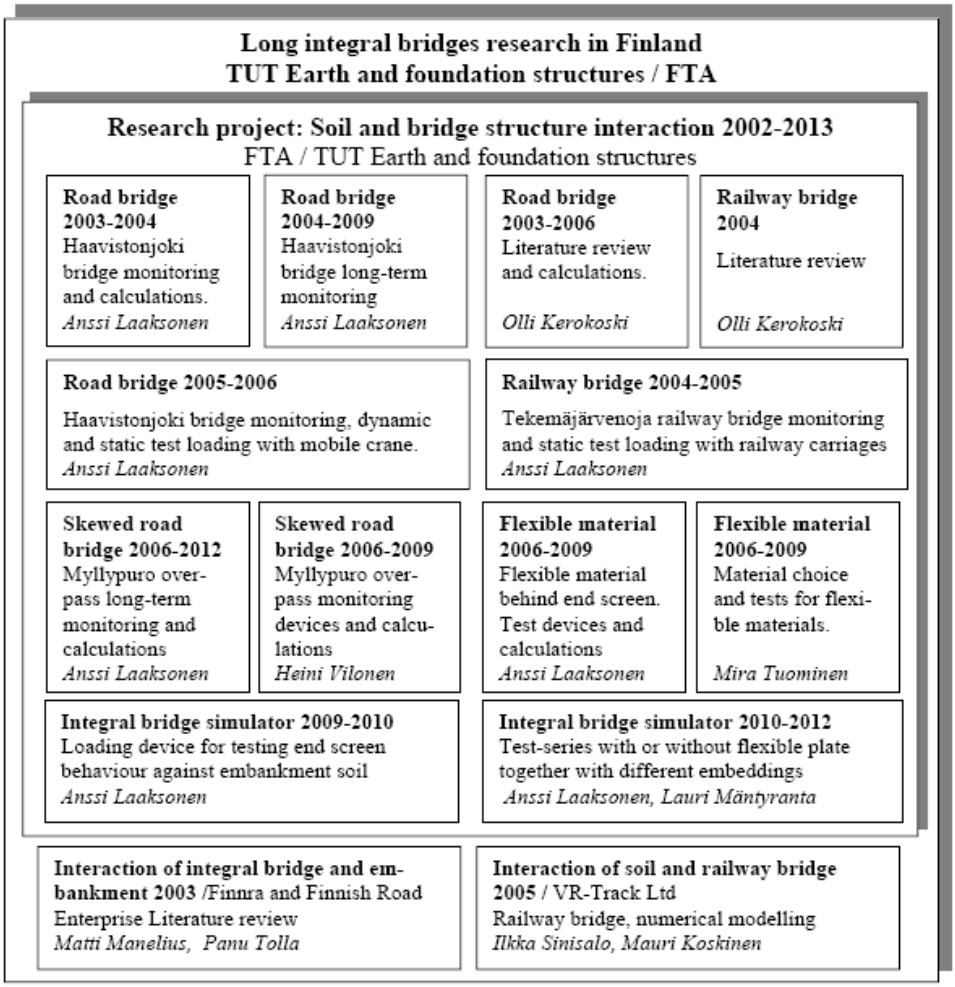

Figure 1.5. Main parts of the integral bridges research project.

Most of the work has been done at the Unit of Earth and Foundation Structures of Tampere University of Technology. A dissertation focussed on the geotechnical aspects of integral abutment bridges was completed in 2006 [75]. A railway bridge oriented dissertation was

completed before this research project in 1997 [80]. The Finnish Road Administration (Finnra) and Finnish Rail Administration (RHK) became part of the Finnish Transport Agency (FTA) on 1.1.2010.

1.4 Research process

The research process of the dissertation and its relationship to the development process are shown in Figure 1.6. As a process, this research is complex. It should be noted that the process of developing integral bridges by no means ends with this study. It is advantageous for the development process that it has included several simultaneous studies which has broadened the researchers' views in many respects.

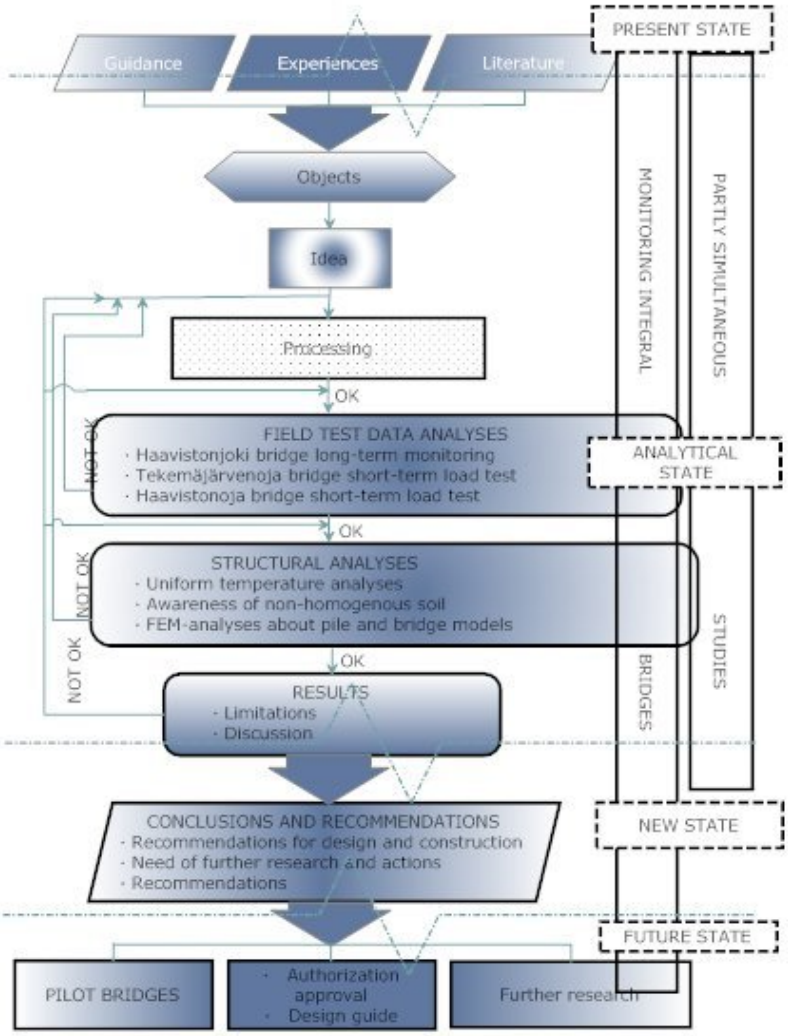

Figure 1.6. Research process and its relationship to the integral bridges development process.

The fact that this project involves only two long-term monitored integral bridges is a problem. It would have been better to have several monitored bridges. However, that was not possible because the monitoring of a problem of the studied type is quite expensive. Yet, different research methods together prove that the idea of this study is sound. This study is

based on constructional science where defining a goal is important in terms of the research method [70]. Then, one does not know the result at the beginning, but knows how to get it. This study involves three research methods: literature research, experimental research (field tests) and calculational analysis (structural analyses). The literature research consists of a short literature review. The main emphasis of this study is on field tests and structural analyses.

1.5 Scope of the study

This study focusses on the straight and straight-ended, cast-in-place concrete, fully integral road bridges. The studied bridge ends are also symmetrical, i.e. end screen height, H, and width, B, of both bridge ends are equal. The term fully integral is also explained in [6]. The results are to some extent applicable also to semi-integral bridges [83]. Skewed bridges are discussed in another part of the research project, see Figure 1.5. The superstructure is either a beam-and-slab or a slab structure. The surface of the superstructure is limited to a type 1 of appendix 4.1 in [48]. The limitation was made due to the surface's influence on the thermal behaviour of the superstructure [2, 1, 116, 109, 12].

Superstructure and end screen dimensions were not optimised in this study. The superstructure dimensions were chosen on the basis of experience to meet the requirements of Finnish guidelines [34, 41]. It was also important that the bridge could be built with typical Finnish construction methods. It was assumed that the bridge ends are founded on steel pipe piles, which behave much like beams of infinite length, i.e. the piles are long enough for infinite laterally loaded pile behaviour.

Thermomechanical analyses of the bridge superstructure were excluded from this study. The approach of the study is something like that of a bridge designer stressing the utilitarian aspects. The main focus of the study is on the structural side but geotechnical aspects are also of great importance in soil-structure interaction (SSI). One goal of the study is to prove that the used research process is suitable for the studied problem. Further limitations are presented later on in the appropriate context.

2 BACKGROUND OF THE STUDY

2.1 Present state

2.1.1 Overview

There are more than 20,000 bridges in Finland [71, 49, 40]. That is an approximate estimate since there are no exact statistics on all bridges. On 1.1.2010, the Finnish Transport Agency owned 14,625 road bridges, of which 11,512 were actual bridges and 3113 tubular bridges [49]. On 1.1.2010 there were 2297 railway bridges, of which 899 were overpasses (roughly 800 of the latter are included in the number of road bridges) [40]. There are also bridges along municipal, private, forest and railway maintenance roads. Approximately 2000 of the road bridges were integral ones [47]. The number includes slab and beam-and-slab bridges over 20 m in sum of span lengths. Bridges (a) and (b) of Figure 1.3 are not included because they are more suitable for shorter span lengths in Finnish circumstances as well as for shorter bridges. It should be noted that European bridges are generally rather long (type a) [137, 23]. There is a growing need to repair bridges and especially their expansion joints [44]. That makes it even more important to build easily maintainable and economical bridges [5, 105].

2.1.2 Finnra design guidelines

The present Finnish bridge design guidelines are maintained by Finnra [13]. Essential issues related to integral bridges design are dealt with in [48, 46]. Allowable thermal expansion length is limited to 35 m with road bridges and to 45 m with light traffic bridges. Accordingly, it is possible to build a 70 m total thermal expansion length symmetrical integral bridge. An embankment of the same rigidity can be modelled at both ends when a bridge interacts symmetrically in the structural model. A few longer pilot bridges have been constructed and their behaviour have been satisfactory [139, 47]. The maximum length of these bridges is 106 m [47]. Eurocodes were adopted as the only bridge design guidelines on 1.6.2010. This study follows the Finnra guidelines in force before 1.6.2010.

Earth pressure behind the end screen is assumed to develop linearly in [23]. An extra load from cyclic development of passive earth pressures is also included. That was done on the basis of the preliminary results of the current research project. The possible gap between the end screen and the embankment was mentioned in the guidelines [4] but it was elimi-

nated in connection with the updating of the guidelines because the significance of the load is taken into consideration as part of earth pressure development. An integral bridge has to withstand interaction forces due to the 30°C uniform superstructure temperature change [4].

In practice, structural design models are linear and perfectly plastic. That allows applying the principle of superposition. Accordingly, load combinations can be calculated directly based on each load case by post-processing. Afterwards it can be checked whether the yield point was exceeded and the structural model can be updated.

Stub-type integral bridges are often founded on steel pipe piles, which are commonly used in foundations of integral bridges. They provide foundations good bearing capacity and quite good flexibility [79, 69]. The piles are usually composite structures. The composite action is fairly firm [78]. The corrosion allowance of the guidelines is relatively conservative. Steel components cannot be used in structural dimensioning if a bridge falls within the two highest winter operation classes [48]. The guidelines are valid for ice-control salt coverage areas. The corrosion allowance was more moderate until 2002, and over dimensioning of piles in terms of corrosion was allowed [43]. It is highly probable that the corrosion rate based on winter operation classes [88, 134] is still lower than in the guidelines valid until 2002. The corrosion rate of this study is based on the guidelines valid until 2002 [43] because the rather conservative approach of the new guidelines may distort the results, and this study concentrates on the serviceability limit state, not on the ultimate limit state where strains exceed the yield point.

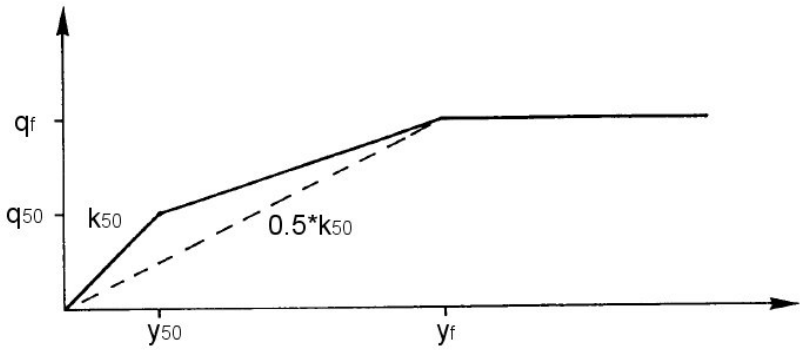

Figure 2.1. Lateral subgrade reaction of pile in cohesionless soil. Notations as in Paragraphs 2.2.4 and 6.3.4 [43, 79].

Guidelines for the steel pipe piles are given in [43]. The development of lateral resistance as a function of lateral displacement in cohesionless soil is presented in Figure 2.1. Stiff-

ness increases as depth increasing. The bi-linear form of lateral pile behaviour was developed during studies [80] and [79].

2.1.3 Standard SFS-EN 1990

It has been possible to apply standard SFS-EN 1990 (Eurocodes) in house building in Finland from 1.11.2007. In bridge construction, Eurocodes were adopted only as design standard on 1.6.2010. Several structural analyses for comparing the old guidelines and the Eurocodes were made before 1.6.2010.

The essential Eurocodes from the viewpoint of this study are Basis of structural design SFS-EN 1990 [115], Action on structures SFS-EN 1991 [2, 117], Design of concrete structures SFS-EN 1992 [119, 118], Design of composite steel and concrete structures SFS-EN 1994 [120] and Geotechnical design SFS-EN 1997 [121].

Complete guidelines for integral bridges are not given in Eurocodes. Allowable length limits for integral road bridges are not mentioned. The allowable thermal expansion length of railway bridges based on simplified calculations is 40 m [117]. If the bridge is symmetrical, this result in an allowable length of close to 80 m. The allowable thermal length would be 90*2 = 180 m for concrete and composite bridges based on more accurate calculations if the intermediate support is rigid [135]. It should be noted that the limiting criterion of allowable length is different due to the different circumstances of railroad bridges compared to road bridges.

A short description of soil-structure interaction is given in Annex G [118] of SFS-EN 1992-1-1. Sections 2.6 and 5.1.2 of the concrete design guidelines further state: “Where ground-structure interaction has a significant influence on the function of the structure, the properties of the soil and the effects of the interaction shall be taken into account in accordance with EN 1997-1”. According to SFS-EN 1997-1 [121]: “An analysis of the interaction between structure, pile foundation and ground can be necessary to prove that the limit state requirements are met”. Full passive earth pressure behind a moving wall is a function of the angle of friction and the shear resistance between ground and wall.

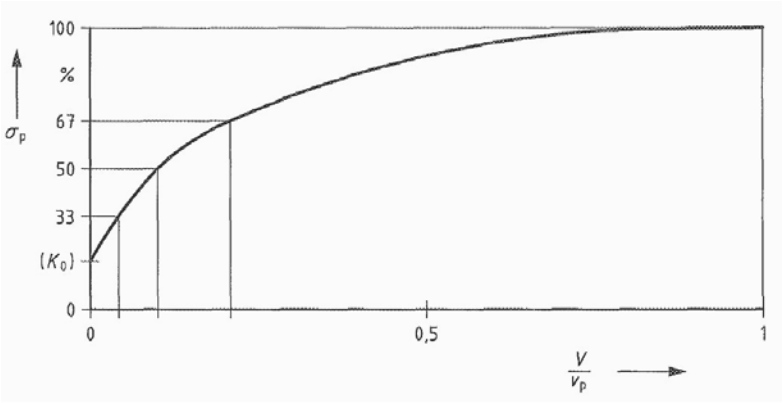

Figure 2.2. "Development of passive earth pressure of non-cohesive soils versus normalised wall displacement v/v_p"[121].

Figure 2.2 [121] presents the general passive earth pressure development as a function of wall displacement according to SFS-EN 1997. Wall displacements are indicated as percentages of wall height at points where passive earth pressure is 50% or 100% of full passive earth pressure. An uplifting component of passive earth pressure is also presented in SFS-EN 1997 [121]. The uplifting component of passive earth pressure occurs as a result of a failure mechanism of the passive state. However, it is not mentioned how this phenomenon changes in a cyclic loading case.

The pile design guidelines of SFS-EN 1997 are quite limited compared to present Finnish guidelines such as the Geotechnical design requirements for bridges [46], Supplementary bridge design instructions [48] and Steel pipe piles [43]. There are plenty of verbal instructions in SFS-EN 1997 but no exact design guidelines with formulas for the calculation of laterally loaded piles. The following phenomena must be taken into account according to SFS-EN 1997 [50]:

- Non linear soil
- Flexural stiffness of the piles
- Fixity conditions (connections)
- Group effect
- Load reversals and cyclic loading

According to SFS-EN 1991-1-5 [116] the superstructure temperature components are:

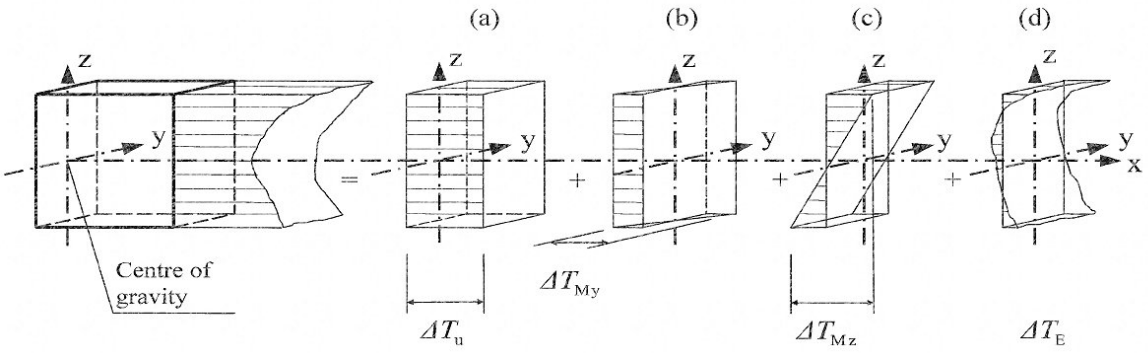

Figure 2.3. Superstructure temperature components [116].

Here, the temperature field is divided in four parts. The most significant part in terms of this study is uniform temperature change, component ΔT_U. The non-linear temperature component, ΔT_E, causes part of the uniform temperature change. Hence, the components cannot be calculated directly by means of superposition but the combination factors given in [116] have to be used. The range of the superstructure uniform temperature is presented in Figure 2.4.

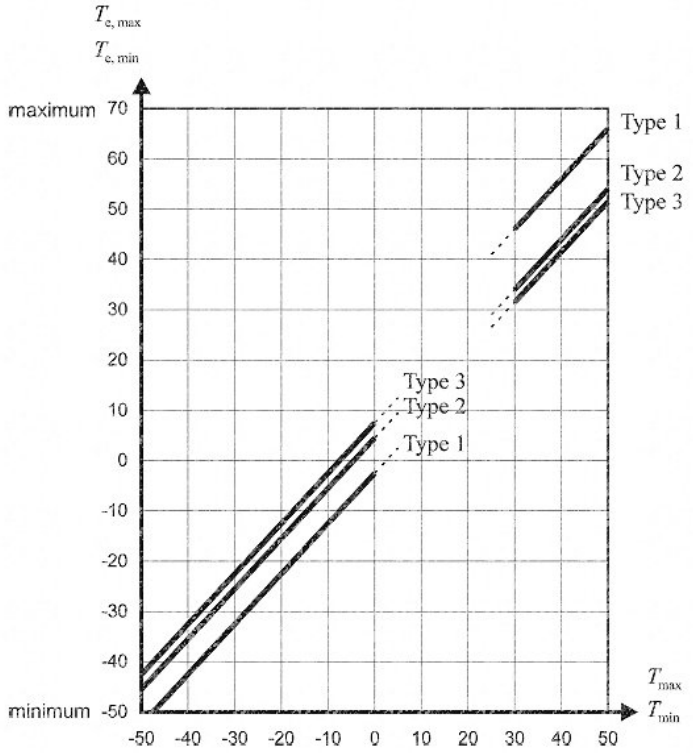

Figure 2.4. Superstructure uniform temperature range $T_{e,min}$ and $T_{e,max}$ [ºC] [116].

The presented superstructure uniform temperature component, T_e, depends on structure type and maximum T_{max} or minimum T_{min} shade air temperature of fractiles 0.98 and 0.02 of prevailing climate. The temperature components T_M and T_E of this study are presented in Appendix 1. The maximum and minimum shade air temperatures in Finland are given in the National Annex to SFS-EN 1991-5 [102].

2.1.4 United States practice

The United States has rather many design and construction practices in terms of integral bridges [32, 100]. Design is based on AASHTO LRFD Bridge Design Specifications [2]. Normally the allowable length of an integral bridge is from 100 m to 180 m depending on valid state guidelines. The total lengths and allowable displacements of abutments are being discussed in the United States, and it is expected that the allowable displacement limit for an abutment will be 0.05 m [140]. The suggested limit would lead to relatively long integral bridges. Figure 2.5 presents a stub-type abutment according to [2].

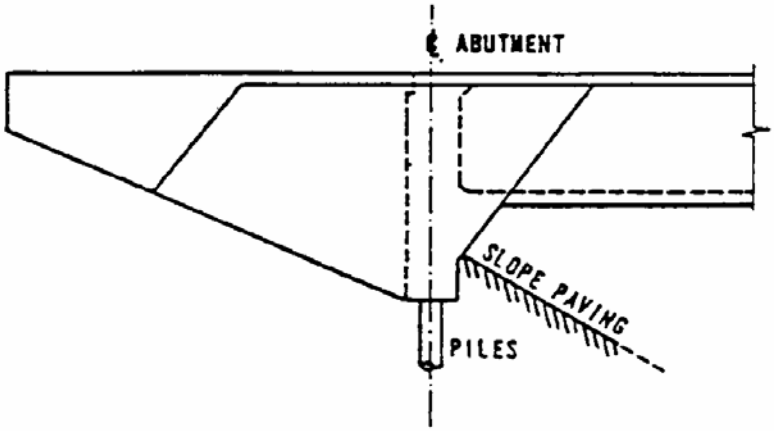

Figure 2.5. Stub-type abutment [2].

HP piles are commonly used to support abutments in the US today, and research there very often focusses on the behaviour of HP piles [110]. Piles are oriented either for weak or strong axis along abutment centreline or in the direction of movement. The piles in Figure 2.6 are oriented for the weak axis.

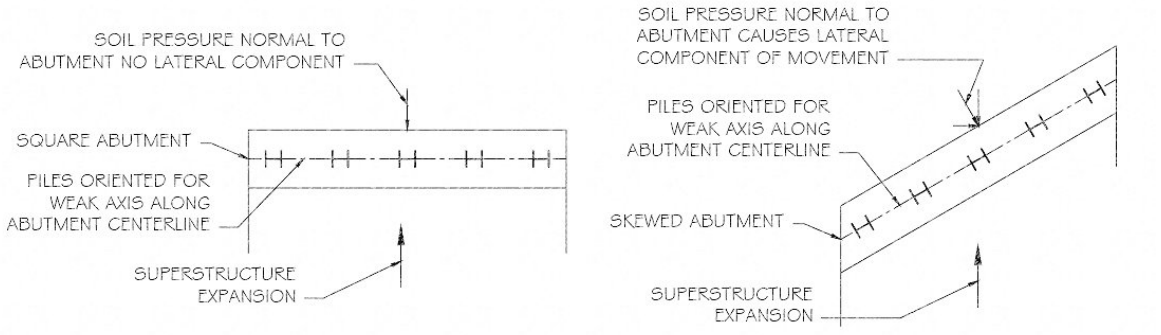

Figure 2.6. HP pile orientations in US Practice [106].

Displacement of 1% of end screen height is required to reach full passive earth pressure behind end screen in dense sand [2]. A simplified design method is given for laterally loaded piles.

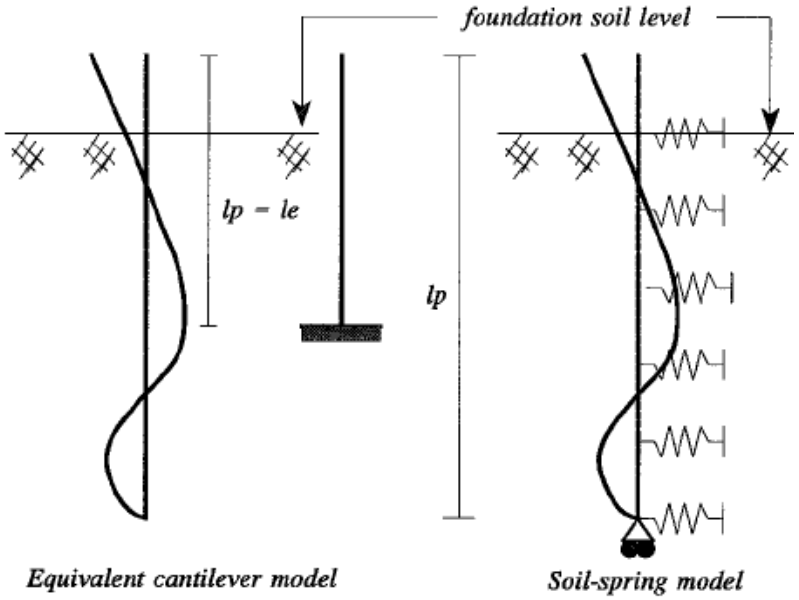

Figure 2.7. Equivalent cantilever model [28, 21].

An equivalent cantilever model is presented in Figure 2.7. The pile is assumed to have a rigid connection at a certain depth. The equivalent length depends on soil and pile properties:

For clays:

$$l_e = 1.4 * \sqrt[4]{\frac{E_p I_p}{E_{cl}}} \qquad [2] \ (2.1)$$

For sands:

$$l_e = 1.8 * \sqrt[5]{\frac{E_p I_p}{n_h}} \qquad [2] \ (2.2)$$

where:
E_p = modulus of elasticity of pile [MN/m^2]
I_p = moment of inertia of pile cross section [m^4]
E_{cl} = soil modulus for clays [MN/m^2]
n_h = constant of lateral subgrade reaction [MN/m^3]

The roots are the stiffness factors of a pile in spring-supported media, compare Formula 2.2 to Formula 2.22 [95, 99, 62, 21]. This phenomenon is discussed more in Paragraph 2.2.4 and Chapter 6. The soil-spring model fundamentals are also presented. The temperature components of the superstructure are relatively similar to EN 1991-1-5 [2]. There are also supplementary design guidelines [1] for basic temperature calculations. The US state of Maine gives allowable pile load as a function of bridge length as presented in Figure 2.8.

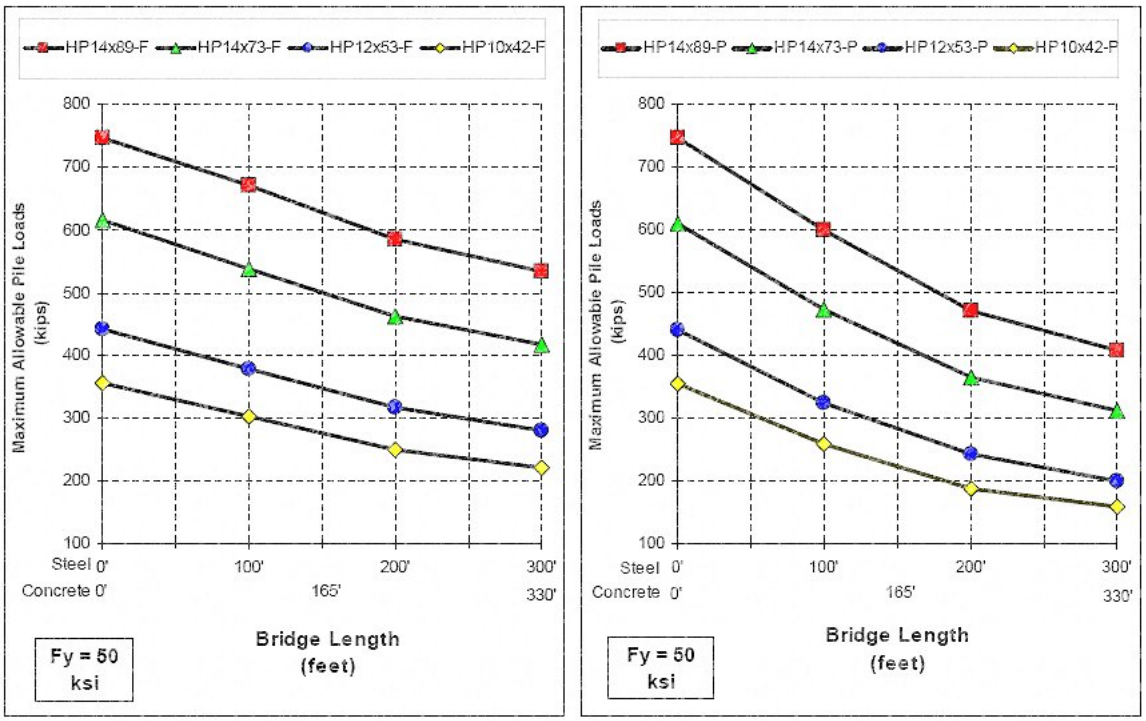

Figure 2.8. The allowable pile load for a fixed (on left) and a pinned (on right) head in dense sand when bending is about the weak axis. The steel grade yield stress is 50ksi = 345MPa. [94].

The allowable load on the pile decreases as bridge length increases. Allowable pile load is smaller when head rotation fixity is released. Stresses on piles are higher in a fixed type connection at the same pile top displacement level, which is opposite behaviour compared to Figure 2.8, see Formulas 6.54-6.57. The main reasons for it are that the stability of a rigidly connected pile is not as sensitive as that of a hinged connection, and that the hinge is located at the top of an end screen (see Figure 2.43 left) when passive earth pressure behind the end screen induces significant moments on the piles [66]. The allowable total thermal expansion lengths in the northern regions of the US are presented in Table 2.1.The length limits in the US state of Tennessee where the longest integral abutment bridge is located are also presented. The lengths were obtained from DOT's guidelines and the bridge is assumed to be made of concrete elements. Construction temperature is assumed to be 10˚C and shrinkage and creep after construction 0.25 ‰ and half of the creep to be included in D_X values. Displacement values are analysed by Formula 6.3. The coefficient of thermal expansion in the analysis is 10*10-5 [1/C]. It is further assumed that the centre of thermal movements is located at the middle of the bridge length.

Table 2.1. The allowable thermal expansion lengths of concrete integral abutment bridges in some northern US states.

Reference	State DOT	AASHTO [1, 2]						
State	Max L_{exp} [m]	T_{max} [ºC]	T_{min} [ºC]	ΔT_U+ [ºC]	ΔT_U- [ºC]	D_{Xshr} [m] (2	D_{X+} [m] (2	D_{X-} [m] (2
Maine	101	36	-29	26	39	-0.013	0.032	-0.007
Massachusetts	183	38	-18	28	28	-0.023	0.048	-0.014
Michigan	120	41	-23	31	33	-0.015	0.035	-0.011
Minnesota	91	45	-34	35	44	-0.011	0.032	-0.010
New York	183	39	-18	29	28	-0.023	0.048	-0.015
Iowa	175	43	-23	33	33	-0.022	0.051	-0.018
Tennessee	244	43	-12	33	22	-0.031	0.057	-0.025
Tennessee(1	358	43	-12	33	22	-0.045	0.084	-0.037

1) World's longest integral abutment bridge, longer than allowed by guidelines
2) See Figure 6.59 for sign

There is a difference between allowable length and abutment displacement. Displacement is affected by climate and shrinkage and creep. The effects of shrinkage and creep are significant. Displacements of bridge ends in Tennessee with a total thermal expansion length L_{exp} = 244 m are 19% higher than in Massachusetts with a maximum value L_{exp} = 183 m (although total thermal expansion length in Tennessee is 33% higher).

2.2 Earlier research

2.2.1 Overview

A short literature review is presented here. Some further references to literature will also be made in the following chapters in appropriate contexts.

Interest toward integral bridge monitoring and design models has increased in recent years as more attention has been paid to the overall costs of bridge maintenance.

2.2.2 Temperature components

Temperature changes in superstructures cause cyclic displacements of abutments. Temperature changes, again, are caused by environmental factors. The environmental factors that affect bridge temperature are presented in Figure 2.9.

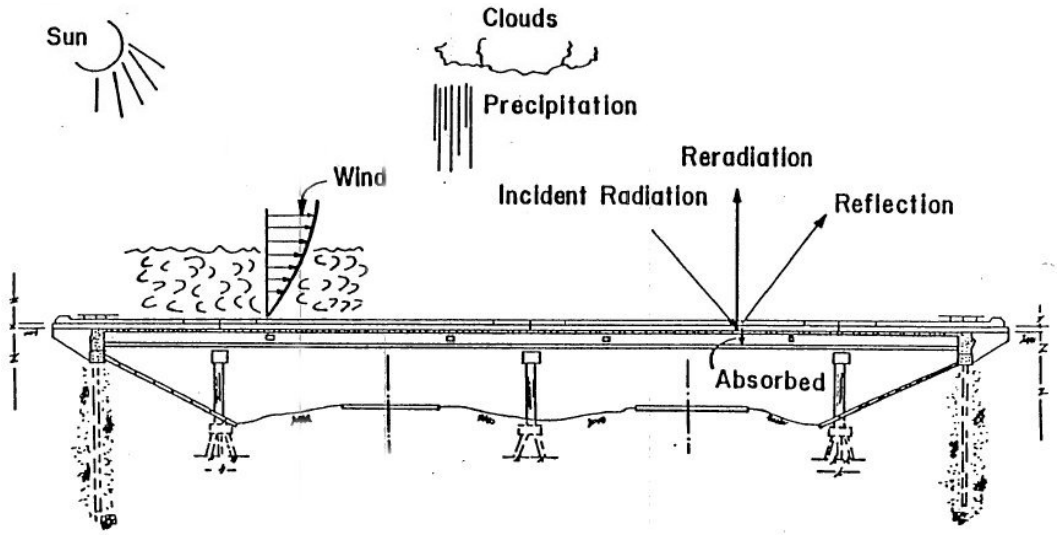

Figure 2.9. Environmental factors that affect bridge temperature according to [68].

The temperature range of composite bridges is wider than that of concrete bridges. The reason behind that are the different material properties and cross sections of concrete and composite bridges. Steel's thermal conductivity is about 30 times higher and specific heat capacity half of concrete's. And the cross section area of the superstructure of a composite bridge is smaller than that of a concrete bridge.

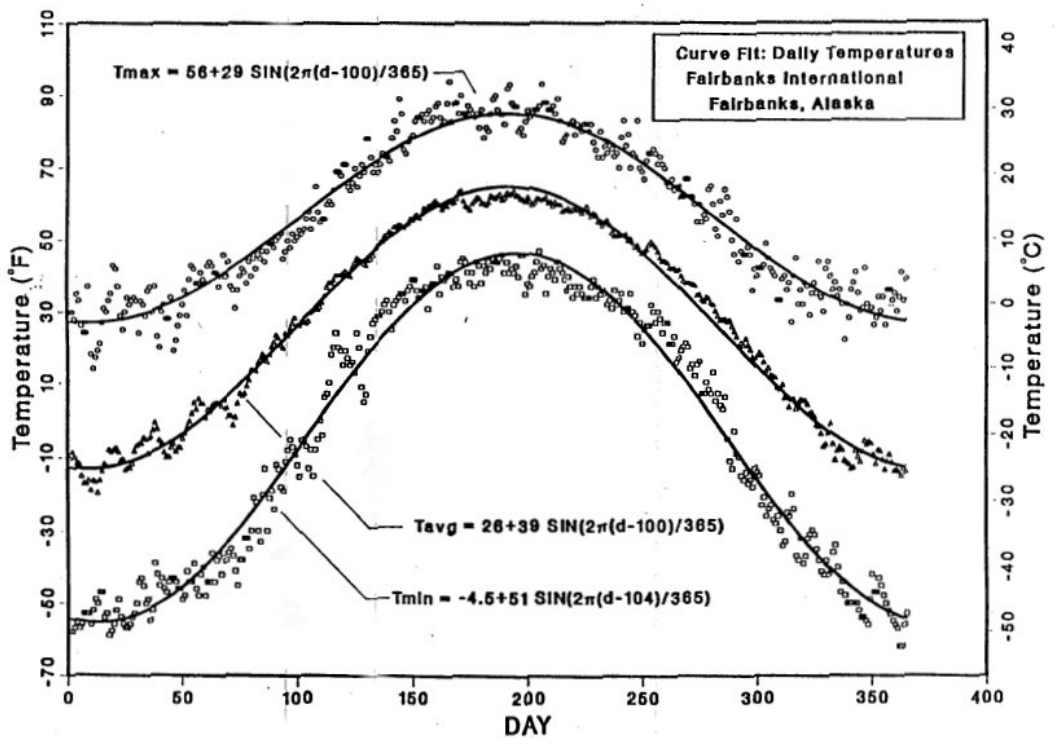

Figure 2.10. Daily ambient air temperature in Fairbanks, Alaska, USA [68].

The lower and upper fractiles of ambient air temperature in Fairbanks, Alaska, USA are presented in Figure 2.10 over the 25-year period 1952-1976 [68, 67]. In this study ambient air temperature refers to air temperatures measured in the shade. The best curve fit with the trigonometric function is also presented. Fractiles in the referred document were chosen for

a 10-year recurrence interval to illustrate a technique for defining temperature gradients of structures. The seasonal and diurnal fluctuation can be seen from both Figure 2.10 and Figure 2.11. Weekly fluctuation in bridge superstructure temperatures would be a more suitable term than daily or diurnal fluctuation because significant uniform temperature changes take a few days to develop due to the quite big specific heat capacity of a bridge superstructure.

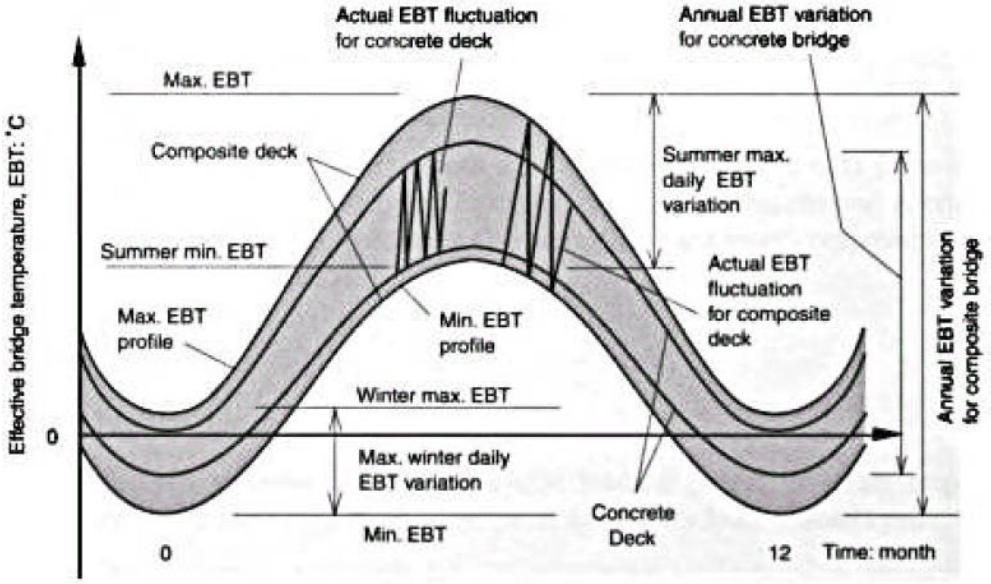

Figure 2.11. Effective bridge temperature (EBT) as a function of time. Seasonal and diurnal variations for bridge superstructure are shown [31]. In this dissertation EBT is the uniform temperature, T_U.

The extreme values of the uniform temperature component of the superstructure are represented by certain fractiles which have a specific recurrence time according to present guidelines. According to [103], the uniform temperatures for concrete superstructures are:

$$T_{e,\min} = 1.0 * T_{\min} + 5°C \qquad \text{[103] (2.3)}$$

$$T_{e,\max} = 0.97 * T_{\max} - \frac{5}{3}°C + \Delta T_{u,solar} \qquad \text{[103] (2.4)}$$

$$\Delta T_{solar} = 0.26 * T_1 \qquad \text{[103] (2.5)}$$

$T_{e.max}$ = maximum uniform bridge temperature component [°C]
$T_{e.min}$ = minimum uniform bridge temperature component [°C]
$\Delta T_{u,\,solar}$ = uniform temperature change from direct solar radiation [ºC]
T_1 = solar increment temperature at top of structure [2, 1] [ºC]

T_{min} and T_{max} in the referred document are based on the 0.05 and 0.95 fractiles departing from the EN1990 referred to earlier. The additional part of the uniform temperature calculation, solar increment $\Delta T_{u,solar}$, is the result of direct solar radiation [103].

2.2.3 Long-term monitored integral bridges

The following long-term monitored bridge is located in Central Pennsylvania in the USA [107, 33]. It is a prestressed concrete girder bridge. The total thermal expansion length of the bridge is 53.5 m. The long-term monitoring earth pressure results [107] are presented in Figure 2.12. The shown earth pressure cells are at a depth of 3 m.

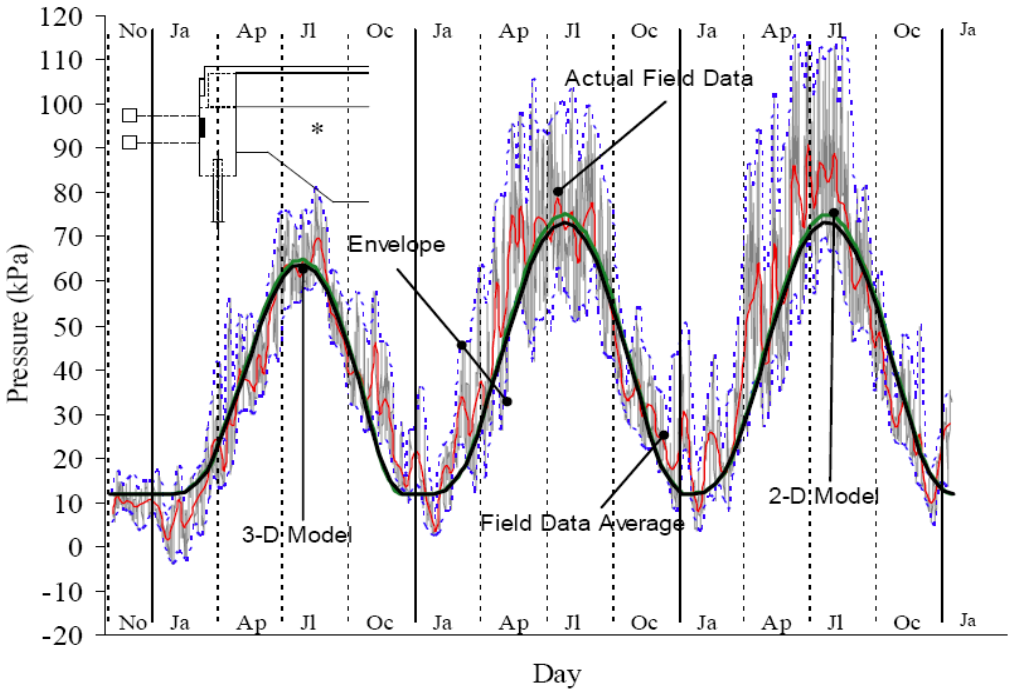

Figure 2.12. Earth pressure behind end screen. Bridge No.203 [107].

The effect of the seasons is also displayed. In summer the bridge expands to its maximum length. Then, the displacement stage of the end screen exerts high passive earth pressures on the embankment. In winter, earth pressure is lower because the displacement stage is smaller. The weekly and diurnal behaviour of earth pressure is also shown.

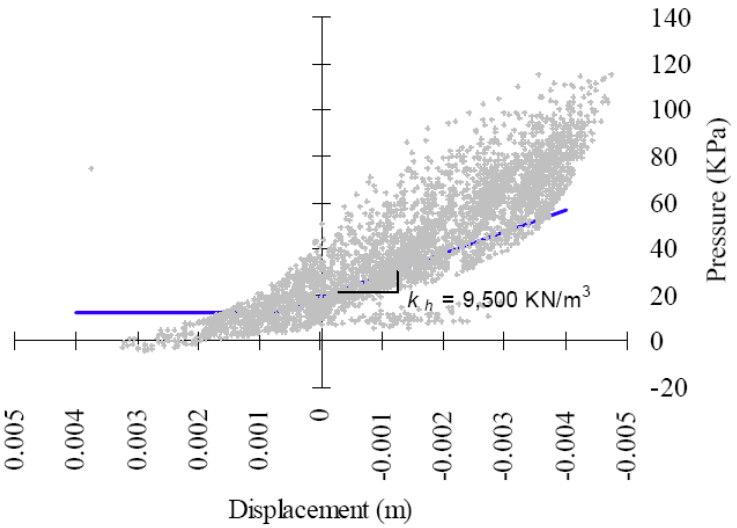

Figure 2.13. Earth pressure behind end screen as function of end screen displacement. Bridge No.203 [107].

Earth pressure behind end screen as function of end screen displacement is presented in Figure 2.13. The value is greatly influenced by hysteresis phenomena. The outside temperature varied during the presented monitoring season from -22 to +32˚C. The temperature range resembles that of southern Finland. The Orange-Wendell (OW) Bridge in the US state of Massachusetts was monitored from 2002 on [13]. The composite bridge's total thermal expansion length is 83.7 m.

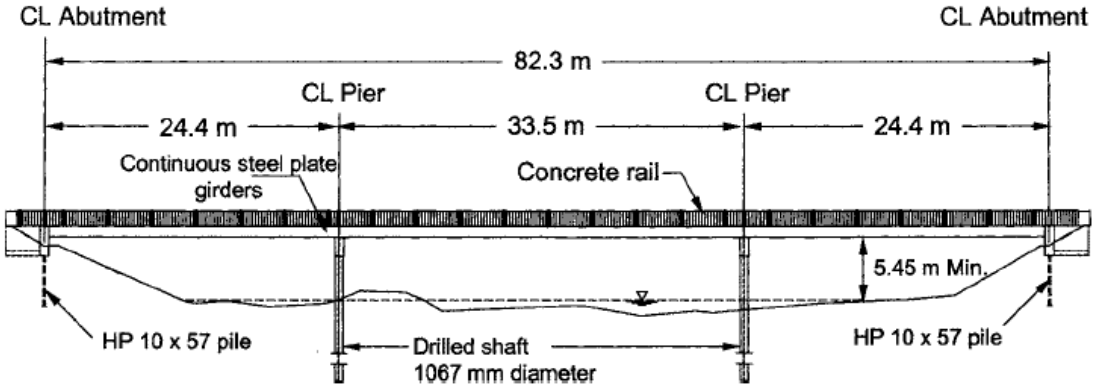

Figure 2.14. Massachusetts OW Bridge elevation [13].

The bridge was monitored with 85 gauges. The displacements of abutments are presented in Figure 2.15. They are not symmetrical to the bridge centre. Abutment displacements also differed during the monitoring period. Thus, it can be concluded that the centre of thermal movements shifts along the bridge length.

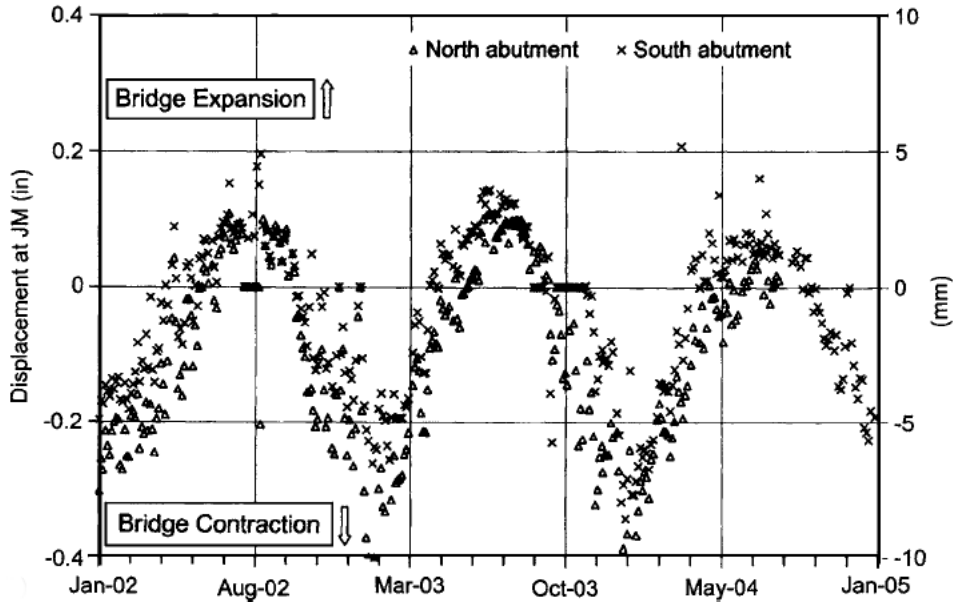

Figure 2.15. Displacements of Massachusetts OW Bridge [13].

An instrumentation drawing-in section of the long-term monitored Scotch Road Bridge is shown in Figure 2.16. The total thermal expansion length of the composite girder bridge is 90.9 m [76]. It is located in Trenton, New Jersey, USA.

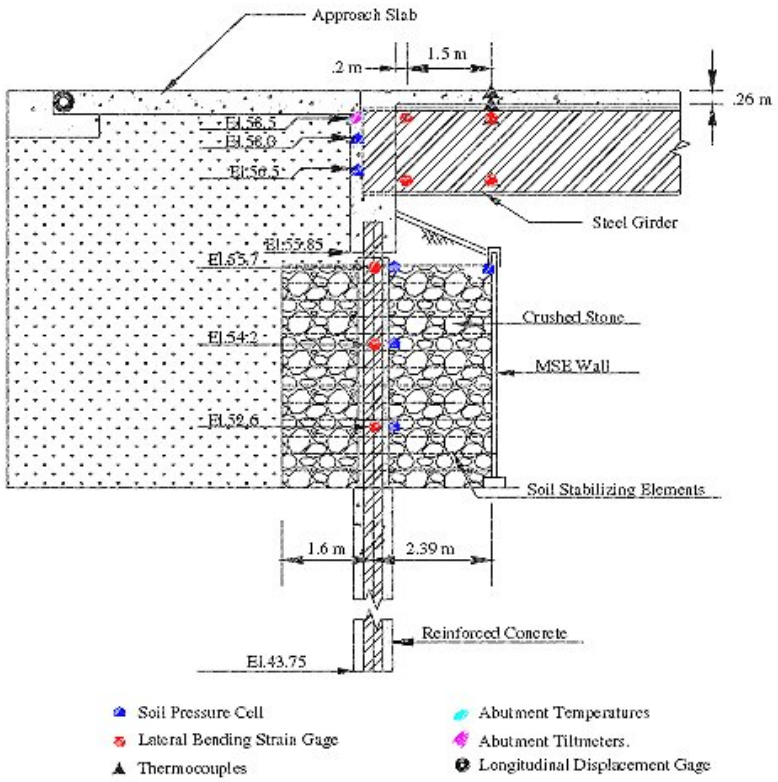

Figure 2.16. An instrumentation drawing-in section of Scotch Road Bridge [76].

Soil pressure behind the abutment developed as function of displacement of abutment, see Figure 2.17. In summer when the bridge is at its maximum length, earth pressure is rather high. Yet, the highest earth pressure was measured in winter. This is due to the freezing of the embankment which allows a small displacement to cause high earth pressure [58].

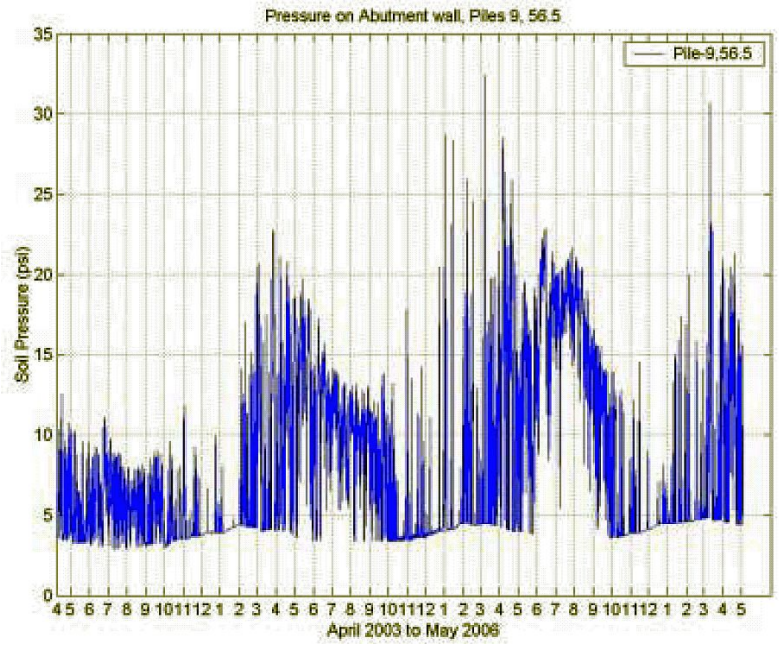

Figure 2.17. Earth pressure behind abutment in Scotch Road Bridge [58].

The supporting piles have bent considerably. The average measured and analysed bending moments of the supporting piles in June-July are presented in Figure 2.18.

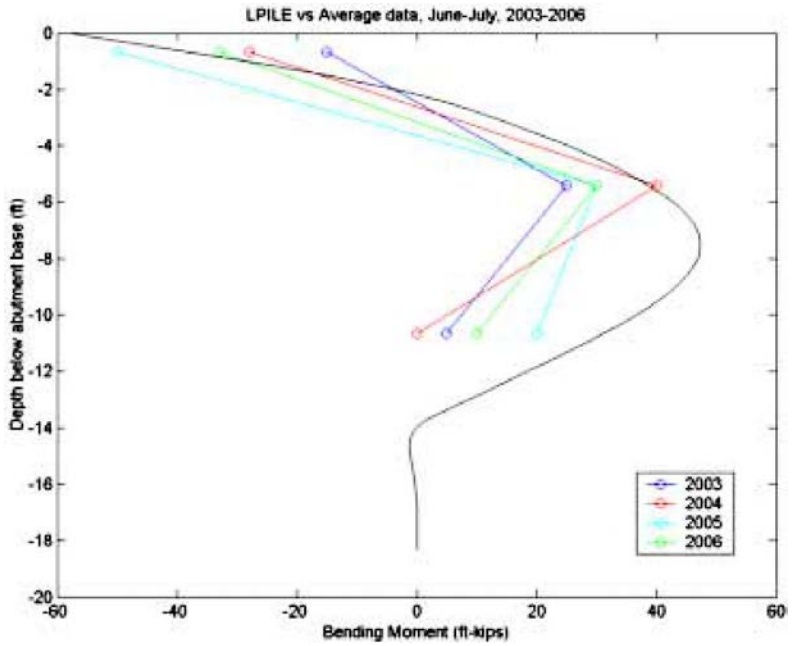

Figure 2.18. Average bending moments of supporting piles of Scotch Road Bridge in June-July. The values were calculated by the LPILE program. [59].

The bending moments are distributed along the pile length. The biggest bending moments were measured at pile tops. However, abutment rotations shifted the biggest moments to lower sections of piles [59]. Ambient air temperature varied during the monitoring period from -16 to +35°C. An elevation of the #55555 Bridge in Rochester, Minnesota, USA is shown in Figure 2.19 [66].

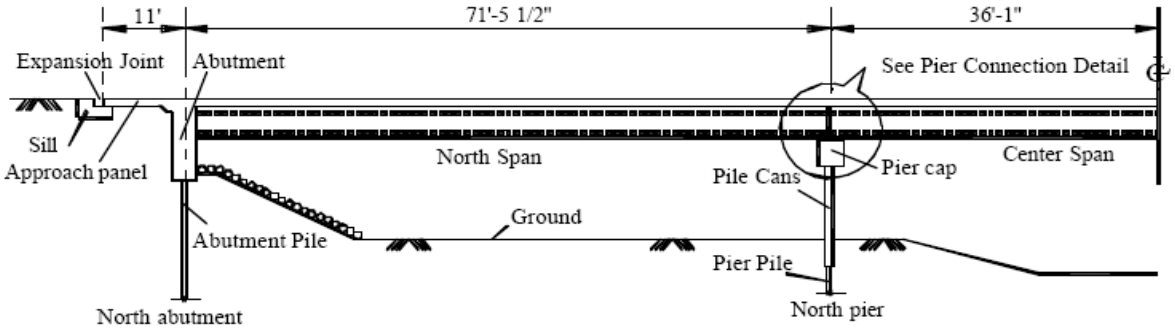

Figure 2.19. #55555 Bridge elevation [66] p. 87.

The prestressed concrete girder bridge has a total expansion length of 66.9 m. It is made of prestressed concrete girder elements and a cast-in-place concrete deck. In the referred report, the monitoring period is rather long, eight years. [66]

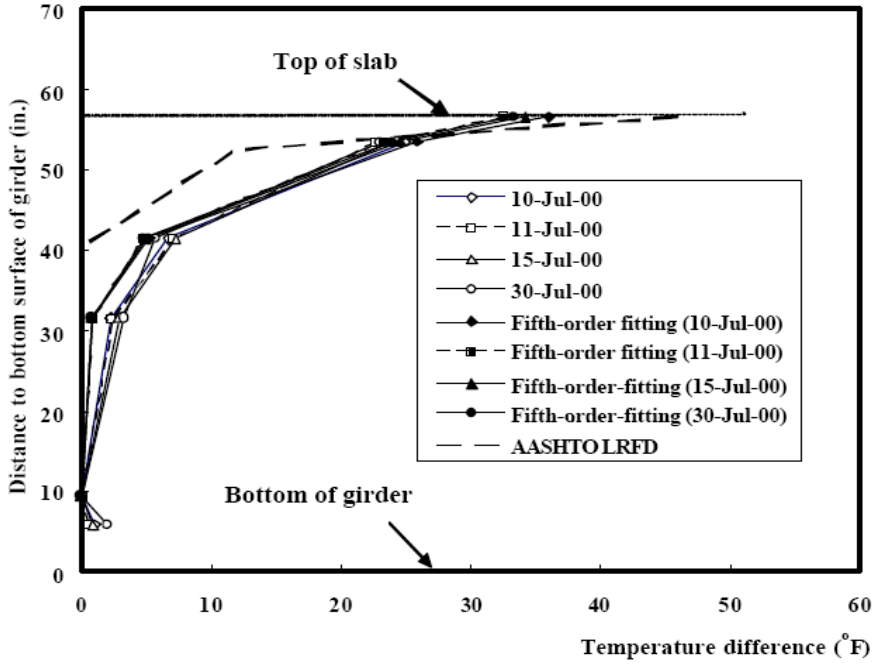

Figure 2.20. Maximum positive temperature difference components [66] p. 205.

The maximum temperature difference components for #55555 Bridge at various dates are presented in Figure 2.20. They differ from local AASHTO guidelines. Temperature difference components are affected by superstructure girder and slab dimensions [66]. Supporting pile curvature is presented as function of time in Figure 2.21.

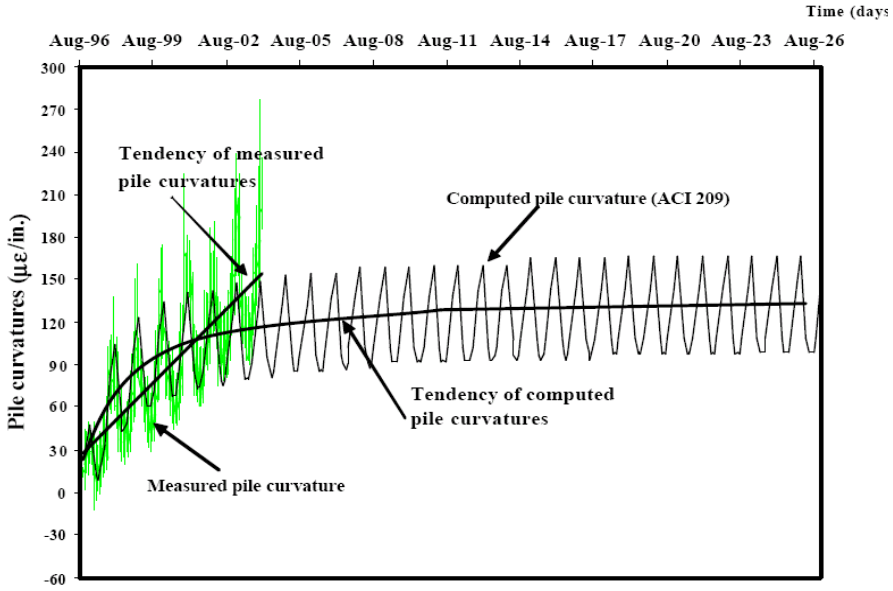

Figure 2.21. Tendencies of computed and measured pile curvatures [66].

Pile curvature remains positive almost constantly since construction, see Figure 6.59 for sign. Shrinkage and creep of the prestressed concrete superstructure exert heavy strains on the supporting piles. Further, the earth pressure behind the end screen may have caused rotation of the abutment and increased positive pile curvatures. Hysteretic behaviour of soil was also assumed. [66]

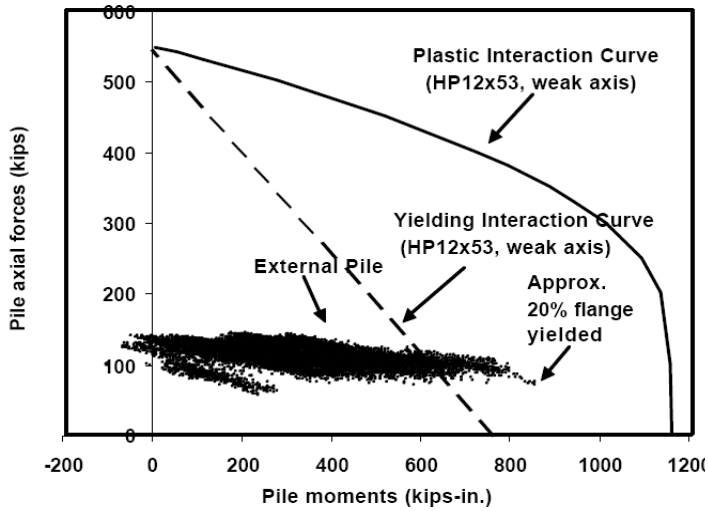

Figure 2.22. Measured interaction curve of the supporting pile [66].

Yield stresses of the pile were exceeded, see Figure 2.22. The risk of low-cycle fatigue failure due to thermal-induced minor or large strain cycles existed [56, 5]. The piles were still sufficiently safe under service conditions according to [66]. However, the referred document did not mention that pile yield might lead to increased excessive eccentricities of pile due to cyclic displacement and cinematic non-linear soil behaviour in case the durability and safety of the structure decreases.

An idealised development of thermal-induced strains on the supporting piles of a fully integral abutment is presented in Figure 2.23 [3, 26].

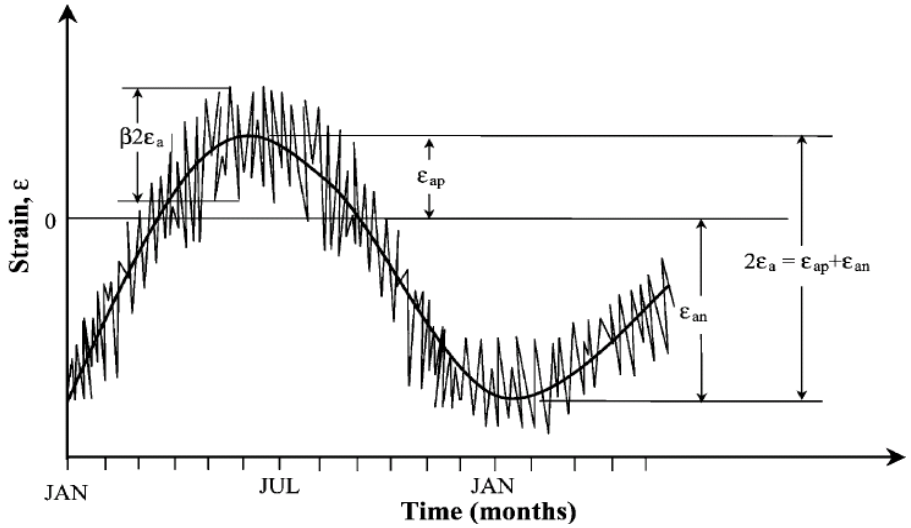

Figure 2.23. Idealised strain on supporting piles as function of time in a fully integral bridge [3, 26].

Strain cycles are divided into large and small ones. It is assumed that a small strain cycle occurs weekly (52 times a year) and a large one once a year. The model is based on two long-term monitored bridges in Iowa, USA [53]. The bridges were prestressed or composite girder bridges. The monitoring results demonstrated that the small strain cycles fall within 20-40% of the large strain cycles, which is indicated by factor β, a positive constant

between small and large strain cycle amplitudes, in Figure 2.23. However, it was also mentioned that this phenomenon is affected by the climate conditions of the location of the bridge.

Table 2.2. Results of FEM analyses on displacement capacity of supporting piles driven in sand which bend about their strong axis. Steel grade yield stress is 248 MPa. Data were taken from [3].

	Pile type	HP310x125	HP280x85
Pile top connection	k_h [MN/m^3](1	$y_{top,all}$[m] (2	$y_{top,all}$[m] (2
Rigid	2000	0.057	0.044
	6000	0.038	0.030
	12000	0.027	0.022
	18000	0.023	0.019
Hinged	2000	0.173	0.158
	6000	0.113	0.099
	12000	0.085	0.072
	18000	0.071	0.060

1) See Formula 2.6
2) Pile top lateral displacement capacity $y_{top,all}$ [m]

Analysed displacement capacities of pile top for fully integral bridge supporting piles driven in sand are presented in Table 2.2. Capacities based on FE model fatigue analyses are given in Figure 2.23. It is assumed that normal stress on piles is $0.3*f_y$. Factor β was assigned the average value 0.3 based on measurements. It can be seen that both soil stiffness and structure stiffness affect pile top displacement capacity.

2.2.4 Static laterally loaded pile behaviour

In laterally loaded soil behaviour earth pressure is related to the coefficient of lateral subgrade reaction by Formula 2.6:

$$p = k_h * y \tag{2.6}$$

where:
p = earth pressure [MN/m^2]
y = displacement of pile [m]
k_h = coefficient of lateral subgrade reaction [MN/m^3]

The general relationships of lateral subgrade reaction behaviour are presented in Formula 2.7 (valid for Case of Figure 6.18a) and Table 2.3.

$$k_s = cc_c * k = cc_c * k_h * D = cc_s * n_h * \left(\frac{z}{D}\right) * D \tag{2.7}$$

The terms and relations are presented in Table 2.3:

Table 2.3. Formulas related to behaviour of lateral subgrade reaction of piles.

Name		Unit	Common expression
Spring stiffness	k_s	[MN/m]	$F = k_s*y$ F = **force [MN]**
Modulus of lateral subgrade reaction	k	[MN/m^2]	$q = k*y = k_h*D*y$ $= n_h*(z/z_{ref})*D*y = y*k_s/cc_s$ when, $k = k_h*D$ and, $k = k_s/cc_s$ cc_s = spring division along pile length [m] D = pile diameter [m] q = **force per unit length [MN/m]**
Coefficient of lateral subgrade reaction	k_h	[MN/m^3]	$p = k_h*y$ [MN/m^2] and, $p = k*y/D$ p = **pressure [MN/m^2]**
Constant of lateral subgrade reaction (1	n_h	[MN/m^3]	$k_h = n_h*(z/D)$ (1 [MN/m^3] z = depth co-ordinate [m] k_h depends on depth z n_h is constant along depth z
Modified constant of lateral subgrade reaction	m_h	[MN/m^3]	$k_h = m_h*z*D^{0.5}$ [MN/m^3] (2 m_h is constant along depth z

1) In cases where the coefficient of lateral subgrade reaction k_h is linearly distributed along pile length, see Figure 6.14a
2) Here, behaviour of non-cohesive soils is presented in a case where the coefficient of lateral subgrade reaction k_h is linearly distributed along pile length, see Figure 6.14a

The behaviour of laterally loaded piles in integral bridges is important because soil-structure interaction forces exert stresses on piles. If the piles were in an elastic media where lateral soil stiffness per unit length k and pile flexural stiffness E_pI_p are constant, the following differential equation could be written:

$$E_P I_P \frac{d^4 y}{dz^4} + k * y = q \qquad \text{[99, 62, 60] (2.8)}$$

where:
q = load distribution along pile [MN/m]
k = modulus of lateral subgrade reaction (Winkler type soil stiffness against pile per unit length) [MN/m^2]

By further introducing a dimensionless variable

$$\xi_1 = \lambda_1 * z \qquad \text{[99, 62] (2.9)}$$

where

$$\lambda_1 = \sqrt[4]{\frac{k}{4 * E_P I_P}} \qquad \text{[99, 62] (2.10)}$$

and q = 0, we get a linear and homogenous form of the differential equation:

$$\frac{d^4 y}{d\xi_1^4} + 4 * y = 0 \qquad \text{[99, 62] (2.11)}$$

where
λ_1 = characteristic value when the coefficient of lateral subgrade reaction is constant [1/m]

Further, it is defined:

$$\phi = \frac{dy}{dz}, M = EI\frac{d^2y}{dz^2}, V = EI\frac{d^3y}{dz^3}, q = EI\frac{d^4y}{dz^4} \qquad (2.12, 2.13, 2.14, 2.15)$$

The solution of Formula 2.11 is presented in [99, 62]. Examples of results produced by Formulas 2.12-2.15 (derivates of pile deflection line for a single pile) are presented in Figure 2.24.

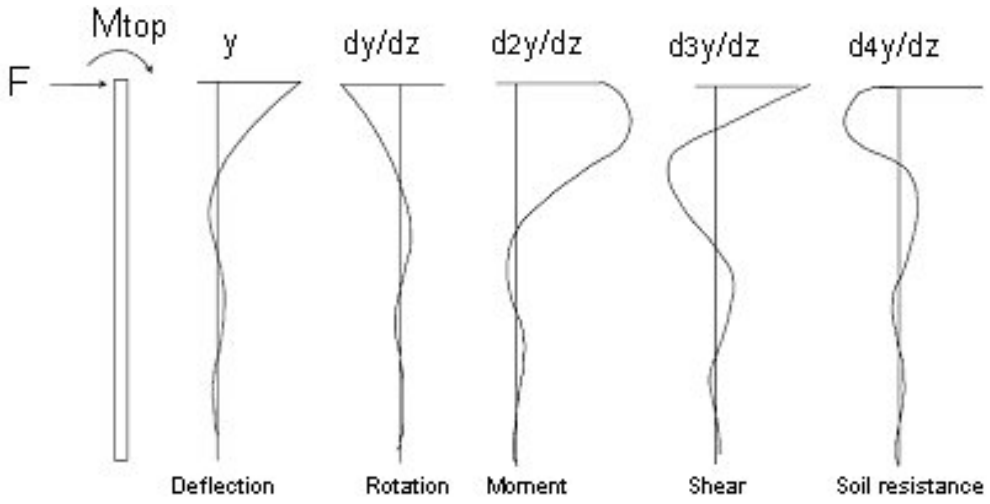

Figure 2.24. Example of overall results on the pile solutions [95].

The results in Figure 2.24 are damped along depth. The characteristic variable λ is called a damping factor in [62]. When the modulus of lateral subgrade reaction is linearly distributed along depth (see Figure 6.18a) and q = 0, the following differential equation can be written [133, 104]:

$$E_p I_p \frac{d^4y}{dz^4} + k * y = 0 \qquad [133, 104] (2.16)$$

$$E_p I_p \frac{d^4y}{dz^4} + n_h * z * y = 0 \;\|:* \frac{1}{n_h * L_P}$$

$$\frac{E_p I_p}{n_h * L_P} * \frac{d^4y}{dz^4} + \frac{n_h * z}{n_h * L_P} * y = 0$$

By introducing a dimensionless variable,

$$\xi_2 = \frac{z}{L_P} \qquad [133, 104] (2.17)$$

then

$$\frac{d^4y}{dz^4} = \frac{d^4y}{d\xi_2^4} * \left(\frac{d\xi}{dz}\right)^4 = \frac{d^4y}{d\xi_2^4} * \frac{1}{L_P^4} \qquad [62] (2.18)$$

and differential Formula 2.16 leads to

$$\frac{E_p I_p}{n_h * L_P} * \frac{1}{L_P^4} * \frac{d^4 y}{d\xi_2^4} + \xi_2 * y = 0 \;\|: * n_h * L_P^5 \qquad (2.19)$$

$$\frac{d^4 y}{d\xi_2^4} + \frac{n_h * L_P^5}{E_p I_p} * \xi_2 * y = 0$$

which is then solved by defining

$$\lambda_2 = \sqrt[5]{\frac{n_h}{E_p I_p}} \qquad [104] (2.20)$$

and finally a linear and homogenous form of the differential equation is obtained with Formulas 2.19 and 2.20:

$$\frac{d^4 y}{d\xi_2^4} + (\lambda_2 * L_P)^5 * \xi_2 * y = 0 \qquad [104] (2.21)$$

where
L_p = length of pile, when s = 0 and co-ordinate z extends from ground level downwards, see Figure 6.18 [m]
s = length of pile above ground level, see Figure 6.18 [m]
λ_2 = characteristic value when coefficient of lateral subgrade reaction is linearly distributed [1/m]

Solutions derived from and/or principles of Formula 2.21 are presented in [62, 104, 133, 141]. The solutions require series development. Solutions for cases where the modulus of lateral subgrade reaction is distributed along the pile length are presented in [95, 96]. Power functions and distributions of modulus of lateral subgrade reaction in cohesionless soils are presented in Figure 2.25.

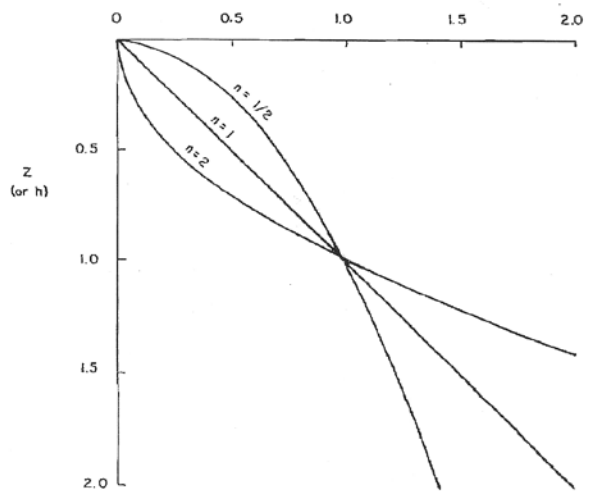

Figure. 2.25. Power functions of modulus of lateral subgrade reaction [95].

According to [95], when the modulus of lateral subgrade reaction is linearly distributed along pile length, stiffness factor T_a is:

$$T_a = \sqrt[5]{\frac{E_p I_p}{n_h}} \qquad \text{[95, 96, 10, 82, 133, 21] (2.22)}$$

Other references [96, 10, 82, 133, 21] also present views similar to those of Formula 2.22. On the basis of Formula 2.22 and [10, 57, 15] it can be concluded that the stiffness factor is an inverse of the characteristic value λ_2 when the modulus of lateral subgrade reaction is linearly distributed.

The distribution of the modulus of lateral subgrade reaction along the pile length has a significant effect on pile behaviour [95]. The effect of the top part of a pile supporting the modulus of lateral subgrade reaction in particular is of great importance [95]. Different distributions of the modulus of lateral subgrade reaction are presented in Figure 2.26.

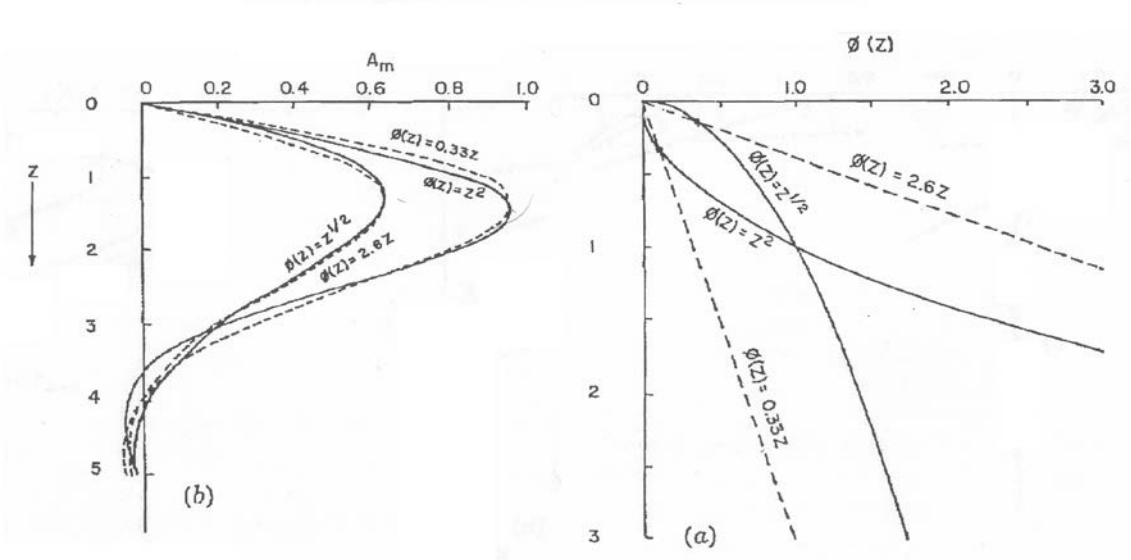

Figure 2.26. Comparison of moment values of different distributions of modulus of lateral subgrade reaction [95]. Pile has hinged top connection. Loading is a lateral force on top of pile. On the left, unitless moment values; on the right, distributions of modulus of lateral subgrade reaction.

First, the moment values of two distributions of the modulus of lateral subgrade reaction are calculated with exponents 2 and ½. Second, the modulus of lateral subgrade reaction is solved as linearly distributed so that the same maximum moment values are obtained. Then, it can be noticed that the upper parts of supporting springs have an essential effect on pile behaviour. Further, highly different distributions of the modulus of lateral subgrade reaction produce highly similar moment distributions which can lead to wrong conclusions during field testing. In the presented case, the loading was a lateral force on top of the pile. However, in the case of the fully integral bridge, the loading causes a forced displacement resulting in different phenomena. The pile can be assumed to behave like a pile of infinite length if:

In the constant modulus of lateral subgrade reaction case (case b in Figure 6.18),

$$\lambda_1 * L_p \geq 5$$

$$\sqrt[4]{\frac{k}{4 * E_p I_p}} * L_p \geq 5 \qquad \text{[96, 62] (2.23)}$$

and in the linearly distributed modulus of lateral subgrade reaction case (case a in Figure 6.18),

$$\lambda_2 * L_p \geq 5$$

$$\sqrt[5]{\frac{n_h}{E_p I_p}} * L_p \geq 5 \qquad \text{[95, 16] (2.24)}$$

In the linearly distributed case, the value 4 is included in addition to 5 [142]. The presented solutions of differential equations assume that soil behaves linearly elastically. However, the lateral subgrade reaction is not elastic, but the presented solutions are appropriate for preliminary examinations and give a picture of the influence of the behaviour of piles of infinite length. A general hyperbolic force-displacement relationship of lateral subgrade reaction is presented in Figure 2.27.

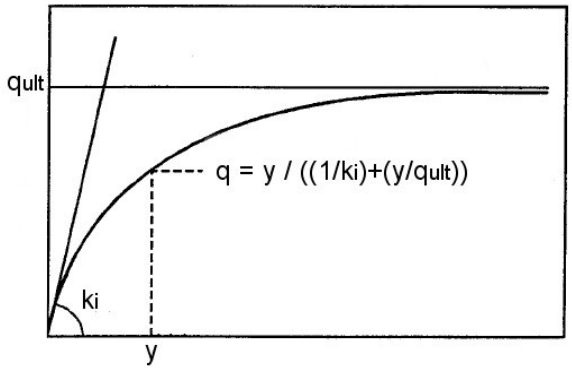

Figure 2.27. Force-displacement relationship of pile-soil-interaction, for terms see Formula 2.25 [20].

Hyperbolic behaviour is rather widely accepted is soil mechanics [17, 123]. Both initial stiffness and ultimate resistance affect the force-displacement relationship along different strain stages. The force-displacement relationship of lateral subgrade reaction is based on tri-linear behaviour in the Finnish guidelines [43, 75], see Figure 2.1. The general hyperbolic behaviour formula is:

$$q = \frac{y}{\frac{1}{k_i} + \frac{y}{q_{ult}}} \qquad \text{[17, 123] (2.25)}$$

where:
k_i = initial modulus of lateral subgrade reaction [MN/m^2]
q_{ult} = lateral soil resistance, asymptote of hyperbolic behaviour [MN/m]

However, the developed pressure does not reach asymptote maximum lateral pressure q_{ult}. Hence a scaling parameter R_f has been introduced.

$$q = \frac{y}{\frac{1}{k_i} + R_f \frac{y}{q_f}} \qquad \text{[30] (2.26)}$$

$$R_f = \frac{q_f}{q_{ult}} \qquad \text{[30, 123, 130] (2.27)}$$

where
q_f = lateral soil failure resistance [MN/m], and R_f is obtained from

$$R_f = 1 - \frac{k_f}{k_i} \qquad \text{[130] (2.28)}$$

where:
k_f = secant modulus of lateral subgrade reaction at failure point [MN/m^2]

Lateral soil failure resistance of cohesionless soil may be calculated as follows:

$$q_f = 3...5 * D * \gamma' * z * K_p \qquad \text{[43, 89, 124, 52, 92] (2.29)}$$

where:
γ' = effective unit weight of soil [MN/m^3]
K_p = passive earth pressure coefficient [-]

$$K_p = \frac{1 + \sin\phi_s}{1 - \sin\phi_s} \qquad (2.30)$$

where:
ϕ_s = soil internal friction angle [^{o}]

And the resistance of cohesive soils is:

$$q_f = 6...9 * D * s_U \qquad \text{[43] (2.31)}$$

where:
s_U = undrained shear strength of cohesive soil [MN/m^2]

The hyperbolic stress-strain relationship with scaling parameter R_f is presented in Figure 2.28.

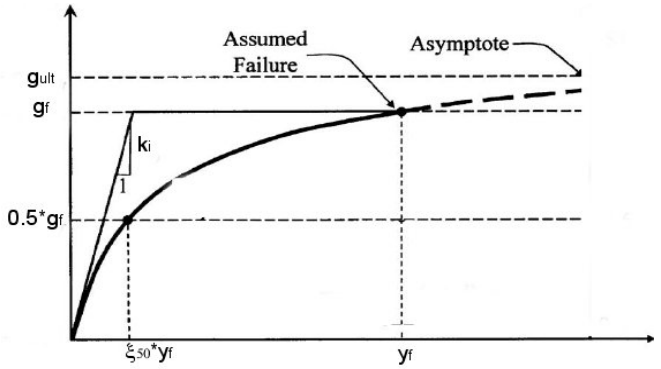

Figure 2.28. Hyperbolic stress– strain relationship with scaling parameter R_f. The figure is based on [123].

Parameter ξ_{50} is obtained from:

$$\xi_{50} = \frac{y_{50}}{y_f} \qquad [130] \ (2.32)$$

where:

y_f = lateral displacement at failure point [m]

y_{50} = lateral displacement of pile at stage when $0.5*q_f$ is reached [m]

The value of $\xi_{50} = 0.25$ is found appropriate for common cohesionless soils [30]. Finnish guidelines also present a corresponding value [43, 79]. Accordingly, the relation of initial stiffness to ultimate secant stiffness, k_i/k_f, is three.

The impact of pile diameter on the modulus of lateral subgrade reaction has been the subject of the foregoing discussion. In present Finnish guidelines, the diameter of a pile has no effect on the modulus of lateral subgrade reaction in cohesionless soils in the case of the upper part of a pile, which has a significant impact on pile behaviour. The basis of the behaviour has been continuum bulb pressure. That pressure at two different pile diameters is presented in Figure 2.29.

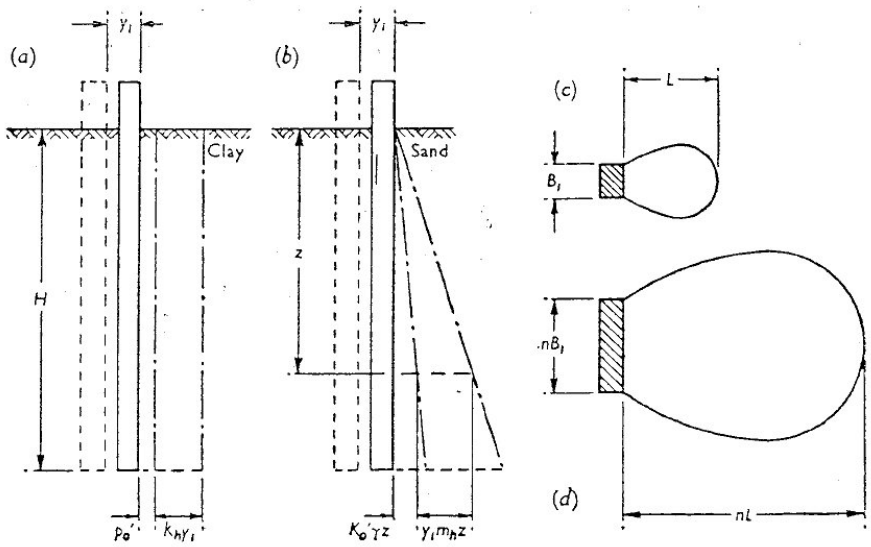

Figure 2.29. Influence of Pile Diameter on Dimensions of Bulb Pressure [129].

Bulb length is assumed linearly proportional to pile diameter in Figure 2.29. Then, the effective length in lateral loading is linearly proportional to pile diameter. Thus, it can be concluded that in lateral displacement rigidity against the pile per unit length is approximately the same for different pile diameters. However, reaction against the pile is not quite that straightforward. The reaction of soil-pile interaction to lateral movement can be expressed in two parts: frontal normal reaction and side friction and normal reaction [144, 9, 11, 14].

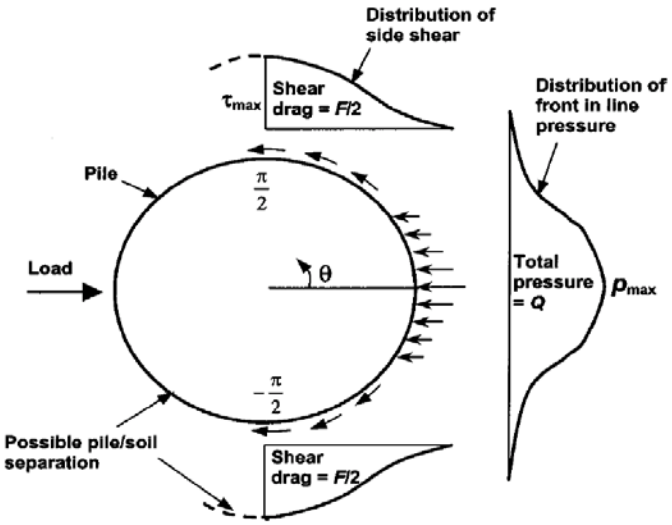

Figure 2.30. Distribution of front earth pressure and side shear around pile subjected to lateral load [125].

It is doubtful whether Terzaghi's [129] assumptions are applicable to these components, especially circular piles. References [8, 143] mention that pile diameter has a negligible effect on the initial modulus of lateral subgrade reaction in cohesionless soils. But it may be concluded from presented results in [8] that in the ultimate loading situation the secant modulus is affected by pile diameter because ultimate strength does depend on pile diameter. The results were based on FEM analyses and full-scale tests. The initial modulus of lateral subgrade reaction was not independent of pile diameter, nor was it linearly proportional to pile diameter [7]. Several formulas for modulus of lateral subgrade reaction have been presented and the familiar ones are presented in [92]. In the study conducted parallel to this integral abutment development process, it was observed that pile diameter has an effect on the ultimate secant modulus of lateral subgrade reaction in cohesionless soils [75]. The shape of the pile cross section also affects lateral behaviour [9].

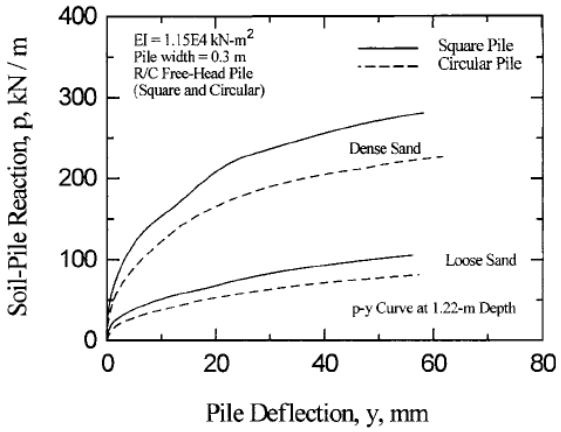

Figure 2.31. Effect of pile cross section on q-y curve [9]. Loose sand $\phi = 30^o$ and dense sand $\phi = 40^o$.

The effect of cross section shape is presented in Figure 2.31. A multiplier of approximately 0.8 was obtained to developed the q value between square and circular cross section. The

analysis in [9] is based on the Strain Wedge method. In [124] a multiplier of 0.75 for normal stresses and 0.5 for shear stresses was recommended, compare to Figure 2.30.

2.2.5 Cyclic laterally loaded pile behaviour

Hysteretic behaviour in cyclic loading of a laterally loaded pile was observed in [124, 112, 52, 81, 72]. The principles of hysteretic backbone curve and behaviour in fully reversed loading are presented in Figure 2.32. A backbone curve represents the relationship in monotonic loading.

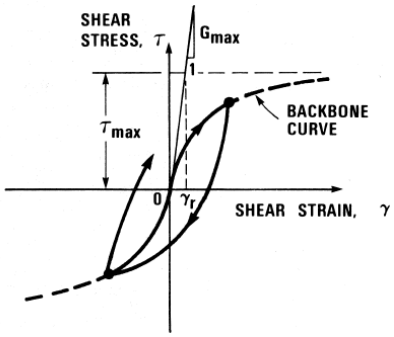

Figure 2.32. Hysteretic backbone curve [130].

Loading sequence affects the p-y relationship. Two cases of pressure-strain relationship of a laterally loaded structure are presented in Figure 2.33, fully reversed and one-sided cyclic loading.

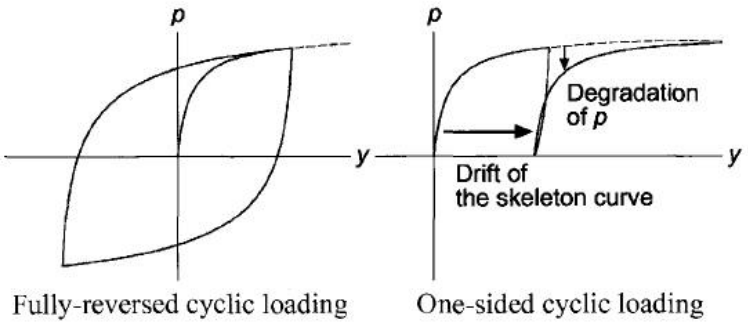

Figure 2.33. Schematic p-y behaviours based on experiments [124].

The behaviour of materials follows kinematic rules, i.e. loading and unloading take different paths in q-y diagrams. The drift of the backbone curve (skeleton curve in Figure 2.33) in one-sided loading leads to low earth pressure at large displacement stages at the beginning of reloading. The behaviour of materials in fully reserved cyclic loading creates a full hysteretic loop in the q-y diagram. Behaviour at the integral bridge end piles is a mixture of the two above cases. The behaviour of earth pressure behind the end screen is closer to that in one-sided loading. The behaviour of q-y loops changes along pile depth. The development of a gap in a q-y loop has an effect on the upper part of the pile. The stage is called non-confined. In the lowest part behaviour is almost elastic while clear hysteretic loops

develop in the middle. These stages are called confined stages. The different stages are presented in Figure 2.34.

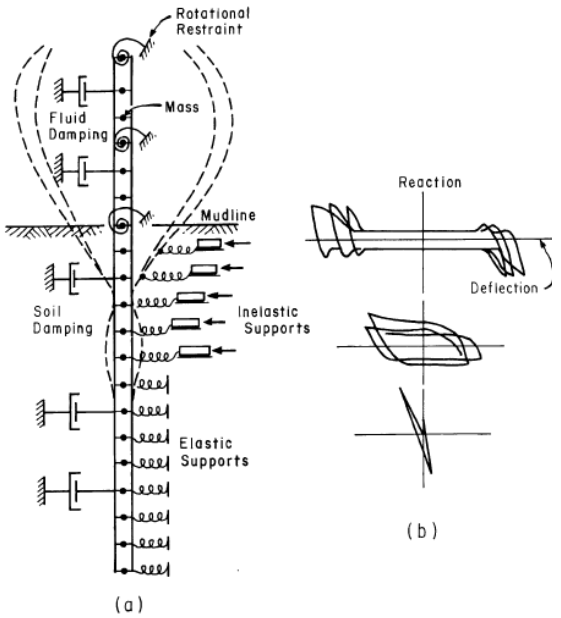

Figure 2.34. a) Soil-pile superstructure model b) variation in q-y curves along depth [97].

Hysteretic behaviour is rather complex and involves many parameters as pointed in [128, 124, 98]. The modulus of lateral subgrade reaction has been modelled with a group of elasto-plastic springs in [97], see Figure 2.35.

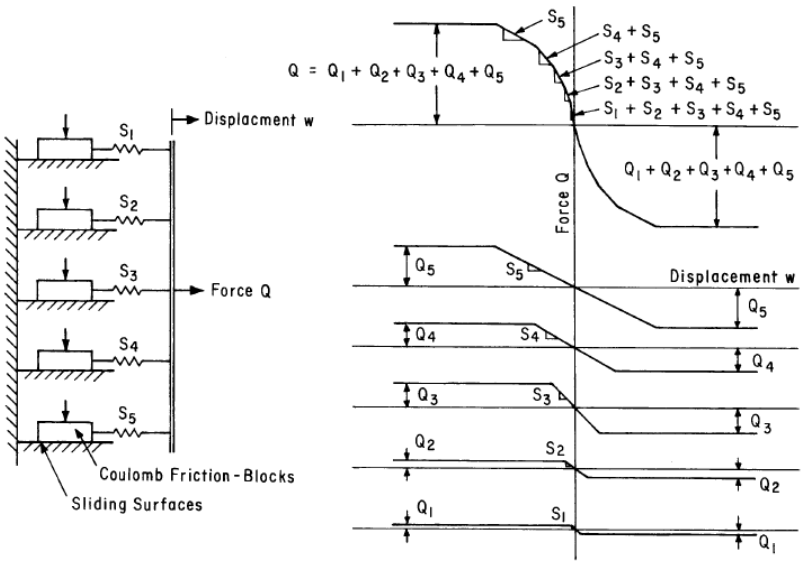

Figure 2.35. Non-linear spring model [97].

The solution consists of several springs connected to the same node. The method allows hyperbolic-like behaviour with simple elasto-plastic springs in the model. All springs are in the elastic section with small displacements. The springs yield at different displacement stages as displacement increases. This method is used in the analyses of this study in Paragraph 6.3.5.

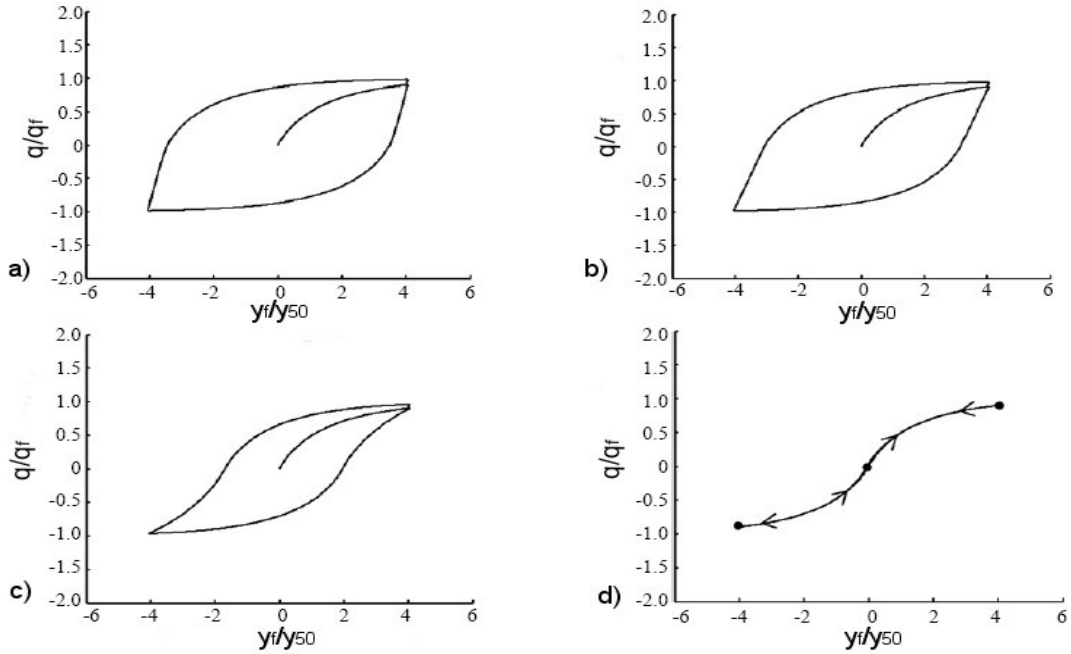

Figure 2.36 a-d. General hysteresis loops of q-y [52].

Different general types of fully reversed hysteretic loops are presented in Figure 2.36. Both the initial modulus of subgrade reaction k_i and the ultimate load q_f are doubled at the beginning of the first reloading in Figure 2.36a [52]. Only q_f is doubled in Figure 2.36b. The behaviour of Figure 2.36c is non-linear but elastic and resembles the backbone curve. The behaviour of Figure 2.36c is in between elastic and pure hyperbolic behaviour. Hyperbolic behaviour at first loading in all cases corresponds to parameter $\xi_{50} = 0.25$. The behaviour in Figure 2.36b is said to correspond to Masing's rule [52]. The behaviours of Figure 2.36 are in confined stages and soil-structure interaction on both sides of piles is summed up. The front side and backside of the laterally loaded pile behave differently during loading. Roughly speaking, the front side is a passive case and the backside an active case. The hysteresis loops of different sides of a pile are presented in Figure 2.37.

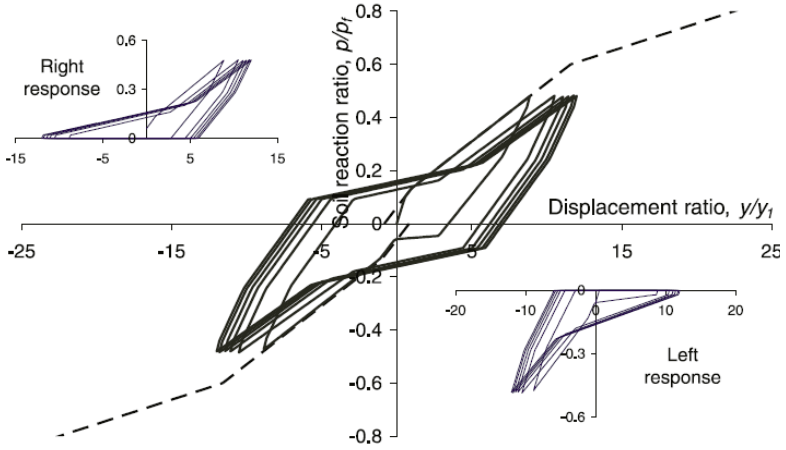

Figure 2.37. Hysteresis loops of q-y with components of different pile sides [4].

The laterally loaded pile has alternating passive and active cases on each side during the loading sequence. Different behaviour on different sides generates non-symmetrical q-y loops. At higher depths, the hysteretic loops become more symmetrical, see Figure 2.34.

2.2.6 Laterally loaded pile as part of fully integral bridge

The supporting piles of the fully integral bridge's ends are monolithically connected to the bridge end screen or to the bridge deck, and laterally loaded mainly by uniform temperature changes. This does not mean that pile tops are rigidly connected against rotation because the bridge end is rotated by loadings and the bridge has a certain stiffness against rotations. Rotation of the bridge end screen decreases the curvature of the top of supporting piles, see Figure 2.38.

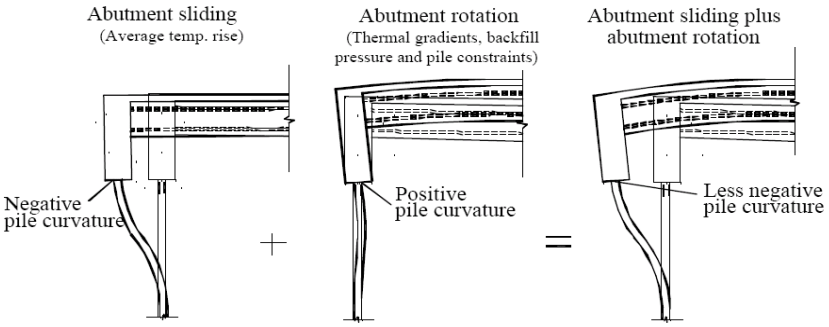

Figure 2.38. Effect of fully integral bridge end rotations on pile curvatures [66].

A deformed shape caused by a live load on a single span fully integral bridge is presented in Figure 2.39. The end screen rotates, the pile head is subjected to displacement and rotation, and the superstructure is displaced under the live load.

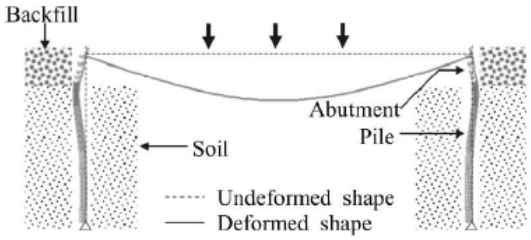

Figure 2.39. Soil-structure interaction behaviour of a single-span fully integral bridge under live load [29].

The distribution of the effects of a live load depends on the stiffness relations between different structural parts. Different properties of backfill soil have only a small effect on the bending moment of a girder at mid-span with different superstructure stiffenesses and pile sizes. The end screen of the single span bridge was 5 m tall and pile sizes were HP250x85 and HP310x125. The influence of the backfill on the bending moments of piles was moderate. The influence of different subsoil properties on the girder moments and pile bending moments was also moderate. [29]

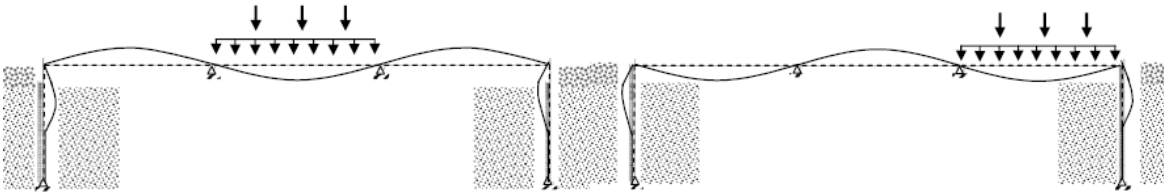

Figure 2.40. Soil-structure interaction behaviour of a three-span integral bridge under live load [27].

The distribution of the effects of a live load is different with multiple span integral bridges than with single span ones due to superstructure continuity, see Figure 2.40. Different properties of backfill soil have only a negligible effect on the bending moment of the girder at intermediate supports. However, subsoil properties have a considerable impact on forces exerted on piles. The influence of subsoil and backfill properties is the greater, the closer the observation point on the bridge end is. [27]

2.2.7 Structural details of releasing soil-structure interaction forces

Details for releasing soil-structure interaction forces are referred to in practises. In US practice predrilled holes are used with piles filled with granular material. A fully integral bridge whose piles were assembled in predrilled holes is shown in Figure 2.41. The function of a predrilled hole is to reduce the modulus of lateral subgrade reaction when supporting piles are subjected to smaller strains from temperature and live loads.

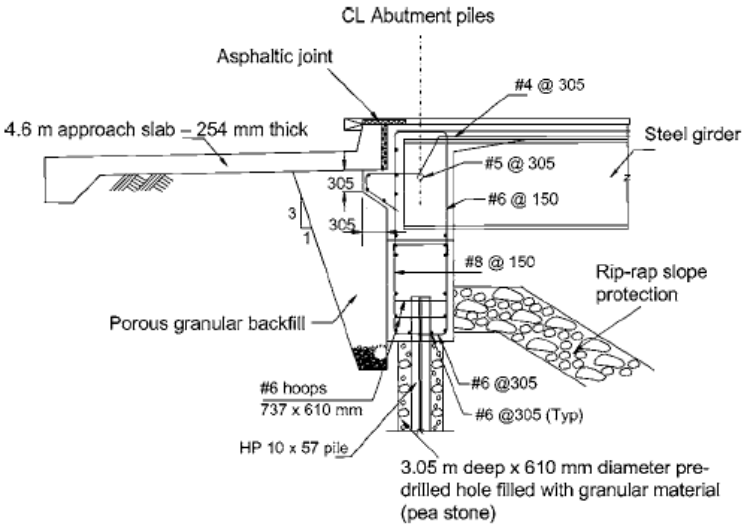

Figure 2.41. Massachusetts OW Bridge abutment and approach slab details [22].

Fill material should be fairly loose and non-compacting [22]. The drilled hole diameter was 0.61 m [22]. However, movements of embankment soil may induce higher strains than calculated also when there are no predrilled holes.

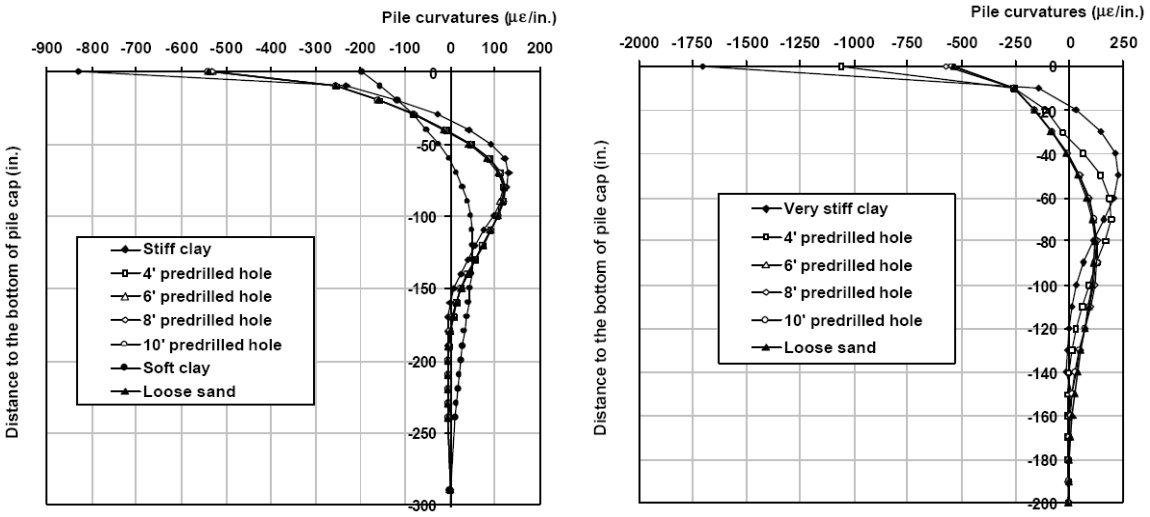

Figure 2.42. Calculated effects of predrilled holes on pile curvature at falling uniform temperature 27.8ºC for the 66.9 m total expansion length. On the left stiff clay, on the right very stiff clay [66].

The effect of the predrilled holes on supporting pile curvatures is presented in Figure 2.42. The predrilled holes are from 1.2 m (4 ft) to 3.0m (10 ft) deep measured from ground level. The left curvature diagram depicts a supporting pile in stiff clay. It can be seen that the predrilled hole decreases the curvature about 20%. The right curvature diagram depicts a supporting pile in very stiff clay. Predrilled holes longer than 1.2 m are shown to reduce pile stresses more than 30%. An interesting observation is that the upper part of the pile has great significance because a longer predrilled hole does not make a substantial difference in the biggest curvatures.

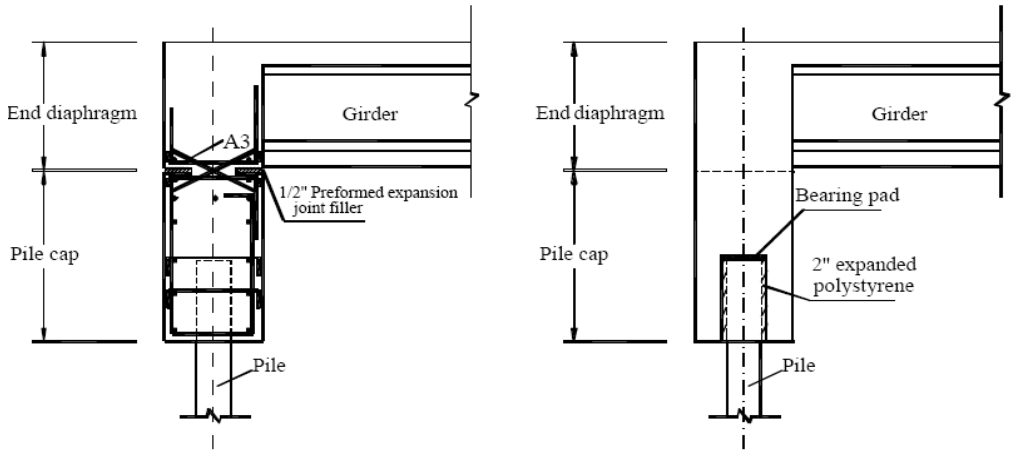

Figure 2.43. Details of abutment that allow partial rotation of pile head [66].

Two details of an abutment that allow partial rotation of pile head are presented in Figure 2.43 [66]. Here, the pile head is treated as a partly hinged connection with limited hinge rotation. Pile head rotation reduces pile curvature at the top of the pile and increases it at the lower pile section. The hinged connection used in the Australian practice is shown in Figure 2.44 [25].

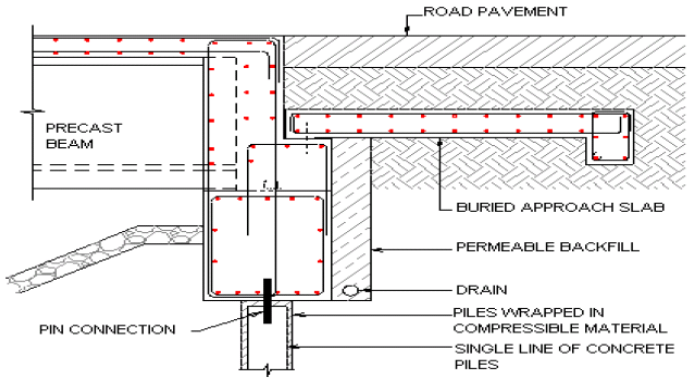

Figure 2.44. Abutment with hinged support at top of pile [25].

A flexible plate has been used behind the end screen to relieve soil-structure interaction forces [25]. It has been observed that the material used should have good flexibility and strength [18]. In a monitored bridge along route 60 over the Jackson River, Alleghany County, Virginia, USA, the flexible plate relieved approximately 85% of maximum earth pressures compared to a case without flexible plate behaviour during a 5-year monitoring period [65].

2.2.8 Approach and transition slabs

A transition slab is a common part of Finnish bridge engineering practice, see Figure 1.4. Approach and transitions slabs are also part of US practice. The transition slab is the one closer to the bridge. It levels out most of the settlement difference between superstructure and embankment. The transition slab is often rigidly connected to the longitudinal movement. Expansion is allowed at the joint between a transition and an approach slab. This is because water is preferred to leak onto the slabs than on the superstructure. Then the slabs instead of the superstructure are exposed to the elements.

2.3 Conclusions

The fact that maintenance costs will rise as bridges become older has further increased the interest for the integral bridge concept. However, all standards do not give accurate design guidelines – they generally only mention that the structure has to withstand occurring interaction forces. There are various design proposals for integral bridges which depend on the environment. The guidelines and research interests are strongly affected by climate and practices.

3 DEFINITION OF THE PROBLEM

3.1 Aim of the study

The aim is to prove that the different properties of the embankment soils between the ends of a fully integral bridge have a significant impact on structural behaviour. Eccentric displacements around the centre of thermal expansion are the result of uniform temperature changes due to the different properties of the soils between the integral bridge ends. This should be taken into account in the construction of integral bridges.

Another goal was to show that the allowable total thermal expansion length of a fully integral bridge can be determined by the presented research process on the basis of structural behaviour. The main methods of the process are bridge monitoring (field tests), structural analysis and review of literature and guidelines, see Figure 1.5. The allowable total thermal expansion length is a safe estimate of the distance between the end screens' outer surfaces, see Figure 1.3.

A further goal was to provide a substantial portion of the information required for integral bridge design guidelines. The presented process was built on the basis of the research problem and related studies, see Figure 1.4 [75, 84, 73, 74, 139].

3.2 Objectives

This study deals with the structural behaviour of a fully integral bridge. Its main objectives are:

- To increase knowledge about the structural behaviour of integral bridges
- To develop systems and devices for the monitoring of bridges
- To develop background material for integral bridge design methods and structural solutions for integral concrete bridges
- To combine a global structural bridge model and soil behaviour using kinematic formulas

The economical benefits of an integral bridge are undoubtedly an important issue, but economic analysis was excluded from this study. The unit of analysis is uniform temperature change and concrete creep and shrinkage which cause strains on the bridge superstructure, which, again, generate interaction forces between the bridge structures and soil. The structural design methods are discussed under the present theme, and recommendations for bridge design and construction are also made. The development of structural details was excluded from this study.

4 FIELD TEST PROGRAMMES

4.1 Overview

The research questions that rose in response to the research problem required also conducting full-scale field tests on the integral bridges. Phenomena can be calculated and studied by many research methods. However, reasonable certainty is ultimately achieved by field tests. Uncertainty is smaller and can be better considered in field tests because the measured results reflect an actual case. On the other hand, most of the necessary measuring techniques did not exist. The monitoring of bridges also requires quite a lot of time in order that sufficient reliability of the measured results can be ensured.

Many of the monitoring and measuring gauges were developed during the research project which made them suited for the full-scale tests.

The objective of this study is not to describe the monitoring devices used in the full-scale field tests on the integral bridges with the finest documentation. Full documentation of the Haavistonjoki Bridge monitoring devices is provided in [84], while the devices used at Tekemäjärvenoja Bridge are documented in [85] and those used at Myllypuro Overpass in [139]. The monitored bridges were chosen based on bridge structure, location and construction time. This chapter presents a major part of the monitoring devices used this study so that the tests may be repeated.

4.2 Haavistonjoki Bridge

4.2.1 Field test programme

The Haavistonjoki (Road) Bridge was chosen as a long-term monitoring target and the monitoring was implemented by TUT in 2003. The bridge is situated about 60 km northeast of Tampere on Highway 9 leading to Jyväskylä. The Haavistonjoki Bridge is a continuous reinforced concrete slab bridge with fully integral abutments. It is founded on 0.711 m diameter steel pipe piles. The horizontal clearance of the bridge is 11.0 m and the structural height of the concrete slab is 0.86 m. The bridge's total thermal expansion length is 51.2 m. Other main dimensions are presented in Figure 4.1.

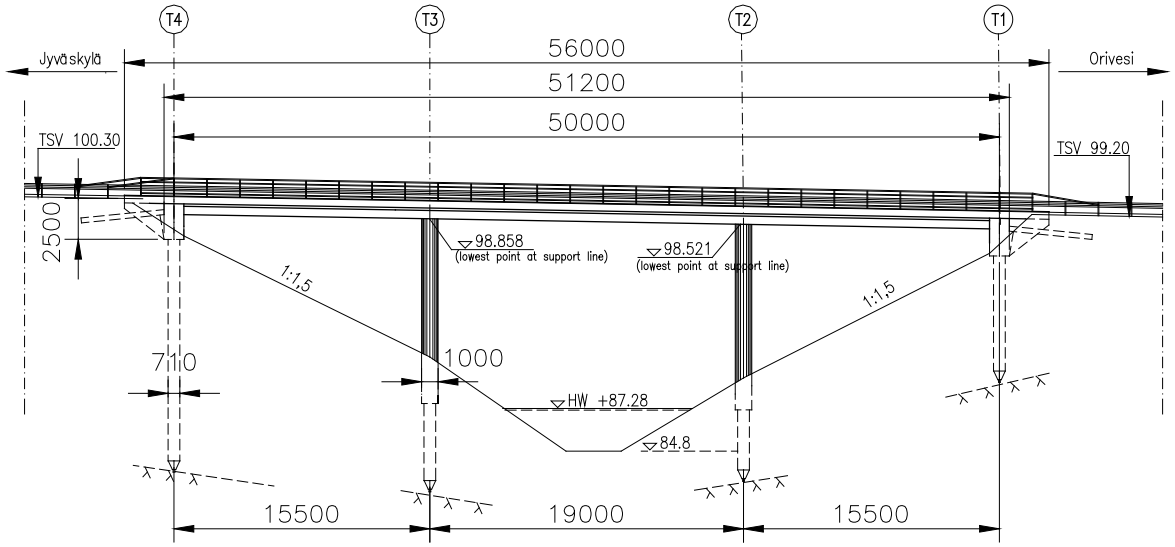

Figure 4.1. Elevation of Haavistonjoki Bridge.

The bridge is monitored by a total of 186 gauges. Monitoring focusses on abutment T4 because displacements were expected to be bigger there. The hypothesis was selected because the height of embankment T1 is lower. The monitored values are:

- Earth pressure between end screen and embankment, 12 gauges
- Earth pressure at bottom of column against embankment, 2 gauges
- Possible gap between end screen and embankment, 6 gauges
- End screen displacements, 2 automated gauges and 12 manual gauges
- Bridge length, by a laser measuring device, 1 piece
- Superstructure temperatures, 16 gauges
- Ambient air temperature, 5 gauges
- Embankment soil temperatures near end screen, 28 gauges
- Transition slab temperatures, 4 gauges
- Displacements between transition slab and end screen, 2 gauges
- Strains on steel pipe pile, 24 gauges
- Steel pipe pile temperatures, 8 gauges
- Strains on superstructure, devices marked as strain bars, 32 gauges (or 64 gauges because strain gauge couples measure separately)

However, the superstructure and steel pipe pile strain gauges could not be made to work properly. Thus, the number of working gauges was 98.Theodolite-tacheometric surveys were also done to determine possible displacements of the whole bridge and embankment slopes as well as road surface settlement at the top of the embankment near the end screen from 8, 13 and 20 locations, respectively. Some problems in measuring ambient air tem-

perature were encountered due to solar radiation. The measuring devices were calibrated at the facilities of the Unit of Earth and Foundation Structures. Reduced size field test drawings are presented in Appendix 2 of [84]. The monitoring devices included also a computer, three data loggers and shelters for the devices. The devices saved measurement results at 15 minute intervals.

The locations of earth pressure cells (EPC) are presented in Figure 4.2. The EPC devices were grouted to the end screen after stripping the superstructure formwork.

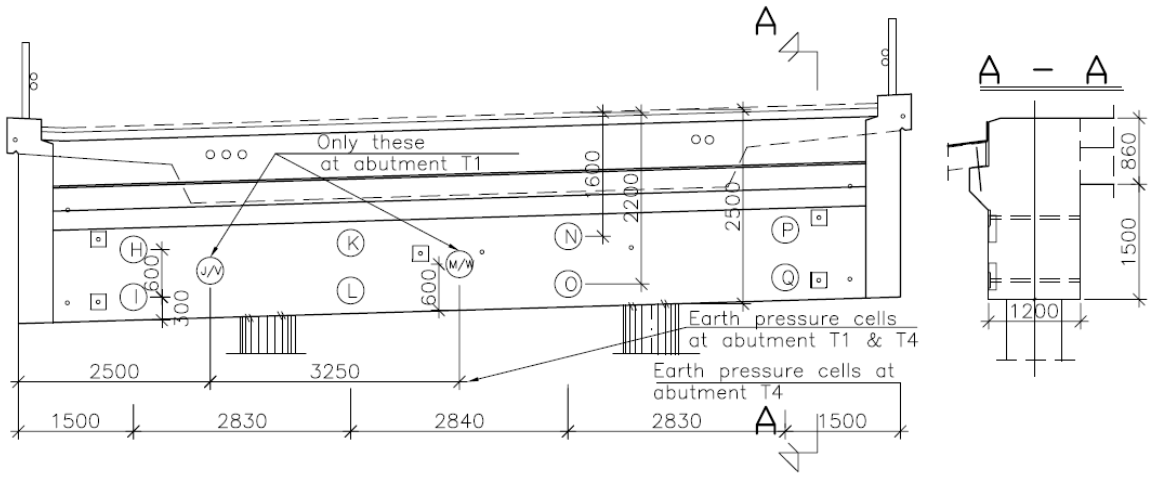

Figure 4.2. EPC locations at Haavistonjoki Bridge abutments. H to Q at abutment T4, V and W at abutment T1.

The earth pressure cells were developed at the Unit of Earth and Foundation Structures of TUT so that they measured earth pressures accurately and were durable [84]. The locations of end screen displacement gauges are presented in Figure 4.3.

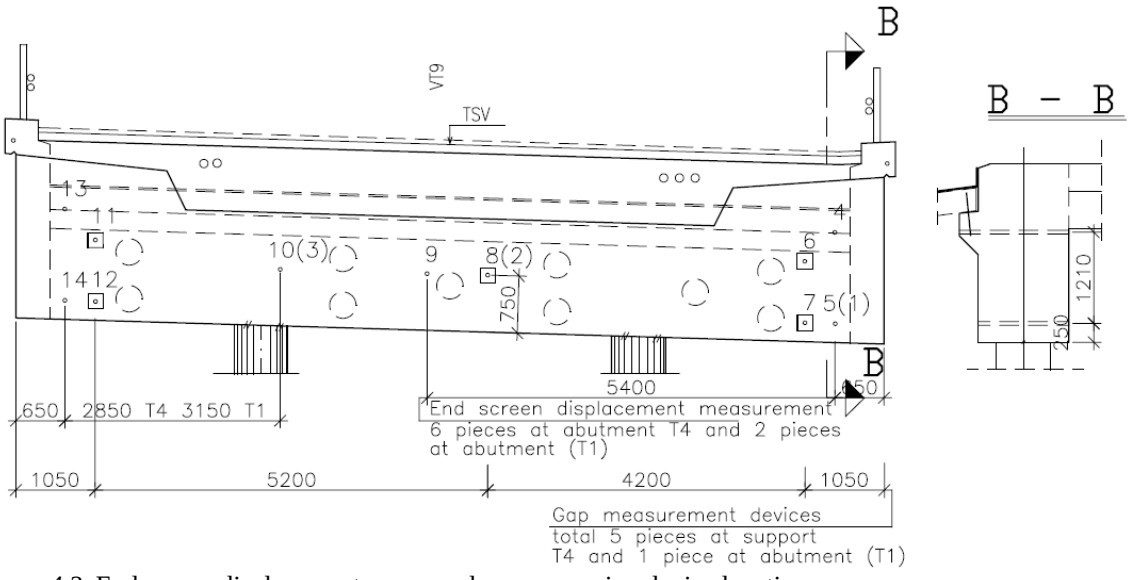

Figure 4.3. End screen displacement gauge and gap measuring device locations.

Gauges 8 and 2 are monitored with data loggers. The rest of the devices are measured by sliding gauges during check surveys. The devices are placed so that end screen rotation

may be read from the sliding gauges. The devices measuring the possible gap between the end screen and the embankment are boxed in Figure 4.3. These devices are read during check surveys. Locations of the superstructure temperature and strain gauges are presented in Figure 4.4.

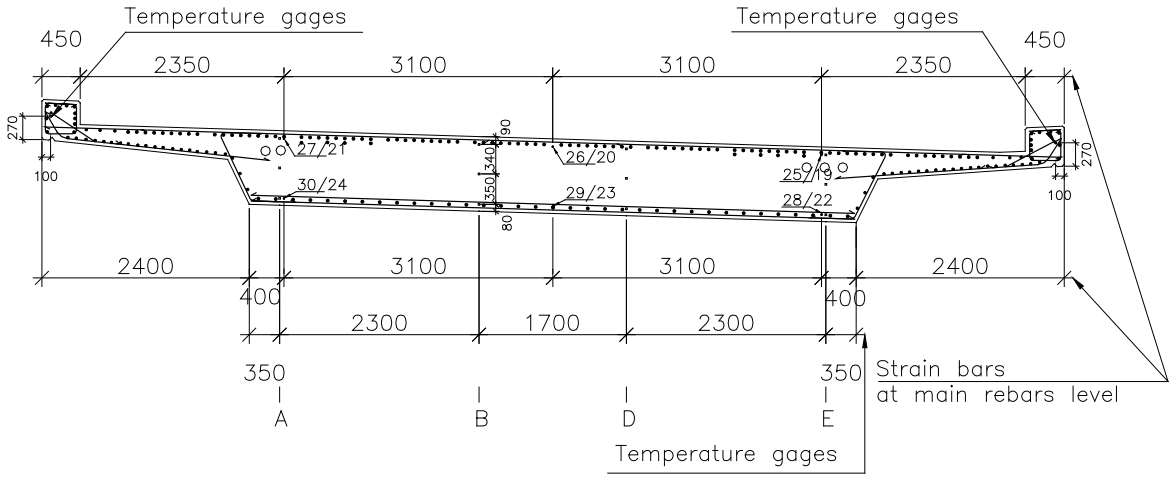

Figure 4.4. Strain bars and temperature gauges of the superstructure.

Temperature gauges were installed at the top, centre and bottom of the deck slab. Gauges were also installed in edge beams. Gauge locations were chosen based on the approximated temperature field of the superstructure [84]. Temperature gauge locations in embankment T4 are presented in Figure 4.5.

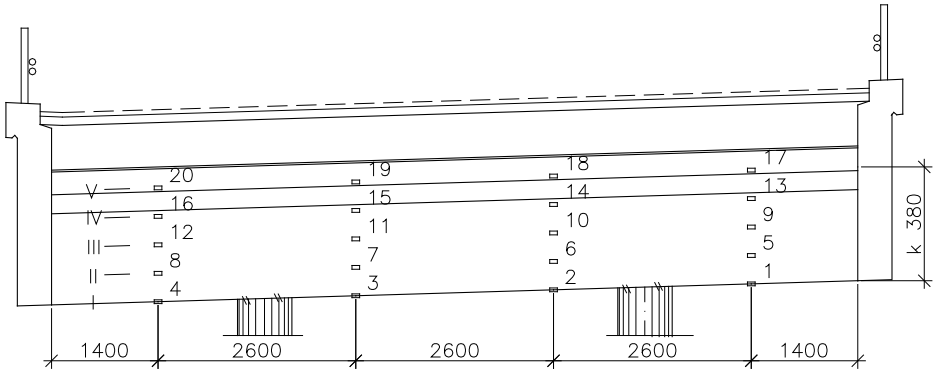

Figure 4.5 Temperature gauges in embankment T4 2.4 m from outer surface of end screen..

The locations of gauges were chosen so that freezing behaviour of the embankment could be studied. A photograph taken prior to construction of embankment T4 approach fill is presented in Figure 4.6.

Figure 4.6. Installation of abutment EPCs, temperature gauges and gap measuring devices between the abutment and the embankment prior to approach fill construction. Anchor bars of end screen displacement measuring devices are also visible.

The gap measuring devices, the temperature gauges of the embankment and the first anchor bars for end screen displacement measuring devices have been installed in Figure 4.6. The approach fills at embankment T1 and T4 were compacted in layers by turns.

4.2.2 Test loading arrangements

This paragraph presents a major part of the monitoring arrangements of the test loadings of this study. The finest descriptions are found in [86]. The Haavistonjoki Bridge was test loaded with a mobile crane at 6.10.2005. The loading time was chosen based on the state of displacement of the end screen. At the loading time, in autumn, the end screen was no longer in the extreme position as the superstructure had started to contract as the uniform temperature had fallen since summer [86]. Three types of loading were implemented with a mobile crane:

2. Braking test
3. Overrun test
4. Static test

The purpose of the braking test was to measure integral bridge behaviour in dynamic longitudinal loading. The magnitude of the developed braking force was also examined. In the braking test, the mobile crane came at a certain speed to the top of the abutment and started to brake whereby it exerted a longitudinal force on the superstructure. This force caused a longitudinal movement in the bridge and interaction forces between soil and the bridge.

The purpose of the overrun tests was to measure integral behaviour under moving traffic load at different speeds of the loading vehicle. The static tests were arranged so that it was possible to measure the live-load induced horizontal earth pressure against the end screen. This study deals with the braking and overrun tests of the presented three test types.

Dynamic test loading required rearrangement of the measuring devices. Data loggers were replaced by faster ones. One kHz was selected as the measuring frequency for the braking tests.

Figure 4.7. The mobile crane equipped with a speed measuring wheel during the braking test at Haaviston-joki Bridge. Mobile crane: Liebherr LTM 1090, dead weight 56 tonnes.

The mobile crane was equipped with speed measuring wheel as can be seen from Figure 4.7. A further requirement was that there was data transmission from the mobile crane to the data logger.

4.3 Tekemäjärvenoja Bridge

4.3.1 Field test programme

The Tekemäjärvenoja (Railway) Bridge was chosen as a short-term monitoring target, and the monitoring was implemented by TUT in 2004. The bridge is situated about 15 km south from the centre of the City of Lahti. Test loading was done on 30.10.2004 – long-term monitoring devices were not installed because the focus was on the short-term test loading. The goal was to measure the distribution of loading to different structural parts and strains on the rails. The relationship between earth pressure and end screen displacement is important for this study. The Tekemäjärvenoja Bridge is a continuous reinforced concrete slab bridge with fully integral abutments. The bridge is a founded on ground

slabs. The horizontal clearance of the bridge is 11.9 m and the structural height of the concrete slabs is 0.93 m. The bridge's total thermal expansion length is 28.8 m. Other main dimensions are presented in Figure 4.8.

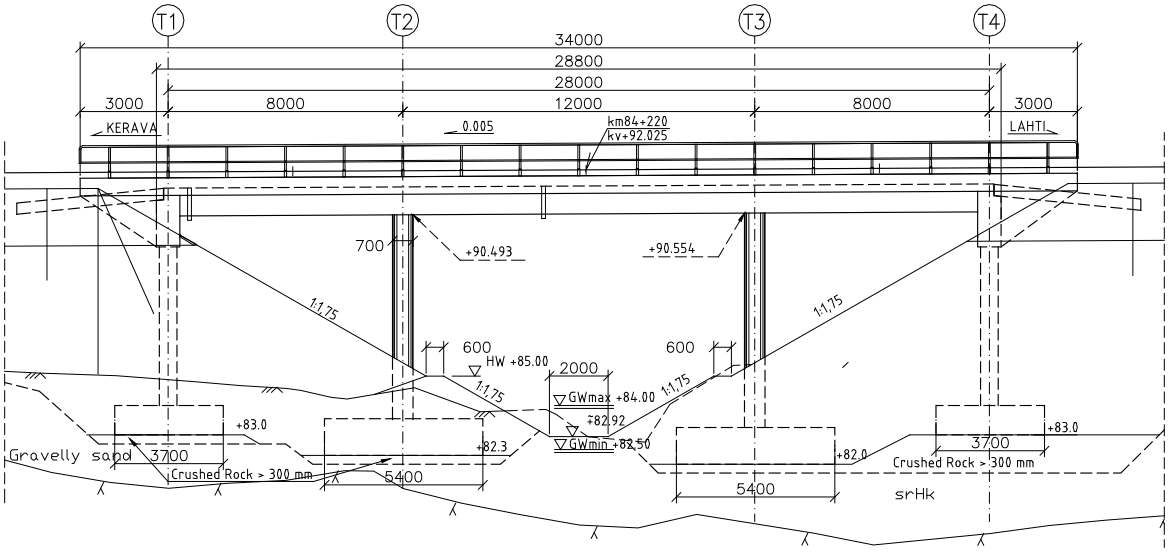

Figure 4.8. Elevation of Tekemäjärvenoja Bridge.

The bridge was monitored with a total of 53 gauges. Monitoring focussed on abutment T4 because the direction of test loading was against embankment T4. The values monitored in this study were:

- Earth pressure between end screen and embankment, 8 gauges
- End screen displacements, 2 gauges
- Embankment soil temperature near end screen, 6 gauges

Locations of earth pressure cells (EPC) are presented in Figure 4.9. Two gauges were at abutment T1 and six at abutment T4.

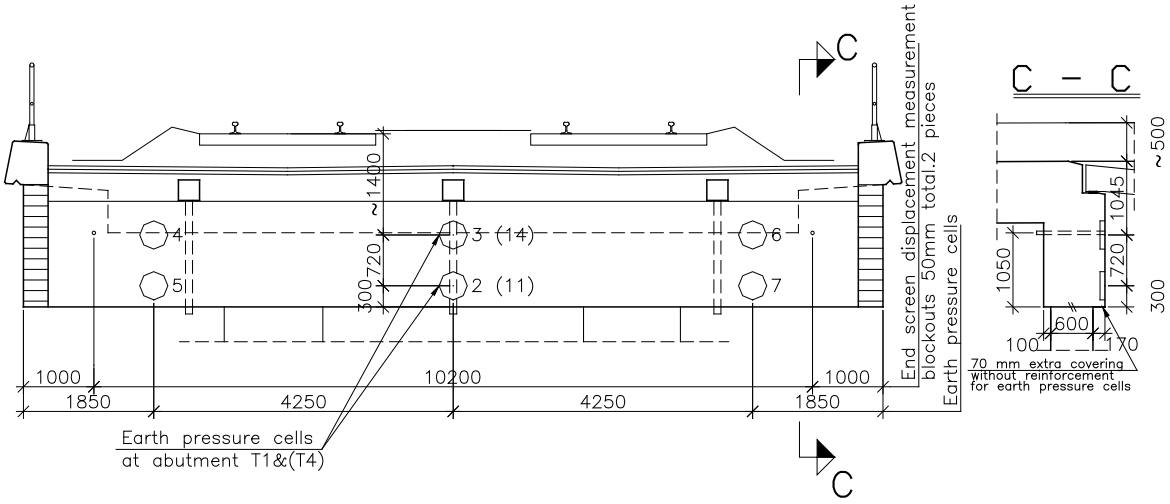

Figure. 4.9 EPC locations at end screen.

End screen displacements were measured at end of the end screen at abutment T4. Further details of monitoring devices are presented in Appendix 3 [85].

4.3.2 Test loading

Short-term loading was implemented with a railway gravel waggon and a post-tensioning jack. Four waggons were parked on the bridge with their brakes on. Eight waggons were parked as counterweights 120 m from abutment T4 so that the induced loading on the bridge corresponded to a braking load situation, see Figure 4.10.

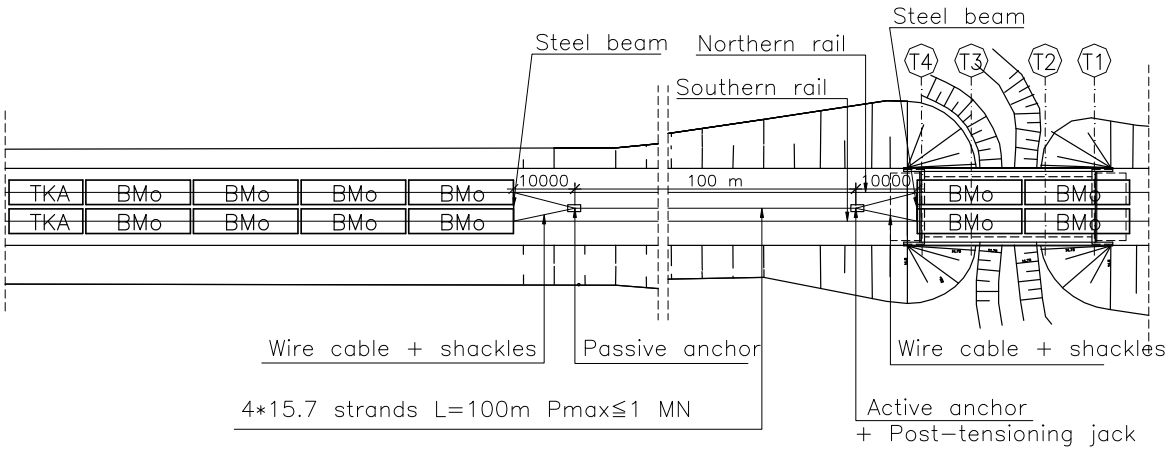

Figure 4.10. Load arrangement plan at Tekemäjärvenoja Bridge. Bmo = Railway gravel waggon, Tka = Railway engine.

Post-tensioning strands with load transfer equipment were placed between the waggon groups. A load between the counterweights and the waggons on the bridge was built up with the post-tensioning jack, see Figure 4.11.

Figure 4.11. Load test at 30.10.2004 on the Tekemäjärvenoja Bridge site. On the left, counterweights. In the middle, post-tensioning jack with a load cell. On the right, railway waggons on the bridge.

The total weight of the railway waggons on the bridge deck was 75 tonnes. The load transfer equipments were designed for 1 MN force. The one-day loading tests were possible because the railway line had not yet been opened to traffic.

4.4 Myllypuro Overpass field test programme

The Myllypuro Overpass (Road bridge) was chosen as a long-term monitoring target in 2007. The bridge is situated about 10 km east of the centre of the City of Tampere on

Highway 3 leading to Ylöjärvi. The Myllypuro Overpass is a continuous post-tensioned concrete beam-and-slab bridge with skewed semi-integral abutments. The bridge is a founded on ground slabs. The horizontal clearance of the bridge is 11.5 m and the structural height of the concrete beams is 1.85 m. The bridge's total thermal expansion length is 70.0 m. Other main dimensions are presented in Figure 4.12.

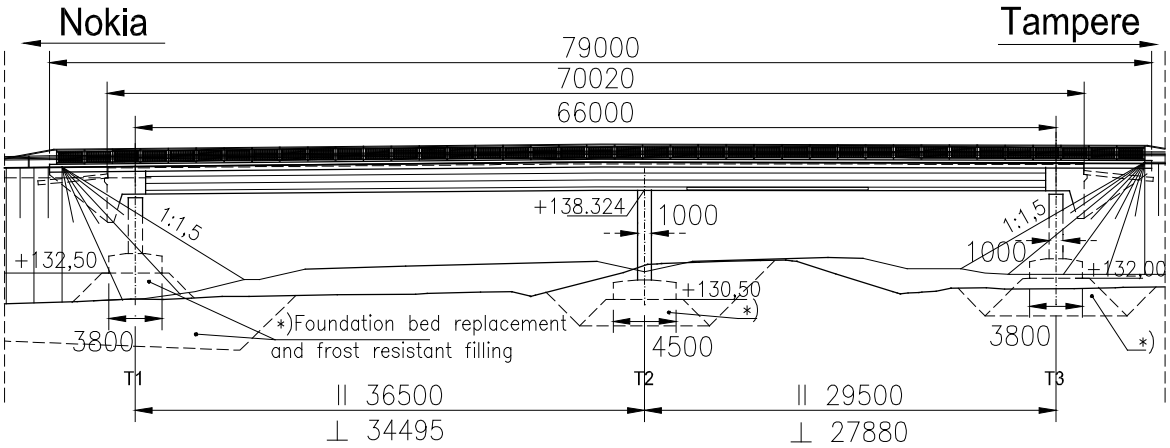

Figure 4.12. Elevation of Myllypuro Overpass. II = Span length ⊥ = Perpendicular length.

The bridge will be monitored with a total of 82 gauges. Monitoring focusses on abutment T3 because it was expected that transversal displacements would be bigger there. The hypothesis was selected because the height of piles at T1 is higher than the height of piles at T2 when longitudinal stiffness is lower. The monitored values are:

- Earth pressure between end screen and embankment, 11 gauges
- Earth pressure between wing wall and embankment, 6 gauges
- End screen displacements, perpendicular (at end screen) and longitudinal (in direction of superstructure centre line), 12 gauges
- Transversal (in direction of superstructure centre line) displacement of superstructure, 2 gauges
- Superstructure temperatures, 18 gauges
- Ambient air temperature, 4 gauges
- Embankment soil temperatures near end screen, 27 gauges
- Displacements between transition slab and end screen, 2 gauges
- Bridge length change measurement during check surveys, 2 positions at edge beams

Monitoring of the bridge started is autumn 2007 with the measurement of superstructure and ambient air temperatures. The rest of the gauges were installed in summer 2008 when

construction of the bridge and its embankments had proceeded so far that it was possible to install gauges.

The locations of the EPCs and end screen displacement gauges are presented in Figure 4.13. The EPCs were grouted to the end screen after stripping the superstructure formwork. Blockouts for end screen displacement gauges were installed in the formwork.

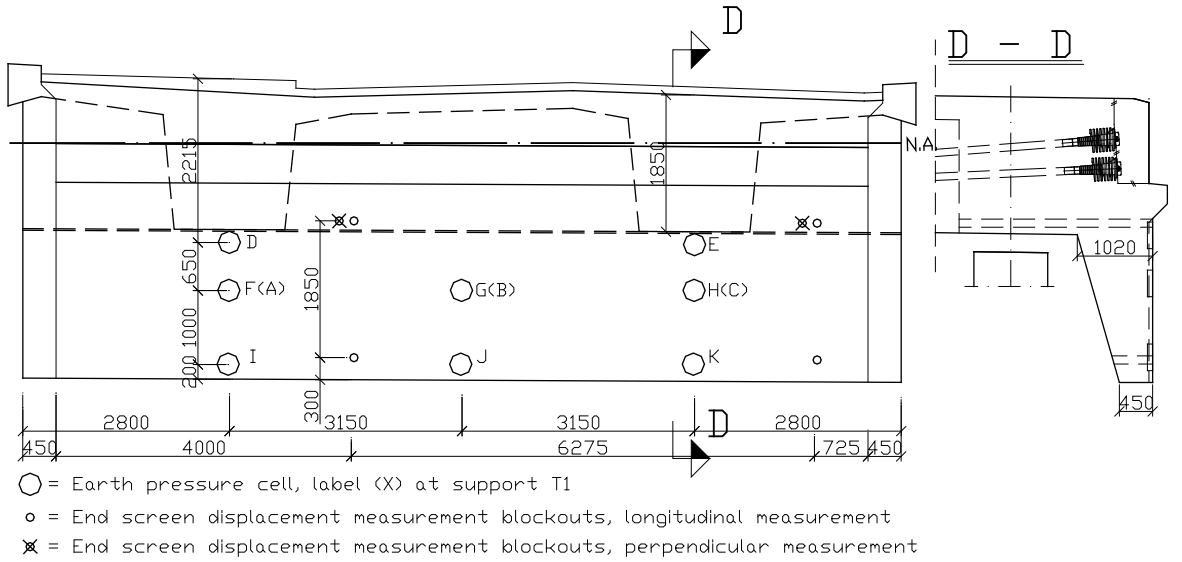

Figure 4.13. EPC and screen displacement gauge locations at Myllypuro overpass abutments.

Six EPCs were installed in the wing walls. The locations of these EPCs are presented in Appendix 4. Superstructure temperature gauge locations are presented in Figure 4.14.

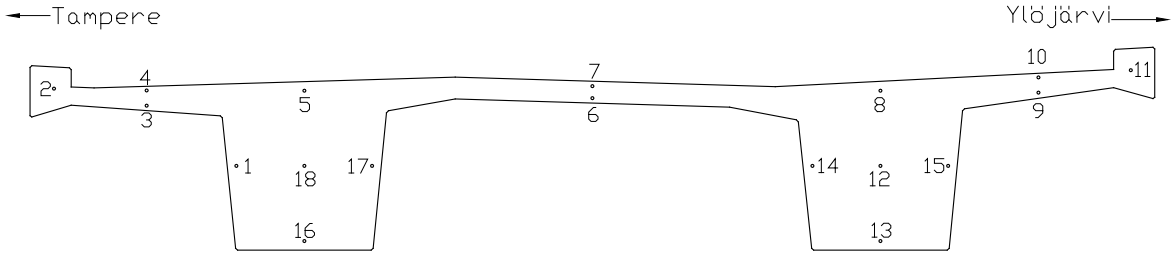

Figure 4.14. Temperature gauges of the superstructure.

Temperature gauge locations were selected so that they can approximate the uniform temperature of the superstructure. They will also be able to monitor the temperature field of the superstructure. Length change of the bridge is measured from the edge beams during check surveys. The goal of these observations is to determine the magnitude of shrinkage and creep in the post-tensioned integral bridge. Further monitoring details are presented in Appendix 4 and [139].

4.5 Conclusions

A lot of new information on integral bridge behaviour was obtained. The monitoring programme covers three bridges, two of which will be monitored over the long term. Some setbacks were also suffered. The measurements on steel pipe piles did not produce the expected results.

Both reinforced and post-tensioned bridge types are monitored including slab and beam-and-slab superstructures.

Both the long-term and short-term monitoring efforts were rather successful under strict timetables, and construction of the bridges was not delayed by the installation of the monitoring devices.

The high temperatures prevailing during the casting of the Myllypuro Overpass were noticeable in the measurement results because the first results were recorded during that phase. Temperature differences across the superstructure cross section were also large. But those results are not part of this study.

5 DATA ANALYSIS

5.1 Overview

The main monitoring period of this study is 10.10.2003-10.10.2007. The monitoring period started with the launching of full monitoring at Haavistonjoki Bridge. The end time was selected so that the monitoring period consisted of full years and the results could be used in this study. Further, the state of end screen displacement was average at the monitoring period time limits.

This chapter examines briefly the Haavistonjoki and Tekemäjärvenoja Bridge test-loading data concerning behaviours linked to the analyses of this study.

This chapter also looks at data from the Finnish Meteorological Institute (FMI) regarding ambient air temperatures. As noted in Section 4.2, the displacements of abutment T4 were excepted to be bigger than those of abutment T1.

5.2 Long-term monitoring data on Haavistonjoki Bridge

5.2.1 Superstructure temperatures

Uniform superstructure and ambient air temperature during the monitoring period are presented in Figure 5.1. Uniform superstructure temperature was calculated from the measurement data according to [84].

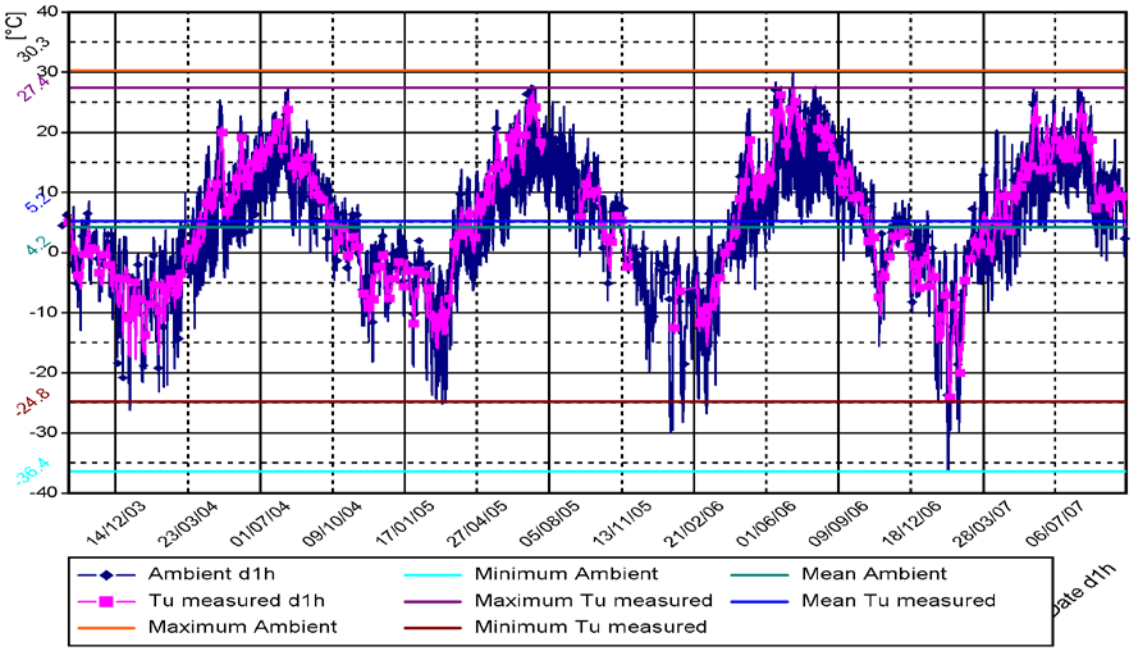

Figure 5.1. Uniform superstructure and ambient air temperature during the monitoring period 10.10.2003-10.10.2007.

The ambient air temperature range was wider than the uniform superstructure temperature range. The maximum ambient air temperature was 30.3°C and the maximum uniform superstructure temperature 27.4°C during the monitoring period. The minimum ambient air temperature was -38.4°C and the minimum uniform superstructure temperature -24.8°C. The minimum values of ambient air and uniform superstructure temperature varied yearly more than maximum values. The average uniform superstructure temperature was 1.0°C higher than the average ambient air temperature during the monitoring period. That is probably due to the thermomechanical behaviour of the superstructure and solar radiation. The effect of solar radiation can be seen in Figure 5.2.

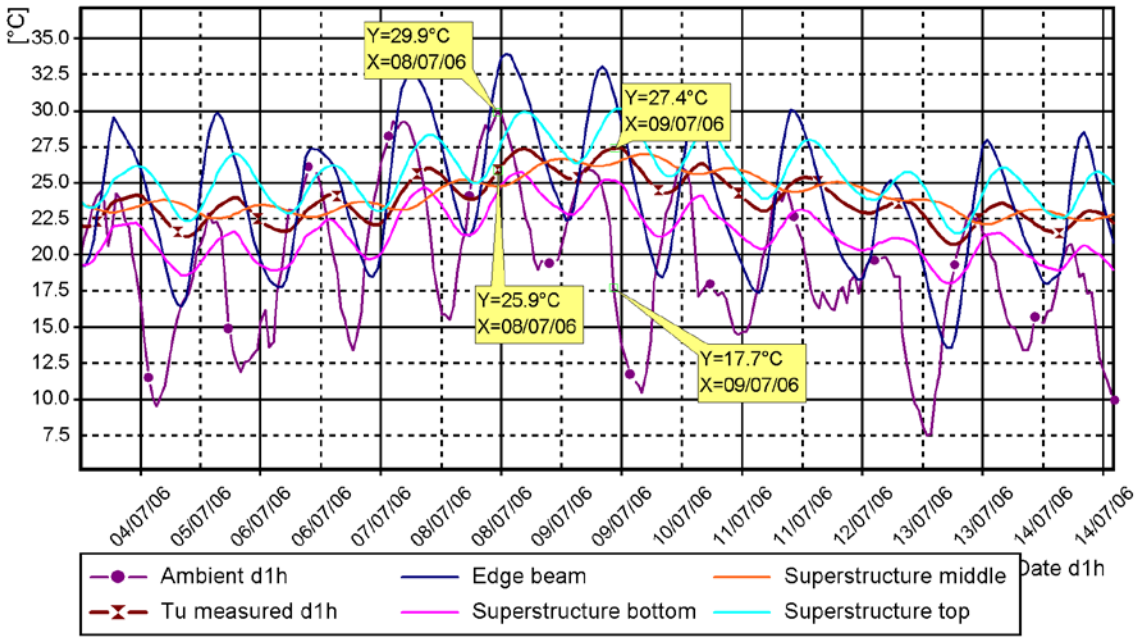

Figure 5.2. Ambient air and uniform temperatures of different superstructure parts during the period 3.7.06-14.7.06.

Figure 5.2 shows that the temperatures of the upper parts of the superstructure vary more than those of the lower and inner parts. The values for structural part are average values from each measuring points in each structural part. The temperature values in yellow boxes are at the time of the highest ambient and uniform bridge superstructures. Temperatures in the upper part of the slab structure vary more than in the lower part and edge beam temperatures vary the most. Solar radiation is absorbed effectively by the asphalt layer and it heats the upper part of the slab structure more than ambient air heats the bottom part of the superstructure. The temperature in the middle part of the superstructure is closest to the superstructure's uniform temperature. A phase difference can also be detected between ambient air and uniform temperature. The uniform temperature lags behind ambient air temperature. This phenomenon is probably the result of the thermomechanical properties

of the superstructure. The superstructure takes time to heat up and cool down, and the phase difference occurs between the ambient and the bridge temperatures. The ambient air and uniform temperatures of different superstructure parts are also presented by year during the monitoring period in Appendix 5.1. Figure 5.3 shows the linearly interpolated temperature field of the superstructure during the warm period.

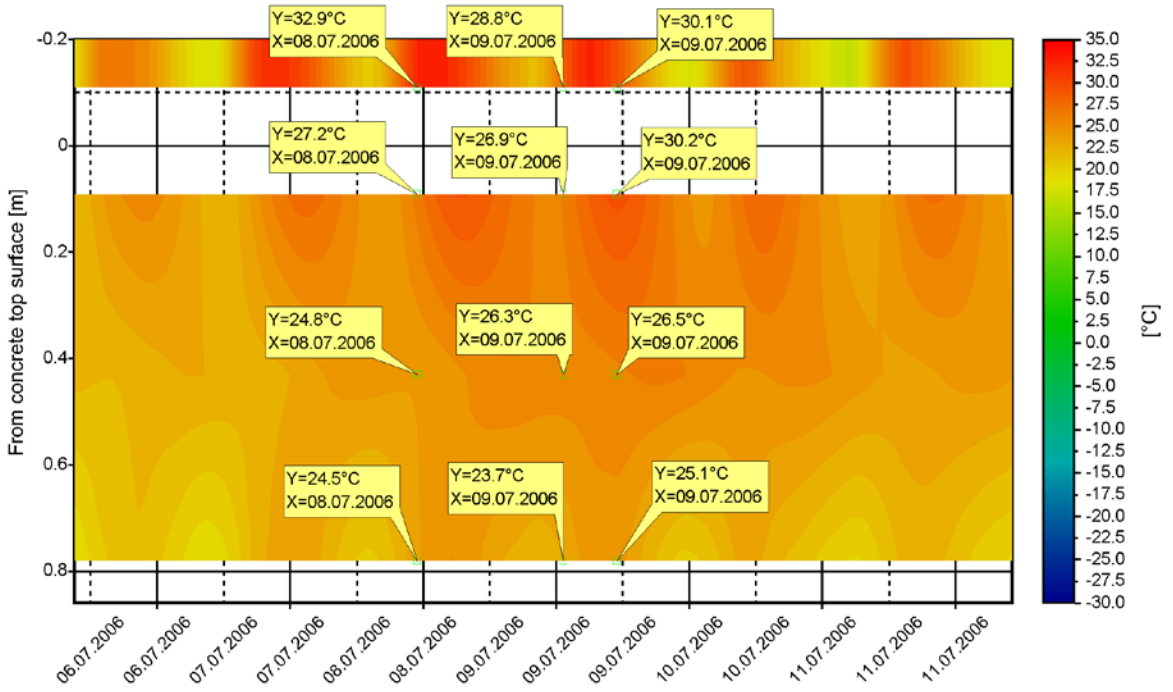

Figure 5.3. Linearly interpolated temperature field at vertical section based on measured temperatures of superstructure during the period 6.7.06-12.7.06. The upper part contour depicts the edge beam. The superstructure concrete top is at level 0.0 m and the bottom at level 0.86 m.

The values of the first column were measured during the warmest ambient air temperature presented in Figure 5.3. The values of the last column represent the time when the uniform temperature was highest during the studied period. The values of the middle column were measured on the same day when ambient air was at its warmest. The measurements show that it takes time for heat energy to travel to the inner parts of the superstructure. In addition, the edge beam cooling rate is higher than those of other parts. The temperature of the superstructure increases also through the bottom induced by ambient air. Further, the time of the warmest ambient air temperature is not the same as the time of the highest uniform temperature. A high positive temperature difference, meaning the temperature of the top part of the structure is higher than that of the lower parts, occurs at the same time as the highest uniform temperature. This phenomenon will be discussed later in this paragraph. Figures 5.4 and 5.5 show the ambient air and uniform temperatures of the different superstructure parts and the linearly interpolated temperature field of the superstructure during the lowest uniform temperature.

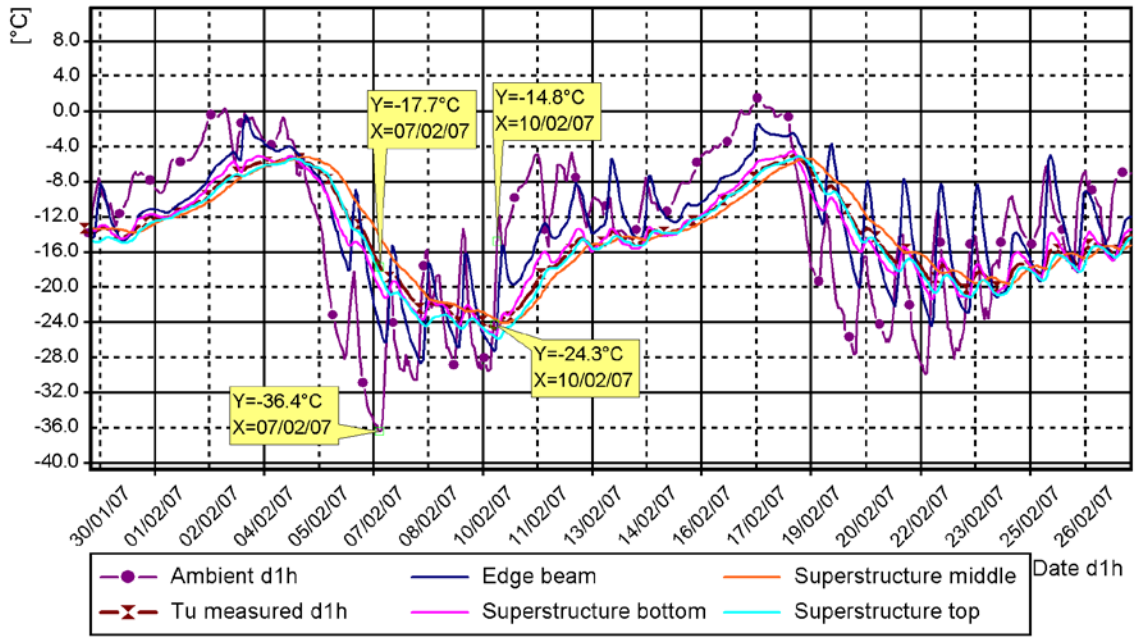

Figure 5.4. Ambient air and uniform temperatures of different superstructure parts during the period 30.1.07-27.2.07.

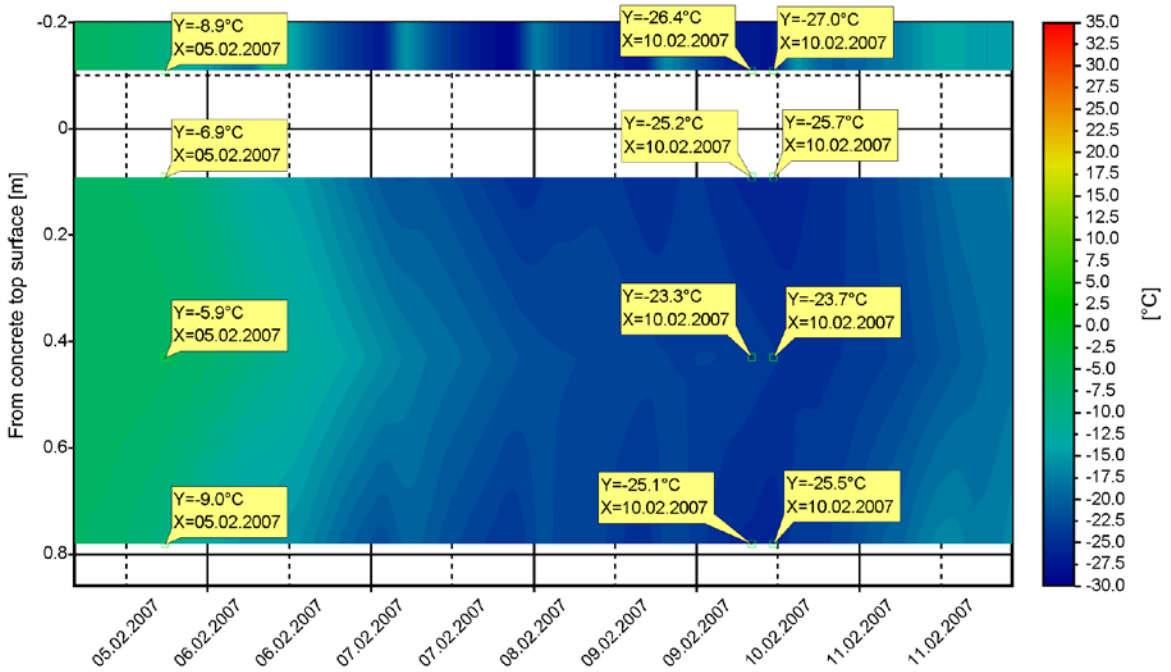

Figure 5.5. Linearly interpolated temperature field at vertical section based on measured temperatures of superstructure during the period 4.2.07-12.2.07. The upper part contour depicts the edge beam. The superstructure concrete top is at level 0.0 m and the bottom at level 0.86 m.

The values of the columns in yellow boxes represent the period of lowest ambient air and uniform temperatures in wintertime. Ambient air temperature changed rapidly during the studied period in Figure 5.5. Cooling speed at the top and bottom of the slab was of the same magnitude. Temperature difference was not at its highest negative value during the studied low uniform temperature period in Figure 5.5. Temperature difference between the

top and bottom levels of the superstructure slab as function of uniform temperature is presented in Figure 5.6.

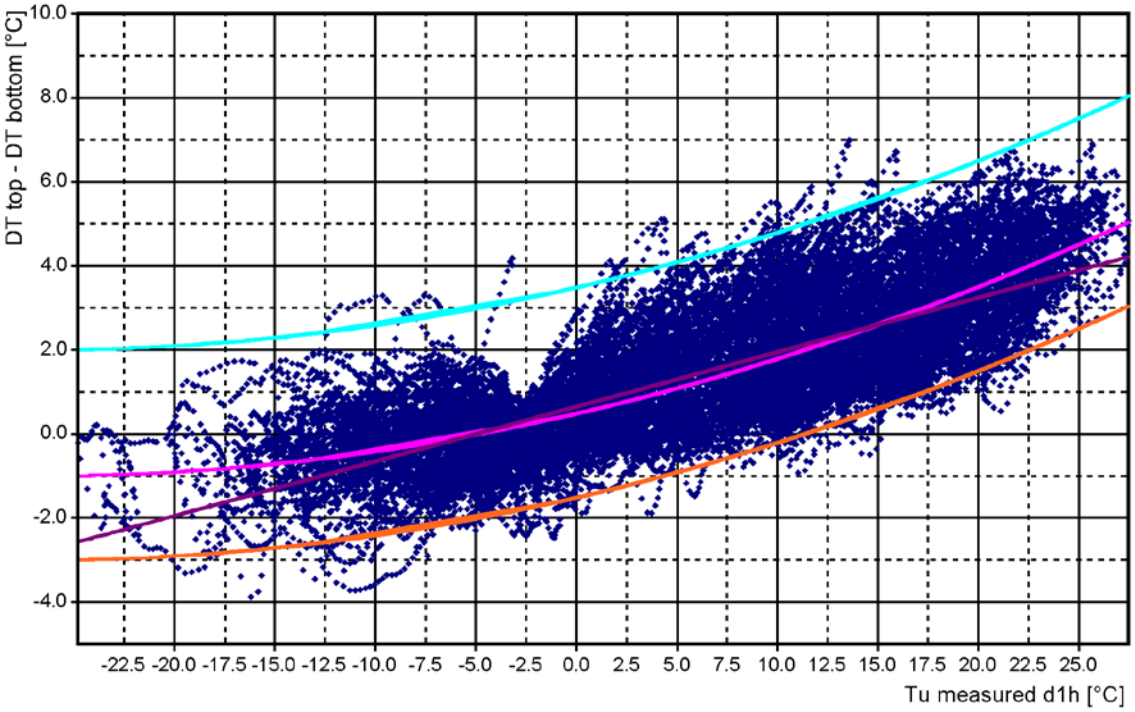

Figure 5.6. Temperature difference between top and bottom levels of the superstructure slab during the monitoring period 10.10.2003-10.10.2007.

High positive temperature differences occurred at times of high uniform temperatures. Negative temperature differences did not occur during high uniform temperatures. In the fully integral bridge, a positive temperature difference reduces abutment pile bending stresses induced by positive uniform temperature changes [66]. A negative temperature difference would be unfavourable for the abutment piles of the fully integral bridge in case of a positive uniform temperature change. Correspondingly, a negative temperature difference will reduce pile bending stresses at a low uniform temperature change in the fully integral bridge. However, a negative temperature difference may not coincide with the lowest uniform temperature. A straight and a parabolic regression line are also shown. The parabolic regression is shown also with offsets of -2ºC and +3ºC.

Figure 5.7 shows the linearly interpolated temperature fields of the superstructure at the time of the highest positive and negative temperature differences.

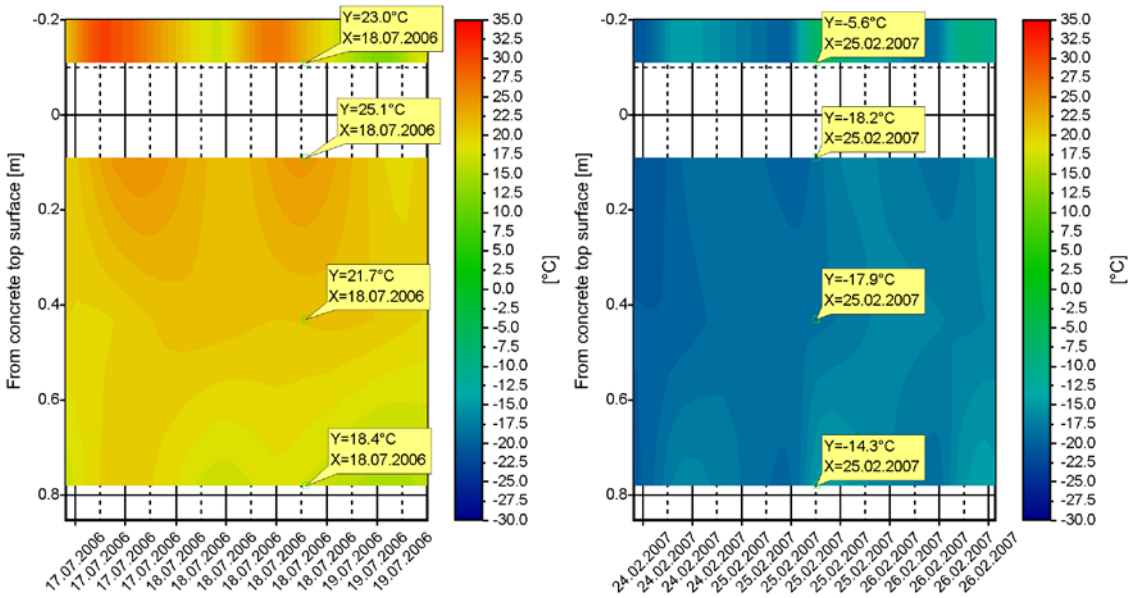

Figure 5.7. Linearly interpolated temperature field of vertical section based on measured temperatures at highest positive and negative temperature differences between measured top and bottom levels of superstructure slab. Positive difference at 18.7.06 and negative at 25.2.07.

Uniform temperature in the high positive temperature difference state was 21.6°C and –15.9°C in the high negative temperature difference state. The high positive temperature difference occurred when ambient air temperature had decreased rapidly. In that state the asphalt layer may have absorbed thermal energy which provided it some insulating effect against cooling. Probably the most important factor as regards the high temperature difference is the effect of solar radiation, especially on the asphalt layer. When ambient air temperature decreases, the decrease in solar radiation may be minimal during a whole day if the weather stays clear. The temperature of the bottom of the slab falls more rapidly than the top part's because ambient air warms the bottom surface while solar radiation warms the top. The impact of the solar radiation was not measured. A corresponding effect occurs also in the high negative temperature difference state.

Before the high positive temperature difference state, ambient air temperature changed from 18.5°C to 10.7°C within 14 hours, and before the high negative temperature difference state it changed from -18.2°C to -8.8°C within 7 hours.

The edge beam behaved most actively, but its effect on the behaviour of the whole superstructure was quite small because the edge beam affected the superstructure's moment of inertia rather little. Further, it is recommended to design the stresses of the whole superstructure without considering the edge beam, which is a “sacrificial” structural part [48]. On these grounds, the edge beam was excluded from the temperature difference calculations.

Yet, this study is not focussed on the size of temperature differences because uniform temperature is more determinant. An important finding is how closely correlated temperature difference and uniform temperature are.

5.2.2 Embankment temperatures

The temperatures of the embankment were measured 2.4 m from the outer surface of the end screen. The linearly interpolated temperature field of the embankment during the monitoring period is presented in Figure 5.8.

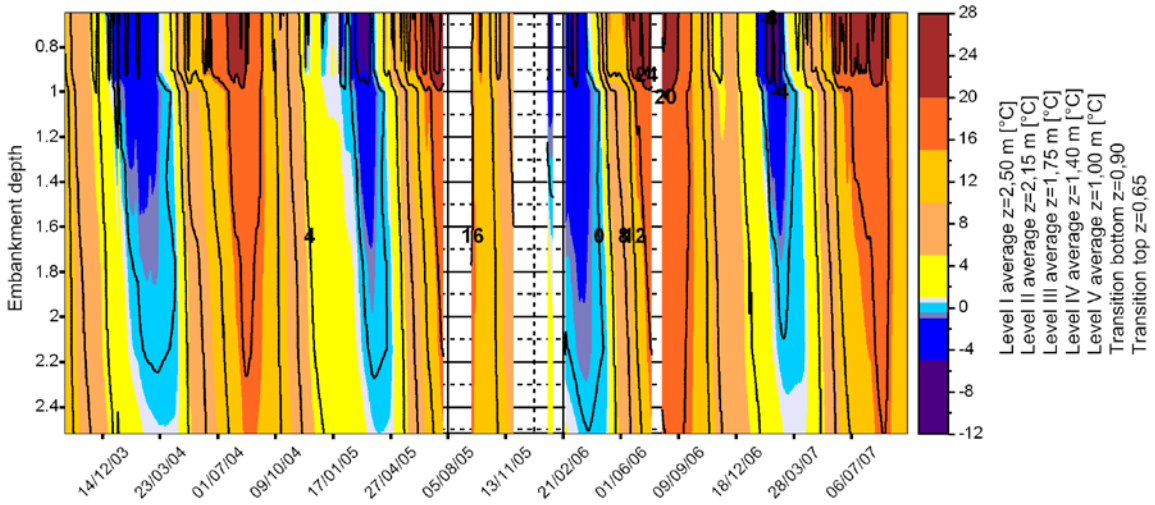

Figure 5.8. Linearly interpolated embankment temperature field at vertical section based on measured temperatures of embankment 2.4 m from end screen during the monitoring period 10.10.2003-10.10.2007.

The finest divisions of the temperature colour legend near 0°C are: -1.0, -0.5, 0.5 and 1.0 °C based on soil behaviour near the freezing point. Phase transition of water between liquid and solid, or vice versa, in soil requires energy absorption to water or from water. This leads to a phenomenon where temperature changes quite slowly near 0°C. An important factor related to embankment temperatures is the frost penetration depth behind the embankment soil which has a impact on the stiffness of the embankment soil. The average maximum annual frost penetration depth during the monitoring period was 2.2 m. Frost penetration depth at abutment T1 was of the same magnitude, see Appendix 5.1. The quite deep frost penetration compared to building foundations is the result of the energy flow through and beneath the end screen to ambient air combined with the lack of a snow cover on the road surface. Figures 5.9 and 5.10 show the linearly interpolated temperature fields of the embankment at the time of deepest frost penetration during the studied period at 29.3.2006 and the subsequent thawing state at 24.4.2006.

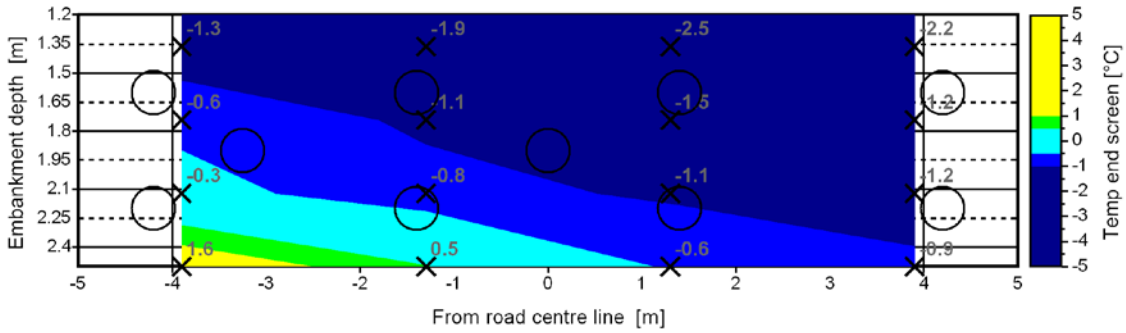

Figure 5.9. Linearly interpolated embankment temperature field based on measured temperatures of embankment 2.4 m from end screen at 29.3.2006. Frost was at its deepest during the monitoring period. Circles mark EPC locations. Crosses mark temperature gauge locations.

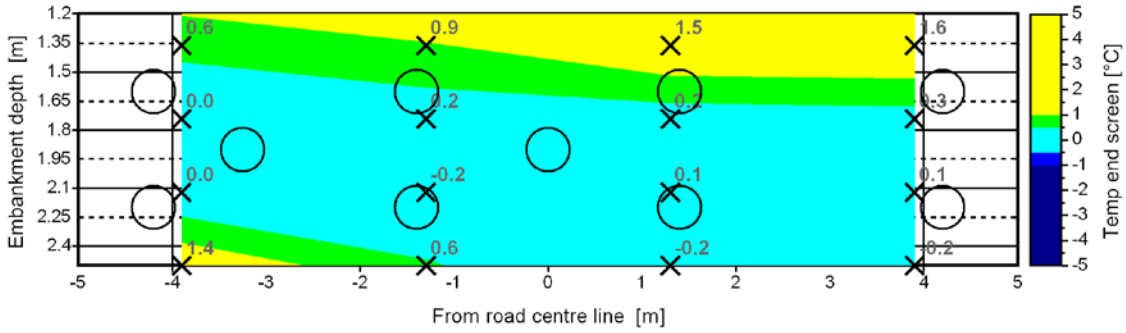

Figure 5.10. Linearly interpolated embankment temperature field based on measured temperatures of embankment 2.4 m from end screen at 2.5.2006. Frost is in melting stage. Circles mark EPC locations. Crosses mark temperature gauge locations.

Frost has penetrated quite deeply when ambient air and solar radiation conditions are intensive in spring. This affects earth pressure development behind the end screen. The phenomenon is discussed in Paragraph 5.2.4. All in all, the embankment is heavily frozen near the bridge end screen. Thawing starts both at the top and the bottom. Uneven freezing of the embankment leads to uneven earth pressure distribution and abutment displacements. The linearly interpolated temperature field of the embankment after a rapid ambient air temperature decrease in February 2007 is presented in Figure 5.11.

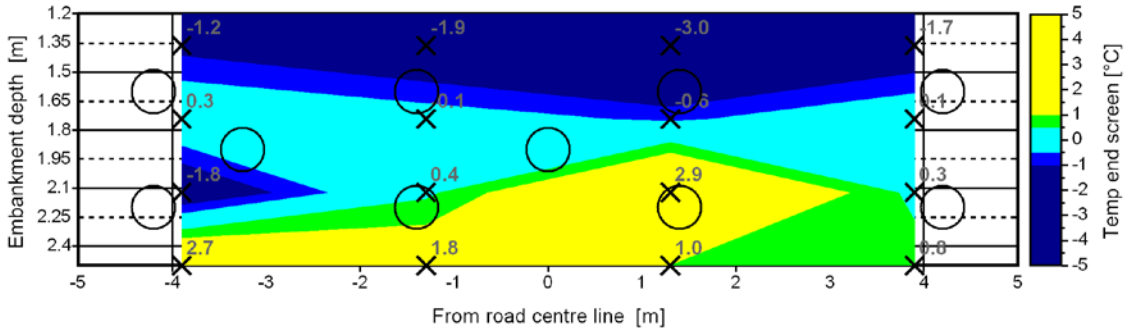

Figure 5.11. Linearly interpolated embankment temperature field based on measured temperatures of embankment 2.4 m from end screen at 28.2.2007. Frost is at a rapid propagation stage. Circles mark EPC locations. Crosses mark temperature gauge locations.

Compared to Figure 5.9, the temperature gradient at the top is heavier because the weather had changed rapidly. There was also a cold zone at a depth of 2.1 m depth in the end

screen area. It may be the result of a thermal energy flow beneath the end screen or the wing wall through the embankment slope. Uneven snow cover on the embankment slope may also contributed to the freezing of the embankment soil.

5.2.3 Superstructure end screen displacements

Displacements of end screens (abutments) during the monitoring period are presented in Figure 5.12. Measurement results “Meas bar 3 surveys”, “Meas T1 change” and “Calc T1 change” concern abutment T1 (see Figure 4.1) while “Meas bar 10 surveys” and “Meas T4 change” concern abutment T4 (see Figure 4.1). In “surveys” indices were measured at the same locations where monitoring devices measured T1 and T4 changes. That was done to guarantee the accuracy of the results.

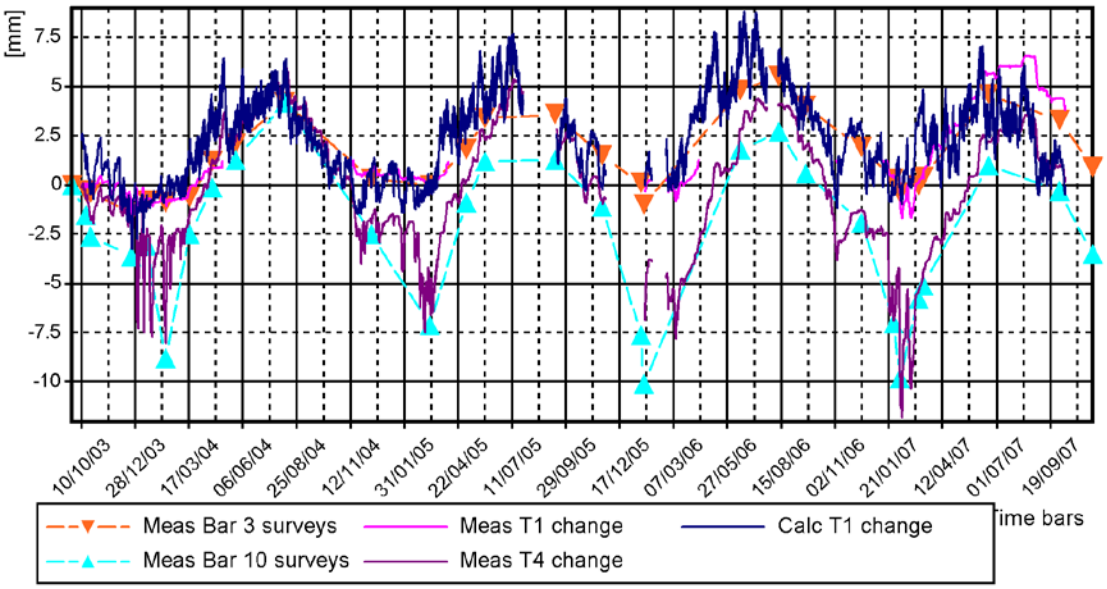

Figure 5.12. Displacements of abutments during the monitoring period 10.10.2003-10.10.2007. “Meas T1 change” and “Meas T4 change” were measured with monitoring devices. “Meas bar 3 surveys” and “Meas bar 10 surveys” changes were measured with a sliding gauge during check surveys at the same locations where automatic measurements took place.

Here, the designations of abutment displacements are different than in structural analyses because a more descriptive designations are better when discussing monitoring data. For example, in structural analyses D_X stands for “meas T4 change”. Measured changes at abutment T4 and measured uniform temperature are presented in Appendix 5.1, Figure 13. The automatic measuring gauge for “Meas T1 change” did not work properly at the longest elongations of the bridge. Abutment T1 displacements have been replaced with “Calc T1 change” values calculated from bridge superstructure temperature changes. As can be seen in Figure 5.12, the calculation was sufficiently accurate. The range of abutment T4 displacements was: 6 - (-12) = 18 mm and that of abutment T1: 8 - (- 4) = 12 mm. Abutment

T4 moved more than abutment T1. The overall trend for abutment T4 has been decreasing while that for abutment T1 has been increasing compared to the initial state. They are the result of longitudinal movement of the superstructure. Long-term longitudinal displacement stands at 3 mm as can be noticed from Figure 5.13. Figure 5.13 shows abutment T4 displacement as function of bridge length change.

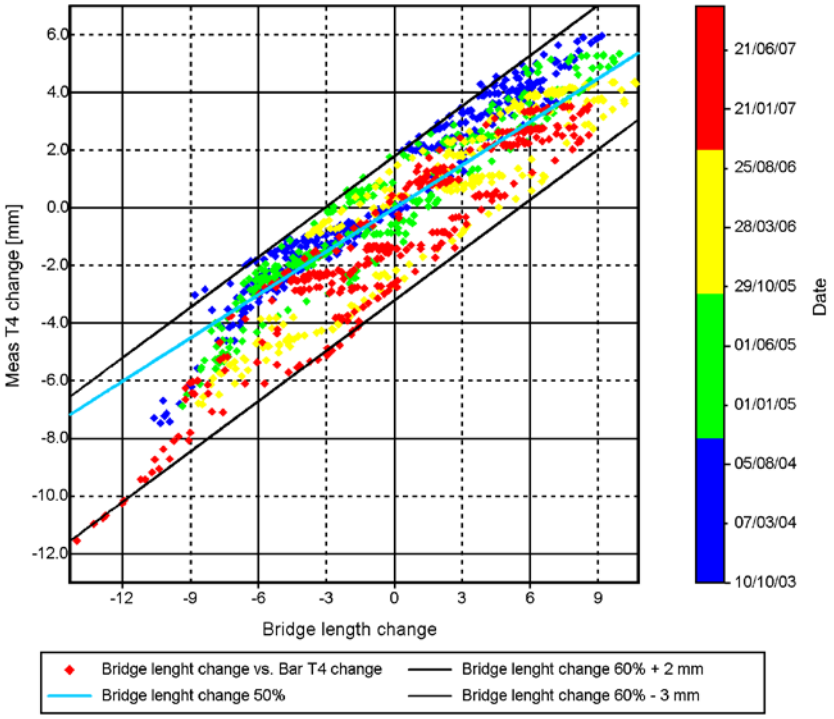

5.13. Bridge length change compared to abutment T4 displacements during the monitoring period 10.10.2003-10.10.2007. Bridge length refers here to the total thermal expansion length.

The longitudinal displacement of the bridge superstructure varied depending on displacement state of abutments. The vertical difference between the 50% bridge length change line and the measured results consists of the longitudinal movements and shrinkage of the concrete bridge superstructure. The difference was at its biggest 5 mm during the coldest time of the monitoring period and 2 mm during the warmest period. Concrete shrinkage cannot be determined from the results because of the malfunctioning of a measurement gauge at abutment T1. Further, it can be seen that the displacements of abutment T4 were 60% of bridge length changes based on regression calculations. That would make displacements of abutment T4 (60/(100-60)) = 1.5 times larger than those of abutment T1 excluding longitudinal movements and concrete shrinkage. However, that relationship changed continuously between states. Further, the displacements of ”Meas T4 change” include part of the rotation of abutment T4 and possible displacement of the anchor plate of the end screen displacement gauge. However, an important finding is that bridge abut-

ment displacement proportions vary from one state to another and especially that some abutment displacements are much bigger than others.

Rotation values of abutment T4 are presented in Figure 5.14. They were calculated from sliding gauge measurements at the bridge. Rotation is calculated on the basis of measured displacements at different levels from the initial position with the formula:

$$r_{end} = \frac{\Delta_{top} - \Delta_{bottom}}{d_m} \quad (5.1)$$

where
Δ_{top} = measured displacement change at top measuring point [m]
Δ_{bottom} = measured displacement change at bottom measuring point [m]
d_m = distance between measurement points [m]
r_{end} = rotation of end screen [rad]

Uniform temperature T_U of the bridge at measurement times is also presented in Figure 5.14.

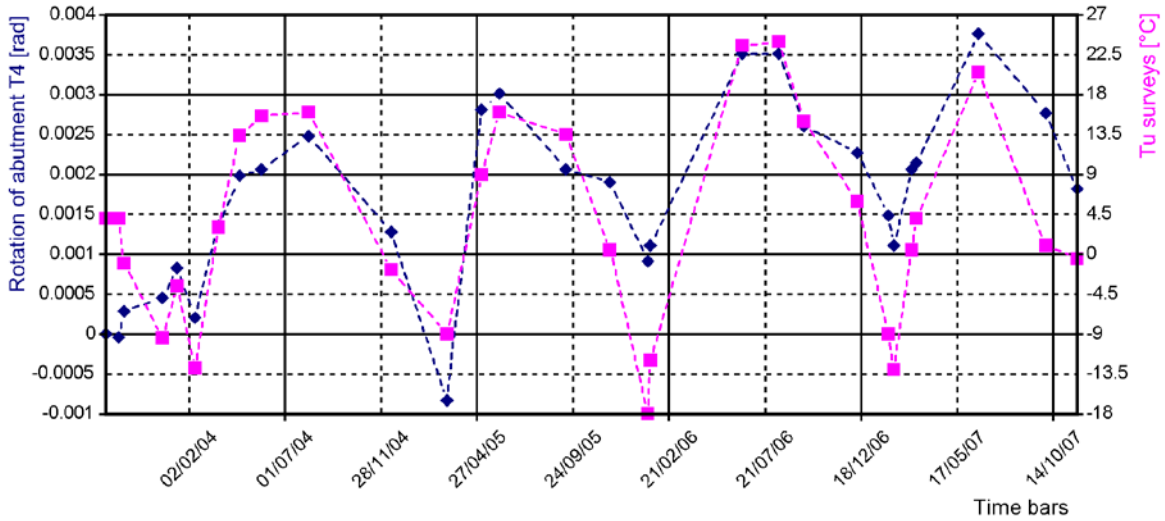

Figure 5.14. Rotation of abutment T4. Values were calculated from sliding gauge measurements during the period 10.10.2003-20.11.2007.

The rotation of abutment T4 increased during the monitoring period, probably due to movements of the embankment and compaction of embankment soil. The uniform temperatures show that the change was not caused by changes in uniform temperatures. The rotation was 0.0025 rad higher at the end of the period than at the beginning. The longitudinal movement of abutment T4 also decreased rotation.

5.2.4 Earth pressures

Earth pressures between end screens and embankments varied during the monitoring period, the values are presented in Figure 5.15. The range of earth pressures was 145 - 0 = 145 kPa. High earth pressures were observed from January to September. Low earth pres-

sures were observed between autumn and winter months. Yearly cycles of earth pressure values can be observed. Some earth pressure cells, e.g. the EPC K, measured higher maximum values in summer while some, e.g. the EPC J, recorded lower values. Average maximum earth pressures in summer rose slightly during the monitoring period. The average earth pressure values measured by the EPC H, I, K, L, M, N, O, P, and Q are presented in Appendix 5.1.

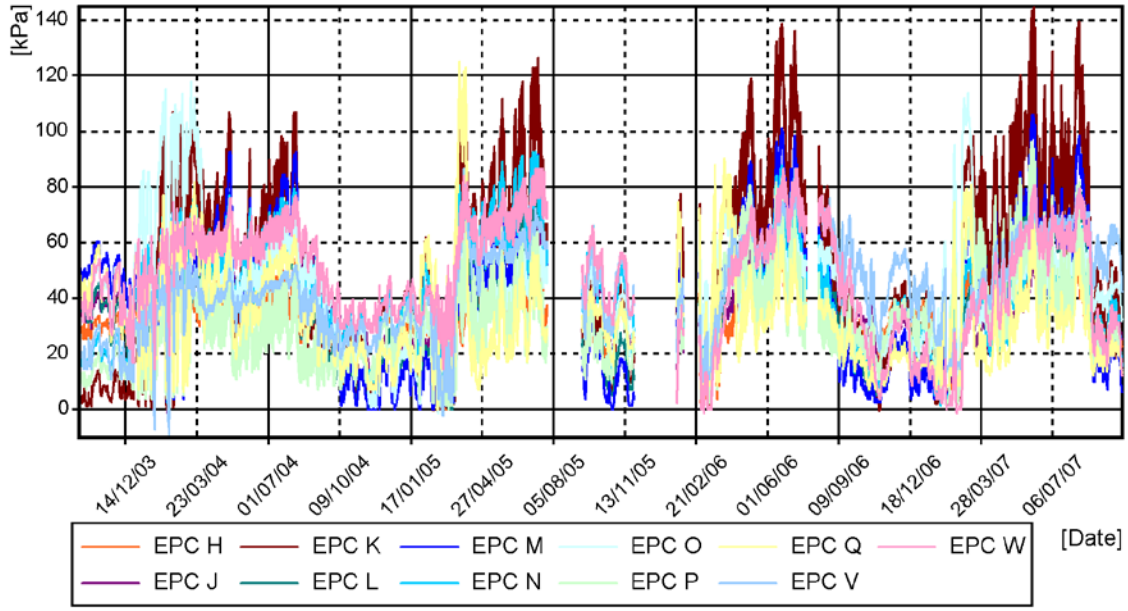

Figure 5.15. Earth pressures between end screen and embankment during the monitoring period 10.10.2003-10.10.2007. Locations of EPCs are presented in Figure 4.2.

The embankment probably compacted during the monitoring period. The compaction was also observed in the related section of the main project [75]. Yearly earth pressure values during the monitoring period are presented in Appendix 5.1. Earth pressures at the bottom of columns at intermediate support T3 against the embankment are also presented in the diagrams discussed in [75]. Earth pressure developments in summer winter at a depth of 1.6 m are presented in Figures 5.16 and 5.17.

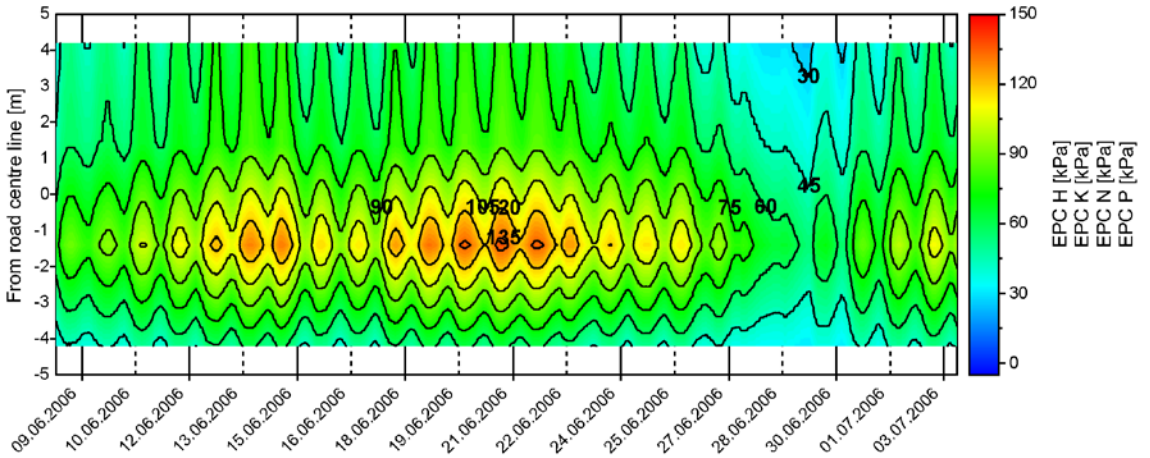

Figure 5.16. Linearly interpolated earth pressure field at horizontal section z = 1.6 m based on measured earth pressures between end screen and embankment during the period 9.6.2006-5.7.2006.

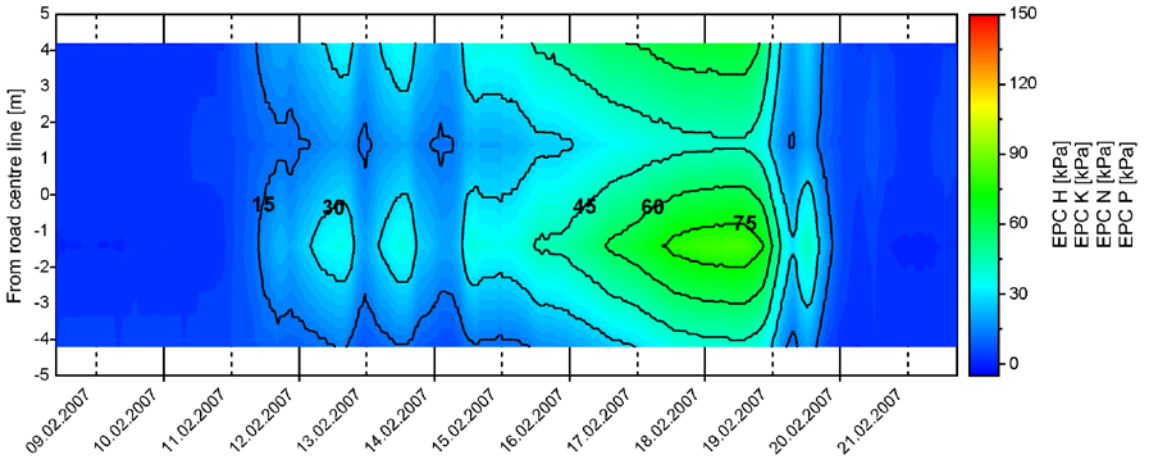

Figure 5.17. Linearly interpolated earth pressure field at horizontal section z = 1.6 m based on measured earth pressures between end screen and embankment during the period 9.2.2007-23.2.2007.

Daily earth pressure changes were rather clear in summer. The uniform temperature of the superstructure varied in daily cycles and induced varying earth pressures against the end screen. Earth pressures concentrated on the middle part of the end screen in the lateral direction of the bridge. Temperature changes were not as regular and the earth pressure distribution against the end screen was not as symmetrical in winter as in summer. Similar behaviour was recorded by the EPCs also at another depth. The vertical sections of the earth pressure distribution determined for the same period as the horizontal sections presented above are shown in Appendix 5.1. Earth pressure development due to displacement in winter differs from that occurring in summer due to the freezing of soil. Earth pressure distribution against the end screen at the beginning of the monitoring period (hereafter the initial stage) is presented in Figure 5.18.

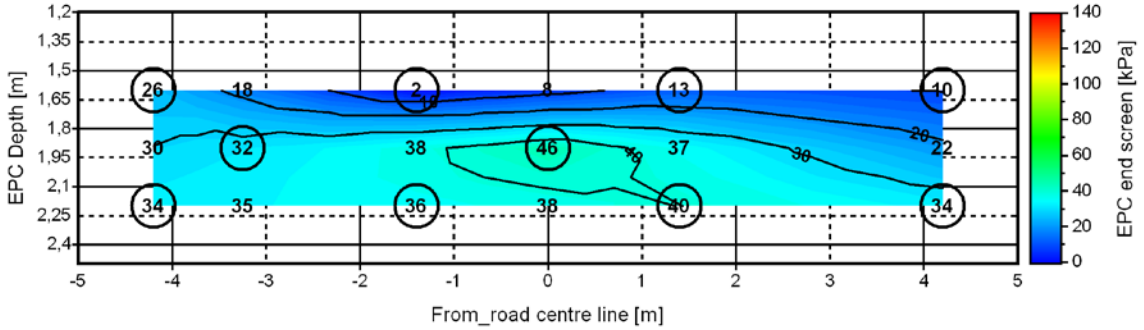

Figure 5.18. Linearly interpolated earth pressure field at the end screen at the beginning of the monitoring period on 10.10.2003.

The initial stage earth pressure distribution was rather linear compared to earth pressure increases along the depth. However, some temperature change induced displacements had developed before the first measurements of the monitoring period at Haavistonjoki Bridge. After several displacement cycles, earth pressure distribution changed. Earth pressure distribution when earth pressures were at their highest during the monitoring period is presented in Figure 5.19. In deviation from the non-rotational wall subject to a single loading cycle, the highest earth pressure occurs at the top of the measurement area of the end screen.

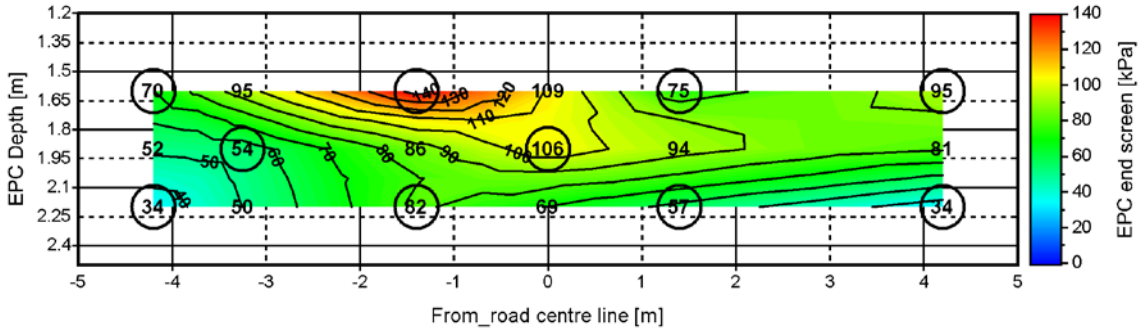

Figure 5.19. Linearly interpolated earth pressure field at the end screen at 6.6.2007 when earth pressures were at their highest during the monitoring period.

The maximum value is 145 kPa. At the bottom of the measurement area of the end screen, the maximum value is 82 kPa. The average change from the initial stage is 83 kPa at the top and 34 kPa at the bottom of the measurement area of the end screen. Similar behaviour was observed during other high earth pressure stages in summer. The high earth pressures at the upper part are probably caused by the transition slab. It is a very rigid component of the abutment structure in the embankment soil [75]. The soil must have compacted against the transition slab during displacement cycles. This is suggested by the development of the EPC K values in Figure 5.15 and the displacements between the transition slab and end screen in Paragraph 5.2.6. The earth pressure distribution during the high-pressure frozen

soil stage is more uneven than during the high-pressure unfrozen stage as can be seen in Figure 5.20.

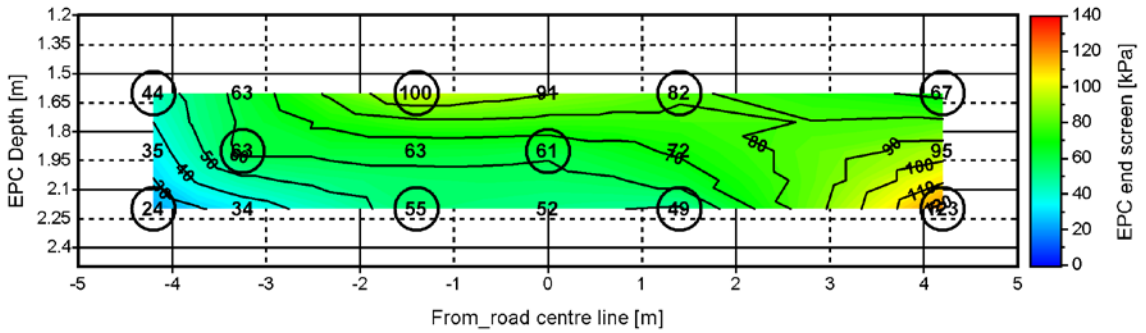

Figure 5.20. Linearly interpolated earth pressure field at end screen at 3.4.2005 when earth pressures were their highest in the frozen soil stage of the monitoring period.

The maximum value is 123 kPa. At the top of the measurement area of the end screen, the maximum value is 100 kPa. The average change from the initial stage is 61 kPa at the top and 54 kPa at the bottom of the measurement area of the end screen. The high earth pressure distribution that developed in the frozen soil stage was induced by simultaneous freezing of the embankment soil and displacement of the abutment due to uniform temperature changes in the superstructure. Probability calculations are excluded from this study, but the probability of a large increase in uniform temperature combined with a frozen embankment may be rather high, and may lead to higher earth pressures in spring than in summer. The deviations of the high earth pressure distribution between yearly frozen soil stages are relatively large compared to the high earth pressure stage of the unfrozen period. The high earth pressure distributions and changes from the initial stage to summer stage and high earth pressure stage to frozen soil stage are presented in Appendix 5.2. The deviation between frozen soil stages is probably due to the uneven freezing of the embankment soil. Earth pressure development as function of abutment displacement at abutment T4 at EPCs K and L is presented in Figure 5.21. Corresponding figures for EPCs N and O are presented in Appendix 5.3.

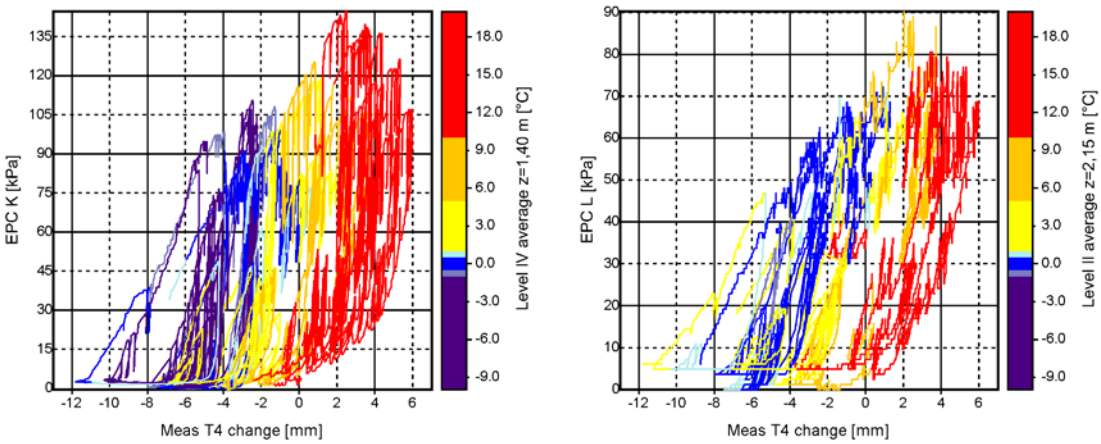

Figure 5.21. Earth pressure displacement as function of soil temperature at the locations of EPCs K (z = 1.6 m) and L (z = 2.2 m). Displacement refers to displacement of abutment T4.

The displacement-earth pressure behaviour is very hysteretic. The hysteresis loop remains much the same the year round during the monitoring period. Earth pressures have increased during the monitoring years at the locations of EPCs K and L. Displacement-earth pressure behaviour of EPC K and L with a colour legend indicating monitoring year are presented in Appendix 5.3. The colour legend of Figure 5.21 indicates soil temperature at the depth of the presented EPCs. At the frozen soil stage, earth pressures are higher compared to the unfrozen stage, the displacement level being the same, see Figures 5.22 and 5.21. Two displacement-earth pressure hysteresis loops can be observed in the frozen and unfrozen soil stages. In measurement results, the behaviour resembles co-ordinate transformation between these two stages. In spring when soil is in the thawing stage, earth pressure creeps from the frozen (blue) to the unfrozen (yellow) soil hysteresis loop. The displacement-earth pressure relationship with a seasonal colour legend is presented in Figure 5.22. Corresponding figures for EPCs K, L, N and O are presented with a colour legend indicating monitoring years in Appendix 5.3.

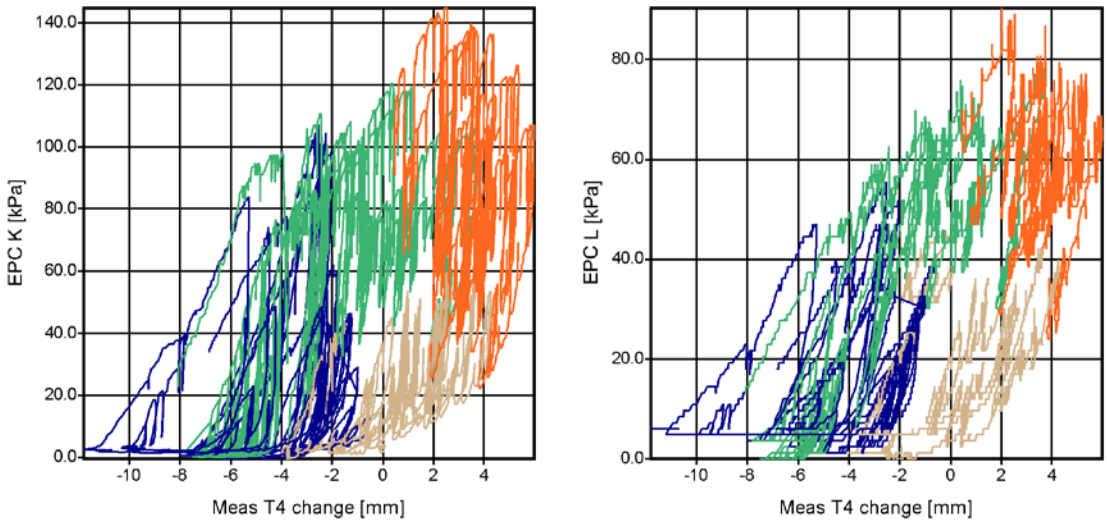

Figure 5.22. Earth pressure displacement as function of seasons at the locations of EPCs K (z = 1.6 m) and L (z = 2.2 m). Displacement refers to displacement of abutment T4. Brown = Sep-Nov, Blue = Dec-Feb, Green = Mar-May and Orange = Jun-Aug.

The seasonal colour legend shows that high earth pressures occurred at the frozen soil stage while rather small abutment displacements developed during the winter and spring seasons. The highest earth pressures developed in summer resulting in much larger displacements than during the frozen soil stages. The viscous behaviour of the frozen soil is also significant [75]. The displacement rate of the end screen is very slow compared to the viscous properties of soil at the time when the creep of soil benefits integral bridges [75].

Earth pressures between end screens and embankments at T1 and T4, in the corresponding locations at a depth of 1.6 m, are presented in Figure 5.23.

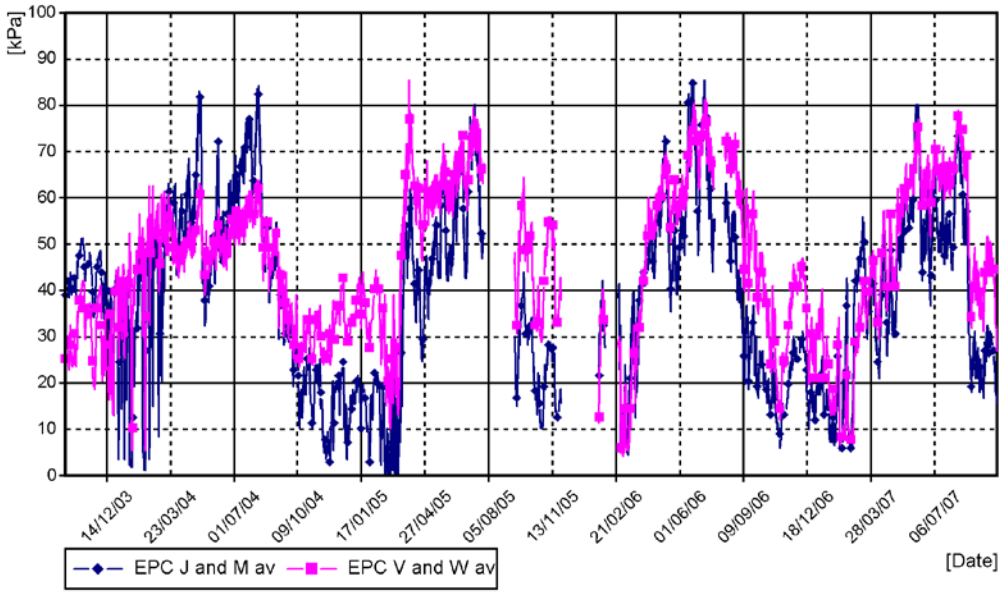

Figure 5.23. Average earth pressures between end screen and embankment during the monitoring period 10.10.2003-10.10.2007 at EPCs J, M, V and W at a depth of z = 1.9 m.

Earth pressures between abutments differed most during the first two monitoring years. In summer 2004, earth pressure was higher at abutment T4 while in winter 2004-2005 and summer 2005 it was higher at abutment T1. During the last two monitoring years earth pressures became more even. A certain longitudinal equilibrium between embankment stiffnesses probably developed due to the longitudinal displacements of the bridge superstructure. Further, slope T4 underwent downward displacements, especially during 2005. Slope T1 also underwent downward displacements but their magnitude was smaller than at abutment T4. Displacements probably increased the horizontal force against the piles more at abutment T4 than at abutment T1. Thereby the longitudinal equilibrium of the superstructure was balanced by the higher earth pressure against abutment T1. However, the larger displacements of abutment T4 than abutment T1 were probably the result of different modulus of subgrade reaction between embankment soils behind the end screens. Further, it is possible that the difference between the earth pressure resultants for the whole end screen at the abutments is not very large because earth pressures were measured only at two locations at abutment T1 while earth may have been distributed differently between the abutments.

5.2.5 Measured gap between embankment and end screen

The gap between the embankment and the end screen was measured by a sliding gauge during check surveys. The measured values are presented in Table 5.1. along with uniform temperature of superstructure and displacement stage (change from initial stage) of abutment T4.

Table 5.1. Measured gap between embankment and end screen. Locations during check surveys are presented in Figure 4.3.

	Loc. 2	Loc. 6	Loc. 7	Loc. 8	Loc. 11	Loc. 12	T_U	T4
Date	[mm]	[mm]	[mm]	[mm]	[mm]	[mm]	[ºC]	[mm]
12.2.2004	-	-	0.2	-	0.1	0.6	-12.9	-7.8
19.1.2006	-	-	-	1.4	0.5	0.3	-10*	-6.6
7.2.2007	-	0.4	0.2	1.4	0.3	0.6	-13.0	-8.8

*An estimate, the measuring devices did not work properly

The size of the gap was relatively small compared to the range of bridge abutment displacements. However, the gap may not have been at its biggest during check surveys. Earth pressures between embankment and end screen and the displacement stage of abutment T4 at the coldest time of the monitoring period, February 2007, are presented in Figure 5.24.

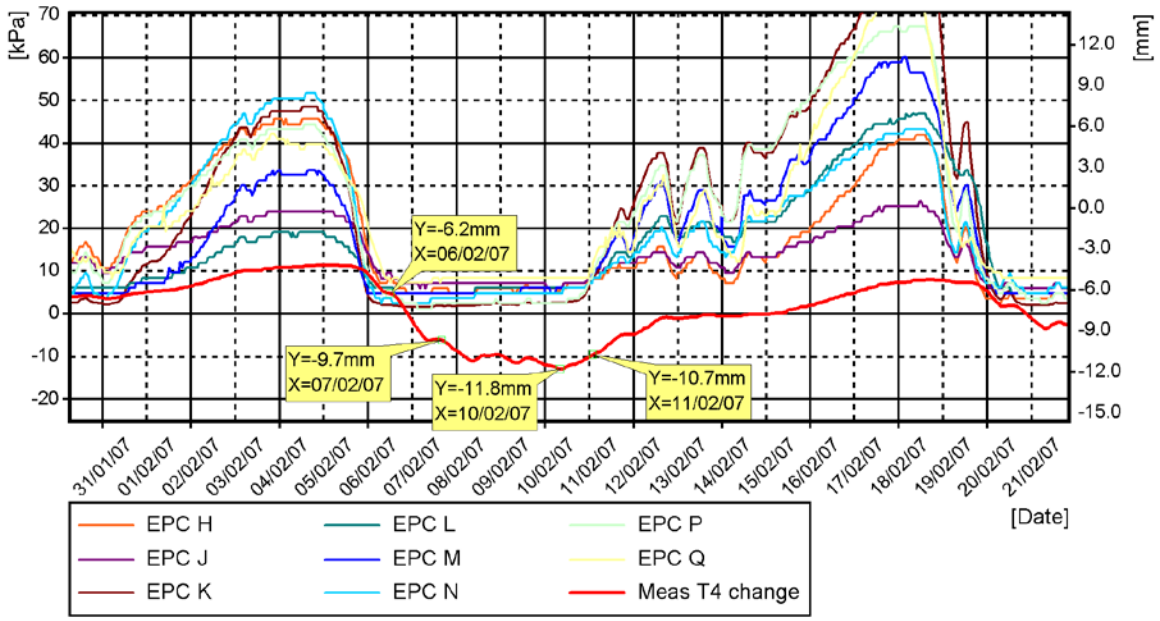

Figure 5.24. Earth pressures between end screen and embankment and displacement stage of abutment T4 during the period 30.1.2006-22.2.2007.

At 6.2.2007 the EPCs measured zero pressures within the limits of measuring accuracy. From that time forward, the superstructure contracted more due to thermal shrinkage. From 6.2.2007 to 10.2.2007 abutment T4 moved 11.8 – 6.2 = 5.6 mm away from the embankment. Only a displacement of 11.8 – 10.7 = 1.4 mm was required when the superstructure started to expand to make earth pressures increase. That means that the embankment had deformed against the end screen while it was still frozen. However, it should be noted that the embankment had not yet reach its deepest stage of frozenness in February 2007, see Figure 5.11. Similar behaviour was observed in February 2004. The result and the closest previous results from 2005 and 2006 are presented in Appendix 5.4.

5.2.6 Displacements between transition slab and end screen

The displacements of abutment T4 and those between the transition slab and the end screen are presented in Figure 5.25 during the first two monitoring years. The measuring devices did no work properly during the last two monitoring years. The sign of the displacement between the transition slab and the end screen is the same as that of the abutment T4 displacement change if the transition slab stays in place in the embankment.

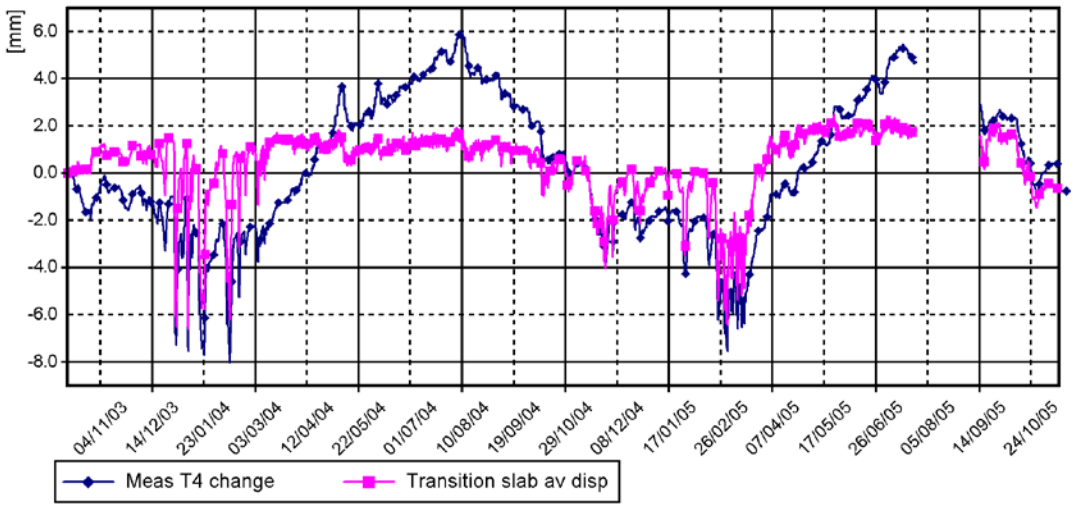

Figure 5.25. Displacements between transition slab and end screen and displacement stage of abutment T4 during the period 10.10.2003-10.10.2005.

At the beginning of the monitoring period, the transition slab almost stayed in place in the embankment if initial settling is ignored. The transition slab was in relatively rigid contact with the end screen during the two following summer stages. Probably the contact via connection dowels of the transition slab was induced by high earth pressures especially against the top part of the end screen, see Figure 5.19. The transition slab is strongly attached to the embankment during winter probably partly due to the freezing of the embankment. The rotation of the end screen is indicated by the displacement changes during winter stages. For example, in January 2004 the displacement change between the transition slab and the end screen was larger than the displacement change of abutment T4: the upper parts had moved more than the lower abutment T4.

5.2.7 Other observations

The need of guidelines and closer supervision of design and building was noted during the monitoring of the integral bridges. The same need was also noticed in [87].

Displacements of slopes were observed at Haavistonjoki Bridge and Myllypuro Overpass. The displacements were clearly visible at support T4 of Haavistonjoki Bridge. The displacements were measured but are not within the scope of this study. Settlements in the road behind the end screen probably contributed to the slope displacements.

A crack was observed in the road surface at the top joint of the transition slab and the end screen. It was bigger in the cold period and smaller or negligible in the warm period.

5.3 Test-loading data on Haavistonjoki Bridge

5.3.1 Braking test

Several braking and overrun tests were performed on Haavistonjoki Bridge. This section provides a short summary of a few representative tests.

The brakes of the loading vehicle produced a deceleration that transmitted a longitudinal force to the superstructure. E.g., the average deceleration and average longitudinal force of the braking test in Figure 5.26 can be calculated as follows:

$$a = \frac{v - v_0}{t - t_0} \tag{5.2}$$

$$F_{brake} = ma \tag{5.3}$$

where:

m = mass of loading vehicle

F_{brake} = 56000kg * (16.2-0) / (9.6-5.2) = 56000kg * 3.7 m/s^2 = 206 kN

The end time of braking (when the vehicle stopped) was determined by linear interpolation because the results of Figure 5.26 include minor inaccuracies due to the measuring devices. The developed force was rather significant compared to the mass of the loading vehicle, and the 500 kN braking force for this type of bridge was given in the guidelines [42].

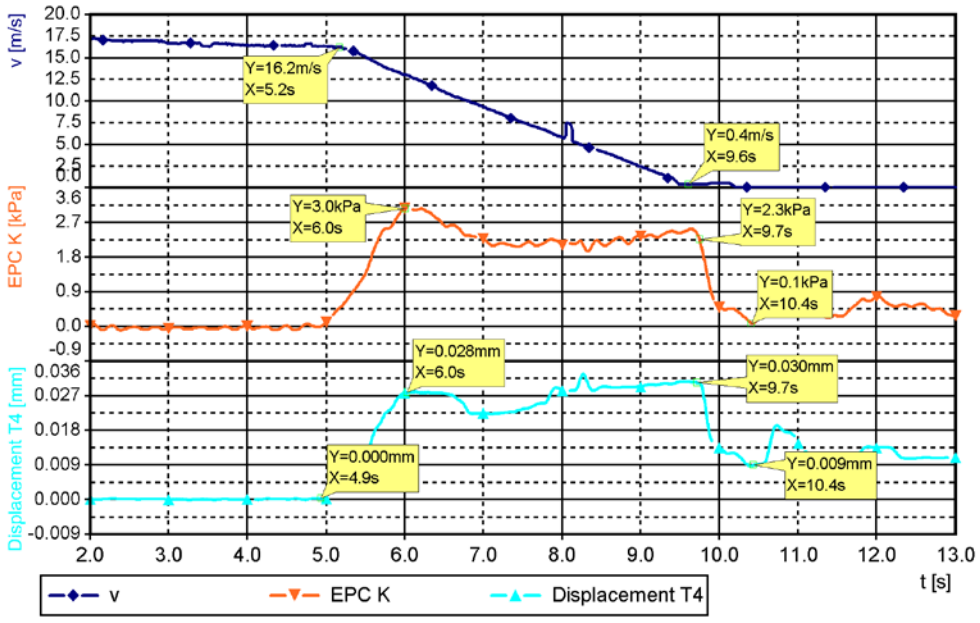

Figure 5.26. Speed of loading vehicle, change of earth pressure between end screen and embankment at EPC K and displacement of superstructure at measurement location 10 of abutment T4 in the braking test.

The braking force induced a longitudinal displacement in the superstructure against abutment T4. The magnitude of the displacement was 0.03 mm. It was very small compared to the long-term displacements of the superstructure. The developed earth pressure was about

3 kPa. The gauge measuring end screen displacement was near EPC K. Thus, the average coefficient of lateral subgrade reaction at the used braking load at the location of EPC K was $k_{h,K}$ = 3kPa/0.03 mm = 100 MN/m^3. Average corresponding stiffnesses from 80 to 280 MN/m^3 were observed at other locations [86] and in the overrun test, see Paragraph 5.3.2. The embankment was very stiff at the examined loading and strain stage of the embankment. The loading also produced a vertical displacement of the superstructure which caused abutment rotations. This is indicated by the changes in earth pressures in Figure 5.27.

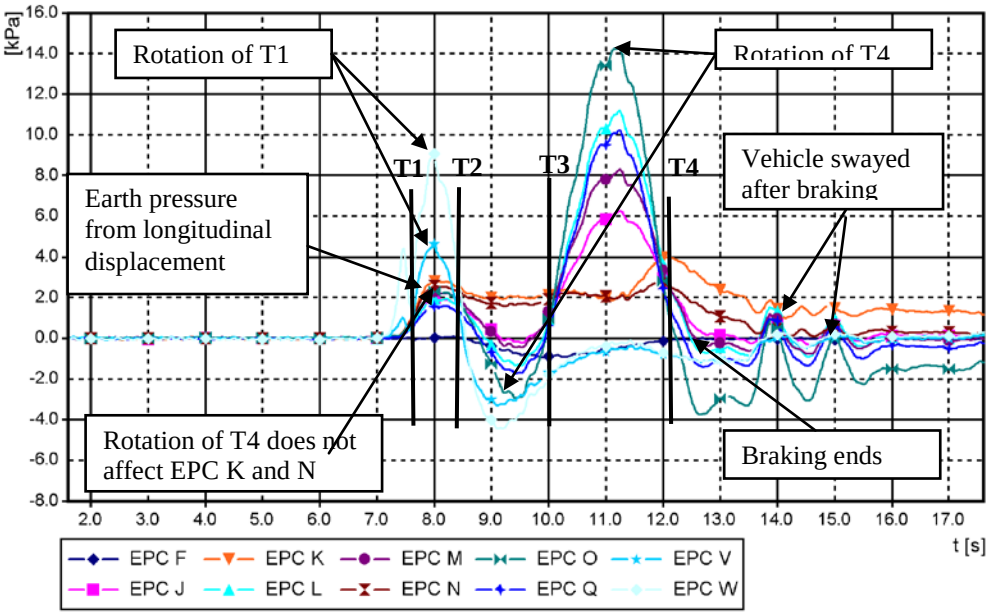

Figure 5.27. Changes in earth pressures between end screen and embankment at used braking load. Locations of abutments and intermediate supports in relation to centre of loading vehicle are indicated by the names of the supports.

The rotations of abutment T4 affect little the earth pressures at EPCs K and N due to their locations which were near the level of the rotation centre during the braking test. The effect of positive and negative rotation is presented schematically in Figure 5.28.

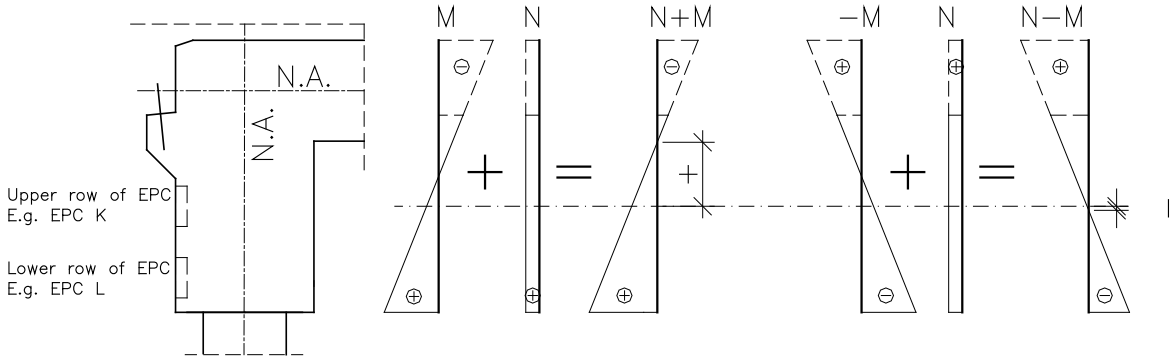

Figure 5.28. Effect of rotations on earth pressure changes between end screen and embankment.

It was possible to calculate the rotations from the measurement results because displacements were measured from two different levels and earth pressures from three different

levels. However, the end screen was assumed to rotate as a straight block, which caused small inaccuracies in the measurement results. Further, the overrun test gave data about loading involving no braking force which confirmed the phenomena. EPCs K and N measured only minor effects from rotations. The lower row of EPCs measured the bigger effects. However, the earth pressure induced by the longitudinal braking force can be determined rather well from the measurements of EPCs K and N.

5.3.2 Overrun test

The overrun test was made using different speeds. No big difference between the various speeds and measured values were observed. Earth pressure-displacement relationships at the locations of EPCs L, O and Q at depth z = 2.2 m from the road surface are presented in Figure 5.29. Corresponding results for the locations of EPCs K, M, N and J and regression curves for J, K, L, M, N and Q are presented in Appendix 6.1.

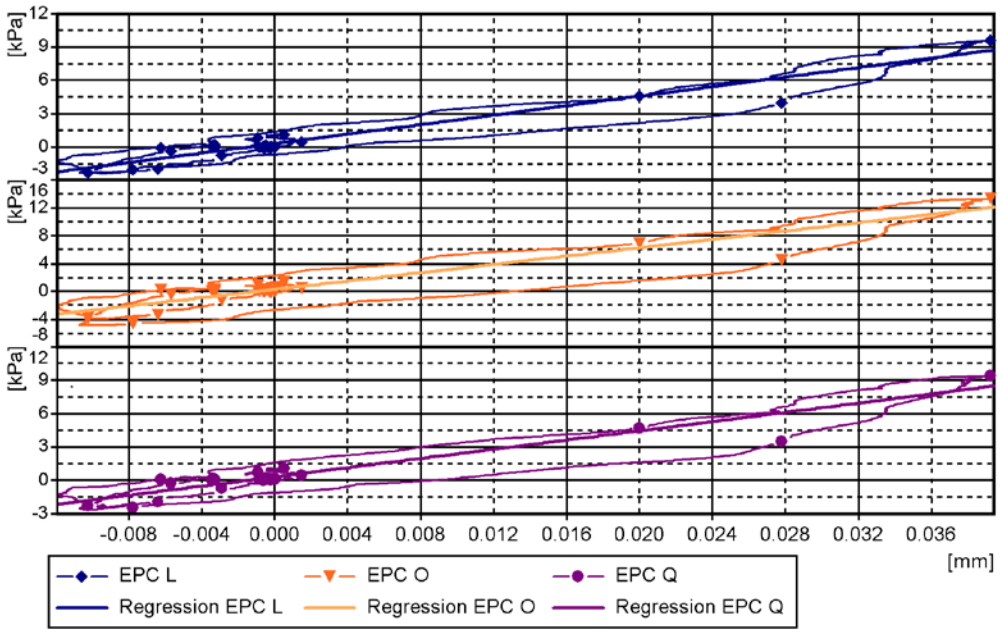

Figure 5.29. Earth pressure-displacement relation in the overrun test at loading vehicle speed 17 m/s at the locations of EPCs L, O and Q when z = 1.6 m.

It can be observed that earth pressure development during the overrun test was rather linear. Displacements were small and the coefficient of the lateral subgrade reaction of the embankment k_h as high as in the braking tests [86]. Average lateral stiffnesses at the locations of EPCs L, O and Q were: $k_{h,L}$ = 7 kPa/0.032 mm = 220 MN/m^3, $k_{h,O}$ = 9 kPa/0.032 mm = 280 MN/m^3 and $k_{hb,Q}$ = 7 kPa/0.032 mm = 220 MN/m^3. Average stiffness $k_{,I}$ varied from 80 to 300 MN/m3 during the overrun tests [86].

In general, stiffnesses in the loading tests were higher than long-term monitoring embankment stiffnesses at larger displacements. However, the lateral embankment stiffness of the loading test was quite similar as to that at small displacements during the weekly thermal induced re-loading in long-term monitoring.

5.4 Test loading data on Tekemäjärvenoja Bridge

The test loading was arranged so that the direction of loading was toward abutment T4 (EPC 4 – EPC 14). Earth pressure development between end screen and embankment as function of loading force is presented in Figure 5.30. The longitudinal loading force of the loading system (see Paragraph 4.3.2) was distributed to the rails, the ballast, the transition slab, the end screen and the substructures of the bridge. Earth pressure changes between end screen and embankment reflect the force acting through the end screen.

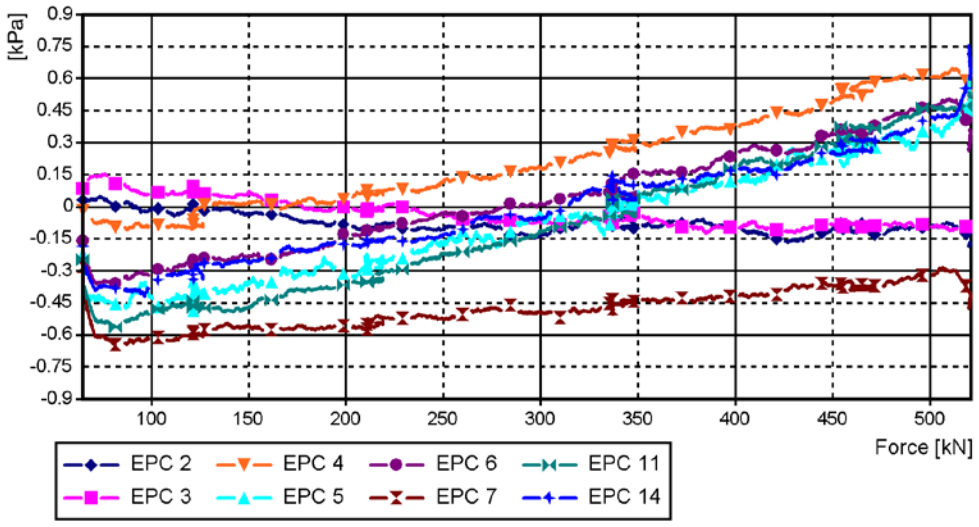

Figure 5.30. Earth pressure changes between end screen and embankment during longitudinal test loading.

Earth pressures increased between end screen and embankment at abutment T4 and decreased slightly at abutment T1. Thus, the interaction force at abutment end screens was: F_{Σ} = H*B*p = 11.8*2*(0.6+0.15) = 18 kN. This force is 3% of the loading force. The percentage amount of force varied between 3-5% of loading force during repeated loading tests. The lateral average coefficient of lateral subgrade reaction of embankment at the location of EPC 6 can be derived from Figure 5.31: $k_{h,6}$ = 0.6/0.06 = 10 MN/m3.

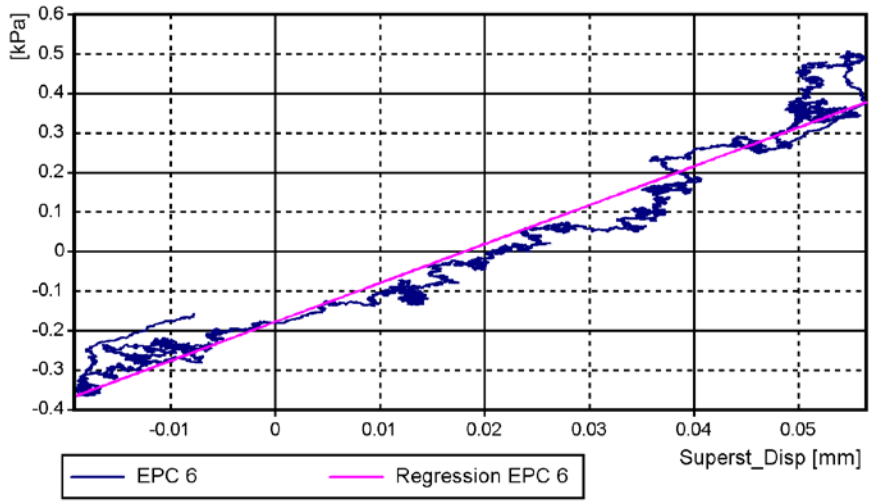

Figure 5.31. Earth pressure-displacement relationship in the loading test at the location of EPC 6 when z = 1.4 m (from sleeper upper surface).

Similar regressions for the earth pressure-displacement relationship were also obtained at other EPC locations. The lateral average coefficients of lateral subgrade reaction were lower, 9 to 13 MN/m3, than those measured in Haavistonoja Bridge test loading [85]. That is probably due to a different strain stage of embankment soil against end screen and differences in fill materials and compacting work.

5.5 Long-term monitoring data on Myllypuro Overpass

The long-term monitoring of Myllypuro Overpass is working fine and measurements have been successfully recorded since November 2008. The field test results are not included in this study because the timetables of monitoring and this study do not coincide. The field test results from the monitoring period (2008-2013) will be published during the monitoring of Myllypuro Overpass.

5.6 Uniform temperature analysis based on ambient air temperature data

5.6.1 Overview

The uniform temperature of Haavistonjoki Bridge has been monitored from 2003 to 2007 as mentioned in Paragraph 5.2.1. The ambient air temperature T_{amb} measurements at Haavistonjoki Bridge produced inaccurate results due to the measurement arrangements. The calibration devices were assembled on 24.10.2007 and ambient air temperature calibration data was obtained from the Finnish Meteorological Institute (FMI). Ambient air tempera-

ture data was measured at FMI Juupajoki-Hyytiälä meteorological station 18 km north-west from the bridge and was reported in Coordinated Universal Time (UTC) as follows:

- 1959-2007 UTC 06, 12 and 18
- 1981-2007 UTC 00, 06, 12 and 18
- 2001-2007 UTC on the hour

Other long-term climatological statistics on solar radiation, etc. were not available from the Juupajoki-Hyytiälä meteorological station. The ambient air temperature data from 1959 on were used for the long-term calculations of Paragraph 5.6.4.

The monitoring period included a rather cold period in February 2007. The average ambient air temperature in February at the bridge location was statistically 6.7ºC colder than the average February ambient air temperature during the observation period 1971-2000. Several of the coldest days were in the coldest 2.5% fractile compared to the normal period 1971-2000 in the Jyväskylä area (100 km north-east of the bridge location). The Haavistonjoki Bridge monitoring period also included a rather warm period in June 2006. Then ambient air temperature exceeded the 25ºC limit during 12 days. The average number of days was five in June during the observation period 1971-2000. In June 2006 there were also several consecutive days when average daily temperature was in the warmest 3.0% fractile compared to the normal period 1971-2000 in the Jyväskylä area. [38, 39]

5.6.2 Method for uniform temperature calculation

The uniform temperature of a bridge superstructure is the result of several environmental factors, see Paragraph 2.2.2. Only ambient air temperatures were available for this study. An analysis method which estimates the uniform temperature T_U of the bridge superstructure based on ambient air temperature was developed. The analysis parameters were derived from Haavistonjoki Bridge monitoring and FMI ambient air temperature data. It is assumed that the other climatological factors affecting the extreme uniform temperature of the bridge superstructure are rather similar to those affecting the extreme uniform temperatures of Haavistonjoki Bridge during monitoring. It should also be noted that the analysis parameters calculated in this study are valid only for the superstructure type of Haavistonjoki Bridge at its location. More calculations will, however, be done during the research project e.g. concerning Myllypuro Overpass.

It is assumed that the change speed of T_U is directly proportional to the temperature gradient between T_U and T_a with constant A, which produces the function:

$$d_T = \left| T_U - T_{amb} \right| * A_{+/-} \tag{5.4}$$

where:
T_U = uniform temperature of bridge superstructure [ºC]
T_{amb} = ambient shade air temperature [ºC]
d_T = change speed of uniform temperature [ºC/h]
$A_{+/-}$ = step constant, A_+ at rising uniform temperature stage and A_- at falling stage [1/h]

Now the constant $A_{+/-}$ can be calculated from measured data with Formula 5.5:

$$A_{+/-} = \frac{d_T}{\left| T_U - T_{amb} \right|} \tag{5.5}$$

A function was also applied instead of step constant $A_{+/-}$ but it did not produce significantly better results compared to the step constant. That is probably due to the other environmental factors, which were partially ignored. Solar radiation has a significant effect on T_U. It was observed that in addition to the warm day ambient air temperature T_U, the calculation must include an offset $\Delta T_{u,solar}$, see Formula 2.5 [103]. This offset for warm days is obtained by comparing measured results to calculated results in the following paragraph. Finally, T_U can be calculated with the following step function:

$$T_{U,n} = T_{U,n-1} + \left| T_{U,n-1} - T_{amb,n} \right| * A_{+/-} + \Delta T_{u,solar} \tag{5.6}$$

Where $\Delta T_{u,solar}$ is a function of T_{amb}, see Figure 5.34

The change in uniform temperature with Formula 5.6 is bigger when the temperature difference between ambient air and uniform temperature is larger.

5.6.3 Implementation of method using monitored data from Haavistonjoki Bridge

An essential result concerning this study is first of all the annual extreme values i.e. outer fractiles of T_U. Hence, the T_U change speed as function of gradient $T_{amb} - T_U$ out a 90% confidence interval of measured T_U values (–11.1ºC and 21.3ºC during the four-year monitoring period of one-hour intervals) is presented in Figure 5.32.

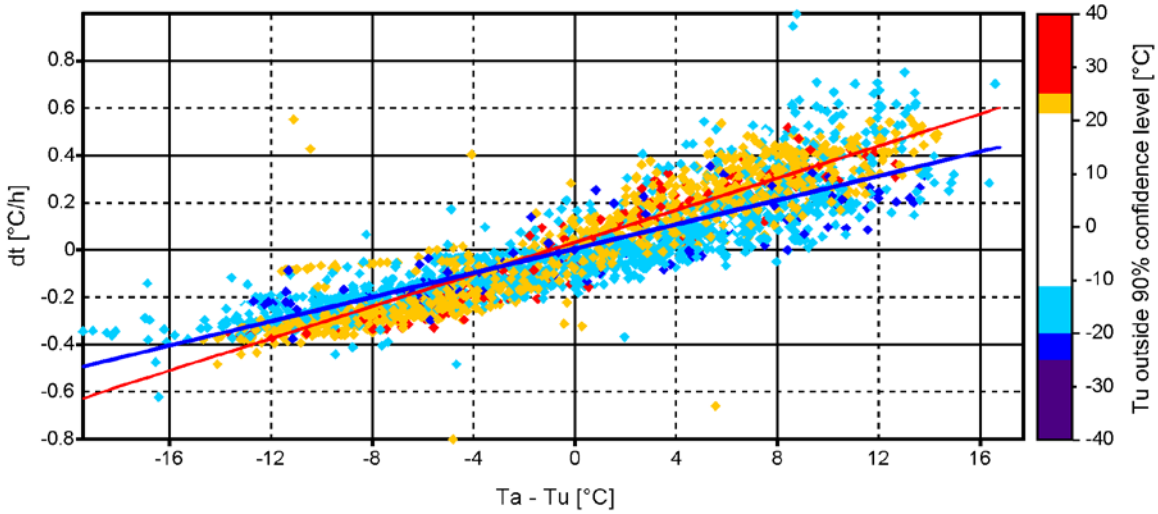

Figure 5.32. Change speed of uniform temperature T_U as function of gradient between ambient air T_a and uniform temperature. Values presented outside a 90% confidence level of T_U during the four-year monitoring period

There are two regression lines in Figure 5.32. The first one represents the upper fractile of T_U and the second one the lower fractile of T_U. Constant A is the slope of the regression lines. Constant A is bigger for higher T_U values which change faster compared to the lower fractile values of T_U. Constants A for high and low T_U values can be calculated as follows: $A_- = 0.8/32 = 0.025$ 1/h $A_+ = 1.1/32 = 0.034$ 1/h. The results in Figure 5.32 scatter rather strongly especially at the superstructure warming up stage (positive gradient T_{amb}-T_U). This is probably mainly due to the fact that the measured results were strongly affected by solar radiation. Hence, constant A was calculated based on all results with a one-hour interval in Figure 5.33 which made T_U calculation results more accurate than the values of Figure 5.32.

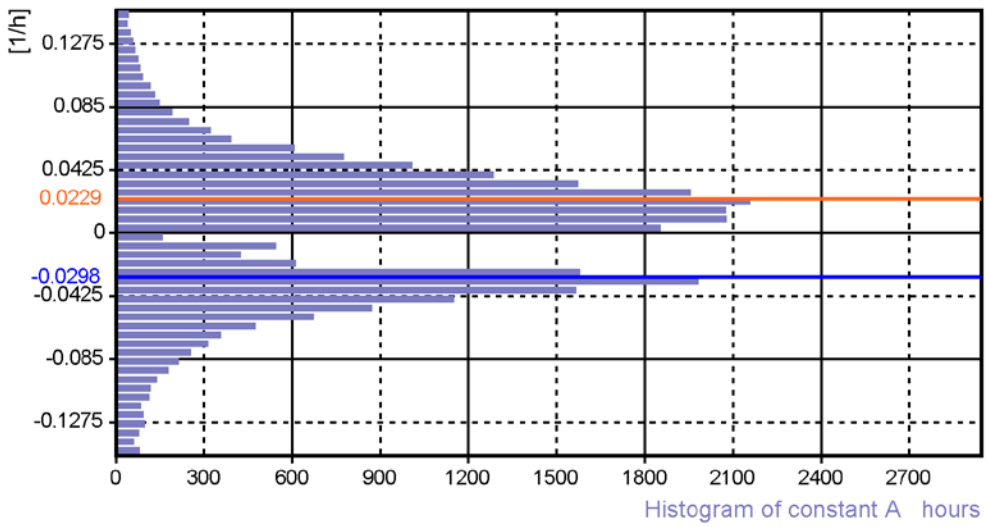

Figure 5.33. Hourly calculated constant A values during four-year monitoring period and selected values for T_U rise and fall stages at distribution peaks.

The values at the distribution peaks were found during calibration calculations to be most suitable. The selected values of $A_{+/-}$ from Figure 5.33 distribution peaks are:

$A_+ = 0.023$ 1/h and $A_- = -0.030$ 1/h.

These values mean that, on average, with the same temperature gradient, the T_U fall rate of of the superstructure is higher than its T_U rise rate. The data obtainable from FMI have different steps as mentioned earlier. Steps of the calculations of the analysis were selected according to obtainable data steps and measured data with on-the-hour steps:

- d1h UTC on the hour
- d6h UTC 00, 06, 12 and 18
- d12h UTC 06 and 12
- d24h UTC 18 and d24h UTC 06

The steps of d12h and d24h were set on the basis of the presented UTC because it was noticed during the analysis that they produced the results with smallest errors in the following data analyses. In the analysis with a d24h time step, the time of day was set at UTC 18 or 06. UTC 00 (and UTC 12) produced larger errors. That is probably due to daily temperature changes. The ambient air temperature at UTC 18 in d24h and UTC 06 and 18 in d12h analyses describes best the average ambient air temperature concerning T_U. Three different values of constant $A_{+/-}$ were used in T_U analyses:

1. Calculated value of $A_{+/-}$, see Figure 5.33, hereafter: mean value
2. 75% of calculated value $A_{+/-}$, hereafter: low value
3. 125% of calculated value $A_{+/-}$, hereafter: high value.

The $\Delta T_{u,solar}$ was determined by an iterative process in connection with the T_U analysis. Results of different steps were compared with various $\Delta T_{u,solar}$ values. The initial magnitude was determined using the $\Delta T_{u,solar}$ value given in [24]. $\Delta T_{u,solar}$ is given in [24] as function of thickness of concrete structure at Finnish climate. A corresponding T_{amb} value is estimated on the basis of Figures 5.32 and 5.34.The determined $\Delta T_{u,solar}$ values of the analysis are presented.

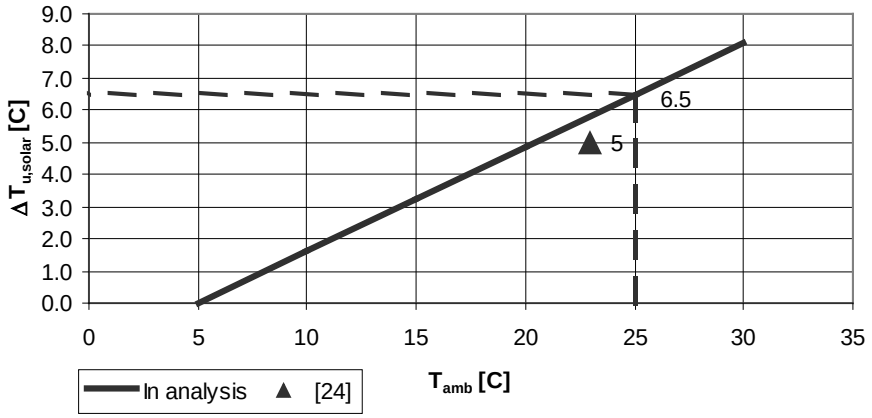

Figure 5.34. $\Delta T_{u,solar}$ as function of T_{amb}.

It was necessary to give $\Delta T_{u,solar}$ as function of T_{amb} instead of as a single value because the analysis is based on a step function where values of previous nodes affect the calculated ones. $\Delta T_{u,solar}$ may be solved more accurately by thermal analysis of the superstructure and accurate solar radiation data, but it was not necessary for the purposes of this study. Further data on $\Delta T_{u,solar}$ will be obtained from Myllypuro Overpass in future. Calculated T_U values of the fourth monitoring year are presented in Figure 5.35.

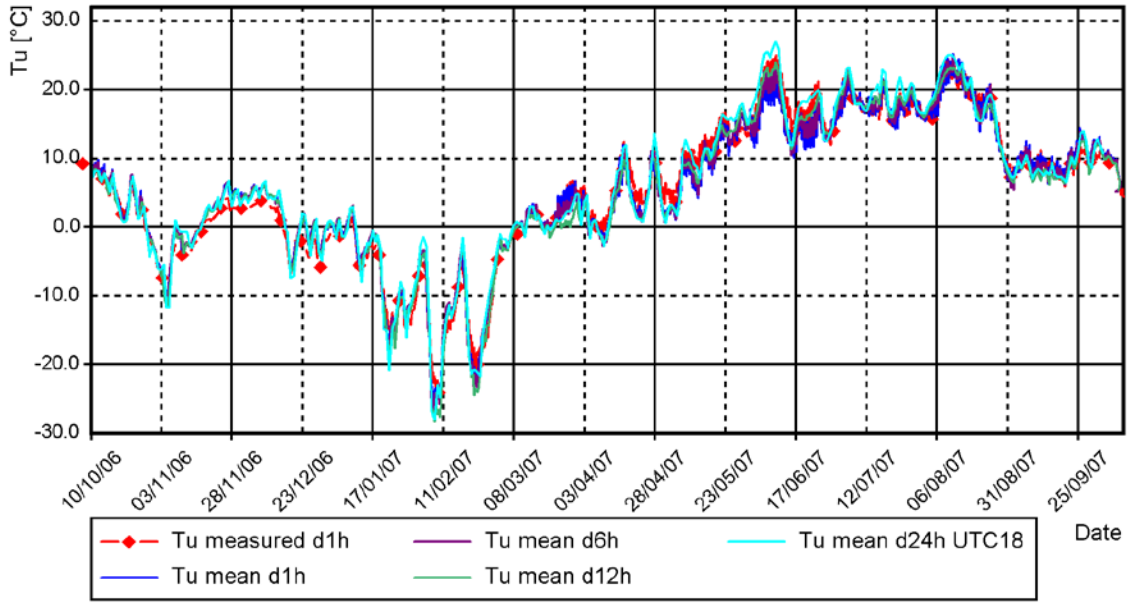

Figure 5.35. Calculated and measured T_U values with different time steps during the fourth monitoring year.

The calculation results are rather precise. Time step d24h produces the largest errors. Time steps d1h, d6h and d12h produce tolerable results considering the overall annual trend. However, the calculated results differ from the measured ones. Calculated T_U values are presented in Figure 5.36 during typical shorter periods of time when T_U was neither high nor low. Calculation results for d24h are presented with UTC 18 and UTC 06 calculation steps. Calculation steps d24h at UTC 12 produced excessively high results in the warm period probably due to daily temperature changes.

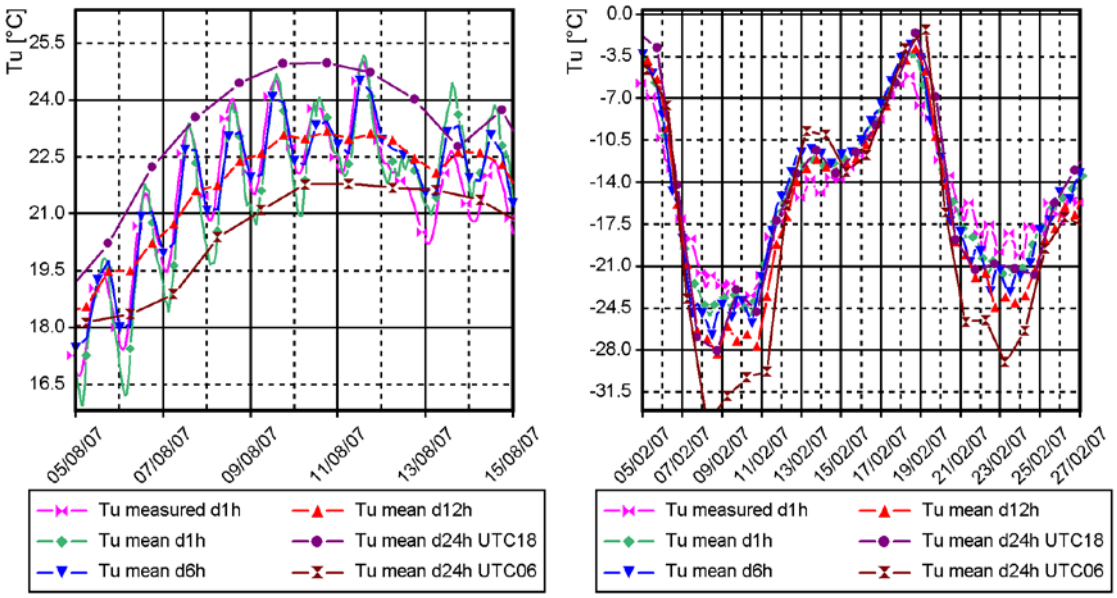

Figure 5.36. Calculated and measured T_U values with different time steps during the warm and cold period.

Calculation with one-hour time steps gives the daily changes in T_U during the warm period. Calculation step d6h follows daily cycles but does not give ultimate daily peaks. Calculation step d12h does not follow daily cycles but larger cycles. The problem with the d24h calculation step is the input ambient air temperature value. Ambient air temperature at UTC 06, 12 and 18 does not produce an average daily T_U value with d24h as with d12h because at the UTC times ambient air temperature is not the average daily value for T_U. In addition, calculation with one-hour time steps gives the best approximation for T_U during the cold period. Calculation step d6h gives too low T_U values as does d12h. Ambient air temperature at UTC 18 in the analysis with d24h also gives results with rather small errors, but with UTC 06 the T_U values are way too low.

Available FMI data from 1959 on was exploited with a constant time step of d12h. This was done because the calculation could be made more straightforward than it would have been with the uneven calculation step. The effect of different constant $A_{+/-}$ values is presented in Figure 5.37.

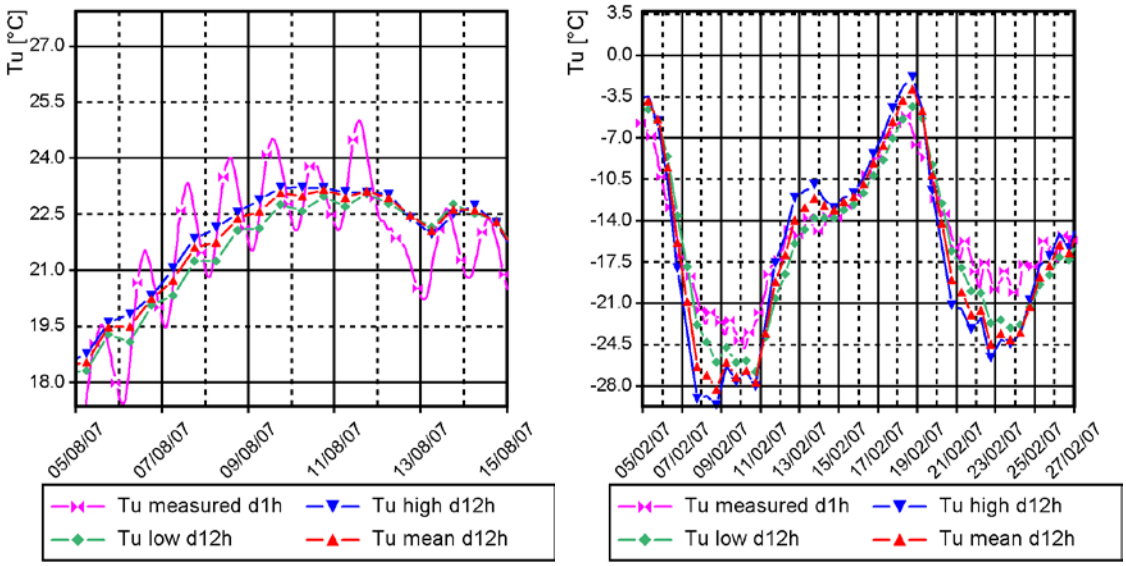

Figure 5.37. Calculated and measured T_U with time step d12h and different constant $A_{+/-}$ values during warm and cold period.

The results show that the analysis is not very sensitive to changes in constant $A_{+/-}$. The calculation step d12h is usable but an extra offset $\Delta T_{u,\,d12h}$ was required in both the warm and cold period. The $\Delta T_{u,\,d12h}$ values were calculated from measured results, but they scattered quite strongly. This is probably due to differences in other environmental factors between extreme T_U periods, which were omitted in this calculation, see Figure 2.9. However, the offset value $\Delta T_{u,\,d12h}$ was approximated to be 1°C because with that value errors in extreme T_U values became small. The offset $\Delta T_{u,\,d12h}$ is hereafter referred to as the "off" index in T_U calculation results. The results of T_U calculations during the fourth monitoring year are presented in Figure 5.38. The first to third monitoring year results are shown in Appendix 7.1.

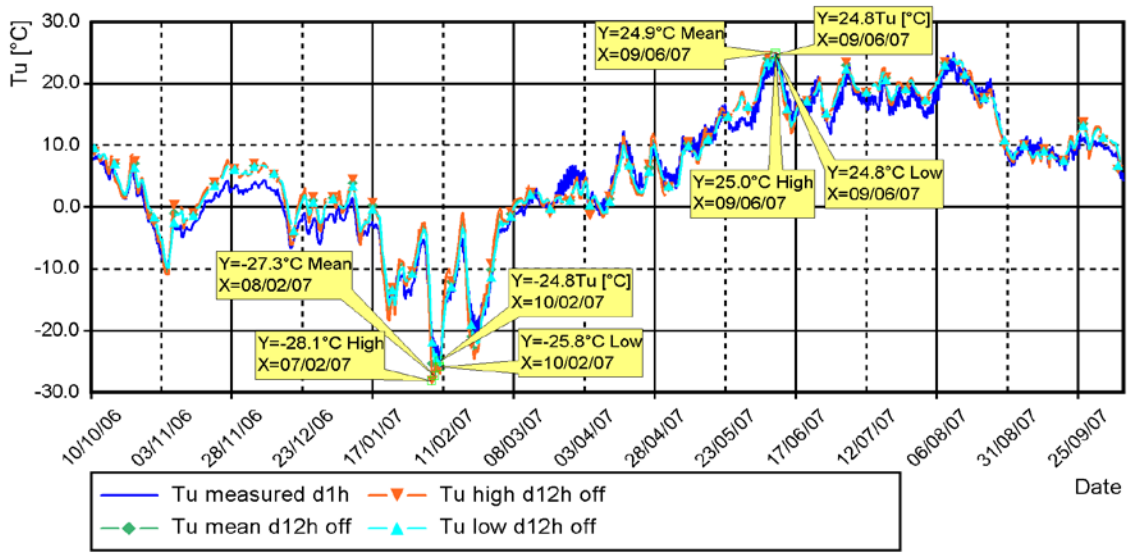

Figure 5.38. Calculated and measured T_U with time step d12h, different constant $A_{+/-}$ values and offset value during the fourth monitoring year.

The results of extreme T_U value calculations are accurate enough for calculating abutment displacements. Extreme T_U values measured and calculated by year are presented in Table 5.2.

Table 5.2. Calculated and measured extreme T_U values during the four-year monitoring period [˚C]. Monitoring year changes on 10th of October.

Year	2003-2004		2004-2005		2005-2006		2006-2007	
Mon.Year	1st min	1st max	2nd min	2nd max	3rd min(*	3rd max	4th min	4th max
Meas. T_U	-17.3	24.4	-15.5	26.0	-15.6	**27.3**	**-24.8**	24.8
T_U low	-16.1	24.4	-18.3	26.2	-18.8	**28.1**	**-25.8**	24.8
Error	1.2	0	-2.8	0.2	-3.2	0.8	-1	0
T_U mean	-18.7	24.7	-19.4	26.8	-19.7	**28.6**	**-27.3**	24.9
Error	-1.4	0.3	-3.9	0.8	-4.1	1.3	-2.5	0.1
T_U high	-20.4	24.8	-20.3	27.5	-20.3	**28.9**	**-28.1**	25
Error	-3.1	0.4	-4.8	1.5	-4.7	1.6	-3.3	0.2

*) Compared at time when monitoring devices were measuring properly and T_U was not at its lowest.

The errors have been calculated by deducting the measured values from the calculated ones. The largest error occurred during the cold T_U period. The low $A_{+/-}$ values produced the best results in both warm and cold periods. The smallest $T_{U,\,low}$ error during the cold period was produced at the lowest T_U. The smallest error during the warm period was correspondingly produced at the highest T_U. However, the significance of the errors is not directly proportional to the error in degrees because the initial temperature $\Delta T_{u,\,0}$ of a cast-in-place bridge is often assumed to be 10ºC [2, 102]. Then, the percent error decreases because e.g. the range of T_U temperatures at the bridge location is from -30ºC to 30ºC meaning temperature range for contraction of -30-10 = -40ºC and a temperature range for expansion for 30-10 = 20ºC. In any case, errors are bigger during the cold T_U period.

5.6.4 Uniform temperature analysis with FMI ambient air temperature data

The measured T_U values were obtained during a four-year monitoring period. Long-term data are required to define the extreme dimensioning temperatures $T_{U,min}$ and $T_{U,max}$. The long-term analysis was made with d12h time steps and with a $\Delta T_{u,\,d12h}$ of 1°C. Data from 1959 on were available at FMI Juupajoki-Hyytiälä meteorological station. The annual maximum values with different $A_{+/-}$ values of T_U are presented in Figure 5.39. Calculated data by decades starting from 1959 are presented in Appendix 7.2.

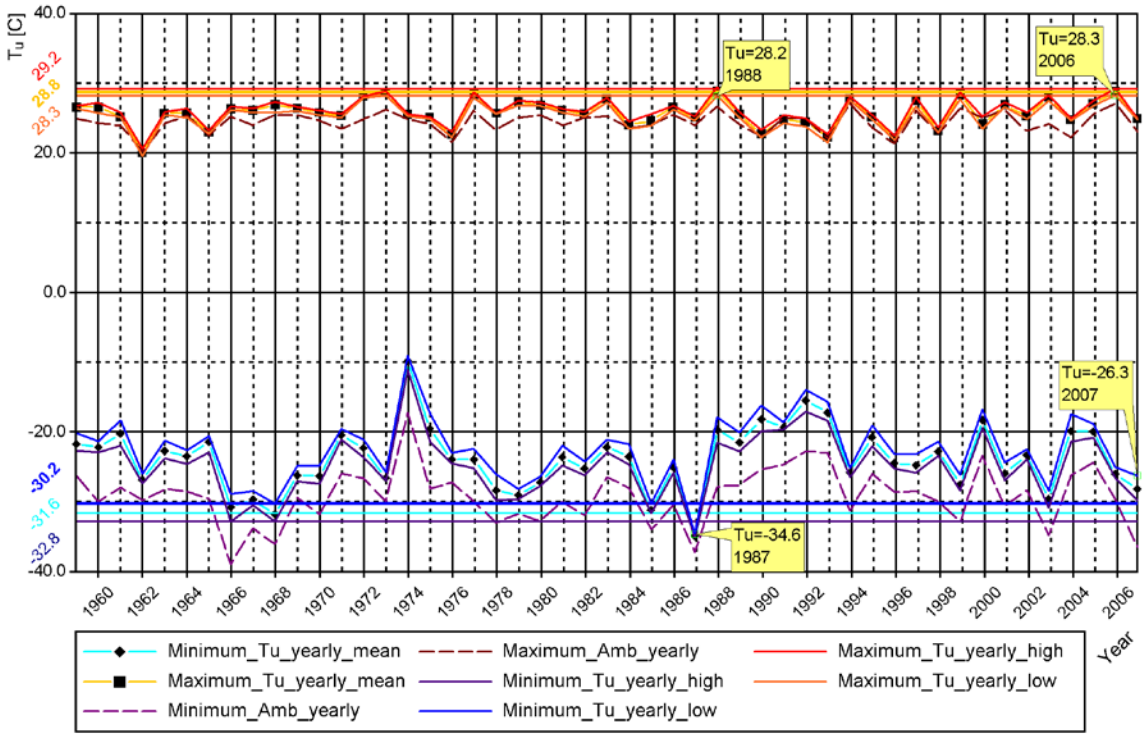

Figure 5.39. Calculated annual extreme values of T_U from 1959 to 2007. T_U values with low $A_{+/-}$ values are plotted.

The highest calculated T_U value of 28.9ºC occurred in 1988 and the lowest -34.9ºC in 1987. An equally high T_U value of 28.8ºC (within calculation accuracy) was obtained in 2006 during the monitoring period. A relatively low T_U of -28.2ºC was also obtained in 2007. It can be noted that the calculated values differ slightly from the measured ones because the ambient air temperature is different. The maximum annual values do not vary as much as the minimum values. On the other hand, values close to the maximum value are obtained quite often. The error of the analysis is probably negative at low T_U values and slightly positive at maximum ones. Hence, T_U values with low $A_{+/-}$ are used to define dimensioning values. Fractiles 0.02 and 0.98 were selected as dimensioning values so as to make the results comparable to the values of the Eurocode [102] which makes them different from the fractiles 0.05 and 0.95 of the Finnish guidelines [34].

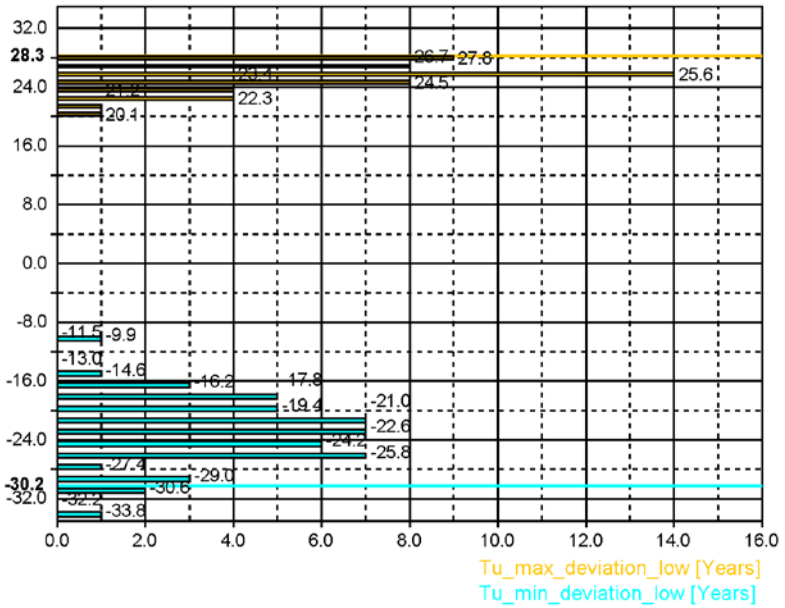

Figure 5.40. Calculated dimensioning values $T_{e,min}$ and $T_{e,max}$ with 0.02 and 0.98 fractiles.

The T_U values of the 0.02 and 0.98 fractiles (i.e. $T_{e,min}$ and $T_{e,max}$) are -30.2ºC and 28.3ºC whereas with 0.05 and 0.95 fractiles the values are -29.7ºC and 28.1ºC, see Figure 5.40. It should be noted that the presented values may be different if the period of analysis were longer (i.e. if the data were available) which would make the distribution more accurate. However, the results of a 48-year period are much more precise than those of a four-year monitoring period concerning the dimensioning values of T_U. The range of T_e is wider than the -25 to 25ºC uniform temperature range of Finnish guidelines for the bridge location [42].

A comparison of the values from the analysis and EN1991-1-5 [102] is made in Figure 5.41. The annual extreme values of T_U are presented as function of annual extreme ambient air temperatures. The T_e extreme values according to [102] are represented by lines as function of ambient air temperature and the annual probability of them being exceeded is 0.02. In addition, the values of Haavistonjoki Bridge location are plotted. The ambient air values used to define T_e values in the Eurocode are the extreme temperatures during the 48-year period. These ambient air temperature values may not correspond to the 0.02 or 0.98 fractile values because they refer to an annual probability of them being exceeded twice in 100 years and they do not necessarily correspond to the maximum values occurring once in 50 years (or once in 48 years). However, the approximation of extreme ambient air temperatures gives accurate enough results.

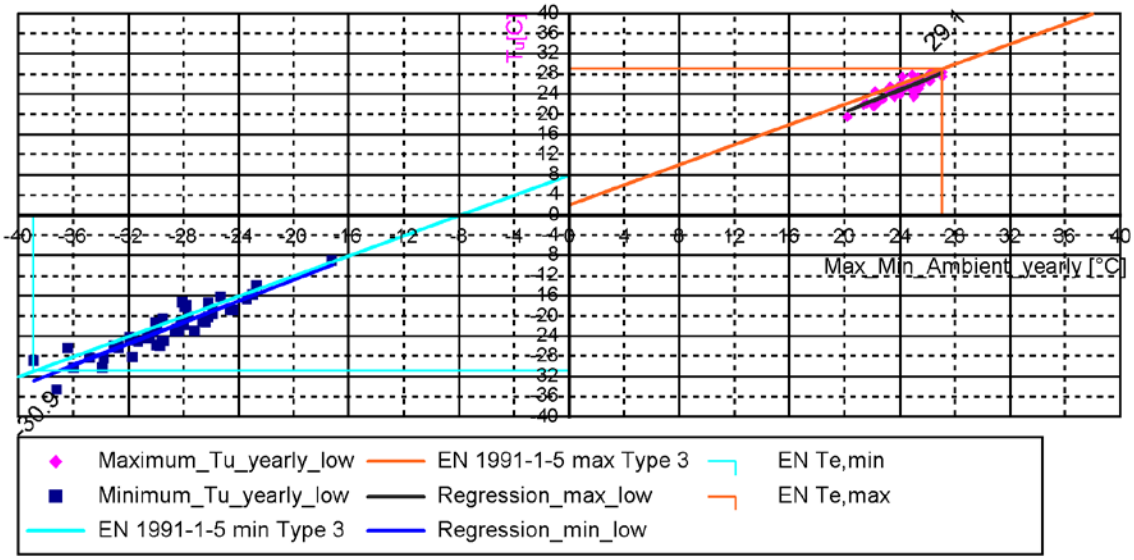

Figure 5.41. Calculated annual extreme values of T_U from 1959 to 2007 as function of annual extreme values of ambient air temperature and T_U values according to Eurocode [102].

The Eurocode [102] gives a range of T_e from –30.9 to 29.1ºC. These values are rather close to the calculated T_e values. The relation based on regression between calculated annual extremes of T_U and T_{amb} is close to the relation presented in the Eurocode. The estimated dimensioning values based on the analysis of uniform superstructure temperatures of Haavistonjoki Bridge are:

$$T_{e,min} = -30 \pm 2\ ^{o}C$$

$$T_{e,max} = 28 \pm 1.5\ ^{o}C$$

The error limits of $T_{e,min}$ are made wider compared to $T_{e,max}$ because of the scattering of $T_{U.min}$ values based on the analysis.

5.7 Conclusions

The bridge monitoring systems provided new data. Superstructure temperature follows seasonal and diurnal cycles. The temperature range was found to be wider than defined in present Finnish guidelines. Embankment temperature follows seasonal cycles, and temperatures below freezing point strongly affect earth pressure development. Further, new knowledge was obtained from simultaneous values of the uniform superstructure temperatures and temperature difference between top and bottom surfaces.

Displacements of integral bridge abutments due to temperature changes do not develop symmetrically from the bridge centre. Displacements of each end develop during each stage depending on the prevailing stiffness of each component of the bridge system. Hence, the centre of thermal movements shifts along the bridge and causes uneven dis-

placement of the abutments. The effect of shrinkage cannot be defined on the basis of measurements.

The proposed schematic behaviour model of Figure 5.42 of high earth pressure mean and boundary values distribution was built based on Haavistonjoki Bridge measurements. "Top" refers to a point 0.5 m below the transition slab bottom and "bottom" refers to a point 0.5 m from the bottom of the end screen.

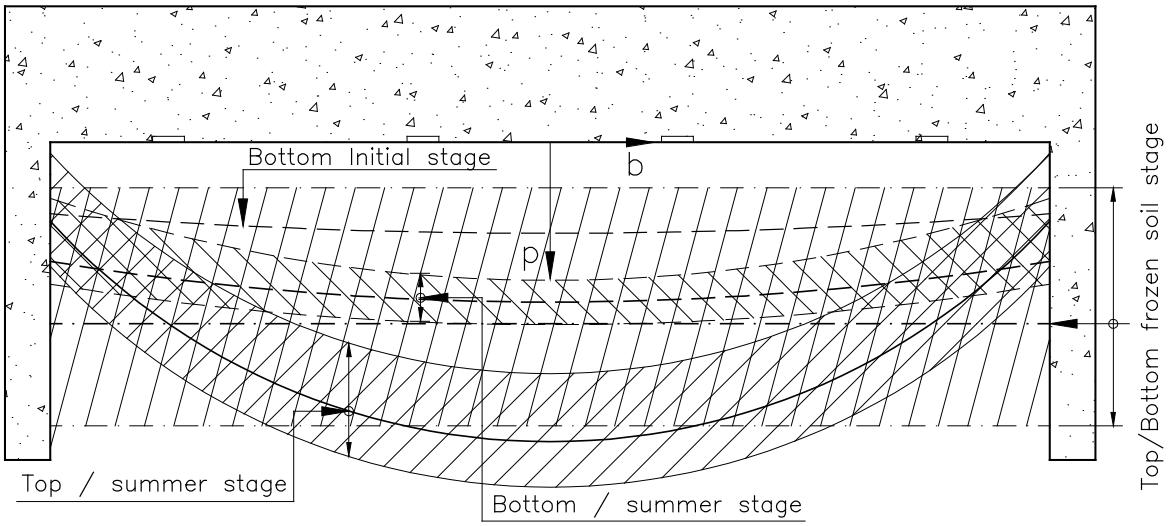

Figure 5.42. Schematic behaviour model of Haavistonjoki Bridge high earth pressure mean and boundary values distribution between end screen and embankment at abutment (top view) based on measurements.

High earth pressures developed at the summer stage in the top part of the end screen but, at the same time, the bottom part was subjected to lower earth pressures. At the frozen soil stage, maximum values vary a lot along the end screen. Hence, it is possible that the earth pressure resultant for the whole end screen is higher if embankment frost penetration depth is very great accompanied by end screen displacements. However, on average, the high maximum earth pressure resultant is slightly lower at the frozen soil stage, see Appendix 5.1.

General observations related to earth pressures:

- Hysteretic development as function of abutment displacement
- Effect of frozen soil
- Uneven distribution against end screen partly affected by transition slab
- Possible difference in magnitude between abutments accompanied by longitudinal equilibrium of superstructure

A schematic description of earth pressure between end screen and embankment is presented in Figure 5.43.

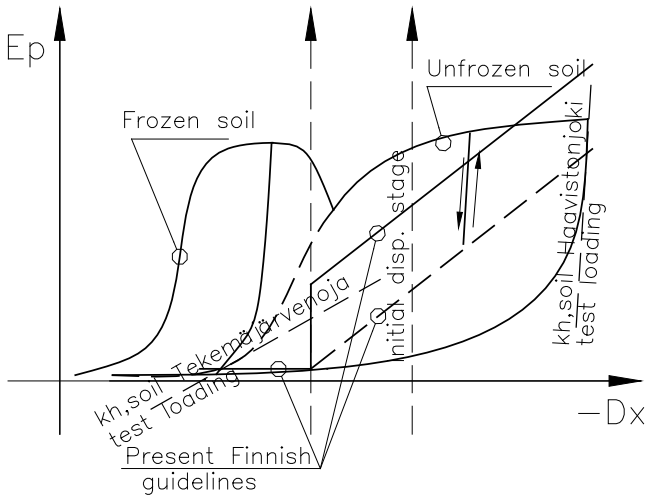

Figure 5.43. Earth pressure-displacement relation between end screen and embankment as measured and presented in Finnish guidelines [46].

Earth pressure is very high although displacement is small at the frozen soil stage. The initial stage of displacements is in the middle of the earth pressure hysteretic development.

The transition slab affects significantly the earth pressure distribution along the end screen. At the unfrozen stage, the upper part of the end screen takes the maximum earth pressure. The stabilisation effect of the transition slab became apparent because the soil of the embankment could not expand easily upward at the passive earth pressure stage which prevented the loosening of the embankment.

The gap measurement results suggest that the possible gap may be at its biggest in winter during the first months of moderate frost, when the embankment freezes to a relatively deep level, and then in spring its temperature falls rapidly even lower. However, the size of the gap will probably be small compared to the range of abutment displacements. Moreover, if the superstructure is affected by a braking load, the stiffness of the embankment is very high after gap closure in the winter stage.

Displacements in the braking tests on Haavistonjoki Bridge and Tekemäjärvenoja Bridge were very small. Integral bridges are very stiff under short-term loading. Dynamic behaviour had a slight influence on the loading data.

The uniform temperature of a concrete bridge superstructure can be determined based on ambient air temperature data if the bridge superstructure has been monitored for a few years. The accuracy of such an analysis is adequate for many purposes. A reasonable accuracy of uniform temperatures at Haavistonjoki Bridge location and the structure type of Haavistonjoki Bridge was obtained for determining the allowable length of an integral bridge. Temperatures can be determined for different locations in Finland which was not

within the scope of this study. The parameters of uniform temperature analysis will also be determined for a beam-and-slab structure based on the monitoring of Myllypuro Overpass and the uniform temperature limits will be determined during the research project.

6 STRUCTURAL ANALYSIS

6.1 Overview

This chapter includes a structural analysis of laterally loaded steel pipe piles and fully integral bridges founded on steel pipe piles. Steel pipe piles are encased in reinforced concrete. A few analytical formulas based on linear material properties have been presented in Section 6.2 for thermal expansion of bridge superstructure. Analyses of laterally loaded piles are presented in Section 6.3 and analyses of fully integral bridges in Section 6.4.

6.2 Analytical superstructure calculations

6.2.1 Centre of thermal movements

The centre of thermal movements and thermal expansion length (see Figure 1.4) are solved on the basis of linear material properties and total stiffnesses of bridge structures and embankments in Paragraph 6.2.1.

An estimate for the centre of thermal movements may be calculated according to Figure 6.1. The analysed bridge has two spans of unequal length. An assumption of infinite axial stiffness of the bridge superstructure is made.

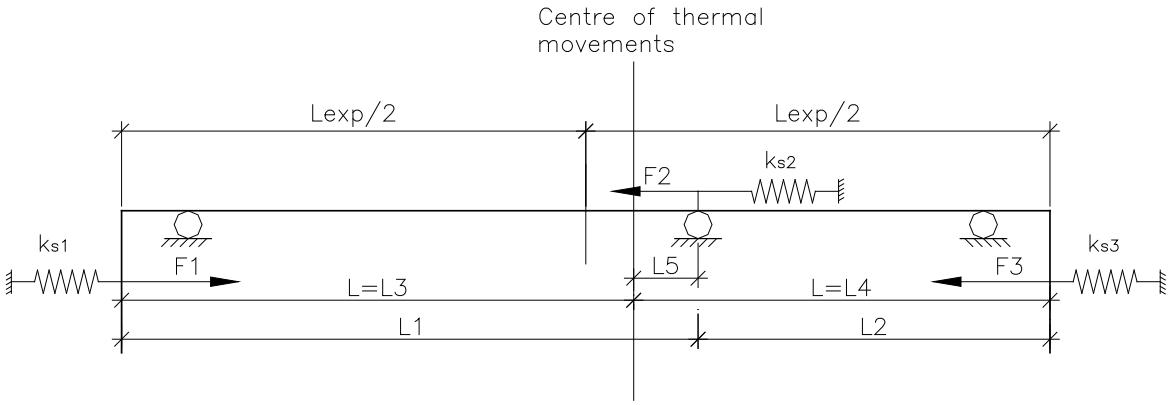

Figure 6.1. Parameters in the analysis of the centre of thermal movements.

All supports have stiffness k_s [MN/m] against longitudinal displacements. Then the longitudinal force equilibrium can be expressed as:

$$\rightarrow: F_1 - F_2 - F_3 = 0 \tag{6.1}$$

and it yields:

$$F = k_s x \tag{6.2}$$

$$\Delta_T = \alpha_{cT} * L * \Delta T_U \tag{6.3}$$

where:

α_{cT} = coefficient of thermal expansion for concrete structures
10*10-6 [1/C] [35]
L = thermal expansion length L3 or L4 [m]
L_{exp} = total thermal expansion length of bridge superstructure [m].

Then, by introducing Formulas 6.1, 6.2 and 6.3 we get:

$$k_{s1} * \Delta_1 - k_{s2} * \Delta_2 - k_{s3} * \Delta_3 = 0 \quad (6.4)$$

$$k_{s1} * L_3 * \alpha_{cT} * \Delta T - k_{s2} * L_5 * \alpha_{cT} * \Delta T - k_{s3} * L_4 * \alpha_{cT} * \Delta T = 0 \,\|: \alpha_{cT} * \Delta T$$

$$k_{s1} * L_3 - k_{s2} * L_5 - k_{s3} * L_4 = 0$$

Figure 6.1 yields:

$$L_5 = L_1 - L_3 \quad (6.5)$$

$$L_4 = L_{exp} - L_3 \quad (6.6)$$

Then, by introducing Formulas 6.4, 6.5 and 6.6 the following is obtained:

$$k_{s1} * L_3 - k_{s2}(L_1 - L_3) - k_{s3}(L_{exp} - L_3) = 0 \quad (6.7)$$

$$L_3 = \frac{k_{s3} * L_0 + k_{s2} * L_1}{k_{s1} + k_{s2} + k_{s3}}$$

Formula 6.7 is valid if analysis is linear or stiffnesses are analysed step by step in a non-linear analysis. Length $L_3 = (2 / 3) * L_{exp}$ if $k_{s3} = 2 * k_{s1}$ and $k_{s2} = 0$, i.e. displacements of support 1 are double compared to those of support 3 due to thermal expansion.

6.2.2 Superstructure contraction due to from soil-structure interaction forces

The amount of contraction of the bridge superstructure from soil-structure interaction forces, i.e., how large displacements are compared to free thermal expansion, is approximated in Paragraph 6.2.2.

A contraction due to normal force from soil-structure interaction was studied with the following simplified analysis, where the axial stiffness of the bridge superstructure is not infinite. A behaviour model is presented in Figure 6.2.

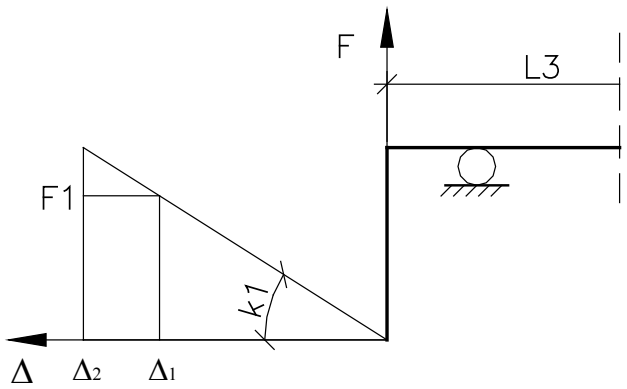

Figure 6.2. Simplified check for contraction of bridge superstructure.

The displacement of end screen Δ_2 represents a case without embankment soil. i.e. thermal expansion is free. The displacement of end screen Δ_1 represents a case with embankment

soil. The difference from Δ_1 to Δ_2 results from the contraction of superstructure. Then, the formula for a concrete bridge superstructure may be written:

$$\Delta_2 - \Delta_1 = \frac{F_1}{k_{ss}} \tag{6.8}$$

$$k_{ss} = \frac{E_c * A_{c,ss}}{L_3} \tag{6.9}$$

where
k_{ss} = axial stiffness of bridge superstructure [MN/m]
E_{ce} = elastic modulus of concrete, see Formula 6.87 [MN/m^2]
$A_{c,ss}$ = cross sectional area of superstructure [m^2]

F_1 is also obtained with formula

$$F_1 = k_{s1} * \Delta_1 \tag{6.10}$$

Together with Formulas 6.8 and 6.10 we get:

$$k_{s1} * \Delta_1 = k_{ss}(\Delta_2 - \Delta_1) \tag{6.11}$$

$$\frac{\Delta_1}{\Delta_2} = \frac{k_{ss}}{k_{ss} + k_{s1}}$$

The relation Δ_1/Δ_2 = 0.92 is obtained with rough input values from Section 6.4 for k_{ss} = (31600*12 /80) = 4740 MN/m and k_{s1} = H*B*$k_{h,s1}$ = 3*13.9*9.3 = 390 MN/m, where B is the width of the end screen and H is the height of the end screen. The effect is smaller if expansion length is smaller. The contraction of concrete superstructure slightly reduces the displacements from thermal expansion. Further, the rotation of the end screen reduces the value k_{s1}, and the soil behind the end screen yields when the previous relation is closer to one. Formulas 6.8-6.11 are valid if analysis is linear or with stiffnesses analysed step by step in non-linear analysis.

6.3 Laterally loaded pile behaviour

6.3.1 Scope

The analysed piles are steel pipe piles with composite action. This selection was made because the present pile type is commonly used, its availability is good, and experiences from the pile type are good. Further, the steel material is effectively used across the cross section. On the other hand this leads to relatively high stiffnesses of piles, which again leads to relatively high moments in constrained lateral motion. Corrosion allowance of 4 mm in normal corrosion conditions is obtained from [43], Paragraph 5.3.1, Table 6 soil corrosion conditions. The selected cross sections are presented in Figure 6.3. In addition, the rein-

forced concrete section used in the pile and bridge models of Section 6.4 is shown in Figure 6.3.

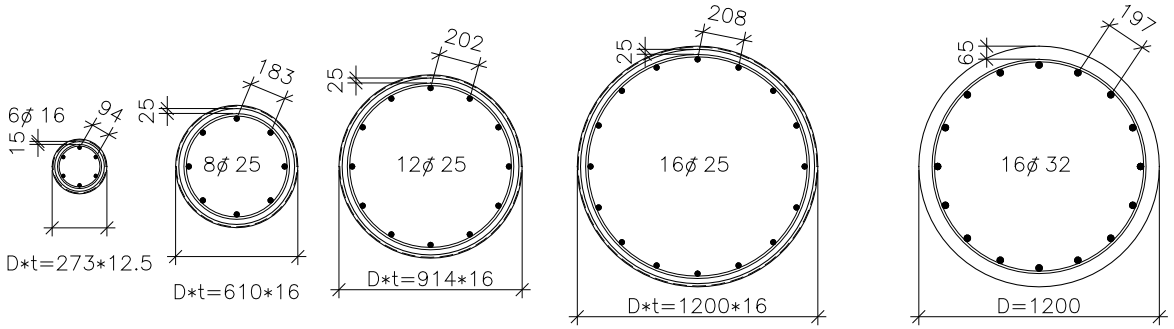

Figure 6.3. Cross section in analyses, stirrups ϕ = 12 except in D*t = 273*12.5 where stirrups ϕ = 8.

The concrete class is K35-2 [35]. The structural steel grade is S355J2H and reinforcement steel A500HW. The yield strength / elastic modulus of S355J2H is 355 MPa/210Gpa [108] and that of A500HW is 500 MPa/205GPa [35]. A dimensioning limit was determined for the yielding of structural steel at cross section edge in the short-term serviceability limit state. This section focusses on the pile cross-section and laterally loaded pile behaviour.

6.3.2 Capacity of composite cross section

Capacities (Moment-normal force diagram) for pile composite cross-section in ultimate limit state (ULS) and serviceability limit state (SLS) are analysed in Paragraph 6.3.2. The principles of analysis in ULS were the same as those given in the Finnish guidelines [35]. A similar method was used to define capacities in SLS, the limit at which structural steel does not yield under SLS loads.

The capacity for bending and normal force of a composite cross section (Pile) was calculated with the following strain stages in ULS and SLS. Calculations between stages were made in several steps. The normal force and bending moment, which correspond to the presented stages, were obtained by integrating corresponding strain stage stresses, see Figure 6.4.

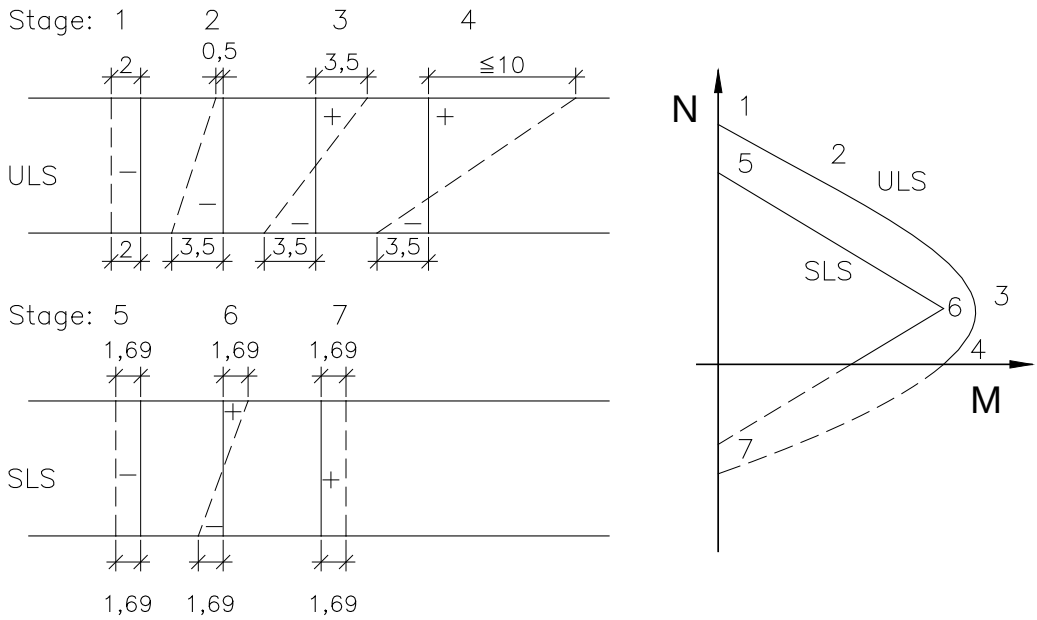

Figure 6.4. Strain stages for capacity calculations of composite pile cross section. Strain unit is [‰]. Tension is positive.

At ultimate limit state [35] it is required that strain at neutral axis does not exceed the value -2 ‰ and -3.5 ‰ at the edge of the cross section with normal strength ($f_{ck,cube}$ < 60 MN/m^2) concrete. At serviceability state the limit ±1.69 ‰ was obtained from the yield strain ε_y of S355 structural steel:

$$\varepsilon_y = \frac{f_s}{E_s} = \frac{355}{210} = 0.00169 \tag{6.12}$$

where:

f_s = yield strength of structural steel [MN/m^2]

E_s = elastic modulus of structural steel [MN/m^2]

The limit of f_s was set to avoid excessive displacements of the pile, which would develop with cyclic displacement in SLS. Further, a fatigue break might develop more easily if the yield strain of structural steel were exceeded during load cycles [56, 5]. A stress-strain relationship is obtained from Formula 6.13 for normal strength concrete in compression [45]:

$$\sigma_c = f_{ck}\left[1-\left(1-\frac{\varepsilon_c}{-0.002}\right)^2\right] \tag{6.13}$$

$$\sigma_c = f_{ck}, \text{if } \varepsilon_c \le -0.002$$

where:

σ_c = compressive stress of concrete [MN/m^2]

f_{ck} = characteristic compressive cylinder strength of concrete at 28 days [MN/m^2]

ε_c = strain of concrete ≤ 0.0035 [-]

$$f_{ck} = 0.7 * f_{ck,cube} \tag{6.14}$$

where:

$f_{ck,cube}$ = characteristic compressive cubic strength for 0.15*0.15*0.15 m^3 test specimen of concrete at age of 28 days [MN/m^2]

Furthermore, it is assumed that concrete is not assumed to exhibit tensile strength at cross section. Structural steel and reinforcement are assumed to behave as linear elastic and ideal plastic materials. The short-term tension stiffness of composite cross section EA_0 in pure compression is expressed as:

$$EA_0 = E_c A_c + E_s A_s + E_y A_y \tag{6.15}$$

where:

E_c = secant modulus of concrete at age of 28 days, which is derived from Formula 6.13 using formula $E_c = \sigma_c / \varepsilon_c$ [MN/m^2]

A_c = cross sectional area of concrete [m^2]

A_s = cross sectional area of structural steel section [m^2]

E_y = elastic modulus of reinforcement [MN/m^2]

A_y = cross sectional area of reinforcement [m^2]

Concrete creep was taken into account as a factor increasing steel stresses in serviceability state, which reduces the capacity of the cross section. The long-term tension stiffness of composite cross section EA_{00} in pure compression is expressed as:

$$EA_{00} = E_{cc} A_c + E_s A_s + E_y A_y \tag{6.16}$$

where:

$$E_{cc} = \frac{E_c}{1+\phi} \tag{35} (6.17)$$

E_{cc} = secant modulus of concrete with creep effect [MN/m2]

ϕ = creep coefficient of concrete at time $t = \infty$ with constant stress σ_c [-]

A change in tension stiffness $\Delta EA_{0->00}$ of composite cross section due to concrete creep is obtained from:

$$\Delta EA_{0->00} = EA_0 - EA_{00} = E_c A_c - E_{cc} A_c \tag{6.18}$$

Due to the lowering of tension stiffness, the compression strain of cross section increases. Stresses of concrete are reduced and those of structural steel as reinforcement get higher. The increase of compressive strain $\Delta\varepsilon_{tot}$ is obtained from:

$$\Delta\varepsilon_{tot} = \left(\varepsilon_{00} - \varepsilon_0\right) = \left(\frac{F_X}{EA_{00}} - \frac{F_X}{EA_0}\right) = EA_0\varepsilon_0\left(\frac{1}{EA_{00}} - \frac{1}{EA_0}\right) = \varepsilon_0\left(\frac{EA_0}{EA_{00}} - 1\right) \tag{6.19}$$

where:

F_x = normal force of pile [MN]

ε_0 = initial strain of column from force F [-]

The increase in steel compression stress $\Delta\sigma_s$ is then obtained from:

$$\Delta\sigma_s = \Delta\varepsilon_{tot} E_s \tag{6.20}$$

However, in Formula 6.17 the creep factor is defined with constant stress. Then compressed concrete final strain at t = ∞ would be:

$$\varepsilon_{cc} = \varepsilon_0 (1 + \phi) \tag{35} (6.21)$$

where:

ε_{cc} = strain of concrete at time t = ∞ with constant stress σ_0 [-]

The concrete stress gets lower because the structural steel and the reinforcement resist the increase of compressive strain in composite cross sections. If the tension stiffness of the structural steel and the reinforcement in the cross section were infinite, the increase of compressive strain of the cross section would be nil. In that case, the behaviour of the concrete would be called relaxation. If the tension stiffness of the structural steel and the reinforcement in the cross section were nil, then the increase of compressive strain of the cross section would be $\phi * \varepsilon_0$. The situation in the composite cross section falls between the previous situations. The relation between concrete relaxation and creep may be expressed as:

$$\psi = \frac{\phi}{1 + \rho\phi} \tag{131} (6.22)$$

where:

ψ = relaxation coefficient of concrete [-]

ρ = ageing coefficient of concrete [-]

The relaxation coefficient of concrete defines the decrease of concrete stress with constant strain:

$$\psi = \frac{\Delta\sigma_c}{\sigma_c} \tag{131, 111, 77} (6.23)$$

where:

$\Delta\sigma_c$ = decrease of concrete stress [MN/m^2]

Further studies on correlations of creep and relaxation may be found in [77, 111]. The ageing coefficient ρ of concrete has been found to be between 0.6-0.9 [131, 111]. In this study the following behaviour is assumed to simplify the analysis:

$$\sigma_{c1} = \frac{\sigma_c}{1 + 0.5\phi + 0.5\phi_{\text{mod}}} \tag{6.24}$$

and:

$$\varepsilon_{c0}(1 + \phi_{\text{mod}}) = \varepsilon_{c0} + \Delta\varepsilon_{tot} = \varepsilon_{c1} = \frac{\sigma_{c1}}{E_c} \tag{6.25}$$

$$\phi_{\mathrm{mod}} = \frac{\Delta\varepsilon_{tot}}{\varepsilon_{c0}}$$

where:

σ_{c1} = final compressive stress in composite cross section at t = ∞ [MN/m^2]
ϕ_{mod} = modified creep coefficient of concrete at time t = ∞ with stress σ_{c1}[-]
ε_{c0} = initial strain of concrete [-] = ε_0
ε_{c1} = final strain at t = ∞ with stress σ_{c1} [-]

In Formula 6.24, the creep is divided into two parts: the first part 0.5*ϕ represents the relaxation and the second part 0.5*ϕ_{mod} takes into consideration that stress of concrete gets lower with time. With ϕ = ∞ the formula gives σ_{c1} = 0 and with infinite tension stiffness of the structural steel and the reinforcement in the cross section $\sigma_{c1} = \sigma_c/(1+0.5\phi)$. The behaviour is similar to what has been described previously. The following schematic behaviour in Figure 6.5 presents the effect of different values of E_sA_s if E_yA_y is ignored.

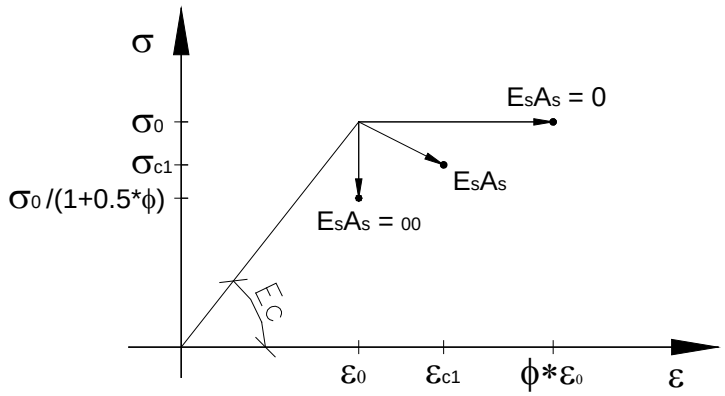

Figure 6.5. Concrete behaviour in composite column.

The creep factor ϕ = 1 for composite columns was used in this study. Shrinkage has been assumed negligible in the composite column. The circumstances of concrete of the composite column are favourable from the viewpoint of creep and shrinkage (lead to small creep factors and shrinkage) because drying and carbonation in a steel pipe is limited. The capacities of Figures 6.6-6.9 below of cross-sections presented in Figure 6.3 were obtained based on the previous dimensioning principles. In the diagrams the different stages of cross-section M-N interaction curves are labelled:

D_0 = capacity in SLS	D_{0c} = capacity in SLS with corrosion
D_1 = capacity in SLS with ϕ = 1	D_{1c} = capacity in SLS with ϕ = 1 and corrosion
D_{00} = capacity in SLS with ϕ = ∞	D_{00c} = capacity in SLS with ϕ = ∞ and corrosion
D_d = capacity in ULS	D_{dc} = capacity in ULS with corrosion

where D is diameter of pile, SLS is serviceability limit state and ULS is ultimate limit state. Calculation points are presented at Curves D_{1c} and D_{dc} include calculation points that

are used later for defining capacities of structures. $\Delta\sigma_s$ was analysed so that the whole concrete area was involved. $\Delta\sigma_s$ at stage D_{1c} is presented for different cross sections in Table 6.1.

Table 6.1. $\Delta\sigma_s$ at stage D_{1c}

Cross section	ϕ_{mod}	$\Delta\varepsilon_s$	$\Delta\sigma_s$
D*t = 1200*16(*	0.42	0.69	150
D*t = 914*16	0.35	0.58	120
D*t = 610*16	0.26	0.43	90
D*t = 273*12.5	0.14	0.21	45

*) Cross section dimensions in Finnish manufacturing are D*t = 1219*16

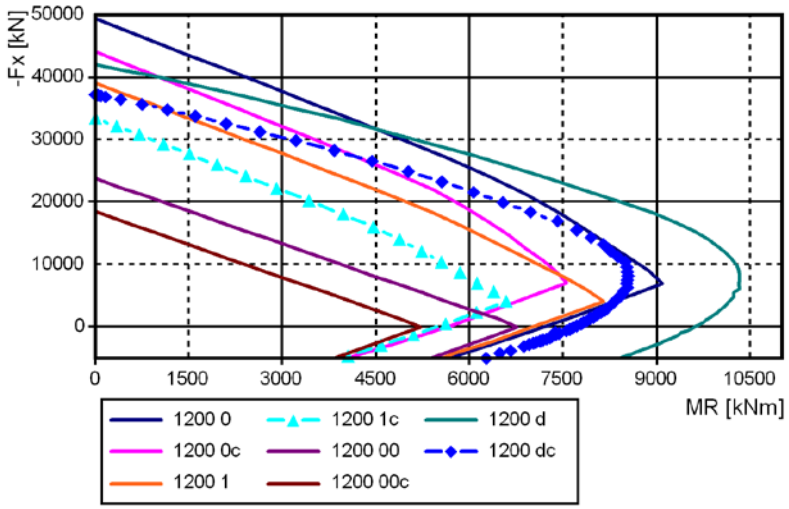

Figure 6.6. Interaction curves for composite column cross section D*t = 1200*16 M-N.

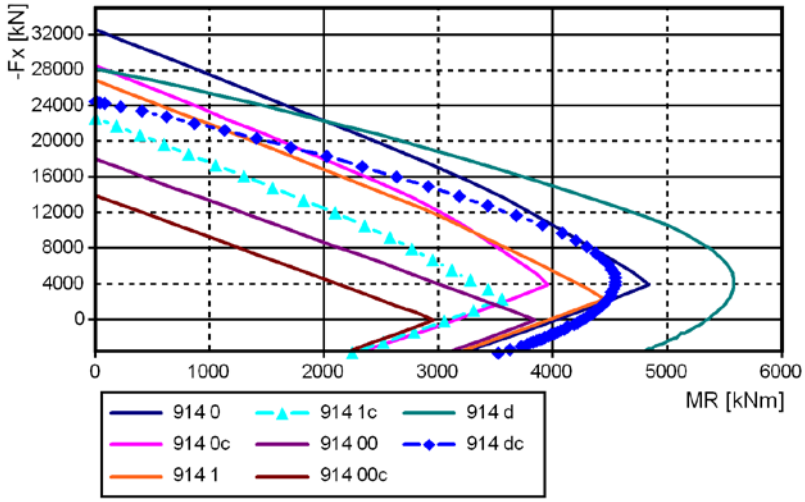

Figure 6.7. Interaction curves for composite column cross section D*t = 914*16 M-N.

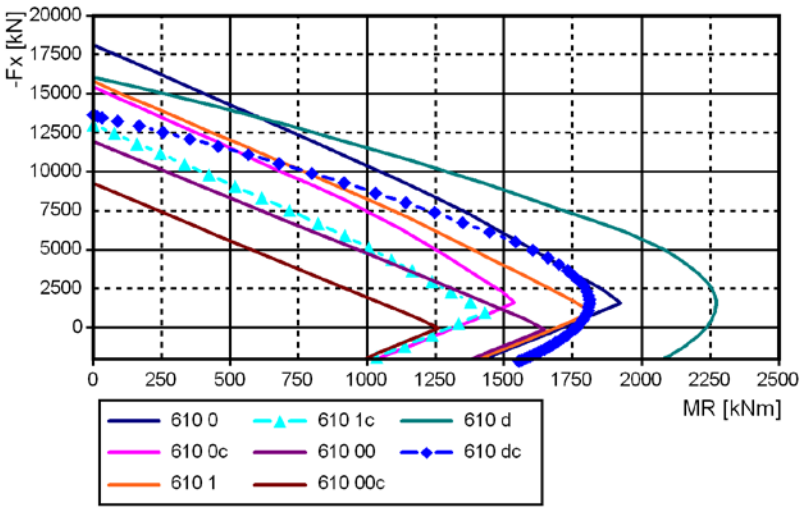

Figure 6.8. Interaction curves for composite column cross section D*t = 610*16 M-N.

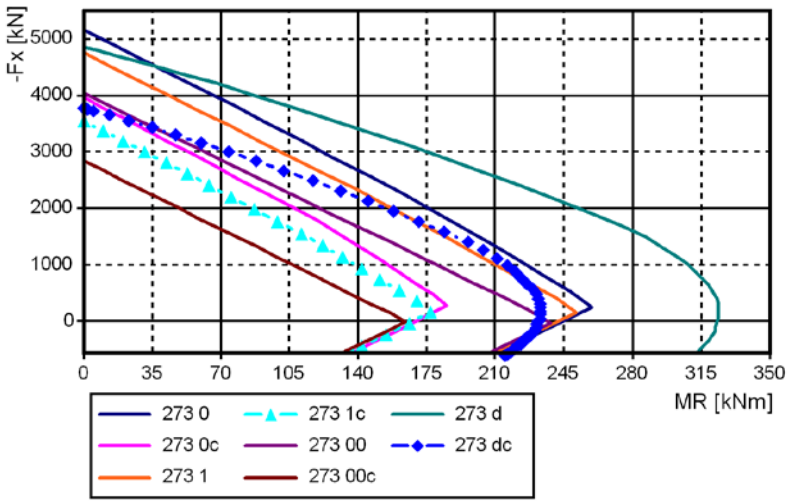

Figure 6.9. Interaction curves for composite column cross section D*t = 273*12.5 M-N.

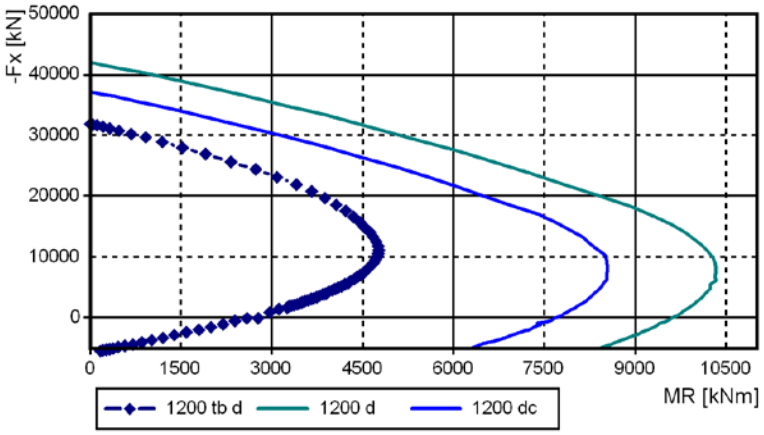

Figure 6.10. Interaction curve for concrete column cross section D = 1200 M-N and interaction curves in ultimate limit state for composite column D*t = 1200*16.

Curves D_{00} and D_{00c} present the capacity of steel section and reinforcement, in other words, limit of capacity for steel stresses, and Formula 6.26 is valid when only structural steel is acting:

$$\sigma_s = \frac{F_x}{A_s} + \frac{M_R}{W_s} \tag{6.26}$$

where:

W_s = elastic section modulus of structural steel [m^3]

M_R = resultant moment of cross section [MNm], if moment axes are y and z then

$$M_R = \sqrt{\left(M_y^2 + M_z^2\right)} \tag{6.27}$$

The concrete in the cross section increases the moment capacity significantly under normal force. The relation A_c*E_c / (A_s*E_s + A_y*E_y) is higher in larger diameter composite columns, which increases the advantage of concrete compared to smaller diameter composite columns. However, the disadvantage of the higher effect of creep is more prevalent in larger diameter cross sections. The highest moment capacity in SLS stages was obtained with compressive strain ε_y on one side of the cross section and tension strain ε_y on the other side. In D_0 and D_{0c} states at maximum moment value, the normal force F_x is carried by concrete and the external moment is carried by the structural steel part of the cross section and the eccentricity of the concrete force resultant, if the reinforcement capacity is neglected. In stage D_0 the maximum moment capacity $M_{o,max}$ was obtained with normal forces $N_{0,opt}$ as shown in Table 6.2.

Table 6.2. Composite cross section capacity with component N [kN] and M [kNm]

Cross section	$N_{0,opt}$	$N_{0,opt2}$	$M_{0,max}$	$M_{0,max3}$	$M_{0,s}$	$M_{0,c}$	$M_{0,max2}$	$N_{1c,opt}$	$M_{1c,max}$
D*t = 1200*16(*	7220	7000	9150	8530	6170	2410	8580	4260	6630
D*t = 914*16	4060	3990	4870	4560	3535	1035	4570	2450	3580
D*t = 610*16	1690	1710	1940	1820	1535	295	1830	1060	1440
D*t = 273*12.5	290	320	260	250	225	25	250	190	178

*) Cross section dimensions in Finnish manufacturing are D*t = 1219*16.

$N_{0,opt2}$ is calculated with the simplified formula:

$$N_{0,opt2} = 0.5\pi\left(\frac{D}{2} - t\right)^2 * f_{ck} * 0.8 * \frac{2}{3} \tag{6.28}$$

where:

$0.5\pi\left(\frac{D}{2} - t\right)^2$ = half of concrete area A_c [m^2]

0.8 = factor that accounts for the concrete stress-strain behaviour along cross section [35]

2/3 = the volume of cylindrical hoof / the volume of wedge = (2/3*r^2*h) / (r^2*h)

Formula 6.28 gives a rather good approximation of normal force $N_{0,opt}$. $M_{0,max2}$ is calculated with the simplified formula:

$$M_{0,\max 2} = M_{0,s} + M_{0,c} \tag{6.29}$$

where:

$M_{0,s} = W_s * f_s$ = the moment capacity of structural steel [kNm] (6.30)

$M_{0,c} = N_{o,opt2} * e_c$ = the moment capacity of concrete [kNm] (6.31)

where:

e_c = concrete force resultant distance from centre axis of composite cross section, assumed to be as in a cylindrical hoof [m]:

$$e_c = \frac{3}{16} * \pi * r \tag{6.32}$$

$M_{0,max3}$ in the Table 6.2 is calculated in stage D_0 without reinforcement. Formula 6.29 gives a very good approximation of moment $M_{0,max}$. Most of the capacity $M_{0,max2}$ is due to structural steel. $N_{1c,opt}$, and $M_{1c,max}$ is calculated in stage D_{1c}. These capacities are used in defining the utilisation rate of the pile cross section in Paragraph 6.4.11. The wall thickness in the cross-section is assumed to be sufficient for stress at SLS with respect to local stability, which was not discussed in this study. The ULS capacities were analysed with a partial safety factor in structural class 1 $\gamma_s = 1.1$ for structural steel, $\gamma_y = 1.1$ for reinforcement and $\gamma_c = 1.35$ for concrete. However, the casting of concrete of structural class 1 [35] may cause problems with the pile. The capacity in ULS was presented to offer a general view of cross section capacities, while the forces and utilisation rates in ULS did not fall within the scope of this study. However, the forces at ULS are also important in analysing the piles of a fully integral bridge [54]

6.3.3 Bending stiffness of composite cross section

The bending stiffnesses of pile composite cross sections in Paragraph 6.3.3 were analysed in a similar way as the capacities in Paragraph 6.3.2.The partial safety factor was 1.0 in defining each curvature-moment relationship. The bending stiffnesses were analysed with different normal forces because they have an effect on the results. The bending stiffness field (moment-curvature relationship with different normal forces) in stage D_0 was inputted in FE analyses.

The bending stiffness of the composite cross section (pile) was calculated at stage D_0. The moment-curvature relationship was analysed with several steps for obtaining a reasonable moment-curvature relationship for FE analyses as in reference [64]. The moment-curvature relation in Figure 6.11 was obtained for a D*t = 1200*16 composite cross section:

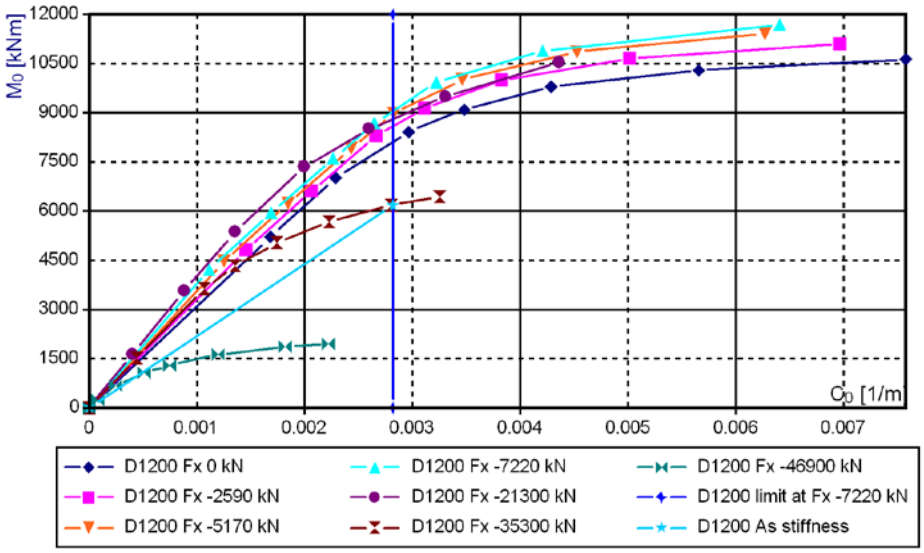

Figure 6.11. Moment-curvature relation for composite cross section D*t=1200*16 at stage D_0. $N_{0,opt}$ = 7220 kN.

The cross section has a high curvature capacity with normal force $N_{0,opt}$. The curvature C_0 is:

$$C_0 = \frac{\left|\varepsilon_{s,t} - \varepsilon_{s,b}\right|}{D} \tag{6.33}$$

where:

$$\varepsilon_{s,t} = \frac{\sigma_{s,t}}{E_s} \text{ and } \varepsilon_{s,b} = \frac{\sigma_{s,b}}{E_s} \tag{6.34}$$

where:

$\varepsilon_{s,t}$ = strain of structural steel at top of composite cross section [-]
$\varepsilon_{s,b}$ = strain of structural steel at bottom of composite cross section [-]
$\sigma_{s,t}$ = stress of structural steel at top of composite cross section [MN/m^2]
$\sigma_{s,b}$ = stress of structural steel at bottom of composite cross section [MN/m^2]

The bending stiffness of the cross section is a secant modulus of each strain stage in Figure 6.11. Also the stiffness of structural steel of cross section is presented until strain limits $\varepsilon_{s,t,}$ and $\varepsilon_{s,b}$ are achieved without normal force F_x. A vertical line represents the limit where both $\varepsilon_{s,t}$ and $\varepsilon_{s,b}$ are at limit ε_y with normal force $N_{0,opt}$. Similar results for all studied cross sections are presented in Appendix 8.1. The equivalent composite cross section properties, moment of inertia I_0 and section modulus of composite cross section W_0, if all parts of cross sections were structural steel at stage D_0, are presented in Table 6.3. E_sI_s is bending stiffness of the steel part of the composite cross section and EI_0 is bending stiffness of the composite cross section at stage D_0.

Table 6.3. Composite cross section properties in bending

	$\varepsilon_s \leq \varepsilon_y$	At stage D_0 when $M_0 = M_{0max}$ (and $N_0 = N_{opt}$)				
Cross section	E_sI_s [MNm^2]	EI_0 [MNm^2]	EI_0/ E_sI_s [1] [-]	I_0 [3] [m^4]	$W_0= 2I_0/D$ [4] [m^3]	$\sigma_0 = M_{0max}/W_0$ [2] [MN/m^2]
D*t = 1200*16	2190	3240	1.48	15.0e-3	26.0e-3	355
D*t = 914*16	956	1320	1.38	6.28e-3	14.0e-3	
D*t = 610*16	277	352	1.27	1.67e-3	5.46e-3	
D*t = 273*12.5	18	21	1.15	1.00e-4	7.32e-4	

1) At present stage also $M_0/M_s = EI_0/EI_s$
2) M_{0max} is obtained from Table 6.1
3) I_0 is moment of inertia of composite cross section if all parts were of structural steel
4) W_0 is section modulus of composite cross section if all parts were of structural steel

The check that yield of structural steel is achieved with presented cross section properties is presented in the last column. This check was made to ensure the accuracy of cross section properties. The moment-curvature relation in Figure 6.12 was obtained for D = 1200 reinforced concrete cross section.

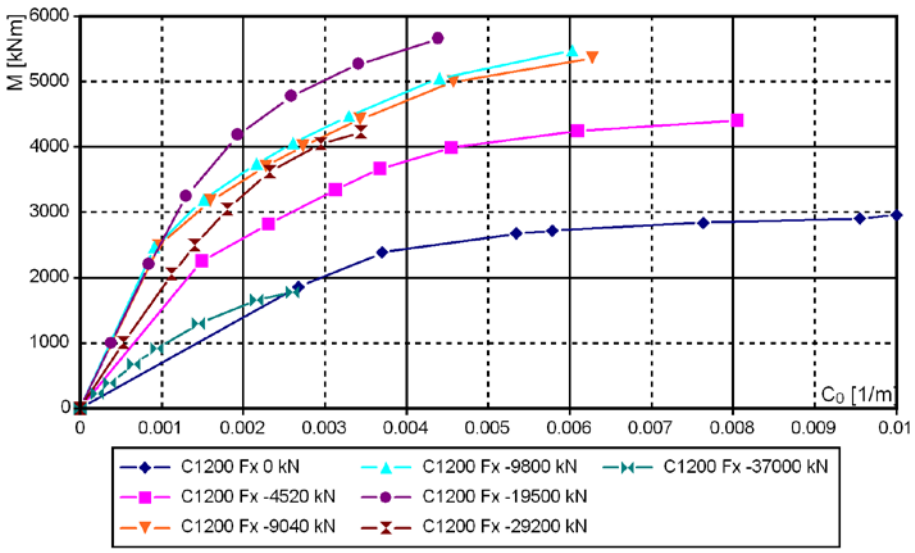

Figure 6.12. Moment-curvature relation of concrete cross section for D=1200.

The stiffness of a reinforced concrete cross section depends more on normal force than that of the composite cross section. The stiffnesses get higher in Figure 6.12 with increasing normal force until a normal curve with a normal force of –19500 kN. The higher the normal force, the less tensile strain in concrete. Stiffnesses get lower with higher normal force values due to the softening of concrete under higher compressive strains.

6.3.4 Modulus of lateral subgrade reaction

The modulus of lateral subgrade reaction for piles is discussed in Paragraph 6.3.4. The modulus of subgrade reaction is inputted to FE analyses together with hyperbolic soil behaviour in Paragraph 6.3.4.

The development and research of modulus of lateral subgrade reaction at piles and screen are not a key point of this study. However, the lateral behaviour of piles and the end screen does have a significant effect on the structural behaviour of integral bridges. Hence, there was a need to pay attention to these behaviours. The behaviours were assigned to the FE model's spring stiffnesses of joint elements with one degree of freedom. Then the behaviour had to be simple enough to be inputted in spring models. In the previous studies of the overall research project it was concluded that pile diameter has an effect on lateral stiffness and strength [75]. Further, the stiffness at a stage representing 50% of ultimate capacity was used in modelling springs at different stages, see Figure 6.13 and 2.35. The behaviour of lateral subgrade reaction is expressed in this study for non-cohesive soils by Formulas 6.35-6.42:

$$M_{50} = m_{50} * \sigma_0 * \left(\frac{\sigma_v}{\sigma_0} \right)^{1-\beta_{50}} \quad \text{[30] (6.35)}$$

$$E_{50v} = M_{50} \frac{(1+\upsilon)(1-2\upsilon)}{1-\upsilon} \quad \text{[114] (6.36)}$$

$$E_{50l} = E_{50v} \frac{1-\upsilon-2\upsilon^2}{(1-\upsilon)(1-\upsilon^2)} \quad \text{[126] (6.37)}$$

$$\sigma_v = \gamma' * z \quad (6.38)$$

And the constant of lateral subgrade reaction n_{h50} when 0.5* q_f is reached is defined:

$$n_{h50} = \frac{E_{50l}}{z} \quad \text{[43] (6.39)}$$

Factor n_{h50} depends on depth z, thus the factor m_{h50} which is independent of depth z is defined:

$$m_{h50} = \frac{n_{h50}}{z^{-\beta_{50}}} * \zeta^{-\beta_{50}} = \frac{E_{50l}}{z^{1-\beta_{50}}} * \zeta^{-\beta_{50}} \quad \text{[51, 127, 10] (6.40)}$$

The coefficient of lateral subgrade reaction is then obtained for general cohesionless soils:

$$k_{h50} = m_{h50} * \frac{z^{\beta_{50}}}{D^{0.5}} => m_{h50} * \left(\frac{z}{D} \right)^{0.5} \quad \text{[51, 127, 133, 113] (6.41)}$$

The modulus of subgrade reaction is then:

$$k_{50} = k_{h50} * D = m_{h50} * \left(\frac{z}{D} \right)^{0.5} * D \quad (6.42)$$

where

k_{h50} = coefficient of lateral subgrade reaction at a stage where 0.5*q_f is reached [MN/m^3]
n_{h50} = constant of lateral subgrade reaction at a stage where 0.5*q_f is reached, constant at each depth level z [MN/m^3]
m_{h50} = modified constant of lateral subgrade reaction at a stage where 0.5*q_f is reached, constant along depth z [MN/m^3]

k_{50} = modulus of lateral subgrade reaction [MN/m^2]
β_{50} = stress exponent depending on soil type at a stage where 0.5*q_f is reached [-]
m_{50} = modulus number depending on soil type at a stage where 0.5*q_f is reached [-]
σ_0 = reference stress, 0.1 used in this study [MN/m^2]
σ_v = effective vertical stress [MN/m^3]
z = depth from ground surface [m]
E_{50l} = lateral soil modulus [MN/m^2]
E_{50v} = vertical soil modulus [MN/m^2]
M_{50} = odometer soil modulus [MN/m^2]
ν = Poisson's ratio of soil [-]
ζ = 1, factor for correcting units [51] [m]

The parameter 0.5 is used in Formula 6.41 and the effect of pile diameter is included in Formulas 6.41-6.42. A different parameter 0.4 is used instead of 0.5 in [143]. The parameter 0.5 was used in Formula 6.41 because:

- The stress level σ_v does not have an effect on the modified constant of lateral subgrade reaction $m_{,h50}$, i.e., $m_{,h50}$ is constant along the pile length but soil stiffness is not and it is taken into account in Formula 6.41
- The parameter β_{50} describes the stage when 50% of lateral capacity has been reached, see Figure 6.17. Then the pile diameter has an effect on modulus of lateral subgrade reaction even though the initial stiffness were not be affected by pile diameter
- The pile diameter would also have an effect at the initial stage of a laterally loaded pile because it was observed in another part of the research project [75]
- The parameter β_{50} had an effect related to the size of loaded area in solutions of a linear half-space case of vertically loaded foundations [127]

According to references [51, 127, 133, 113] Formula 6.41 will lead to results where pile diameter has a certain effect on modulus of lateral subgrade reaction (soil stiffness per unit length against pile). The factor ζ corrects units of the modified constant of lateral subgrade reaction in Formula 6.40. A commonly used value for β_{50} in cohesive soils at low stress levels is 1.0 and for non-cohesive soils 0.5 [51, 127]. It is probable in the case of cohesive soils that $\beta_{50} \neq 1$ when 50% of the capacity has been reached. The stress level of cohesive soil (subsoil) is small in this study. Formulas 6.39 and 2.20 have been presented in [43]. However, Formulas 6.39 and 6.43 together lead to a situation where pile diameter does not affect the modulus of lateral subgrade reaction k because the diameter will be reduced at the top part of the pile when depth is smaller than 10*D and loading below ultimate resistance, see also Figure 6.18, case d.

$$k_{50} = n_h * \left(\frac{z}{D} \right) * D = n_h * z \qquad [43] (6.43)$$

and when z $\geq$ 10*D

$$k_{50} = n_h * \left(\frac{10 * D}{D} \right) * D = n_h * 10 * D \qquad [43] (6.44)$$

The modulus of lateral subgrade reaction of Formulas 6.35-6.42. is obtained with Formula 6.45 and $\beta_{50} = 0.5$:

$$k_{50} = \frac{E_{50l}}{z} * \frac{1}{z^{-\beta_{50}}} * \zeta^{-\beta_{50}} * \left(\frac{z}{D} \right)^{0.5} * D = m_{h50} * z^{0.5} * D^{0.5} \qquad (6.45)$$

In the case of Formula 6.45 pile diameter affects modulus of lateral subgrade reaction in non-cohesive soils. A formula for spring stiffness k_{s50} of non-cohesive soils is obtained using Formulas 2.7 and 6.45:

$$k_{s50} = cc_c * k_{50} = cc_s * m_{h50} * \left(\frac{z}{D} \right)^{0.5} * D = cc_s * m_{h50} * \sqrt{D * z} \qquad (6.46)$$

The modulus of lateral subgrade reaction is assumed to be independent of pile diameter in cohesive soils in this study using Formula 6.47. The result corresponds to the elastic continuum solution where:

$$k_h = \frac{E_s}{D} \qquad [43] (6.47)$$

In [132] a soil stiffness per unit area has been presented with the following equation for elastic continuum and rectangular areas:

$$\frac{\Delta}{P} = \frac{m_s \left(1 - \nu^2\right)}{E\sqrt{A}} \qquad [43] (6.48)$$

$$\frac{PA}{\Delta} = \frac{E}{m_s \left(1 - \upsilon^2\right)\sqrt{A}} = k_h \qquad (6.49)$$

where:
P = vertical loading [MN]
Δ = displacement [m]
E = elastic modulus of continuum [MN/m^2]
A = loaded area [m^2]
m_s = shape factor depending on shape of loaded area [-]

At A = D*3D and m = 0.82, Formula 6.49 is of the form:

$$k_h = \frac{0.65 E_s}{D\left(1 - \nu^2\right)} \qquad [138] (6.50)$$

In [11, 92] it has been suggested that the factor 0.65 should be 1.3 because the pile is in contact at both sides. In [19, 92] it has been suggested based on a full-scale test that factor 1.0 gives the closest agreement:

$$k = k_h * D = \frac{E_s}{(1-\nu^2)} \qquad [138]\ (6.51)$$

The modulus of subgrade reaction based on the theory of elasticity is obtained with Formula 6.51.

6.3.5 Hyperbolic and cyclic lateral soil behaviour

The loads of pile and bridge models are cyclic. Thus the soil properties have to be taken into account observing kinematic rules for soil material behaviour. Hyperbolic behaviour is part of cyclic lateral soil behaviour.

In this study, soil pressure development against pile is assumed hyperbolic, as described in Paragraph 2.2.4. The initial modulus of lateral subgrade reaction k_i is calculated based on k_{50}. The relation between the k_{50} value and hyperbolic behaviour is presented in Figure 6.13.

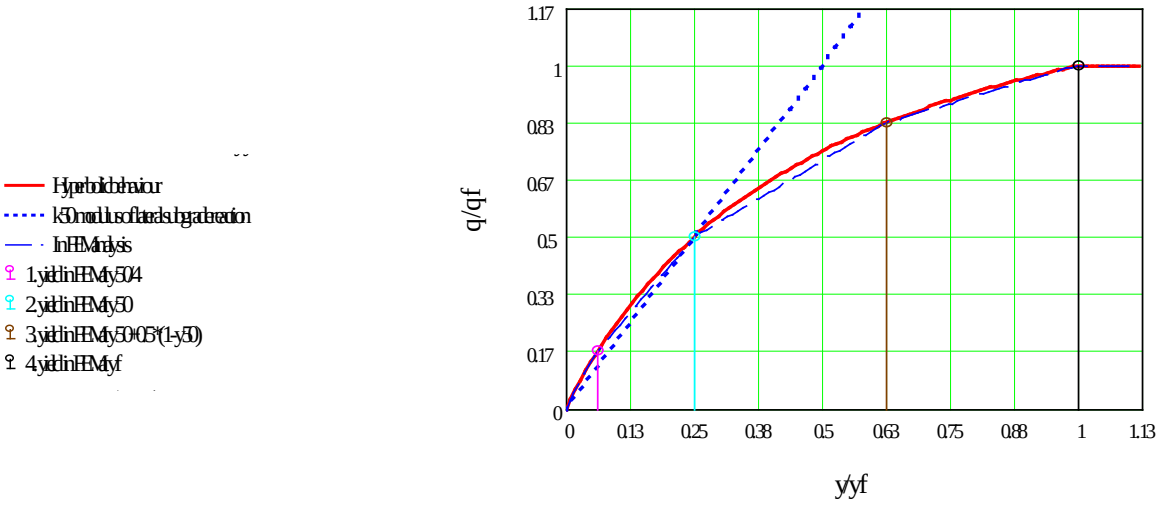

Figure 6.13. Hyperbolic lateral soil behaviour at ξ_{50} = 1/2.

In the analysis of this study, soil behaviour is modelled with four different elasto-plastic springs at the same node as in Figure 2.35 and in [33]. Then the behaviour presented in Figure 6.13 is obtained. As the limits of the turning points were selected $y_{50}/4$, y_{50}, $y_{50}/2$ + 0.5 and y_f so that the behaviour is close to hyperbolic. q_f is calculated with Formula 2.29 using factor 4.4 [43]. The behaviour is analysed with Formula 2.26. Cyclic behaviour is assumed symmetrical as in Figure 2.34b and Figure 6.14.

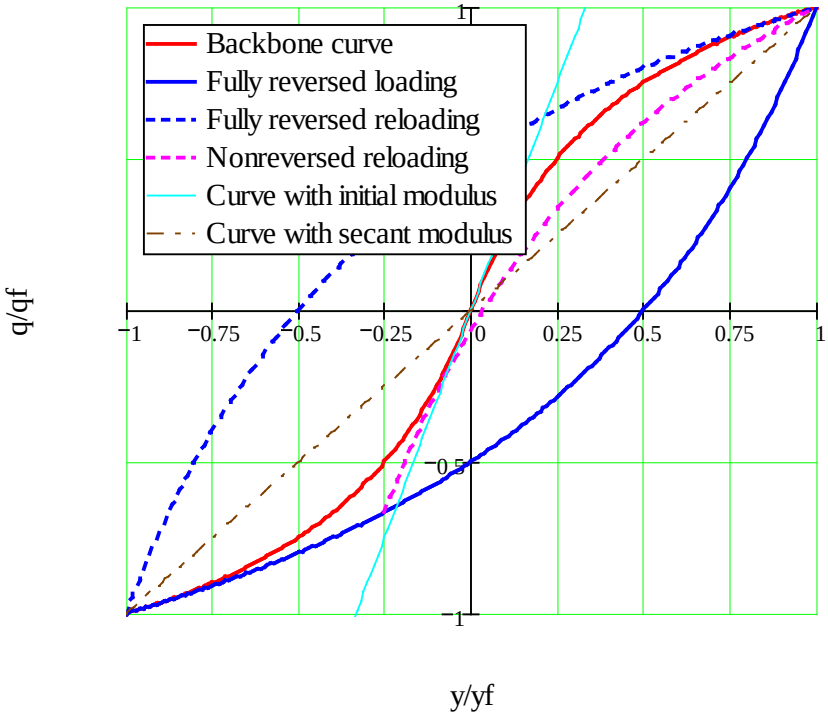

Figure 6.14. Cyclic lateral soil behaviour of q-y loops at ξ_{50} = 1/2 and R_f = 2/3.

In the first loading of Figure 6.14, the q-y relationship is shown by the red curve according to Formula 2.26. In the first fully reversed loading, q-y is shown by the blue curve according to Formula 6.52:

$$q = 1 - \frac{1-y}{\frac{1}{k_i} + R_f \frac{|1-y|}{2q_{ult}}} \tag{6.52}$$

If loading is fully reversed, the reloading curve is similar to the fully reversed curve but mirrored against the secant curve in a fully loaded case. If loading is not fully reversed before reloading, the formula is:

$$q = q_r + \frac{y-y_r}{\frac{1}{k_i} + R_f \frac{|y-y_r|}{2q_{ult}}} \tag{6.53}$$

where:
q_r = lateral soil reaction at the beginning of reloading [MN/m]
y_r = lateral displacement at the beginning of reloading [m]

If the lateral soil reaction exceeds the value q_{ult}, then the q-y behaviour is assumed fully lateral. At the beginning of reverse loading the behaviour is similar as in Figure 6.14 in fully reversed loading, see Figure 6.15.

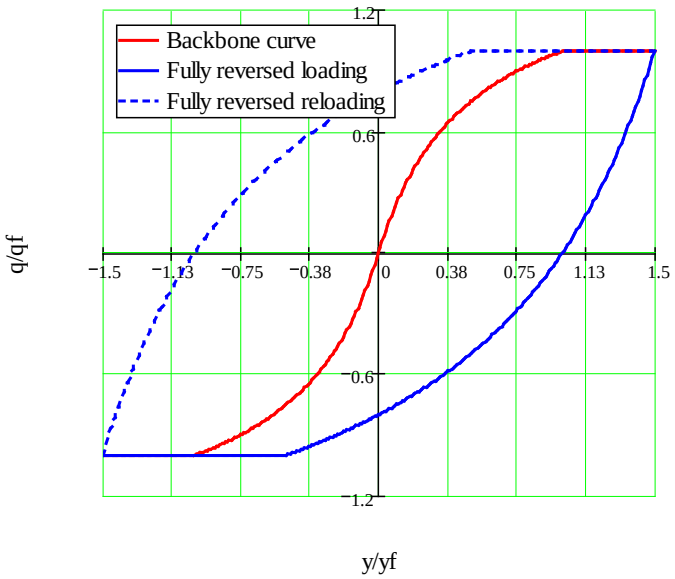

Figure 6.15. Cyclic lateral soil behaviour of q-y loops where y_f is exceeded at ξ_{50} = 1/2 and R_f = 2/3.

The drawback of the behaviour is that it does not take into account the gap formation behind a laterally loaded pile. However, in Figure 6.14, in the fourth curve of partly reversed loading, load q exceeds q_f at y_f although degradation is present in monotonic loading [52], see Figure 2.34b. In the case of the piles of an integral bridge end, the loading is between monotonic and fully reversed. The non-symmetrical loading is due the fact that the construction-period temperature of the bridge was not in the middle of the temperature range and shrinkage and creep range of concrete. Further, the soil of the slope is relatively loose. A multiplier has been estimated in Paragraph 6.4.6 partly due to these reasons for permanent loadings, which affect longitudinal displacements. The influence of different values of k_i and q_{ult} on the hyperbolic curve is presented in Figure 6.16.

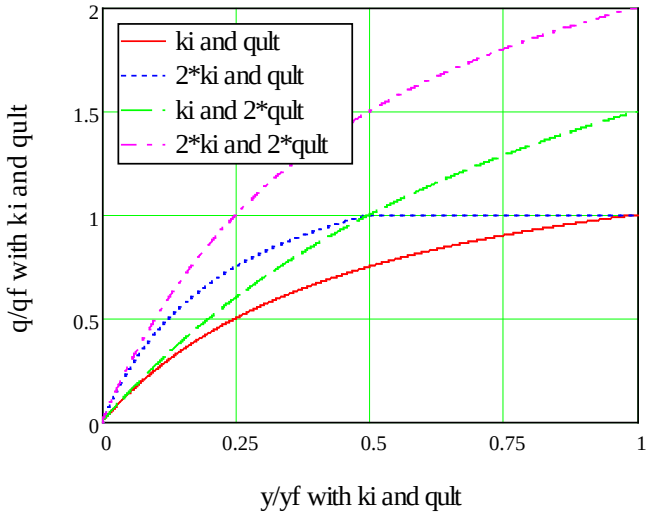

Figure 6.16. The influence of different k_i and q_{ult} on hyperbolic soil behaviour at ξ_{50} = 1/2 and R_f = 2/3.

It may be observed that q_{ult} has a strong influence on hyperbolic behaviour. The lateral behaviour of the top part of the pile plays a significant role in the present problem, as noted in Figures 2.26 and Paragraph 6.3.7. Soil strains are at their highest and q_f is reached or almost reached along top part of the pile when lateral capacity has a relatively strong influence compared to initial stiffness k_i.

6.3.6 Soil and lateral soil properties in analysis

The lateral soil properties were inputted as function of Global co-ordinates (with depth co-ordinate z) and pile diameter to FE analyses. The lateral soil properties were analysed in Paragraph 6.3.6.

Three different soil properties were used in the laterally loaded pile analysis. The selected soil properties are presented in Table 6.4. Factor 0.8 was used for k_i and q_f because the cross section is circular, see Figure 2.31. In addition, subsoil properties, SS, of the bridge model analysis have been presented. Only one set of subsoil properties were used in the analyses because subsoil properties have only a small influence on laterally loaded pile behaviour in the studied dimensions, as noted in Paragraphs 2.2.4 and 6.3.8.

Table 6.4. Soil and lateral soil reaction properties in the case of piles

	Soil properties							Lateral soil reaction properties (1		
	ϕ_s	s_U	m_{50}	β_{50}	γ'	ν	ξ_{50}	k_{50} (2	q_f	$y_{50} = 0.5*q_f/k_{50}$
	°	MN/m^2	-	–	kN/m^3	–	-	MN/m^2	MN/m	m
WS	36	0	400	0.5	18	0.3	0.25	$8.23*\sqrt{(z*D)}$	0.244*z*D	$0.0148*\sqrt{(z*D)}$
NS	37	0	700	0.5	19	0.3	0.25	$14.8*\sqrt{(z*D)}$	0.269*z*D	$0.0091*\sqrt{(z*D)}$
HS	40	0	1000	0.5	20	0.3	0.25	$21.7*\sqrt{(z*D)}$	0.324*z*D	$0.0075*\sqrt{(z*D)}$
SS(3	0	20	50	1.0	15	0.3	0.17	2.43	0.128*D	$0.0026*\sqrt{(z*D)}$

1) Calculated as defined in Paragraphs 6.3.5 and 6.3.6
2) See Figure 6.17c
3) Subsoil of bridge model in Section 6.4

The general behaviour of lateral subgrade reaction for pile diameters D and 2D is presented in Figure 6.17. k_{50} as well as y_f and y_{50} are $\sqrt{2}$-fold when the pile diameter is doubled. Resistance q_f is doubled when pile diameter is doubled.

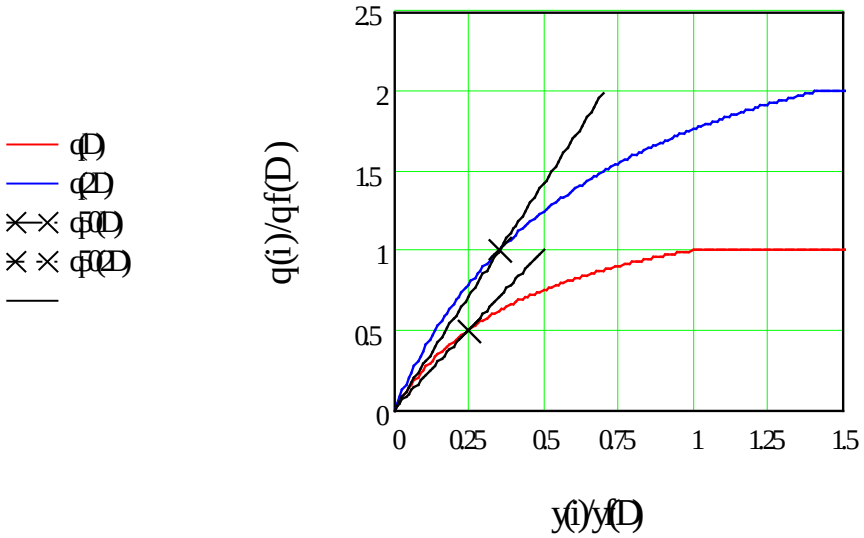

Figure 6.17. General behaviour of lateral subgrade reaction for pile diameters D and 2D.

The slope of curves $q_{50}(D)$ and $q_{50}(2D)$ is the modulus of lateral subgrade reaction, as in Table 6.4.

6.3.7 Distribution of modulus of lateral subgrade reaction along pile length

Different distributions of modulus of lateral subgrade reaction are presented in Paragraph 6.3.7. Solutions for a laterally loaded pile with linear material properties are presented based on [104]. Further, the effect of the unsupported (out of soil) top part of the pile on laterally loaded pile behaviour is discussed.

The distribution of modulus of lateral subgrade reaction affects the laterally loaded pile behaviour. Four different types of distribution are presented in Figure 6.18.

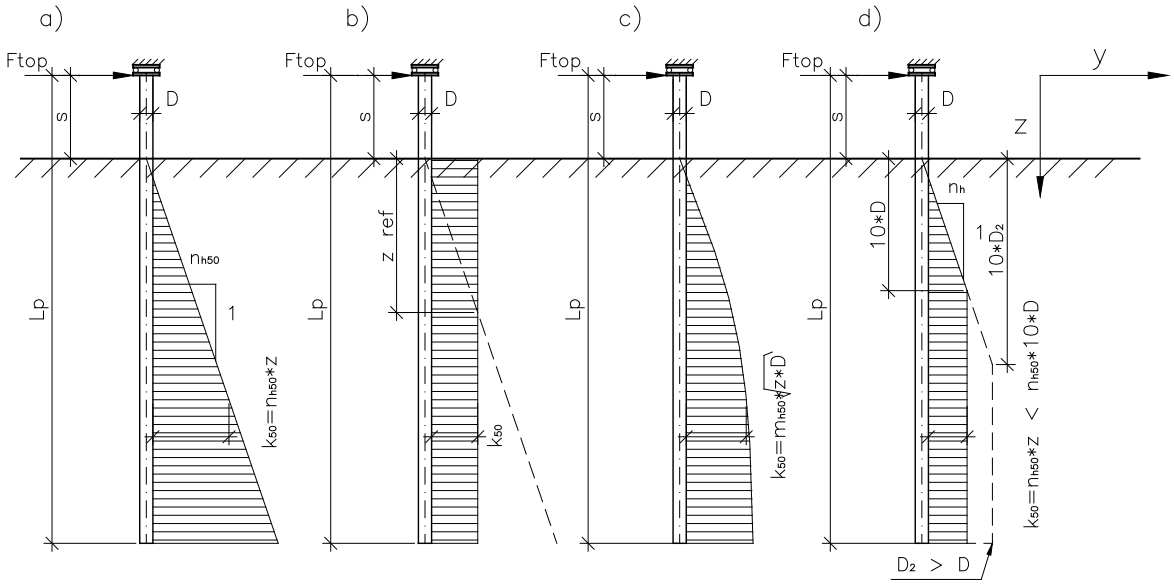

Figure 6.18 a)-d) Linear, constant, parabolically distributed modulus of lateral subgrade reaction according to Finnish guidelines [43]. In the Figure the pile is rotationally supported from the top of pile.

Figure 6.18b corresponds to Formula 6.51. Figure 6.18c corresponds to Formula 6.45. Figure 6.18d corresponds to the Finnish guidelines [43]. Figure 6.18a present the Gibson's soil

model. At a fully integral bridge end, the abutment piles are monolithically connected to the end screen or to the superstructure. The top part of the pile may be above ground level, or modelled as if it extended beyond the soil distance s, see Figure 6.18 and 6.19

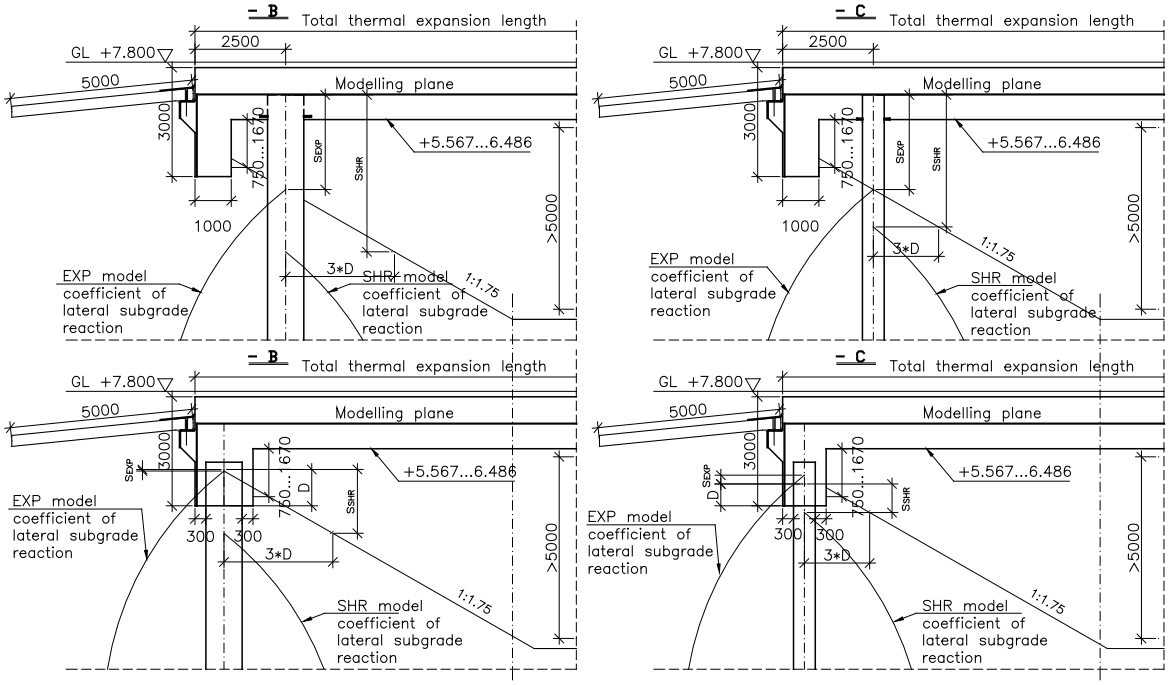

Figure 6.19. Piles at a fully integral bridge end. The distribution of modulus of lateral subgrade reaction against pile depends on pile displacement direction. The upper one are type T2 and the lower one are T1, see Section 6.4. The ones on the left are larger piles than the ones on the right. Names of section marks refer to Figure 6.39.

The modulus of lateral subgrade reaction distribution depends on pile displacement direction because of the slope effect. Soil at the slope side is not as stiff and firm as at the embankment side. They are calculated with separate models in the analysis: SHR for superstructure shrinking and EXP for expanding effect on piles at bridge end. The selection was made more simple structural models. Figure 6.15 shows a bridge type without a cantilever span, type T1, and one with a cantilever span, type T2. The level z = 0 of the modulus of lateral subgrade reaction is at the slope's upper bound in models EXP_T2, see Figure 6.19, upper types. It is assumed that the end screen affects the upper part of the pile because the end screen pushes the embankment as the pile moves towards the embankment [75]. The level of the modulus of lateral subgrade reaction z = 0 when soil distance between pile centreline and slope upper bound is 3*D in the SHR models. The value for the distance in stabilised state in the Finnish guidelines is 5*D [46]. The smaller distance is selected so that the results of present analyses would be on the safe side concerning the pile stresses from the displacements. The level z = 0 of modulus of lateral subgrade reaction is at the extended slope upper bound in models EXP_T1 because the end screen effect is similar to that mentioned earlier. Values of s in different models are presented in Table 6.5.

Table 6.5. Distances s [m], according to Figures 6.18 and 6.19

	Model type			
Cross section	s, T1 SHR	s, T1 EXP	s, T2 SHR	s, T2 EXP
D*t = 1200*16	2.36	0.300	4.66	2.25
D*t = 914*16	1.58	0.014	4.17	2.25
D*t = 610*16	0.756	-0.290	3.65	2.25
D*t = 273*12.5	-0.159	-0.627	3.08	2.25

Values of s are measured from the superstructure neutral axis (T2) and end screen bottom level distance D inside the end screen (T1). This offset was performed so that a connection of the pile would develop rotational fixity. If it is assumed that s = 0 and the structure is like in Figure 6.18 a and b and the pile top has lateral displacement y_{top}, then the highest moment develops at the top of pile:

$$M_{top,a} = y_{top} * \lambda_2^2 * EI_p = y_{top} * (\frac{d}{dz} k_a)^{\frac{2}{5}} * (EI_p)^{\frac{3}{5}} \quad \text{in case a)} \quad [104]\ (6.54)$$

$$M_{top,b} = y_{top} * \lambda_1^2 * EI_p * 2 = y_{top} * \sqrt{k}_b * \sqrt{EI_p} \quad \text{in case b)} \quad [104]\ (6.55)$$

and in case the pile top is hinged

$$M_{\min,a} = -0.305 * M_{top,a} \quad \text{in case a)} \quad [104]\ (6.56)$$

$$M_{\min,b} = -0.322 * M_{top,b} \quad \text{in case b)} \quad [104]\ (6.57)$$

$$\frac{d}{dz} k_a = n_{h,a} (* \quad [104]\ (6.58)$$

where:

EI_p = bending stiffness of pile cross section [MNm^2]

$M_{top,a}$ = bending moment at top of pile when modulus of lateral subgrade reaction is linearly distributed along pile length [MNm]

$M_{top,b}$ = bending moment at top of pile when modulus of lateral subgrade reaction is constant along pile length [MNm]

$M_{min,a}$ = minimum bending moment of pile when modulus of lateral subgrade reaction is linearly distributed along pile length [MNm]

$M_{min,a}$ = minimum bending moment of pile when modulus of lateral subgrade reaction is constant along pile length [MNm]

k_a = modulus of lateral subgrade reaction when modulus of lateral subgrade reaction is linearly distributed along pile length [MN/m^2]

k_b = modulus of lateral subgrade reaction when modulus of lateral subgrade reaction is constant along pile length [MN/m^2]

$n_{h,a}$ = modified constant of lateral subgrade reaction when modulus of lateral subgrade reaction is linearly distributed along pile length [MN/m^3]

*) Derivate based on Formula 2.7: $\frac{d}{dz} k_a = n_h$, see Figure 6.18 case a.

The moment at the top of the pile is determined to be equal in case a) and case b) in Figure 6.18, i.e. $M_{top,a} = M_{top,b}$, using Formulas 6.54 and 6.55. Further, the modulus of subgrade reaction in case a) is determined using m_h in case b):

$$k_b = z_{ref} * \frac{d}{dz} k_a = z_{ref} * n_{h,a} \tag{6.59}$$

then z_{ref} is obtained from Formulas 6.54. 6.55 and 6.59:

$$z_{ref} = \sqrt[5]{\frac{EI_p}{n_{h,a}}} = \frac{1}{\lambda_a} = T_a \tag{6.60}$$

where

z_{ref} = reference depth, see Figure 6.18 [m]

Compare Formula 6.60 to Formulas 2.20 and 2.22. If value s is taken into account, then values of z_{ref} may be obtained from Figures 6.20. The analysis is based on the differential equation solution in [104].

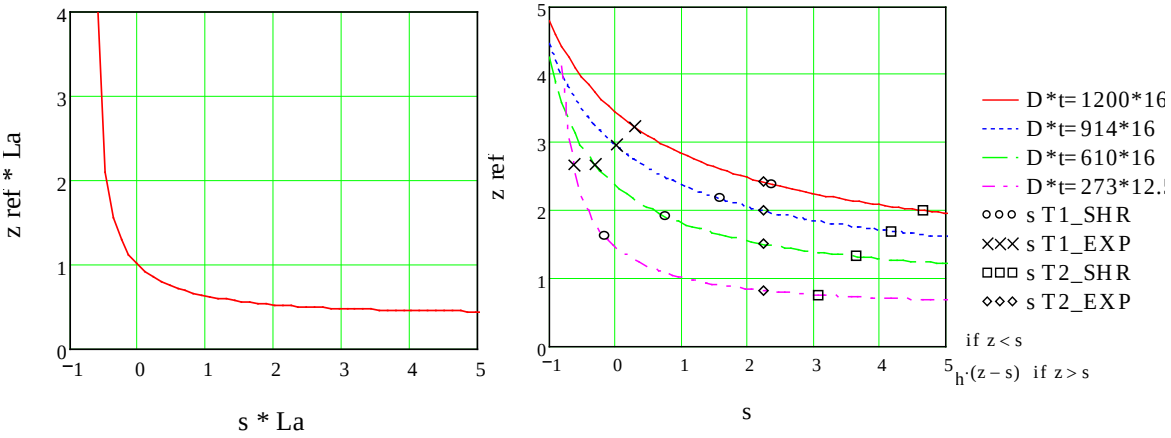

Figure 6.20. Left: Relative values of z_{ref} at different values of s (L_a in figure is λ_a). Right: Values of z_{ref} [m] at different values of s [m] and d(k)/dz = 6 [MN/m^2].

If d(k)/dz = 6*D$^{0.5}$ MN/m^2 and composite cross section stiffness is EI_0, then values s = -1 to 5 m z_{ref} are obtained from Figure 6.20. The level of z_{ref} is relatively high along pile length and the upper part of modulus of lateral subgrade reaction has a strong influence on laterally loaded pile behaviour as noted in [95]. The values of s from Table 6.5 are presented in Figure 6.20, right side. The value of $1/\lambda_a = T_a$ may be read from Figure 6.20, right side, when s = 0. The value of s has a significant decreasing effect on moment at the pile top M_{top} at prevailing forced pile top displacement y_{top}. The decrease of M_{top} when value of s increases at d(k)/dz = 6*D$^{0.5}$ MN/m^2 is presented in Figure 6.21 in cases a) and b) of Figure 6.18.

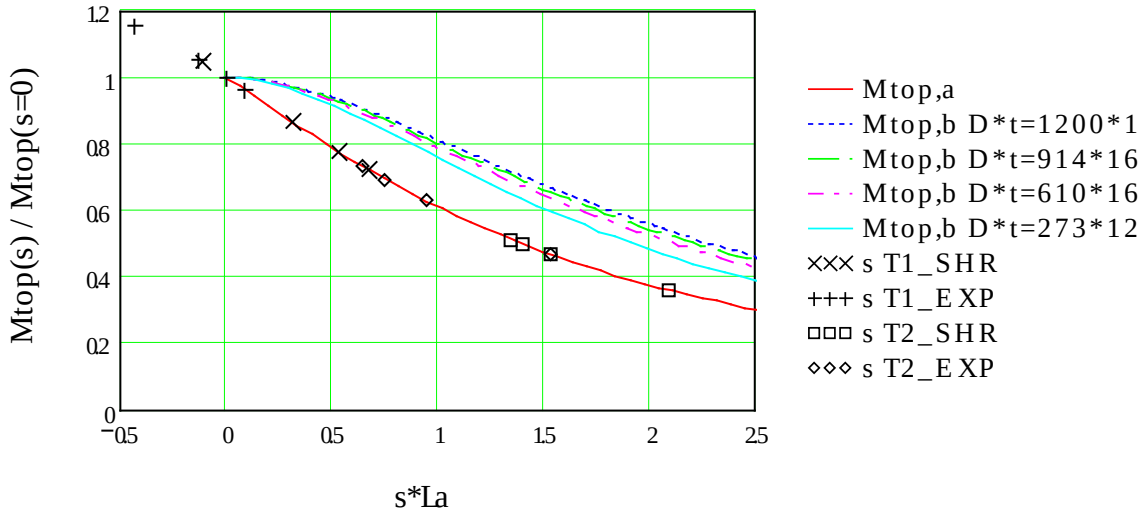

Figure 6.21. $M_{top,a}(s)/M_{top,a}(s=0)$ and $M_{top,b}/ M_{top,b}(s=0)$ (L_a in figure is λ_a).

It may be noted from Figure 6.21 that the increasing of s affects moment $M_{top,a}$ more than $M_{top,b}$ when the moments at the initial stage are equal to z_{ref} in Formula 6.60. A relatively small value of s decreases the moment value at forced displacement y_{top} at pile top. The decrease in moments due to the value of s is largest with models T2_SHR.

If it is assumed that s = 0 and the structure is like in Figure 6.18a and 6.18b, and the pile top is subject to lateral force F_{top}, then the highest moment develops at the top of pile:

$$M_{top2,a} = 0.93 * \frac{F_{top}}{\lambda_2} = 0.93 * \sqrt[5]{\frac{EI_p}{n_h}} * F_{top} \quad \text{in case a)} \qquad [104]\ (6.61)$$

$$M_{top2,b} = \frac{F_{top}}{2 * \lambda_1} = 0.5 * \sqrt[4]{\frac{4 * EI_p}{k_b}} * F_{top} \quad \text{in case b)} \qquad [104]\ (6.62)$$

and in a case when the pile top is hinged

$$M_{min\,2,a} = -0.80 * M_{top2,a} \quad \text{in case a)} \qquad [104]\ (6.63)$$

$$M_{min\,2,b} = -0.64 * M_{top2,b} \quad \text{in case b)} \qquad [104]\ (6.64)$$

The effect of the bending stiffness of pile cross-section and the modulus of subgrade reaction is opposite to the moment at the pile top in the case where loading to pile is F_{top} compared to the case where the pile top is subject to forced displacement y_{top}. The decrease of moments between the rigid and hinged cases with load Ftop is smaller than with pile top displacement y_{top}.

6.3.8 Finite element models (FEM)

A cyclic FE analysis with LUSAS (14.3-2 kit242) has been carried out. Models consist of thick nonlinear beam elements (BTS3), joint elements (JSH4), support conditions, material

properties and geometric properties [93]. A mesh of the model with supporting conditions is presented in Figure 6.22.

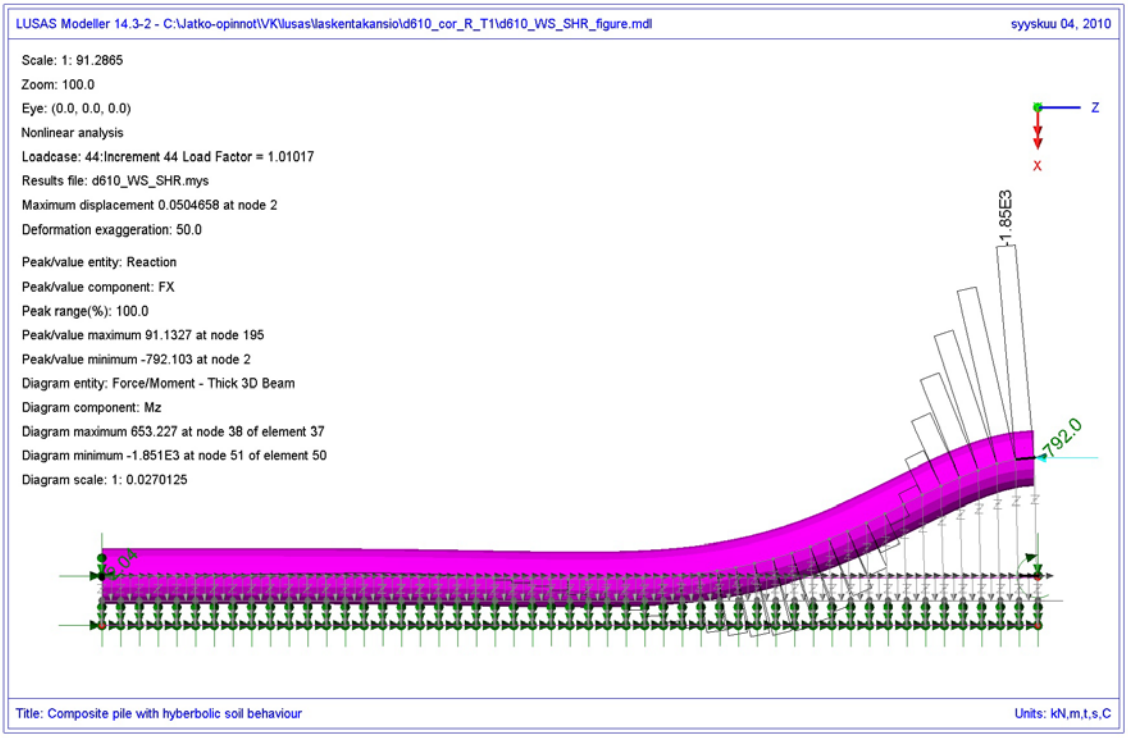

Figure 6.22. T1_D610_R_WS_SHR_cor with 4 mm corrosion FE model in LUSAS at increment where pile top displacement is 50 mm. Main moment M_z in black (beam local z-co-ord.) and support reaction FX in green (Global X-co-ord.) at pile ends are visible.

Supports are shown in green and the pile in pink. The joint elements of the pile are supported with continuous support in all translate and the rotational Z-direction. The pile bottom is supported in all translate directions, and the pile top in translate X- and Y-directions and in the rotational Y-direction. A lateral load was given as the displacement of the pile top support. The lateral displacement of the pile top in X-direction was 0.05 m forward and fully reversed to –0.05 m position in T1 models. The displacement value was 0.1 m in T2 models. A 20 m pile length was selected in the model to ensure that the behaviour would be near infinite. The selection was made with help of Formulas 2.22 and 2.23. A mesh division of 50 was selected, which is relatively fine due to the nature of nonlinearity. Several mesh divisions were tested to ensure accurate results. A sufficient mesh division would be from three to five along one characteristic half-wave length (half-wave length = $\pi/\lambda = \pi*T$) according to [62, 66]. In the present analysis, the mesh division is greater than 10 along one half-wave, see T_a for D*T=273*12.5 from Figure 6.20, right side. Four elastic-plastic joint elements were connected to the same nodes in beam elements as described in Paragraph 6.3.6. The values s in Table 6.5 were taken into account as an offset of the Z –coordinate in the FE model. The bending stiffness was modelled as function of normal force

according to Paragraph 6.3.3. The normal force was set at N_{opt}. Both rotationally rigid pile top R and hinged pile top F models were analysed. In the project a total of 192 pile models were analysed including the following:

- 4 pile sizes: D*t = 273*12.5, D*t = 610*16, D*t = 914*16, D*t = 1200*16
- Pile cross section with or without corrosion (with corrosion: cor)
- 3 soil types: WS, NS, HS
- Main displacement directions of pile top: SHR, EXP
- Bridge type with or without cantilever span: T1, T2
- Rotationally rigid or hinged pile top: R, F

Total: 4*2*3*2*2*2 = 192 models

This study is mainly focussed on rotationally rigidly connected piles (R models) but models with corrosion (cor models) were also taken into account as a factor which lowers the capacity of the cross section. The forces used in dimensioning were, however, taken from the model without corrosion. This selection was made because it is possible that corrosion takes place at only one level of the cross-section while forces develop as in models without corrosion.

6.3.9 FEM results on laterally loaded piles

The results for one example pile size, D*t = 914*16, are discussed in Sub-paragraph 6.3.9.1 to simplify the result of Paragraph 6.3.9. All examined pile diameters are discussed in Sub-paragraph 6.9.3.2.

*6.3.9.1 Results for pile size D*t = 914*16*

Lateral q-y loops at different depths in models T1_D914_R_NS_EXP- and T1_D914_R_WS_SHR are presented in Figure 6.23.

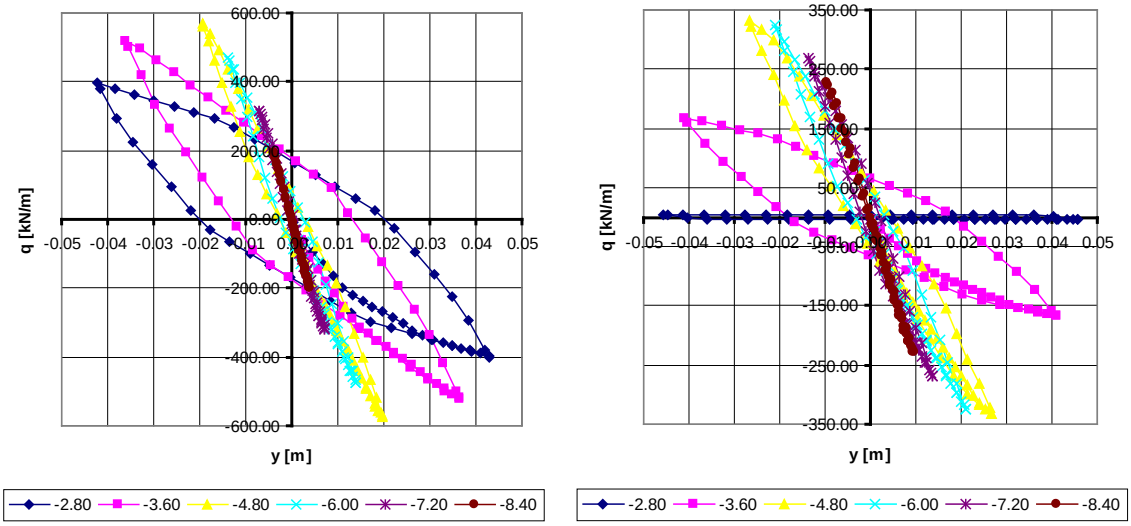

Figure 6.23 q-y loops at different depths Z. Left, T1_D914_R_NS_EXP model where s = 0.014. Right, T1_D914_R_WS_SHR -model where s = 1.58.

The q-y loops are for the same level Z but the value s is according to Table 6.5. The behaviour is as described in Paragraph 6.3.6. The behaviour is more elastic when Z decreases. The upper part of the lateral subgrade reaction has yielded over the 3rd yield point, see Figure 6.13. Developed max q-values are remarkably lower in the model WS_WHR than in NS_EXP. In other pile models, the behaviour is similar to the above ones'. The developed moment values M_{top} as function of y_{top} at the pile top of EXP model are presented in Figure 6.24.

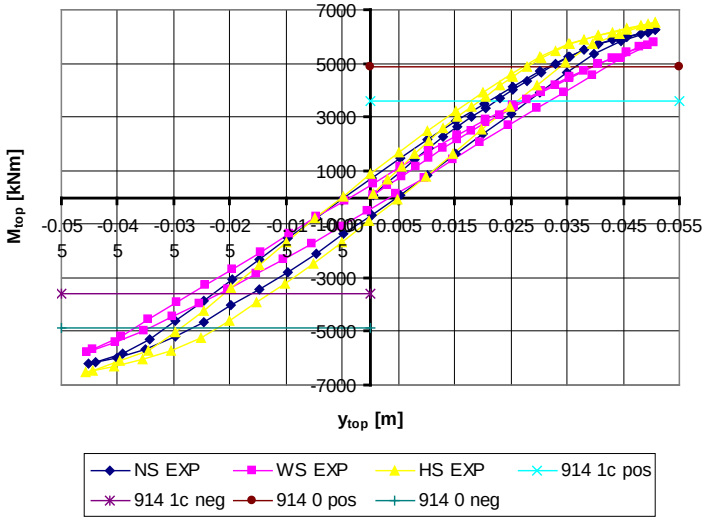

Figure 6.24. M_{top} as function of y_{top} in different soil types in T1_D914_R _EXP models.

The behaviour of moment M_{top} is rather linear as function of y_{top} of the pile compared to q-y loops. The behaviour reveals that the effect of pile bending stiffness is rather significant as with the linear behaviour in Formula 6.54. The capacities of the cross section D*t = 914*16 in the stages D_0 = 4870 kNm and the D_{1c} = 3580 kNm are also presented in Figure

6.24. Lateral displacement capacities at D_{1c} vary from 0.013 to 0.033 m and from 0.029 m to 0.039 m at D_0. The developed moment values as function of y_{top} at the pile top in the SHR model are presented in Figure 6.25.

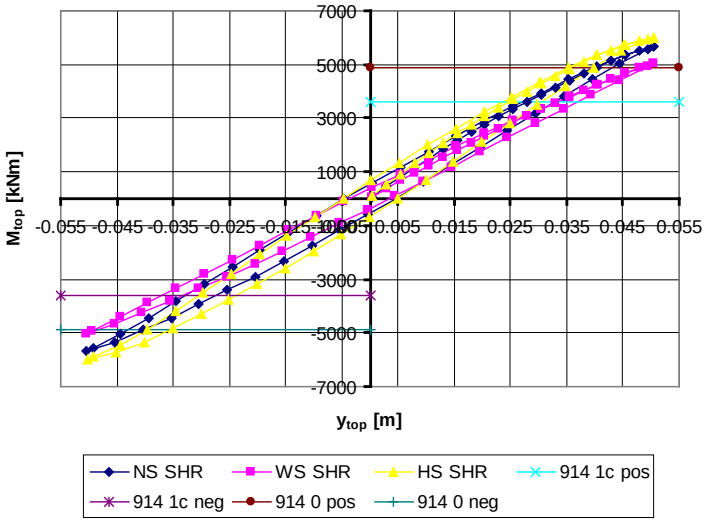

Figure 6.25. M_{top} as function of y_{top} in different soil types in T1_D914_R _SHR models.

In the SHR model, the behaviour of the moment is also rather linear. The lateral displacement capacities at D_{1c} vary from 0.025 to 0.037 m and from 0.035 m to 0.049 m at D_0. The moment values between EXP and SHR models are rather similar. Similar results for other cross section are presented in Appendix 8.2. The values of the later developed force at the pile top F_{top} as function of y_{top} scattered more than the moment values, see Figures 6.26 and 6.27.

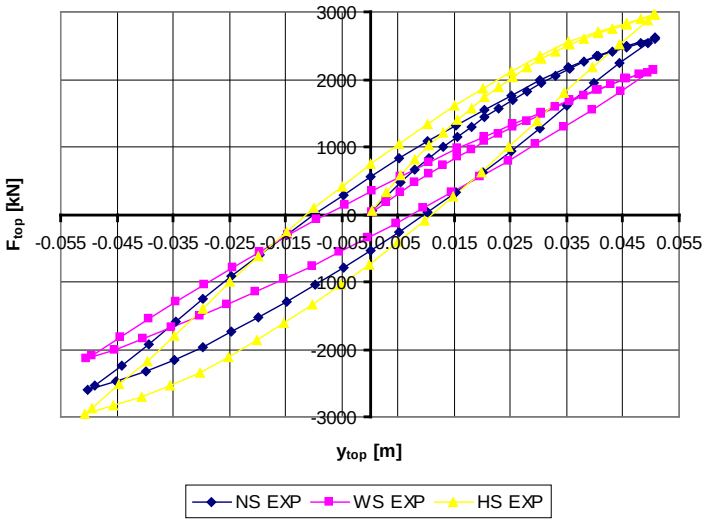

Figure 6.26. F_{top} as function of y_{top} in different soil types in T1_D914_R_EXP models.

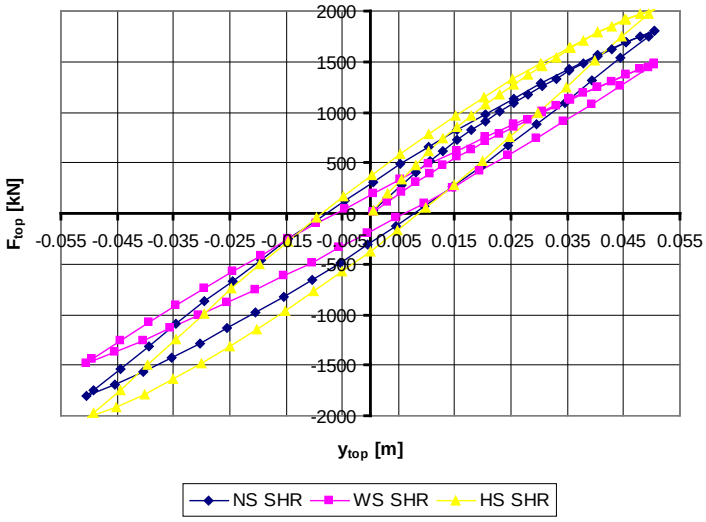

Figure 6.27. F_{top} as function of y_{top} in different soil types in T1_D914_R_SHR models.

The differences between the EXP and SHR models are bigger in the values of F_{top} than those of M_{top}. The differences have an effect on global bridge analysis especially in type T1 bridges, see Figure 6.19, where the lateral force has an influence on bridge end rotations. Moment values developed as function of y_{top} from model T2_D914_R_NS_EXP and model T2_D914_R_WS_SHR are presented in Figures 6.28 and 6.29.

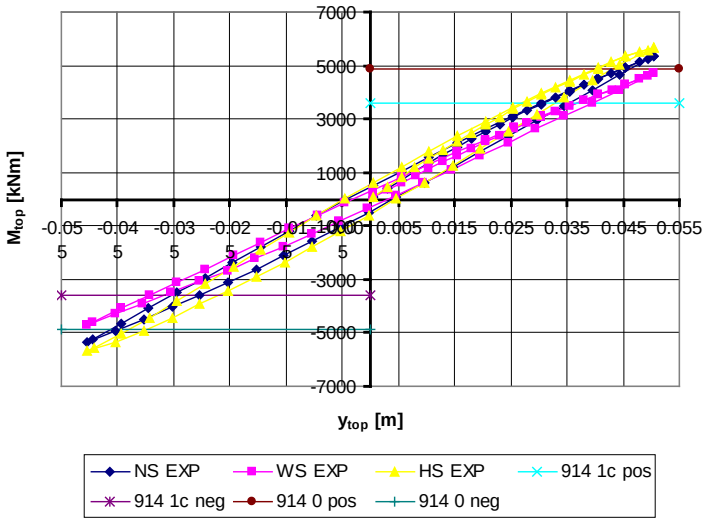

Figure 6.28. M_{top} as function of y_{top} in different soil types in T2_D914_R _EXP models, s = 2.25 m.

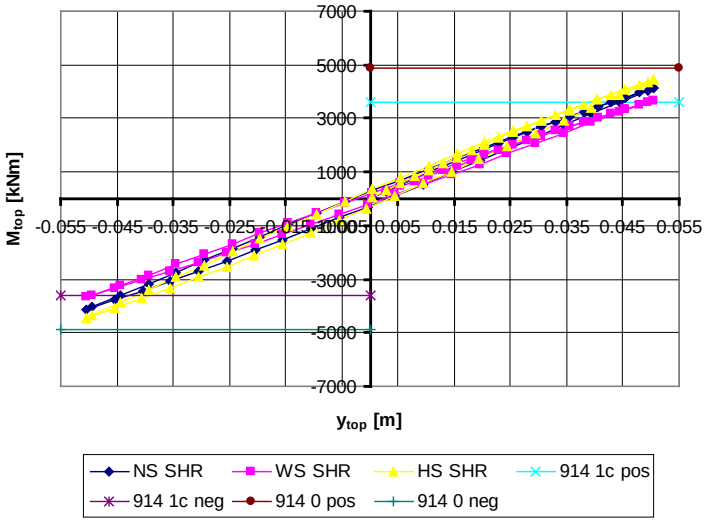

Figure 6.29. M_{top} as function of y_{top} in different soil types in T2_D914_R_EXP models, s = 4.17 m.

In the T2 model, the effect of soil type is smaller than in the T1 model. Displacement capacities of D_{1c} vary from 0.028 to 0.039 m at D_0 in the EXP model and from 0.040 to 0.049 m in the SHR model. The capacity D_{1c} was not obtained in all models with a 0.05 m displacement of the pile top. The structure of T2 is more slender than that of T1 since the developed forces are smaller in T2 models. Similar behaviour was detected with F_{top} values. The slenderness of piles is clearly visible in the F models. The moment values developed as function of y_{top} from models T1_D914_F_NS_EXP and T1_D914_F_WS_SHR are presented in Figures 6.30 and 6.31.

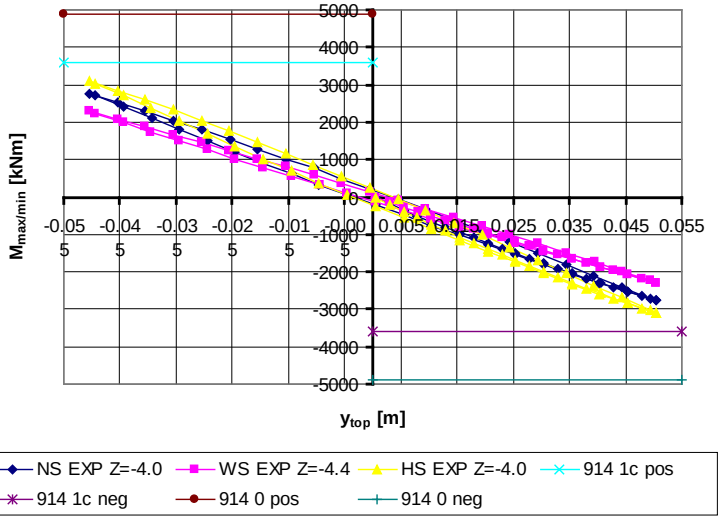

Figure 6.30. $M_{max/min}$ as function of y_{top} in different soil types in T1_D914_F_EXP models, s = 2.25. m

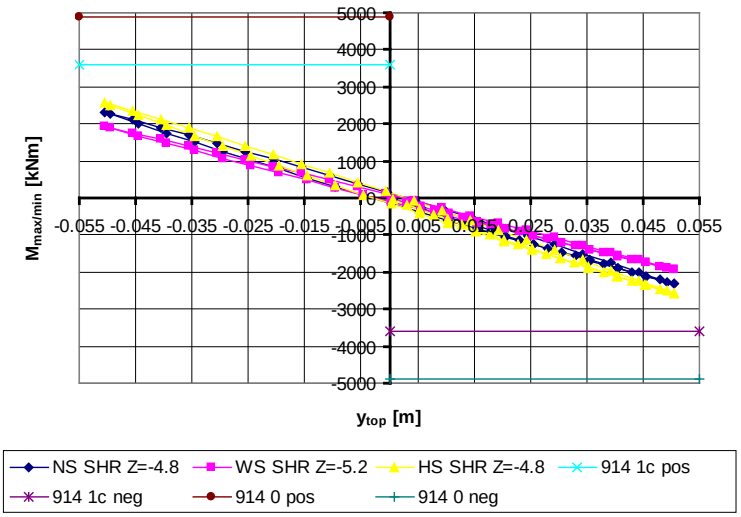

Figure 6.31. $M_{max/min}$ as function of y_{top} in different soil types in T1_D914_F_SHR models, s = 4.17 m.

The values of maximum or minimum moments in the F models are roughly 51-54% of the moments in the R models which corresponds to more than 31-32% with the linear behaviour in Formulas 6.56-6.57 where the distribution of the lateral modulus of subgrade reaction is linear or constant along depth.

6.3.9.2 Results for all pile size cross sections

In Section 4 it was noted that embankments tend to be relatively loose [75, 84]. Hence, analysis of the lateral displacement (y_{top}) capacities was made with soil models WS_SHR and NS_EXP for different pile cross-sections. The limit of pile cross-section in serviceability state capacity was set as the yield of structural steel in this study. If normal force in stage D_0 is N_{opt}, then the yield is obtained from the curvature of Formula 6.33: $C_{0,y} = (|\varepsilon_{y,b}| + |\varepsilon_{y,t}|)/D = (0.00169*2)/D = 0.00338/D$. Values of $C_{0,y}*D$ as function of y_{top} in T1_R models are presented in Figures 6.32 and 6.33.

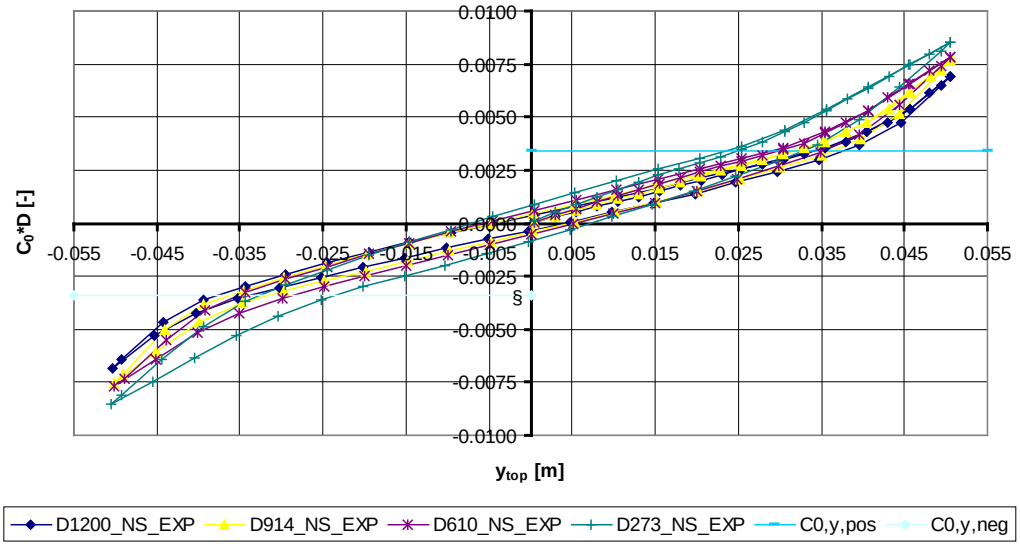

Figure 6.32. $C_{0,y}$*D as function of y_{top} in T1_R_NS_EXP models.

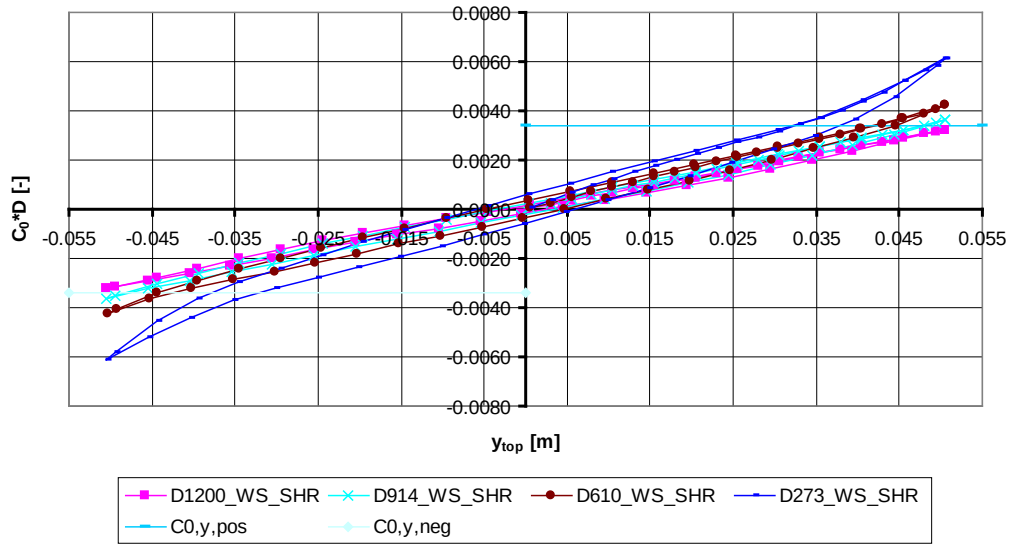

Figure 6.33. $C_{0,y}$*D as function of y_{top} in T1_R_WS_SHR models.

Larger diameter piles have greater lateral displacement capacities than smaller ones. Smaller diameter piles are slender but their damping of lateral displacement along pile length is greater as the second derivate on displacement along depth is also relatively large compared to the bending stiffness of the pile cross section in smaller diameter piles. Values of $C_{0,y}$*D as function of y_{top} in T2_R models are presented in Figures 6.34 and 6.35.

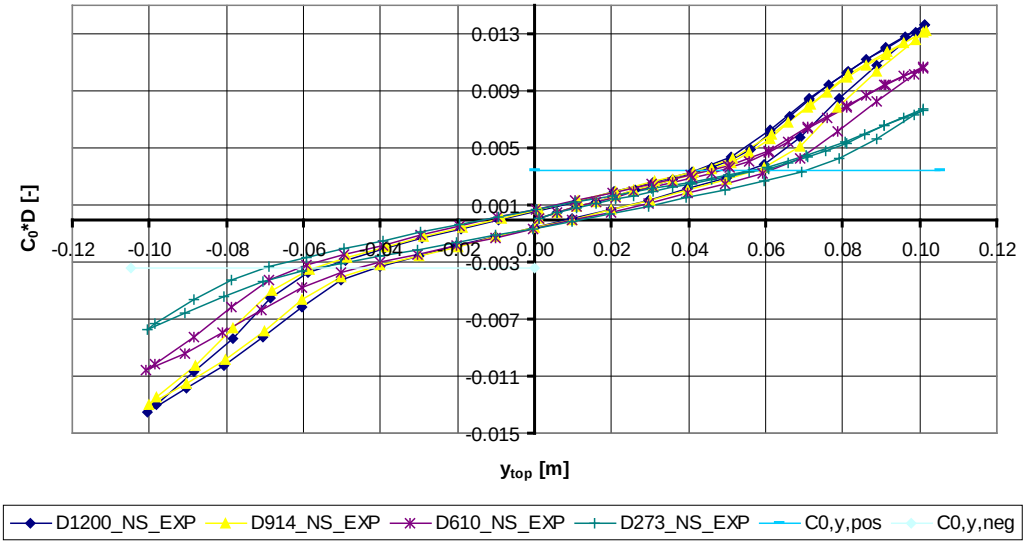

Figure 6.34. $C_{0,y}$*D as function of y_{top} in T2_R_NS_EXP models.

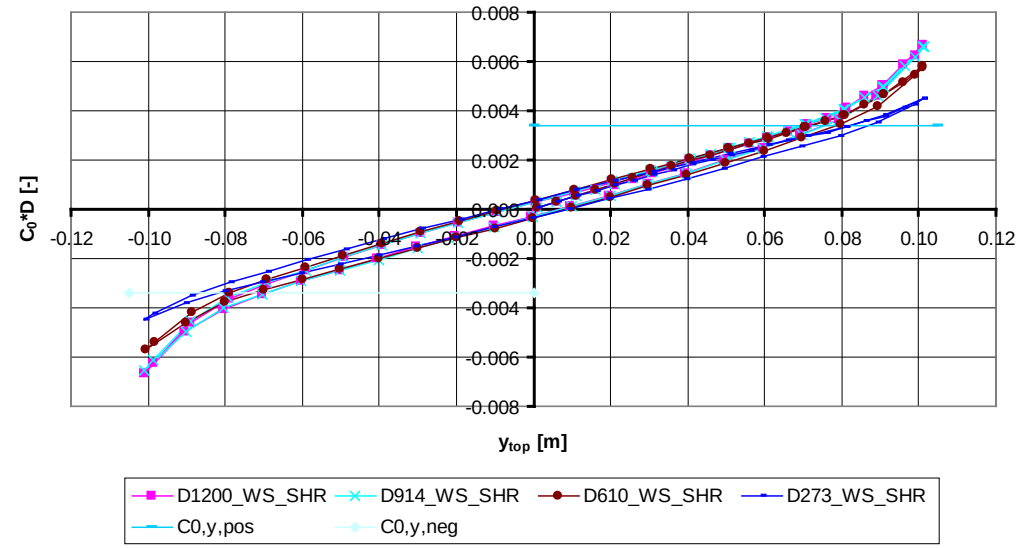

Figure 6.35. $C_{0,y}$*D as function of y_{top} in T2_R_WS_SHR models.

The pile D*t = 273*12.5 has the largest displacement capacity in T2_R models. This is caused by relatively larger values of s in small diameter piles than in large ones. Displacement capacities are larger in T2 than T1 models because of the effect of the value of s. Displacement capacities of y_{top} at D_0 are presented in Table 6.6.

Table 6.6. Displacement capacities [m] of y_{top} at D_0 with N_{opt} in T1_R- and T2_Rmodels

	Model type			
Cross section	T1_WS_SHR	T1_NS_EXP	T2_WS_SHR	T2_NS_EXP
D*t = 1200*16	0.053	0.034	0.069	0.042
D*t = 914*16	0.048	0.031	0.069	0.042
D*t = 610*16	0.042	0.029	0.072	0.046
D*t = 273*12.5	0.032	0.024	0.081	0.056

The presented displacement capacities of y_{top} are calculated only with the load from lateral displacement and normal force N_{opt} of a rotationally connected pile top. The results are only estimates because piles at a fully integral bridge end are also subject to other loads and other normal forces, and the connection of the pile top is not rotationally rigid.

6.3.10 Solution for modulus of lateral subgrade reaction in design

It is not normally possible to do complex non-linear analyses in normal bridge design. A simplified method for considering hyperbolic soil behaviour in design is presented in Paragraph 6.3.10. Here, non-linear soil properties are taken into account in the linear analysis of a normal design process.

The use of complex non-linear analyses may not be a straightforward solution in basic bridge design. The value of s is ignored in Formula 6.54. Solutions of the differential equation in Formula 2.21 with values of s are presented in [104]. It is possible to solve an equivalence value for d/dz(k_a) for a linearly behaving model using the values of Table 6.2 (moment capacity of composite cross section in D_{1c} stage), Table 6.3 (Bending stiffness of composite cross section), Table 6.5 (values of s) and Table 6.6 (displacement capacity of composite cross section in stage D_{1c}). Results for different composite pile cross sections are presented in Figure 6.36.

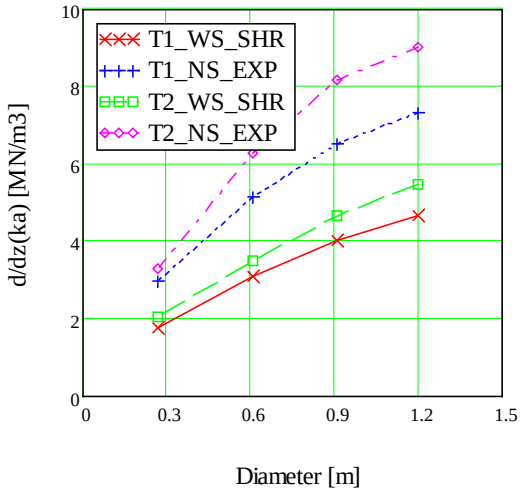

Figure 6.36. Equivalence constant of lateral subgrade reaction d/dz(k_a).

The pile diameter has an effect on the modulus of lateral subgrade reaction as in the non-linear material models. The values of the derivate of lateral subgrade reaction along pile length in the EXP models are higher than in the SHR models and in the T2 than in the T1 models. The relation between models T1 and T2 results from the fact that in the T1 models the soil against the pile yields more than in the T2 models. The values of Figure 6.36 are divided with $D^{0.5}$ in Table 6.7. The obtained values are called m_{heq}, see Table 2.3.

Table 6.7. Equivalent modified constant of lateral subgrade reaction m_{heq} when modulus of subgrade reaction is linearly distributed along pile length [MN/m^3]

	Model type			
Cross section	T1 SHR	T1 EXP	T2 SHR	T2 EXP
D*t = 1200*16	4.2	6.7	5.0	8.2
D*t = 914*16	4.2	6.8	4.9	8.6
D*t = 610*16	4.0	6.6	4.5	8.0
D*t = 273*12.5	3.4	5.7	3.9	6.3

Values of m_{heq} are almost independent of pile diameter in terms of bending moments partly because bending moment is not very sensitive to changes of modulus of lateral subgrade reaction as may be noted from Formula 6.54. Different values of s and different stages of yield among cross sections affect the values. Further, in Section 6.4 it is concluded that the cross section D*t = 273*12.5 is not the best option for a long fully integral abutment bridge. Hence, m_{heq} may be set as an average value of the three largest diameters when the linear elastic and linearly distributed modulus of subgrade reaction is obtained from Formula 6.65:

$$k_{eq} = z * m_{heq} * D^{0.5} \tag{6.65}$$

where

k_{eq} = equivalent linearly distributed modulus of lateral subgrade reaction in the case where the modulus of lateral subgrade reaction is linearly distributed along pile length, see Figure 6.18a [MN/m^2]

m_{heq} = equivalent modified constant of lateral subgrade reaction in the case where the modulus of lateral subgrade reaction is linearly distributed along pile length, see Figure 6.18a [MN/m^3]

In models T1_SHR, T1_EXP, T2_SHR and T2_EXP the values of m_{heq} are 4.1, 6.7, 4.8 and 8.3 MN/m^3, respectively. Values of m_{heq} are fitted to large displacements at the rotationally rigidly connected pile tops and are not applicable in all design, but it is possible to define these values for a larger group of structural cases because the values presented in the foregoing are applicable only at a high displacement stage.

6.4 Bridge models of fully integral bridge

6.4.1 Scope

The finite element bridge models were intended to be the first step in analysing fully integral bridges together with structural behaviour of bridge superstructure and non-linear soil models with kinematic rules in piles and end screens. Further, the effects of the uniform temperature load of Section 5.6 were pointed out. The focus in the analyses was on forces on the piles in the serviceability limit state and the effect of different pile diameters. The

loads were as in the Finnra bridge design guidelines until 1.6.2010 [42, 45, 48, 43, 46, 48]. An ultimate limit state analysis was not included in this study.

A group of bridge types was analysed. This was because it made possible the comparison of the effects of different loadings on different bridge types with a view to their characteristics. In the discussion on the results, the focus will be more on comparing results between bridge types than presenting very detailed results on a few bridge types.

The focus of this section is on analysing forces at pile cross-sections in the case of feasible bridge superstructure cross-sections. The obtained forces are compared to capacities obtained in Paragraph 6.3.2.

6.4.2 Bridge structure types

The bridge superstructure types and span divisions were selected based on existing bridges. The types were selected to represent common overpasses. The orientation of supporting columns and superstructure was set straightforward and rather orthogonal to achieve an easier solution and have more clear results from a large group of bridges. The analysed bridge superstructure types are presented in Paragraph 6.4.2.

The analysed three bridge superstructure types and span division combinations (hereafter "bridge types") are labelled B1, B2 and B3. Type B1 has six spans and B2/B3 types have four. The three analysed total thermal expansion lengths were selected on the basis of Section 6.3. The lengths are L1 = 120 m, L2 = 135 m and L3 = 150 m. The structures of the bridges are symmetrical. The effective width of the bridge was set to 13.5 m so that the length of the end screen would allow using multiple small piles in one row. The skew angle is zero degrees and the end screen is vertical in all types. The height of the end screen H was set to 3.0 m, see Figure 6.40. The thickness of the surface structure was 0.11 m in the analysis. Two different side span ratios were used in the analysis: S1 = 0.85 and S2 = 0.7. This ratio was determined with Formula 6.66:

$$S = \frac{L_r}{L_k} \tag{6.66}$$

where
L_r = span length of side span [m]
L_k = span length of middle span [m]

Middle spans are uniform and the intermediate supports are perpendicular, i.e. skew angles are zero degrees. Two different end types, T1 (without cantilever span) and T2 (with cantilever span) were used in the analysis, see Figure 6.19. The length of the cantilever span

from the support line to the outer surface of the end screen was 2.5 m in all models. The elevations of bridge types used in the analysis are presented in Figure 6.37.

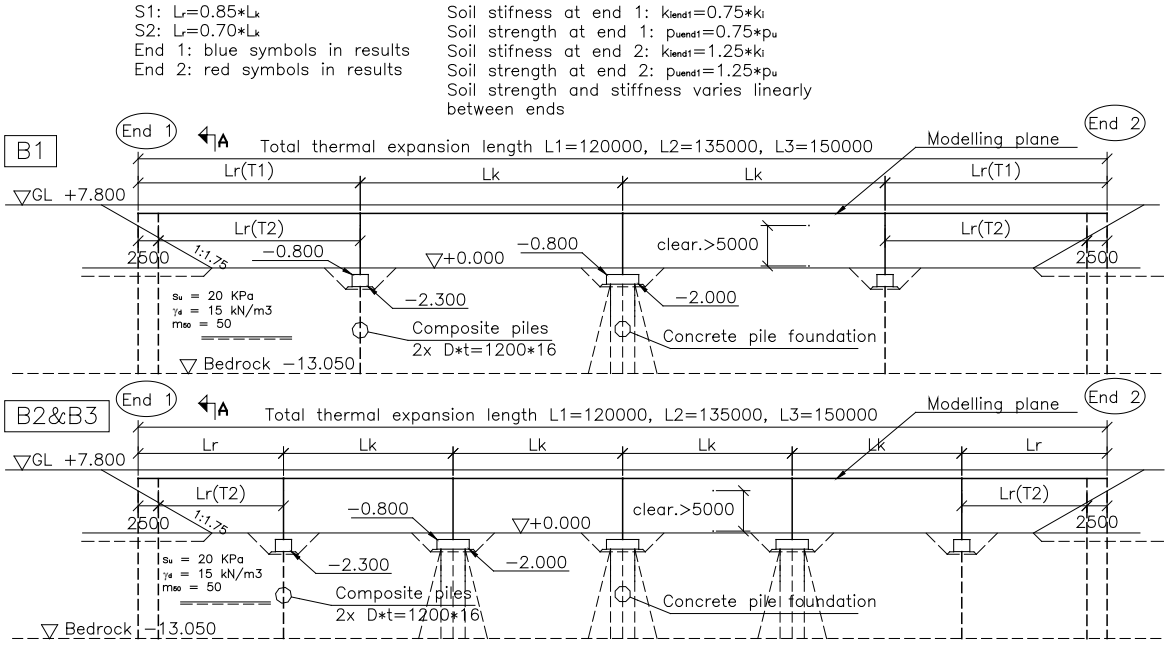

Figure 6.37. Elevations of bridge types in global FE analyses.

Three- and five-span bridges were analysed in the preliminary analysis. However, the three-span type included long spans in the case of the beam-and-slab concrete superstructure, while the focus of this study is on medium length span bridges. The five-span type was rather similar to the six-span type while the difference between the four- and six-span types was greater. In fact, one goal was to determine how different side span lengths affect the fully integral bridge's structural behaviour. The monitored Haavistonjoki Bridge superstructure could actually have been implemented with six spans. The intermediate supports were founded on two large composite steel pipe piles (D*t = 1200*16) or on a concrete pile foundation. The concrete pile foundations were used because their rigidity against support displacement is rather high and thus they resist longitudinal bridge displacements. The composite pile foundation was used in the first intermediate supports because their longitudinal stiffness is lower than that of a concrete pile foundation, which reduces forces at intermediate columns. The intermediate columns' cross section was D1200, see Figure 6.3. A transverse beam width*height*length = 2.0*1.5*9 m^3 was modelled on top of the composite pile foundation at the intermediate supports between piles and columns to take into account the probable tolerances of piles and columns, see Figure 6.37. Furthermore, the longitudinal stiffness of intermediate supports decreases towards the bridge end when lateral forces of intermediate supports are minimised in simultaneous thermal expansion and longitudinal displacement. Moreover, the longitudinal stiffness of the whole bridge

system is adequate. Main dimensions and parameters of modelled bridges are presented in Table 6.8.

Table 6.8. Main dimensions and parameters of the 28 modelled main bridge types

	(1		(2	(3	(4					(5		(6
Model type	L_{exp}		$f_{ck,cube}$	σ_{pt}	Spans	L_r	L_k	L_r/L_k	L_m	h_d	L_m/h_d	$A_{c,ss}$
	[m]			[MN/m^2]	[-]	[m]	[m]	[-]	[m]	[m]	[-]	[m^2]
B1_L1_S1_T1	120	RC Beam	40		4	27.5	32.5	0.85	30.2	2.00	15.1	12.0
B1_L1_S1_T2	120	RC Beam	40		4+(2)	26.4	31.1	0.85	27.8	2.00	13.9	12.0
B1_L1_S2_T1	120	RC Beam	40		4	25.0	35.0	0.71	30.8	2.00	15.4	12.0
B1_L1_S2_T2	120	RC Beam	40		4+(2)	24.0	33.5	0.71	28.4	2.00	14.2	12.0
B1_L2_S1_T1	135	PC Beam	45	3.5	4	31.0	36.5	0.85	34.0	1.80	18.9	11.1
B1_L2_S1_T2	135	PC Beam	45	3.5	4+(2)	29.9	35.1	0.85	31.6	1.80	17.6	11.1
B1_L2_S2_T1	135	PC Beam	45	3.5	4	28.0	39.5	0.71	34.7	1.80	19.3	11.1
B1_L2_S2_T2	135	PC Beam	45	3.5	4+(2)	27.0	38.0	0.71	32.3	1.80	17.9	11.1
B1_L3_S1_T1	150	PC Beam	45	4.0	4	34.5	40.5	0.85	37.7	2.00	18.9	12.0
B1_L3_S1_T2	150	PC Beam	45	3.5	4+(2)	33.4	39.2	0.85	35.3	2.00	17.7	12.0
B1_L3_S2_T1	150	PC Beam	45	4.0	4	31.0	44.0	0.70	38.6	2.00	19.3	12.0
B1_L3_S2_T2	150	PC Beam	45	4.0	4+(2)	30.0	42.5	0.70	36.2	2.00	18.1	12.0
B2_L1_S1_T1	120	RC Beam	40		6	18.0	21.0	0.86	20.1	1.35	14.9	9.1
B2_L1_S1_T2	120	RC Beam	40		6+(2)	17.3	20.1	0.86	18.6	1.35	13.8	9.1
B2_L1_S2_T1	120	RC Beam	40		6	16.0	22.0	0.73	20.4	1.35	15.1	9.1
B2_L1_S2_T2	120	RC Beam	40		6+(2)	15.3	21.1	0.73	18.8	1.35	14.0	9.1
B2_L2_S1_T1	135	RC Beam	40		6	20.5	23.5	0.87	22.6	1.60	14.1	10.2
B2_L2_S1_T2	135	RC Beam	40		6+(2)	19.7	22.6	0.87	21.0	1.60	13.1	10.2
B2_L2_S2_T1	135	RC Beam	40		6	17.5	25.0	0.70	23.1	1.60	14.4	10.2
B2_L2_S2_T2	135	RC Beam	40		6+(2)	16.9	24.1	0.70	21.5	1.60	13.4	10.2
B2_L3_S1_T1	150	RC Beam	40		6	23.0	26.0	0.88	25.1	1.80	13.9	11.1
B2_L3_S1_T2	150	RC Beam	40		6+(2)	22.2	25.1	0.88	23.5	1.80	13.1	11.1
B2_L3_S2_T1	150	RC Beam	40		6	20.0	27.5	0.73	25.5	1.80	14.2	11.1
B2_L3_S2_T2	150	RC Beam	40		6+(2)	19.3	26.6	0.73	23.9	1.80	13.3	11.1
B3_L1_S1_T1	120	RC Slab	40		6	18.0	21.0	0.86	20.1	1.10	18.3	13.8
B3_L1_S1_T2	120	RC Slab	40		6+(2)	17.3	20.1	0.86	18.6	1.10	16.9	13.8
B3_L1_S2_T1	120	RC Slab	40		6	16.0	22.0	0.73	20.4	1.10	18.5	13.8
B3_L1_S2_T2	120	RC Slab	40		6+(2)	15.3	21.1	0.73	18.8	1.10	17.1	13.8

1) Total thermal expansion length, distance between outer surfaces of end screens [m]
2) Concrete cubic strength from 0.15*0.15*0.15 m^3 test specimen [MN/m^2]
3) Average post-tensioning stress σ_{pt} immediately after post-tensioning based on post-tensioning force divided over the whole cross sectional area [MN/m^2]
4) Number of spans, the cantilever spans are in brackets
5) Average structural height h_d along superstructure [m]
6) Cross-sectional concrete area of the whole bridge superstructure $A_{c,ss}$ [m^2]

The uniform span length L_m was calculated with Formula 6.67.

$$L_m = \frac{\sum L_i^2}{\sum L_i} \qquad \text{[37] (6.67)}$$

The selection of structural heights h_d was based on existing bridges and reference [37]. The relations L_m/h_d are presented in Figure 6.38.

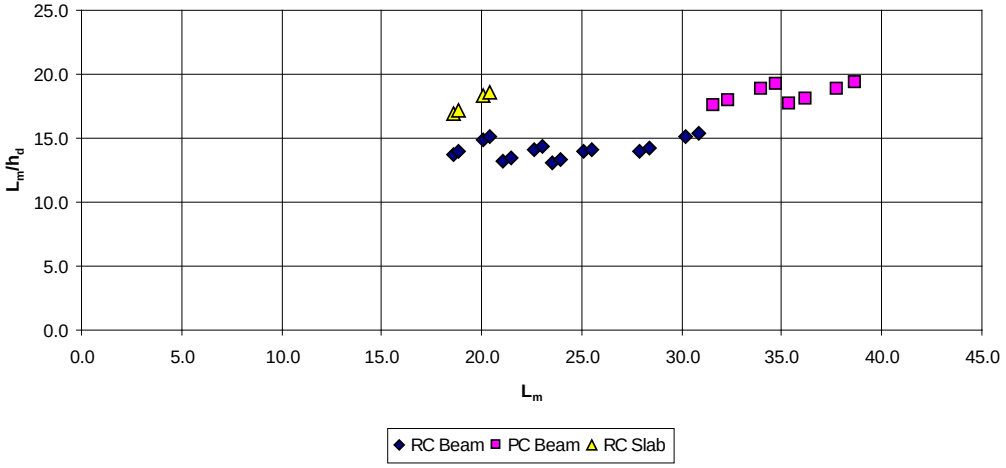

Figure 6.38. Relation L_m/h_d as function of L_m.

The longest L_k spans between 35.1 to 44.0 m are post-tensioned beam-and-slab structures (PC Beam). Reinforced concrete beam-and-slab (RC Beam) structures' L_k spans are from 22.1 to 35.0 m. The longest RC Beam structures may not be as economical in terms of building costs as PC Beam structures, but the RC Beam is expected to allow building longer fully integral bridges due to the effects of post-tensioning force on the bending moments of the piles at bridge ends. Reinforced concrete slab-structures' (RC Slab) L_k spans are from 20.1 to 22.0 m. The RC Slab structures were selected to determine the difference between the RC Beam and the RC Slab structures. The monitored Haavistonjoki Bridge is an RC Slab structure. However, the RC Slab may not be an economical option because of the larger amount of concrete needed compared to RC Slab structures, see Table 6.8, last column. RC Slab structures were analysed only with L1 because other span lengths would be outside the RC Slab range. The cross-sections of the superstructures are presented in Figure 6.39.

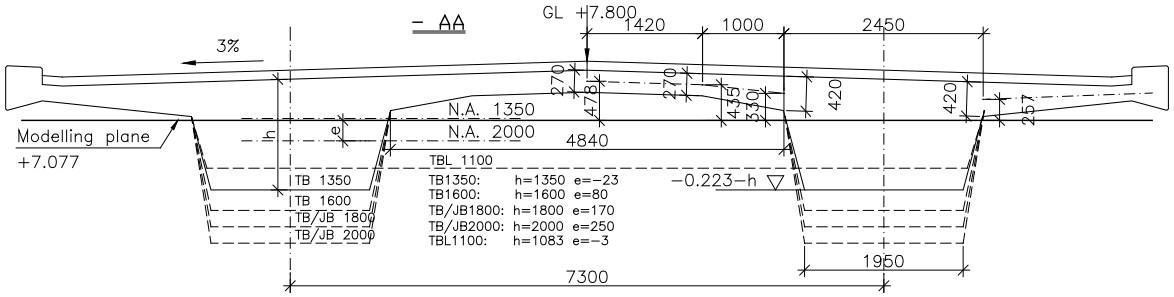

Figure 6.39. Superstructure cross-sections. Names of section marks refer to Figure 6.37.

The beam width of all cross-sections is the same: 2.45 m at top and 1.95 m at bottom. The thickness and other dimensions of the slab in the beam-and-slab structure were selected on the basis of existing bridges. The structural height does not change under one L type for simpler analysis. Pile orientation at bridge ends was modelled as in Figure 6.40.

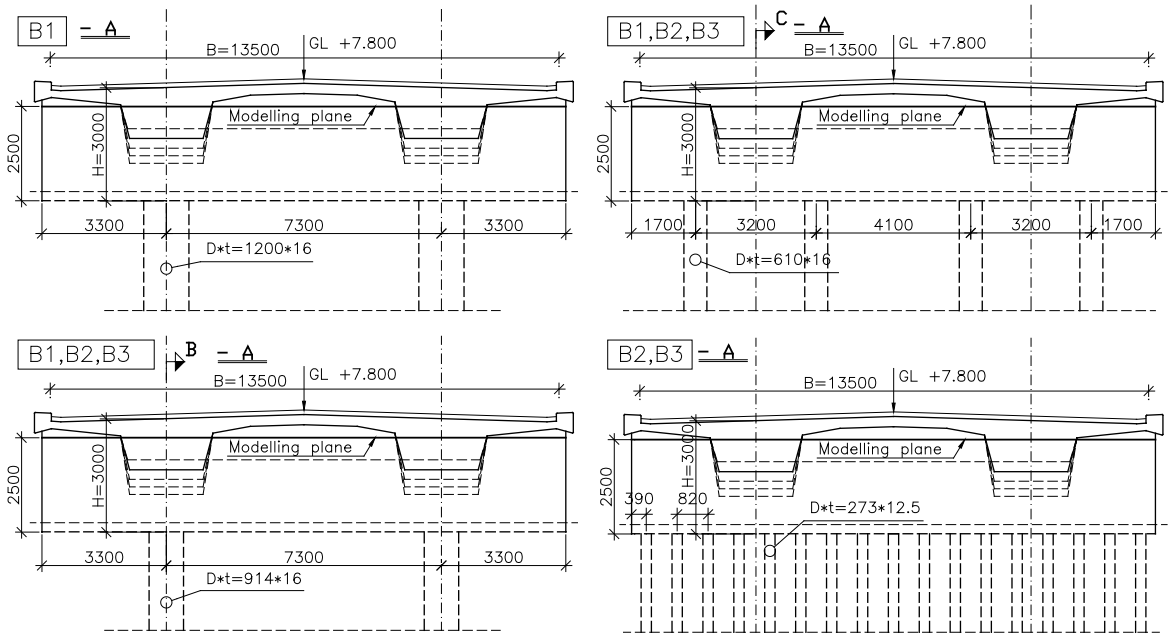

Figure 6.40. Composite piles at fully integral bridge ends. Names of section marks refer to Figure 6.37.

A number of piles were selected knowing N_{opt} in D_0 stage. Several piles were analysed in a simple preliminary analysis of a continuous beam with roughly estimated loads using S2 and L_{exp} = 120 m (Loads are discussed in Paragraph 6.4.5). This analysis served as a magnitude check in the analysis of this study. The estimated number of piles is presented in Table 6.9.

Table 6.9. Selecting the number of piles at bridge ends

Bridge type	B4	**B1**	B5	**B2**	**B3**	
Spans	3	**4**	5	**6**	**6**	
Superstructure	Estimated maximum SLS support reaction at end of bridge [MN]					
PC Beam	9.5	**7.1**	6.1	5.4	-	
RC Beam	10.9	**7.8**	6.4	**5.6**	5.6	
RC Slab	-	-	7.8	6.5	**6.5**	Selected
Cross section	Estimated number of piles with N_{opt} in stage D_0					number
D*t = 1200*16	1.3	**1.1**	0.9	0.8	0.9	2
D*t = 914*16	2.3	**1.9**	1.6	**1.4**	**1.6**	2
D*t = 610*16	5.6	**4.6**	3.8	**3.3**	**3.9**	4
D*t = 273*12.5	33	27	22	**19**	**22**	17

The analysed pile number and the bridge options are in boldface. In addition, bridge types B4 and B5 are shown, although they were excluded as described above. The orientations of piles at bridge ends are assigned structurally reasonable locations, see Figure 6.40. The number of cross-sections D*t = 273*12.5 was selected based on the minimum centre-to-centre spacing according to the piling instructions [43]. However, the selected number probably still causes problems in pile driving. One pile option with D*t = 1200*16 was not a real option due to the effective width of 13.5 m. Soil properties in the bridge models were

set as in Section 6.3 NS_EXP and WS_SHR models. These selections were made because it was noted in Chapters 4 and 5 that the slope tends to be of relatively loose soil material.

Three cross-sections of piles were analysed in the bridge models. The total number of the analysed bridge structural types is thus 28*3 = 84. However, the number of non-linear bridge models in the FEM analyses was 84*2 = 168 pieces. Furthermore, Paragraph 6.4.5 specifies that 84 linear models were analysed for wind and vertical traffic loads. Thus, the total number was 252.

Post-tensioning forces were approximated with the equivalent load method, see Figure 6.41. However, the post-tensioning forces are highly tentative because beams were not designed in this study as the study concentrates on forces on piles at bridge ends. The post-tensioning-force was modelled constant along the beam length for simplicity, i.e. friction losses, lock-off losses and an accurate longitudinal component of curved post-tensioning force were not included in the analysis. The average post-tensioning force immediately after post-tensioning was set in the analysis to $F_{pt} = A_c * \sigma_{pt}$, see Table 6.8. Forces were estimated with simple continuous elastic frame models so that the deflection in the middle of spans from combined displacement from permanent load and post-tensioning force was slightly upwards. This kind of load-balancing method is presented in [90, 91].

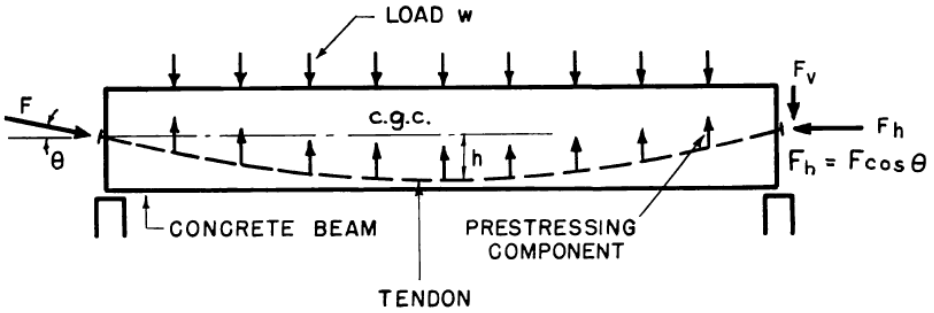

Figure 6.41. Balancing of uniform load, in the figure: $F_h = F_{pt,h}$ [90, 91].

The longitudinal component of post-tensioning force $F_{pt,h}$ in the load balancing method may be calculated with Formula 6.68:

$$F_{pt,h} = \frac{w * L_{pt}^2}{8 * h_j} \qquad \text{[91] (6.68)}$$

where

w = balanced load [MN/m]

L_{pt} = length of post-tensioned span [m]

h_j = height of post-tendon profile [m]

Tendon profiles in this study are 0.15 m from beam upper surface at intermediate supports and 0.15 m from beam bottom surface in the middle of L_k spans. At L_r spans, tendon profiles were set to more than 0.15 m from the bottom surface. Tendons were sett at the neutral axis of the whole cross section at type T1 bridge ends and $h_d/8$ up from the whole cross section's neutral axis at type T2 bridges. Equivalent loads and more precise dimensions in general cases and in post-tensioned bridge types (B1L2 and B1L3) are presented in Appendix 9.1.

6.4.3 End screen and wing wall soil-structure interaction

Lateral soil properties were assigned to end screen and wing walls as with piles in Section 6.3. The lateral behaviour is described in terms of lateral soil modulus and influence length in Paragraph 6.4.3.

The soil-structure interaction in the bridge models was roughly based on behaviour observed in Chapters 2, 4 and 5. Some key points are also presented at the beginning of Paragraph 6.3.4. The behaviour is hysteretic and depends on the height of the end screen H. Thus, it is concluded that lateral modulus of subgrade reaction against embankment behind the end screen increases along with depth [123, 27, 58]. Further, the required displacement of the end screen against the embankment to obtain full passive earth pressure at each depth increases along with depth [123]. However, in [46] the required displacement is independent of depth z. The passive earth pressure capacity behind the end screen is expressed with factor $K_p = 8.0$ with $\phi = 38^\circ$ [75, 48]. The SSI of the end screen and the embankment is widely discussed in dissertation [75] related to the overall research project, see Figure 1.4. This behaviour is not within the scope of this study. Straightforward expressions for end screen SSI are presented in [122]. The average length of influence zone L_{inf} at the embankment behind the end screen is assumed to be 2*H. In [75] L_{inf} is assumed to be H. In this study L_{inf} is defined as:

$$L_{\inf} = \frac{2*H}{z^{1-\beta_{50}}} * \zeta^{1-\beta_{50}} \tag{6.69}$$

L_{inf} = average length of influence zone at embankment [m]
H = height of end screen [m]

Then the coefficient of subgrade reaction against the end screen is obtained from:

$$k_{h50,emb} = \frac{E_{50v}}{L_{\inf}} \tag{6.70}$$

and the spring stiffness is obtained from the formula:

$$k_{s50} = k_{h50,emb} * cc_b * cc_h = \frac{E_{50v} * z^{1-\beta_{50}} * cc_b * cc_h}{2*H*\zeta^{1-\beta_{50}}} \tag{6.71}$$

$$= \frac{E_{50v}}{2 * z^{\beta_{50}} * \zeta^{1-\beta_{50}}} * \frac{z}{H} * A_{cc} = m_{h,emb} * \frac{z}{H} * A_{cc}$$

$$m_{h,emb} = \frac{E_{50v}}{2 * z^{\beta_{50}} * \zeta^{1-\beta_{50}}} \quad (6.72)$$

$$A_{cc} = cc_b * cc_h \quad (6.73)$$

where

cc_b = spring division along end screen width [m]

cc_h = spring division along end screen height [m]

$k_{h,emb}$ = coefficient of lateral subgrade reaction against end screen [MN/m^3]

$m_{h,emb}$ = modified constant of lateral subgrade reaction against end screen [MN/m^3]

A_{cc} = area affected by spring properties [m^2]

The behaviour type 1 of soil backfill (BF_1) in bridge analyses is presented in Table 6.10.The properties of HS from Table 6.4 are also presented.

Table 6.10. Soil and lateral soil reaction properties at end screen (BF_1 and BF_2) and piles (HS)

	Soil properties							Lateral soil reaction properties		
	ϕ	c	m_{50}	β_{50}	γ'	ν	ξ_{50}	k_{s50}/A_{cc}	p_p	$y_{50,end} = 0.5*p_p/k_{s50}$
	o	MN/m^2	-	–	kN/m^3	–	-	MN/m^3	MN/m^2	m
BF_1	40	0	1000	0.5	21	0.3	0.25	13.9*z/H	0.168*z	0.0060*H
Values at depth z = 2/3*H = 2/3*3.12 = 2.08 m								9.27	0.349	0.0187
BF_2	40	0	1000	0.5	21	0.3	0.25	13.9*z$^{0.5}$/H	"	0.0060*H*z$^{0.5}$
Values at depth z = 2/3*H = 2/3*3.12 = 2.08 m								6.43	0.349	0.0270
	ϕ	c	m_{50}	β_{50}	γ'	ν	ξ_{50}	k_{50}	q_f	$y_{50} = 0.5*q_f/k_{50}$
HS	40	0	1000	0.5	20	0.3	0.25	21.7*√(z*D)	0.324*z*D	0.0075*√(z*D)
Values at depth z = 2.08 m and D = 1.0 m								31.3	0.674	0.0108

Lateral soil reaction properties are also calculated with L_{inf} = 2*H [122] in the previous table (BF_2). The lateral displacement $y_{50,end}$ of the end screen at a stage, when 0.5*p_p is reached, is constant along the depth with soil behaviour BF_1, as in [46], whereas with BF_2 it depends on depth as in [123]. The stiffness and strength values of both models are lower per unit area than in the HS model with piles. This is reasonable behaviour because the influence zone in the soil is relatively higher at the end screen than at the piles. The soil model BF_1 was selected for the bridge models because it is recognized and used in literature and practise. However, in Section 6.5 it is noted that behaviour BF_1 may be too stiff and firm. The relations between stiffness k_{s50} and ultimate strength for the whole end screen at height H = z and H = 2z are:

$$BF_1 := \frac{\int_0^{2z} k_{s50}\,dz}{\int_0^{z} k_{s50}\,dz} = 2 \text{ and } BF_2 : \sqrt{2} \tag{6.74}$$

and

$$BF_1 \text{ and } BF_2 : \frac{\int_0^{2z} p_p\,dz}{\int_0^{z} p_p\,dz} = 4 \tag{6.75}$$

The relation of stiffnesses with soil behaviour BF_1 is 2 as in the design guidelines [46]. The relation is $\sqrt{2}$ with soil behaviour BF_2. This behaviour is similar to k_{50} in the case of piles with different diameters. The cyclic behaviour was modelled as with piles in Paragraph 6.3.6 but allowing no capacity for "suction" earth pressures.

The SSI behaviour of wing walls was modelled as that of the end screen except that both the stiffness and strength were multiplied by the factor 0.5 [36]. The SSI behaviours of beams on top of the piles at intermediate supports were modelled as the SSI behaviour of end screens.

6.4.4 Global parameter of SSI

Different soil properties at different ends (actually along bridge length) were described with a global parameter (along the longitudinal axis of the bridge) in FE models. This parameter and the parameter for taking into account the centre-to-centre effect of lateral modulus of subgrade reaction are described in Paragraph 6.4.4.

It was noted in Chapters 4 and 5 that bridge end displacements, e.g. from uniform temperature changes, are partly eccentric compared to the centre of the bridge superstructure. Hence, in the bridge models both the stiffness and the strength of soil are multiplied by 0.75 at end 1 and by 1.25 at end 2. These values are assigned to bridge soil models using multiplier m_G obtained by global Formula 6.76:

$$m_G = 1 + \frac{X}{2 * L_{\text{exp}}} \tag{6.76}$$

where
m_G = multiplier for soil stiffness and strength [-]
X = longitudinal co-ordinate from bridge centre, at bridge end 1 X = $-L_{exp}/2$ and at bridge end 2 X = $L_{exp}/2$ [m]
L_{exp} = total thermal expansion length [m]

This behaviour is also modelled for intermediate support piles and beams, i.e. intermediate supports that are founded on steel pipe piles. The effect of the piles' centre-to-centre spacing (cc) was taken into account with q_f and k_{50} according to the following principles. If normalised pile spacing cc/D was greater than 5, the multiplier m_{cc} for stiffness and strength of soil with normalised spacing was 1.0. With normalised pile spacing 3.0 and with 9 or more piles m_{cc} was 0.65 [55, 101]. The values are presented in Table 6.11.

Table 6.11. Multipliers m_{cc} for q_f and k_{50}

	Model type			
	cc [m]	cc / D [-]	Number	m_{cc}
D*t = 1200*16	7.3	6.1	2	1.0
D*t = 914*16	7.3	8.0	2	1.0
D*t = 610*16	3.2	5.2	4	1.0
D*t = 273*12.5	0.82	3.0	17	0.65(*

*) Average value $m_{cc,av}$ for entire pile row

The value 0.65 for D*t = 273*12.5 is an average for the entire pile row. In the transverse direction the multiplier m_{cc} was assigned a parabolic function so that the average value was 0.65 while at corner piles it was 1.0. The relation between normalised spacing 3.0 and factor 4.4 in Formula 2.29 [43] is 0.68, which also supports the value 0.65. A parabolic distribution along bridge width was assumed in Figure 6.42.

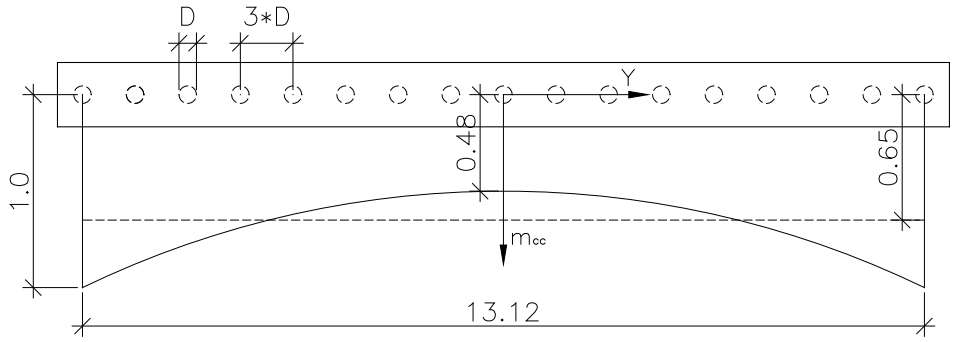

Figure 6.42. Distribution of modulus of subgrade reaction along bridge width when cc/D = 3.0 with piles D*t = 273*12.5.

The factor m_{cc} was set to 1.0 at corner piles and the average value as 0.65. Then, the parabolic distribution was developed as follows:

$$k_{50tot} = m_{cc,av} * 13.12 = 0.65 * 13.12 \tag{6.77}$$

$$k_{50tot} = 13.12 * 1.0 - \frac{2}{3} * 13.12 * (1 - m_{cc,mid}) \tag{6.78}$$

then

$$0.65 * 13.12 = 13.12 * 1.0 - \frac{2}{3} * 13.12 * (1 - m_{cc,mid}) \tag{6.79}$$

$$m_{cc,mid} = 0.48$$

where

$k_{50,tot}$ = total lateral modulus of subgrade reaction of piles at bridge end at stage when $0.5*q_f$ is reached [MN/m^2]
$m_{cc,mid}$ = multiplier for stiffness and strength of soil with normalised pile spacing at location of middle pile [-]
$m_{cc,av}$ = average multiplier for stiffness and strength of soil with normalised pile spacing [-]

The transverse global co-ordinate of bridge models is Y and the origin is at the centre of the bridge, see Figure 6.44 and 6.45. The parabolic formula for multiplier m_{cc} is:

$$m_{cc,mid} + a * \left(\frac{13.12}{2} \right)^2 = 1.0 \tag{6.80}$$

$$a = \frac{1 - m_{cc,mid}}{6.6^2} = 0.012$$

then

$$m_{cc} = m_{cc,mid} + a * Y^2 = 0.48 + 0.012 * Y^2 \tag{6.81}$$

and

$$2 * \int_0^{\frac{13.12}{2}} 0.48 + 0.012 * Y^2 dY = 0.65 * 13.12$$

A similar multiplier was assigned to all depths z and displacement stages.

6.4.5 Loads in general

All modelled loads of bridge models are listed in Paragraph 6.4.5. The loads are according to the Finnish bridge design guidelines except for the uniform temperature load, which is defined in Section 5.6.

The loads for the bridge models were:

Permanent loads:

Dead loads (dead weight in later figures):

- Reinforced and post-tensioned concrete structures ρ = 25 kN/m^3 [42]
- Embankment layers above transition slab ρ = 21 kN/m^3, 30% of the load above L = 5 m transition slabs is supported on bridge ends [48]
- Surface structures of superstructure: 2.7 kN/m^2 (the 1 kN/m^2 of the optional extra pavement was ignored) [42]
- Bridge parapets: 0.75 kN/m on each side
- Buoyancy of piles below average ground water level: -10 kN/m^3

Earth pressure:

- Earth pressure at rest of end screen excluding effects of transition slab (EP at rest end screen in later figures) [46]

- Uneven earth pressure at rest of piles at abutments (EP at rest piles in later figures) [46]

Temperature load (T_U drop at cast in later figures):

- Temperature drop during curing of concrete by -25˚C to an average temperature of 5.2˚C

Concrete creep and shrinkage:

- Concrete creep, creep factor $\phi = 1.4$, [35]
- Concrete shrinkage

Post-tensioning force:

- Post-tensioning force at t = 0 and at t = 00, 15% losses from creep and shrinkage were assumed between t = 0 and t = 00
- Effect of creep on bridge length

Live loads:

Traffic loads:

- Normal traffic load Lk1 for road bridge, three 210 kN axle loads and surface load 3 kN/m^2 [42]
- Traffic load earth pressure on end screen from surface load of 20 kN/m^2 [42] (TLEP later on)
- Traffic load earth pressure on piles at abutments from surface load of 20 kN/m^2 [46]

Temperature loads:

- Uniform temperature T_U change from -30 to 28˚C, see Paragraph 5.6.4 (T_U in later figures)
- Average temperature 5.2˚C, see Figure 5.1
- Linear temperature difference +5˚C at T_U = 30˚C and 0˚C at T_U = -28˚C, see Figure 5.6 and [42]

Wind load:

- Wind load in transverse direction on lateral surface of superstructure and columns: 1.6 kN/m^2 [42]
- Wind load on bridge parapets: 0.8 kN/m^2 for both bridge parapets.

6.4.6 Permanent loads affecting longitudinal displacements of piles

It is noted that the modulus of subgrade reaction is probably too stiff for cyclic loading, and the creeping and cracking of concrete releases forces i.e. decrease the bending stiffness (bending stiffness was modelled in the FE models with short-term concrete material

properties). A multiplier for taking these issues into account with Formula 6.54 (linearly behaving modulus of subgrade reaction) is introduced in Paragraph 6.4.6. This multiplier decreases the loads to yield correct results with modelled properties.

The multiplier m_d in the bridge model was used for the following loads: temperature drop at curing time of concrete, shrinkage and creep in post-tensioned structures, due to reasons presented in Paragraph 6.3.5 and the effect of creep of concrete. Formula 6.54 in Paragraph 6.3.7 gives us:

$$M_{top,a,1} = M_{top,a,2} \tag{6.82}$$

$$y_{top,1} * (\frac{d}{dz} k_{a,1})^{\frac{2}{5}} * (EI_1)^{\frac{3}{5}} = y_{top,2} * (\frac{d}{dz} k_{a,2})^{\frac{2}{5}} * (EI_2)^{\frac{3}{5}}$$

$$m_d = \frac{(\frac{d}{dz} k_{a,2})^{\frac{2}{5}} * (EI_2)^{\frac{3}{5}}}{(\frac{d}{dz} k_{a,1})^{\frac{2}{5}} * (EI_1)^{\frac{3}{5}}} = \frac{\left(\frac{\frac{d}{dz} k_{a,cyclic}}{\frac{d}{dz} k_{a,staat}}\right)^{\frac{2}{5}}}{1^{\frac{2}{5}}} * \frac{\left(\frac{1}{1+0.5*\phi_{av}}\right)^{\frac{3}{5}}}{1^{\frac{3}{5}}}$$

$$m_d = \frac{\left(\frac{1}{2}\right)^{\frac{2}{5}} * \left(\frac{1}{1+0.5*1}\right)^{\frac{3}{5}}}{1} = \frac{0.76*0.78}{1} = 0.6$$

where

$$m_d = \frac{y_{top,1}}{y_{top,2}} \tag{6.83}$$

$M_{top,a,1}$ = bending moment at top of pile when modulus of lateral subgrade reaction is linearly distributed along pile length with full soil stiffness and non-creep concrete (as in bridge FE model) and reduced pile top displacement [MNm]

$M_{top,a,2}$ = bending moment at top of pile when modulus of lateral subgrade reaction is linearly distributed along pile length with reduced soil stiffness and concrete with creep and full pile top displacement [MNm]

$k_{a,staat}$ = static modulus of lateral subgrade reaction when modulus of lateral subgrade reaction is linearly distributed along pile length [MN/m^2]

$k_{a,cyclic}$ = cyclic modulus of lateral subgrade reaction when modulus of lateral subgrade reaction is linearly distributed along pile length [43, 63] [MN/m^2]

EI_1 = bending stiffness of structure without creep effect [MNm^2]
EI_2 = bending stiffness of structure with creep effect [MNm^2] [45]
ϕ_{av} = 1, average creep factor of pile and superstructure [-]
m_d = 0.6, m_d multiplier for bridge model loads: temperature drop at curing time of concrete, shrinkage and creep in post-tensioned structures [-]

The relation between the static and cyclic modulus of lateral subgrade reaction is from 1/4 to 1/2 [43, 63]. It is assumed in this study that permanent loads, which cause longitudinal

displacements of piles and develop during loading cycles, develop moments on abutment piles with the presented lower modulus of lateral subgrade reaction. The average creep factor of structures is estimated so that the moments of piles would be close to a case where the superstructure and the piles are affected by creep. The cross section properties in the bridge model are assigned without creep, and the modulus of lateral subgrade reaction is full in terms of the cyclic loading in the bridge models, which is why the multiplier m_d has been applied. The discussed loads were assigned to the FE model with temperature drop ΔT_{mod}, which is the equivalent temperature drop ΔT_{eq} multiplied with m_d. The temperature drop values and corresponding strains are presented in Table 6.12.

Table 6.12. Strains and equivalent temperature drops

	ε_i[-]	ΔT_{eq} [˚C]	ΔT_{mod} [˚C]	$\varepsilon_{i,mod}$ [-]
Curing of concrete	-0.00025	-25	-15	-0.00015
Shrinkage	-0.00025	-25	-15	-0.00015
Creep	-0.00017	-17	-10	-0.00010
Σ	-0.00067	-67	-40	-0.00040

The shrinkage strain $\varepsilon_{c,shr}$ of concrete is set to -0.00025 [-] [35, 45]. Then the equivalent temperature drop $\Delta T_{eq,shr}$ is:

$$\Delta T_{eq,shr} = \frac{\varepsilon_{c,shr}}{\alpha_{cT}} = \frac{-0.00025}{10*10^{-6}} = -25°C \tag{6.84}$$

Similarly, the creep of the superstructure concrete in the post-tensioned bridge types:

$$\varepsilon_c = \frac{\sigma_c}{E_{ce}} = \frac{-4}{33500} = -0.00012$$
$$\varepsilon_{cc} - \varepsilon_c = \varepsilon_c * \phi = -0.00012 * 1.4 = -0.00017 \tag{6.85}$$

$$\Delta T_{eq,cc} = \frac{-0.00017}{\alpha_{cT}} = -17°C \tag{6.86}$$

where

$$E_{ce} = 5000 * \sqrt{f_{ck,cube}} \quad \text{[35] (6.87)}$$

This method means that only the creep part of the strain caused by post-tension was reduced. All analyses of post-tensioned bridge types were made with the $\Delta T_{mod,cc}$ value of -10˚C, which corresponds to post-tensioning stress 4 MN/m^2, and the temperature drop was modelled for the whole cross section for the sake of simplicity.

6.4.7 Traffic load earth pressure

Normally the traffic load earth pressure is analysed using the rest earth pressure coefficient when it is assumed that the structure is rigid. The traffic load earth pressure is defined in Paragraph 6.4.7 when the structure moves away from the embankment simultaneously with a traffic load on the embankment surface.

The following schematic model for traffic load earth pressure $\Delta\sigma_{x1}$ from traffic load at embankment $\Delta\sigma_{z1}$ at only one end of the bridge, with elastic material behaviour, is presented in Figure 6.43.

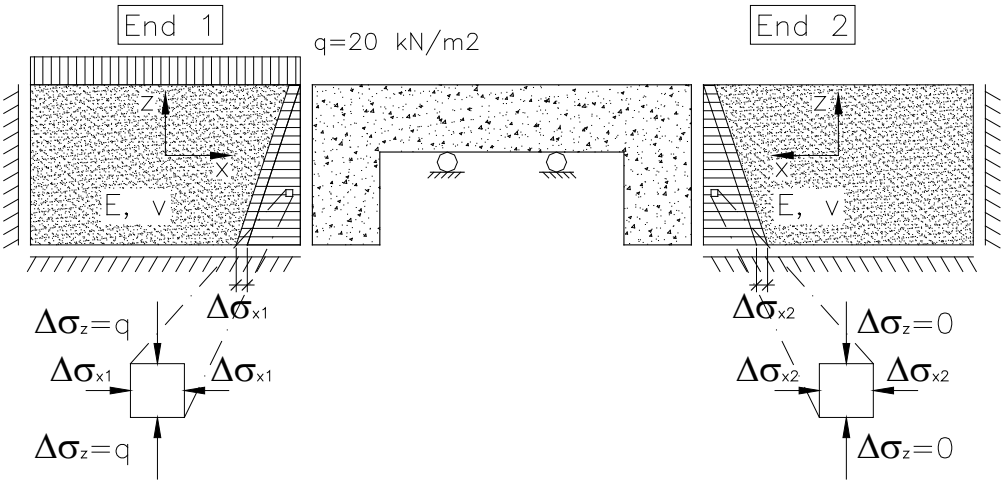

Figure 6.43. Traffic load earth pressure behind end screen at bridge end 1.

Hooke's Law and the co-ordinates of Figure 6.43 yield for bridge end 1 the following:

$$\varepsilon_{x1} = \frac{1}{E}\left(\sigma_{x1} - \nu * \left(\sigma_{y1} + \sigma_{z1}\right)\right) \tag{6.88}$$

if boundary condition $\sigma_{x1} = \sigma_{y1}$ is set then with Formula 6.88 we get:

$$\Delta\varepsilon_{x1} = \frac{1}{E}\left(\Delta\sigma_{x1} * (1-\nu) - \nu * \Delta\sigma_{z1}\right) \tag{6.89}$$

$$\Delta\sigma_{x1} = \frac{E * \Delta\varepsilon_{x1} + \nu * \Delta\sigma_{z1}}{1-\nu}$$

and because the structure moves away from the embankment, the longitudinal strain changes at end 2:

$$\Delta\varepsilon_{x2} = \frac{\Delta\sigma_{x2}}{E} \tag{6.90}$$

and for the longitudinal equilibrium of bridge structure condition $\Delta\sigma_{x2} = \Delta\sigma_{x1}$ is valid. Then with condition $\Delta\varepsilon_{x1} = -\Delta\varepsilon_{x2}$ and Formula 6.89 and 6.90 we get:

$$\Delta\sigma_{x2} = \Delta\sigma_{x1} = \frac{-\Delta\sigma_{z2} + \nu * \Delta\sigma_{z1}}{1-\nu} = \frac{\nu}{2-\nu} * \Delta\sigma_{z1} \tag{6.91}$$

if $\Delta\varepsilon_x = 0$ then based on Formulas 6.89 and 6.90:

$$\Delta\sigma_{x1} = \frac{\nu}{1-\nu} * \Delta\sigma_{z1} \tag{6.92}$$

If boundary condition $\sigma_{x1} = \sigma_{y1}$ is eliminated and boundary condition $\Delta\varepsilon_{y1} = 0$ is set, we obtain again from Hooke's Law:

$$\Delta\varepsilon_{y1} * E = \left(\Delta\sigma_{y1} - \nu * \left(\Delta\sigma_{z1} + \Delta\sigma_{x1}\right)\right) = 0 \quad (6.93)$$

$$\Delta\sigma_{y1} = \nu * (\Delta\sigma_{z1} + \Delta\sigma_{x1})$$

and $\Delta\sigma_{y1}$ is inputted to Formula 6.88 with Formula 6.90 when $\Delta\sigma_{x2} = \Delta\sigma_{x1}$:

$$\Delta\varepsilon_{x2} = \frac{1}{E}\left(\Delta\sigma_{x2} - \nu * \left(\nu * (\Delta\sigma_{z1} + \Delta\sigma_{x2} + \Delta\sigma_{z1})\right)\right) = \frac{\Delta\sigma_{x2}}{E} \quad (6.94)$$

$$\Delta\sigma_{x2} = \Delta\sigma_{x1} = \frac{\nu^2 + \nu}{2 - \nu^2} * \Delta\sigma_{z1}$$

Formulas 6.88-6.94 are rough because the transition slab and the piles are neglected, and the boundaries of soil elements behind the end screen are frictionless, but they offer a perspective to the behaviour of TLEP. Moreover, the assumption $\sigma_{x1} = \sigma_{y1}$ is not valid when the bridge superstructure moves in the longitudinal direction. Formula 6.92 is an equation for the rest earth pressure factor when a wall (or the end screen) against the soil is rigid. Formula 6.91 is an equation for the case where the structure between the embankments is supported on bearings through which a longitudinal movement is released. If Formula 6.91 is divided by Formula 6.92 we get the relation R :

$$R_1 = \frac{\nu}{2 - \nu} * \frac{1 - \nu}{\nu} = \frac{1 - \nu}{2 - \nu} \quad (6.95)$$

with ν = 0.3 R = 0.4

A corresponding relation based on Formulas 6.94 and 6.92 is:

$$R_2 = \frac{\nu^2 + \nu}{2 - \nu^2} * \frac{1 - \nu}{\nu} = (1 + \nu) * \frac{\nu - 1}{\nu^2 - 2} \quad (6.96)$$

R = relation of traffic load earth pressure to rigid wall and integral bridge end screen [-]

When ν = 0.3, R_1 = 0.41 and R_2 = 0.48, 41/48% of the general rest earth pressure from traffic load is mobilised to structure in Figure 6.43. The mobilised rest earth pressure from traffic load to the superstructure of a fully integral abutment bridge may be between 20 and 100%, depending on the stiffness relations between soil at the embankments, the transition slab and the structures of the bridge. If the traffic load affects simultaneously both abutments, then the traffic load earth pressure is 100% compared to the general rest earth pressure [84]. Half of the traffic load earth pressure was modelled in the bridge model because in the load combination rules [42] temperature change was assumed to be the determining load.

6.4.8 Finite element models

FE analyses of the bridge models were made with LUSAS (14.3-2 kit242). Basic models of bridges were built with the normal modelling procedure of the FE models in LUSAS.

Modification of basic models and creation of different bridge types were mostly performed with programs and subprograms written in the "Visual Basic Script" programming language. These programs controlled LUSAS in repetitive analyses. The material properties of the concrete in the bridge models are presented in Table 6.13.

Table 6.13. Material properties of concrete in bridge models

Structural part	$f_{ck,cube}$ [MN/m^2]	E_{ce} [MN/m^2](1	ν_c	G_{ce} [MN/m^2](2	ρ_c [kN/m^3]
Superstructure PT	45	33500	0.3	12900	2.5
Superstructure RC	40	31600	0.3	12200	2.5
End screen and wing walls	40	31600	0.3	12200	2.5
Substructures of intermediate supports	35	29600	0.3	11400	2.5

1) Calculated as in [35] and Formula 6.87

2) Elastic shear modulus of concrete G_{ce} is based on the theory of elasticity for simplicity of analyses. The relation between elastic and dimensioning shear modulus is presented in [35].

Axial stiffnesses of columns and piles were modelled with elastic material properties and bending properties as described in Paragraph 6.3.3. General views of bridge models B1 and B2 with a deformed shape at loading time t = 575 s are presented in Figures 6.44 and 6.45. Loading time is explained in Paragraph 6.4.9.

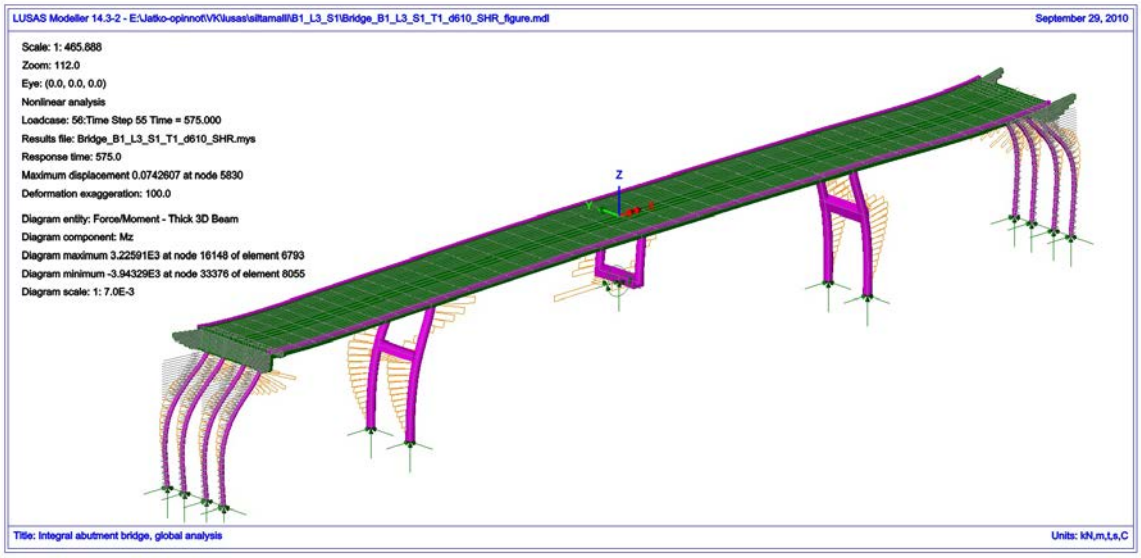

Figure 6.44. Bridge model B1_L3_S1_T1_d610_SHR at loading time t = 575 s, deformation exaggeration 100. Main moments of piles and columns M_z are also shown.

Figure 6.45. Bridge model B2_L3_S1_T1_d610_SHR at loading time t = 575 s, deformation exaggeration 100. Main moments of piles and columns M_z are also shown.

The middle spans are of equal length as defined in Table 6.8. The supports, which are founded on the concrete pile foundation, are modelled with rigid supports together with rigid beams at bottom of columns, see Figures 6.44 and 6.45 Bridge type B1_L3 is post-tensioned and type B2_L2 a reinforced concrete superstructure. The effect of post-tensioning may be seen in the displacement differences between Figures 6.44 and 6.45 (with deformation exaggeration value 100). The cross section of bridge type B1_L3 is presented in Figure 6.46 and the cross section of bridge type B3_L1 in Figure 6.47.

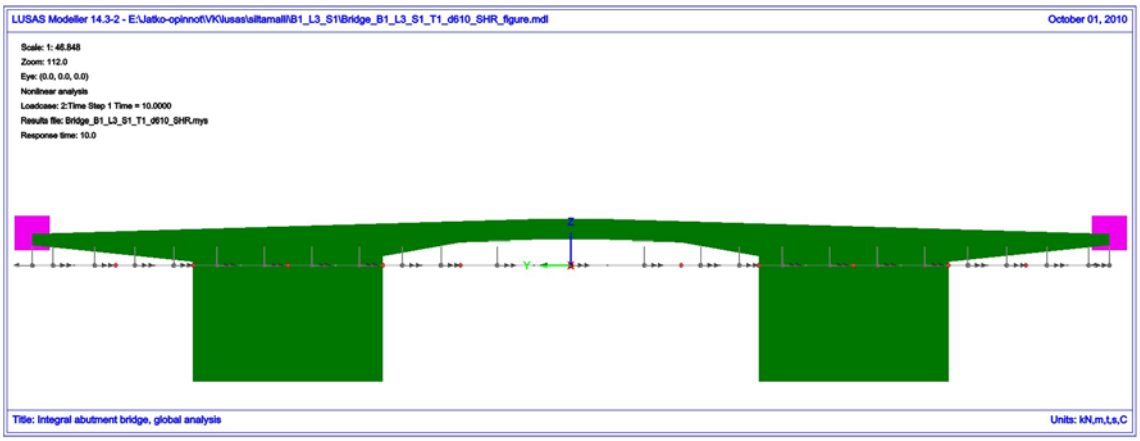

Figure 6.46. Cross-section of superstructure in model B1_L3_S1_T1_d610_SHR.

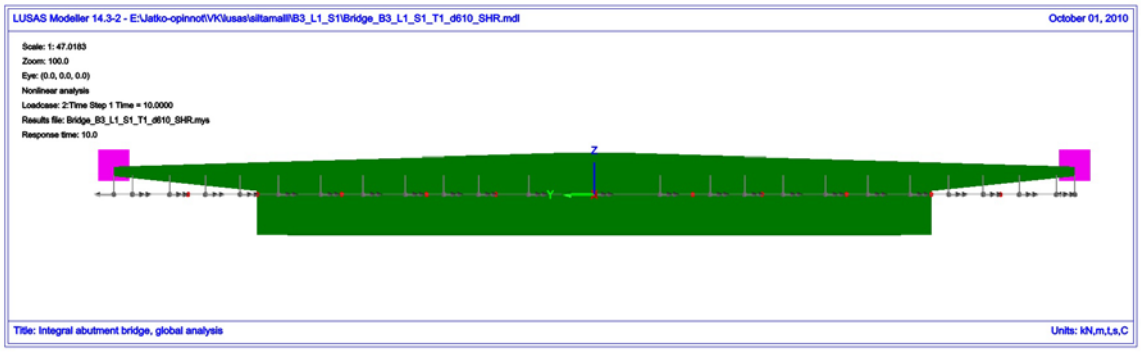

Figure 6.47. Cross-section of superstructure in model B3_L1_S1_T1_d610_SHR.

All cross sections were modelled to the modelling plane, see also Figures 6.19, 6.37, 6.39 and 6.40. The difference between cross-sections of different beam-and-slab structures was the distance between the modelling plane and the bottom of the beam part in terms of modelling the cross sections. The difference between cross sections in bridge models B3 and B1 and B2 is that the intermediate slab bottom level is even between the cantilever slab spans. The beams and slabs were modelled with slab elements (thick shell elements QTS4) and the edge beam with beam elements (thick non-linear beam element BTS3) [93]. The abutments of bridges were modelled by including all studied piles in all models but setting them active or inactive depending on the model. Piles were embedded 0.5 m (D*t = 273) or 1.0 m in the end screen in bridge models T1 or supported on a separate beam in bridge models T2, see Figure 6.48. The embedding in models T1 was made so that the connection between the end screen QTS4 elements and piles BTS3 elements would be stiff enough.

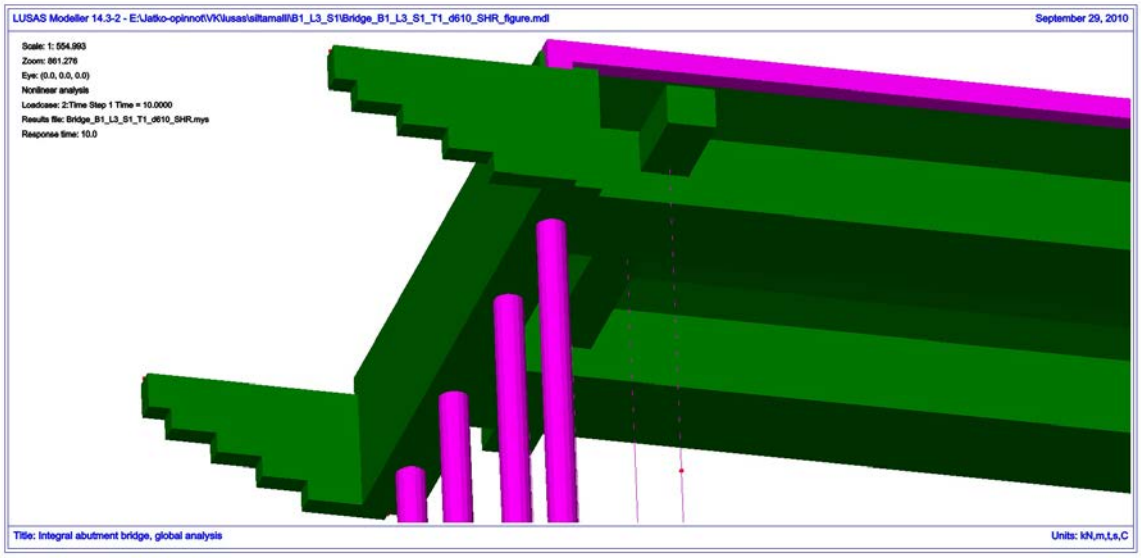

Figure 6.48. Abutment pile and structure orientation in model B1_L3_S1_T1_d610.

The wing walls and end screens were modelled with QTS4 elements. The bottom edge of the wing wall was modelled in steps to avoid an irregular and non-coincident mesh with

joint elements (Joint element JSH4). These joint elements were modelled between the structure, wing wall and end screen, elements and support level of the joint elements. The joints for wing walls were modelled opposite to the soil to avoid collapsing of the mesh, see Figure 6.49.

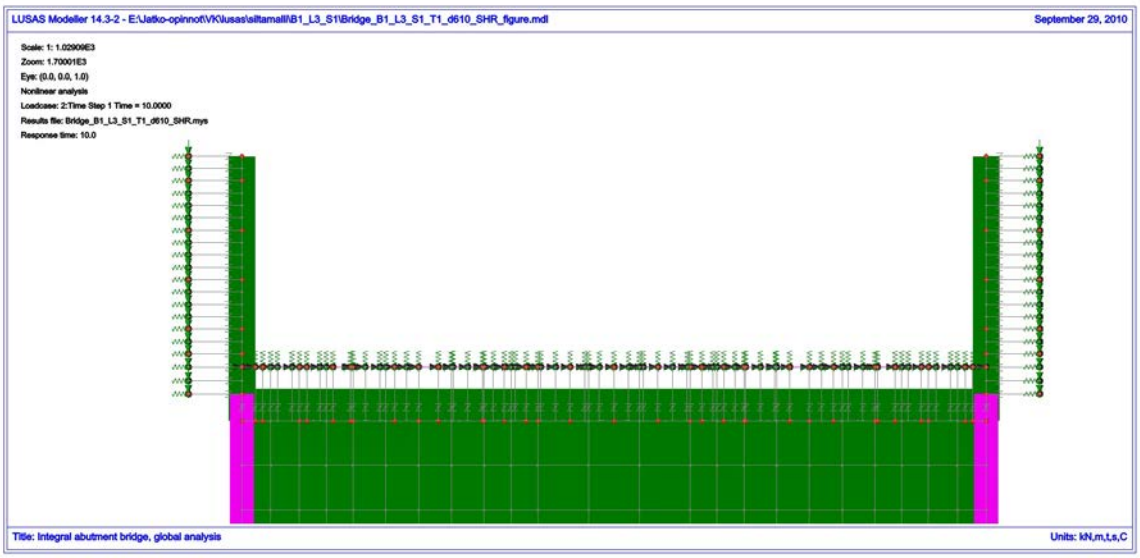

Figure 6.49. Abutment structure orientation and supporting levels of wing walls and end screen in model B1_L3_S1_T1_d610_SHR.

Further, the joints were not modelled for the full length of the wing wall and end screen because the effects of thicknesses of slab elements, i.e., wing walls and end screen neutral axes, were modelled to the modelling plane and half of the thickness of the connecting parts was modelled without joints, see Figures 6.49 and 6.50.

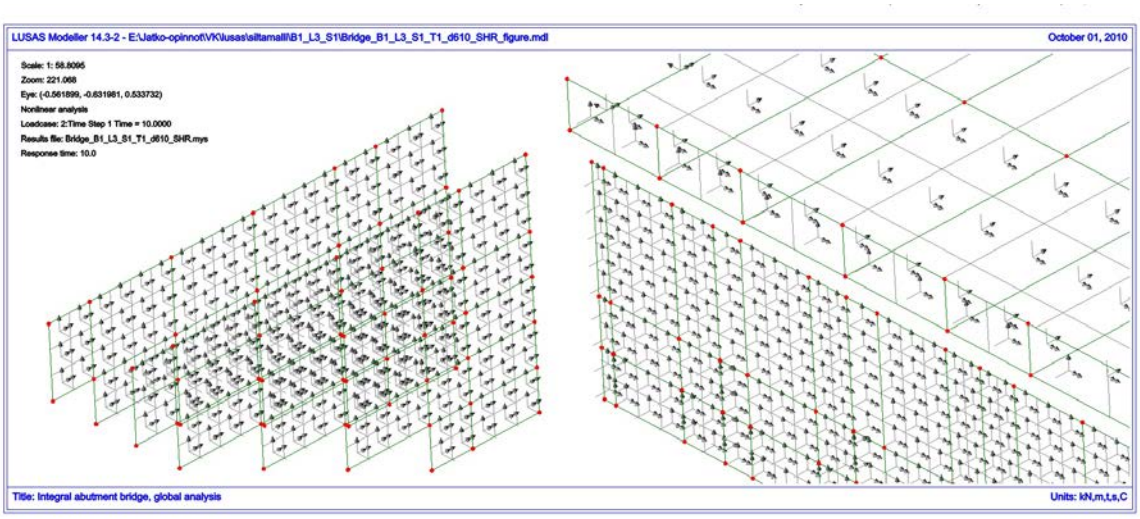

Figure 6.50. Mesh of wing wall, supporting level of wing wall joints and end screen in model B1_L3_S1_T1_d610_SHR.

The top part of the end screen was modelled directly connected to superstructure elements and the bottom part with a small gap for avoiding irregular meshes at joints as was men-

tioned earlier. The principle of meshes of piles at abutments and structures at the first intermediate supports is seen in Figure 6.51.

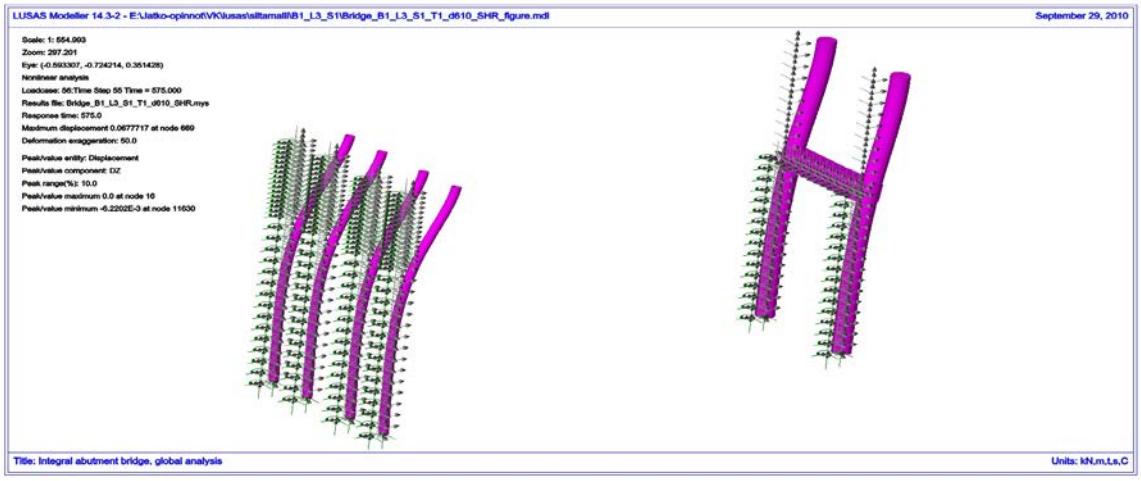

Figure 6.51. Meshes of piles and structures at first intermediate support in model B1_L3_S1_T1_d610_SHR.

Lateral longitudinal joints of piles were modelled between a supporting line of joints and the pile, as in the case of the modelling of wing walls and end screens. Transverse supports of piles were modelled with simple continuous elastic supports of stiffness k_{50} for simplicity of the models. Longitudinal joints of the transverse beam at the top of piles at intermediate supports were modelled to one line because the structural part was modelled as a beam. The stiffness of joints was integrated from end screen behaviour and material between the top and bottom level of the transverse beam. Thereby the stiffness is slightly lower because the longitudinal stiffness of soil above the top part was neglected. The effective width of the superstructure was the reason for modelling the superstructure with slab elements. A rough effective width is included in the analyses. Stress contours at the top of the superstructure in model B2_L3_S1_T2_d914_SHR are presented in Figure 6.52.

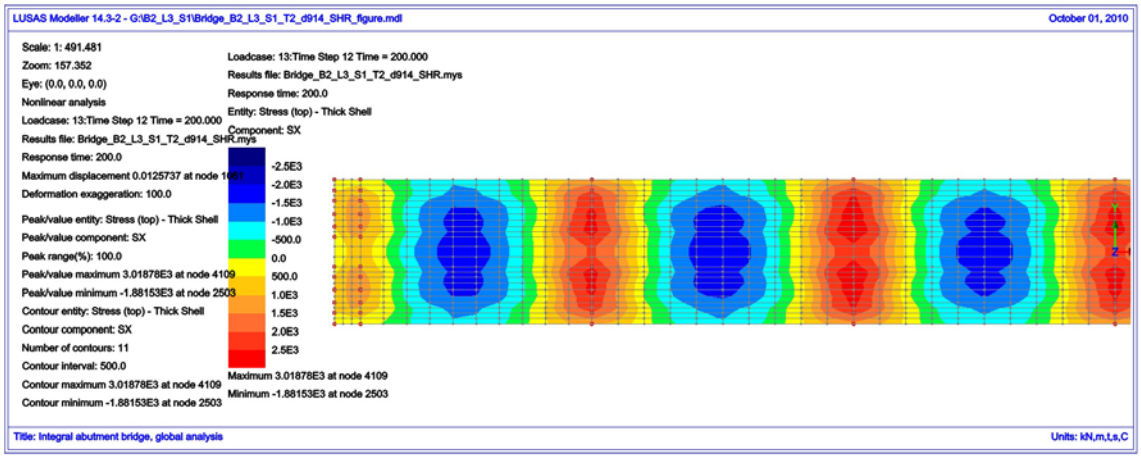

Figure 6.52. Longitudinal stresses at top of superstructure in model B2_L3_S1_T2_d914_SHR at loading time t = 200 s. Contour range is from –2.5 to 2.5 MN/m^2.

It may be noted that stresses are not evenly distributed along the cross section because shear lag and level of top surface have an effect. Figure 6.52 shows a reinforced concrete superstructure and Figure 6.53 shows a post-tensioned one.

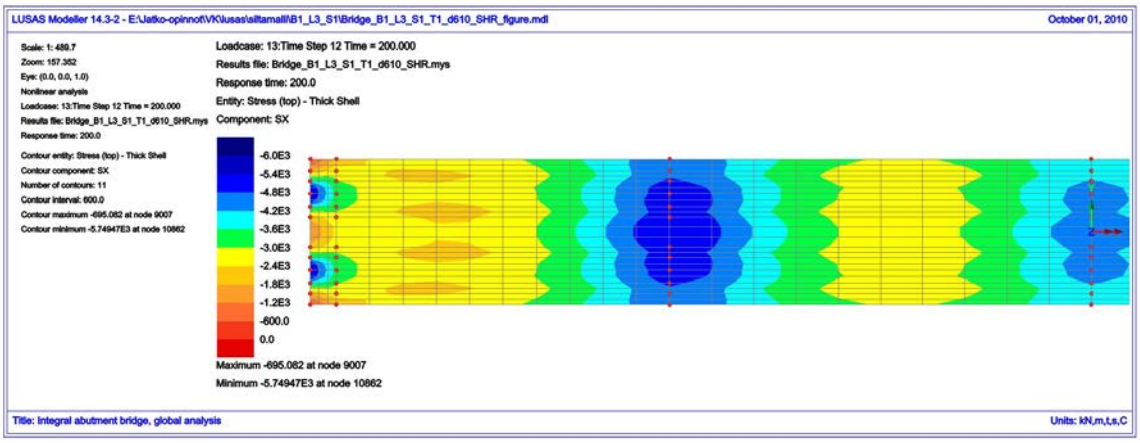

Figure 6.53. Longitudinal stresses at top of superstructure in model B1_L3_S1_T1_d610_SHR at loading time t = 200 s. Contour range is from 0 to 6.0 MN/m^2.

The behaviour of a post-tensioned superstructure is different from that of a reinforced concrete superstructure in terms of effective width. The longitudinal stresses are rather concentrated near anchors of tendons at bridge ends and by contrast rather evenly distributed farther from bridge ends. With rough checks of the longitudinal stresses of superstructure, the average effective width of cantilever and intermediate slabs was 30 to 60% of slab widths in reinforced concrete superstructures and 30 to 90% in post-tensioned superstructures. The values are only suggestive because the slabs were modelled with linear elastic material properties while assuming that they are accurate enough for the purposes of the serviceability analyses of this study.

Wind loads and vertical traffic loads were analysed with linear elastic models for simplicity because traffic loads have several possible positions and they cause many different load combinations on the bridge. Further, the effect of the traffic load on internal stresses is not very big compared to e.g. the temperature load, and vertical traffic load does not directly affect the longitudinal displacement at the pile top. Thus, the error due to this simplification is tolerable. In addition, wind loads are not as definitive as other loads, which makes it is proper to use the linear elastic model in the analysis. The effect of vertical traffic load pattern Lk1 [42] 3*210 kN axles with spacing of 6.0 and 2.5 m was analysed, see different spacings (points in loading lanes) in Figure 6.54.

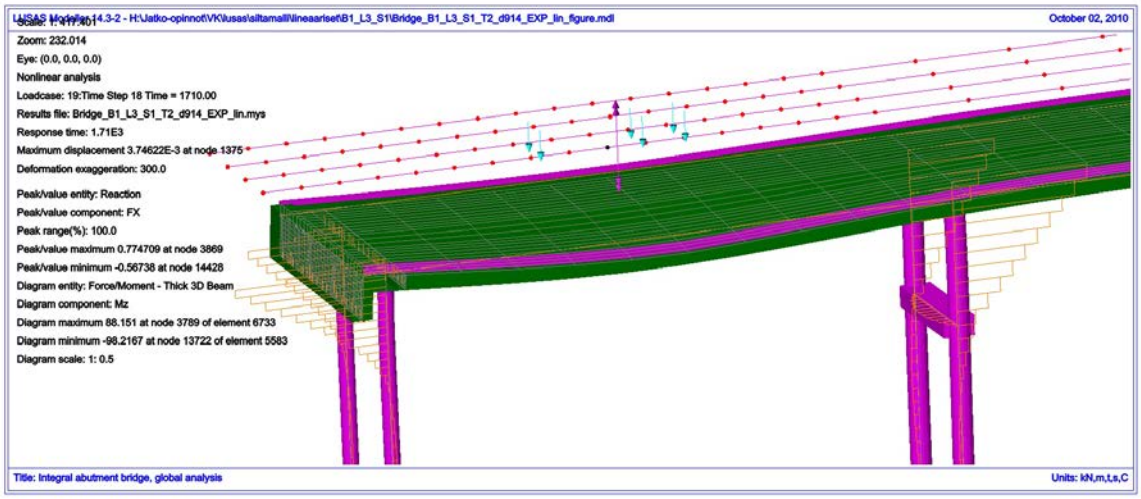

Figure 6.54. Bridge model B1_L3_S1_T2_d914_EXP with Lk1 loading pattern at first span, deformation exaggeration 300. Main moments of piles and columns M_z are also shown.

Positions of Lk1 loading pattern in bridge models were assigned with finer divisions at bridge ends than in the central section of the bridge, see Figure 6.54. This was made to shorten the analysis time, and results for piles at bridge ends were analysed with reasonable accuracy. The assign point (the location where the load was assigned) of the axle group was at the middle of the loading pattern of Lk1, see black point in Figure 6.54. Four 3 m wide loading lanes were assigned at the other side of the bridge's effective width 13.5 m. The lengths of different sections L_{sec}, load assign divisions (section length L_{sec} divided by 16) and lengths of loading lines L_{line} are presented in Table 6.14.

Table 6.14. Load positions of loading pattern Lk1 at one loading lane

	L_{exp}	L_{line} (1	$L-L_{line}/2$ (5	$L_{sec,1}$ (2	$L_{sec,1}/16$	$L_{sec,2}$ (3	$L_{sec,2}/16$	n_{Lk1} (4
	[m]	[m]	[m]	[m]	[m]	[m]	[m]	
L1	120	132	6.0	32	2.00	68	4.25	48
L2	135	144	4.5	34	2.13	76	4.75	48
L3	150	160	5.0	36	2.25	88	5.50	48

1) L_{line} is length of loading lane [m]
2) $L_{sec,1}$ is length of first (end) part of loading lane [m]
3) $L_{sec,2}$ is length of second (middle) part of loading lane [m]
4) N_{Lk1} is number of different locations of loading pattern Lk1 at one loading lane [-]
5) Distance of beginning of loading lane from end screen outer surface [m]

Totally 48 load positions along a single loading line were analysed. A uniformly distributed part of vertical traffic load, 3 kN/m^2 [42], was assigned with width of loading line 3 m and length of each span. Then the number of load cases on the uniformly distributed part of one loading lane was 4/6 with bridge type B1T1/B1T2 and 6/8 with bridge types B2T1/B2T2 and B3T1/B3T2. The most determining load combination was combined from the previous load, separate load cases of axle groups, and uniformly distributed load. The

wind loads were assigned in transverse direction of the bridge. The linear models were modified from non-linear models with the following changes:

- Longitudinal non-linear modulus of lateral subgrade reaction of piles was replaced by elastic stiffness $k_{50}/4$. Transverse elastic modulus of lateral subgrade reaction k_{50} stayed the same as in non-linear models.
- Non-linear modulus of lateral subgrade reaction of end screen was replaced by elastic stiffness $k_{50}/4$
- Non-linear modulus of lateral subgrade reaction of wing walls was replaced by elastic stiffness $k_{50}/4$, here k_{50} is the modulus of the end screen.
- Linear bending stiffnesses of piles were determined based on the third normal force level and half of the ultimate moment capacity with corresponding normal force as shown in Figure 6.11, in Paragraph 6.3.3 and Appendix 8.1.
- Linear bending stiffnesses of concrete columns were determined based on the second normal force level and half of the ultimate moment capacity with corresponding normal force as shown in Figure 6.12 and Paragraph 6.3.3.

The value of $k_{50}/4$ was assigned to the end screen because values of the linear model are calculated together with values of the non-linear models, see Paragraph 6.4.9. In determining cases, soil is either remarkably yielding or at an active state in the non-linear models when values of the linear models are applied. Then a value lower than k_{50} was assigned to the end screen. The value of $k_{50}/4$ (instead of the $k_{50}/(2*4)$ of the non-linear analysis) was assigned to end wing walls because of the nature of the wind load and low yield of the soil in the non-linear model load combinations. The bending stiffnesses of the piles and columns were set so that the normal force level was below the target value N_{opt} because some normal force values were obtained from the linear model.

The total number of degrees of freedom in the bridge models B1/B2/B3 was 67608/70848/70848. The total number of nodes was calculated by dividing the above numbers by six. Most nodes were concentrated on bridge ends and substructures (piles, end screens, wing walls and intermediate supports). Approximately 75% of the degrees of freedom were at the bridge ends and substructures.

6.4.9 Load combinations in FEM

Bridge structures are analysed normally with linear models in bridge design when the method of superposition is valid and it is possible to use e.g. influence lines. However, the method of superposition is not valid in non-linear analysis, and Paragraph 6.4.9 defines how loads were combined in the structural analyses of this study.

Loads were assigned in non-linear models (NL) as function of time because the superposition method does not work in combining results from separate load cases of non-linear

analyses. The non-linear analyses were performed as quasi-static, i.e., the loads were assigned so slowly that mass matrix and damping matrix did not have noticeable effects, because velocity and acceleration were small, and each load was entered separately as function of time and the result at each point in time corresponds to one load combination. The variation of loading as function of time is called a load curve in LUSAS. The load curves of the analyses are presented in Figure 6.55.The output times of results are presented in Figure 6.55.

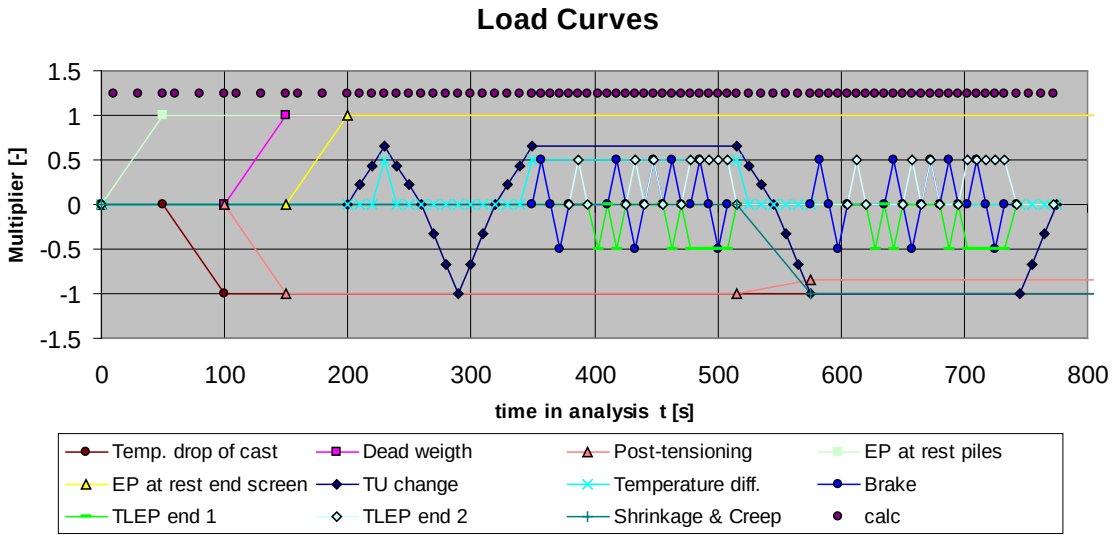

Figure 6.55. Load curves of non-linear models. In the figure EP = rest earth pressure, TLEP = traffic load earth pressure and calc = output times of results.

Some loads are presented with a negative multiplier to simplify Figure 6.55. The change of T_U was modelled between -30°C and 28˚C with an initial temperature of 5.2˚C, then (28-5.2)/(-30-5.2) = 22.8/35.2 = 0.65, which is the maximum positive multiplier of T_U in Figure 6.55, i.e., the temperature attribute of the non-linear bridge model was 35.2˚C. Half of the positive temperature difference was modelled together with the maximum value of T_U while none of the negative temperature difference was modelled with the minimum value of T_U, because temperature difference decreases the moment values of piles resulting from a change of T_U. The most determining load case was selected for piles in terms of temperature difference (minimum value together with T_U), see Figure 5.6. The total temperature change DT in the FE models during loading time t is presented in Figure 6.56.

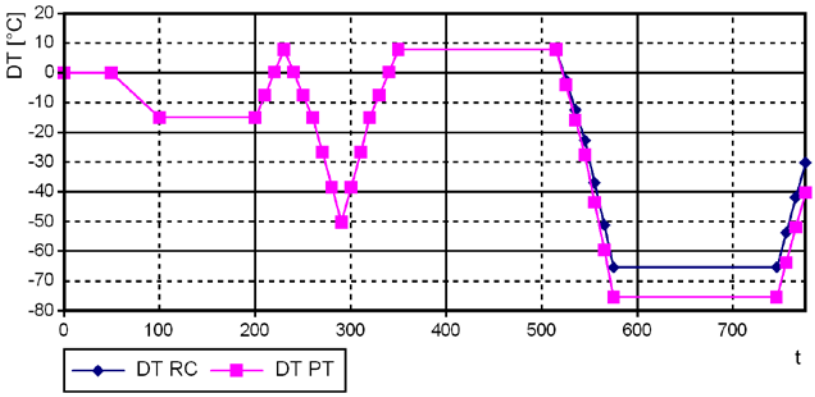

Figure 6.56. Temperature change in reinforced (RC) and post-tensioned (PT) bridges.

The total temperature change is strongly on the negative side. The loading sequence maximum positive change from initial stage is 7.8ºC and maximum negative change 65.4ºC with reinforced concrete structures, and 75.5ºC with post-tensioned concrete structures. It is obvious that the negative temperature change has a major effect on dimensioning. The group of traffic load earth pressure combinations (TLEP) at both ends and brake load were assigned with both maximum and minimum values of T_U. The multiplier with previous loads was from -0.5 to 0.5 because of the combination rules in [42]. The creep and shrinkage were activated between t = 510 s and t = 575 s, and at the same time the post-tensioning force multiplier decreased from 1.0 to 0.85 due to long-term losses. The results of bridge models were combined into the flowchart in Figure 6.57. The results were analysed for all nodes under consideration.

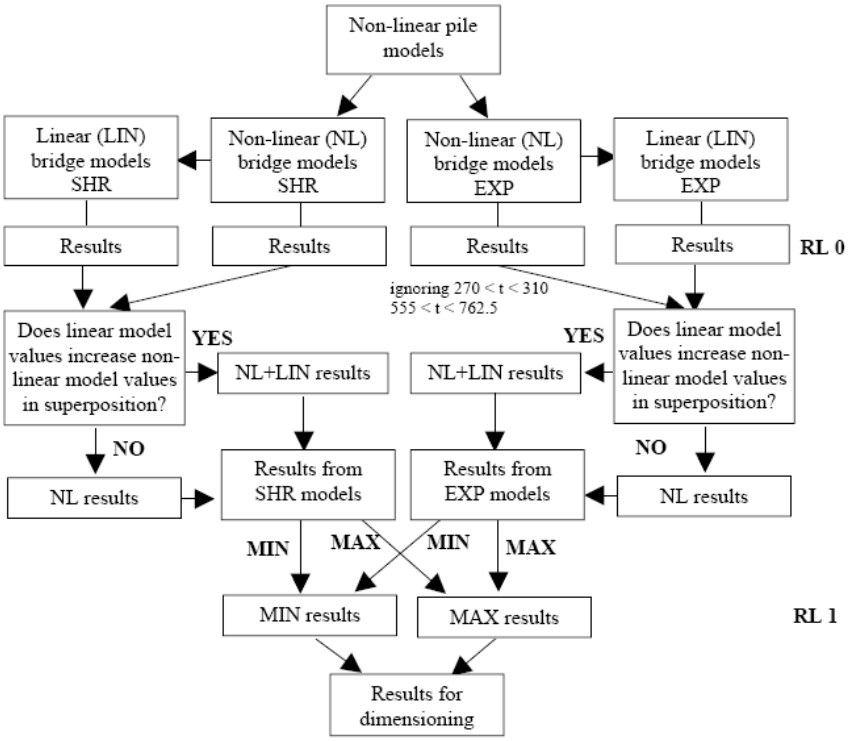

Figure 6.57. Flowchart combining non-linear and linear bridge model results.

The superposition method does not work correctly with non-linear models, as mentioned above. However, in the present study, the results of the non-linear models were much higher than those from linear models (LIN) with their characteristic boundary conditions, and the error in superposition was not very relevant. The stiffnesses of linear models were set so that the error in superposition would not be relevant and misleading. Time gaps 270 < t < 310 and 555 < t < 762.5 were ignored in the non-linear EXP bridge model results because the time gaps of stages were governed by the SHR bridge models, and EXP models are not valid with these time gaps. The time gaps are presented together with results as function of time in Paragraph 6.4.10. The results on traffic and wind loads (LIN) were combined together with full values with results from non-linear models.

6.4.10 Results of FEM

The results from FE analyses are presented in Paragraph 6.4.10. Different levels of results are also defined in Paragraph 6.4.10.

Different levels of results may be observed in the flowcharts of Figures 6.57 and 6.58; these levels 0-3 will be discussed later on. The processing of pile results from FE analyses is described in the flowchart of Figure 6.58.

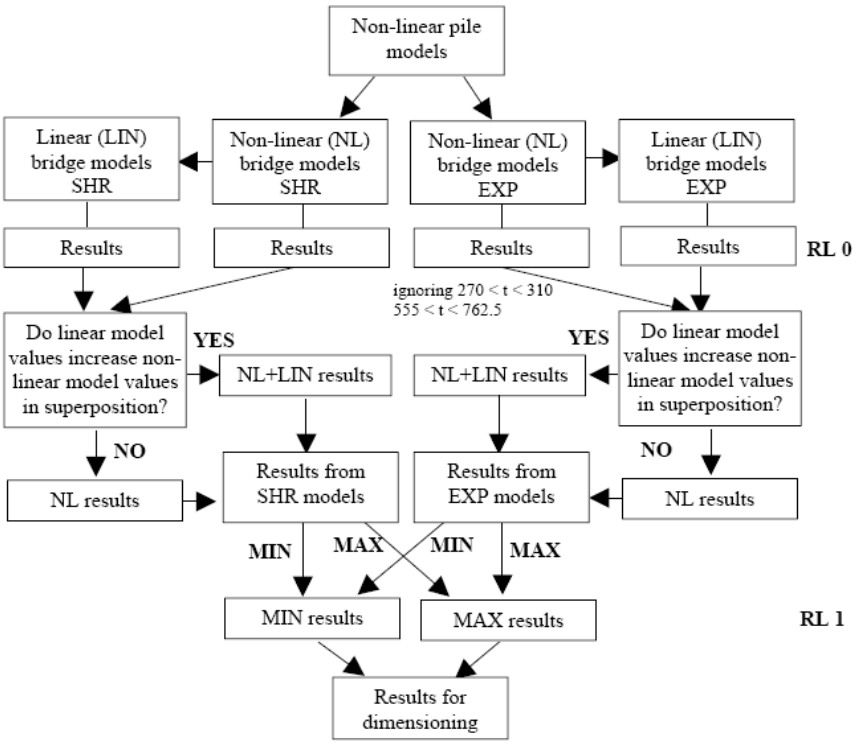

Figure 6.58. Flowchart of pile results.

Results from FE analyses include, for instance, data from all force components (max 6) for all nodes, location in the bridge model (co-ordinates X, Y, Z), loading time (t), and

whether the examined force is a minimum on maximum value. The previous flowchart was made to clarify which results are discussed in each paragraph. The resultant bending moment M_R of pile cross-section was calculated with Formula 6.97:

$$M_R = \sqrt{M_z^2 + M_y^2} \tag{6.97}$$

where
M_z = bending moment around local Z-axis (main direction of piles), see Figure 6.51 and 6.54 [MNm]
M_y = bending moment around local Y-axis [MNm]

Negative signs are not used with Formula 6.97. The sign of M_R is determined by the sign of M_z, as in Figure 6.54. The sign of the main moment of piles M_z and the main moment of bridge superstructure M_Y in the results are determined by the system presented in Figure 6.59. The sign is positive when external fibres on the side indicated by a dashed line are under higher tension than those on the other side.

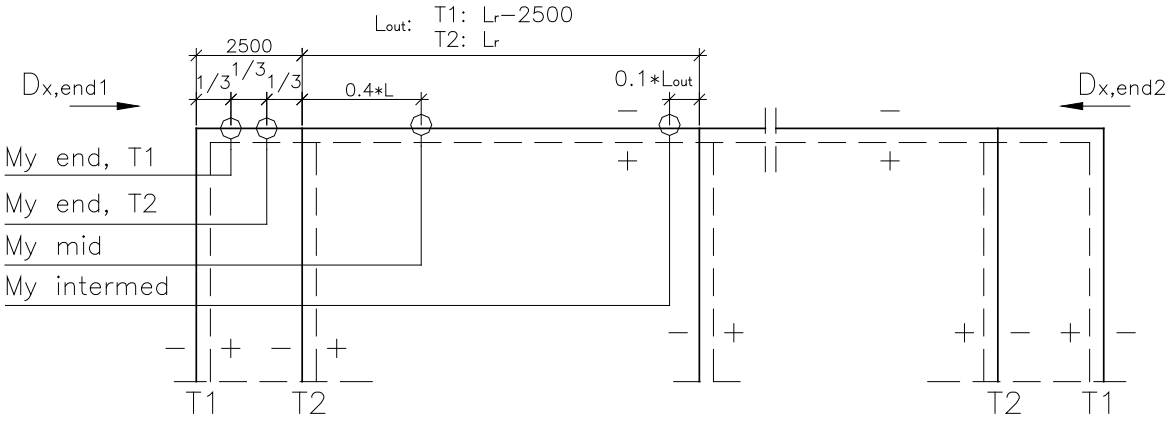

Figure 6.59. Sign of moments M_z and M_Y and positive longitudinal displacement DX directions.

In addition, the positive direction of longitudinal displacements and points of outputting moments of superstructure M_y are defined in Figure 6.59. The present direction was selected for easier interpretation of the results. The time unit of the results is seconds.

6.4.10.1 Bending moments of piles as function of loading time

Results for pile bending moments M_R at the top of pile as function of loading time in Figure 6.60 were obtained from bridge models B1_L1_S1_T1_d914_SHR and -_EXP.

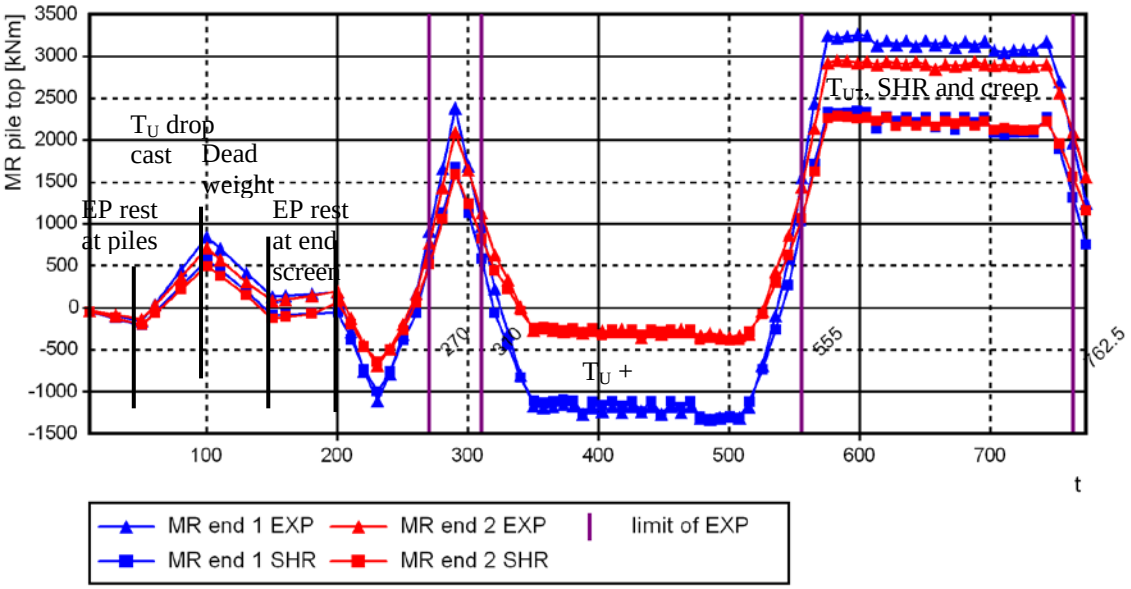

Figure 6.60. Pile bending moments M_R at top of pile in bridge models B1_L1_S1_T1_d914_SHR and _EXP. Result level 0 (RL0). Vertical lines represents starting points of loads. Names are abbreviated. Main affecting load are named in here, compare to Figure 6.55.

The vertical lines are the earlier mentioned time gaps from the results of EXP models, which were ignored. The results with blue labels represent bridge end 1 (where multiplier m_G = 0.75, see Paragraph 6.4.4) and the results with red labels represent bridge end 2 (where multiplier m_G = 1.25, see Paragraph 6.4.4). The results marked with triangles are from the EXP model and those marked with rectangles are from the SHR model.

The effects of different loadings of quasi-static analyses are clearly visible in pile bending moments. Time gaps of first loads are marked by lines and labels in Figure 6.60. The absolute value of bending moment M_R is higher due to the contraction of superstructure than due to the expansion of superstructure. This difference is higher at bridge end 1 because negative M_R values are relatively small. Moments M_R from dead weight at the pile top reduced the maximum M_R values. Moments M_R from the SHR and EXP models were relatively similar in the time gap from t = 340 s to 515 s, whereas in the time gap from t = 555 s to 750 s moments M_R from different bridge ends were relatively similar, but the results from SHR and EXP models were clearly different. The effect of different behaviour in SHR and EXP models is greater at the stage where the bridge superstructure contracts in terms of moment M_R. Earth pressures behind end screens are small during the contraction of the bridge superstructure, and roughly speaking the unequal displacements of bridge ends are balanced with the piles and the columns.

Effects of the traffic load earth pressures and brake loads were relatively small compared to the total values of M_R. The largest effect on maximum positive values of moment M_R

was obtained from brake load at the stage where the superstructure of the bridge was contracted, see time gap from t = 575 s to t = 605 s. This results from the fact that after a large contraction of the bridge superstructure (see Figure 6.56), the brake load needs to resist only one embankment in the model because at the other embankment earth pressure is zero, thus only one embankment has longitudinal stiffness at the present loading stage. The highest effect on minimum values of moment M_R was obtained at the stage where the superstructure of the bridge was expanded, see time gap from t = 477.5 s to t = 507.5 s. The effects of the TLEPs and brake loads have the same sign as the effect of expansion. Similar behaviours were observed in all bridge models. The results for pile bending moments M_R at the top of pile in Figure 6.61 were obtained from bridge models B1_L1_S1_T2_d914_SHR and EXP.

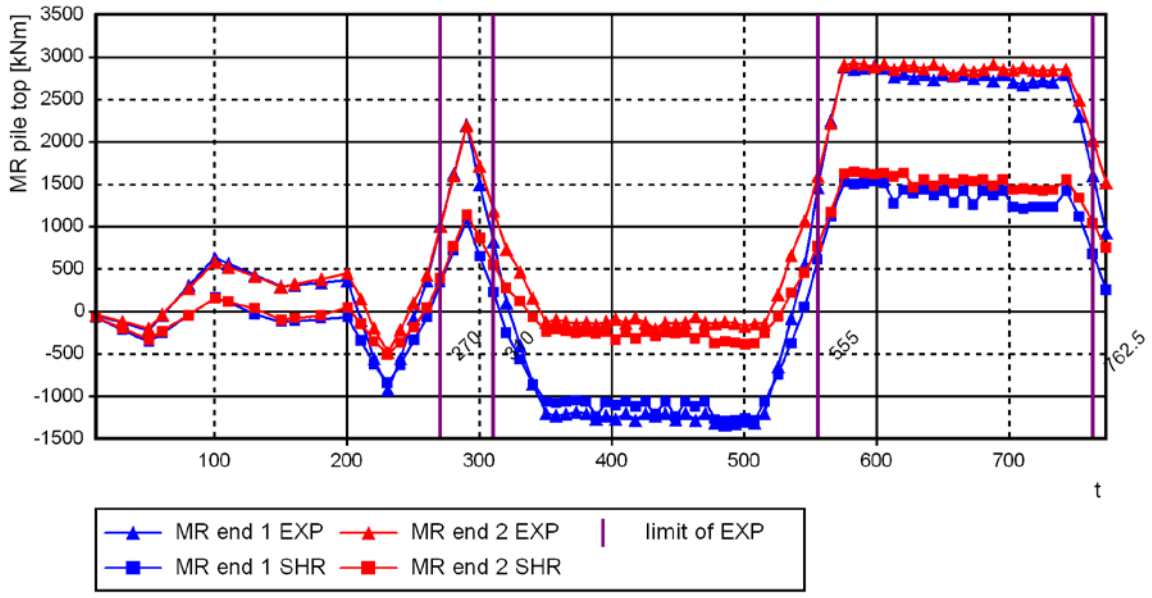

Figure 6.61. Pile bending moments M_R at top of pile in bridge models B1_L1_S1_T2_d914_SHR and _EXP. RL0.

Values of moment M_R at bridge end 2 were more on the positive side in T2 models than in T1 models. The difference between SHR and EXP models was greater in T2 models than in T1 models at the stage where the superstructure of the bridge was contracted. The moments M_R are approximately same in T2 models as in T1 models in the time gap from t = 555 s to 750 s, although the structure is slender in T2 models. This is probably caused by the fact that the rotation of the end screen reduces the moment M_R in T1 models but not in T2 models. Similar results for bridge types B2_L1_S1_d914 and B3_L1_S1_d914 are presented in Appendix 9.2 as in Figures 6.60 and 6.61.

6.4.10.2 Bending moments of bridge superstructure as function of loading time

The results for the bridge superstructure's total main bending moments $M_{y,tot}$ as function of loading time at the end of the bridge $M_{y,end,tot}$, at first intermediate support $M_{y,intermed,tot}$ and at span L_r $M_{y,mid,tot}$ (see Figure 6.59) in Figures 6.62 and 6.63 were obtained from bridge models B1_L1_S1_T1_d914_SHR, EXP and B1_L1_S1_T2_d914_SHR, EXP.

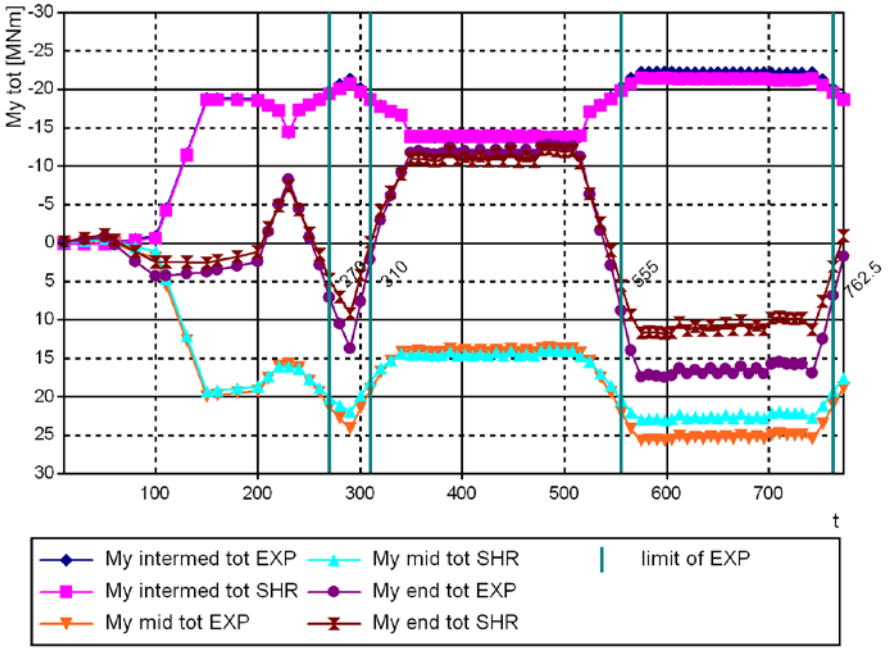

Figure 6.62. Superstructure bending moments M_y in bridge models B1_L1_S1_T1_d914_SHR and EXP. RL0.

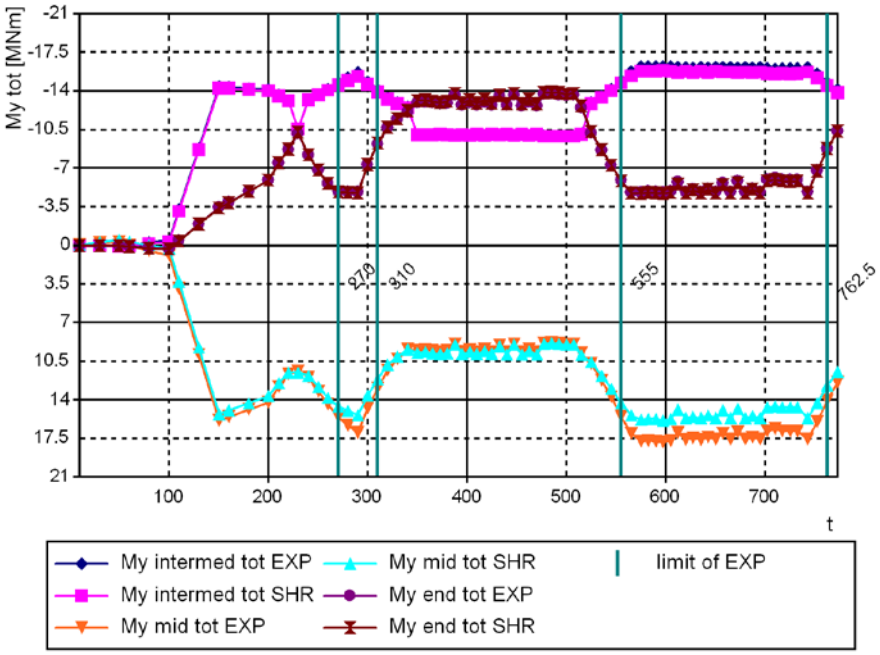

Figure 6.63. Superstructure bending moments M_y in bridge models B1_L1_S1_T2_d914_SHR and EXP. RL0.

The moment $M_{y,end,tot}$ varies remarkably during loading time because of reactions of the piles and earth pressure variations behind the end screen. The longer the distance from

bridge end, the smaller the effects of by loading time and the difference between SHR and EXP models. Generally, the highest absolute values (from observed locations) are at span L_r or at the first intermediate support in bridge type B1. Especially in bridge types B2_T2 and B3_T2 the minimum values of moments $M_{y,end,tot}$ were higher (higher absolute value) than the minimum values of moments $M_{y,intermed,tot}$ and $M_{y,mid,tot}$, see Appendix 9.2. The moment $M_{y,end,tot}$ was rather similar in T1 and T2 models for the time gap from t = 340 s to 515 s, see Figure 6.63. This kind of behaviour was observed in other bridge models, too. It has to be noted that moment $M_{y,end,tot}$ occurs in different locations in models T1 and T2. The highest influence in the SHR and EXP models occurred in the time gap t = 555 s to750 s. However, this time gap is neglected in EXP models.

6.4.10.3 Bending moments of piles as function of pile top lateral displacement

The result matrix in Figures 6.64-6.69 was obtained from bridge models L1_S1_T1_d914_SHR and EXP in terms of the M_R-D_X relation. The longitudinal displacement D_X is from the top of the pile. The matrix-type presentation reveals the effect of two variables on the examined relations. The similar matrices from different results have been used in the results later on, because a lot of result data come from a large number of bridge models. In the following matrix, the left column is for results from T1 models and the right column for results from T2 models. Rows represent different bridge types B1_L1, B2_L1 and B3_L1. The results of the SHR models are marked with rectangles and the results of the EXP models with triangles. The displacement D_X range of bridge end 1 is larger than that of bridge end 2. However, the developed positive moment M_R does not differ very much between the ends of the bridge because the slope of results from bridge end 2 is steeper but the displacement range smaller. Among bridge types T1, the main bridge type B has an effect on the moment M_R values, whereas with bridge types T2 the effect of main bridge type B is small. The difference between bridge types T1 probably results from different bending stiffness of the bridge superstructure of main bridge types B. The difference between SHR and EXP models is remarkable in bridge type T2, in other words, bridge type T2 is more sensitive to changes in supporting conditions. Moments M_R are the same or even higher in bridge type T2 than in bridge type T1.

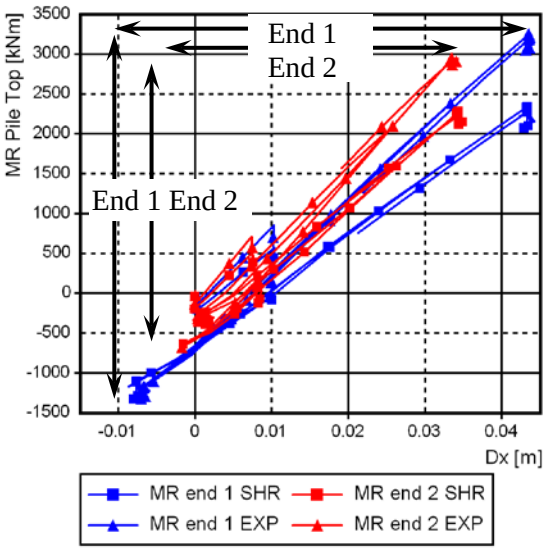

Figure 6.64. M_R-D_X from B1_L1_S1_T1_d914, RL0.

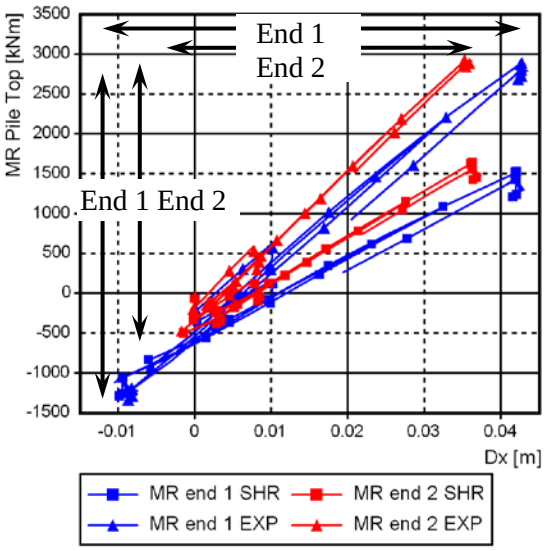

Figure 6.65. M_R-D_X from B1_L1_S1_T2_d914, RL0.

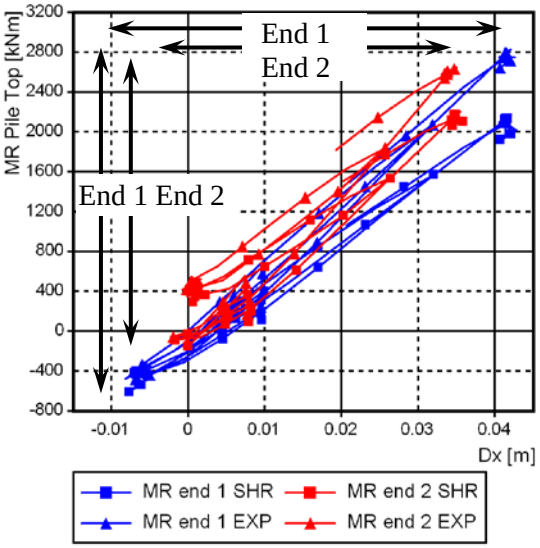

Figure 6.66. M_R-D_X from B2_L1_S1_T1_d914, RL0.

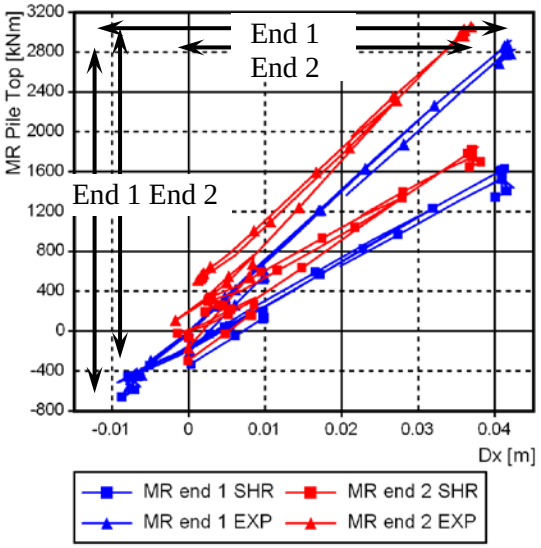

Figure 6.67. M_R-D_X from B2_L1_S1_T2_d914, RL0.

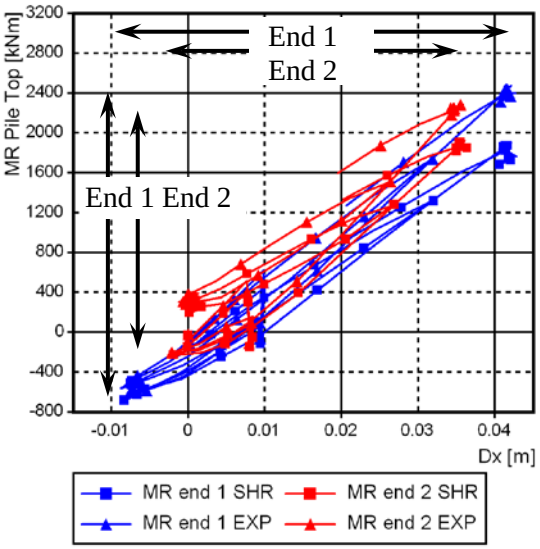

Figure 6.68. M_R-D_X from B3_L1_S1_T1_d914, RL0.

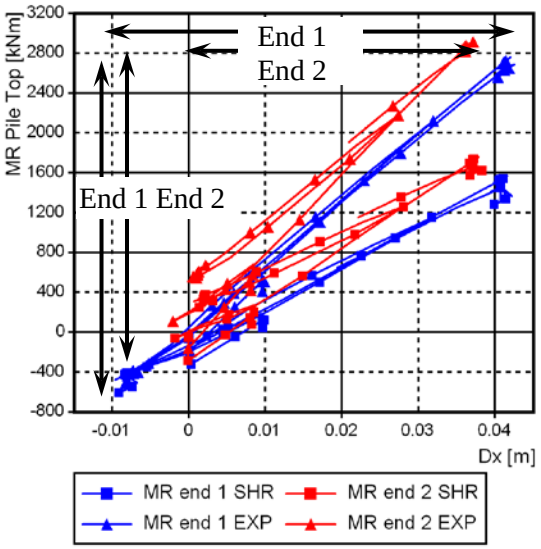

Figure 6.69. M_R-D_X from B3_L1_S1_T2_d914, RL0.

6.4.10.4 Earth pressure behind end screen as function of bridge end displacements

The earth pressure (E_P) displacement (D_X) relationship was obtained from bridge model B2_L1_S1_T1_d914_SHR, see Figure 6.70. Depth z_1 = 2.6 m and z_2 = 1.6 m.

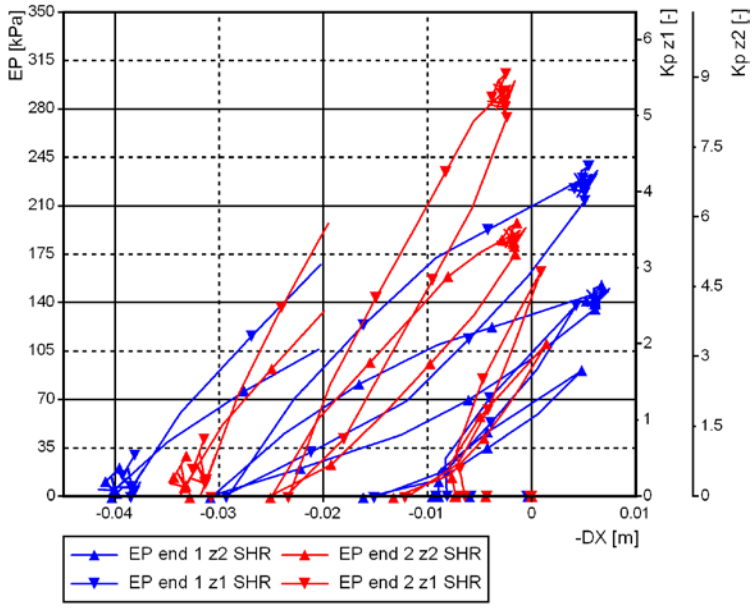

Figure 6.70. E_P-D_X from B2_L1_S1_T1_d914_SHR, z_1 = 2.6 m z_2 = 1.6 m, RL0.

Effects of the global multiplier m_G are clearly visible as a difference between bridge ends in the previous results. The slope of the E_P-D_X relationship is steeper at bridge end 2. The ultimate value of K_p is 0.75*8 = 6 at bridge end 1 and 1.25*8 = 10 at bridge end 2. The developed earth pressures are higher at bridge end 1 in terms of K_P, i.e., the soil strain state is higher at bridge end 1. The E_P-D_X relationship at depth z_1 is presented for bridge models B2_L1-, B1_L2- and B2_L3_S1_T1_d914_SHR in Figure 6.71.

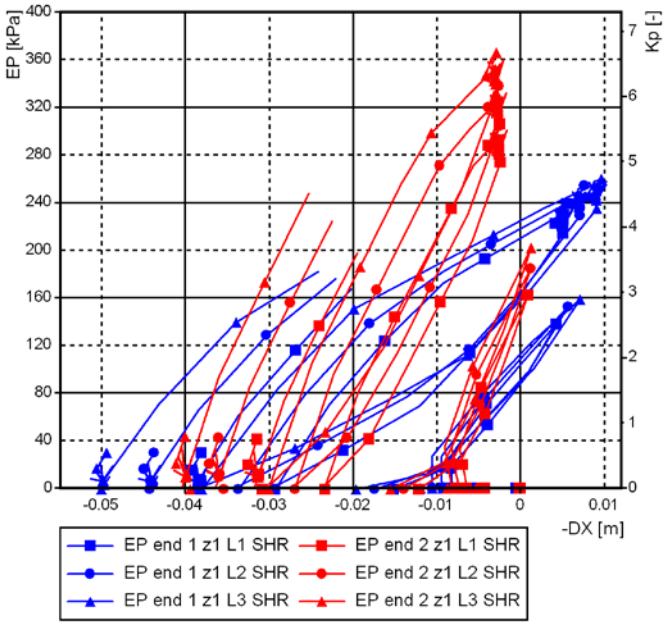

Figure 6.71. E_P-D_X from B2_L1-, B2_L2- and B2_L3_S1_T1_d914_SHR, z_1 = 2.6, RL0.

The maximum earth pressures increase as function of bridge length. The displacement stage increases at bridge end 1 as function of bridge length. At bridge end 2, the developed displacement stage is rather independent of bridge length but the earth pressures increase. A similar behaviour is observed later on in the displacement results.

6.4.10.5 Bending moments of piles as function of depth

The result matrix in Figures 6.72-6.77 for the pile bending moments as function of depth was obtained from bridge models B1_T1_S1 and B1_T2_S1 in terms of moment M_R. In the matrix, the left column is for results from T1 models and the right column for results from T2 models. Rows show different pile types D*t = 610*16, 914*16, and 1200*16. The results of the L1 models are marked with circles, L2 models with rectangles and L3 models with triangles. The results for all piles of each examined pile size are presented in each figure, e.g. results of all nodes in 8 piles (4 per bridge end) are presented in the figures related to the pile size D*t = 610*16. The global co-ordinate Z is the distance from the modelling plane, i.e. Z is a co-ordinate in the FE model. Maximum moments M_R represent the top of pile in bridge models T1 and T2. The maximum moments in bridge models T2 are observed at bridge end 2 (red symbols). Minimum moments M_R are also observed at the top of pile with bridge length L1 at bridge end 1 (blue circles). With lengths L2 and L3 of the bridge, minimum moments M_R are observed at a lower level and extreme values occur at bridge end 2 (red rectangles and triangles). At these lengths, both the minimum moments M_R and the maximum moments M_R are the result of the contraction of the bridge superstructure, not of the expansion of the bridge superstructure as with length L1. The effect of

the post-tensioning is clearly visible in moment M_R ranges. The moment M_R range shifts towards positive values with post-tensioned bridge types (L2 and L3). The maximum moments M_R at the top of the piles in bridge models T2 with lengths L2 and L3 are almost equivalent, but with L3 the range shifts towards negative values. The effects of traffic and wind loads are included in the following results. In this part of the bridge models B1_L1_S1_T1_d914 and -_T2_d914, moment M_R may be obtained as the difference between Figures 6.64-6.65 and Figures 6.74-6.75. This part is small at the positive values of 55 and 50 kNm and moderate at the negative values of 260 and 185 kNm. They result from the behaviour of the continuous superstructure. The effect of the traffic load is greater on negative values because the location of the load is at L_r span (see Figure 6.54) and smaller on positive value because the location of the load is at the first L_k span. There are no negative moments M_R at the top of the piles with bridge types B1_L2_T1 and B1_L3_T1. With bridge types B2 and B3 the positive moments also are occur at the top of the piles, see Appendix 9.3-9.5. Similar results on other bridge types mentioned in Paragraph 6.4.2 are also presented in Appendix 9.

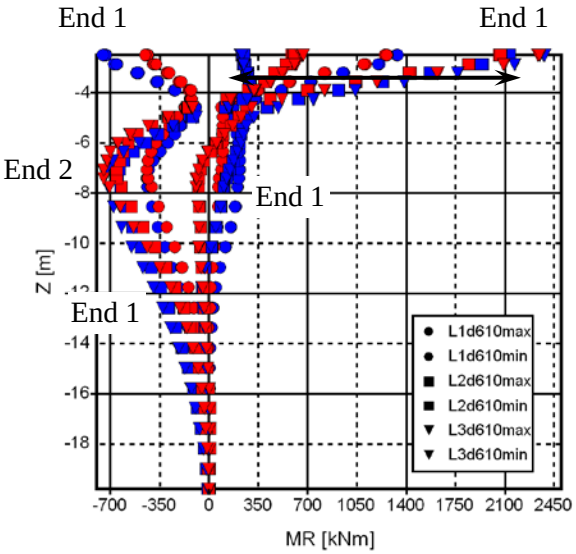

Figure 6.72. M_R-Z from B1_S1_T1_d610, RL1.

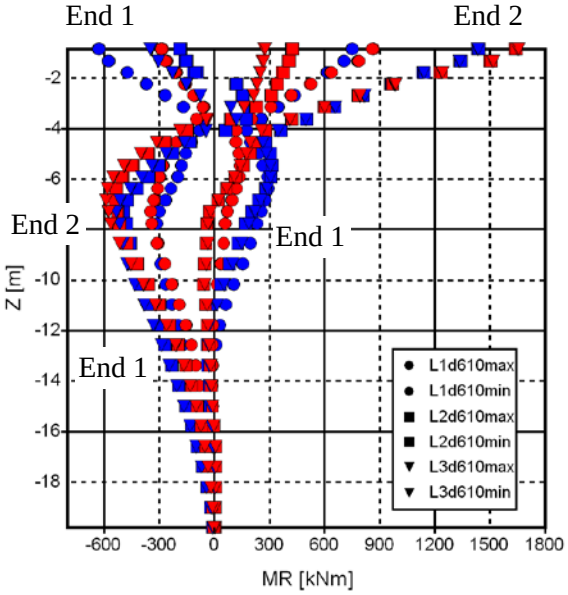

Figure 6.73. M_R-Z from B1_S1_T2_d610, RL1.

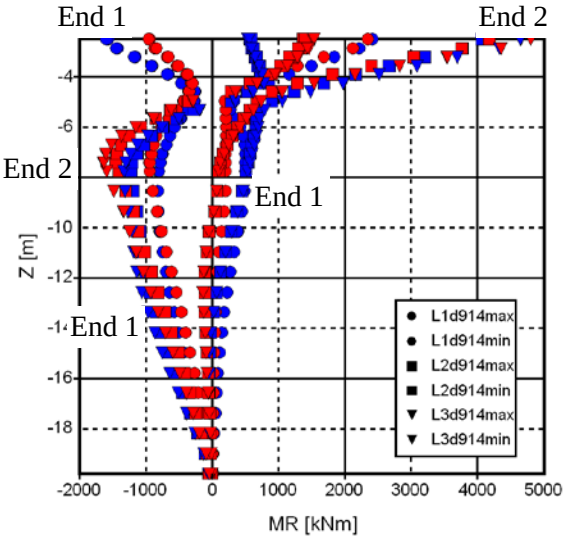

Figure 6.74. M_R-Z from B1_S1_T1_d914, RL1.

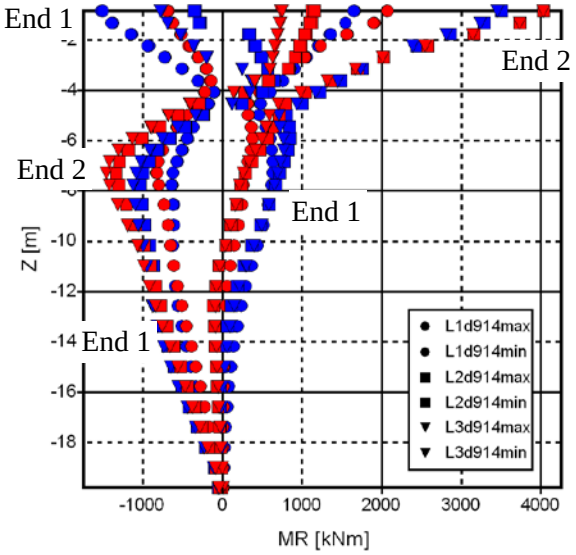

Figure 6.75. M_R-Z from B1_S1_T2_d914, RL1.

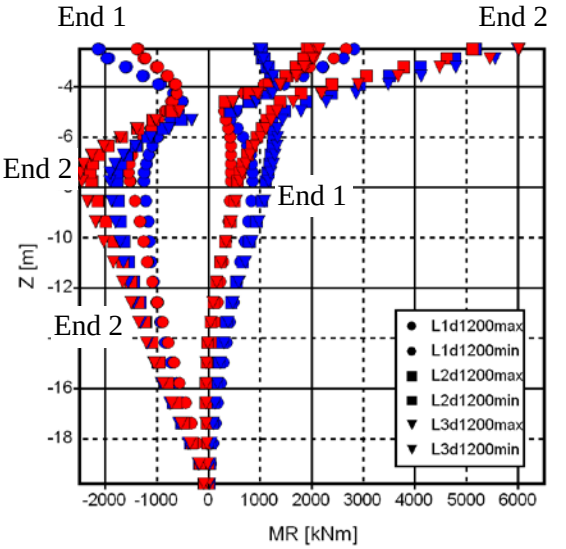

Figure 6.76. M_R-Z from B1_S1_T1_d1200, RL1.

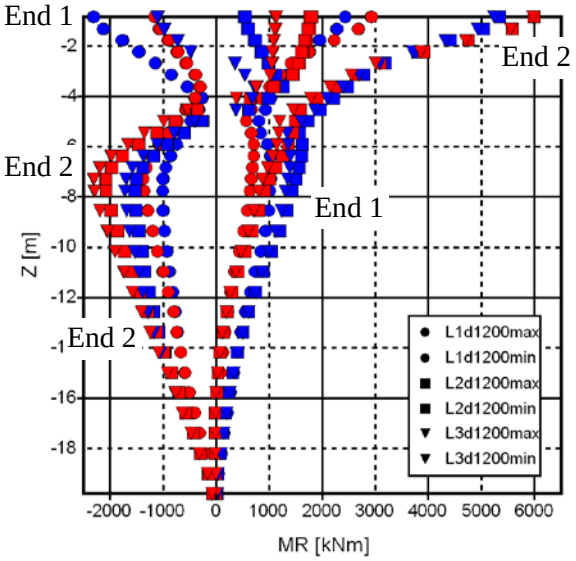

Figure 6.77 M_R-Z from B1_S1_T2_d1200, RL1.

6.4.10.6 M_R-F_X diagrams of pile cross sections

The result matrix in Figures 6.78-6.83 was obtained from bridge models B1_T1_S1 and B1_T2_S1 in terms of M_R-F_X diagrams. The cells and symbols in the diagrams of the following matrix correspond to the previous result matrix. Each result of a bridge model consists of four sub-results, the maximum or minimum of component M_R or F_X and corresponding values of F_X or M_R (see result level RL2 in Figure 6.58). Value F_X is the normal force of the pile. The cross section capacities are presented in stages D_0, D_{0c}, D_1 and D_{1c}, see Paragraph 6.3.2. The maximum moment M_R occurs with small normal force F_X values. These are the result of the structural behaviour of the continuous frame-like bridge superstructure. Normal force F_X is smaller at the piles of the bridge ends when the superstructure is contracted and higher when the superstructure is expanded. This phenomenon may be calculated for bridge B1_L1_S1_T1_d914_SHR from the M_y results in Figure 6.62. The moment $M_{y,end,tot}$ change is 22 MNm and $M_{y,intermed,tot}$ change is 7.5 MNm from t = 515 s to t = 575 s. The distance between these results is $0.9*L_{out} = 0.9*(27.5 - 2.5) = 22.5$ m according to Table 6.8 and Figure 6.59. That allows calculating the change towards smaller normal forces F_X of the piles D*t = 914*16 based on the changes of moments: (22 + 7.5) / (22.5 * 2) = 0.65 MN per pile. By contrast, the maximum normal force was observed at the expanded stage with traffic loads. Extreme effects of traffic and wind loads on the normal forces F_X of bridge B1_L1_S1_T1_d914 were from -1.2 to 0.15 MN. However, the FE models do not take into account the uplifting component of the earth pressure behind end screens. The resultant of the earth pressures at bridge end 1 was 5.7 MN at the loading time t = 575 s; with length L3, the resultant was 5.9 MN. Then the uplifting component of bridge end 1 with length L1 would be 5.7 * (sin38 / 2) = 1.85 MN [46]. The normal force range would be roughly the same at the expanded and the contracted stage with bridge type B1_L1_S1_T1_d914.

Similar results on other bridge types mentioned in Paragraph 6.4.2 are presented in Appendices 9.3-9.5.

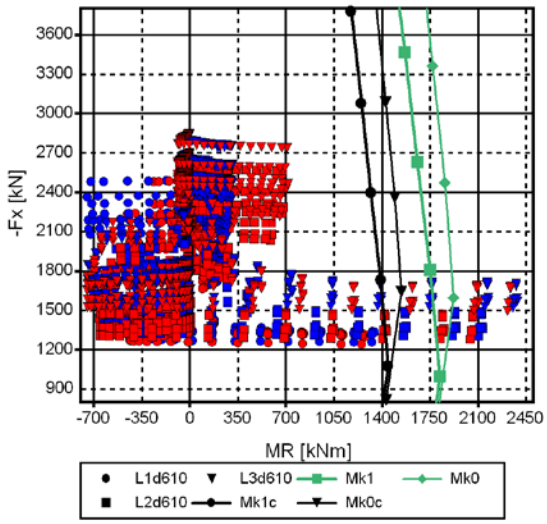

Figure 6.78. M_R-F_X from B1_S1_T1_d610, RL2.

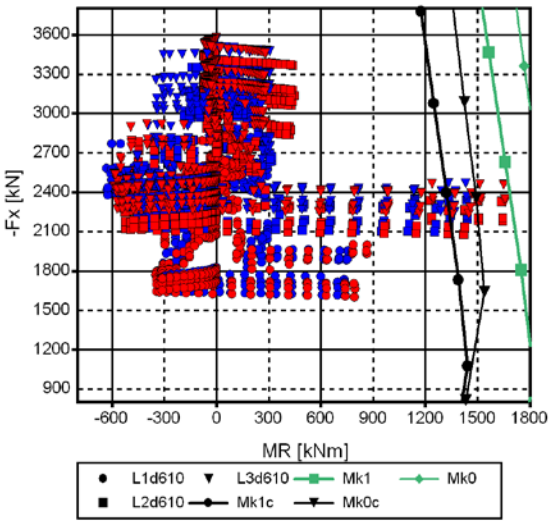

Figure 6.79. M_R-F_X from B1_S1_T2_d610, RL2.

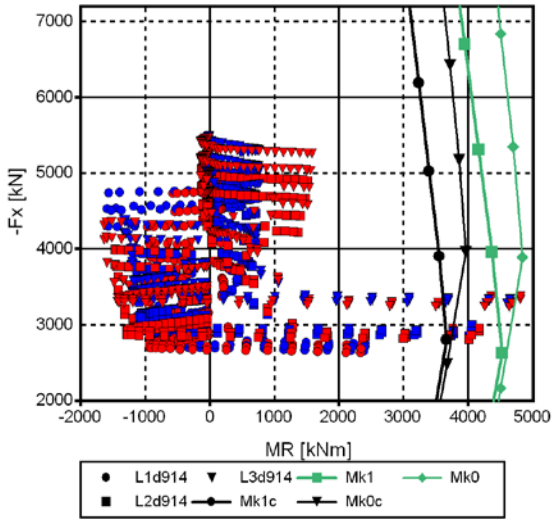

Figure 6.80. M_R-F_X from B1_S1_T1_d914, RL2.

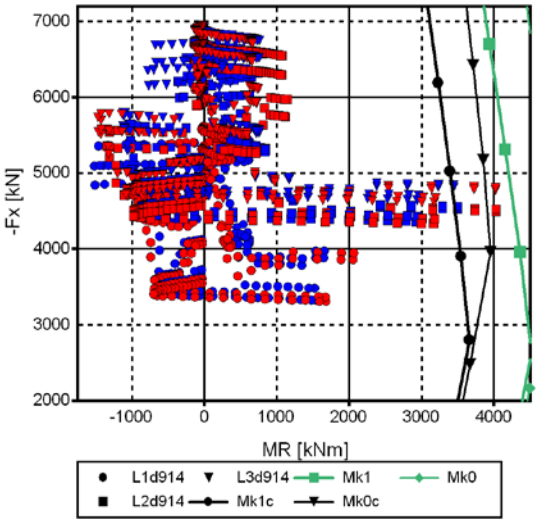

Figure 6.81. M_R-F_X from B1_S1_T2_d914, RL2.

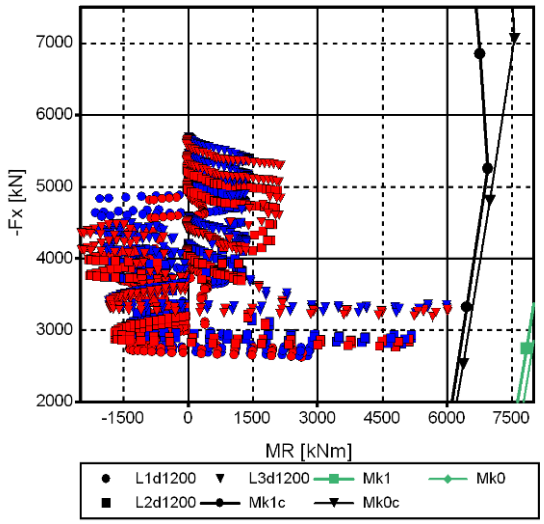

Figure 6.82. M_R-F_X from B1_S1_T1_d1200, RL2.

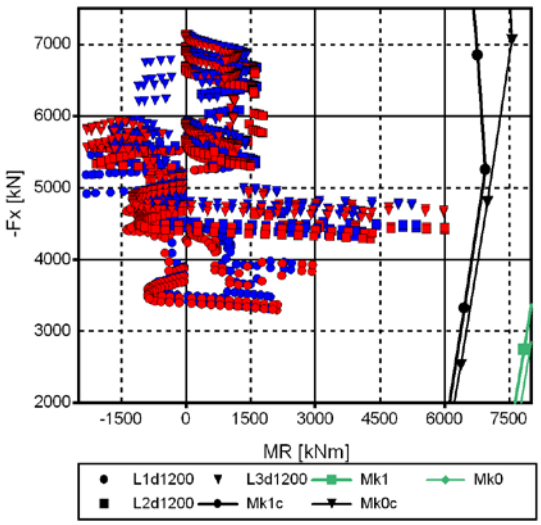

Figure 6.83. M_R-F_X from B1_S1_T2_d1200, RL2.

6.4.10.7 Displacements of bridge ends as function of loading time

The result matrix in Figures 6.84-6.89 for bridge end displacements as function of loading time was obtained from bridge models B1_T1_S1_SHR and B1_T2_S1_SHR in terms of $D_{X,end1}$- $D_{X,end2}$ diagrams. The cells and symbols in the diagrams of the following matrix correspond to the previous result matrices with the difference that the colours of the symbols depend on the loading time t. The line $D_{X,end1} = D_{X,end2}$ indicates where the results should be if the bridge end displacements were centric around the bridge's centre of thermal expansion. The path perpendicular to the previous line is the longitudinal displacement of the bridge superstructure. In addition, the displacement range of each bridge length is presented. The effect of global multiplier m_G is clearly visible in the following results. The displacement range of bridge end 1 is wider than that of bridge end 2. A gap between post-tensioned (L2 and L3) and reinforced concrete structures (L1) is visible at the maximum contraction stage. The difference is not as obvious at the most expanded stage maybe because the loading compared to the initial stage is only slightly or not at all on the expanded side. Displacements of bridge type T2 are more eccentric at the expanding stages, i.e. at the highest earth pressures the slopes of the following diagrams are close to 5/3 when the displacements of bridge ends develop very intensely due to the stiffness relations of the embankment. The relation of global factors m_G behind the end screens is 5/3. Bridge types T1 have a greater elastic stiffness of the piles at the bridge ends, which compensates for the displacements of the bridge ends around the centre of thermal expansion, but the displacements are still eccentric. The bending moments of intermediate columns are roughly symmetrical when the results do not fall on the line $D_{X,end1} = D_{X,end2}$. The longitudinal displacements of the bridge superstructure are very small due to brake and TLEP loads. The displacement from the 500 kN brake load was 0.5 mm at the expanded stage and 0.3 mm at the contraction stage. The maximum displacements from a brake and TLEP load combination in the bridge models was 0.8 mm.

Similar results on other bridge types mentioned in Paragraph 6.4.2 are presented in Appendices 9.3-9.5.

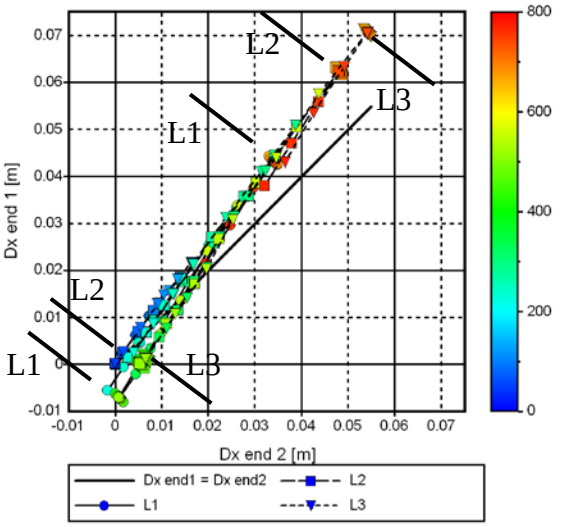

Figure 6.84. $D_{X,end1}$-$D_{X,end2}$ B1_S1_T1_d610_SHR, RL0.

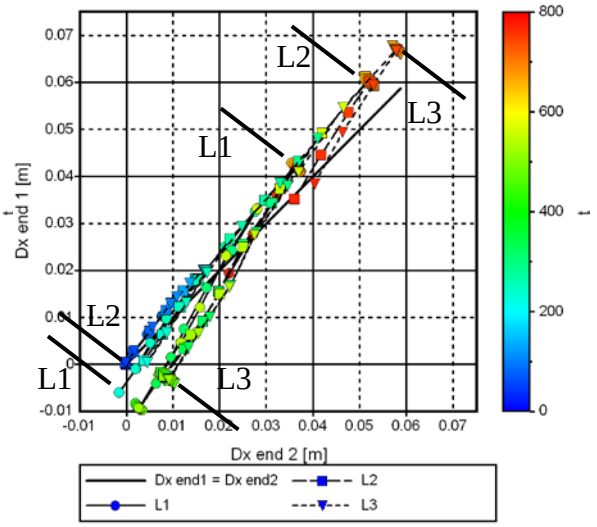

Figure 6.85. $D_{X,end1}$-$D_{X,end2}$ B1_S1_T2_d610_SHR, RL0.

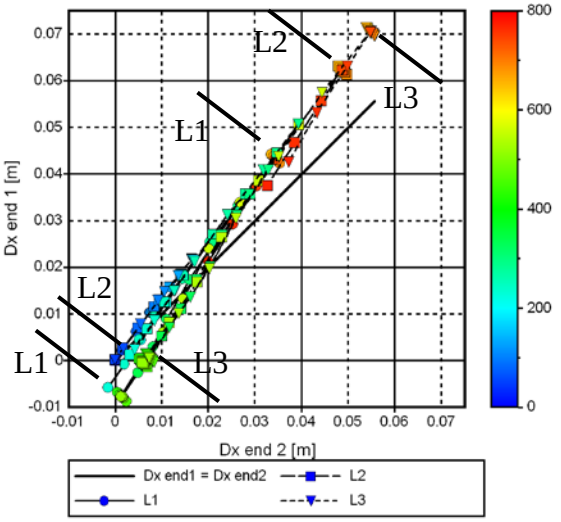

Figure 6.86. $D_{X,end1}$-$D_{X,end2}$ B1_S1_T1_d914_SHR, RL0.

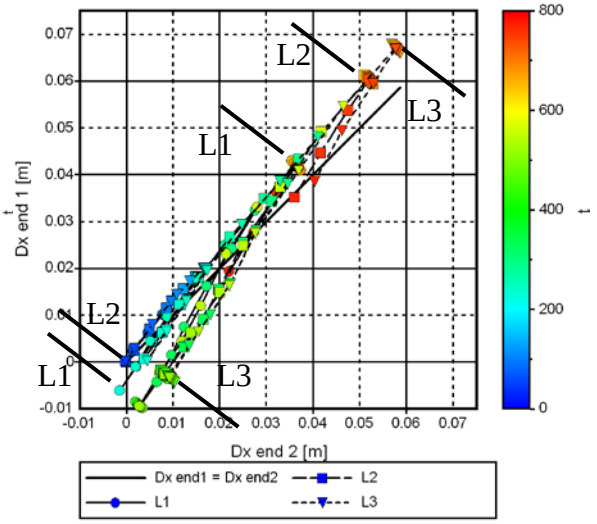

Figure 6.87. $D_{X,end1}$-$D_{X,end2}$ B1_S1_T2_d914_SHR, RL0.

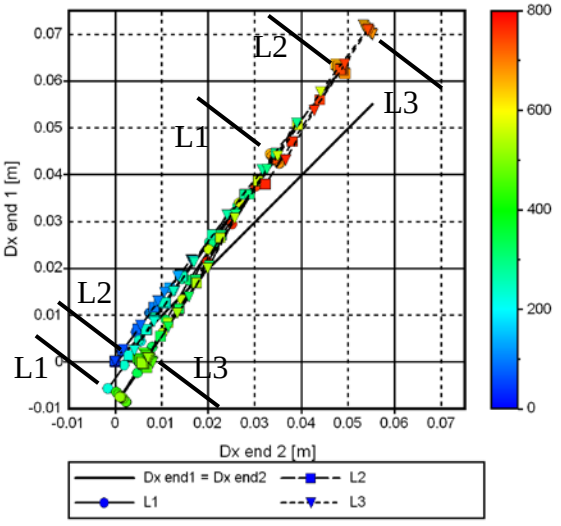

Figure 6.88. $D_{X,end1}$-$D_{X,end2}$ B1_S1_T1_d1200_SHR, RL0.

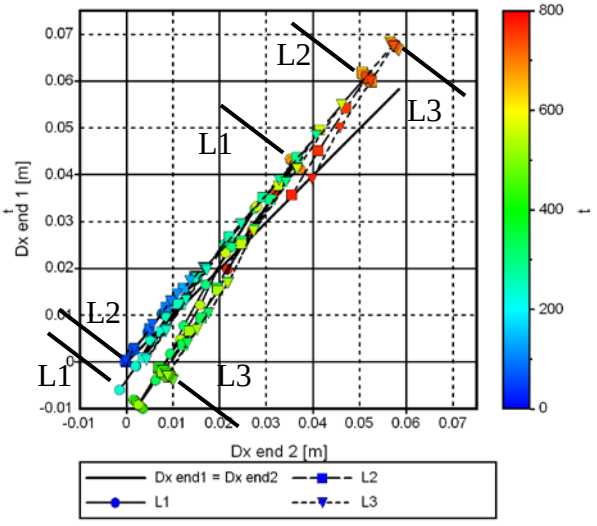

Figure 6.89. $D_{X,end1}$-$D_{X,end2}$ B1_S1_T2_d1200_SHR, RL0.

6.4.10.8 Bridge length changes as a function of loading time

Bridge length changes Δ_L as function of loading time in bridge models B1_S1_T1_d914_SHR are presented in Figure 6.90.

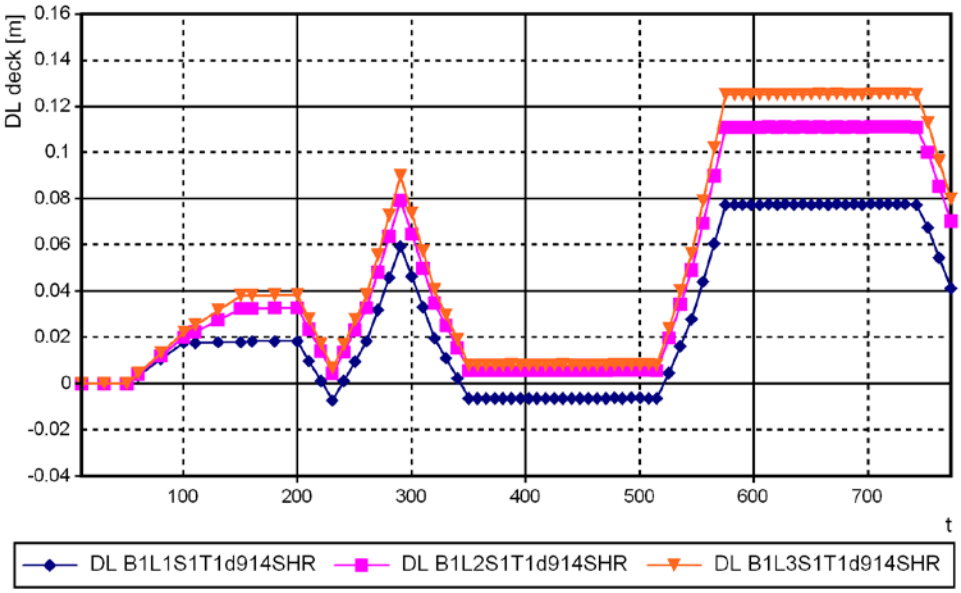

Figure 6.90. Changes in bridge lengths Δ_L in bridge models B1_S1_T1_d914_SHR.

The result is rather similar compared to the loading presented with a uniform temperature drop in Figure 6.56. Longitudinal strains in the bridge superstructure from post-tensioning force prevent negative displacements. Furthermore, the effect of creep on longitudinal strains of the bridge superstructure from post-tensioning force is clearly noticeable (from t = 510 to t = 575).

6.4.11 Utilisation rates of pile cross sections

The total thermal expansion lengths of the analysed bridges were selected so that composite pile cross-section utilisation rate would be exceeded in SLS. When the utilisation rate is 1.0, the loading point in the M_R-F_X diagram is on the SLS capacity curve. A way of defining the utilisation rate when the point does not fall on the SLS capacity curve is described in Paragraph 6.4.11. Results for each analysed bridge model's pile utilisation rates are presented in Paragraph 6.4.11.

The utilisation rate of the pile cross section was defined in the M_R-F_x diagram. The utilisation rate was defined as the relation of the line from the origin to analysed forces to the line from the origin to the capacity line, see the blue line in Figure 6.91.

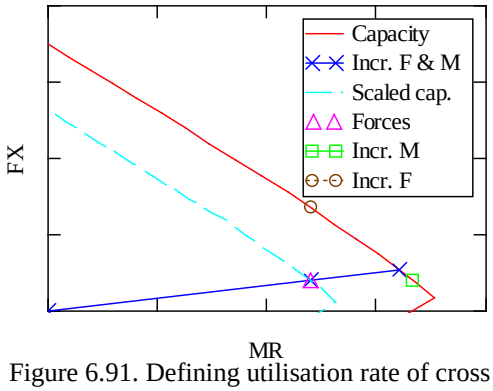

Figure 6.91. Defining utilisation rate of cross section.

Nonlinear behaviour (second order effects, etc.) was omitted in the utilisation rate definition for simplicity and because the relative normal force was small compared to the normal force capacity. The results shown in Figures 6.92 and 6.93 were obtained from the utilisation rates of pile cross-sections in the serviceability limit state based on the results of bridge models B1 and capacity D_{1c} described in Paragraph 6.3.2. The presented result is the highest utilisation rate for all nodes in piles in each bridge model.

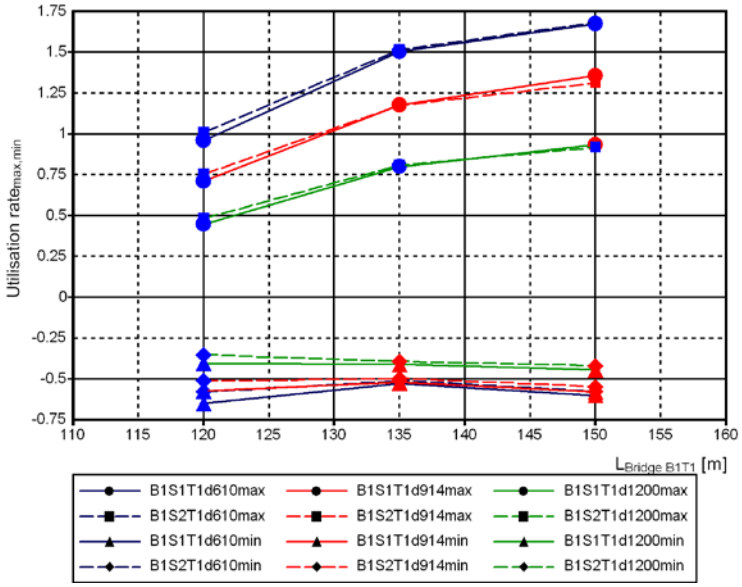

Figure 6.92. Utilisation rates of pile cross-sections in bridge models B1_T1, RL3.

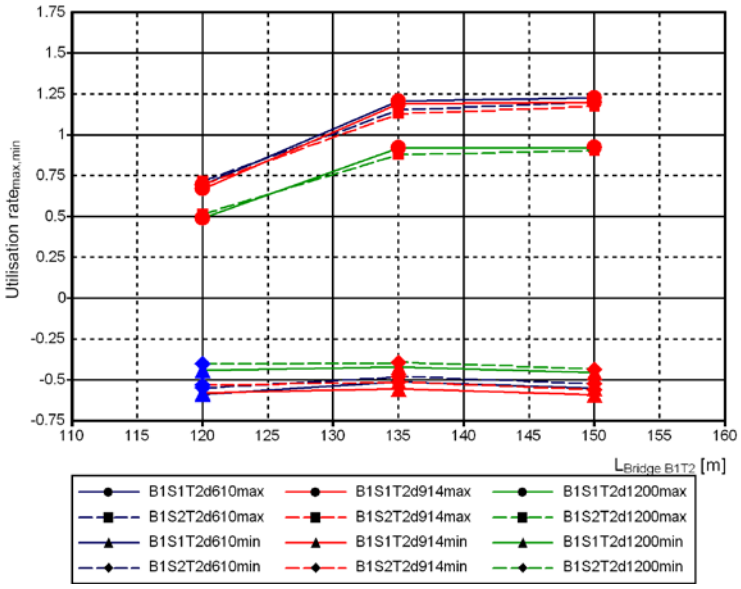

Figure 6.93. Utilisation rates of pile cross-sections in bridge models B1_T2, RL3.

A positive utilisation rate of M_R-F_X is the result of a positive moment M_Z while a negative utilisation rate is the result from a negative moment M_Z, see Figure 6.59. Linear interpolation between the analysed bridge lengths was used. The utilisation rate is lower with larger diameter piles both with the positive and the negative moments M_Z in bridge type B1_T1. The most dimensioning effect was obtained from the stage of positive moment M_Z. The positive utilisation rate is slightly higher and the negative one slightly lower with bridge types S2 because the dead weight moment is less negative with bridge type S2 than bridge type S1. The difference between bridge types T1 and T2 is not big because the useful rotation of the screen is missing in type T2 in terms of moment M_Z. The utilisation rate increases with increasing bridge length. The difference between the reinforced and the post-tensioned concrete structures is noticeable in the great difference between lengths L1 and L2 is compared between bridge types B1 (previous results) and B2 and B3 (later on). There is no clear connection between the positive utilisation rate and which bridge end of bridge types B1_T1 is more dimensioning. In the case of the negative utilisation rate, blue values (bridge end 1) are for tops of piles, and red values (bridge end 2) are for the lower parts of piles. Utilisation rate 1 represents the allowable length of a fully integral bridge in terms of piles in the serviceability limit state. Bridge end 2 is the dimensioning one with bridge types B1_T2. Utilisation rates from bridge models B2 are presented in Figures 6.94 and 6.95.

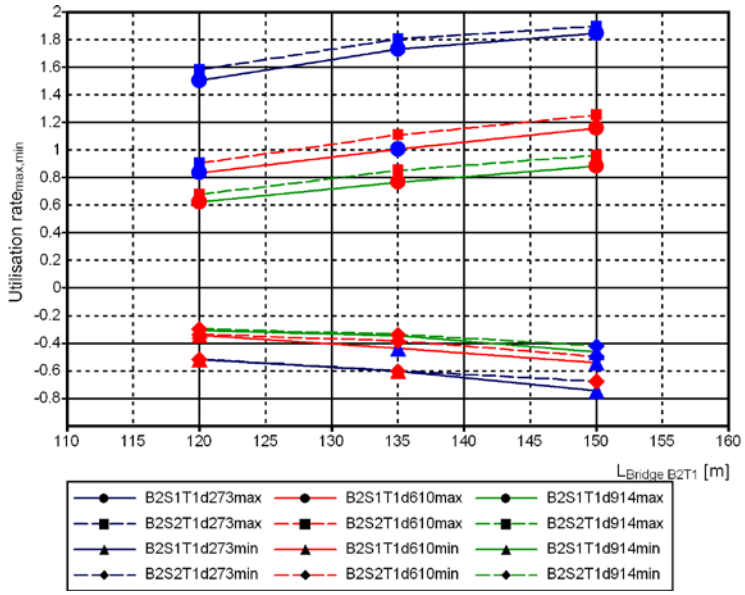

Figure 6.94. Utilisation rates of pile cross-sections in bridge models B2_T1, RL3.

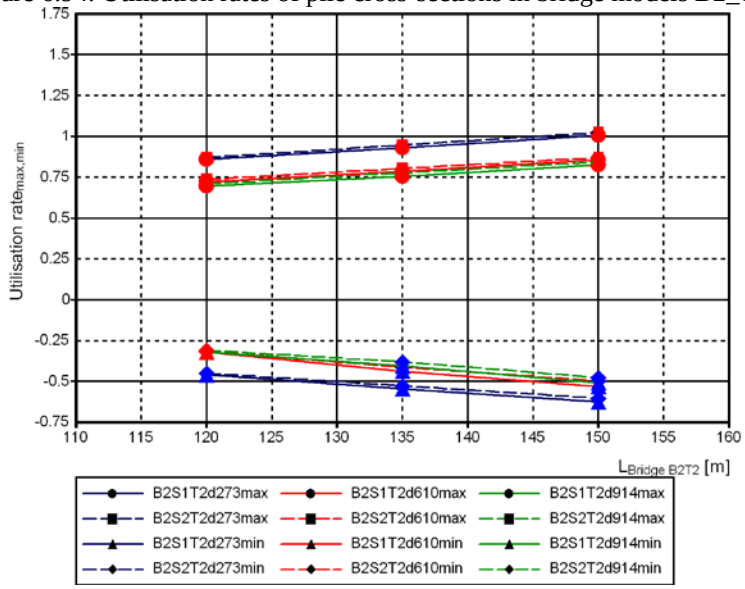

Figure 6.95. Utilisation rates of pile cross-sections in bridge models B2_T2, RL3.

As in the case of the negative utilisation rate of bridge models B1_T1 and B1_T2 , blue values are for the tops of piles and red values for the lower parts of piles. The cross section D*t = 273*12.5 is not possible with the analysed bridge lengths in bridge type B2_T1 but is possible with bridge types B2_T2. Changes in the positive and negative utilisation rates develop more linearly with increasing bridge length in bridge types B2 than bridge types B1.The difference between S1 and S2 is clearer with all bridge lengths of bridge models B2_T1. The positive utilisation rates of bridge type B2 with lengths L2 and L3 are lower than with bridge type B1. Utilisation rates of bridge models L1_T1 and L1_T2 with pile sizes D*t = 273*12.5, 610*16 and 914*16 are presented in Figures 6.96 and 6.97.

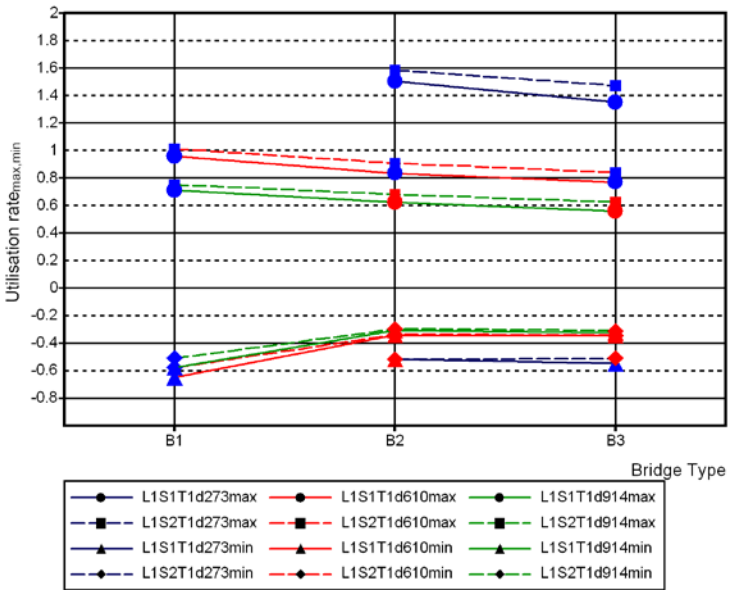

Figure 6.96. Utilisation rates of pile cross-sections in bridge models L1_T1, RL3.

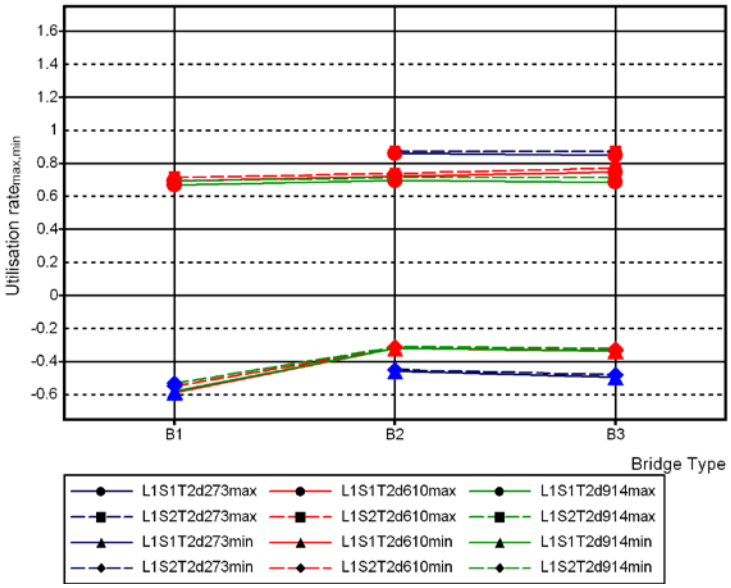

Figure 6.97. Utilisation rates of pile cross-sections in bridge models L1_T2, RL3.

Positive utilisation rates are lower in bridge models B2_L1_T1 and B3_L1_T1 than in B1_L1_T1 but with types T2 the positive utilisation rates are almost equal. The probable reason is the bending stiffness of superstructures. Piles are connected to the lower edge of the end screen the earth pressure behind the screen (at the expanded stage) and reactions from piles cause rotation of the end screen which is related to the stiffness of the end screen and the superstructure. Bridge types B2 and B3 have a lower bending stiffness than bridge type B1. The rotation of the end screen is not particularly useful in bridge types T2. The utilisation rate is lower with higher diameter piles in all bridge types. The difference between piles D*t = 610*16 and 914*16 is relatively small in bridge types T2, whereas in bridge types T1 the difference is more obvious.

6.4.12 Bending stiffness of superstructure

An estimate of correct bending stiffness of the reinforced bridge superstructure is discussed in Paragraph 6.4.12. Bridge superstructures were modelled with elastic material properties, but the loads inducing longitudinal displacements of bridge ends were reduced in Paragraph 6.4.6. Here, an attempt is made to evaluate the suitability of the assumed multiplier for bending stiffness presented in Paragraph 6.4.6 for the analyses of this study.

The superstructure was modelled with linear elastic material properties and the loads were decreased as described in Paragraph 6.4.6. However, the cracked bending stiffness of the reinforced concrete superstructure depends significantly on the reinforcement of the cross section. The effective bending stiffness of the bridge superstructure is estimated based on the formulas of [35]. The formulas and simplifications are presented in Appendix 9.6. Figure 6.98 shows effective bending stiffness as percent of the modelled linear elastic bending stiffness in bridge models B2_T1 at bridge end 1. The symbol colours represents the mentioned percent value and the vertical axis shows the total bending moment value from non-linear analyses.

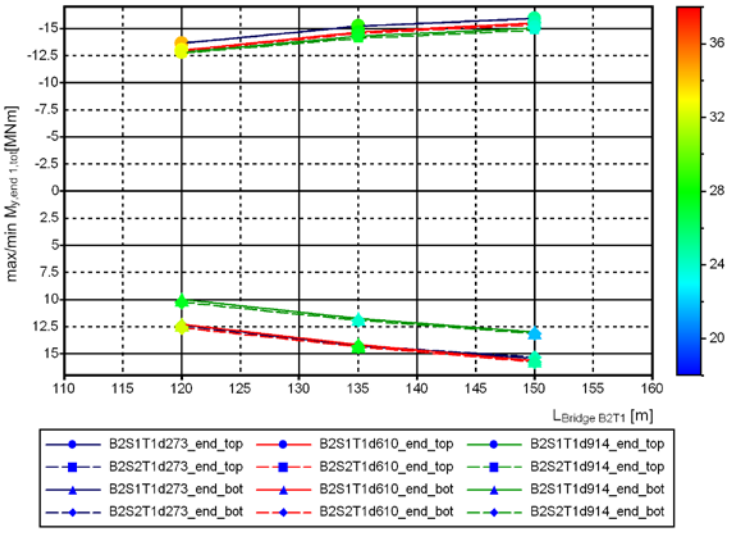

Figure 6.98. Effective bending stiffness of bridge type B2_T1 as percent of modelled bending stiffness.

Only moments at result level RL0 were taken into account, i.e. the moment $M_{y,end,tot}$ does not include moments from traffic loads. The effective stiffness is considerably lower than the modelled stiffness. This behaviour is not as strong in bridge types B1_L2 and B1_L3 because they are post-tensioned concrete structures and there the creep of concrete releases forces. The total bending moment is lower with larger diameter piles.

6.4.13 Bridge versus pile models

The main differences between the pile and bridge models were:

- End screen rotation has a major impact on the moment of the pile in the T1 bridge model
- Only one load type was included in the pile models
- Several soil properties were studied in the pile models
- The effect of the piles' cc-spacing is included in the bridge models with cross section D*t = 273*12.5
- The displacements of the end screen are not equal in the bridge models.

The pile models were made for preliminary analysis and they revealed that modelling of the whole structure (or taking limitations into account) is the preferred way to model soil-structure interaction.

6.4.14 Sensitivity of results

The large number of different pile and bridge models makes estimating of sensitivity possible even though the bridge models were analysed only using a single soil property. The single bridge model had two ends with different soil properties, and each bridge was analysed using both SHR and EXP soil properties. The sensitivity analyses are dealt with in the previous chapters.

The parameters related to soil strength and bending stiffness of the bridge superstructure and the end screens probably had the greatest effect on the results discussed in this study. Here, soil strength is mainly studied in connection with laterally loaded piles, distribution along pile length, and long-term behaviour during many loading cycles, depending on the displacement direction of the pile top. The most dimensioning case for pile bending moments was the contracted stage where a high earth pressure does not occur behind the end screens, which is why soil strength does not have a great effect in terms of pile bending moments. The change of stiffness of soil behind end screens does not have a strong influence on the pile bending moments either because the stiffnesses of embankments are rather dominant compared to other parts of the bridge. A relatively pronounced effect of soil strength and stiffness on the pile bending moment was observed in Paragraph 6.3.9 and in Appendix 8.2. However, the results are from pile models where rotation of the end screen does not occur. Hence, the effect of soil properties in bridge models would be smaller because the rotation of the end screen would also increase with stronger soils. The bending stiffnesses of the end screen and the bridge superstructure have a clear impact on the rotations of the end screens, and the cracked cross section properties are much looser than linear elastic cross section properties.

6.5 Conclusions

The contraction of the bridge superstructure due to normal force does not affect bridge end displacements considerably. Composite piles are a suitable foundation type for integral bridges. The encased concrete in piles enables maximum moment capacity with reasonable normal force. It is reasonable to select the number of the piles so that at the serviceability limit state normal forces are near the value that produces the maximum moment capacity. The hinge at the top of the pile reduces the bending moment of the pile. However, the risk of a longitudinal displacement of the bridge superstructure is probably higher as with bridge types T2. The hinged connection may be an effective solution during the construction stage especially with post-tensioned bridge superstructures.

New perspectives on the modulus of lateral subgrade reaction were presented in Section 6.3. The pile diameter had an influence on it. The behaviour of a laterally loaded pile in a slope also proved important.

Non-linear modelling procedures are rather complex, which may produce many errors. The analyses have to be robust. Special attention also needs to be paid to the modelling of integral bridge ends. The non-linear models are awkward for combining results from different load cases. However, the quasi-static analyses are suitable until a certain limit where the capacity of computers is reached. The non-linear analyses may be a suitable option for the longest integral abutment bridges.

The slab type bridge superstructure was included in the analyses of the shortest length L1 to allow comparison of the effects of different types of superstructures. It also made possible comparison of the results to the Haavistonjoki Bridge. The bridge models were analysed with the selected superstructure type, total thermal expansion lengths and substructure types, and it is probable that the optimum fully integral bridge type will be obtained by optimising the structural parts of the bridge. In fact, it is possible to derive the properties of a fully integral bridge from the analyses because the group of bridges was rather large even though it was essential to limit the group size. Moreover, it is possible to estimate the allowable total thermal expansion length of a fully integral bridge in terms of structural behaviour.

Bridge type T2 was more sensitive to changes in soil properties than bridge type T1. The displacements of bridge type T2 superstructure were more eccentric around bridge centre than those of bridge type T1.Aesthetics was not included as a design basis in this study,

which may cause problems with bridge type T2. The rotations of the end screen release pile moments in bridge type T1 remarkably: when soil stiffness and strength increase, the rotation increases and the increase of pile moments diminishes.

Increasing the integral bridge length increases eccentric displacements around the bridge centre, and the increase bridge end displacements concentrates on the bridge end where soil stiffness and strength are lower. Hence, the observed problems with the integral bridge probably focus on that bridge end. The stiffness of intermediate supports plays a role in longitudinal displacements. The intermediate supports were rather slender in the analysed bridge models compared to the longitudinal stiffness of bridge ends. This kind of behaviour sets requirements for integral bridge designs.

The traffic load did not significantly increase the most dimensioning forces of the piles. The bending moments of the bridge were of same magnitude at the bridge ends and intermediate supports. Hence, concrete is used rather effectively along the whole bridge length.

The longitudinal displacement of the bridge superstructure under a 200 kN brake load in the loading test was 0.03 mm in Paragraph 5.3.1. The corresponding displacement in bridge models under a 500 kN load was 0.3 mm and the corresponding value under a 200 kN load would be 0.08 mm. The end screens are bigger in bridge models, which increases the difference. The effect of the asphalt layer and the transition slab decreases the difference. In both cases the longitudinal displacement values were very small compared to the total displacement stages of the bridge ends.

The total values of the longitudinal displacements of the bridge ends were higher with post-tensioned bridge superstructure types in the bridge models. This may increase the maintenance work on embankments. The total values of the longitudinal displacements are also high with reinforced concrete structures.

The side span ratio S1 (0.85) was slightly better in terms of pile bending moments than S2 (0.7) in the case of bridge type T1 because the dead weight moments on piles at the bridge end had a different sign than in the most dimensioning case at the contraction stage. The bridge length range was suitable in terms of the pile bending moments and in the estimation of allowable fully integral bridge length.

Bridge type B3 was slightly better in terms of pile bending moments. However, the uniform temperature load was equal in different bridge types. The beam-and-slab structure probably behaves differently than the slab structures.

The utilisation rate of larger pile cross-sections was lower than that of smaller ones. However, the effect of local stability of the steel wall was ignored, which probably evens out the differences between different pile sizes in Section 6.4.

The first estimates for the maximum thermal expansion length of fully integral abutment bridges in terms of structural behaviour were presented in Section 6.4. Many parameters have an influence on results, which is why the term "estimate" is justified. A database including numerous FE models was created for fully integral bridge analyses in Section 6.4. The database is useful for further analyses because many limitations were set during the analyses to make them feasible for this study.

The forces on piles at bridge ends were analysed rather reliably but many issues requiring further research were noted.

7 MAIN RESULTS AND DISCUSSION

7.1 Results

7.1.1 Field tests

A durable long-term monitoring system was created. The measuring gauges were still working at the end of 2010 after the main monitoring period at Haavistonjoki Bridge described in Chapter 5. Both long-term and short-term behaviours were observed. The measuring devices also work reliably at the Myllypuro Overpass. The data measured from the three monitored and/or tested bridges will be compared with each other which will increase the reliability of the results. The measured data enable further studies on SSI and thermal behaviour of bridge superstructures. Both long-term and short-term analyses (loading tests) are possible during the lifetime of the monitoring devices. Finally, the large amount of data allow comparisons of data measured at bridges and that measured in laboratory conditions. A key result of this study was that the building of embankments requires careful guidance and supervision. Construction methods also need to be developed.

7.1.2 Uniform temperature analysis

A rather simple uniform temperature analysis based on measured data was developed in Chapter 5. The method allows effective use of the measured ambient temperatures. It is also possible to analyse uniform temperatures during the history of measured ambient temperatures. The obtained uniform temperature range -30…+28ºC to the concrete slab superstructure was higher than -25…+25ºC in Finnish guidelines. The research project also enables extending the uniform temperature analyses to beam-and-slab structures. Thereby the difference between the two basic bridge superstructure types can be observed.

7.1.3 Allowable total thermal expansion length and global behaviour

Estimates of the allowable total thermal expansion length limits of the fully integral bridge were made in terms of structural behaviour in Section 6. The analysed total thermal expansion length range was 120 to 150 m. Some structures were allowable with the selected group of parameters across the selected range. In the light of the studied limits and behaviours, a reasonable limit for the allowable total thermal expansion length is 120 m in circumstances similar to those at Haavistonjoki Bridge. The laterally loaded pile and pile diameter play an important role in structural behaviour.

The eccentric displacement of bridge ends around the centre of the bridge has a significant effect on the structural behaviour of an integral bridge. The eccentricity results from different soil properties at different points of the bridge, see Figure 7.1. The loading in Figure 8.1 results from the uniform temperature change. The elastic stiffness of bridge structures k_{s2} partly offsets the eccentric displacements. The relation between the bridge ends' longitudinal displacements Δ is stronger than the relation between the total failure loads of the embankment behind the end screens F_f due to the yield of soils in a hyperbolic displacement-force relationship.

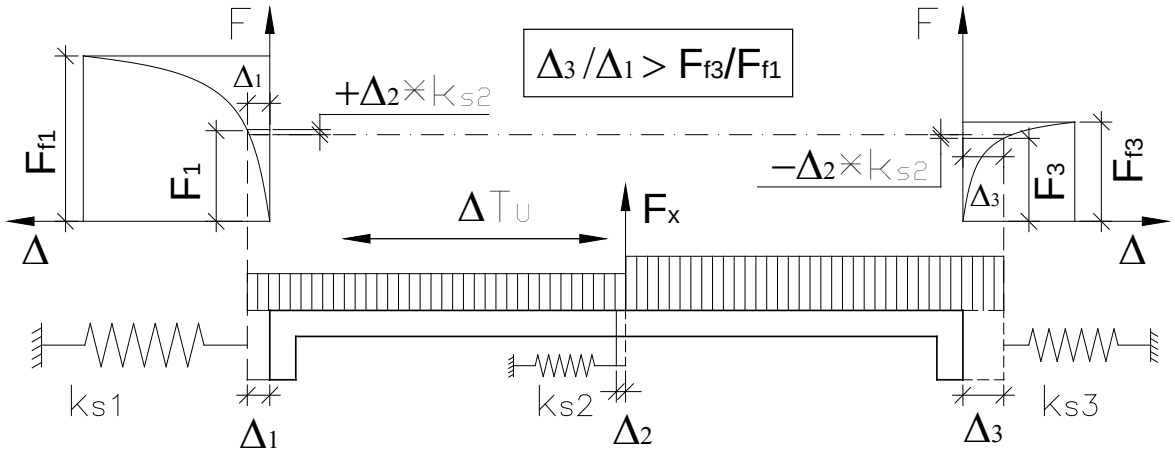

Figure 7.1. The eccentric displacement of the bridge ends around the centre resulting from different soil properties at different ends of the bridge.

Many parameters are involved in the structural behaviour of integral bridges (as indicated, for example, by the large number of Notations). This leads to several limitations in this study. Many subject requiring further research were also discovered.

7.2 Discussion

7.2.1 Field tests

A major deficiency of the field tests was that only two bridges were monitored in the long-term analysis and two bridges in the short-term loading tests. However, it was not possible to expand the number of bridges because of the limited research budget and development funds. Yet, the number of monitored bridges is rather large and the results are quite extensive and cover a long-term compared to earlier field tests in the researches referred to.

The bridges included in the field tests were built under allowable thermal expansion limits of the present design guidelines. Hence, the monitoring of longer bridges was excluded. Monitoring results for different lengths would probably reveal more information on integral bridge behaviour.

The monitoring of steel pipe piles was unsuccessful. The results would have been very important in defining the allowable length of a fully integral bridge.

7.2.2 Uniform temperature

The uniform temperature was determined for the Haavistonjoki Bridge location and naturally for the bridge superstructure type of Haavistonjoki Bridge. Bridge location has an effect on the uniform temperature range, which would have been wider if it had been determined for different locations and superstructures during this study. Thermal analyses were excluded from this study. A thermal analysis might have produced usable information on the uniform temperature and temperature difference.

7.2.3 Limitations and deficiencies of pile and bridge models

The limitations and deficiencies of the bridge models are presented below in the form of a list with rough subheadings. The effects of the listed items on the main results are estimated using rough categories:

1 = the effect is negligible, 2 = the effect is small and 3 = the effect is notable.

Loads:

- The uniform temperature increases first, which does not happen with a bridge completed in the autumn. 2
- Thermal analyses were not included. 3
- The nonlinear part of uniform temperature gradient, as in Figure 2.3 right, is included in measuring results but not in values of SFS-EN 1991-1-5 when comparison results in Figure 5.4. 1
- The post-tensioning force does not change due to strains of the superstructure, i.e. the tendons are not included in the cross section properties. 2
- The creep based on the post-tensioning force was modelled as a uniform temperature drop which also causes contraction in the transverse direction opposite to creep. Moreover, creep is modelled for the whole cross section and independent of stresses. 2
- The shrinkage of a concrete slab superstructure was the same as in a concrete beam-and-slab superstructure. The decreasing effect of reinforcement on shrinkage was ignored. 2
- Different loading sequences of non-linear analyses were not examined. 2
- The different distributions of load patterns in Lk1 axes were ignored. Furthermore, load model Lk1 was determined only in one direction (no forward-reverse analyses). 1
- The models do not include load model Ek1 [42]. 2
- The traffic load earth pressure (TLEP) is a bit higher at bridge end 2 due to the modelling technique. TLEP from the underpassing road was ignored. 2
- The 1 kN/m^2 from the variable extra pavement was ignored. 1
- Load pattern Lk1 locations at the top of the end screen were ignored because the value 20 kN/m^2 was used in the NL calculations of traffic load earth pressure analyses. 2

Soil models:

- The earth pressure against the end screen does not decrease towards the wing walls at the expanded stage. 1
- The earth pressure does not increase against the wing walls because of the passive earth pressure against the end screen. 1
- A bridge model without parameter m_G would have been useful. 3
- Analyses of a different structural part with separate multiplier m_G, i.e., without a global multiplier, might have revealed some dimensional effects. 3
- Active earth pressure and possible gap formation is missing from the soil models. 2
- The soil models are not suitable for a larger number of loading cycles. 2
- A vertical component is missing from the soil behaviour behind the end screen. 2
- The frozen embankment situation was not analysed. 3
- The combined results from the separate SHR and EXP bridge models are rough. 2
- The effect of ground water was ignored. 1
- Soil properties were modelled on the basis of vertical stresses, not based on three-dimensional stresses. 3
- The analysis of the strain stage of embankment soil along pile length may cause certain limitations to lateral displacement capacity. 2

Pile cross sections:

- The effect of local buckling of steel pipes may cause limitations especially to larger diameter piles. 3
- The bending behaviour is elastic non-linear, and kinematic behaviour is ignored. 2
- The bending stiffness of the pile cross section does not change along the pile length. The selected reinforcement would probably be smaller at greater depths. 2
- The effect of low cycle fatigue was ignored. 2
- The elastic modulus E_y for reinforcement was 200 GPa in the analyses but in [12] it is 205 GPa. 1

General:

- The behaviour of the bridge superstructure was linear elastic. 3
- The analyses were made with only one height and thickness of the end screen. 3
- Effects of the tolerances of piles on dimensioning forces were ignored in the analyses. 2
- The analyses of superstructure forces were preliminary and the superstructure moments $M_{y,tot}$ were outputted only for bridge end 1. 2
- The displacements of bridge ends are higher in real case because of reduction used in modelling of the creep and shrinkage, see Paragraph 6.4.6. 2
- Edge beams are involved in cross section behaviour at all stages, i.e. the sacrificial edge beams were ignored. 1
- The end screen's connection to the superstructure is independent of the thickness of the superstructure. Modelling was done using a neutral axis and not e.g. from the bottom of the superstructure beam. 2
- Ultimate limit state analyses and stability were not included in this study, i.e., only the serviceability limit state was included. 3

7.2.4 Advantages and further needs of pile and bridge models

The main advantages of the bridge models were:

- Straightforward bridge analyses were created which are presented in a form that allows using them as input or reference data to assist bridge design in future.
- A way to analyse load combinations in non-linear analyses was presented.
- The non-linear analyses are illustrative of the effects of different loads.
- The effects of embankment behind the end screen and laterally loaded piles are included in the same bridge models.

Bridge models also need the following main features (as well as those described in Paragraph 7.2.3):

- More accurate superstructure bending stiffnesses updated with an iterative process for both post-tensioned and reinforced concrete superstructures
- A deeper analysis of the long-term loads in terms of the release of forces as described in Paragraph 6.4.6.
- Deeper analyses of forces on superstructures
- Analyses of post-tensioned superstructures with more accurate tendons and tendon profiles
- An analysis of intermediate support forces

7.2.5 Allowable total thermal expansion length

The analysed limits were based on the structural behaviour of piles and the behaviour of the bridge superstructure in the limited serviceability limit state. The final allowable length limit is the minimum based on several behaviours, not only structural behaviours. A schematic presentation of the relations between different maximum thermal expansion limits of each integral bridge is shown and the amount of knowledge on different limits produced by this study is also roughly estimated in Figure 7.2.

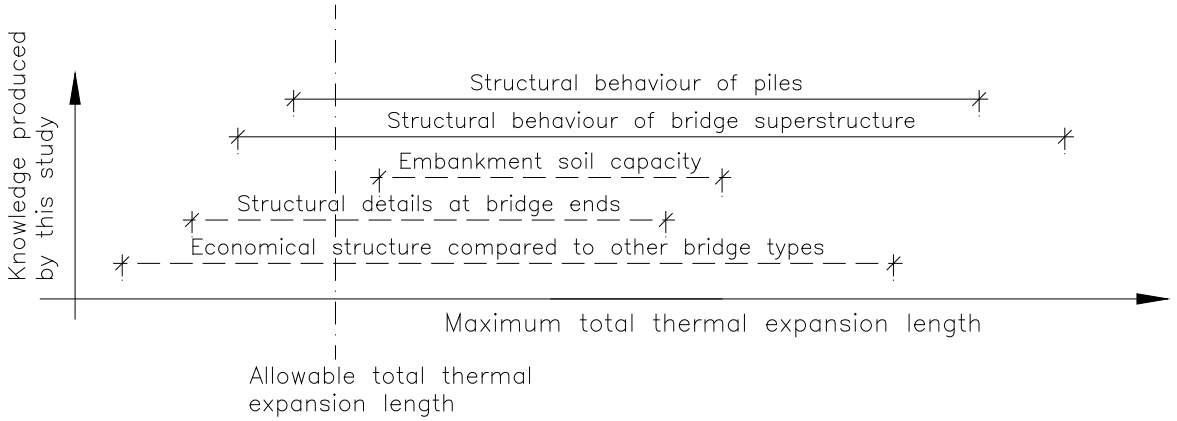

Figure 7.2. Maximum and allowable total thermal expansion length of an integral bridge.

Conditions and bridge super- and substructure combinations have an influence on the maximum total thermal expansion limit of each integral bridge. Examples of conditions:

- Climate: Temperature range
- Bridge site: Requirements of road, span divisions, skew angle, subsoil
- Building time and quality of construction
- Deviation of material properties

- Tolerances
- Subsoil properties

Examples of selections:

- Bridge superstructure type and span divisions
- Pile cross section
- Dimensions of abutments
- Embankment soil properties
- Structural details

The structural analysis of the study already includes selections. Hence, it is justified to regard the results as estimates. The allowable total thermal expansion length of the guidelines has to be reasonable and to a certain degree on the safe side. Further, the limitations and deficiencies presented in Paragraph 7.2.3 have an effect on allowable length. Structural models of design are usually linear which reduces the allowable length based on the analyses of this study, see also Section 8.2.

8 CONCLUSIONS AND RECOMMENDATIONS

8.1 Conclusions

Detailed conclusions have been presented during this study, and the key general conclusions are presented here.

The main results will serve as a guideline for constructing durable and safe integral bridges, which in many cases are an economical option. The increase of the allowable total thermal expansion length from 70 m [48, 46] to around 100 m is a clear advantage as concerns bridges of normal length. The increased total length makes the integral bridge an option for overpasses of motorways. However, other maximum total thermal expansion length limits also need to be determined to make the longest integral bridges possible, see Paragraph 7.2.5.

Important knowledge was acquired on many aspects of bridge engineering, not only on integral bridges, during the research project and this study. The uniform temperature load, the temperature difference, the concurrence of the above loads, and the brake load were analysed in this study. The concrete shrinkage and creep values will be examined during the research project based on the long-term monitoring of Myllypuro Overpass.

New perspectives and knowledge were gained on SSI of the end screen and laterally loaded piles. The viewpoint of the modulus of lateral subgrade reaction will probably increase interest and research into laterally loaded piles. The point of view of composite cross sections may increase the need to update design guidelines and methods.

The analyses in Chapter 6 fulfil the goal of serving as a first step in fully integral bridge modelling with complex soil properties. Soil properties play an important role in the structural behaviour of an integral abutment bridge. New design approaches were found during this study. They are partially applicable to bridge design guidelines.

8.2 Recommendations for bridge design and construction

A principle for determining allowable total thermal expansion length is suggested in Figure 8.1. The main point of the suggestion is that the allowable total thermal expansion length is lower than the limit recognised in the non-linear analysis made for research purposes which included careful analyses of different soil properties at bridge ends.

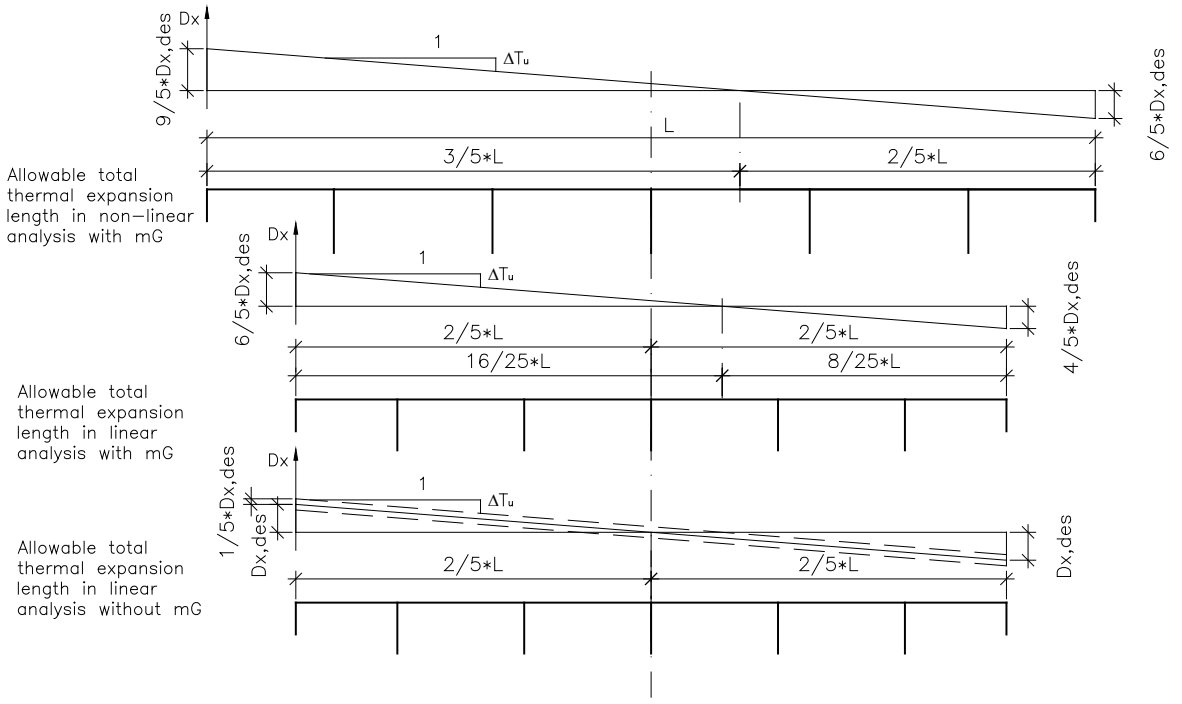

Figure 8.1. Suggested allowable total thermal expansion length in bridge guidelines.

The allowable total thermal expansion length limit L is based on the analyses of this study and other researches. Parameter m_G is as in Paragraph 6.4.4. ΔT_U is the temperature change that causes displacement D_X. Parameter D_X is the longitudinal displacement of linear analyses in normal bridge design. The relation $D_{X,end1} = 1.5*D_{X,end2}$, i.e. relation $m_{Gend2}/m_{Gend1} = 1.5$, is used in Figure 8.1 on the basis of the results discussed in Paragraph 6.4.10. Here, it is suggested that uncertainties and the difference between the non-linear and linear analyses are taken into account in decreasing the allowable thermal expansion limit to twice the shorter thermal expansion length of the non-linear analyses. Thus parameter m_G is left out of the linear analysis in normal design when there is a need for an extra longitudinal displacement, which is $1/5*D_{X,des}$ in the example. $D_{X,des}$ is displacement of the bridge end from ΔT_U when the bridge model is symmetrical. Another option is to increase the value of ΔT_U 6/5-folf in the analysis. The drawback of the last option is that forces on the intermediate supports are underestimated in terms of the temperature difference. Hence, the integral bridge should be designed using asymmetrical conditions to make the forces reasonable along the bridge length. Pilot bridges are recommendable when updating the allowable total thermal expansion length, see Paragraph 8.3.7.

The longest integral bridges can be designed reasonably well using non-linear analyses and/or taking non-linear behaviour into account with different material properties at different points and loading sequences. For example, the signs and values of pile bending moments at the bridge ends have to be considered carefully. The same applies to the earth

pressure behind the end screen. High earth pressures are also present at the initial displacement stage D_x. Detailed conclusions on structural behaviour are presented in Section 6.5.

More detailed guidelines on integral bridges are necessary in the case of longer integral bridges. In addition, the guidelines on integral bridges would be easy to use if all of them were compiled into a single manual. Clear guidance and supervision for the construction of embankments is very important, as mentioned in Paragraph 7.1.1. The slope also needs to be limited below 1:1.5 to ensure the stability of embankments especially in the case of integral bridges. A preliminary design guide for integral abutment bridges is one goal of the overall research project on integral bridges.

8.3 Recommendations of further research

8.3.1 Extension of the research process

An extension of the overall research process is essential. The collected field test data offer possibilities for more detailed analyses of measured data, for example, on the earth pressure-displacement relationship and the thermal behaviour of the superstructure. Long-term changes in the earth pressure-displacement relationship are also an important issue. Future needs for further research and measures should be presented in connection with the needs discussed in Paragraph 8.3.3.

8.3.2 Laterally loaded pile and end screen

Research into the lateral behaviour of piles is highly recommendable. Lateral behaviour is one of the key issues in the structural behaviour of integral bridges. Lateral behaviour is also important in numerous other structures. Consideration of both the cyclic and static behaviour is highly necessary. The research project should preferably consist of the following parts:

- Full-scale lateral loading tests of piles in level ground and at slopes
- Effective implementation of laboratory tests combining tests and theory
- Structural analyses in two-dimensional and continuum models
- Development of theory and methods for laterally loaded pile behaviour

Research on the behaviour of the end screen combined with the above parts would offer more knowledge about the cyclic and static behaviour of the embankment soil.

8.3.3 Structural analyses

The further development of bridge models discussed in Section 6.4 would give more information on the structural behaviour of different bridge types. The development of simple linear elastic or partly linear elastic conditions in bridge design models would provide more tools for the design of integral bridges. The need examined in Paragraph 8.3.2 also has a clear effect on the considered subject. Studies of other than the serviceability limit states are recommendable, especially ones on the ultimate limit state. The skewed integral bridge is a main integral bridge type. Structural analyses would offer more information on the characteristic behaviour of this bridge type, which may differ radically from the studied straight-ended integral bridge. The need for structural analyses of composite bridges and other bridge types is also obvious.

8.3.4 Flexible material

The idea to put a flexible plate behind the integral bridge end screens is addressed in this study. It would decrease the average stress level of the embankments and the thermal expansion eccentricity around the bridge centre, see Figure 8.2. The term ISSI refers to intelligent soil-structure interaction.

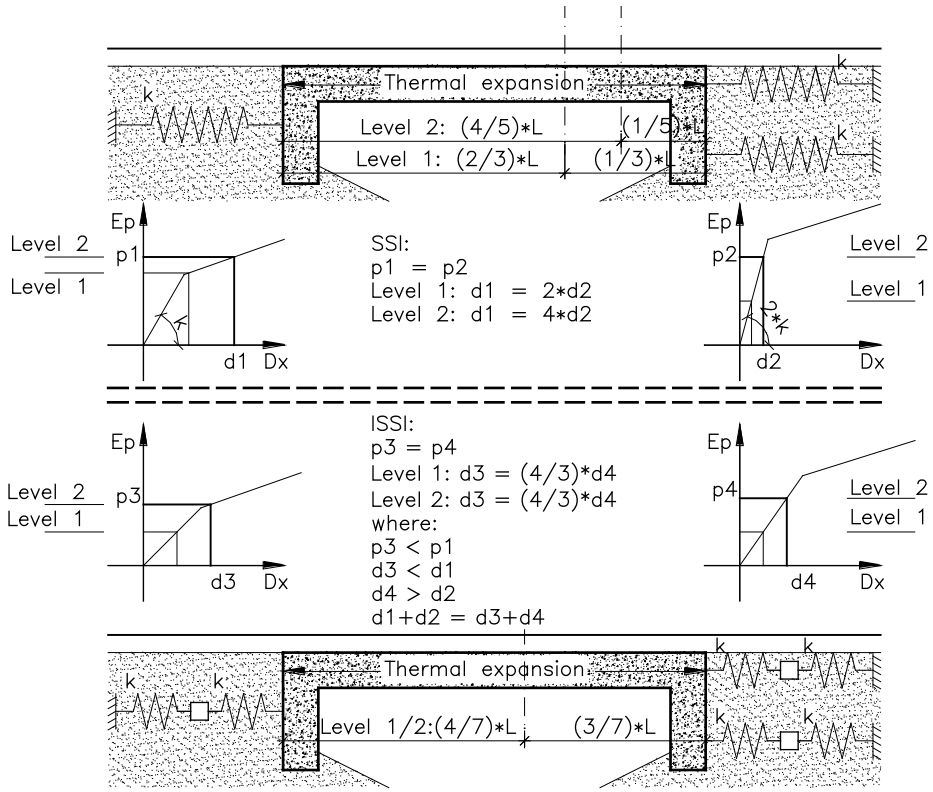

Figure 8.2.Idea of flexible material behind integral bridge end screens.

The upper structure has no flexible plate while the lower one does. E_P-D_x diagrams are presented for each bridge end. In the upper structure the initial stiffness of soil is assumed

to be double at bridge end 2, i.e., the ratio of factors m_G between the bridge ends is two. The stiffness of the flexible plate is assumed equal to soil stiffness at bridge end 1. The figure shows a schematic representation where the stiffnesses of the intermediate supports are ignored. Two displacement stages (stress levels) are presented. The flexible plate may reduce stresses considerably by significantly reducing the deformations of the embankment. The displacements of the bridge ends may also be more equal than without the flexible plate. The use of the plate both improves the integral bridge behaviour and probably enables longer integral bridges.

Research into the presented idea requires a loading device which serves two main objectives. The measured data from field tests and structural analyses can be harmonised with the results of the loading device. The effects of flexible material will be examined. The loading device makes it possible to study the effect of different lengths of integral bridges with different soils, since the results of the two monitored bridges can be generalised to a wider group of integral bridges. A photograph of the testing device is shown in Figure 8.3.

Figure 8.3. Loading device called the “Integral bridge simulator”.

Material tests on the flexible material are an important part of the research. Preliminary studies [136] were done during the study, see Figure 1.4.

8.3.5 Thermal analyses

It is recommendable to repeat the uniform temperature analyses, as those of Section 5.6 on Haavistonjoki Bridge and Myllypuro Overpass, at different locations in Finland. Thermal analyses would also provide more information on the temperature distribution and uniform temperature changes along different cross sections. Here, the thermal analyses refer to a transient temperature field analysis.

8.3.6 Composite column cross section

The cross section behaviour in the serviceability limit state and the ultimate limit state requires further research, especially into the local stability of the steel pipe of the composite cross section. Both static and cyclic tests would give more information on the behaviour of piles of fully integral bridges.

8.3.7 Pilot bridges

Pilot bridges are recommendable if the limit of allowable total thermal expansion length is to be increased. The monitoring of these pilot bridges in situ with systematically (step-by-step) increased lengths would give more confidence to extend bridges. The pilot bridges may be monitored at different levels. The minimum level consists of regular on-site observations at the bridges and the highest level may involve the use of monitoring devices as in Chapter 4.

8.3.8 Structural details

The structural details of integral bridges should be durable and suitable for them. The details include:

- A transition slab for different thermal expansion lengths and bridge superstructures
- Pile connection to superstructure both in bridge type T1 and T2 with or without hinge behaviour
- A possible joint between the transition slab and the superstructure in the case of longest thermal expansion lengths
- Connection details for the flexible plate behind the end screen

Some possible ideas for the details of the transition slab are presented in Figure 8.4.

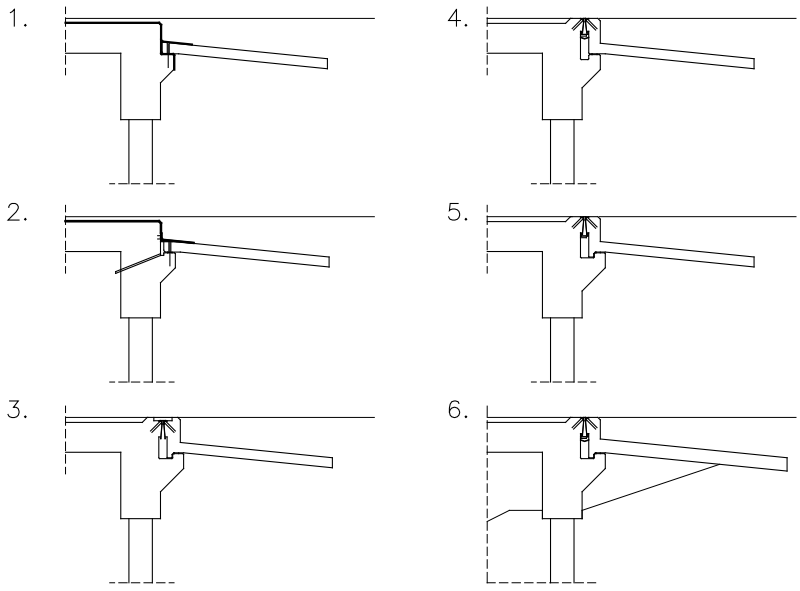

Figure 8.4. Ideas for transition slab connection details.

Thermal expansion length increases with the numbering. Types 1 and 2 are similar to those of the present stage. Type 3 has a mass expansion joint above the joint of the end screen and bridge abutment. Types 4, 5 and 6 have an open gap and gutters on bridge sides. Type 6 has no soil behind the end screen.

REFERENCES

1. AASHTO. 1989. AASHTO Guide Specifications - Thermal Effects in Concrete Bridge Superstructures. Washington, D.C. 60 p.
2. AASHTO. 2007. AASHTO LRFD Bridge Design Specifications, SI units, 4th Edition. Washington, D.C. pp. 3-99 - 3-104.
3. Abhasai, S & Dicleli, M. 2004. Effect of cyclic thermal loading on the performance of steel H-piles in integral bridges with stub-abutments. Journal of Constructional Steel Research. Vol. 60, No. 2., pp. 161-182.
4. Allotey, N. & El Naggar, M. H. 2008. Generalized dynamic Winkler model for nonlinear soil–structure interaction analysis. Canadian Geotechnical Journal. Vol. 45, No. 4, pp. 560-573.
5. Arsoy, S. 2000. Experimental and Analytical Investigations of Piles and Abutments of Integral Bridges. Dissertation. Virginia Polytechnic Institute and State University. 186 p. + 59 app. p.
6. Arsoy, S. et al. 2002. Experimental and Analytical Investigations of Piles and Abutments of Integral Bridges. Virginia Transportation Research Council. Report No. FHWANTRC 02-CR6. 55 p.
7. Ashford, S. & Juirnarongrit, T. 2003. Evaluation of Pile Diameter Effect on Initial Modulus of Subgrade Reaction. Journal of Geotechnical and Geoenvironmental Engineering. Vol. 129, No. 3., pp. 234-242.
8. Ashford, S. 2005. Effect of the pile diameter on the modulus of subgrade reaction. Publication number SSRP–2001/22, University of California, San Diego. 322 p. + 32 app. p. ISBN 952-15-1620-8.
9. Ashour, M. & Norris, G. 2000. Modeling Lateral Soil-Pile Response Based on Soil-Pile Interaction. Journal of Geotechnical and Geoenvironmental Engineering. Vol. 126, No. 5., pp. 420-428.
10. Bouafia, A. 2007. Single piles under horizontal loads in sand: determination of P–Y curves from the prebored pressuremeter test. Geotechnical and Geological Engineering. Vol. 25, No. 3., pp. 283-301.
11. Bowles, J.E. 1982. Foundation Analysis and Design, Chapter 16. pp. 867-968. ISBN 0-07-118844-4
12. Branco, F. & Mendes, P. 1993. Thermal Actions for Concrete Bridge Design. Journal of Structural Engineering. Vol. 119, No. 8, pp. 2313-2331.

13. Brena, S. & Bonczar, C. et al. 2007. Evaluation of Seasonal and Yearly Behaviour of an Integral Abutment Bridge. Journal of Bridge Engineering. Vol. 12, No. 3., pp. 296-305.
14. Briaud, J. L. et al. 1984. Laterally loaded piles and the pressuremeter: Comparison of existing methods. Laterally Loaded Deep Foundations, ASTM STP 835, ASTM, West Conshohocken. pp. 97–111.
15. Broms, B. 1976. Geoteknik, Kompendium Del IV. Kungliga Tekniska Högskolan (Royal Institute of Technology), Stockholm. 92 p. (In Swedish)
16. Budkowska, B. & Szymczak, C. 1995. On first variation of extremum values of displacements and internal forces of laterally loaded piles. Computer & Structures. Vol. 57. No. 2. pp. 303-307.
17. Byung, T.K. et al. 2004. Experimental Load–Transfer Curves of Laterally Loaded Piles in Nak-Dong River Sand. Journal of Geotechnical and Geoenvironmental Engineering. Vol. 130, No. 4., pp. 416-425.
18. Carder, D. et al. 2002. Suitability testing of materials to absorb lateral stresses behind integral bridge abutments. Publication number TRL552, Transport Research Laboratory. 48 p. + 4 app. p. ISSN 0968-4107.
19. Carter, D.P. 1984. A Non-linear Soil Model for predicting lateral pile response. Master's thesis. THESIS 1984-C24. University of Auckland.
20. Castelli, F. 2002. Discussion of ''Response of Laterally Loaded Large-Diameter Bored Pile Groups'' by Charles W. W. Ng, Limin Zhang, and Dora C. N. Nip. Journal of Geotechnical and Geoenvironmental Engineering. Vol. 128, No. 11., pp. 963-964.
21. Chakrabarti, A. et al. 2009. Lateral load capacity estimation of large diameter bored piles and its implementation: a study. IABSE reports = Rapports AIPC = IVBH Berichte, Vol.80 (1999).
22. Civjan, S. & Bonczar, C. et al. 2007. Integral Abutment Bridge Behavior: Parametric Analysis of a Massachusetts Bridge. Journal of Bridge Engineering. Vol. 12, No. 1., pp. 64-71.
23. Clayton, C. & Bloodworth, A. 2006. A laboratory study of the development of earth pressure behind integral bridge abutments. Géotechnique. Vol. 56, No. 8., pp. 561-571.

24. Concrete association of Finland. 1984. Suunnittelun sovellusohjeet, BY 16 (Application note of concrete design). Jyväskylä. 283 p. + 101 app. p. ISBN 951-9365-17-6. (In Finnish)

25. Connal, J. 2004. Integral Abutment Bridges – Australian and US Practice. Austroads 5th Bridge Conference, Hobart, Australia, May 19-21. 19 p.

26. Dicleli, M. & Abhasai, S. 2003. Maximum length of integral bridges supported on steel H-piles driven in sand. Engineering structures. Vol. 25, No. 12. pp. 1491-1504.

27. Dicleli, M. & Ehran, S. 2010. Effect of Soil-Bridge Interaction on the Magnitude of Internal Forces in Integral Abutment Bridge Components due to Live Load Effects. Engineering Structures. Vol. 32, No. 1., pp. 129-145.

28. Dicleli, M. 2000. Simplified model for computer-aided analysis of integral bridges. Journal of Bridge Engineering. Vol. 5, No. 3., pp. 240-248.

29. Dicleli, M. 2008. Effect of Soil and Substructure Properties on Live-Load Distribution in Integral Abutment Bridges. Journal of Bridge Engineering. Vol. 13, No. 5., pp. 527-539.

30. Duncan, J.M. & Chang, C. 1970. Nonlinear Analysis of Stress and Strain in Soils. Journal of the soil mechanics and foundations division, ASCE. Vol. 96, No. 5., pp. 1629-1653.

31. England, G et al. 2000. Integral Bridges; A fundamental approach to the time-temperature loading problem. 129 p. + 23 app. p. ISBN 0-7277-2845-8.

32. Federal Highway Administration. 2005. The 2005 – FHWA Conference, Integral Abutment and Jointless Bridges (IAJB 2005), Baltimore, Maryland, United States 16-18 March. 343 p.

33. Fennema, J. et al. 2005. Predicted and Measured Response of an Integral Abutment Bridge. Journal of Bridge Engineering. Vol. 10, No. 6., pp. 666-677.

34. Finnish environmental administration. 1993-2007. Suomen rakentamismääräyskokoelma, Rakenteiden lujuus, osa B (The National Building Code of Finland, The Strength of Structures. RakMk, part B, in Finnish)

35. Finnish environmental administration. 2004. Suomen rakentamismääräyskokoelma, rakenteiden lujuus, osa B4 Betonirakenteet (The National Building Code of Finland, The Strength of Structures, part B4 Concrete Structures). Helsinki.83 p. (In Finnish)

36. Finnish Association of Civil Engineers. 1989. RIL 179-1989, Sillat (RIL 179-1989, Bridges). Helsinki. 390 p. ISSN 0356-9403. (In Finnish)
37. Finnish Meteorological Institute. 2002. Climatological statistics of Finland 1971-2000. Helsinki.99 p. ISSN 1458-4530. (In Finnish)
38. Finnish Meteorological Institute. 2007. Statistic from Finnish climate, ambient air temperature. Published in the Internet on 5.10.2007 http://www.fmi.fi/saa/tilastot.html
39. Finnish Railway Administration. 1997. Rautatiesiltojen suunnitteluohjeet, RSO, osa 4. (Railway bridge design introductions, RSO, part 4.) VR 2753.11.0, 17 p. (In Finnish)
40. Finnish Transport Agency. 2010. Interviews of bridge experts of bridge engineering.
41. Finnra. 1992-2007. Siltojen suunnitelmat (Designs of bridges). Internet 19.2.2008: http://alk.tiehallinto.fi/sillat/suunnit1.htm (In Finnish)
42. Finnra. 1999. Siltojen kuormat (Loads of bridges). Helsinki. 31 p. ISBN 951-726-538-2. (In Finnish)
43. Finnra. 2000. Steel pipe piles. Helsinki. 81 p. + 3 app.p. ISBN 951-726-617-0.
44. Finnra. 2005. Siltojen ylläpito, Toimintalinjat (Bridge Maintenance, management policies). Helsinki. 28 p. + 10 app.p. ISBN 951-803-461-3. (In Finnish)
45. Finnra. 2006. Betonirakenteiden suunnitteluohjeet (Instructions for concrete structures). Helsinki. 33 p.. ISBN 951-803-580-6. (In Finnish)
46. Finnra. 2007. Sillan geotekniset suunnitteluperusteet (Geotechnical design requirements for bridges). Helsinki. 50 p. + 40 app. p. ISBN 978-951-803-896-5.
47. Finnra. 2008. Siltarekisteri (Bridge register). Compiled from bridge register on 2.4.2008.
48. Finnra. 2008. Sillansuunnittelun täydentävät ohjeet (Supplementary bridge design instructions). Helsinki. 28 p. + 84 app. p. ISBN 978-952-221-035-7. (In Finnish)
49. Finnra. 2010. Sillat 1.1.2010, Liikenneviraston sillaston rakenne, palvelutaso ja kunto (Bridges of Finnish Road Administration on 1.1.2010: structure, service level and condition of the bridge stock). Helsinki. 77 p. + 2 app. p. ISSN 1459-1561. (In Finnish)

50. Frank, R. 2008. Design of pile foundations following Eurocode 7-Section 7. Presentation in workshop “Eurocodes: background and applications” Brussels, 18-20 February 2008. 8-13. 29 p.

51. Gabr, M.A. et al. 1997. Buckling of Piles with General Power Distribution of Lateral Subgrade Reaction. Journal of Geotechnical and Geoenvironmental Engineering. Vol. 123, No. 2., pp. 123-130.

52. Gerolymos, N. et al. 2009. Numerical modeling of centrifuge cyclic lateral pile load experiments. Earthquake Engineering and Engineering Vibration. Vol. 8, No. 1., pp. 61-76.

53. Girton, D. et al. 1989. Validation of design recommendations for integral-abutment piles. Publication number HR-292, Iowa State University. 82 p. + 15 app. p.

54. Greimann, L. & Wolde-Tinsae, A. 1988. Design Model for Piles in Jointless Bridges. Journal of Structural Engineering. Vol. 114, No. 6, pp. 1354-1371.

55. Guo, W. 2009. Nonlinear response of laterally loaded piles and pile groups. International Journal for Numerical and Analytical Methods in Geomechanics. Vol. 33, No. 5., pp. 879-914.

56. Hällmark, R. 2006. Low-cycle Fatigue of Steel Piles in Integral Abutment Bridges. Master’s thesis. Luleå University of Technology. 132 p. + 39 app. p. ISSN 1402-1617.

57. Han, J. & Frost, J. 2000. Load defection response of transversely isotropic piles under lateral loads. International Journal for Numerical and Analytical Methods in Geomechanics. Vol. 24, No. 5., pp. 509-529.

58. Hassiotis, S. & Xiong, K. 2007. Deformation of Cohesionless Fill Due to Cyclic Loading. Stevens Institute of Technology, New York. 83 p. SPR ID# C-05-03.

59. Hassiotis, S. 2007. Data gathering and design details of an integral abutment bridge. Presentation in: 18th Engineering Mechanics Division Conference of ASCE, Blacksburg, Virginia, United States, 3-6 June pp. (EMD2007).

60. Heinisuo, M. 1989. Paalun analysointi kotimikrolla (Pile analysis using a personal computer). Journal of structural mechanics. Vol. 22, No. 2, pp. 23-41. (In Finnish)

61. Helsinki University of Technology. Course material 43.3110, Construct of Concrete Structures. 2009.

62. Hetenyi, M. 1946, renewed 1974. Beams on elastic foundation. Ann Arbor: The University of Michigan Press. 255 p. ISBN 0-472-08445-3

63. Hettler, A. 1986. Sekantenmoduln bei horizontal belasteten Pfählen in Sand berechnet aus nicht-linearer Bettungstheorie. Geotechnik. Vol. 9, No. 1, pp. 20-29.

64. Hilmi, M. 2002. Viscoelastic Behaviour of Composite Piles Used in the Construction of Quays. Turkish Journal of Engineering & Environmental Sciences. Vol. 26, No. 5., pp. 419-427.

65. Hoppe, E. 2005. Field study of integral backwall with elastic inclusion. Publication number VTRC 05-R28, Virginia Transportation Research Council. 27 p. + 10 app.p.

66. Huang, J. et al. 2004. Behavior of Concrete Integral Abutment Bridges. University of Minnesota. 294 p. + 55 app. p. MN/RC - 2004-43.

67. Hulsey, L. 1992. Bridge lengths: Jointless prestressed girder bridges. University of Alaska Fairbanks. Final report No. INE/TRC/GRP-92.04. 36 p. + 22 app. p.

68. Hulsey, L. et al. 1990. The no expansion joint bridge for northern regions. University of Alaska Fairbanks. Final report No. INE/TRC 90.02. 163 p. + 25 app. p.

69. Hyrkkönen, A. 1988. Geotechnical bearing capacity of large steel pipe pile. Master's thesis. Tampere University of Technology 187 p. (In Finnish)

70. Järvinen P. & Järvinen A. 1996. Tutkimustyön metodeista (On Research Methods). Tampere University. ISBN 951-97113-1-7. (In Finnish)

71. Järvinen, V. 2010. Sillansuunnittelun perusteet (Basics of bridge engineering), RTEK-3610. Tampere University of Technology. 89 p. (In Finnish)

72. Kagawa, T., and Kraft, L. (1980). Seismic P-Y Responses of Flexible Piles. Journal of Geotechnical Engineering. Vol. 106, No. 8, pp. 899-918.

73. Kerokoski, O. 2005. Soil–structure interaction of jointless bridges. Literature research. Tampere University of Technology. 150 p. ISBN 952-15-1352-7. (In Finnish)

74. Kerokoski, O. 2005. Soil–structure interaction of jointless bridges with integral abutments. Calculations. Tampere University of Technology. 126 p. Internet 19.2.2008: http://alk.tiehallinto.fi/sillat/julkaisut/silta_ja_maa_lask_06.pdf (In Finnish)

75. Kerokoski, O. 2006. Soil-Structure Interaction of Long Jointless Bridges with Integral Abutments. Dissertation. Publication number 605, Tampere University of Technology 136 p. + 30 app. p. ISBN 952-15-1620-8.F

76. Khodair, Y. & Hassiotis, S. 2005. Analysis of soil–pile interaction in integral abutment. Computers and Geotechnics. Vol 32, No 3. pp. 201–209.

77. Klug, P. & Wittmann, F. 1970. The correlation between creep deformation and stress relaxation in concrete. Materials and Structures. Vol. 3, No. 2, pp. 75-80.

78. Koskinen, M. 1997. Composite action of steel pipe pile. Publication number 45, Tampere University of Technology. 27 p. ISBN 951-722-989-5.

79. Koskinen, M. 1997. Horizontal capacity of steel pipe pile. Licentiate thesis. Tampere University of Technology. 204 p. + 27 app. p. (In Finnish)

80. Koskinen, M. 1997. Soil-Structure Interaction of Jointless Bridges on Piles. Dissertation. Publication number 200, Tampere University of Technology. 184 p. ISBN 951-722-741-8.

81. Küçükarslan, S. et al. 2003. Inelastic analysis of pile soil structure interaction. Engineering structures. Vol. 25, No. 9. pp. 1231-1239.

82. Kumar, S. et al. 2006. Nonlinear response of single piles in sand subjected to lateral loads using k_{hmax} approach. Geotechnical and Geological Engineering. Vol. 24, No. 1., pp. 163-181.

83. Laaksonen, A. & Kerokoski, O. 2007. Long-term Monitoring of Haavistonjoki Bridge. IABSE Symposium, Weimar, Germany. pp. 360-361.

84. Laaksonen, A. 2004. Soil-structure Interaction of Jointless Bridges. Master's thesis. Tampere University of Technology 160 p. + 76 app. p. ISBN 952-15-1338-1. (In Finnish)

85. Laaksonen, A. 2005. Field Test of Tekemäjärvenoja Railway Bridge. Research report. Tampere University of Technology, Earth and Foundation Structures. 25.3.2008, unpublished. Available from Unit of Earth and Foundation Structures TUT. (In Finnish)

86. Laaksonen, A. 2008. Soil-structure interaction of integral bridge: Test loading with mobile crane. Tampere University of Technology, Earth and Foundation Structures. 69 p. + 11 app. p. Published on the Internet, 27.3.2008: http://www.tut.fi/units/rka/mpr/julkaisut/silta_ja_maa_koekuorm.pdf

87. Lawrer, A. et al. 2000. Field performance of integral abutment bridge. Transportation Research Record 1740, paper No. 00-0654. pp. 108-117.

88. Leppänen, M. 1992. Corrosion of steel pipe piles. Master's thesis. Tampere University of Technology 203 p + 19 app.p. (In Finnish)

89. Lianyang, Z. et al. 2005. Ultimate Lateral Resistance to Piles in Cohesionless Soils. Journal of Geotechnical and Geoenvironmental Engineering. Vol. 131, No. 1, pp. 78-83.

90. Lin, T.Y. & Burns, N.H. 1981. Design of prestressed concrete structures. New York. 646 p. ISBN 0-471-01898-8.

91. Lin, T.Y. 1963. Load-Balancing Method for Design and Analysis of Prestressed Concrete Structures. ACI Journal Proceedings (American Concrete Institute). Vol. 60, No. 6., pp. 719-742.

92. Ling, L.F. 1988. Back analysis of lateral load test on piles. Report / University of Auckland School of Engineering 460. University of Auckland. 117 p. + 78 app. p. ISSN 0111-0136

93. LUSAS. 2008. Element reference manual, LUSAS version 14.3: Issue 1. p. 69, 277 and 324.

94. Maine department of transportation (MDOT). 2003. Bridge design guide: Part 5: Substructures. Updated in 2007.

95. Matlock, H. & Reese, L. 1960. Generalized solutions for laterally loaded piles. Journal of the soil mechanics and foundations division, ASCE. Vol. 86, No. 5., pp. 63-91.

96. Matlock, H. & Reese, L. 1961. Foundation analysis of pile supported structures. The Fifth International Conference on Soil Mechanics and Foundation Engineering. Paris. 17-22 July. Volume II, pp. 91-97.

97. Matlock, H. et al. 1979. SPASM 8 - A Dynamic Beam-Column, Program for Seismic Pile Analysis with Support Motion. Fugro, Inc.

98. Meymand, P. 1998. Shaking Table Scale Model Tests of Nonlinear Soil-Pile-Superstructure Interaction In Soft Clay. University of California, Berkeley. 457 p. + 5 app. p.

99. Mikkola, M. 1981. Kimmoisella alustalla oleva palkki (Beam on elastic foundation). Publication number 36, Helsinki University of Technology. 33 p. (In Finnish)

100. Mistry, V. 2005. Integral Abutment and Jointless Bridges. The 2005 – FHWA Conference, Integral Abutment and Jointless Bridges (IAJB 2005), Baltimore, Maryland, United States 16-18 March. pp. 3-11.

101. Mokwa, L. 1999. Investigation of the Resistance of Pile Caps to Lateral Loading. Dissertation. Virginia Polytechnic Institute and State University. 302 p. + 80 app.p.

102. NA SFS-EN 1991-1-5. 2007. Eurocode 1: Actions on structures – Part 1-5: General actions-Thermal actions. Finnish Standards Association, Helsinki. 5 p.

103. Oesterle, R & Volz, J. 2005. Effective temperature and longitudinal movement in integral abutment bridges. The 2005 – FHWA Conference, Integral Abutment and Jointless Bridges (IAJB 2005), Baltimore, Maryland, United States 16-18 March. pp. 302-311.

104. Ollila, M. 1973. Theorie der räumlichen Pfahlwerke im elastischen Kontinuum. Dissertation. Publication number TKK-DISS-278 TES 661, Helsinki University of Technology 78 p. (In German)

105. Petursson, H. & Collin, P. 2002. Composite Bridges with Integral Abutments Minimizing Lifetime Cost. IABSE Symposium, Melbourne, Australia. 9 p.

106. Preston, H. Plastic Design of Steel HP-Piles for Integral Abutment Bridges. The 2005 – FHWA Conference, Integral Abutment and Jointless Bridges (IAJB 2005), Baltimore, Maryland, United States 16-18 March. pp. 270-280.

107. Pugasap, K. 2006. Hysteresis model based prediction of integral abutment bridge behaviour. Dissertation. The Pennsylvania State University. 259 p. + 126 app. p.

108. Rautaruukki Oyj. 2010. Brochure: Large diameter steel pipe piles. Hämeenlinna. 19 p. (In Finnish)

109. Roberts-Wollman, C. & Breen, J. & Cawrse, J. 2002. Measurements of Thermal Gradients and their Effects on Segmental Concrete Bridge. Journal of Bridge Engineering. Vol. 7, No. 3., pp. 166-174.

110. Rodolfo, M. & Samer, P. 2005. Integral Abutments and Jointless Bridges (IAJB) 2004 Survey Summary. The 2005 – FHWA Conference, Integral Abutment and Jointless Bridges (IAJB 2005), Baltimore, Maryland, United States 16-18 March. pp. 12-29.

111. Ross, A. D. 1958. Creep of concrete under variable stress. Vol. 29, No. 9, pp. 739-758.
112. Rovithis, E. et al. 2009. Experimental p-y loops for estimating seismic soil-pile interaction. Bulletin of Earthquake Engineering. Vol. 7, No. 3, pp. 719-736.
113. Rowe, P.W. 1956. The Single Pile Subject to Horizontal Force. Geotechnique. Vol 6, No. 2., pp. 70-85.
114. Sadrekarimi J. & Akbarzad M. 2009. Comparative Study of Methods of Determination of Coefficient of Subgrade Reaction. The Electronic Journal of Geotechnical Engineering. Vol. 14, bundle E., pp. 419-427.
115. SFS-EN 1990. Eurocode 0, Basis of structural design. Finnish Standards Association, Helsinki. 138 p.
116. SFS-EN 1991-1-5. 2003. Eurocode 1: Actions on structures – Part 1-5: General actions – Thermal actions. Finnish Standards Association, Helsinki. 68 p.
117. SFS-EN 1991-2. Eurocode 1: Actions on structures. Part 2: Traffic loads on bridges. Finnish Standards Association, Helsinki. 164 p.
118. SFS-EN 1992-1-1. Eurocode 2: Design of concrete structures - Part 1-1: General rules and rules for buildings. Finnish Standards Association, Helsinki.
119. SFS-EN 1992-2. Eurocode 2: Design of concrete structures – Part 2: Concrete bridges. Design and detailing rules. Finnish Standards Association, Helsinki.
120. SFS-EN 1994-2. Eurocode 4: Design of composite steel and concrete structures – Part 2: General rules and rules for bridges. Finnish Standards Association, Helsinki.
121. SFS-EN 1997-1. Eurocode 7. Geotechnical design – Part 1: General rules. Finnish Standards Association, Helsinki.
122. Shamsabadi, A. & Nordal, S. 2006. Modeling passive earth pressures on bridge abutments for nonlinear Seismic Soil-Structure interaction using Plaxis. Plaxis Bulletin. No. 6., pp. 8-15.
123. Shamsabadi, A. et al. 2007. Nonlinear Soil–Abutment–Bridge Structure Interaction for Seismic Performance-Based Design. Journal of Geotechnical and Geoenvironmental Engineering. Vol. 133, No. 6., pp. 707-720.

124. Shirato, M. et al. 2006. A New Nonlinear Hysteretic Rule for Winkler Type Soil-Pile Interaction Springs that Considers Loading Pattern Dependency. Soils and Foundations, Japanese Society of Soil Mechanics and Foundation Engineering. Vol. 46, No. 2., pp. 173-188.
125. Smith, T. 1987. Pile horizontal modulus values. Journal of Geotechnical Engineering. Vol. 113, No. 9., pp. 1040-1044.
126. Smoltczyk, U. 1992. Grundbau-Taschenbuch, Teil 3. 846 p. Berlin. ISBN 3-433-01412-4 (In German)
127. Stark, R.F. & Booker, J.R. 1997. Surface Displacements of a Non-homogeneous Elastic Half-space Subjected to Uniform Surface Tractions. Part II: Loading on Rectangular Shaped Areas. International Journal for Numerical and Analytical Methods in Geomechanics. Vol. 21, No. 6., pp. 379-395.
128. Taciroglu, E. et al. 2006. A Robust Macroelement Model for Soil-Pile Interaction under Cyclic Loads. Journal of Geotechnical and Geoenvironmental Engineering. Vol. 132, No. 10, pp. 1304-1314.
129. Terzaghi, K. 1955. Evaluation of coefficients of subgrade reaction. Geotechnique. Vol 5, No. 4., pp. 297-326.
130. Terzaghi, K. et al. Soil mechanics in engineering practice. pp.133-134. ISBN 0-471-08658-4
131. The International Federation for Structural Concrete (fib). 1999. Structural Concrete. Textbook on Behaviour, Design and Performance
Vol. 1: Introduction – Design Process – Materials. Stuttgart. ISBN 978-2-88394-041-3.
132. Timoshenko, S. & Goodier, J.N. 1951. Theory of Elasticity. pp. 366-372
133. Titze, E. 1970. Über den seitlichen Bodenwiderstand bei Pfahlgründungen. Bauingenieur-Praxis, 77. Berlin. 118 p. + 18 app. p. ISBN 3-433-00040-9 (In German)
134. Törnqvist, J. 2004. Teräsputkipaalujen korroosio, Mitoitus empiiriseen aineistoon pohjautuen (Corrosion of steel piles, dimensioning on the basis of empirical material). Espoo. 42 p. ISBN 952-5004-53-8. (In Finnish)
135. Tschumi, M. 2008. Railway actions, selected chapters from EN 1991-2 and Annex A2 of EN 1990. Presentation in workshop “Eurocodes: background and applications” Brussels, 18-20 February 2008. 8-13. 37 p.

136. Tuominen, M. 2008. The Utilization of Elastic Material in Integral Abutment Bridges. Master's thesis. Tampere University of Technology 67 p. + 14 app.p. (In Finnish)
137. UK Highways Agency 2003. Design manual for roads and bridges, Volume 1 Section 3 Part 12 BA42/96, The Design of Integral Bridges. The Stationary Office UK. 16 p.
138. Vesic, A.S. 1961. Beams on Elastic Subgrade and Winkler Hypothesis. Proceedings of the Fifth International Conference on Soil Mechanics and Foundation Engineering. Paris. Vol 1, pp. 545-550.
139. Vilonen, H. 2007. Soil-structure interaction of skewed jointless bridges. Master's thesis. Tampere University of Technology. 83 p. + 38 app. p. Internet 19.2.2008: http://alk.tiehallinto.fi/sillat/julkaisut/silta_ja_maa_vino.pdf (In Finnish)
140. Wasserman, E. 2007. Integral abutment design (Practices in the United States). 1st U.S.-Italy Seismic Bridge Workshop, Pavia, Italy, 19-20 April. 12 p.
141. Wiemann, J. et al. 2004. Evaluation of Pile Diameter Effects on Soil-Pile Stiffness. 7th German Wind Energy Conference DEWEK. Wilhelmshaven. 20-21 October. 4 p.
142. Woodward, R. et al. 1972. Drilled Pier Foundations. McGraw-Hill Company. pp. 61-104. ISBN 0-07-071783-4.
143. Yoshida, I. & Yoshinaka, R. 1972. A Method to Estimate Modulus of Horizontal Subgrade Reaction for a Pile. Soils and Foundations, Japanese Society of Soil Mechanics and Foundation Engineering. Vol. 12, No. 3. pp. 1-17.
144. Zhang, L. et al. 2005. Ultimate Lateral Resistance of Piles in Cohesionless Soils. Journal of Geotechnical and Geoenvironmental Engineering. Vol. 131, No. 1., pp. 78-83.

APPENDICES

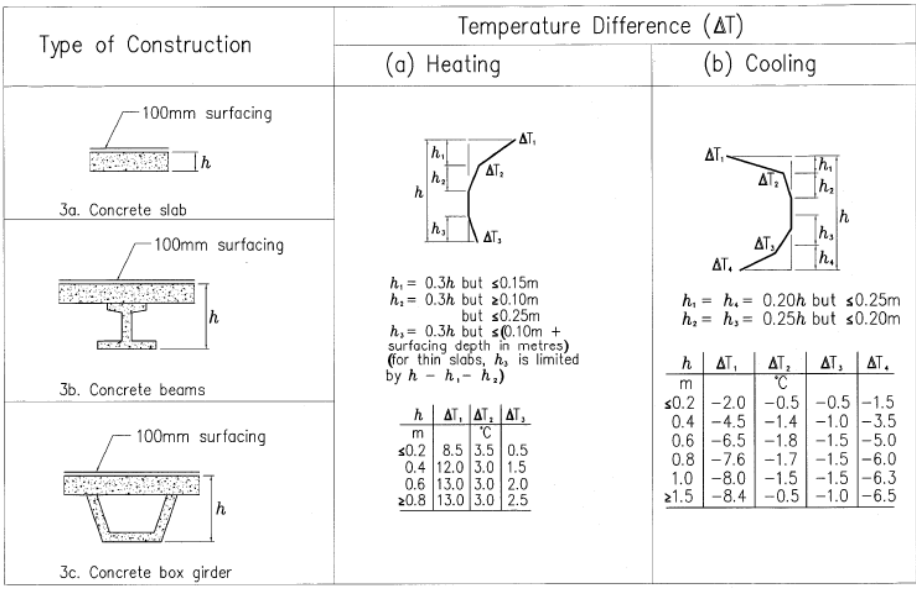

h	ΔT1	ΔT2	ΔT3
m		°C	
≤0.2	8.5	3.5	0.5
0.4	12.0	3.0	1.5
0.6	13.0	3.0	2.0
≥0.8	13.0	3.0	2.5

h	ΔT1	ΔT2	ΔT3	ΔT4
m		°C		
≤0.2	−2.0	−0.5	−0.5	−1.5
0.4	−4.5	−1.4	−1.0	−3.5
0.6	−6.5	−1.8	−1.5	−5.0
0.8	−7.6	−1.7	−1.5	−6.0
1.0	−8.0	−1.5	−1.5	−6.3
≥1.5	−8.4	−0.5	−1.0	−6.5

Figure 6.2c: Temperature differences for bridge decks – Type 3 : Concrete Decks

*Note: The temperature difference ΔT incorporates ΔT_M and ΔT_E (see 4.3) together with a small part of component ΔT_N; this latter part has been included in the uniform bridge temperature component (see 6.1.3).

Figure 1 Cross section types and non-linear temperature differences of cross sections [116]

Table 1 Linear temperature difference values [116]

Table 6.1: Recommended values of linear temperature difference component for different types of bridge decks for road, foot and railway bridges

Type of Deck	**Top warmer than bottom**	**Bottom warmer than top**
	$\Delta T_{M,heat}$ (°C)	$\Delta T_{M,cool}$ (°C)
Type 1: Steel deck	18	13
Type 2: Composite deck	15	18
Type 3: Concrete deck: - concrete box girder - concrete beam - concrete slab	 10 15 15	 5 8 8
NOTE 1: The values given in the table represent upper bound values of the linearly varying temperature difference component for representative sample of bridge geometries. NOTE 2: The values given in the table are based on a depth of surfacing of 50 mm for road and railway bridges. For other depths of surfacing these values should be multiplied by the factor k_{sur}. Recommended values for the factor k_{sur} is given in Table 6.2.		

208 **Appendix 1 2(2)**

Table 2 Multiplier for linear temperature difference in Table 1 [116]

Table 6.2: Recommended values of k_{sur} to account for different surfacing thickness

Road, foot and railway bridges						
Surface Thickness	Type 1		Type 2		Type 3	
	Top warmer than bottom	Bottom warmer than top	Top warmer than bottom	Bottom warmer than top	Top warmer than bottom	Bottom warmer than top
[mm]	k_{sur}	k_{sur}	k_{sur}	k_{sur}	k_{sur}	k_{sur}
unsurfaced	0,7	0,9	0,9	1,0	0,8	1,1
water-proofed [1)]	1,6	0,6	1,1	0,9	1,5	1,0
50	1,0	1,0	1,0	1,0	1,0	1,0
100	0,7	1,2	1,0	1,0	0,7	1,0
150	0,7	1,2	1,0	1,0	0,5	1,0
ballast (750 mm)	0,6	1,4	0,8	1,2	0,6	1,0

[1)] These values represent upper bound values for dark colour

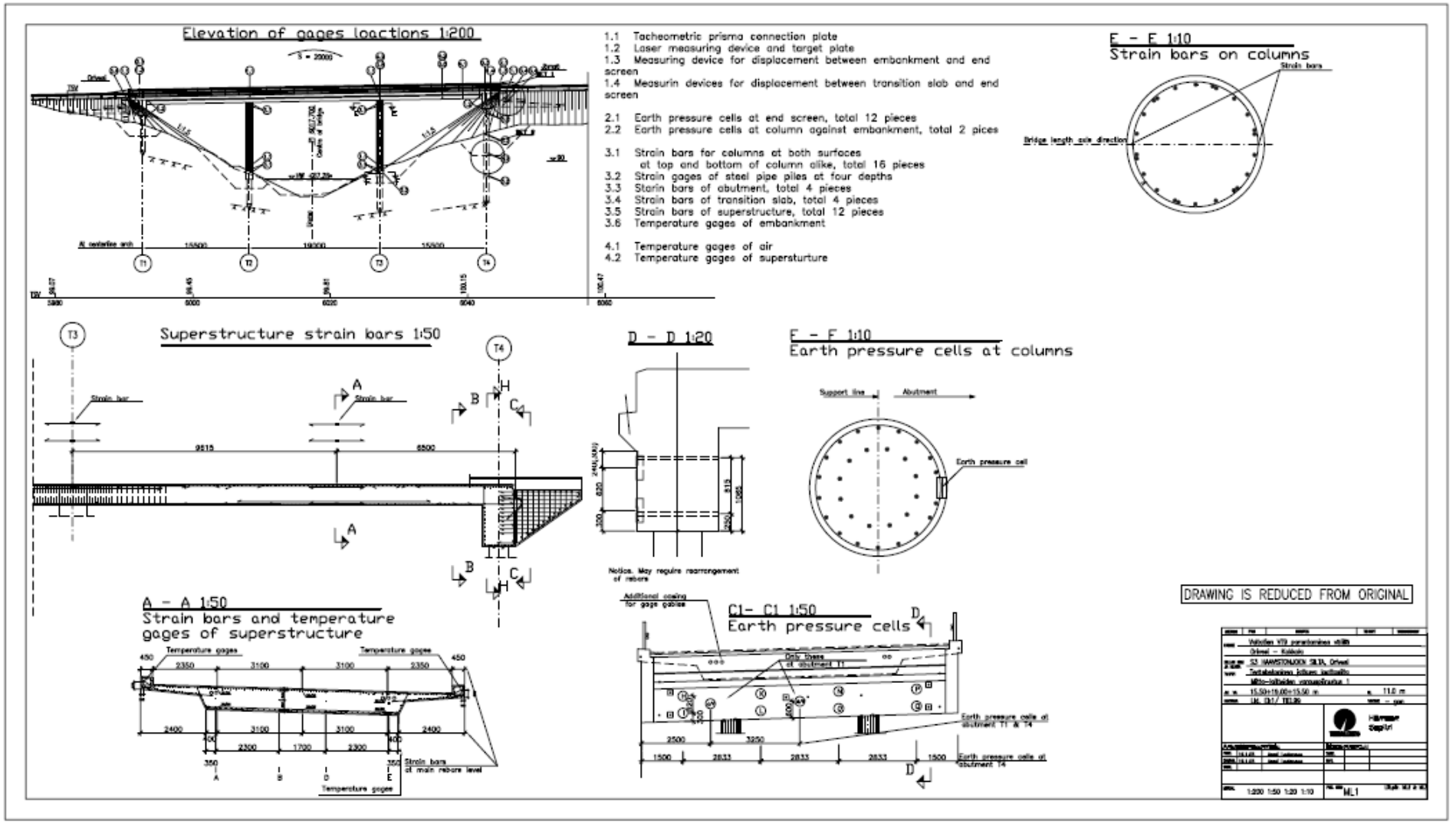
Elevation of gages loactions 1:200
1.1 Tacheometric prisma connection plate
1.2 Laser measuring device and target plate
1.3 Measuring device for displacement between embankment and end screen
1.4 Measurin devices for displacement between transition slab and end screen
2.1 Earth pressure cells at end screen, total 12 pieces
2.2 Earth pressure cells at column against embankment, total 2 pices
3.1 Strain bars for columns at both surfaces at top and bottom of column alike, total 16 pieces
3.2 Strain gages of steel pipe piles at four depths
3.3 Starin bars of abutment, total 4 pieces
3.4 Strain bars of transition slab, total 4 pieces
3.5 Strain bars of superstructure, total 12 pieces
3.6 Temperature gages of embankment
4.1 Temperature gages of air
4.2 Temperature gages of supersturture
E - E 1:10
Strain bars on columns
Strain bars
Bridge length axle direction
Superstructure strain bars 1:50
Strain bar
9515
8500
D - D 1:20
Notice. May require rearrangement of rebars
E - E 1:10
Earth pressure cells at columns
Support line
Abutment
Earth pressure cell
A - A 1:50
Strain bars and temperature gages of superstructure
Temperature gages
Strain bars at main rebars level
C1- C1 1:50
Earth pressure cells
Additional casing for gage cables
Earth pressure cells at abutment 11 & 14
Earth pressure cells at abutment 14
DRAWING IS REDUCED FROM ORIGINAL
1:200 1:50 1:20 1:10
M1.1

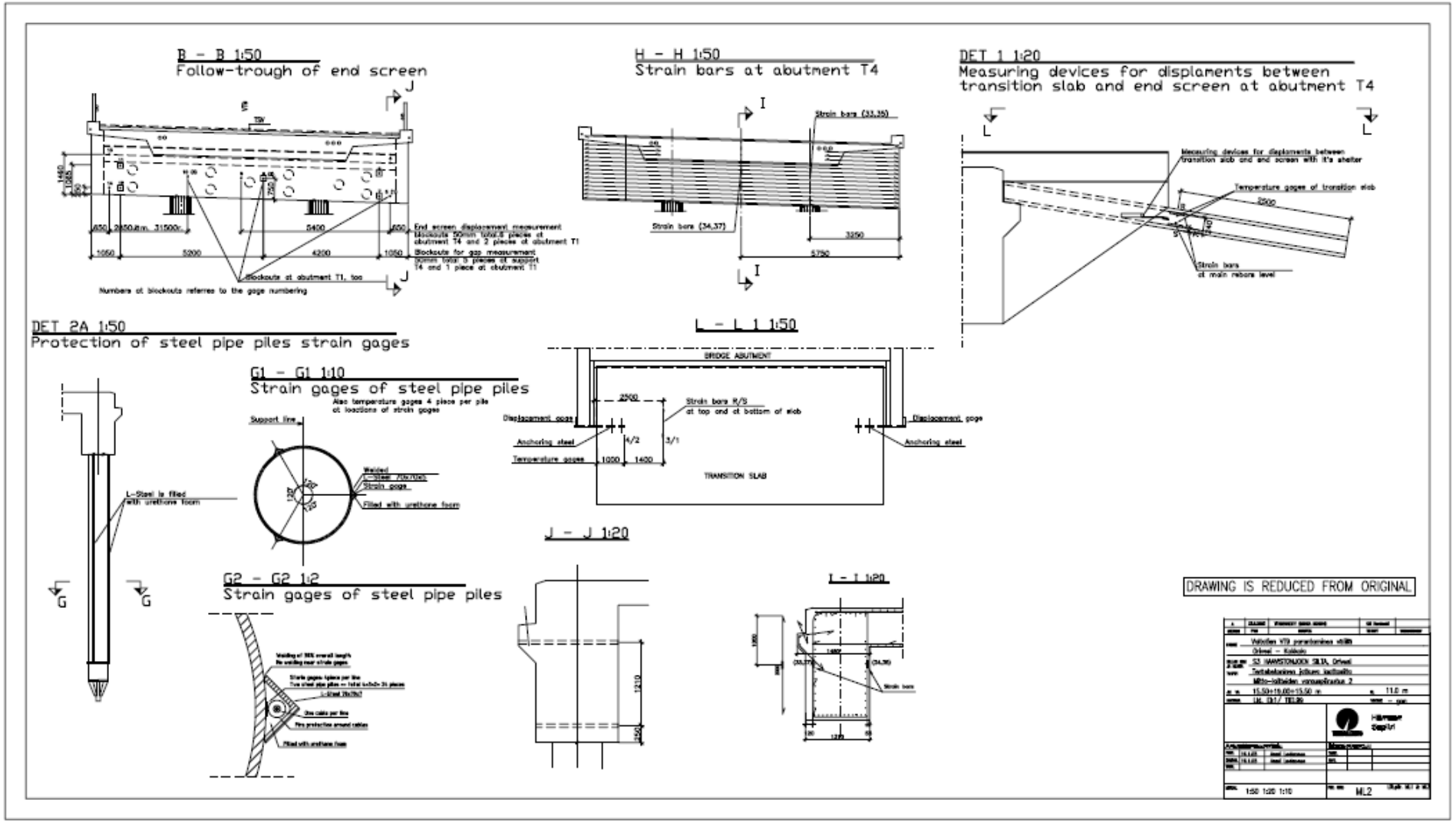
B - B 1:50
Follow-trough of end screen
H - H 1:50
Strain bars at abutment T4
DET 1 1:20
Measuring devices for displaments between transition slab and end screen at abutment T4
DET 2A 1:50
Protection of steel pipe piles strain gages
G1 - G1 1:10
Strain gages of steel pipe piles
L - L 1:50
BRIDGE ABUTMENT
TRANSITION SLAB
J - J 1:20
I - I 1:20
G2 - G2 1:2
Strain gages of steel pipe piles
DRAWING IS REDUCED FROM ORIGINAL

Realized gages loactions 1:200

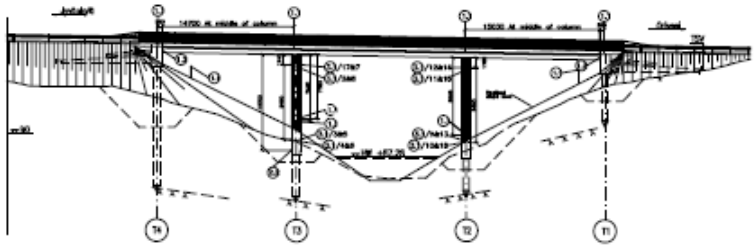

DET 2B 1:50
Realized locations of
Strain and temperature gages
of steel pipe piles

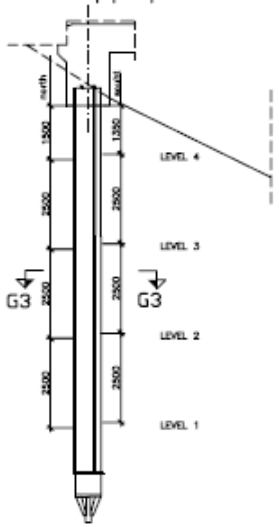

G3 - G3 1:10
Strain gages of steel pipe piles

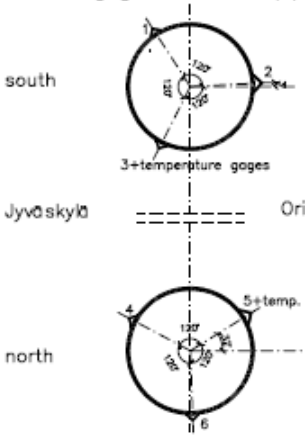

C2 - C2 1:50
Temperature gages at embankment T4

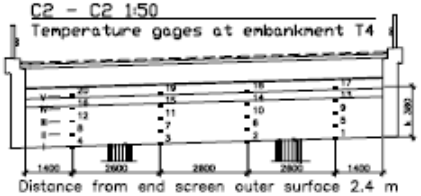

K - K 1:50
Temperature gages at embankment T4

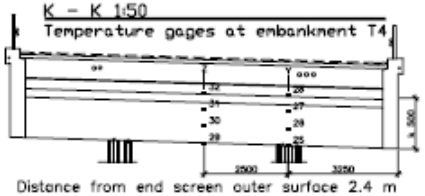

DRAWING IS REDUCED FROM ORIGINAL

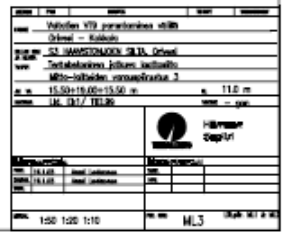

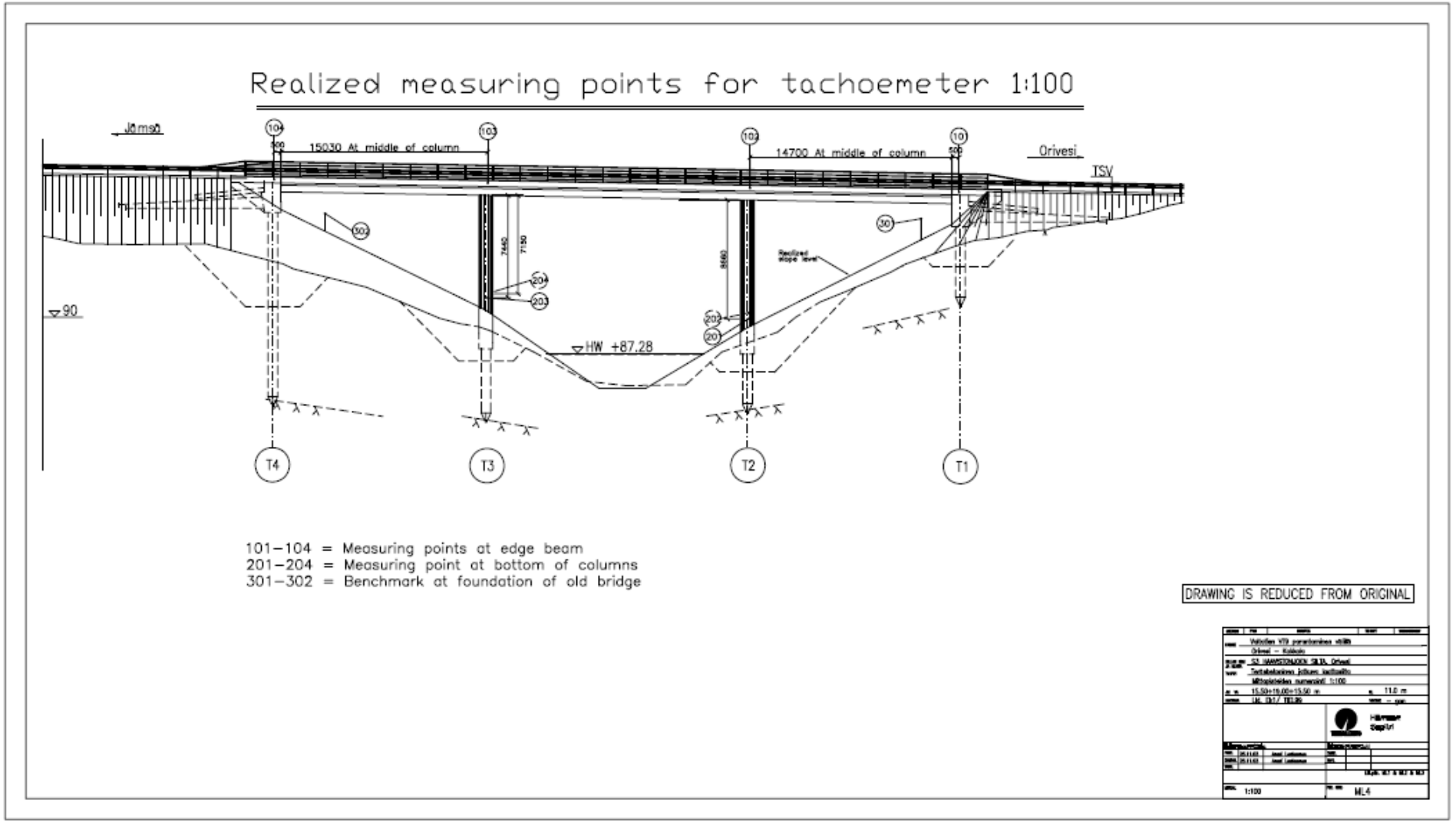
Realized measuring points for tachoemeter 1:100
Järvsö
15030 At middle of column
14700 At middle of column
Orivesi
TSV
90
HW +87.28
T4
T3
T2
T1
101–104 = Measuring points at edge beam
201–204 = Measuring point at bottom of columns
301–302 = Benchmark at foundation of old bridge
DRAWING IS REDUCED FROM ORIGINAL

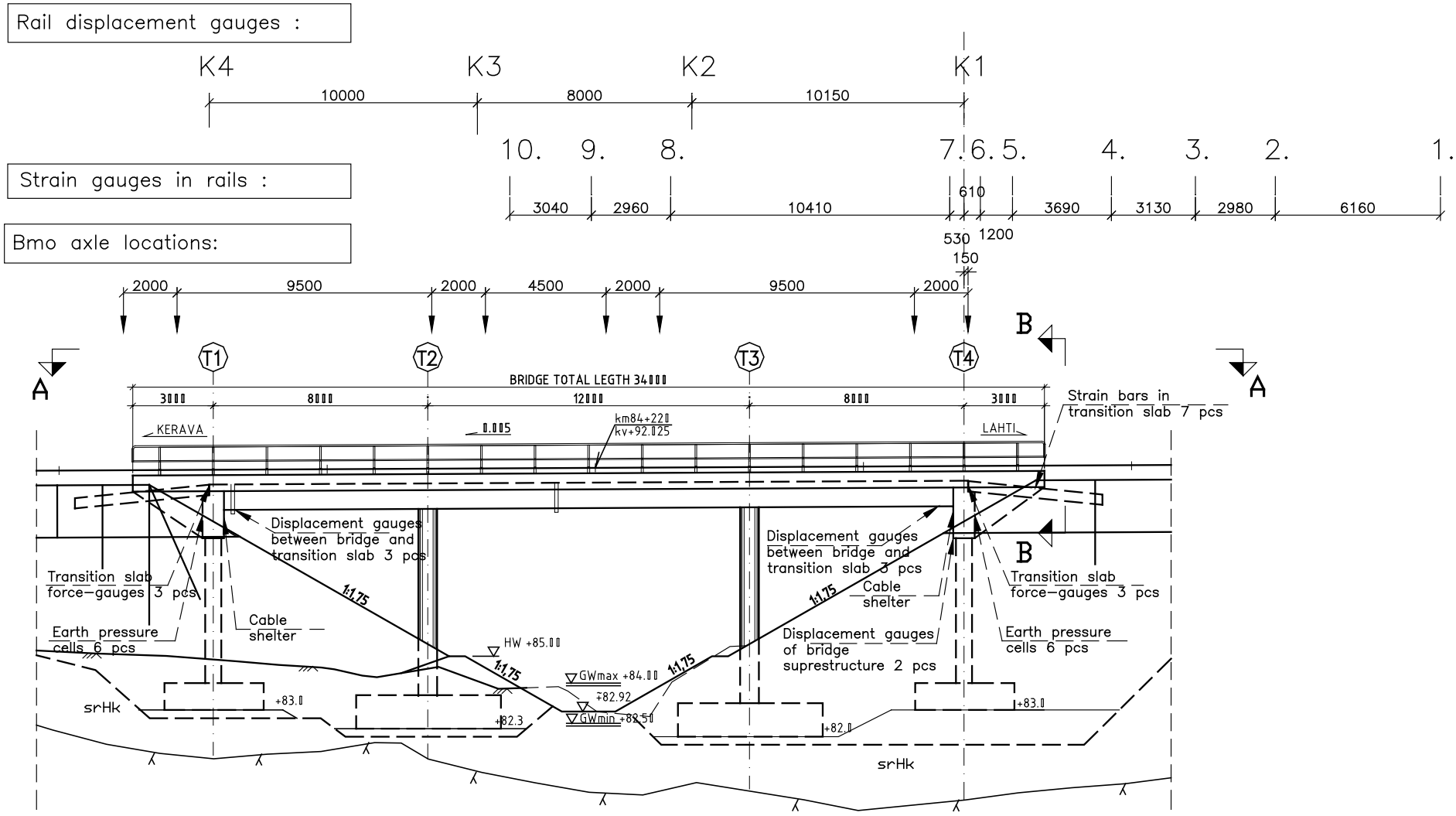

Figure 2 Elevation of monitoring devices

 Appendix 3 2(2) Field test programme details of the Tekemäjärvenoja Bridge

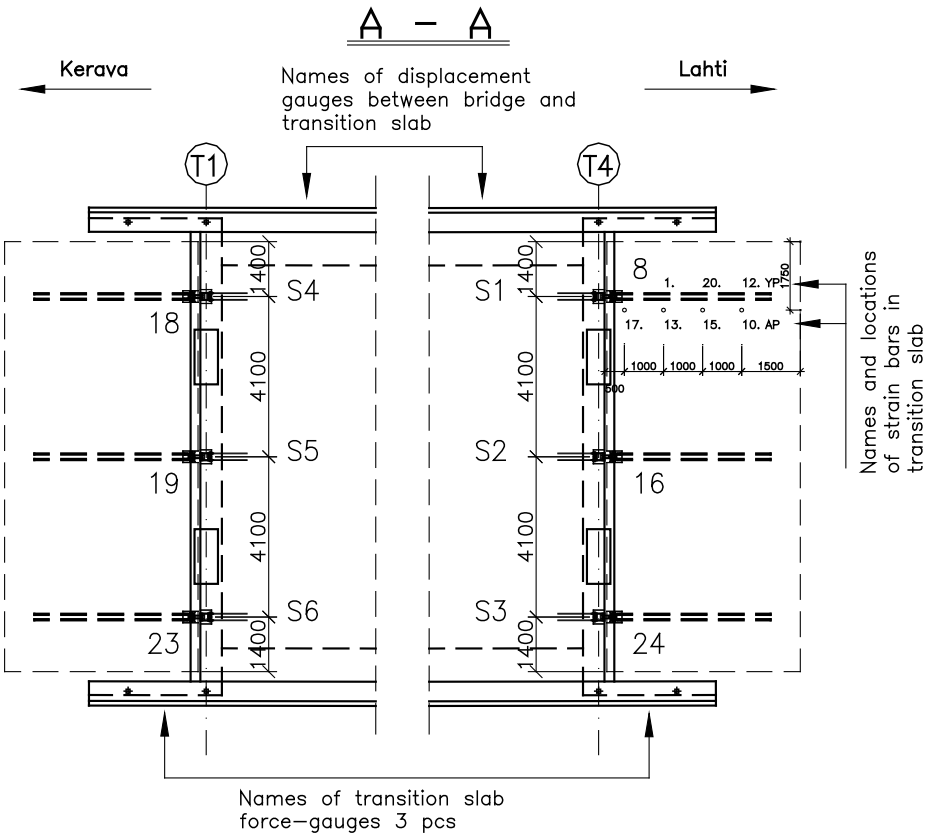

Figure 3 Monitoring devices in transition slab

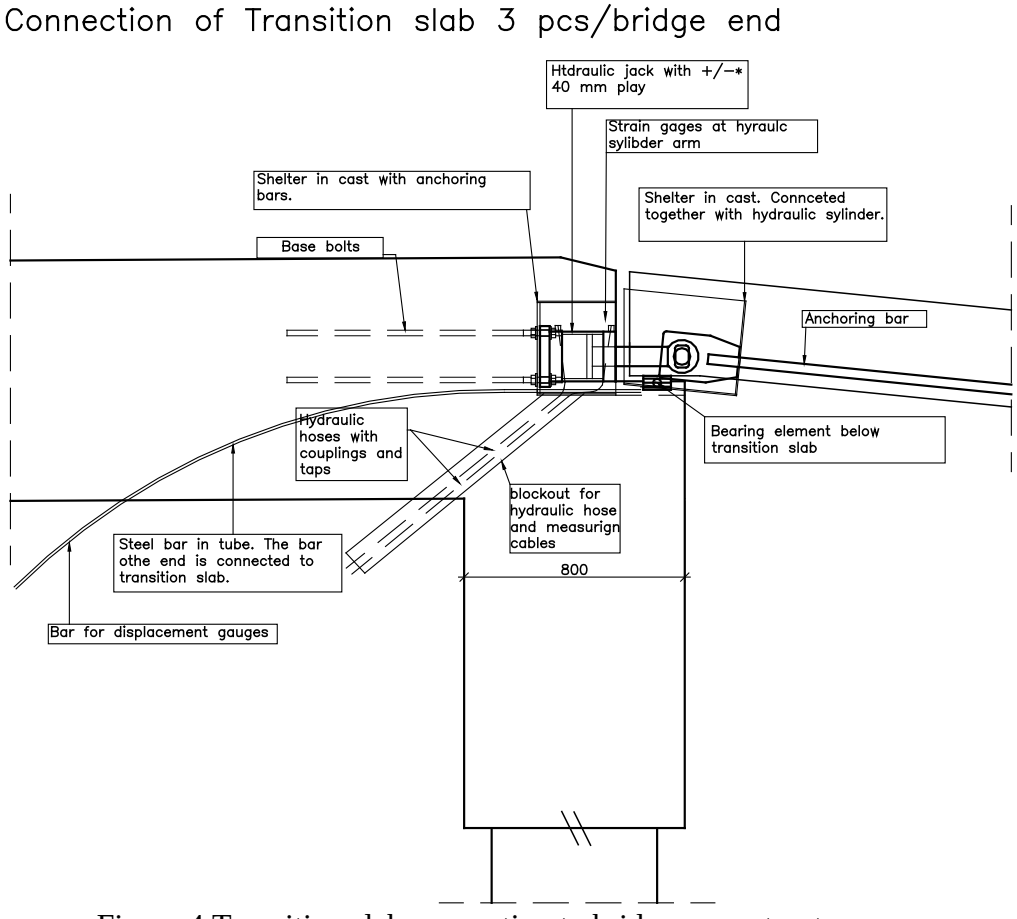

Figure 4 Transition slab connection to bridge superstructure

Appendix 4 1(1) Field test programme details of the Myllypuro Overpass 215

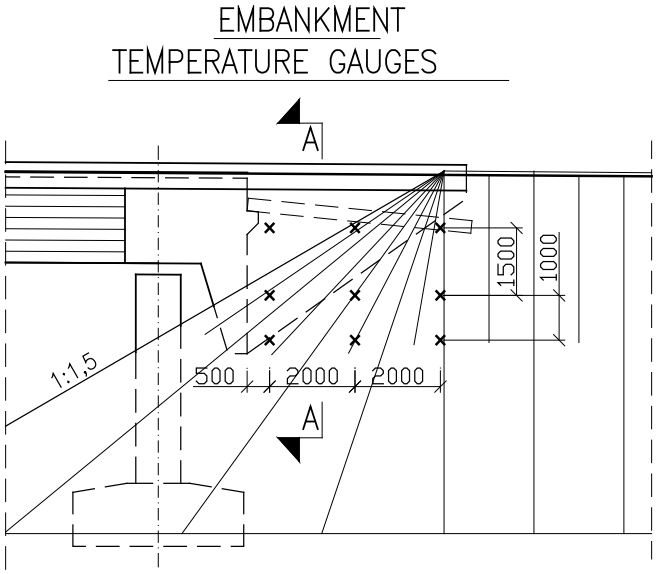

Figure 5 Embankment temperature gauge locations at embankment T3

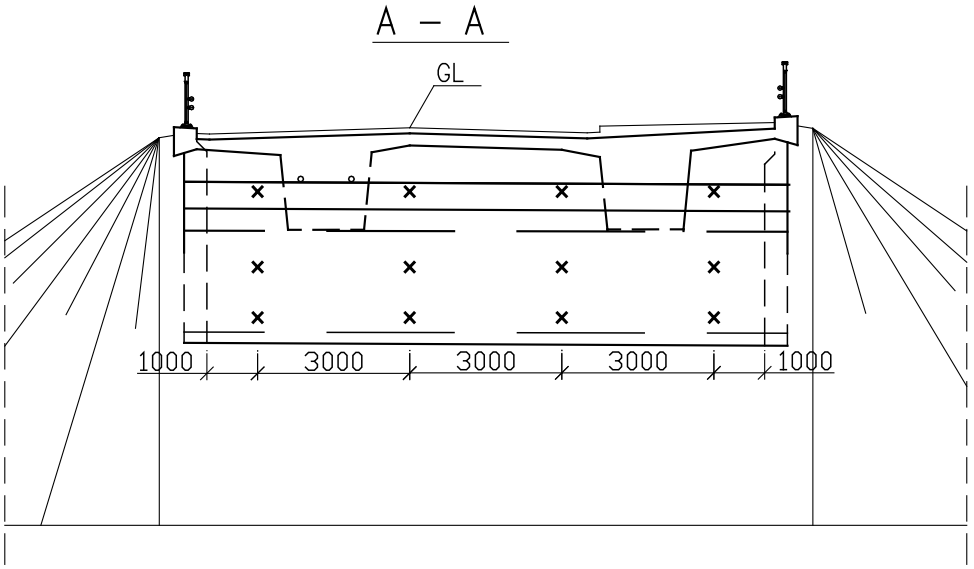

Figure 6 Embankment temperature gauge locations at embankment T3

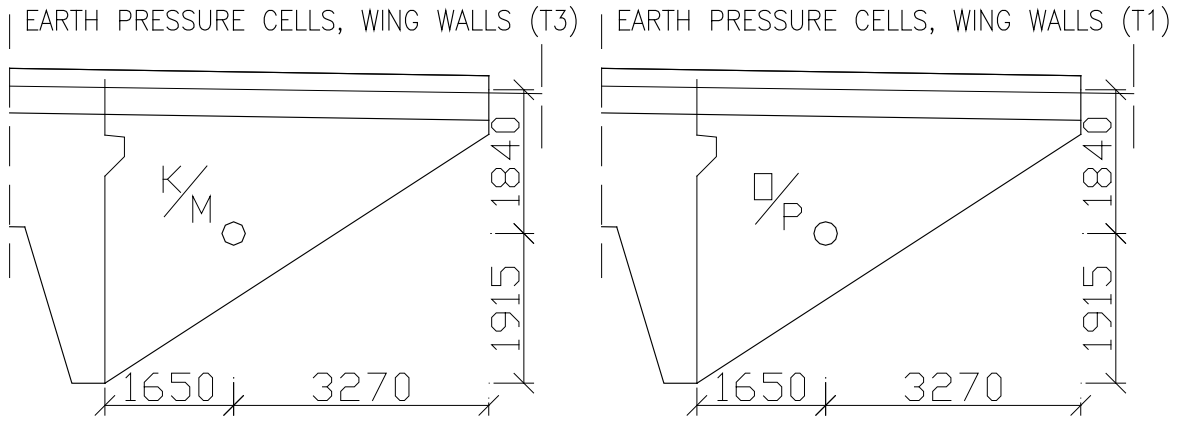

Figure 7 Earth pressure cell at wing walls

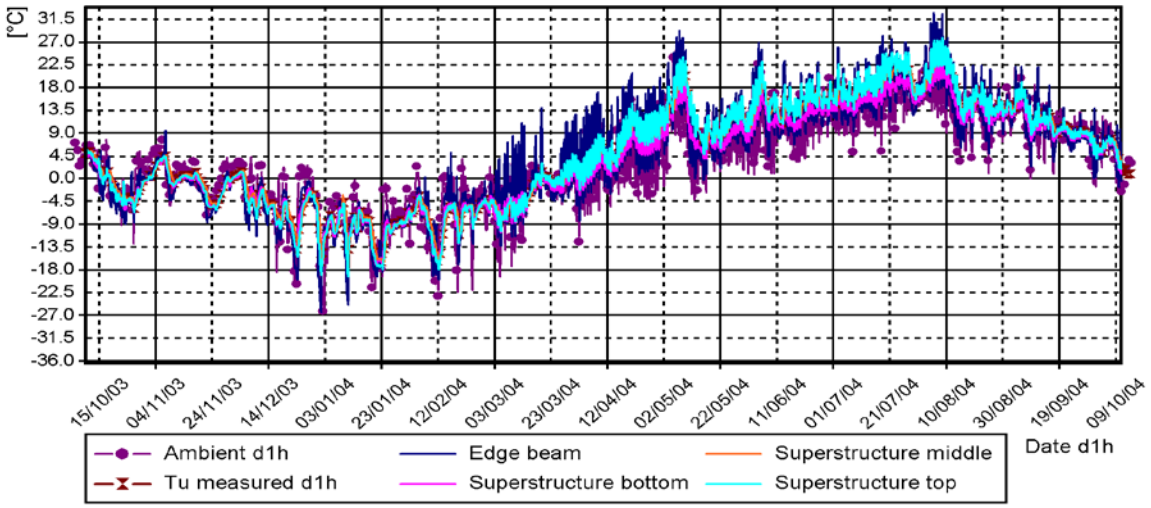

Figure 8 Ambient air and uniform temperatures of different superstructure parts during the period 10.10.03-10.10.04

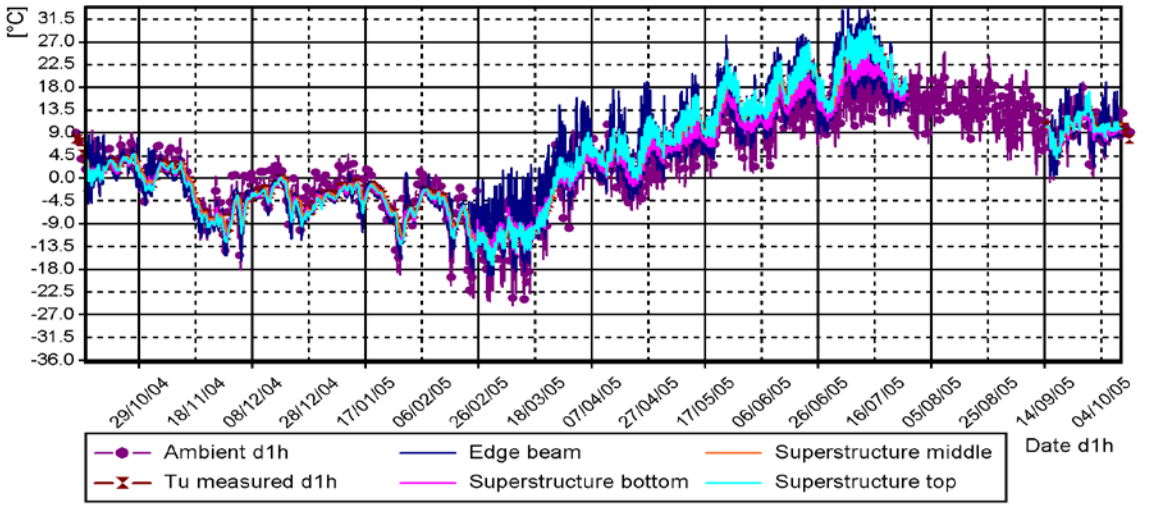

Figure 9 Ambient air and uniform temperatures of different superstructure parts during the period 10.10.04-10.10.05

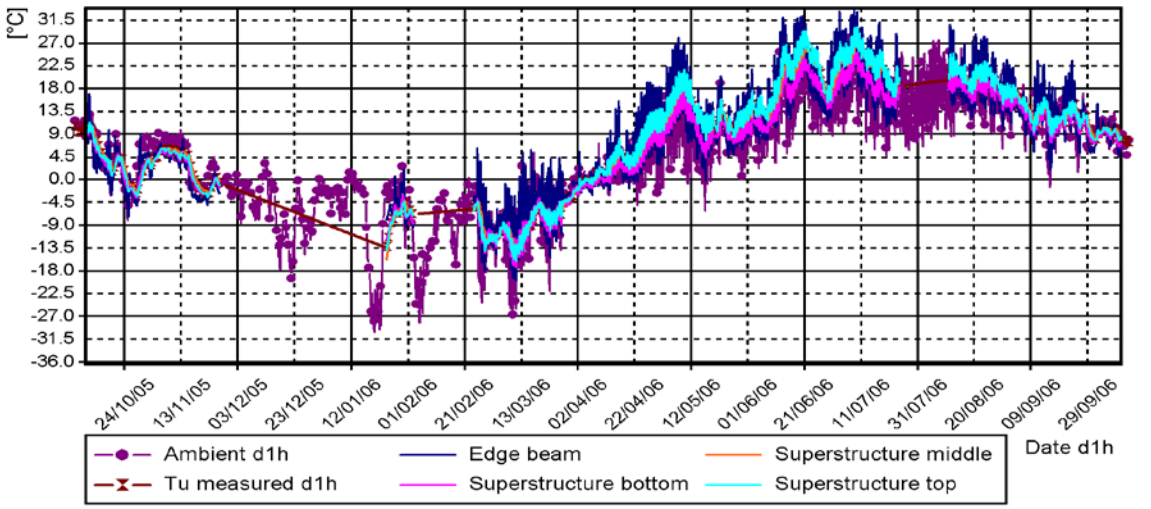

Figure 10 Ambient air and uniform temperatures of different superstructure parts during the period 10.10.05-10.10.06

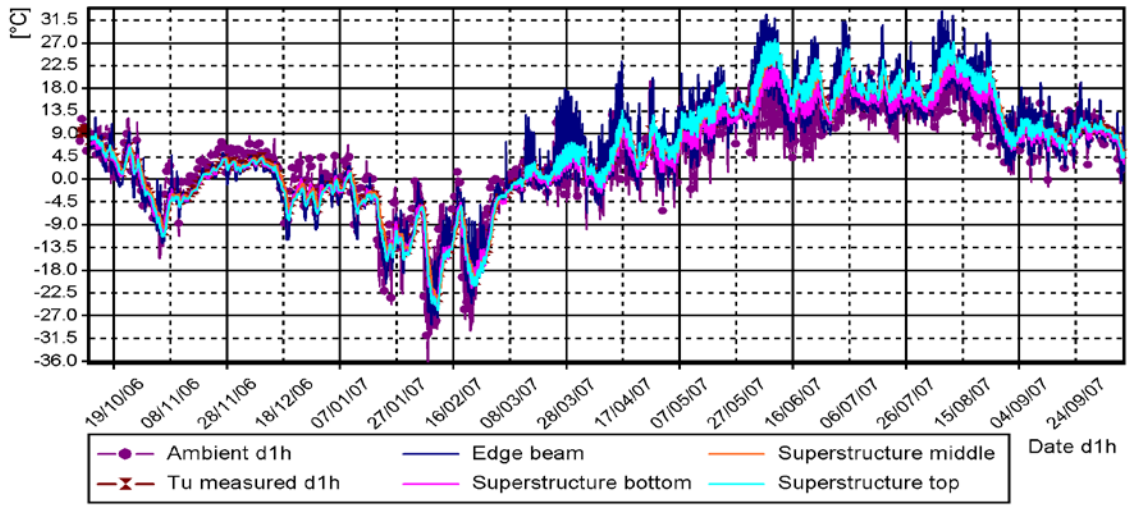

Figure 11 Ambient air and uniform temperatures of different superstructure parts during the period 10.10.06-10.10.07

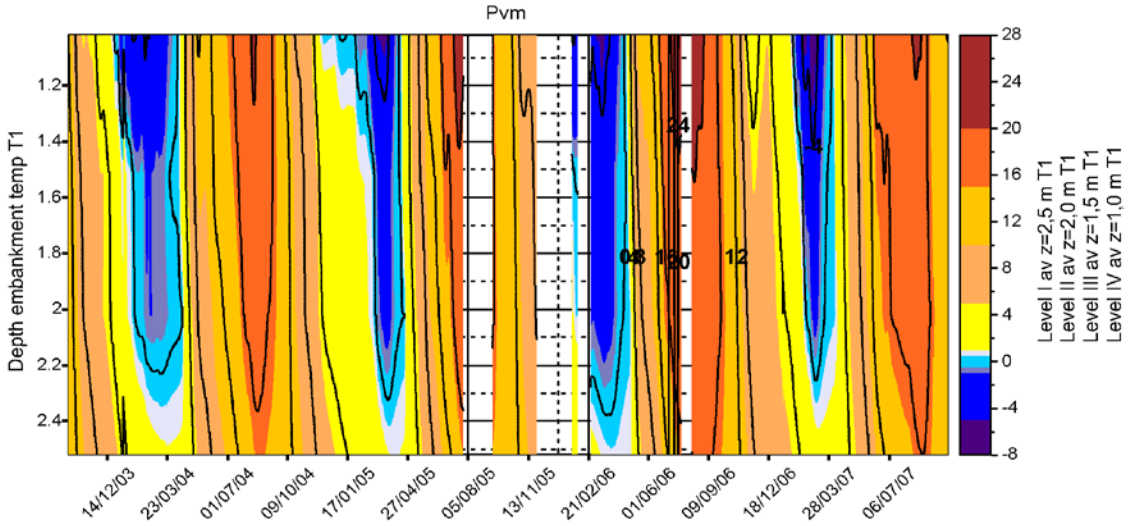

Figure 12 Linearly interpolated embankment temperature field at a vertical section based on measured temperatures of embankment T1 at a distance of 2.4 m from the end screen during the monitoring period 10.10.2003-10.10.2007

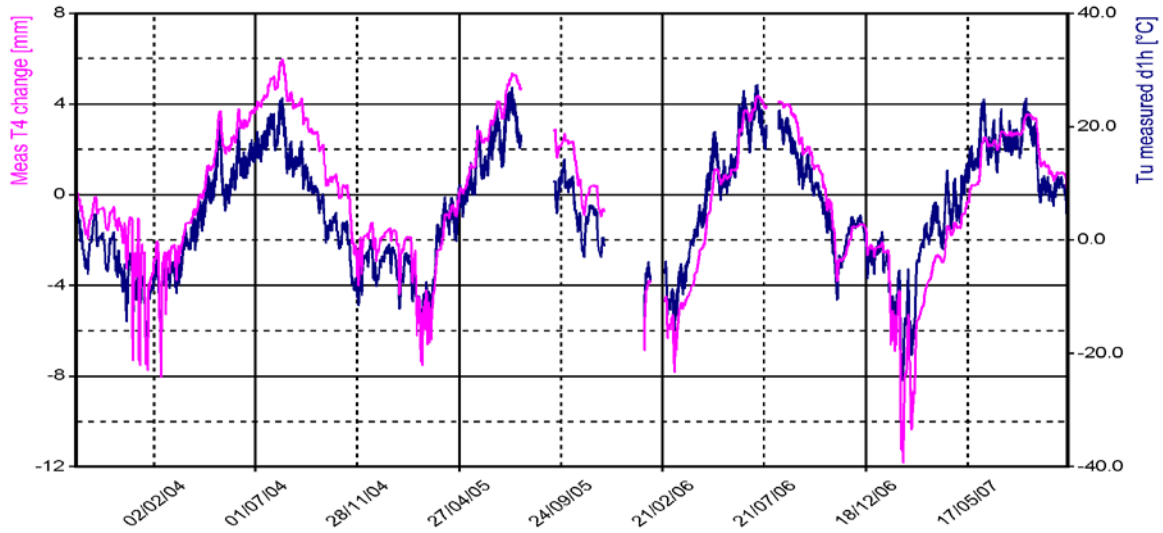

Figure 13 Displacement of abutment T4 and uniform temperature of superstructure during the monitoring period 10.10.2003-10.10.2007

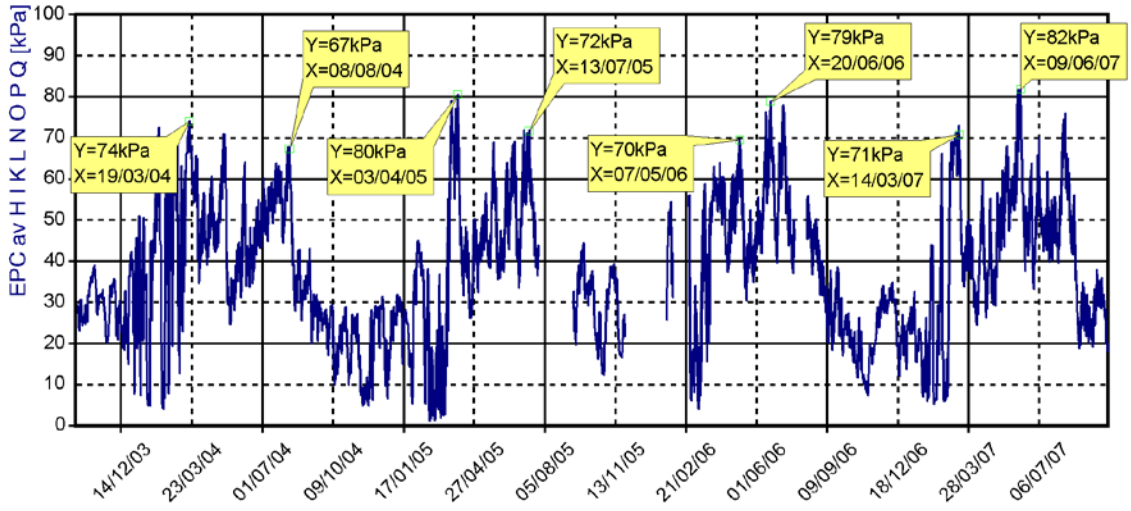

Figure 14 Average earth pressures from EPC H, I, K, L, M, N, O, P and Q between end screen and embankment during the monitoring period 10.10.2003-10.10.2007

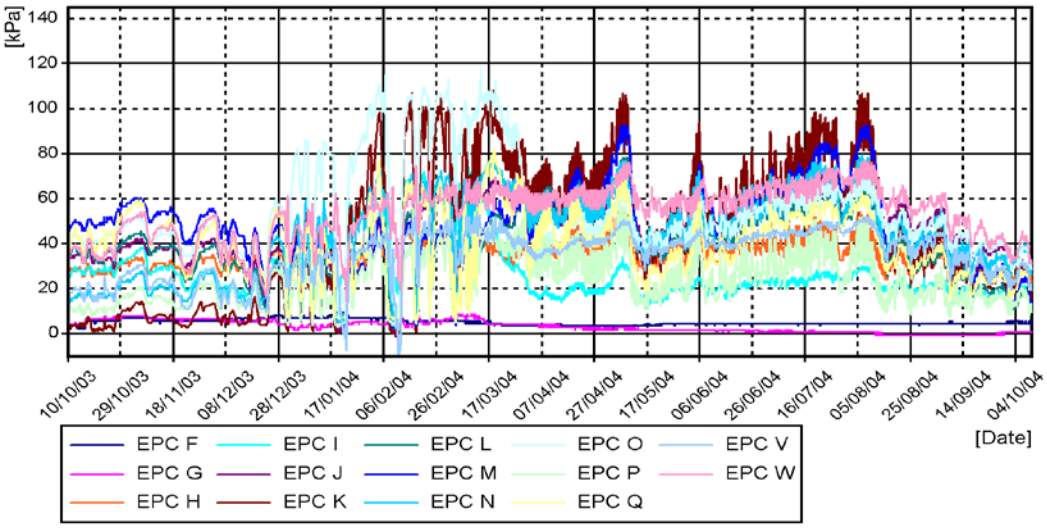

Figure 15 Earth pressures between end screen and embankment during the monitoring period 10.10.2003-10.10.2004

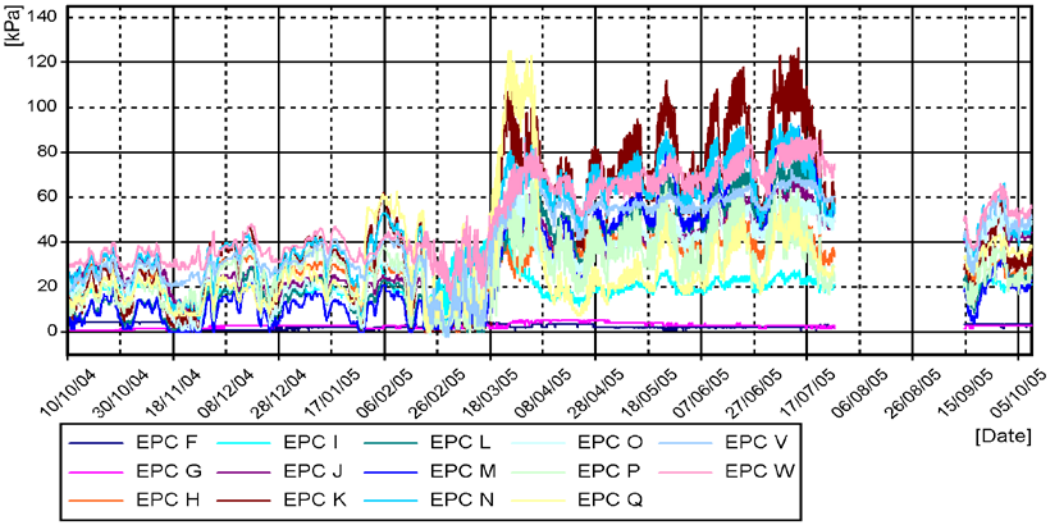

Figure 16 Earth pressures between end screen and embankment during the monitoring period 10.10.2004-10.10.2005

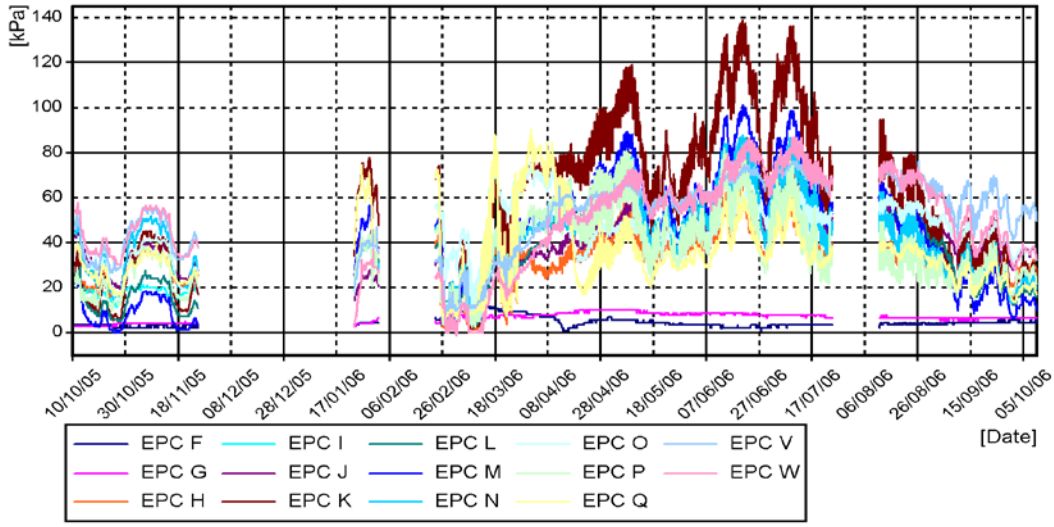

Figure 17 Earth pressures between end screen and embankment during the monitoring period 10.10.2005-10.10.2006

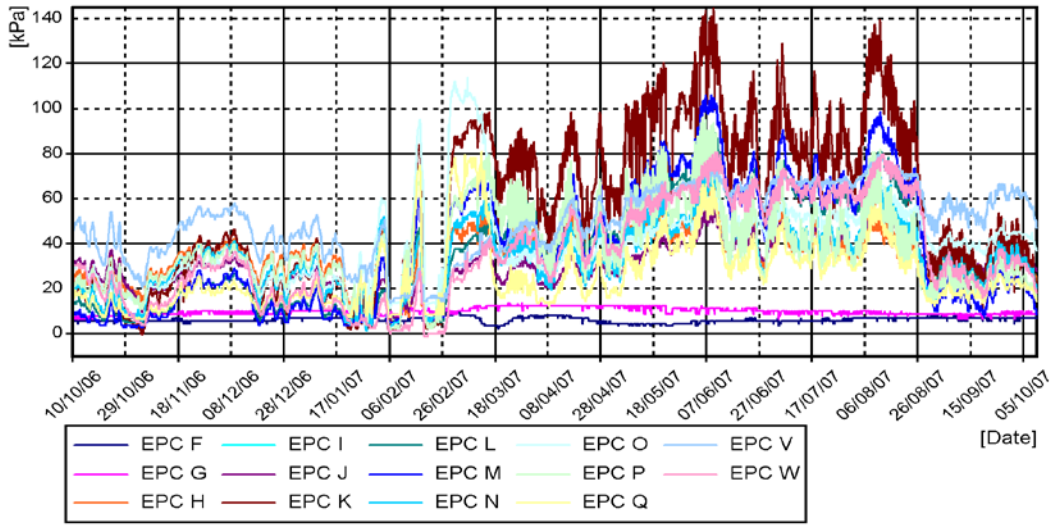

Figure 18 Earth pressures between end screen and embankment during the monitoring period 10.10.2006-10.10.2007

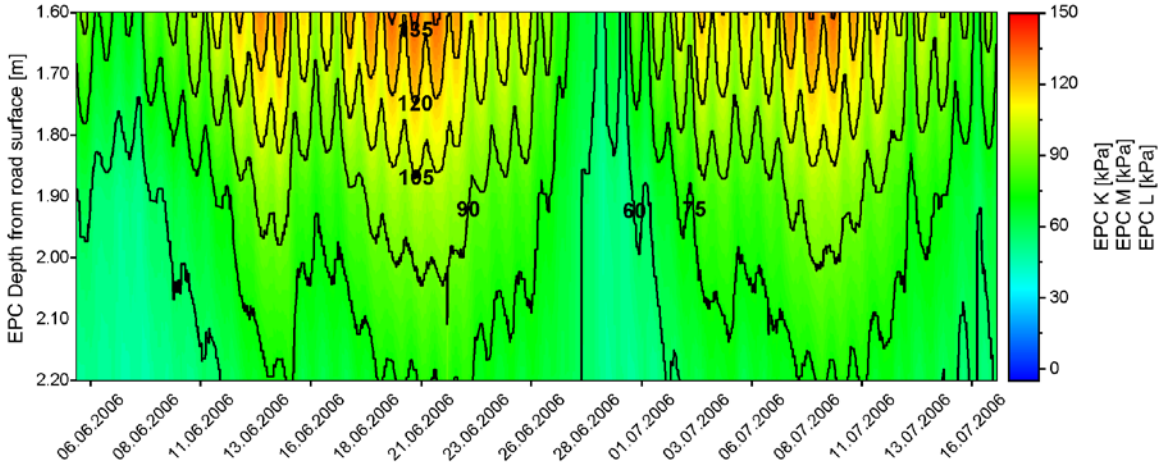

Figure 19 Linearly interpolated earth pressure field at a vertical section based on measured earth pressures between end screen and embankment during the period 9.6.2006-5.7.2006

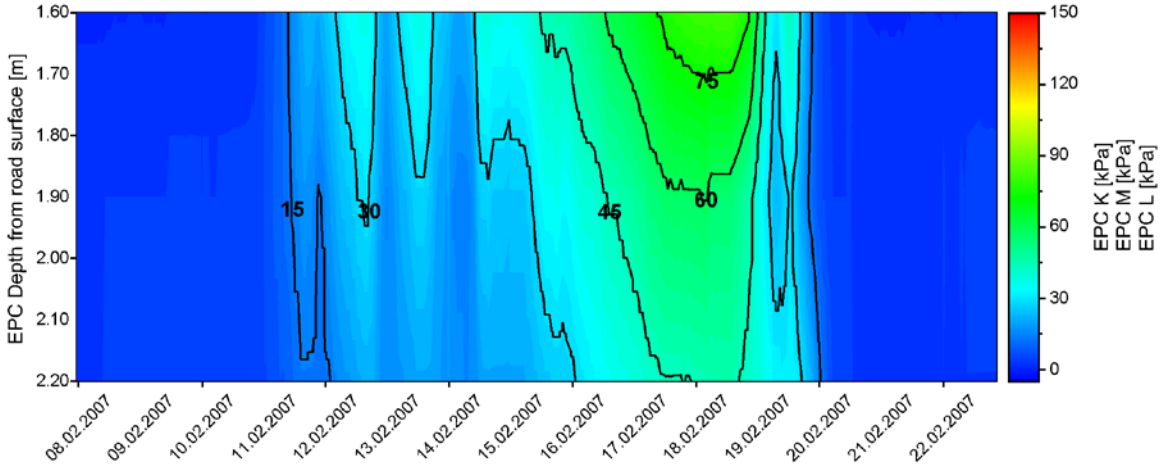

Figure 20 Linearly interpolated earth pressure field at a vertical section based on measured earth pressures between end screen and embankment during the period 9.2.2007-23.2.2007

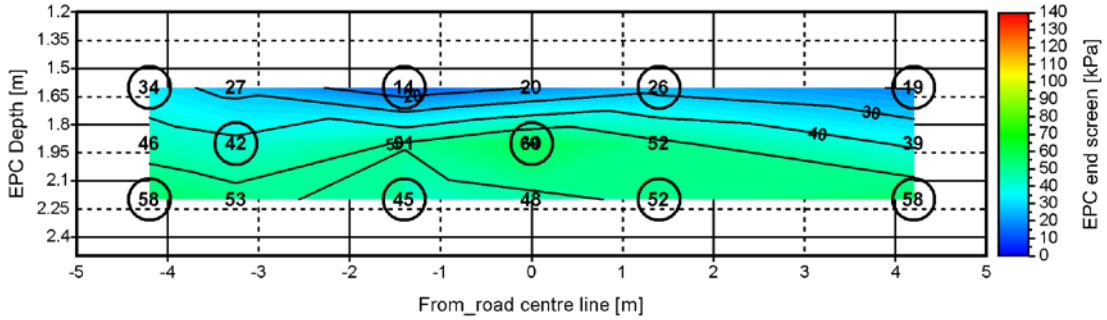

Figure 21 Linearly interpolated earth pressure field at the end screen at 10.10.2003

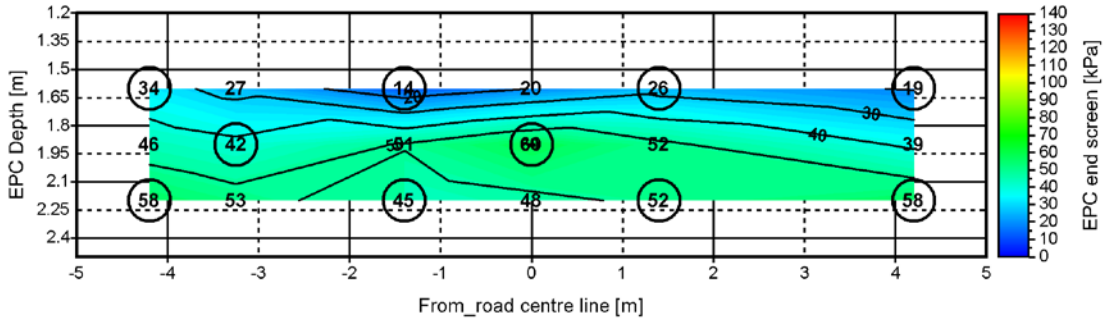

Figure 22 Linearly interpolated earth pressure field at the end screen at 5.11.2003

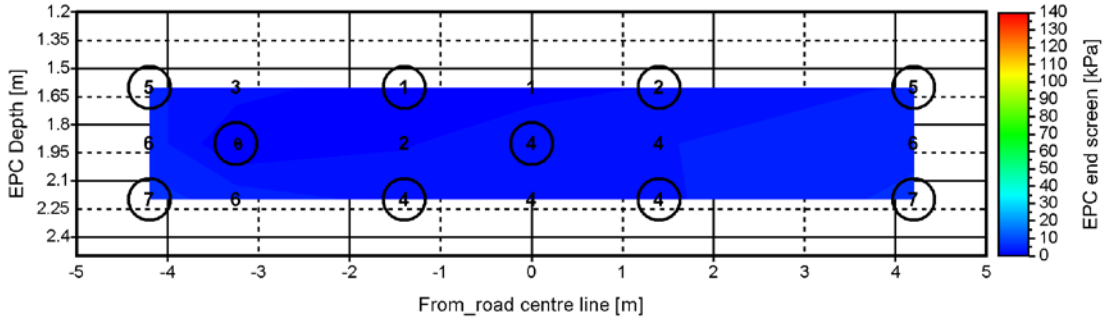

Figure 23 Linearly interpolated earth pressure field at the end screen at 5.2.2004

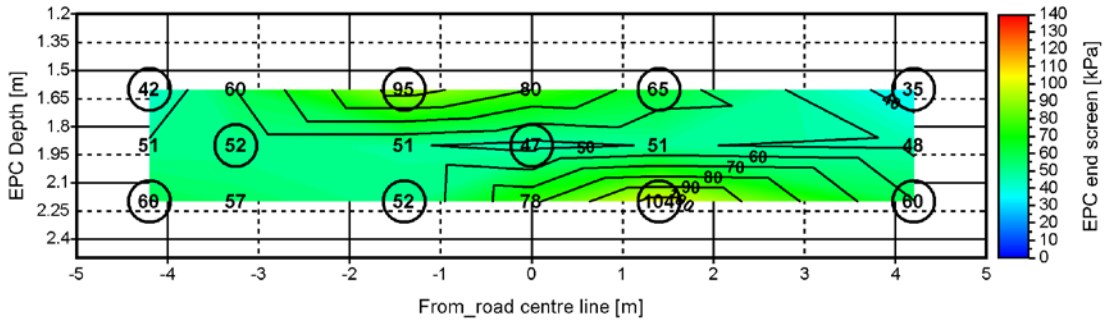

Figure 24 Linearly interpolated earth pressure field at the end screen at 17.2.2004

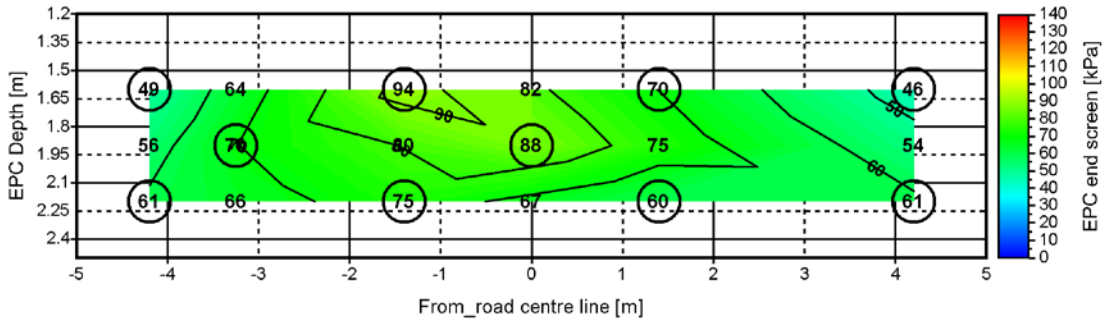

Figure 25 Linearly interpolated earth pressure field at the end screen at 9.5.2004

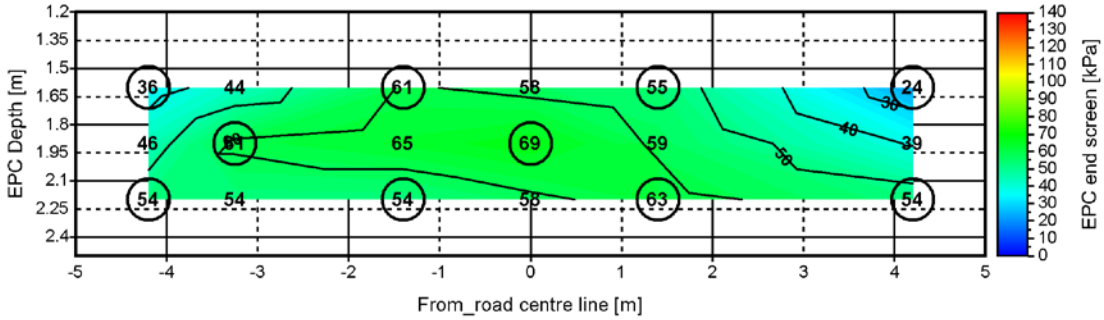

Figure 26 Linearly interpolated earth pressure field at the end screen at 2.8.2004

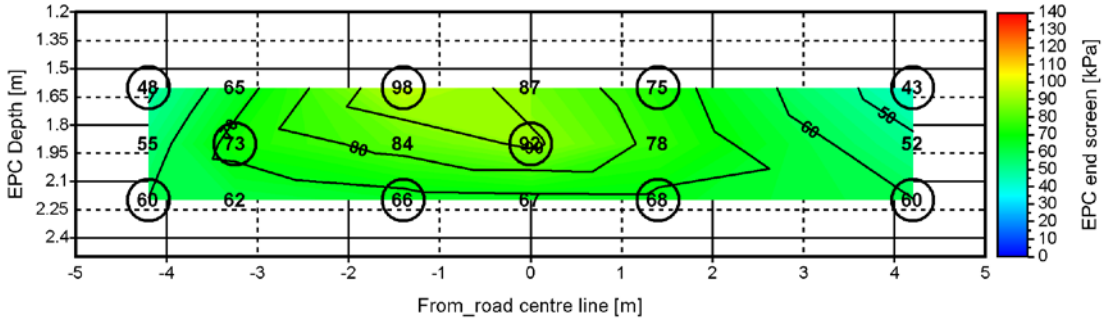

Figure 27 Linearly interpolated earth pressure field at the end screen at 7.8.2004

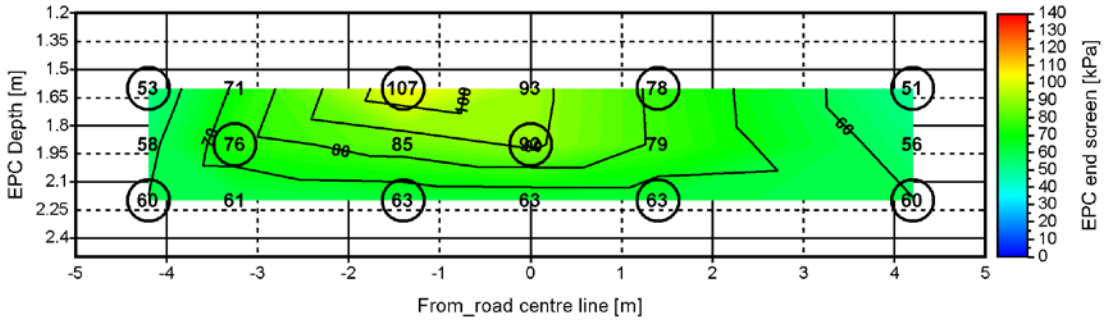

Figure 28 Linearly interpolated earth pressure field at the end screen at 8.8.2004

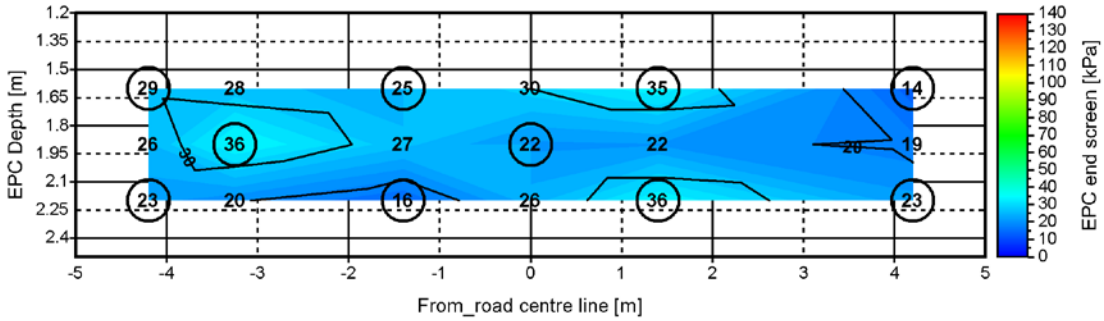

Figure 29 Linearly interpolated earth pressure field at the end screen at 8.10.2004

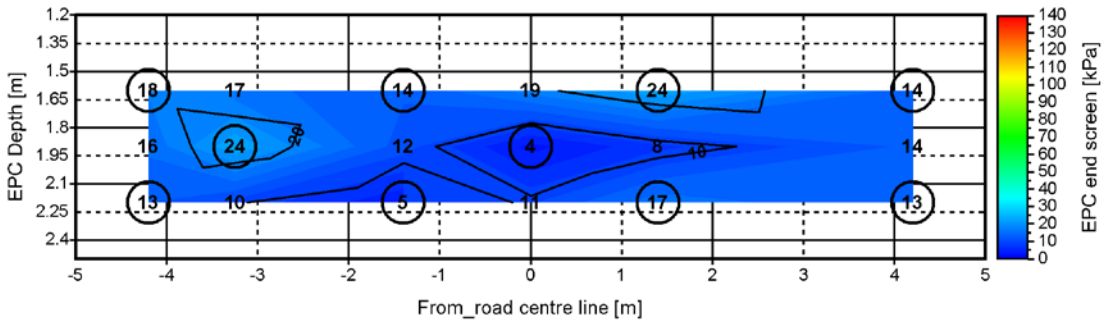

Figure 30 Linearly interpolated earth pressure field at the end screen at 12.10.2004

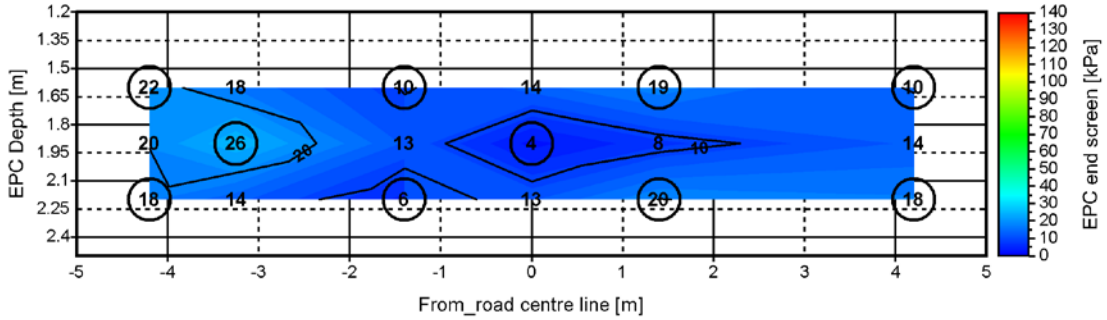

Figure 31 Linearly interpolated earth pressure field at the end screen at 15.11.2004

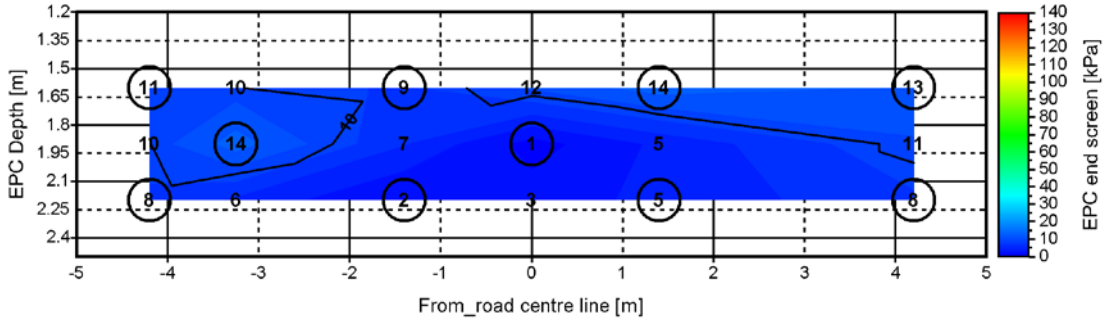

Figure 32 Linearly interpolated earth pressure field at the end screen at 21.11.2004

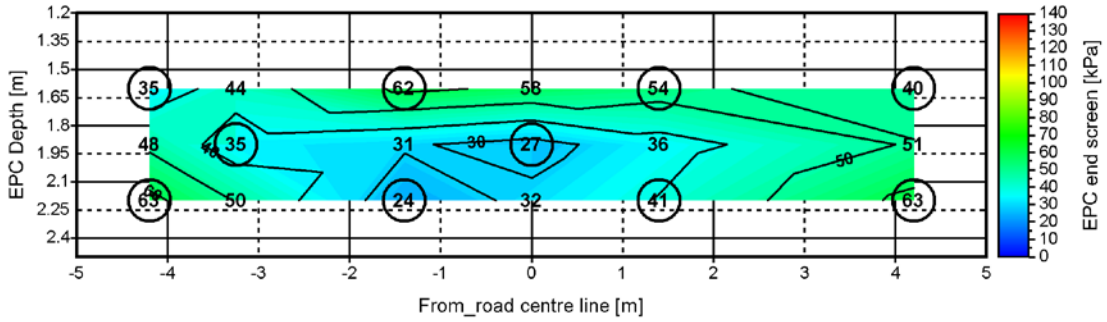

Figure 33 Linearly interpolated earth pressure field at the end screen at 8.3.2005

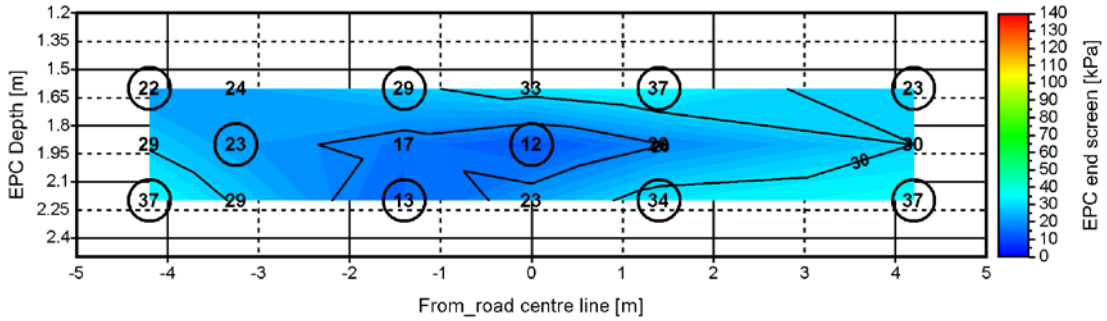

Figure 34 Linearly interpolated earth pressure field at the end screen at 18.3.2005

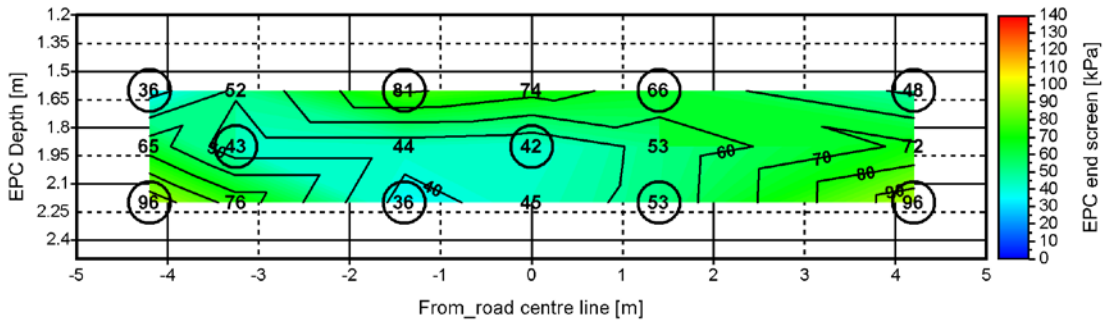

Figure 35 Linearly interpolated earth pressure field at the end screen at 24.3.2005

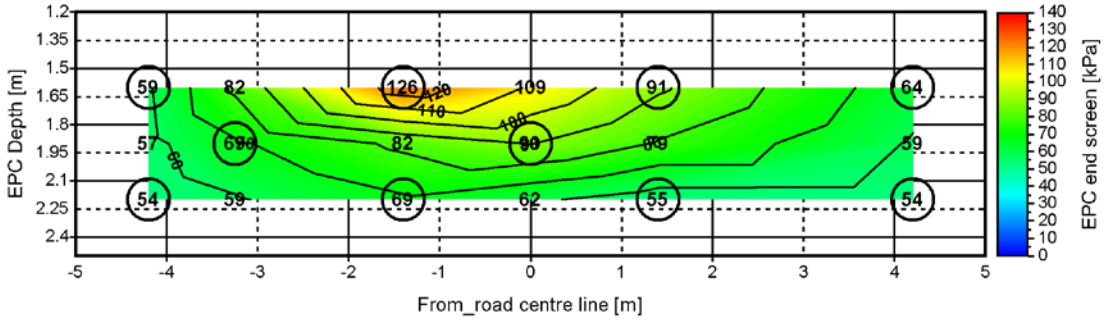

Figure 36 Linearly interpolated earth pressure field at the end screen at 13.7.2005

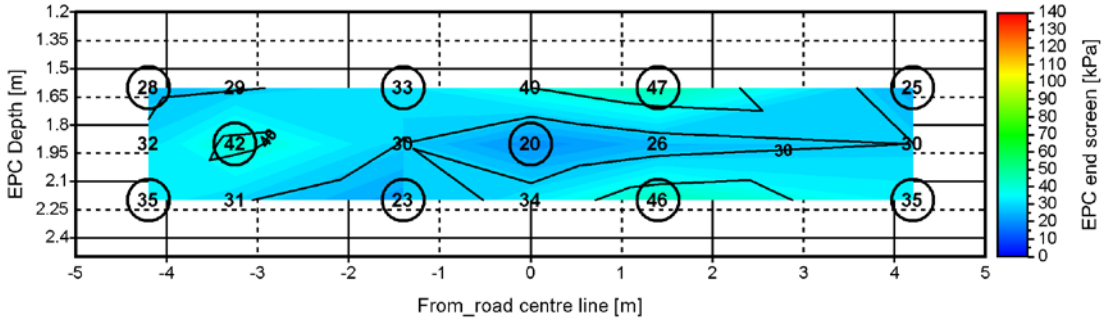

Figure 37 Linearly interpolated earth pressure field at the end screen at 6.10.2005

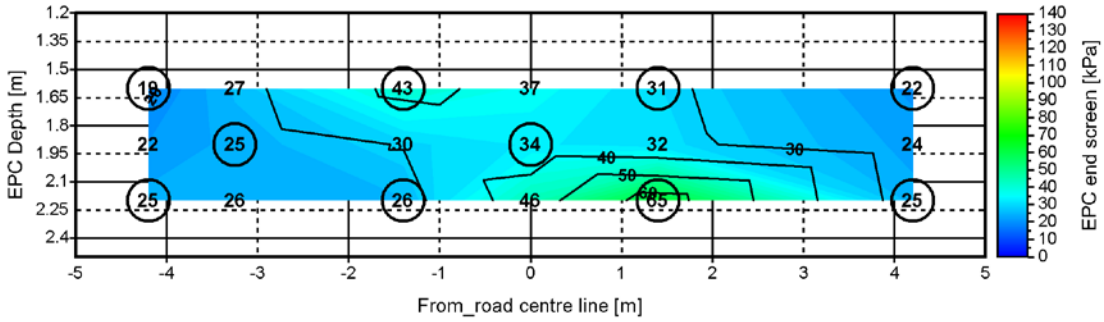

Figure 38 Linearly interpolated earth pressure field at the end screen at 27.3.2006

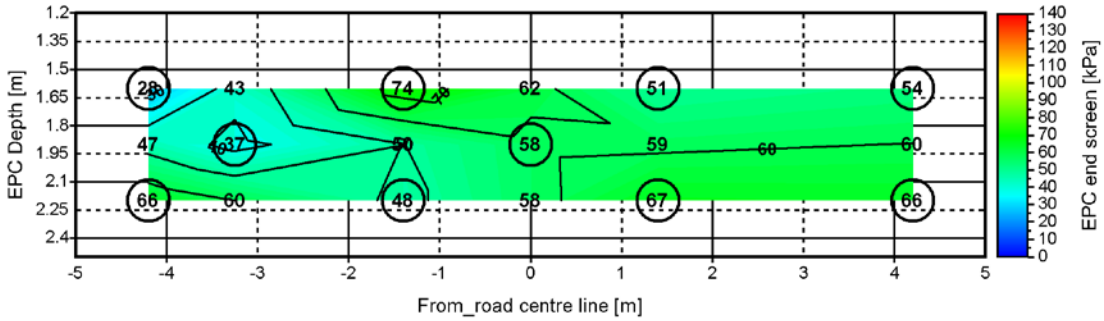

Figure 39 Linearly interpolated earth pressure field at the end screen at 31.3.2006

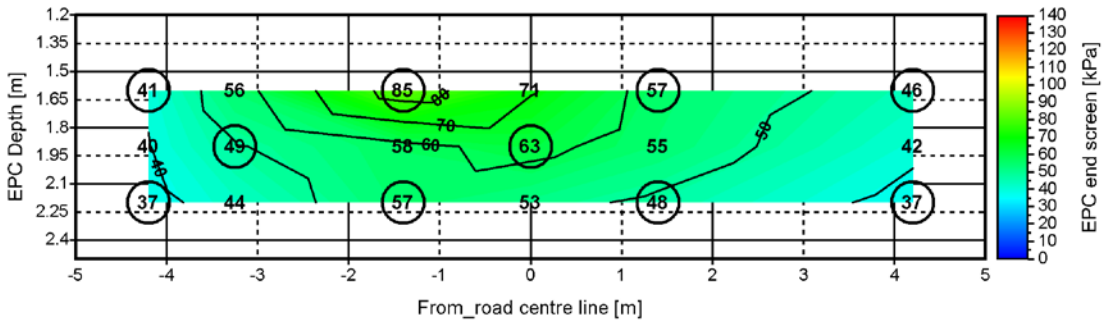

Figure 40 Linearly interpolated earth pressure field at the end screen at 10.6.2006

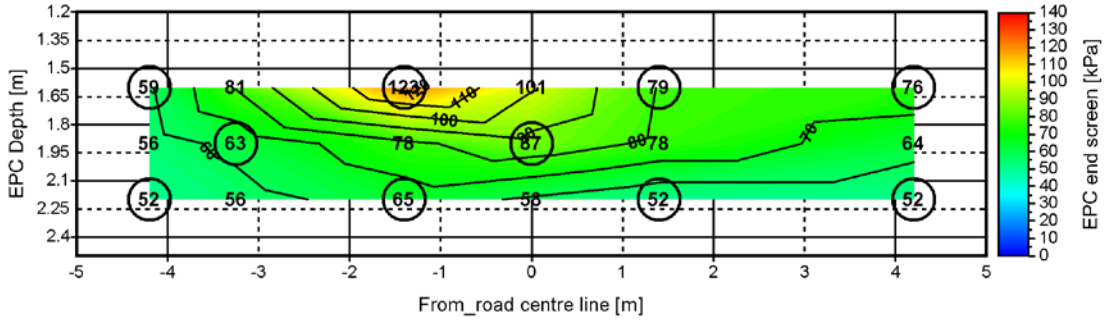

Figure 41 Linearly interpolated earth pressure field at the end screen at 12.6.2006

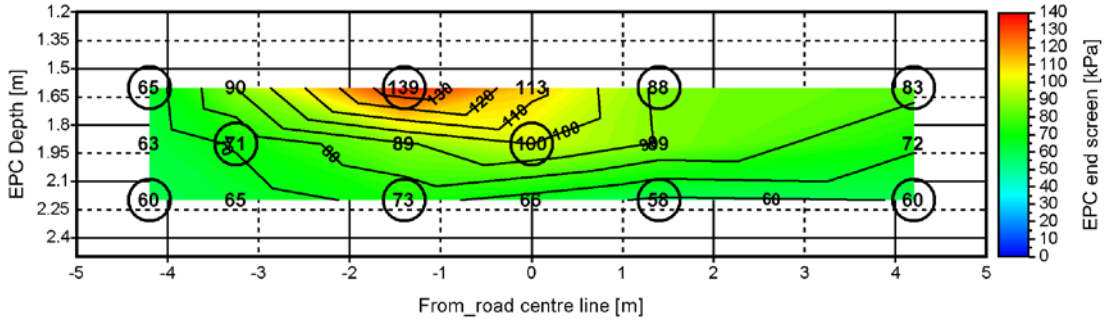

Figure 42 Linearly interpolated earth pressure field at the end screen at 20.6.2006

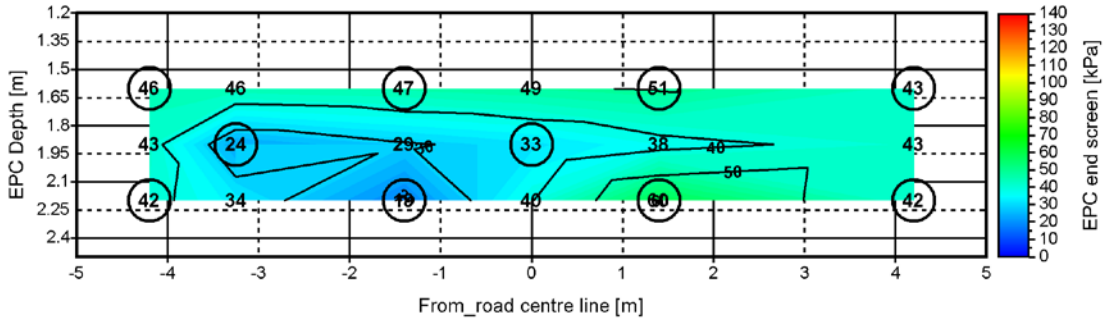

Figure 43 Linearly interpolated earth pressure field at the end screen at 3.2.2007

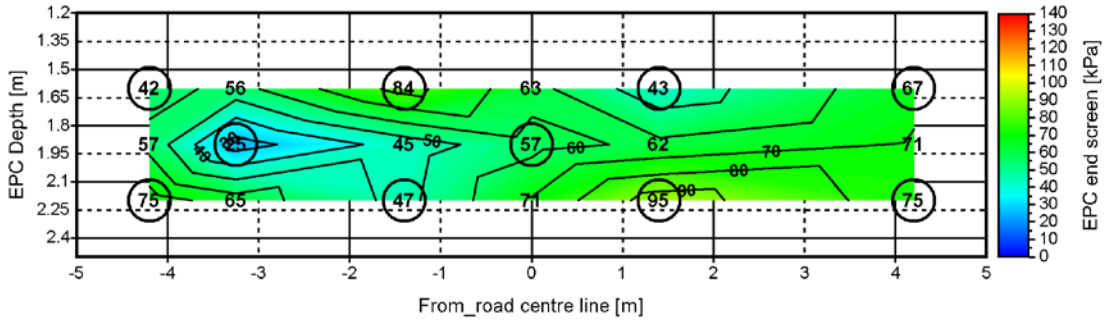

Figure 44 Linearly interpolated earth pressure field at the end screen at 18.2.2007

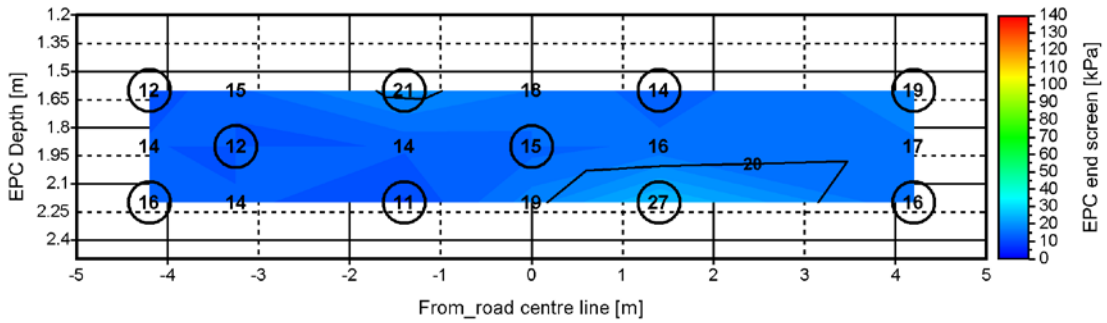

Figure 45 Linearly interpolated earth pressure field at the end screen at 26.2.2007

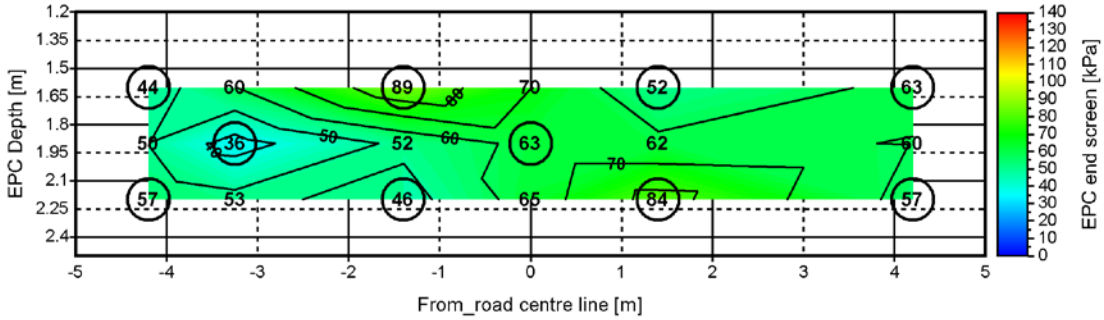

Figure 46 Linearly interpolated earth pressure field at the end screen at 3.3.2007

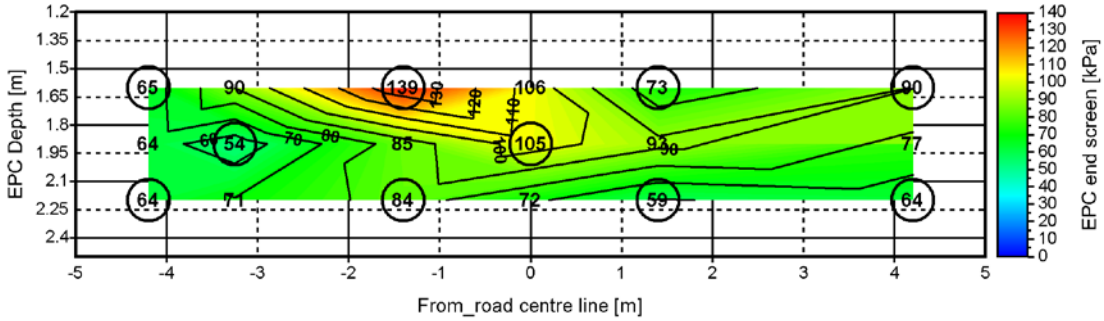

Figure 47 Linearly interpolated earth pressure field at the end screen at 8.6.2007

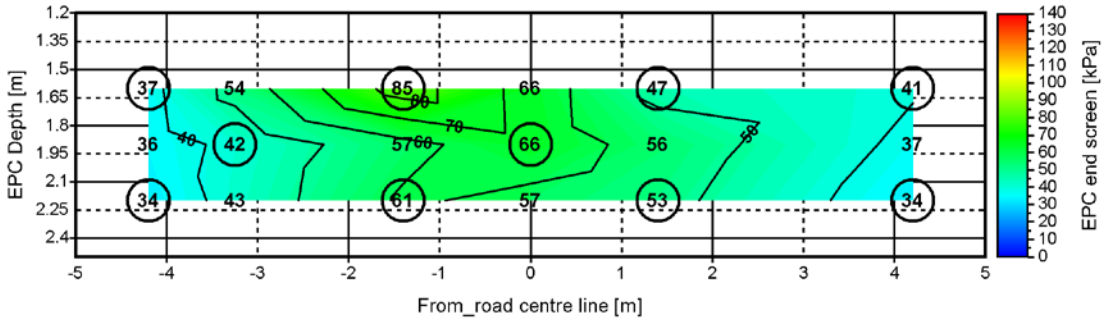

Figure 48 Linearly interpolated earth pressure field at the end screen at 5.8.2007

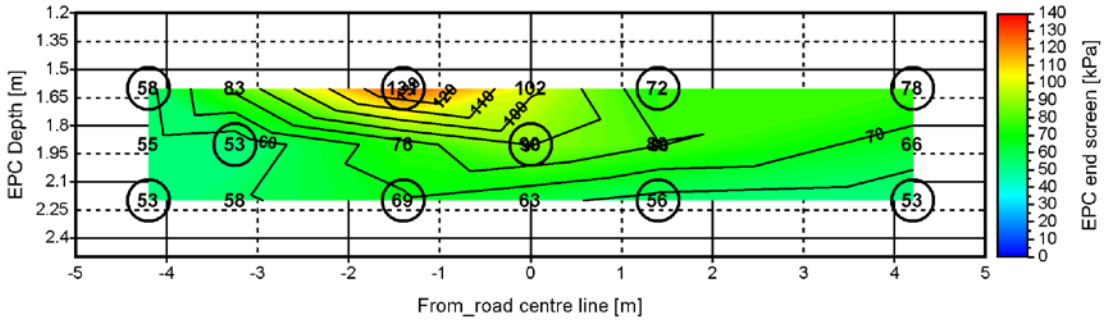

Figure 49 Linearly interpolated earth pressure field at the end screen at 7.8.2007

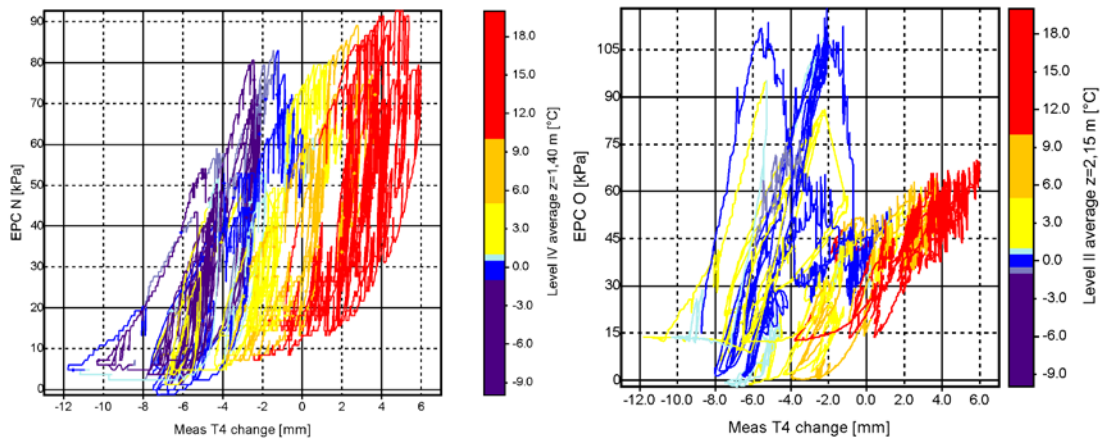

Figures 50 Earth pressure-displacement relation and soil temperature at the locations of EPCs N (z = 1.6 m) and O (z = 2.2 m). Displacement is the displacement of abutment T4.

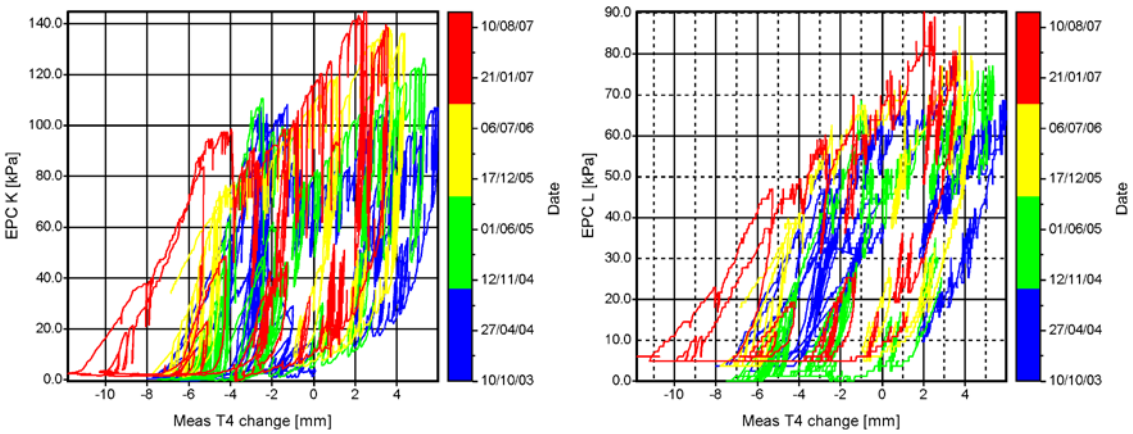

Figures 51 Earth pressure-displacement relation and monitoring years at the locations of EPCs L (z = 1.6 m) and L (z = 2.2 m). Displacement is the displacement of abutment T4.

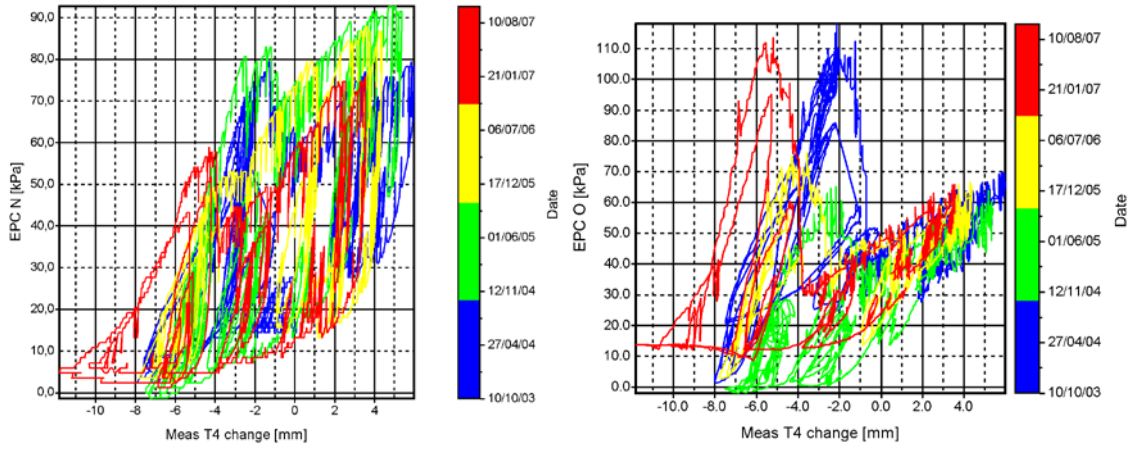

Figures 52 Earth pressure-displacement relation and monitoring years at the locations of EPCs N (z = 1.6 m) and O (z = 2.2 m). Displacement is the displacement of abutment T4.

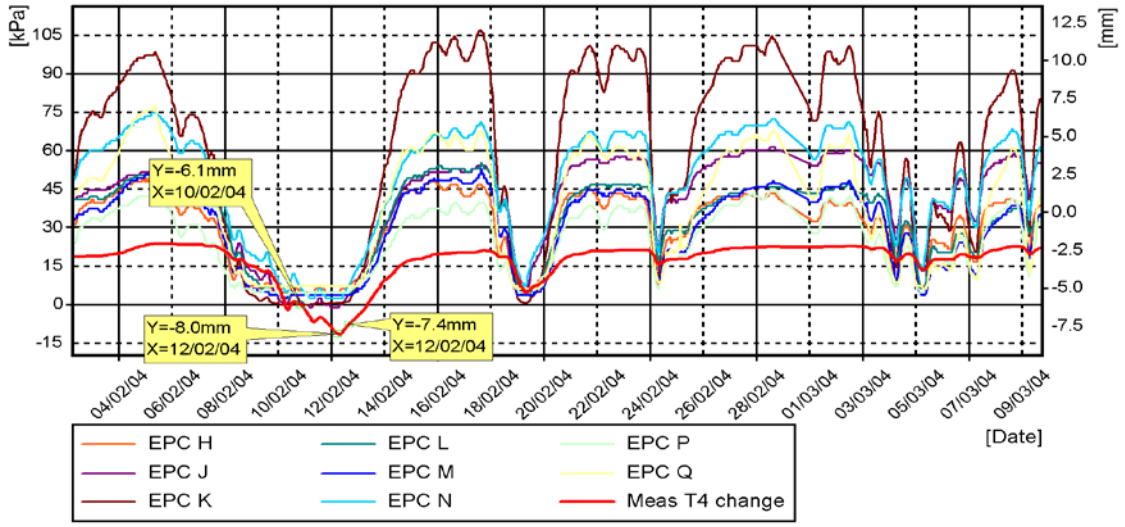

Figure 53 Earth pressures between end screen and embankment and displacement stage of abutment T4 during the period 30.1.2004-10.3.2004

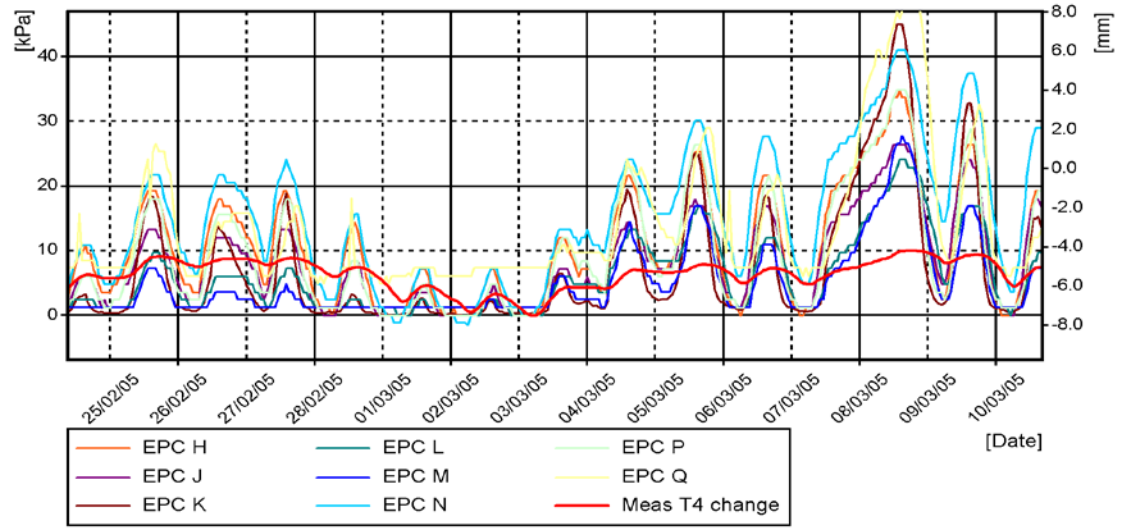

Figure 54 Earth pressures between end screen and embankment and displacement stage of abutment T4 during the period 30.1.2005-10.3.2005

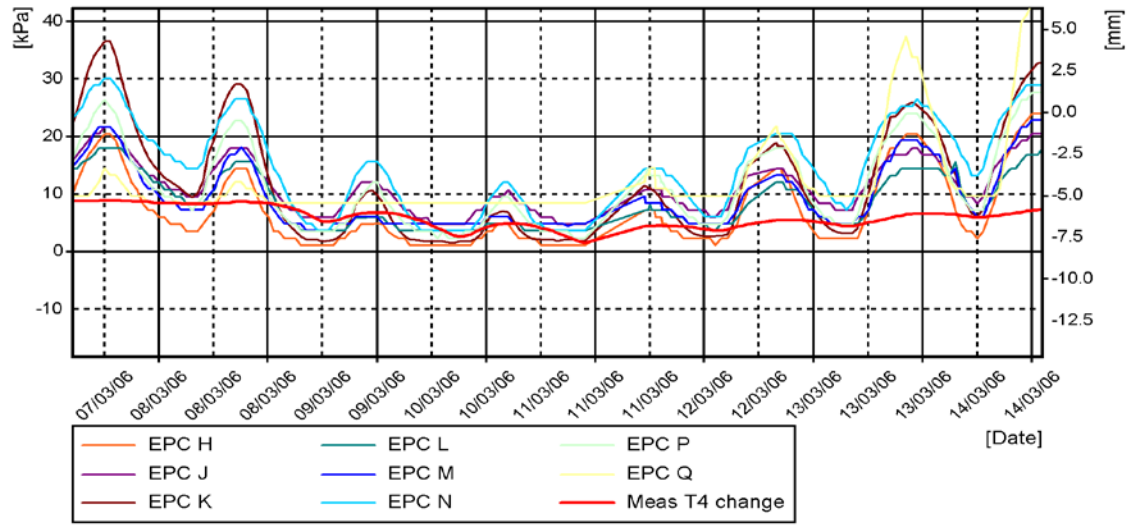

Figure 55 Earth pressures between end screen and embankment and displacement stage of abutment T4 during the period 7.3.2006-14.3.2006

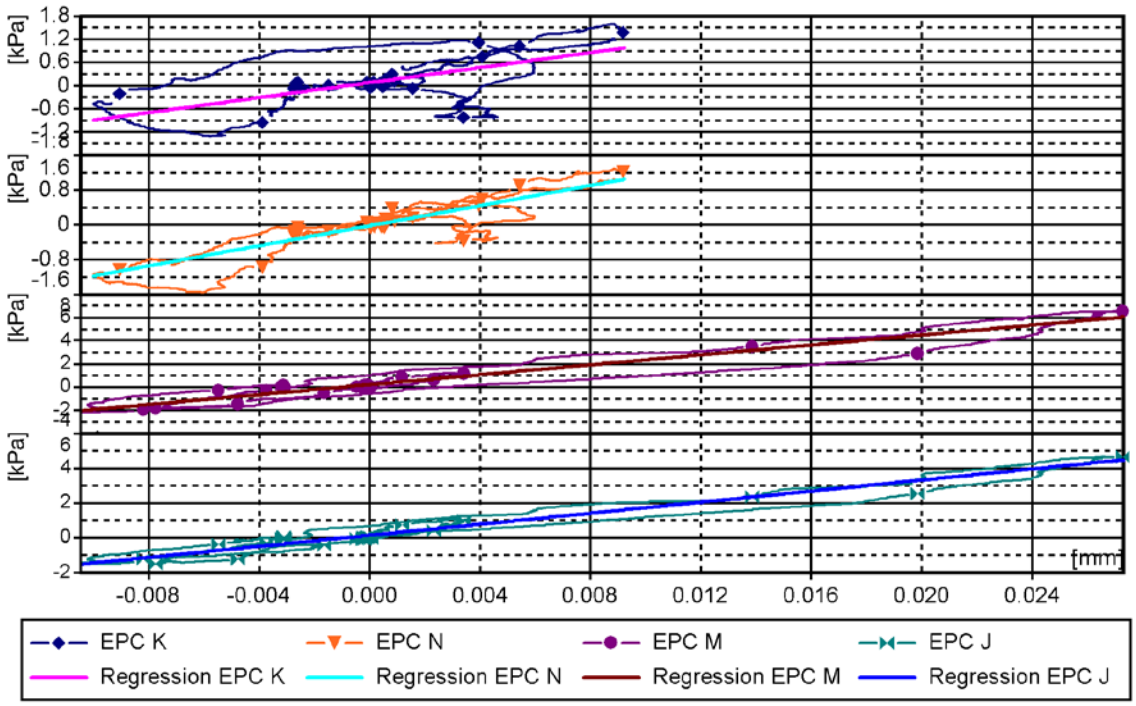

Figure 56 Earth pressure-displacement relation in the overrun test with loading vehicle speed 17 m/s at the locations of EPCs K (z =1.6 m), M (z = 1.9 m), N (z = 1.6 m) and J (z = 1.9 m).

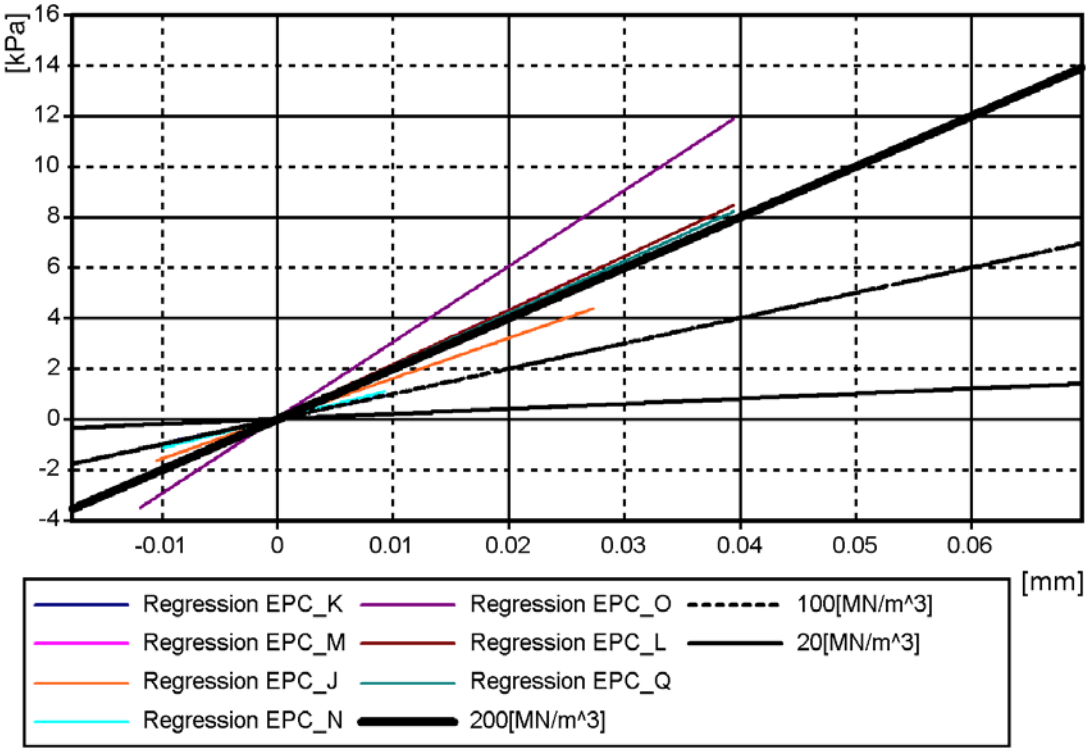

Figure 57 Earth pressure-displacement relation in the overrun test with loading vehicle speed 17 m/s at the locations of EPCs J (z =1.9 m), K (z =1.6 m), L, M (z = 1.9 m), N (z = 1.6 m), O (z = 2.2 m) and Q (z = 2.2 m).

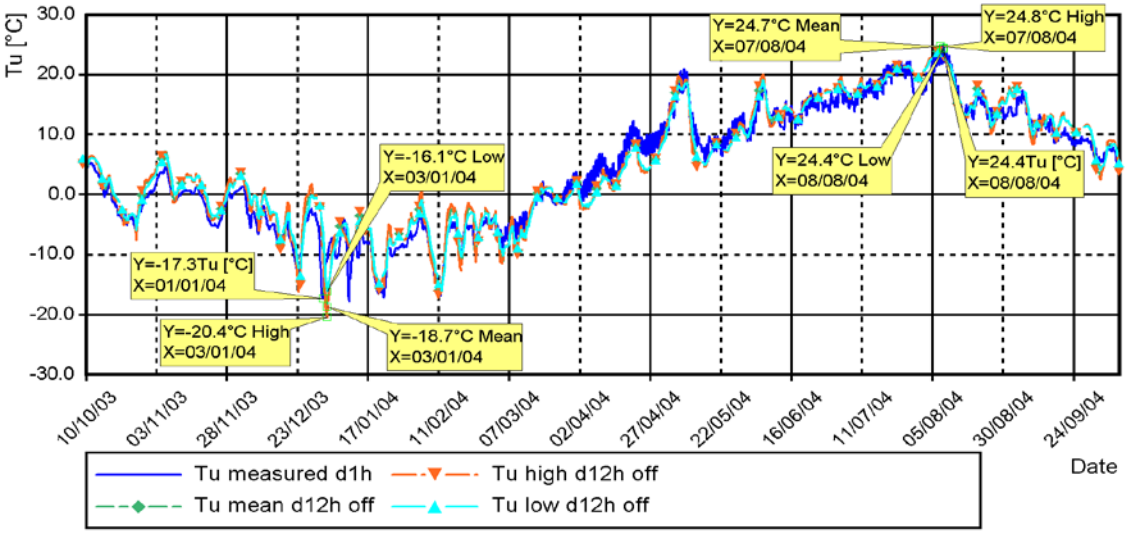

Figure 58 Calculated and measured T_U with time step d12h, different constant $A_{+/-}$ values and offset value in calculation during first monitoring year

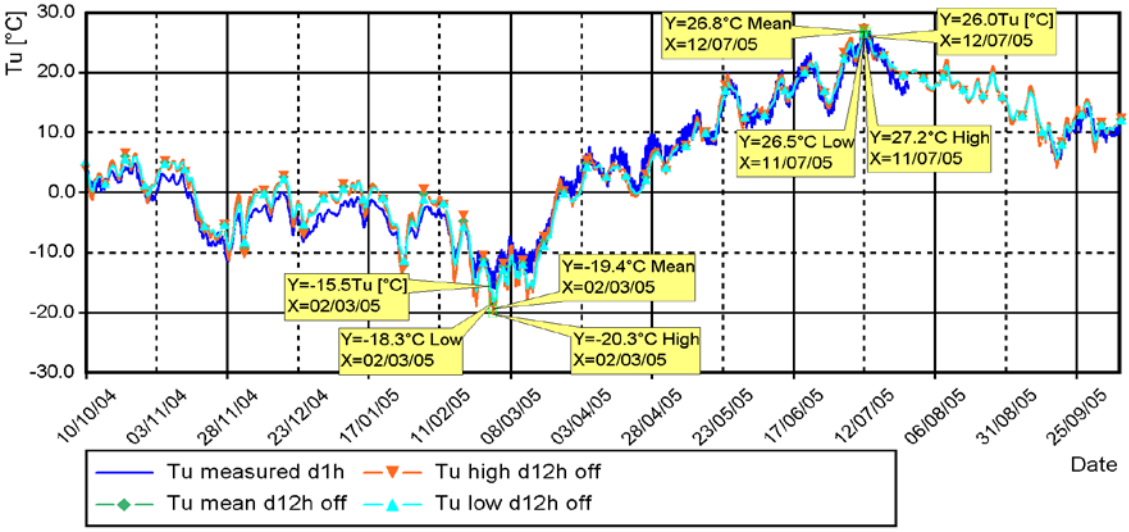

Figure 59 Calculated and measured T_U with time step d12h, different constant $A_{+/-}$ values and offset value in calculation during second monitoring year

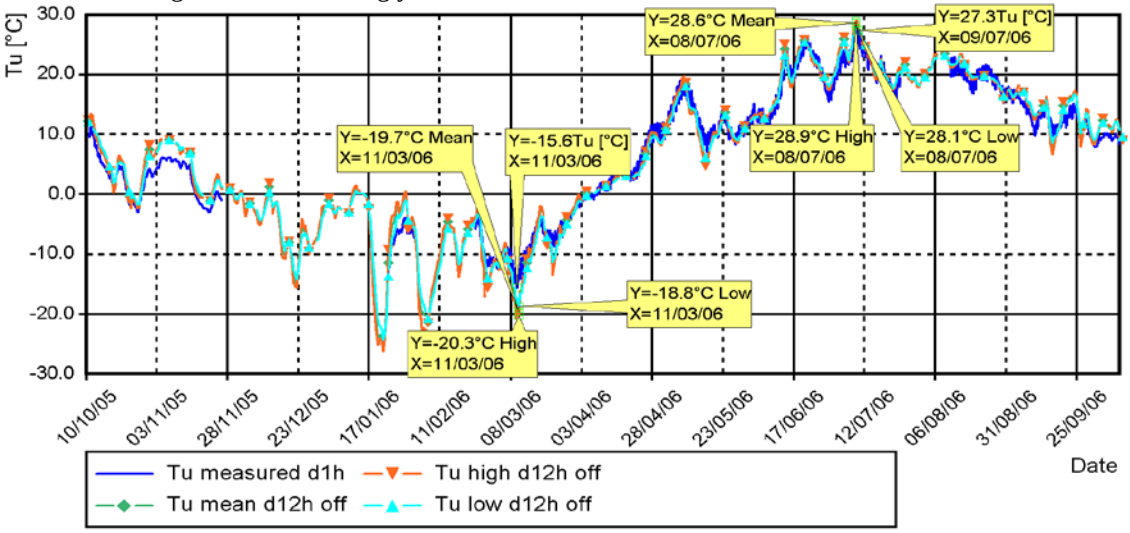

Figure 60 Calculated and measured T_U with time step d12h, different constant $A_{+/-}$ values and offset value in calculation during third monitoring year

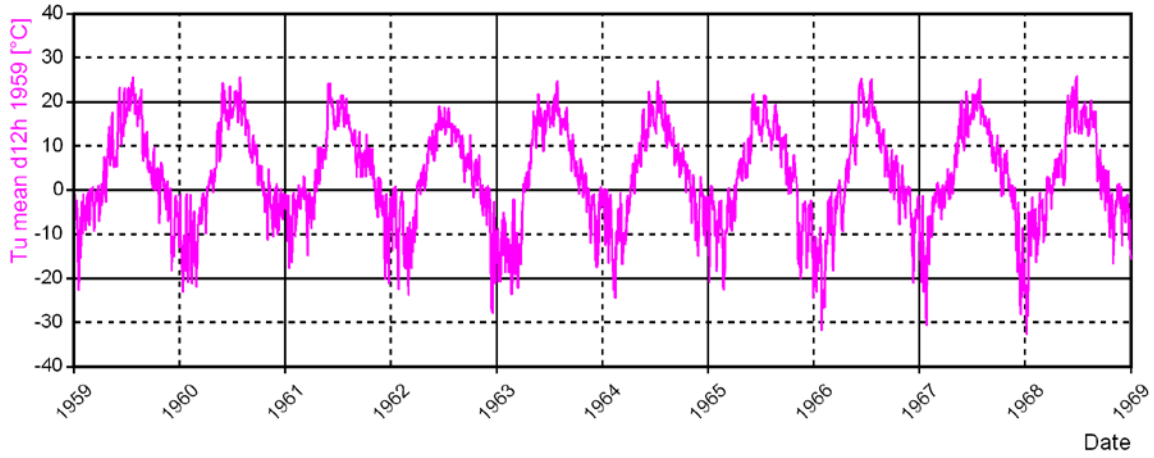

Figure 61 Calculated T_U values from 1959 to 1969

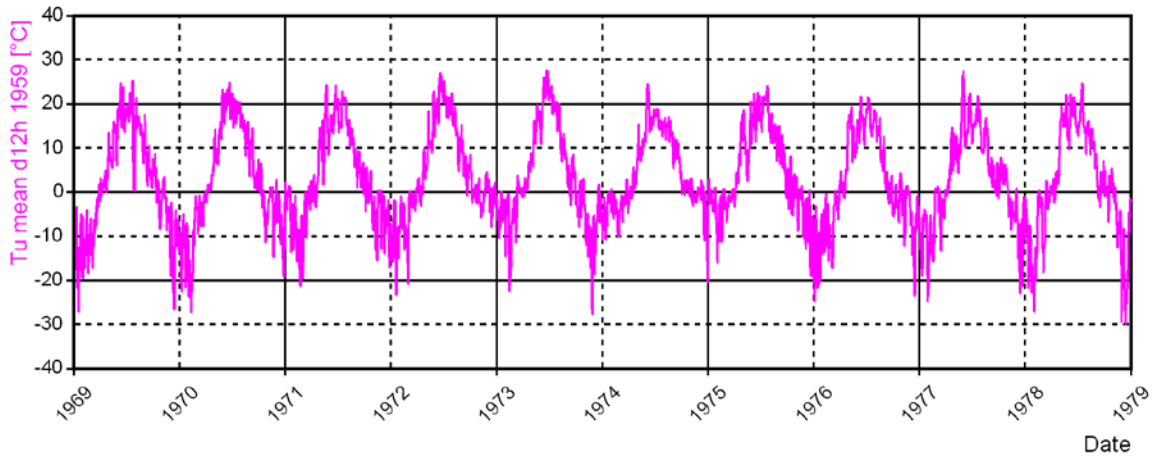

Figure 62 Calculated T_U values from 1969 to 1979

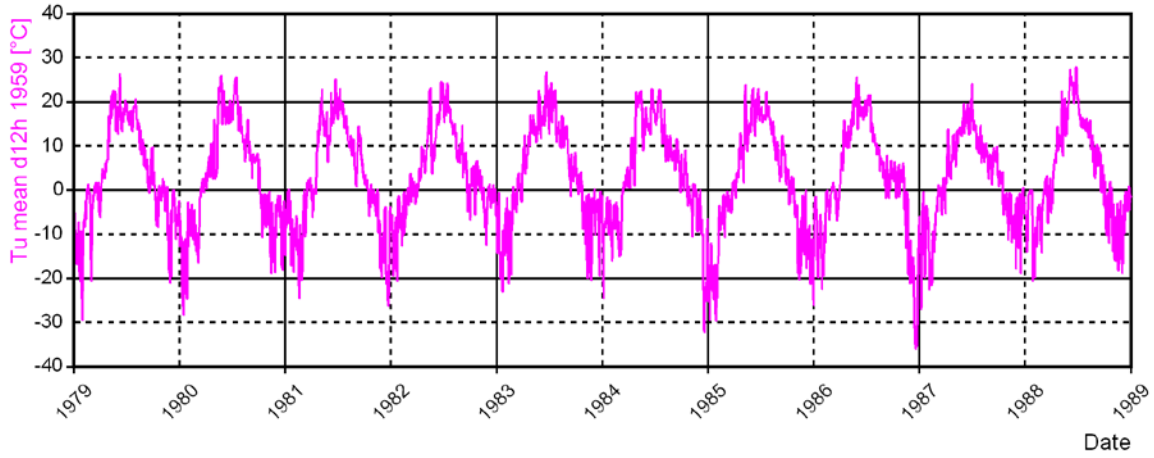

Figure 63 Calculated T_U values from 1979 to 1989

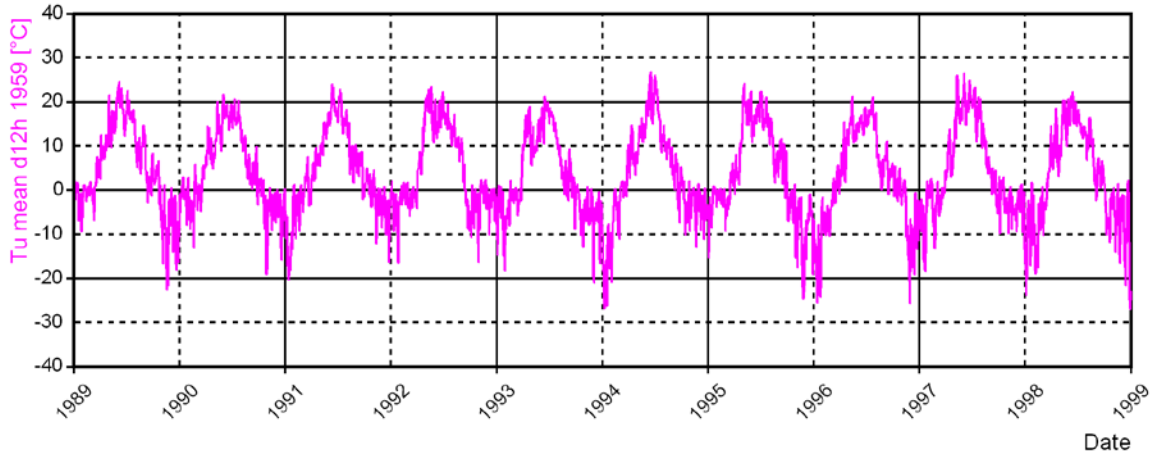

Figure 64 Calculated T_U values from 1989 to 1999

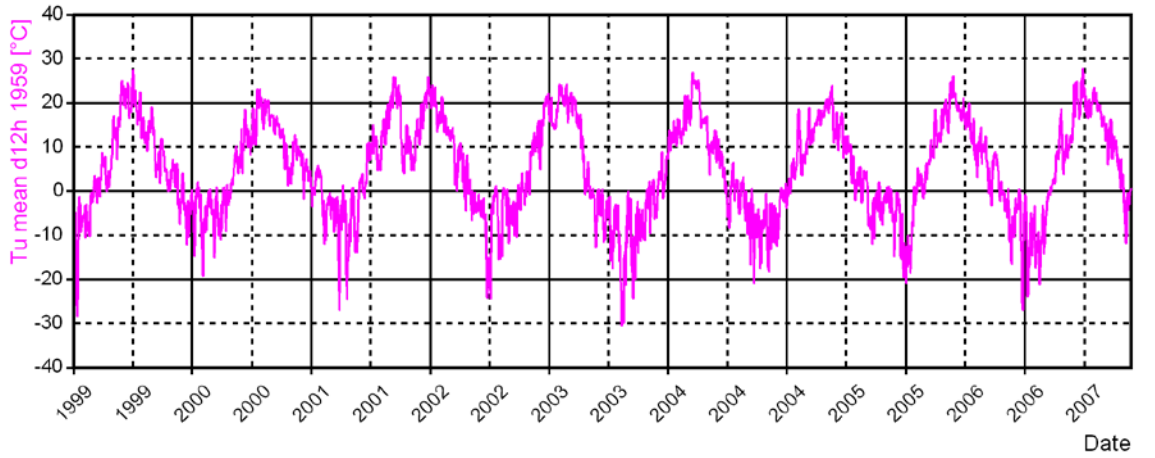

Figure 65 Calculated T_U values from 1999 to 2007

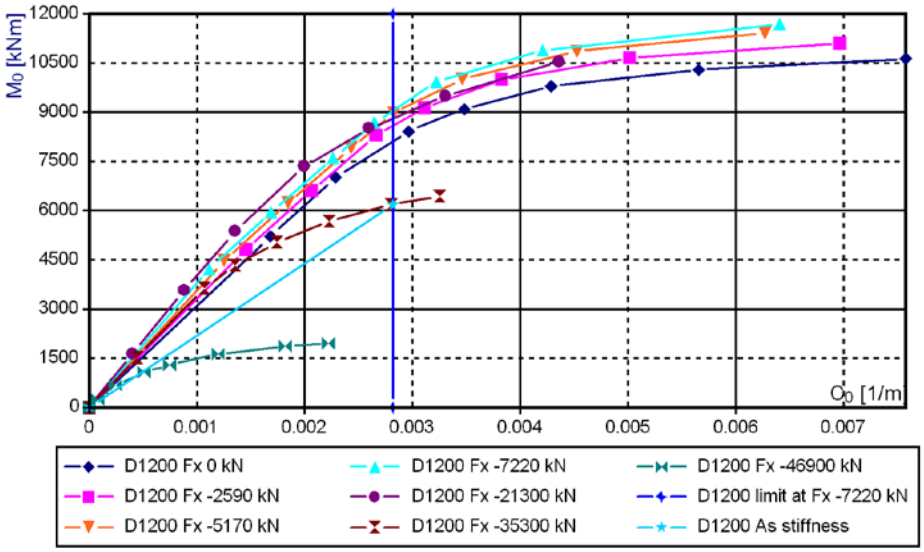

Figure 66 Moment-curvature relation for composite cross section D*t=1200*16 at stage D_0. $N_{0,opt}$ = 7220 kN

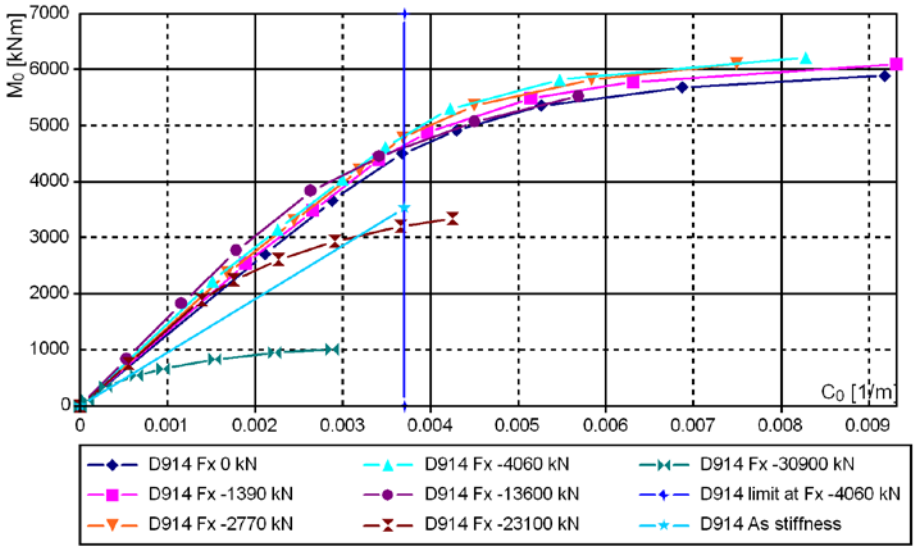

Figure 67 Moment-curvature relation for composite cross section D*t=914*16 at stage D_0. $N_{0,opt}$ = 4060 kN

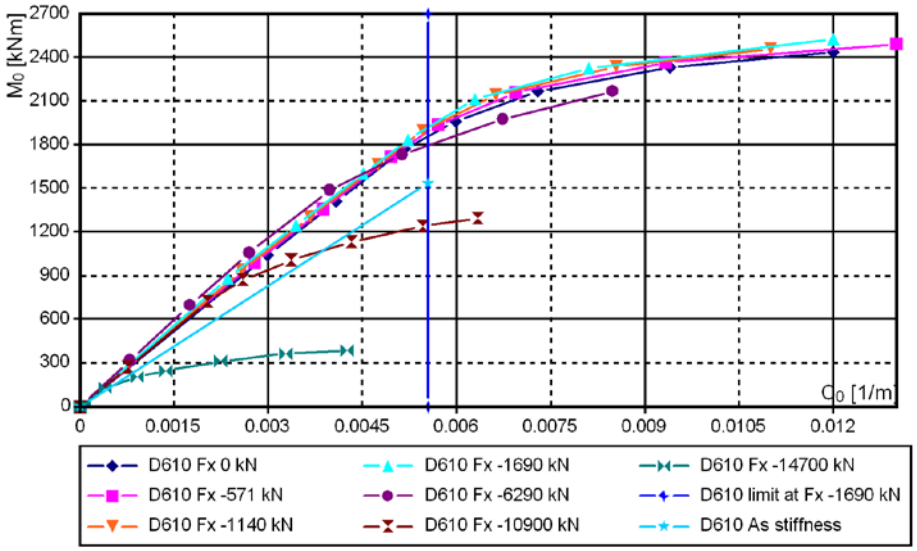

Figure 68 Moment-curvature relation for composite cross section D*t=610*16 at stage D_0. $N_{0,opt}$ = 1890 kN

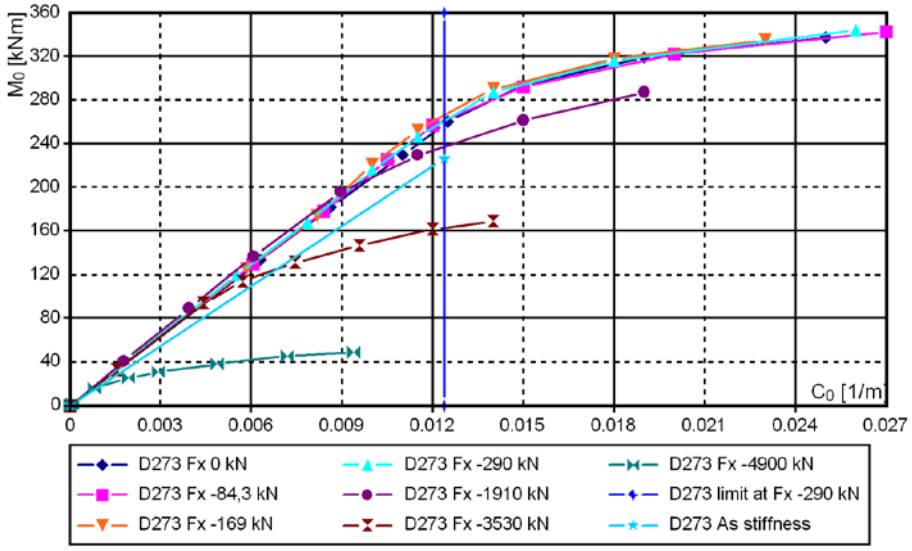

Figure 69 Moment-curvature relation for composite cross section D*t=273*12.5 at stage D_0. $N_{0,opt}$ = 290 kN

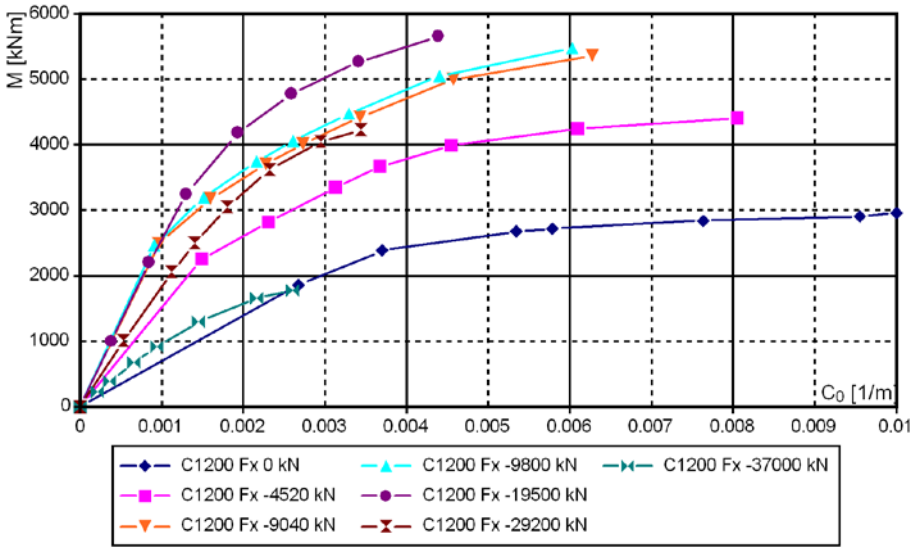

Figure 70 Moment-curvature relation for concrete cross section D=1200

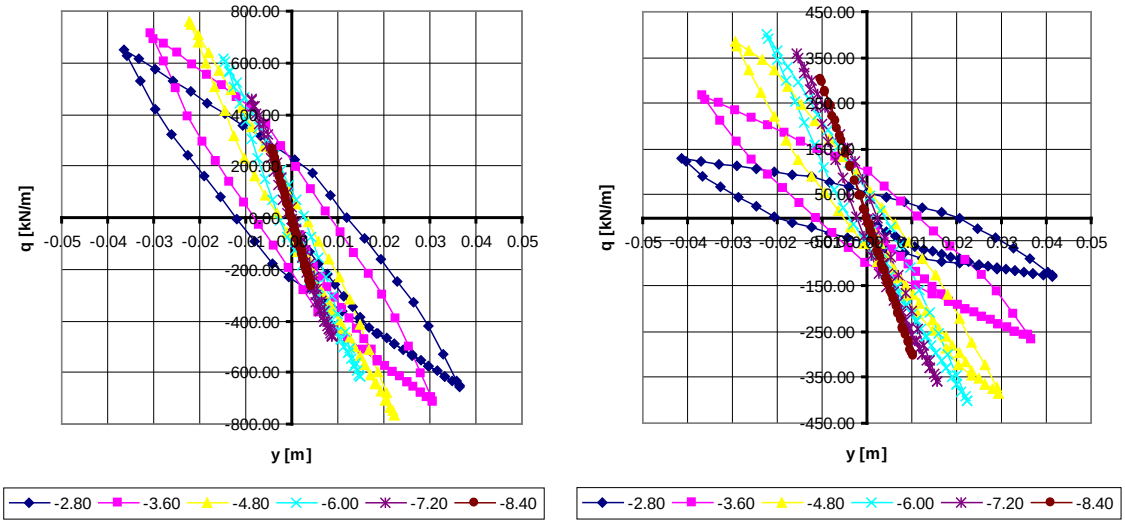

Figures 71 q-y loops at different depths Z. Left: T1_D1200_R_NS_EXP model where s = 0.30. Right: T1_D1200_R_WS_SHR model where s = 2.36.

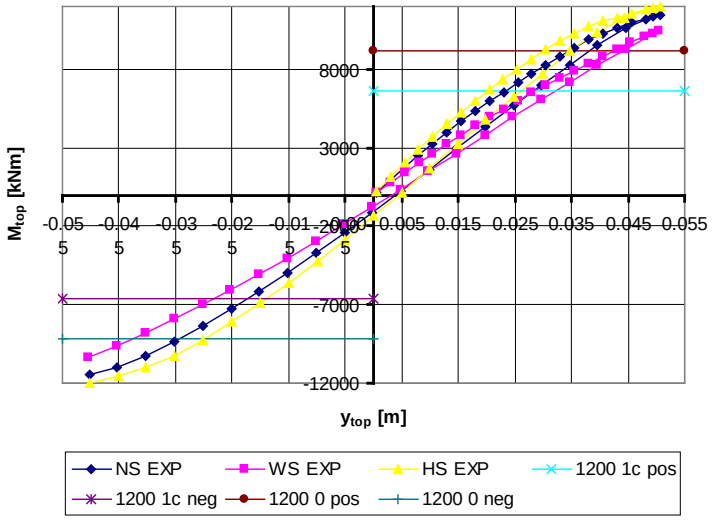

Figure 72 M_{top} as function of y_{top} in different soil types in T1_1200_R _EXP models

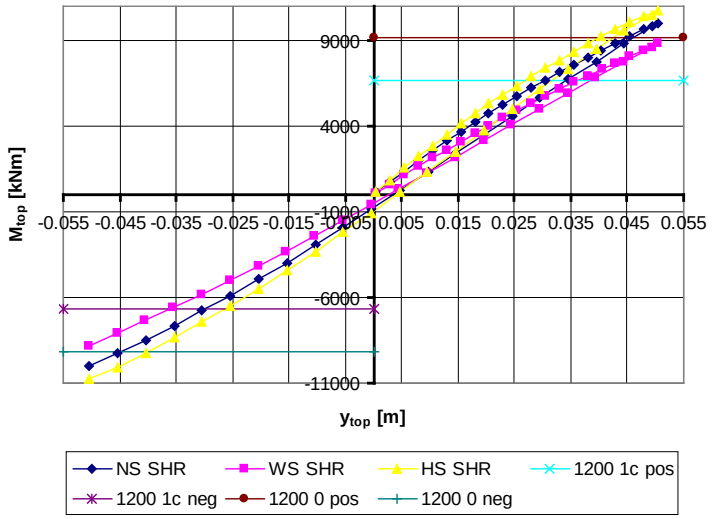

Figure 73 M_{top} as function of y_{top} in different soil types in T1_1200_R _SHR models

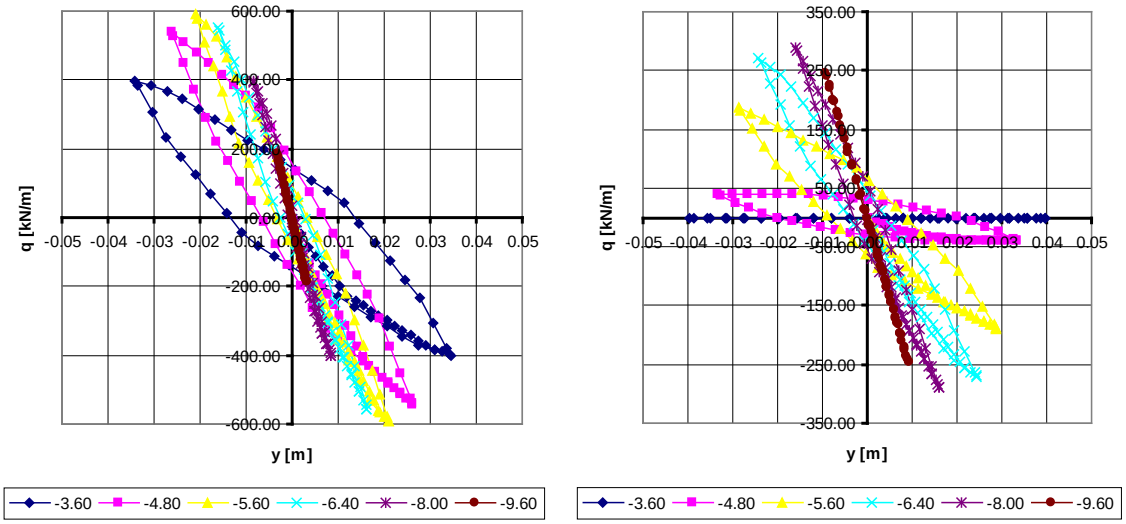

Figures 74 q-y loops at different depths Z. Left: T2_D1200_R_NS_EXP model where s = 2.25. Right: T2_D1200_R_WS_SHR model where s = 4.66.

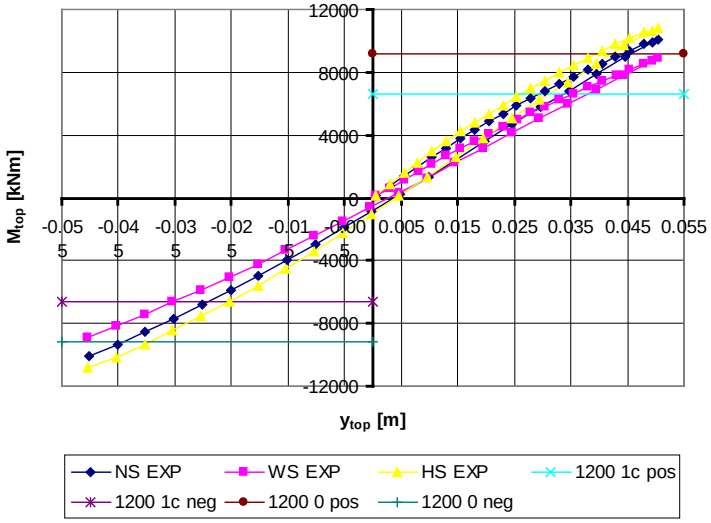

Figure 75 M_{top} as function of y_{top} in different soil types in T2_1200_R _EXP models

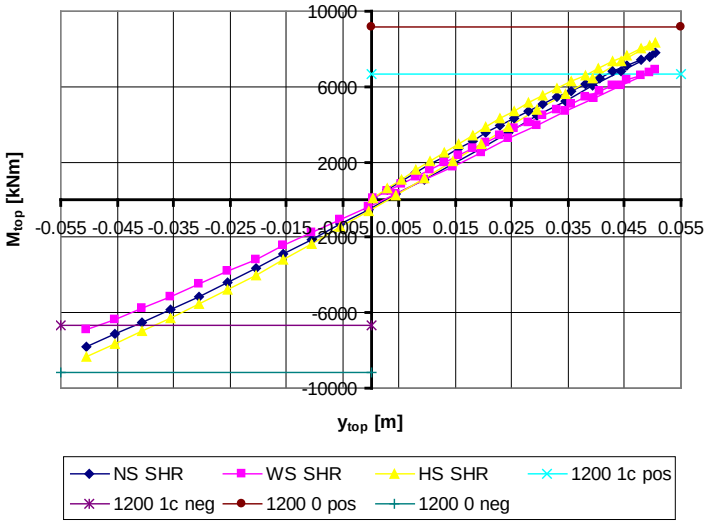

Figure 76 M_{top} as function of ytop in different soil types in T2_1200_R _SHR models

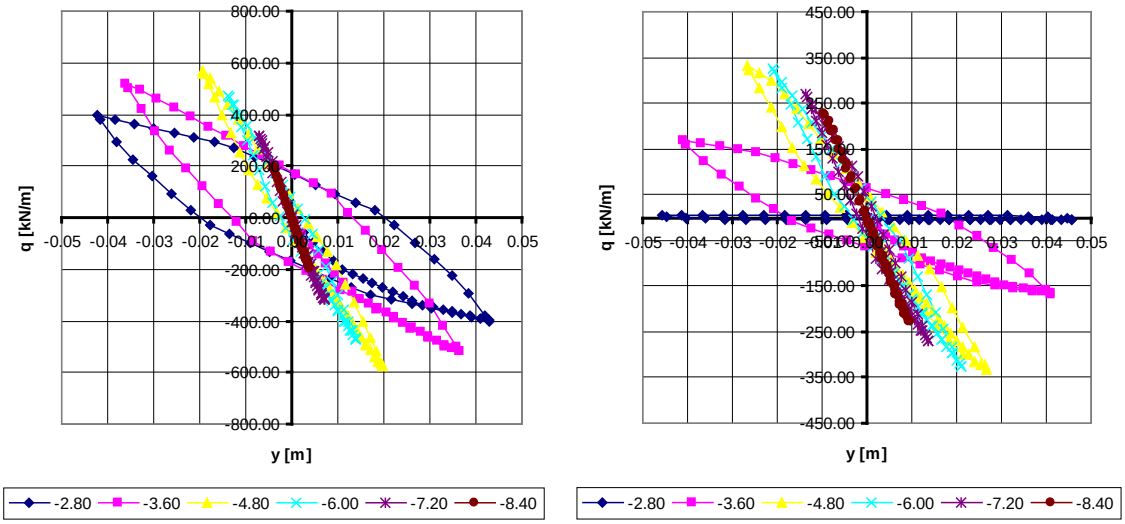

Figures 77 q-y loops at different depths Z. Left: T1_D914_R_NS_EXP model where s = 0.014. Right: T1_D914_R_WS_SHR model where s = 1.58.

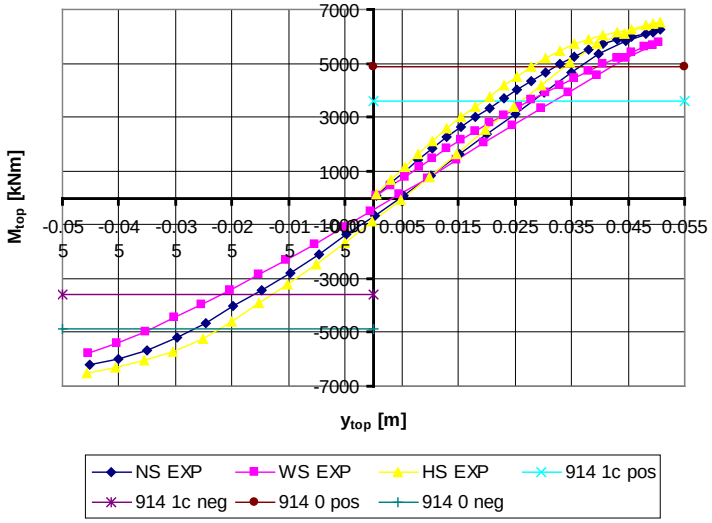

Figure 78 M_{top} as function of y_{top} in different soil types in T1_914_R _EXP models

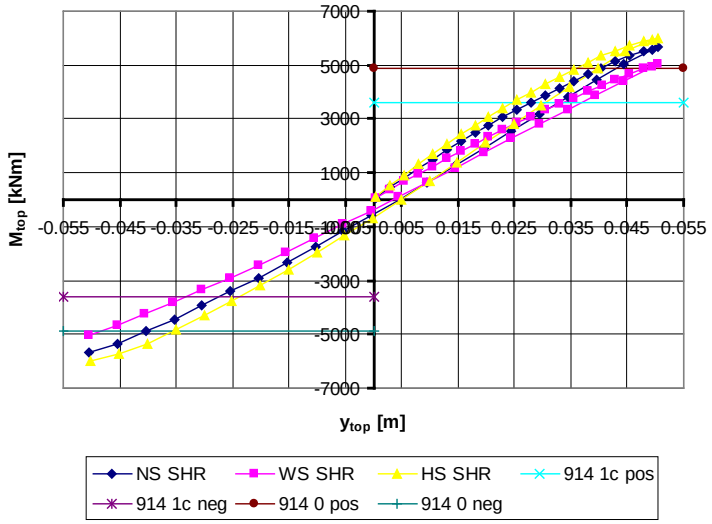

Figure 79 M_{top} as function of ytop in different soil types in T1_914_R _SHR models

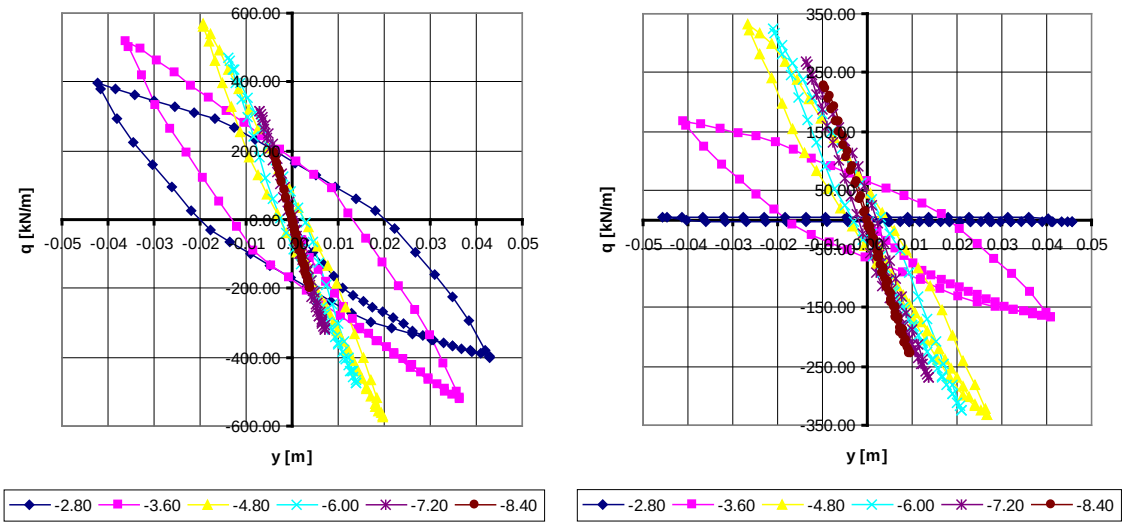

Figure 80 q-y loops at different depths Z. Left: T2_D914_R_NS_EXP model where s = 2.25. Right: T2_D914_R_WS_SHR model where s = 4.17.

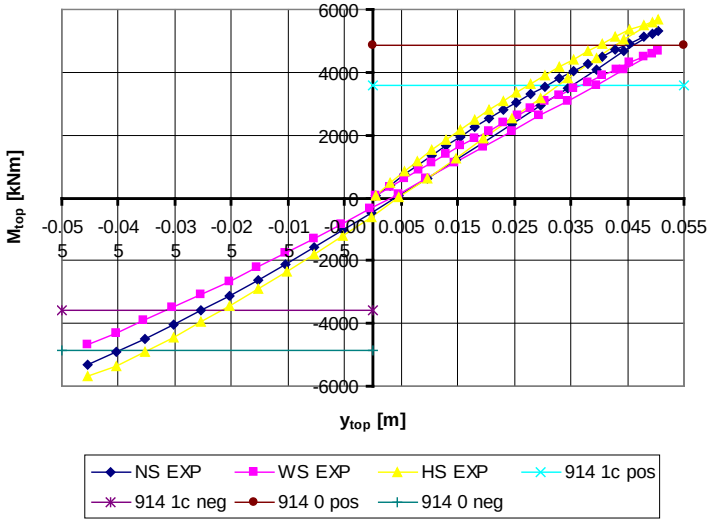

Figure 81 M_{top} as function of ytop in different soil types in T2_914_R _EXP models

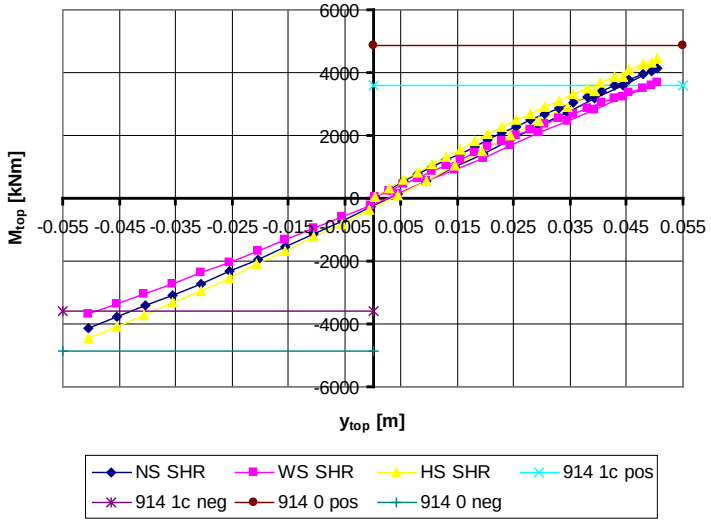

Figure 82 M_{top} as function of ytop in different soil types in T2_914_R _SHR models

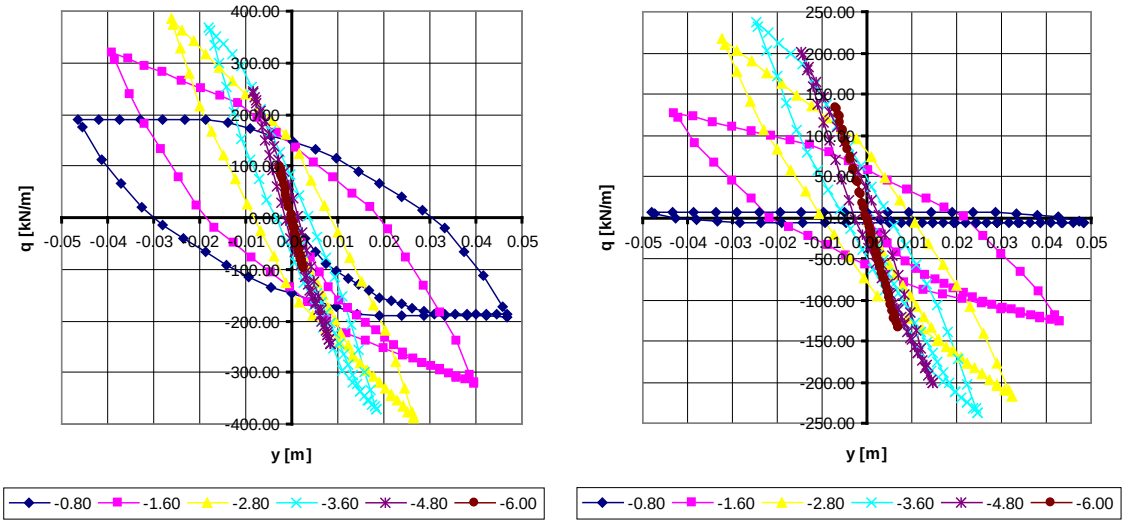

Figure 83 q-y loops at different depths Z. Left: T1_D610_R_NS_EXP model where s = -0.29. Right: T1_D610_R_WS_SHR model where s = 0.76.

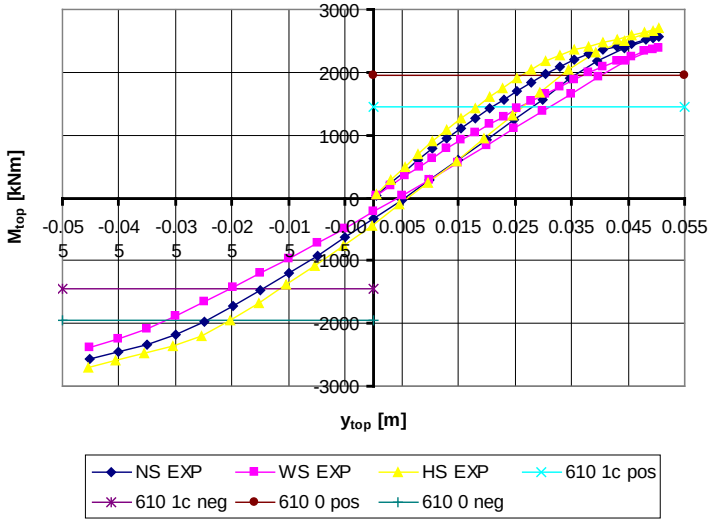

Figure 84 M_{top} as function of ytop in different soil types in T1_610_R _EXP models

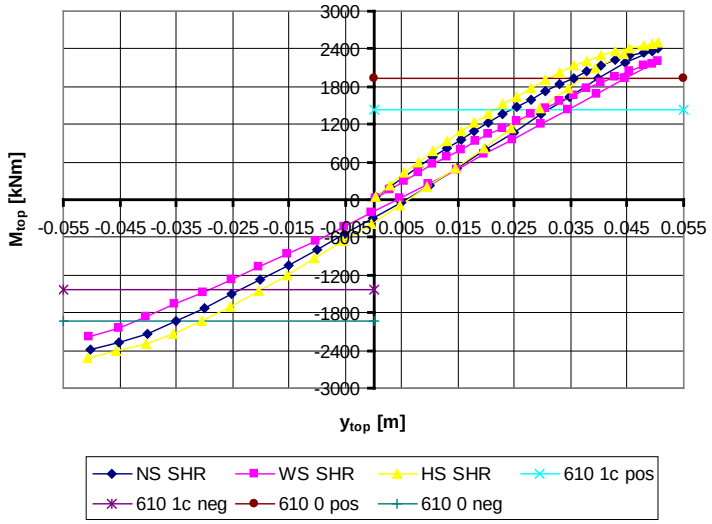

Figure 85 M_{top} as function of ytop in different soil types in T1_610_R _SHR models

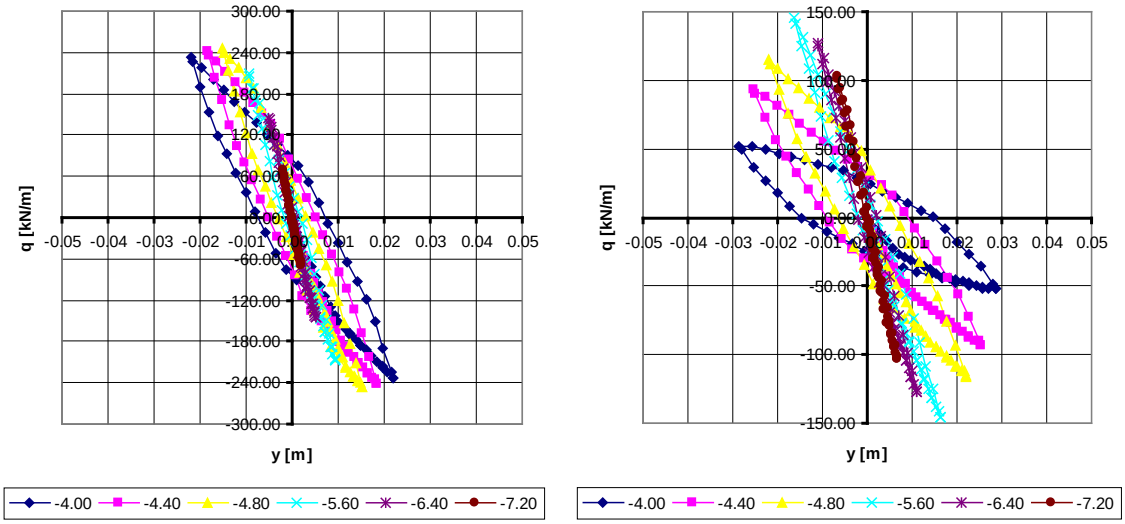

Figure 86 q-y loops at different depths Z. Left: T2_D610_R_NS_EXP model where s = 2.25. Right: T2_D610_R_WS_SHR model where s = 3.65.

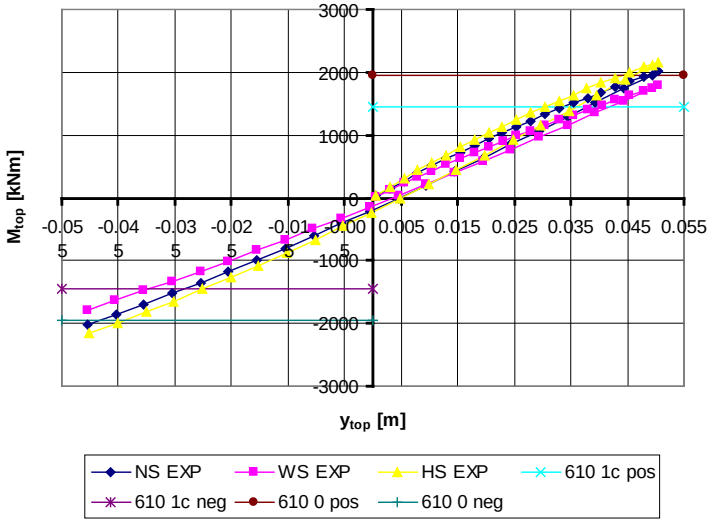

Figure 87 M_{top} as function of ytop in different soil types in T2_610_R _EXP models

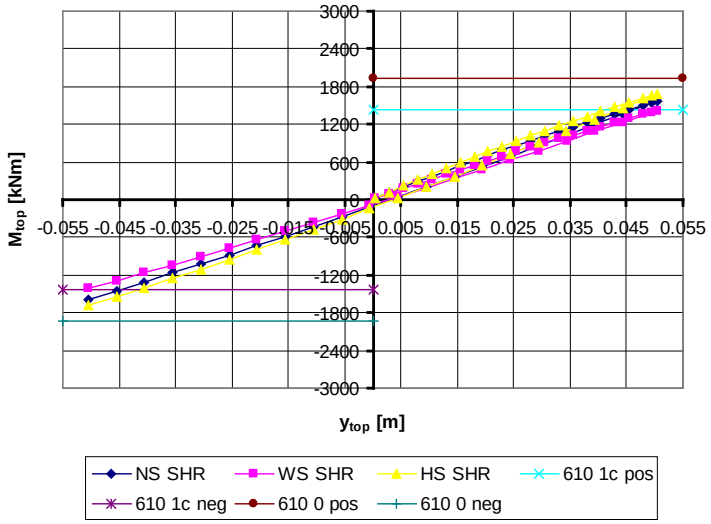

Figure 88 M_{top} as function of ytop in different soil types in T2_610_R _SHR models

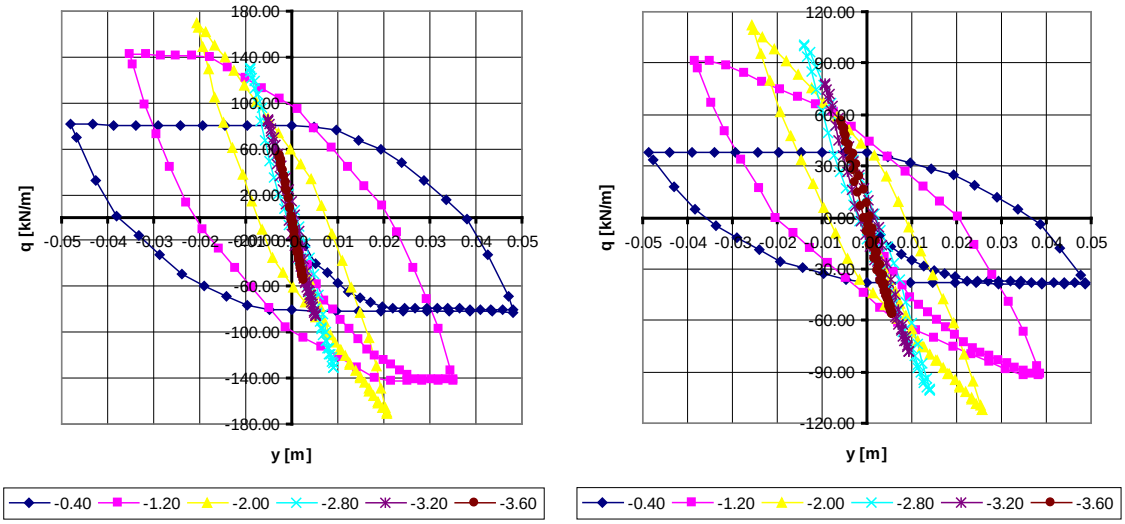

Figure 89 q-y loops at different depths Z. Left: T1_D273_R_NS_EXP model where s = -0.63. Right: T1_D273_R_WS_SHR model where s = -0.16.

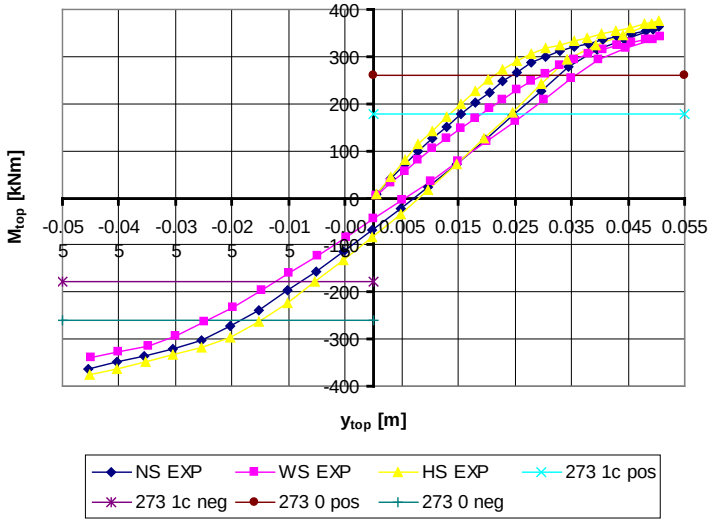

Figure 90 M_{top} as function of ytop in different soil types in T1_273_R _EXP models

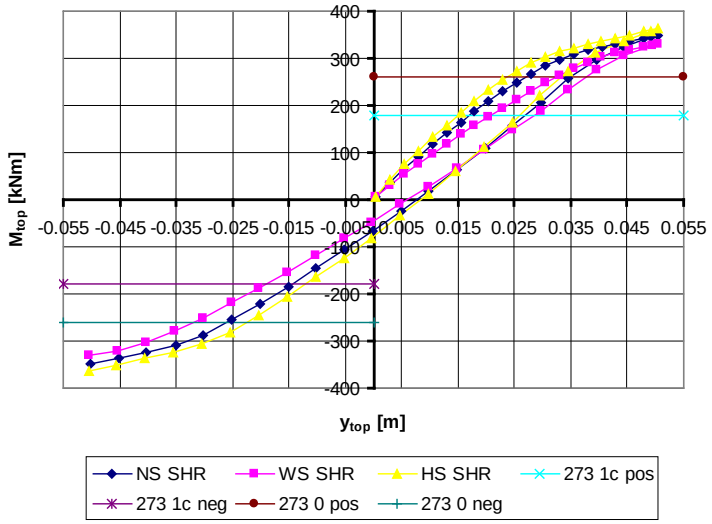

Figure 91 M_{top} as function of ytop in different soil types in T1_273_R _SHR models

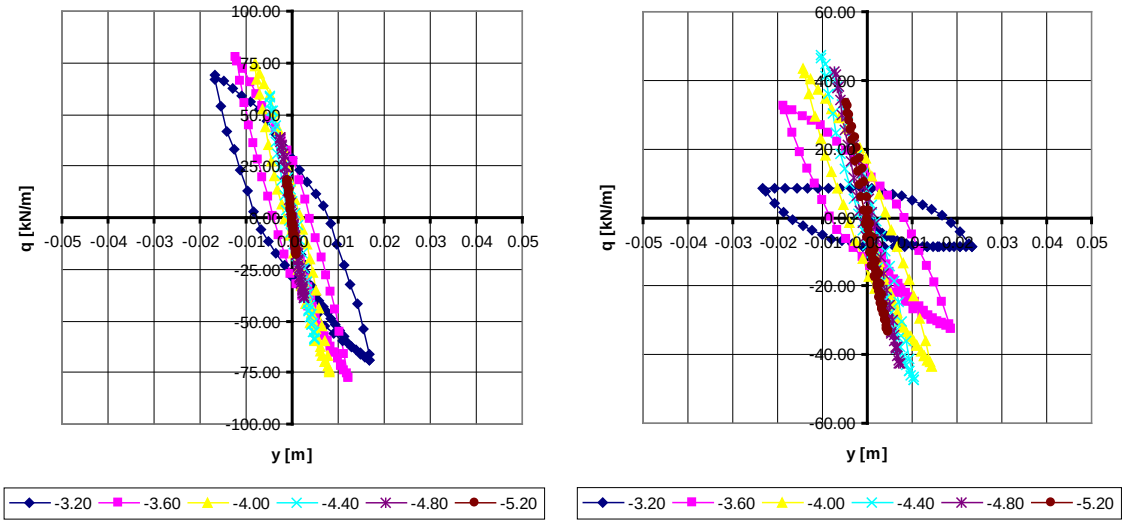

Figure 92 q-y loops at different depths Z. Left: T2_D273_R_NS_EXP model where s = 2.25. Right: T2_D273_R_WS_SHR model where s = 3.08.

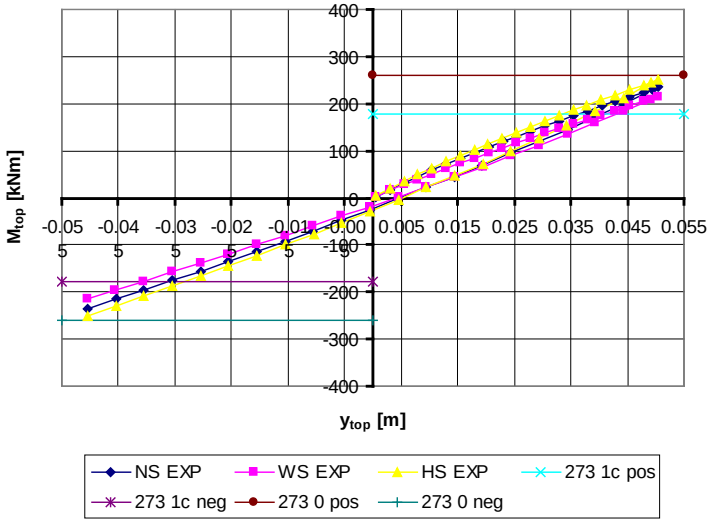

Figure 93 M_{top} as function of ytop in different soil types in T2_273_R _EXP models

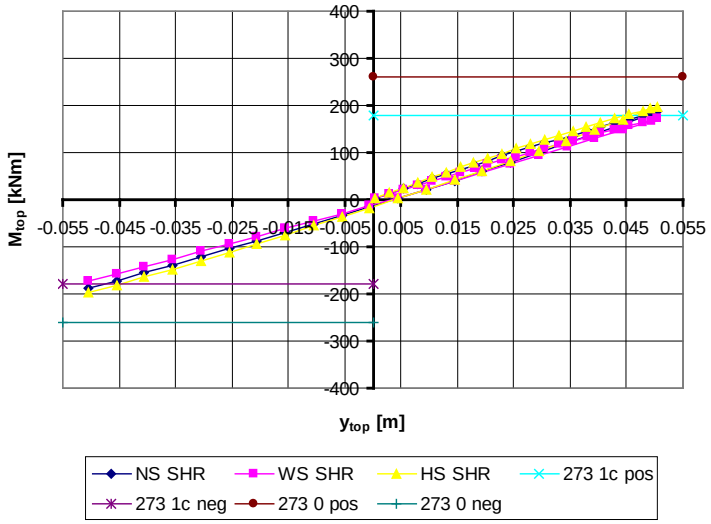

Figure 94 M_{top} as function of ytop in different soil types in T2_273_R _SHR models

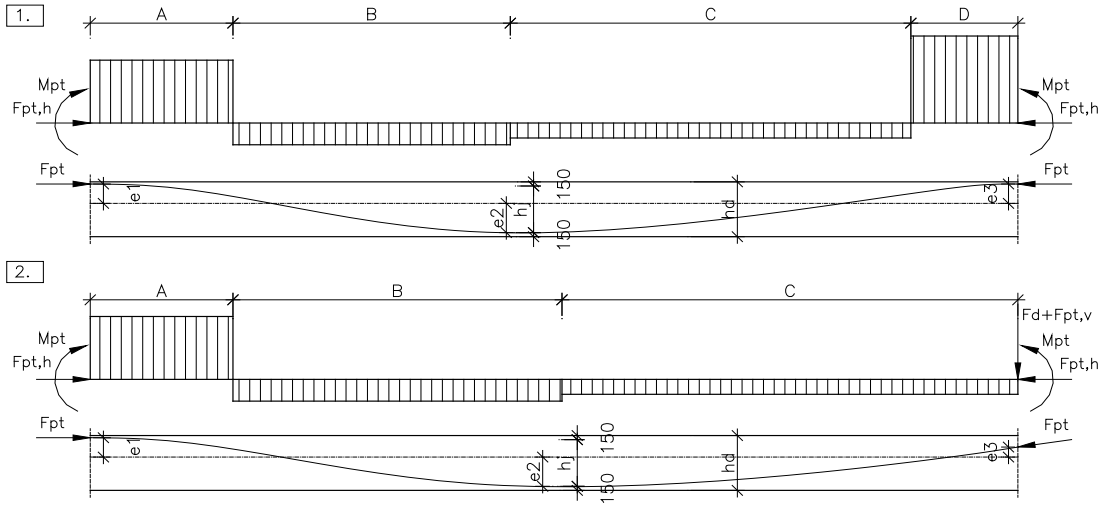

Figure 95 Equivalent loads for post-tensioning forces [90, 91, 61]

Table 3 Dimensions and forces in defining equivalent loads for post-tensioning forces

Last span (L_r), values with second case in Figure 95

	σ_{pt}	$A_{c,ss}/2$	$F_{pt,h}$	e1	e2	e3	e1+e2	e2+e3	a	b	c	d	wa	wb	wc	wd or Fd
B1_L2_S1_T1	3.5	5.6	19.4	0.580	0.919	-0.170	1.499	0.749	1.80	16.80	12.40	0	1.739	0.186	0.189	2.345
B1_L2_S1_T2	3.5	5.6	19.4	0.580	0.806	0.055	1.386	0.861	1.80	16.11	10.74	1.20	1.670	0.187	0.261	2.334
B1_L2_S2_T1	3.5	5.6	19.4	0.580	0.615	-0.170	1.195	0.445	1.80	15.00	11.20	0	1.535	0.184	0.138	1.544
B1_L2_S2_T2	3.5	5.6	19.4	0.580	0.503	0.055	1.083	0.558	1.80	14.38	9.59	1.20	1.444	0.181	0.210	1.674
B1_L3_S1_T1	4.0	6.0	24.0	0.600	1.104	-0.250	1.704	0.854	2.04	18.66	13.80	0	1.937	0.212	0.215	2.972
B1_L3_S1_T2	3.5	6.0	21.0	0.600	0.979	0.000	1.579	0.979	2.04	17.97	11.98	1.36	1.625	0.184	0.257	2.267
B1_L3_S2_T1	4.0	6.0	24.0	0.600	0.751	-0.250	1.351	0.501	2.04	16.56	12.40	0	1.709	0.211	0.156	1.939
B1_L3_S2_T2	4.0	6.0	24.0	0.600	0.626	0.000	1.226	0.626	2.04	15.94	10.63	1.36	1.604	0.205	0.236	1.843

Middle span (L_k), values with first case in Figure 95

e1+e2	e2+e3	a	b	c	d	wa	wb	wc	wd
1.500	1.500	1.20	17.05	17.05	1.20	2.661	0.187	0.187	2.661
1.500	1.500	1.20	16.37	16.37	1.20	2.763	0.203	0.203	2.763
1.500	1.500	1.20	18.55	18.55	1.20	2.459	0.159	0.159	2.459
1.500	1.500	1.20	17.82	17.82	1.20	2.553	0.172	0.172	2.553
1.700	1.700	1.36	18.89	18.89	1.36	2.963	0.213	0.213	2.963
1.700	1.700	1.36	18.22	18.22	1.36	2.682	0.200	0.200	2.682
1.700	1.700	1.36	20.64	20.64	1.36	2.727	0.180	0.180	2.727
1.700	1.700	1.36	19.91	19.91	1.36	2.821	0.193	0.193	2.821

Eccentricities are presented with offset from modelling plane

Neutral axis of whole cross section at bridge ends are below modelling plane:

JB1800 0.17

JB2000 0.25

Values are also presented in Figure 6.38

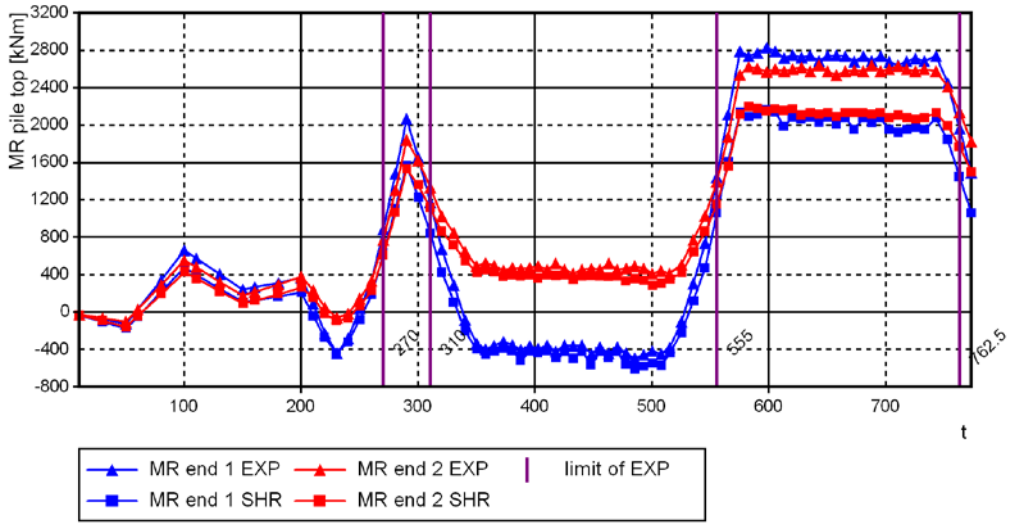

Figure 96 Pile bending moments M_R at top of pile in bridge models B2_L1_S1_T1_d914_SHR and -_EXP. Result level 0 (RL0).

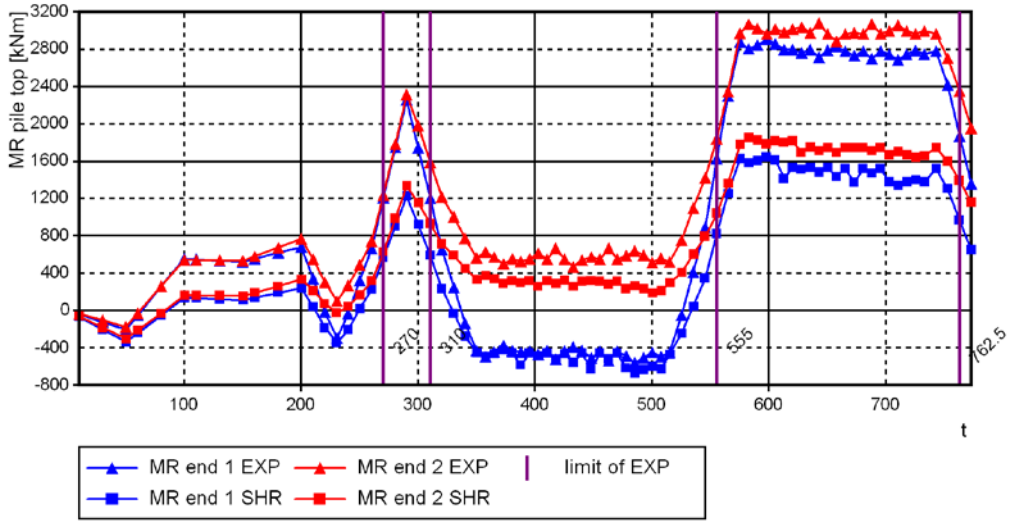

Figure 97 Pile bending moments M_R at top of pile in bridge models B2_L1_S1_T2_d914_SHR and -_EXP. Result level 0 (RL0).

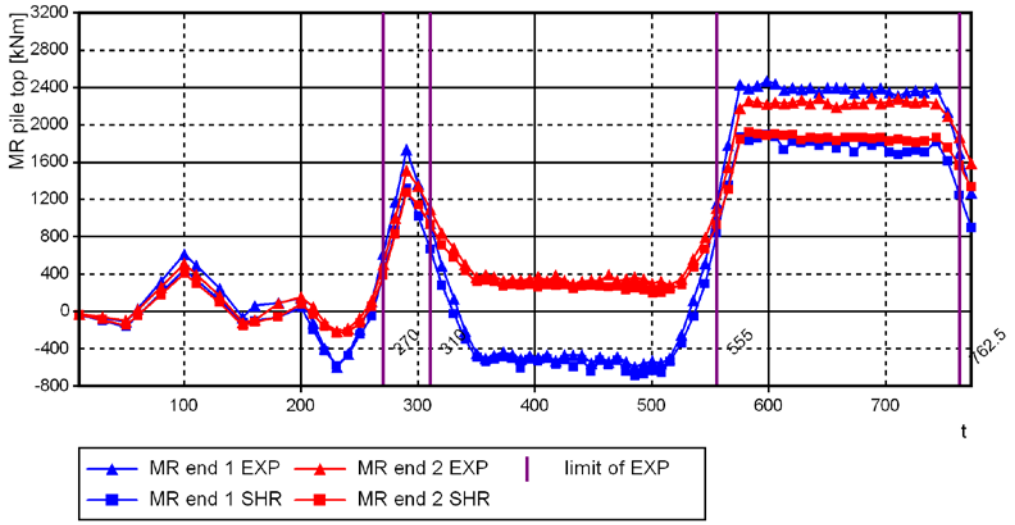

Figure 98 Pile bending moments M_R at top of pile in bridge models B3_L1_S1_T1_d914_SHR and -_EXP. Result level 0 (RL0).

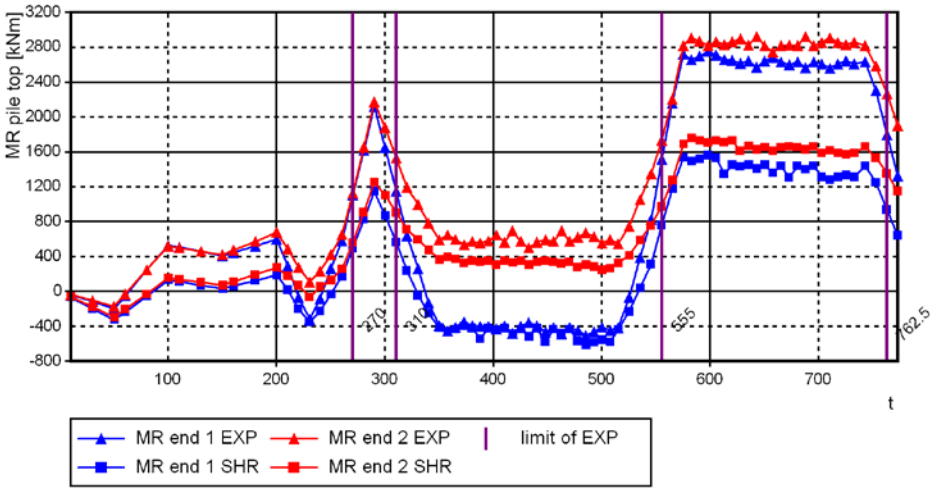

Figure 99 Pile bending moments M_R at top of pile in bridge models B3_L1_S1_T2_d914_SHR and -_EXP. Result level 0 (RL0)

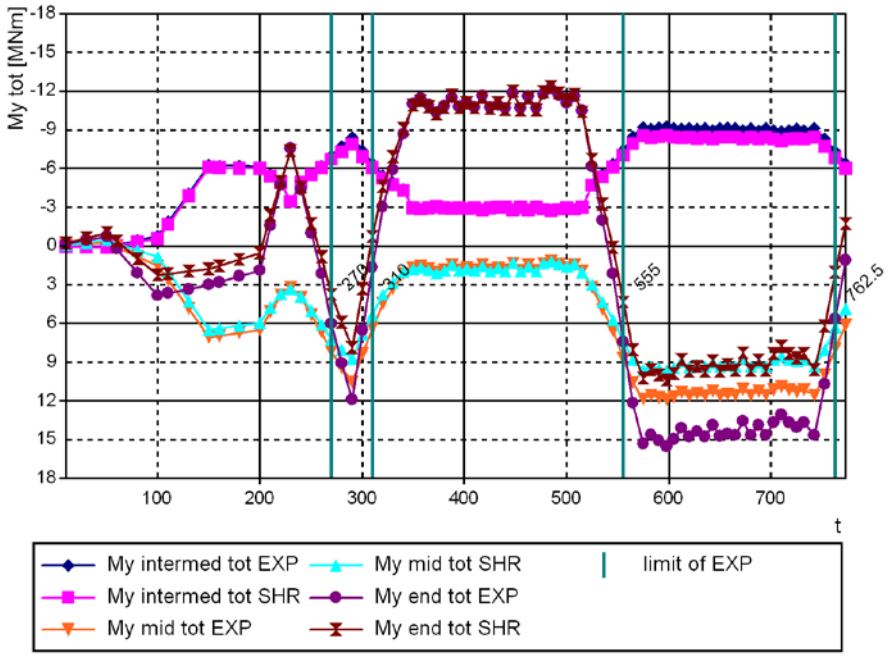

Figure 100 Superstructure bending moments M_y in bridge models B2_L1_S1_T1_d914_SHR and -_EXP. RL0.

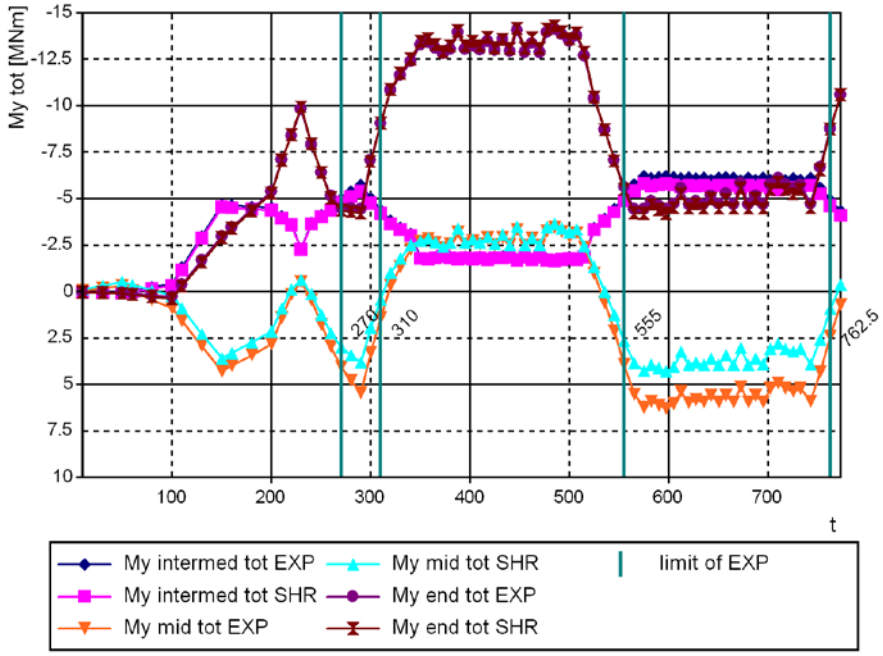

Figure 101 Superstructure bending moments M_y in bridge models B2_L1_S1_T2_d914_SHR and -_EXP. RL0.

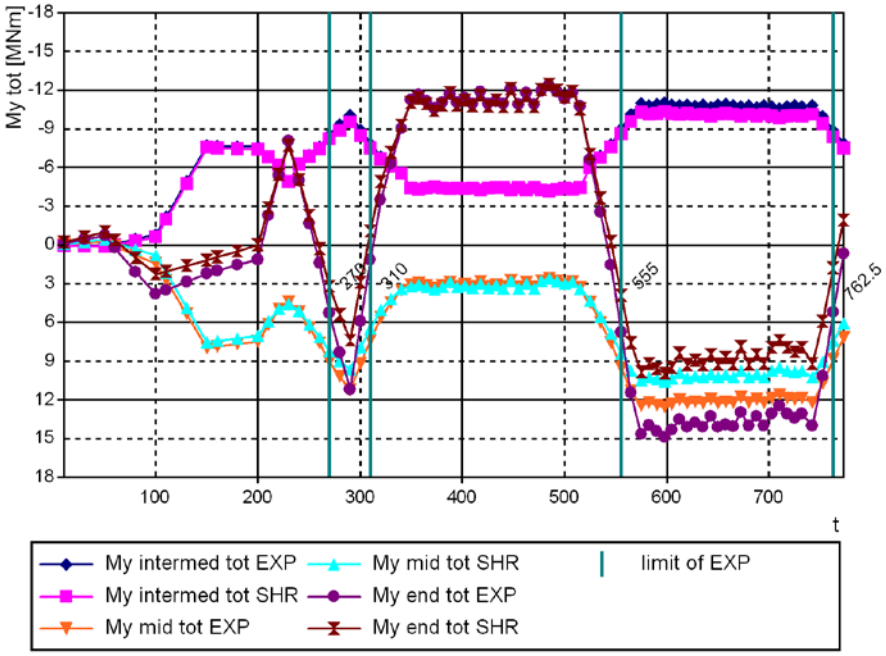

Figure 102 Superstructure bending moments M_y in bridge models B3_L1_S1_T1_d914_SHR and -_EXP. RL0.

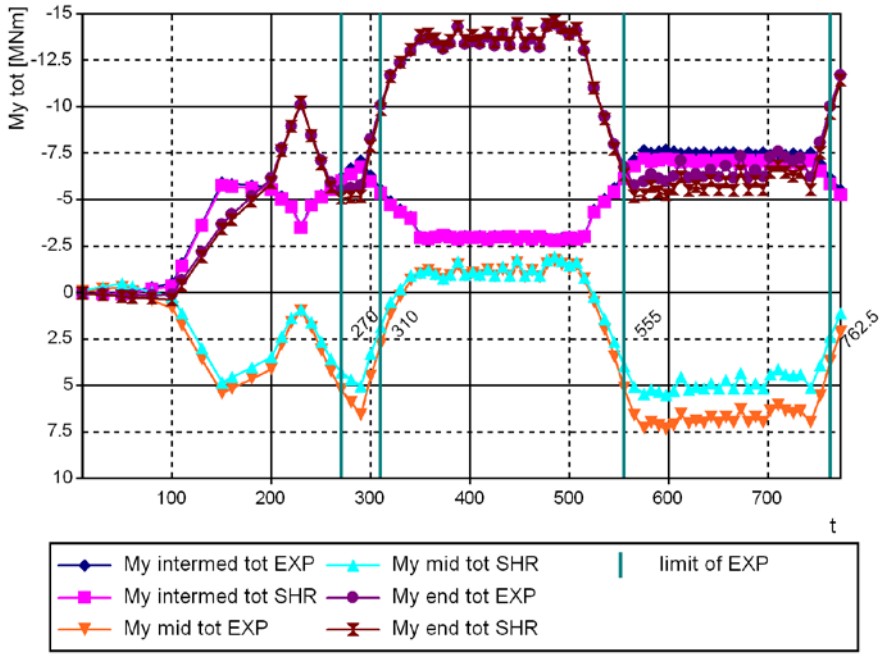

Figure 103 Superstructure bending moments M_y in bridge models B3_L1_S1_T2_d914_SHR and -_EXP. RL0.

 Appendix 9.3 1(5) M_R-Z, M_R-F_X and $D_{X,end1}$-$D_{X,end2}$ diagrams of bridge models B1

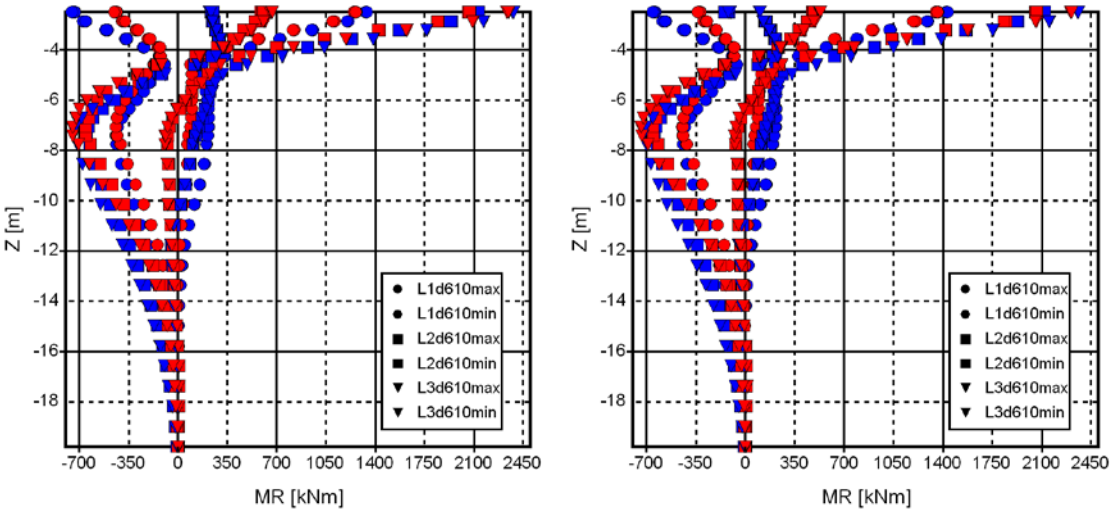

Figures 104 M_R-Z diagrams of bridge models, left B1_T1_S1_d610, right B1_T1_S2_d610, RL1

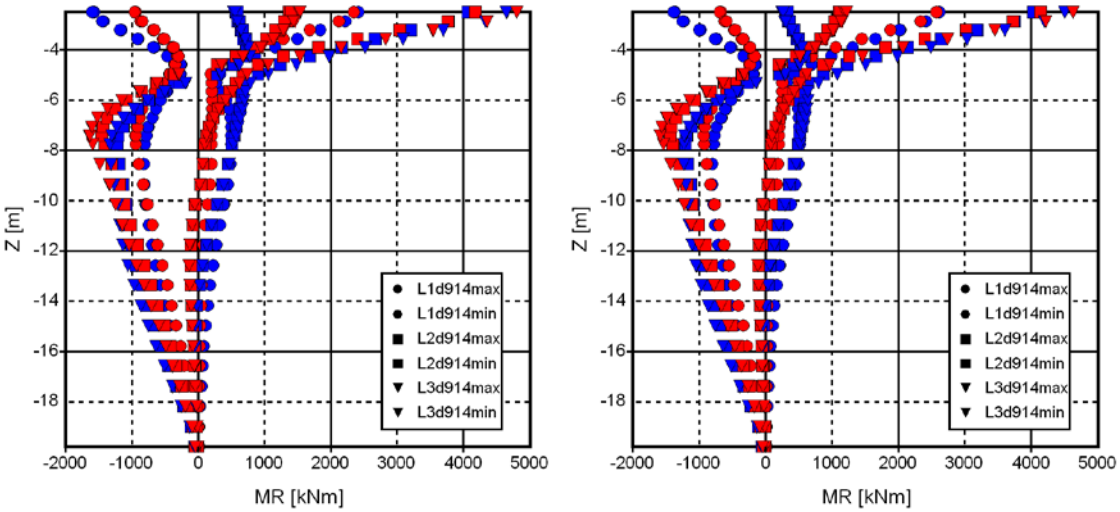

Figures 105 M_R-Z diagrams of bridge models, left B1_T1_S1_d914, right B1_T1_S2_d914, RL1

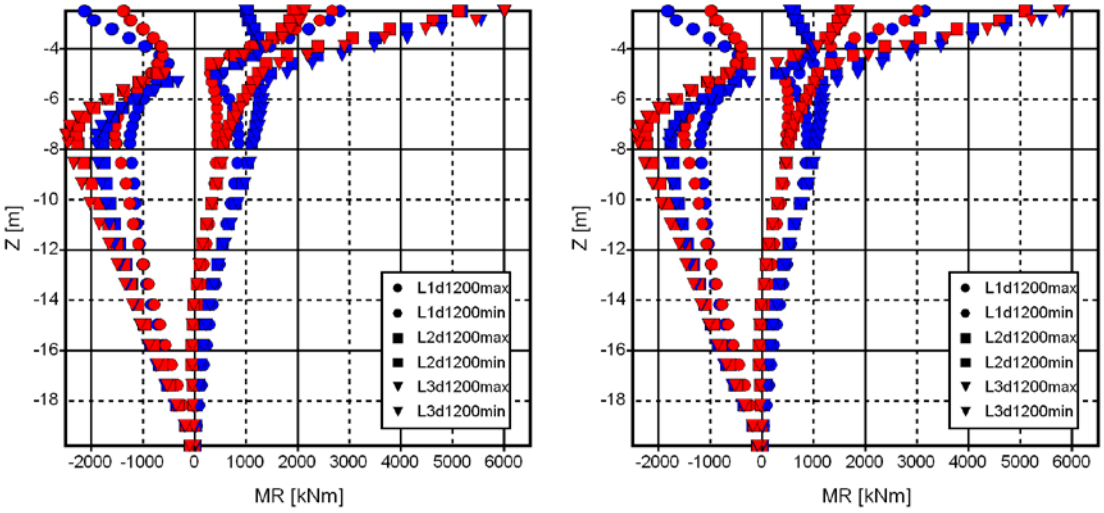

Figures 106 M_R-Z diagrams of bridge models, left B1_T1_S1_d1200, right B1_T1_S2_d1200, RL1

Appendix 9.3 2(5) M_R-Z, M_R-F_X and $D_{X,end1}$-$D_{X,end2}$ diagrams of bridge models B1 249

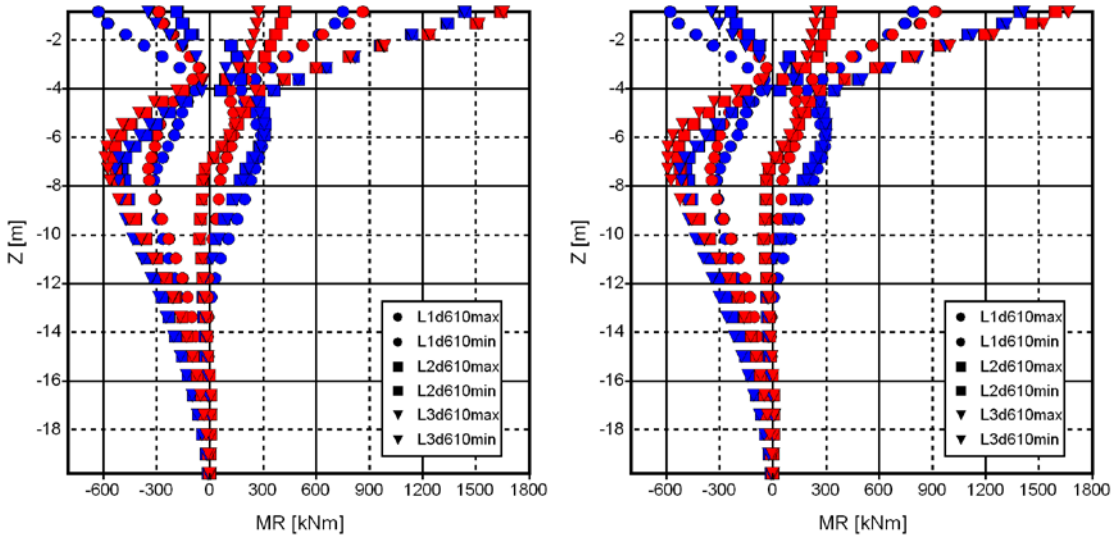

Figures 107 M_R-Z diagrams of bridge models, left B1_T2_S1_d610, right B1_T2_S2_d610, RL1

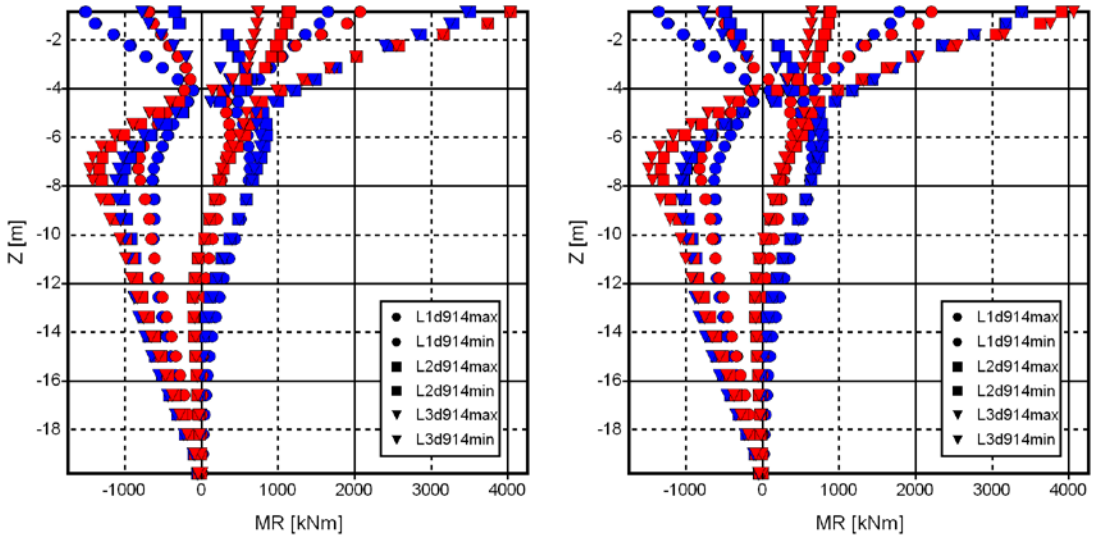

Figures 108 M_R-Z diagrams of bridge models, left B1_T2_S1_d914, right B1_T2_S2_d914, RL1

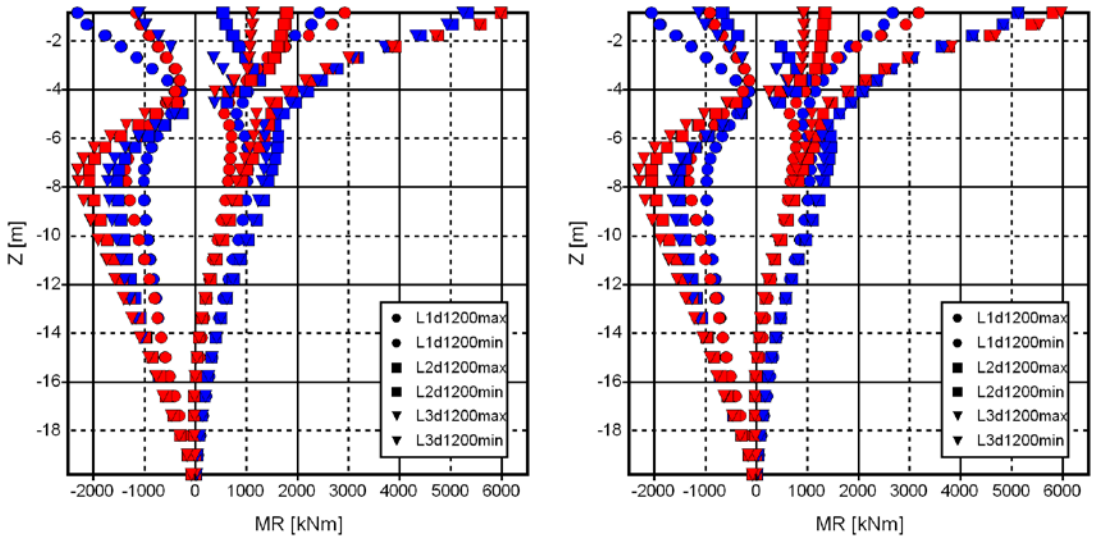

Figures 109 M_R-Z diagrams of bridge models, left B1_T2_S1_d1200, right B1_T2_S2_d1200, RL1

 Appendix 9.3 3(5) M_R-Z, M_R-F_X and $D_{X,end1}$-$D_{X,end2}$ diagrams of bridge models B1

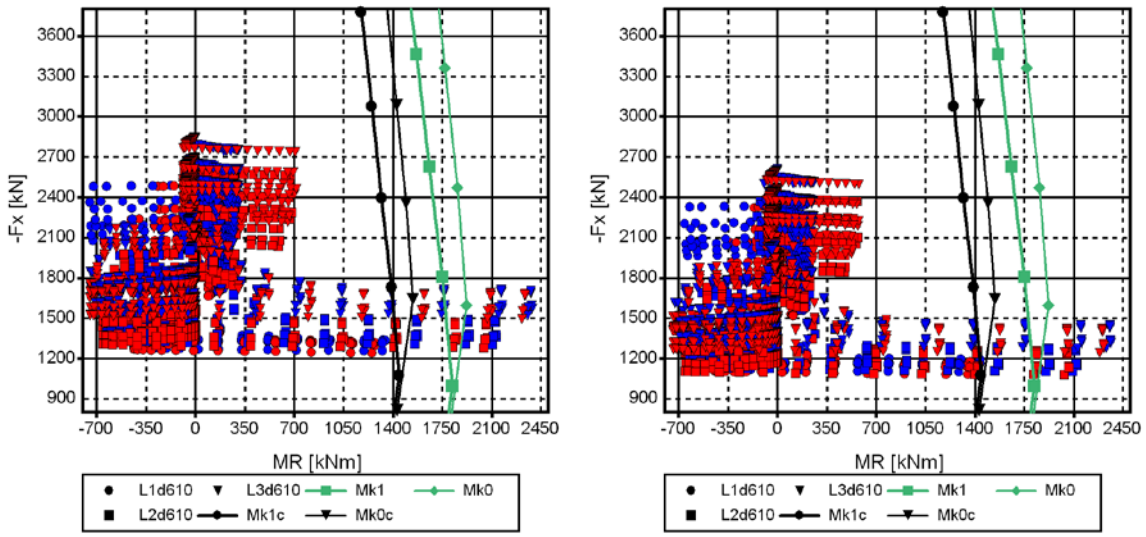

Figures 110 M_R-F_X diagrams of bridge models, left B1_T1_S1_d610, right B1_T1_S2_d610, RL2

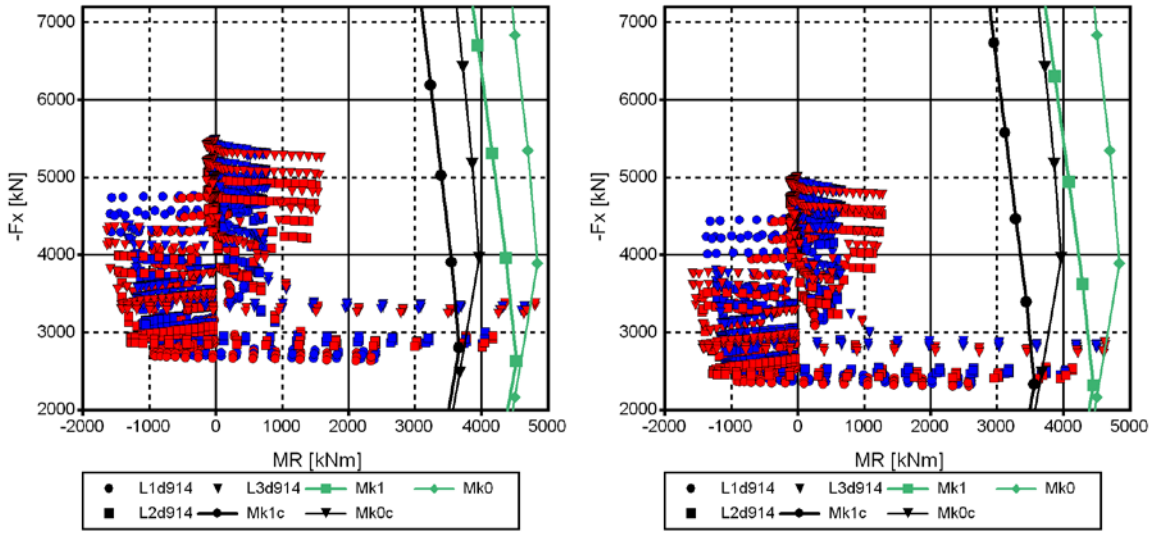

Figures 111 M_R-F_X diagrams of bridge models, left B1_T1_S1_d914, right B1_T1_S2_d914, RL2

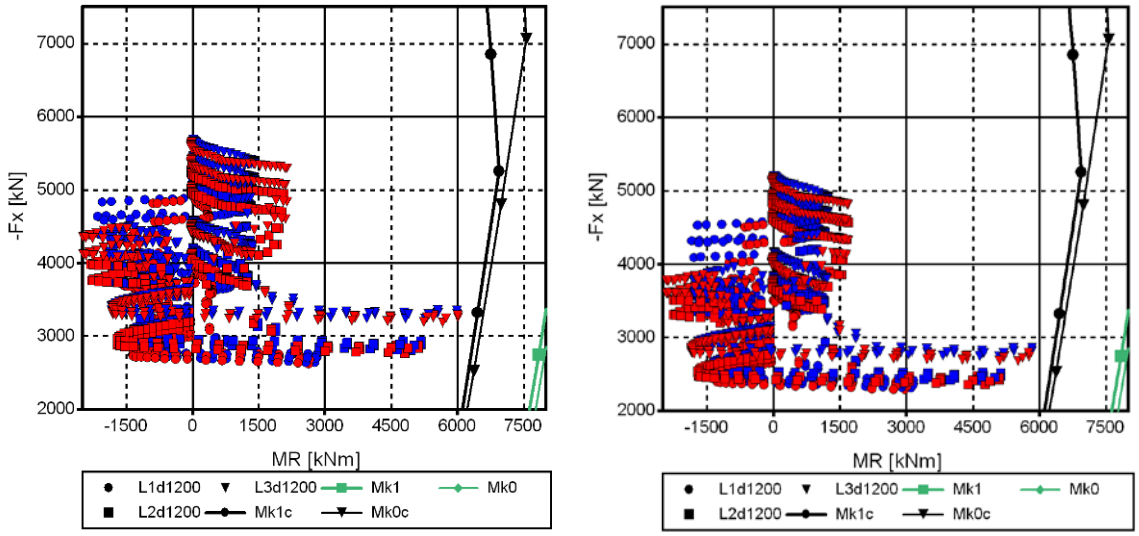

Figures 112 M_R-F_X diagrams of bridge models, left B1_T1_S1_d1200, right B1_T1_S2_d1200, RL2

Appendix 9.3 4(5) M_R-Z, M_R-F_X and $D_{X,end1}$-$D_{X,end2}$ diagrams of bridge models B1 251

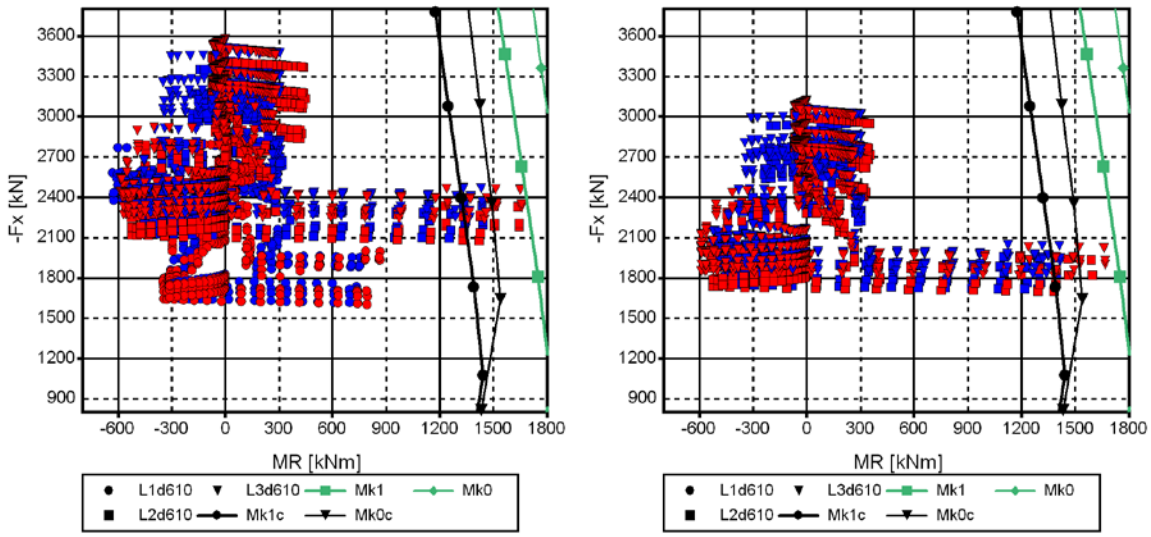

Figures 113 M_R-F_X diagrams of bridge models, left B1_T2_S1_d610, right B1_T2_S2_d610, RL2

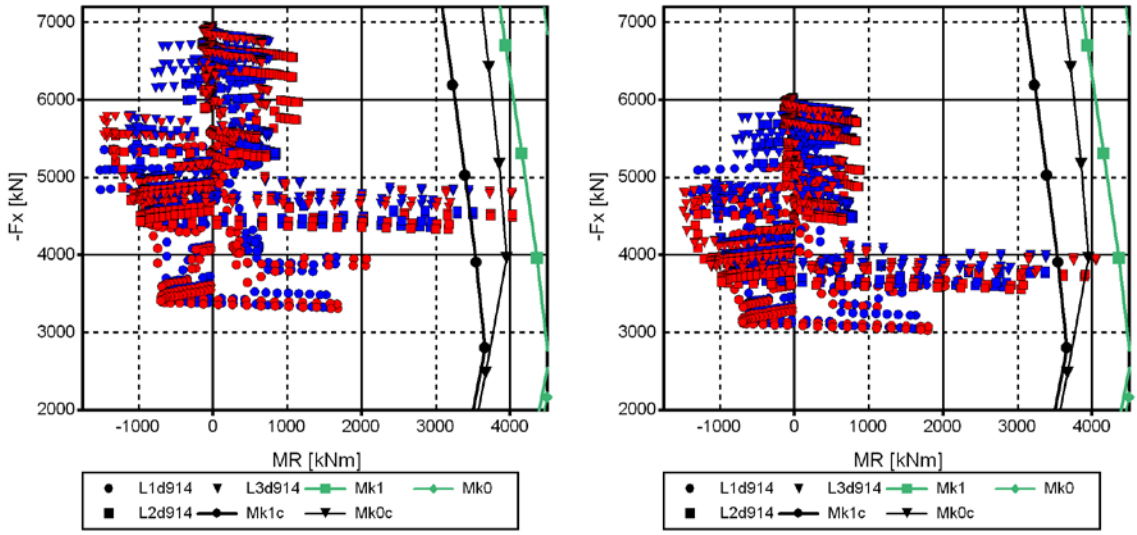

Figures 114 M_R-F_X diagrams of bridge models, left B1_T2_S1_d914, right B1_T2_S2_d914, RL2

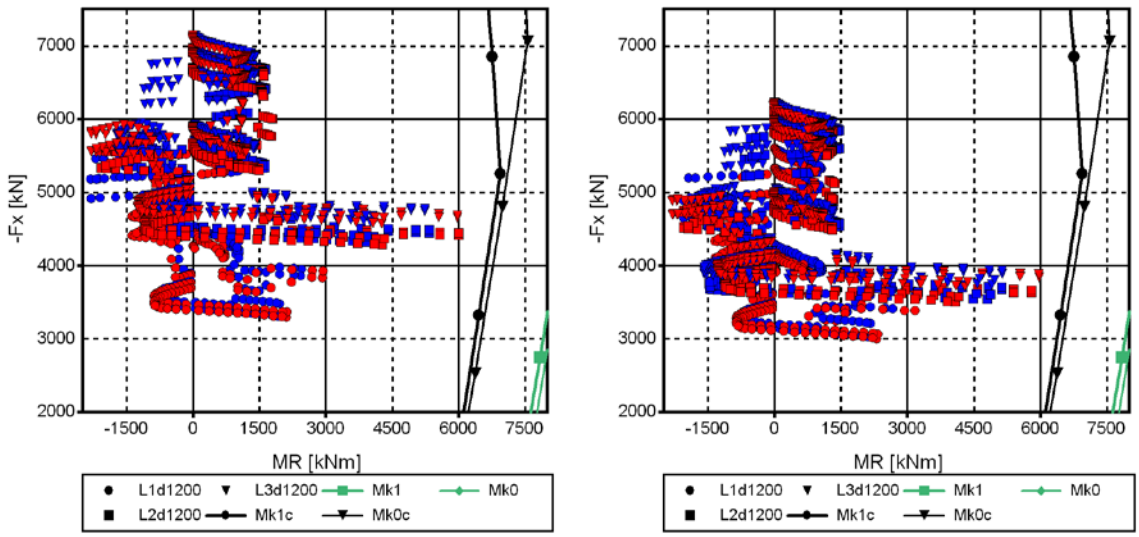

Figures 115 M_R-F_X diagrams of bridge models, left B1_T2_S1_d1200, right B1_T2_S2_d1200, RL2

 Appendix 9.3 5(5) M_R-Z, M_R-F_X and $D_{X,end1}$-$D_{X,end2}$ diagrams of bridge models B1

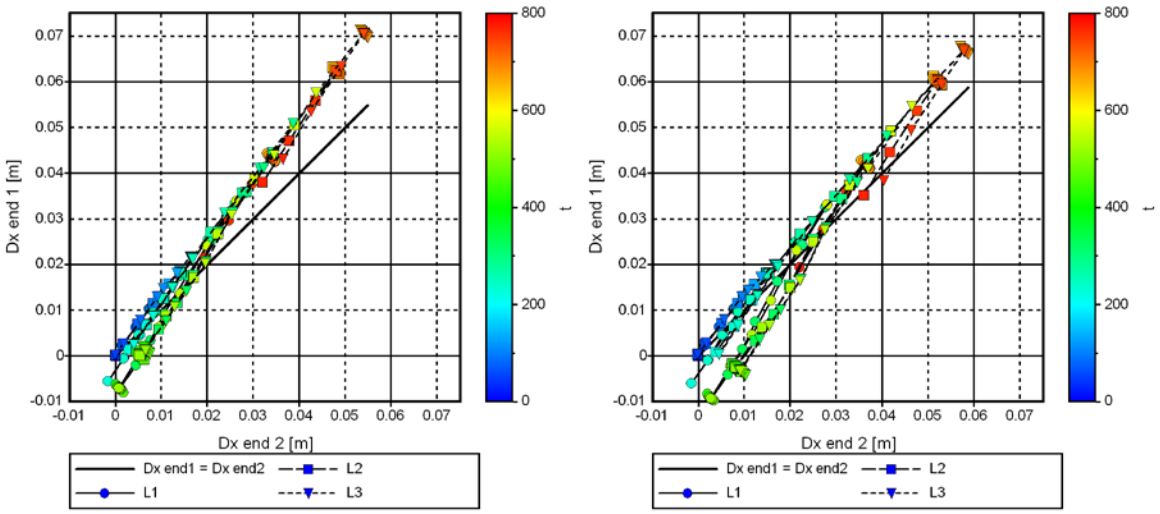

Figures 116 $D_{X,end1}$-$D_{X,end2}$ diagrams of bridge models, left B1_T1_S1_d610_SHR, right B1_T2_S1_d610_SHR, RL0

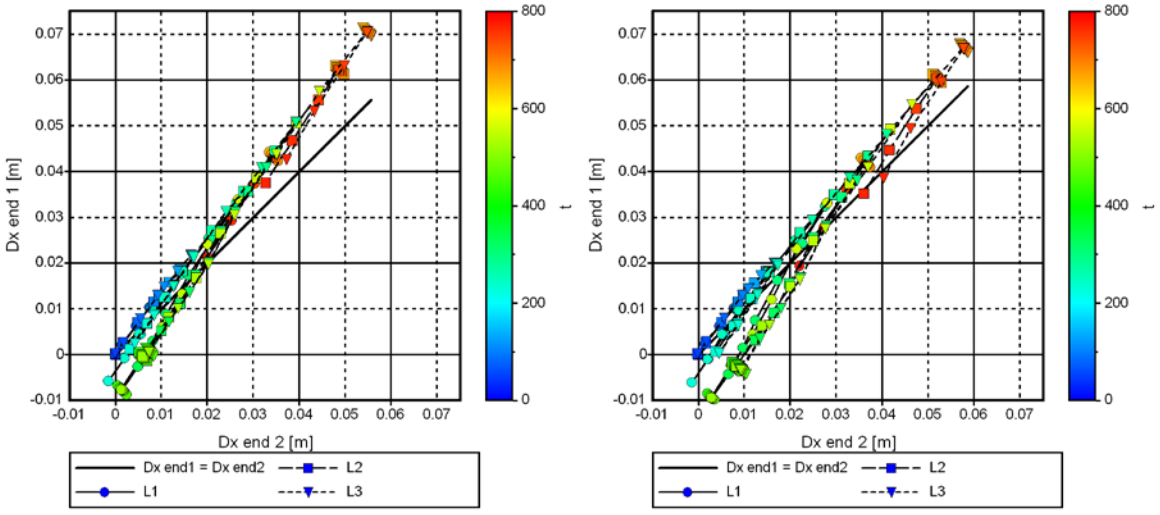

Figures 117 $D_{X,end1}$-$D_{X,end2}$ diagrams of bridge models, left B1_T1_S1_d914_SHR, right B1_T2_S1_d914_SHR, RL0

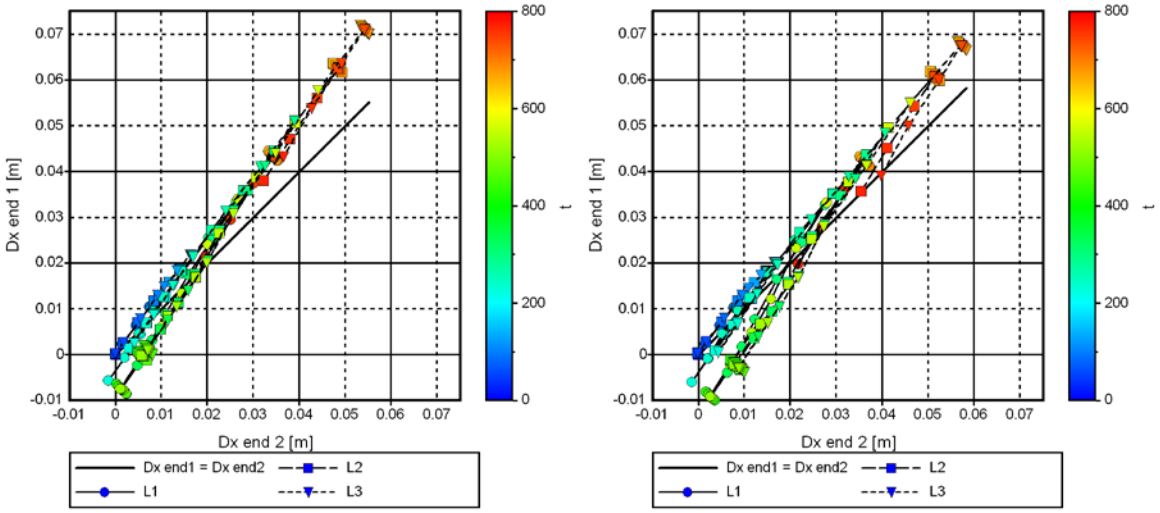

Figures 118 $D_{X,end1}$-$D_{X,end2}$ diagrams of bridge models, left B1_T1_S1_d1200_SHR, right B1_T2_S1_d1200_SHR, RL0

Appendix 9.4 1(5) M_R-Z, M_R-F_X and $D_{X,end1}$-$D_{X,end2}$ diagrams of bridge models B2 253

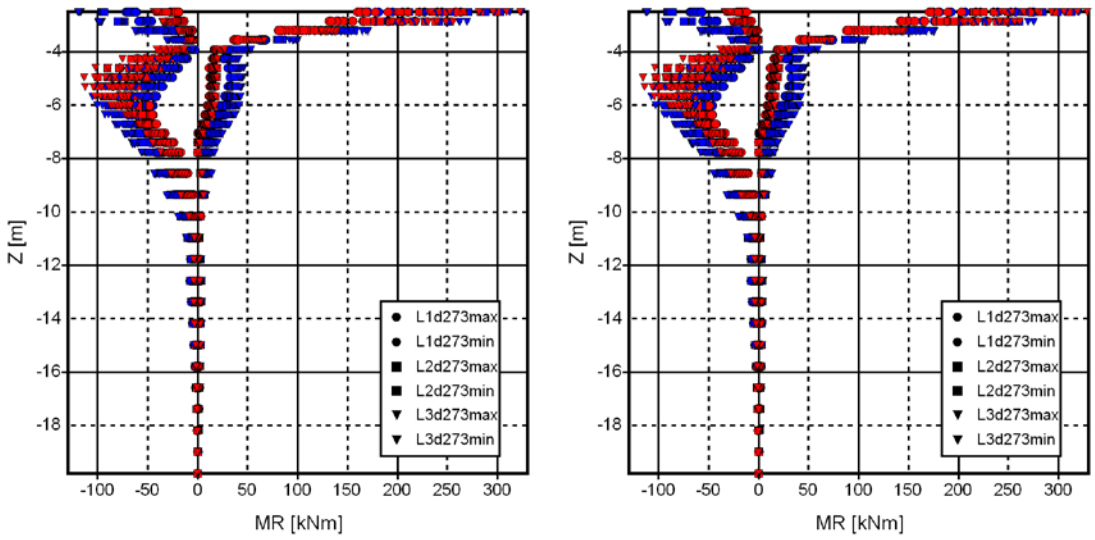

Figures 119 M_R-Z diagrams of bridge models, left B2_T1_S1_d273, right B2_T1_S2_d273, RL1

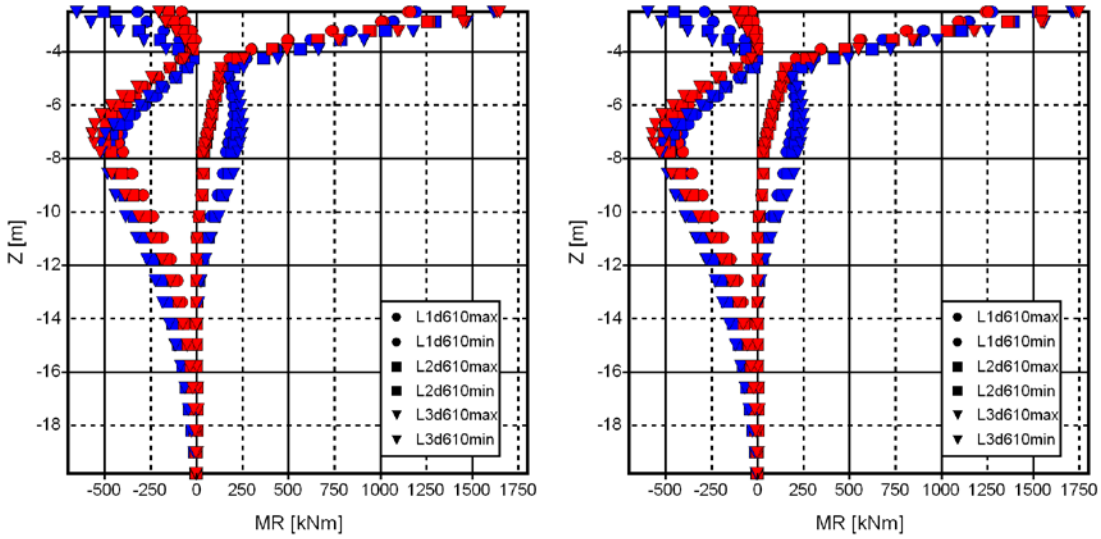

Figures 120 M_R-Z diagrams of bridge models, left B2_T1_S1_d610, right B2_T1_S2_d610, RL1

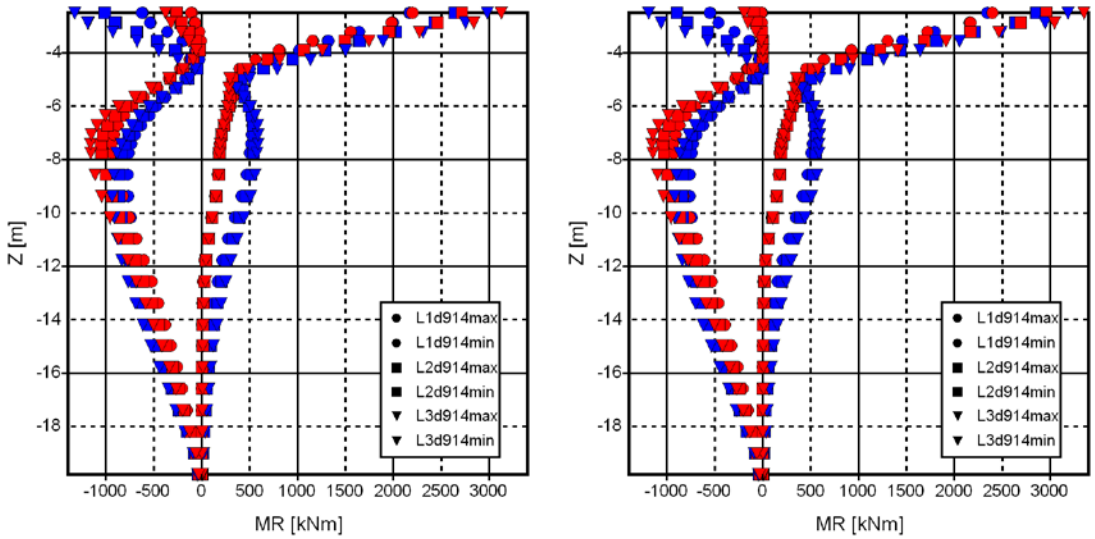

Figures 121 M_R-Z diagrams of bridge models, left B2_T1_S1_d914, right B2_T1_S2_d914, RL1

 Appendix 9.4 2(5) M_R-Z, M_R-F_X and $D_{X,end1}$-$D_{X,end2}$ diagrams of bridge models B2

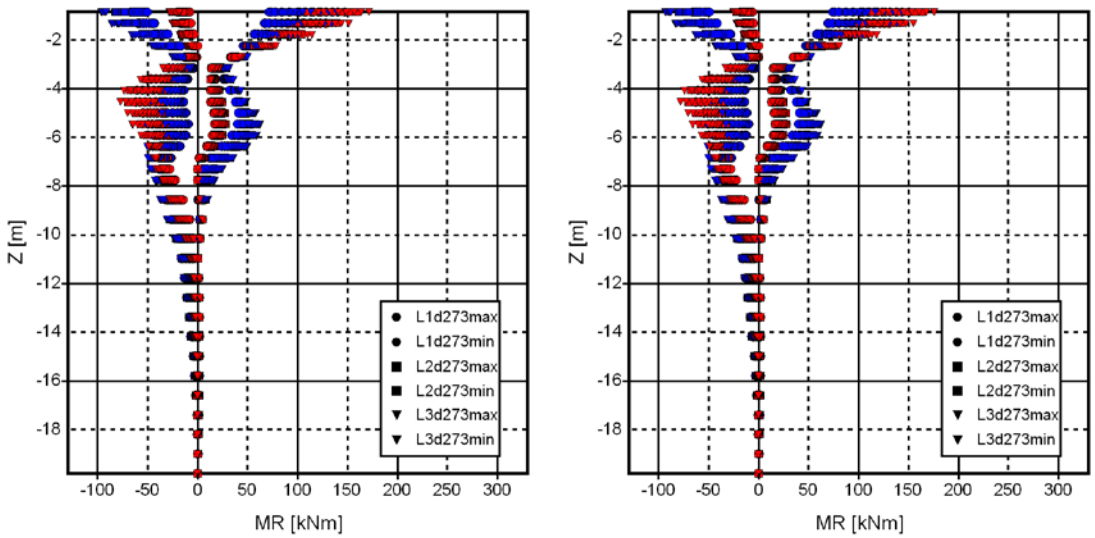

Figures 122 M_R-Z diagrams of bridge models, left B2_T2_S1_d273, right B2_T2_S2_d273, RL1

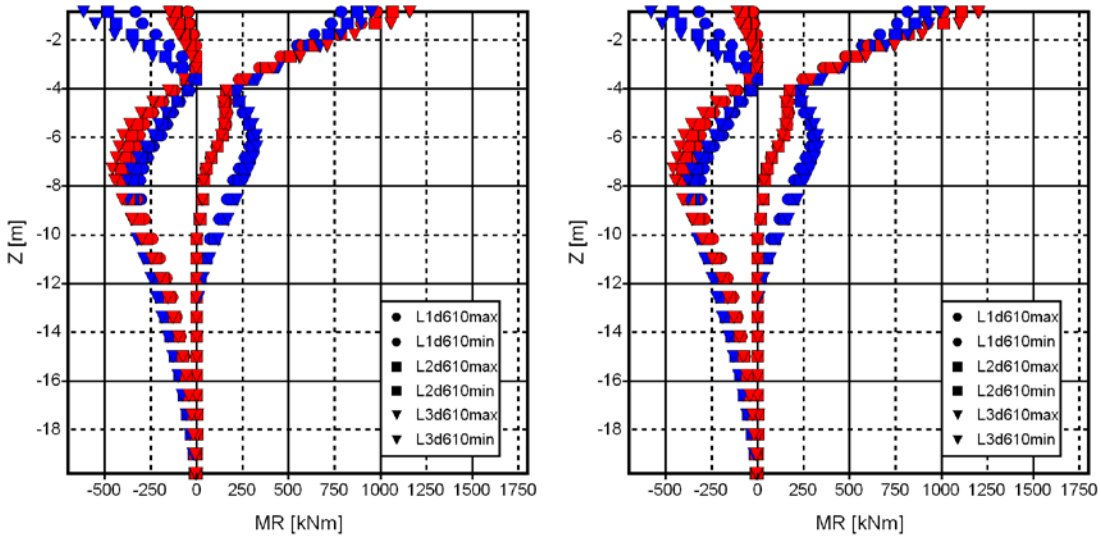

Figures 123 M_R-Z diagrams of bridge models, left B2_T2_S1_d610, right B2_T2_S2_d610, RL1

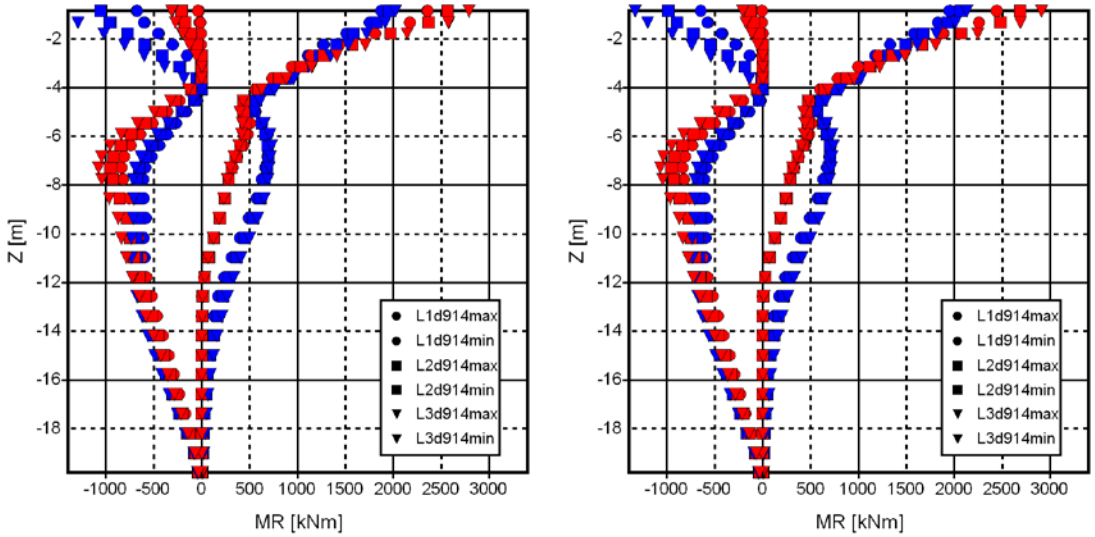

Figures 124 M_R-Z diagrams of bridge models, left B2_T2_S1_d914, right B2_T2_S2_d914, RL1

Appendix 9.4 3(5) M_R-Z, M_R-F_X and $D_{X,end1}$-$D_{X,end2}$ diagrams of bridge models B2 255

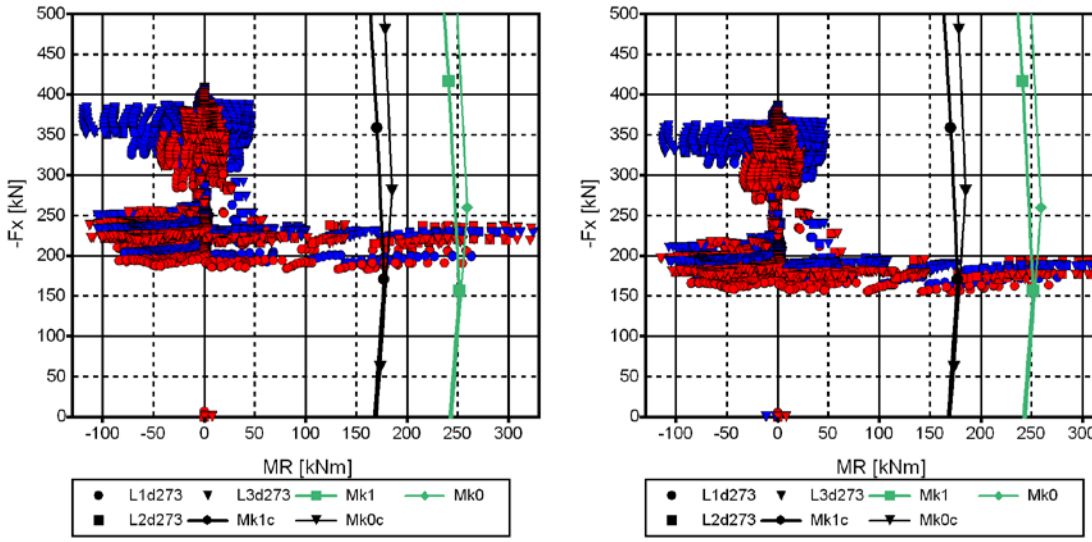

Figures 125 M_R-F_X diagrams of bridge models, left B2_T1_S1_d273, right B2_T1_S2_d273, RL2

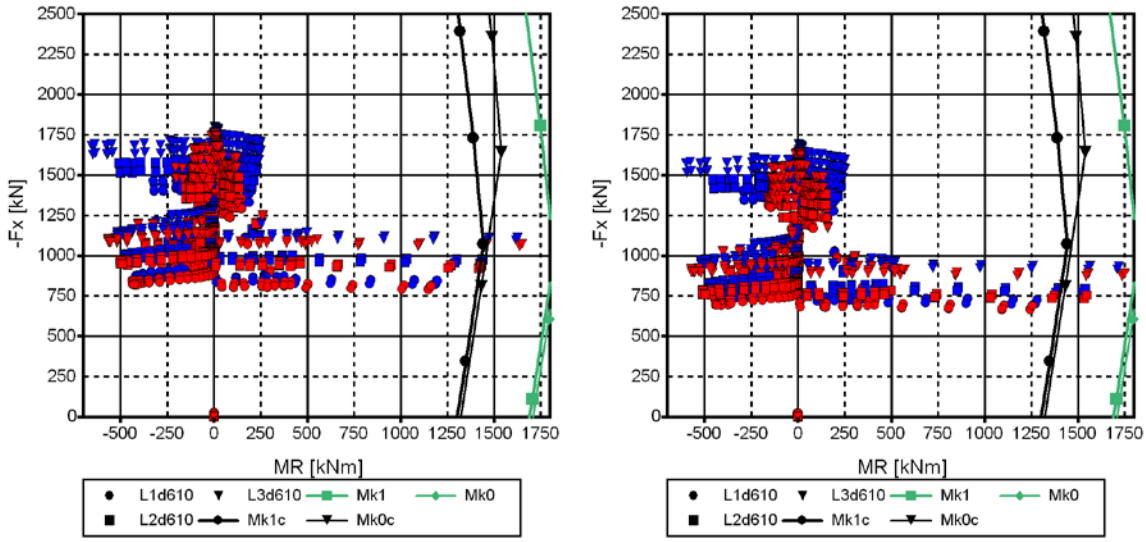

Figures 126 M_R-F_X diagrams of bridge models, left B2_T1_S1_d610, right B2_T1_S2_d610, RL2

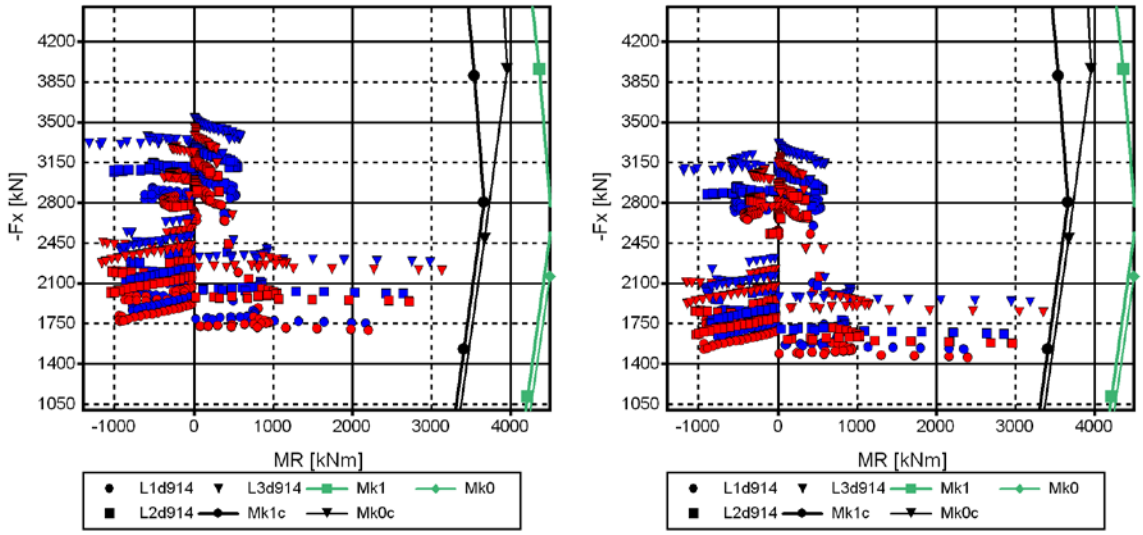

Figures 127 M_R-F_X diagrams of bridge models, left B2_T1_S1_d914, right B2_T1_S2_d914, RL2

 Appendix 9.4 4(5) M_R-Z, M_R-F_X and $D_{X,end1}$-$D_{X,end2}$ diagrams of bridge models B2

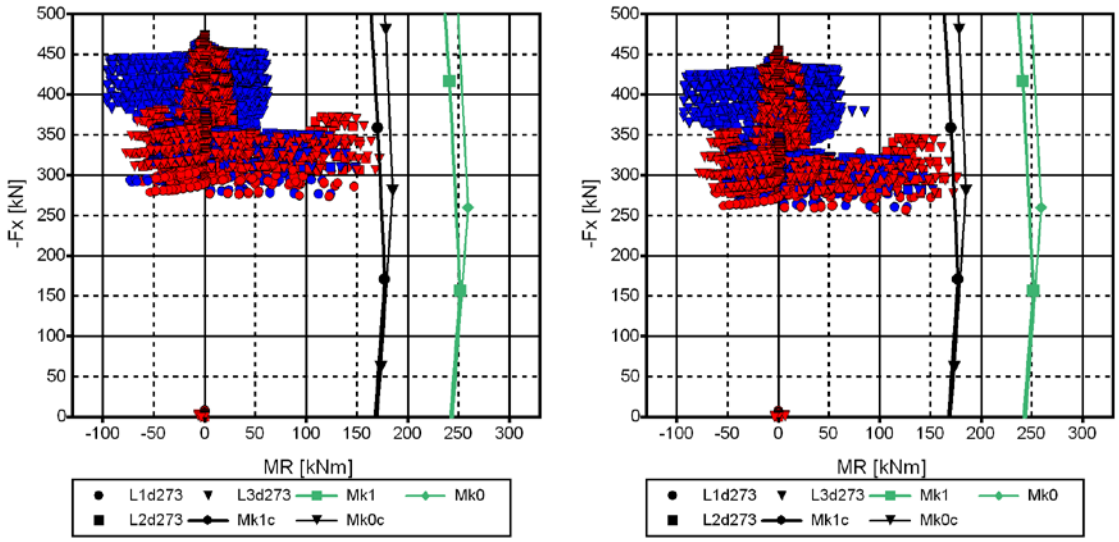

Figures 128 M_R-F_X diagrams of bridge models, left B2_T2_S1_d273, right B2_T2_S2_d273, RL2

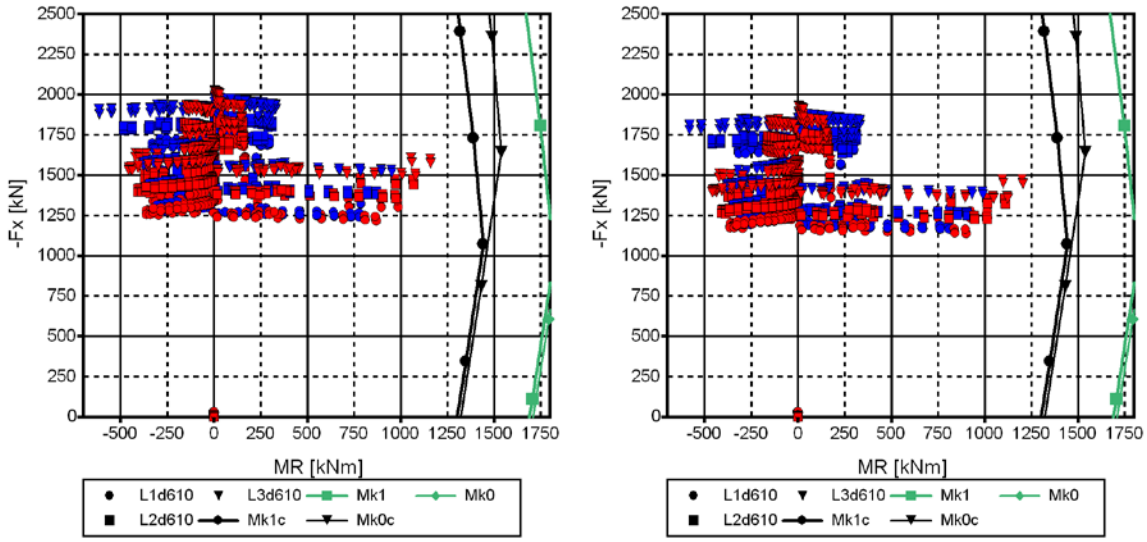

Figures 129 M_R-F_X diagrams of bridge models, left B2_T2_S1_d610, right B2_T2_S2_d610, RL2

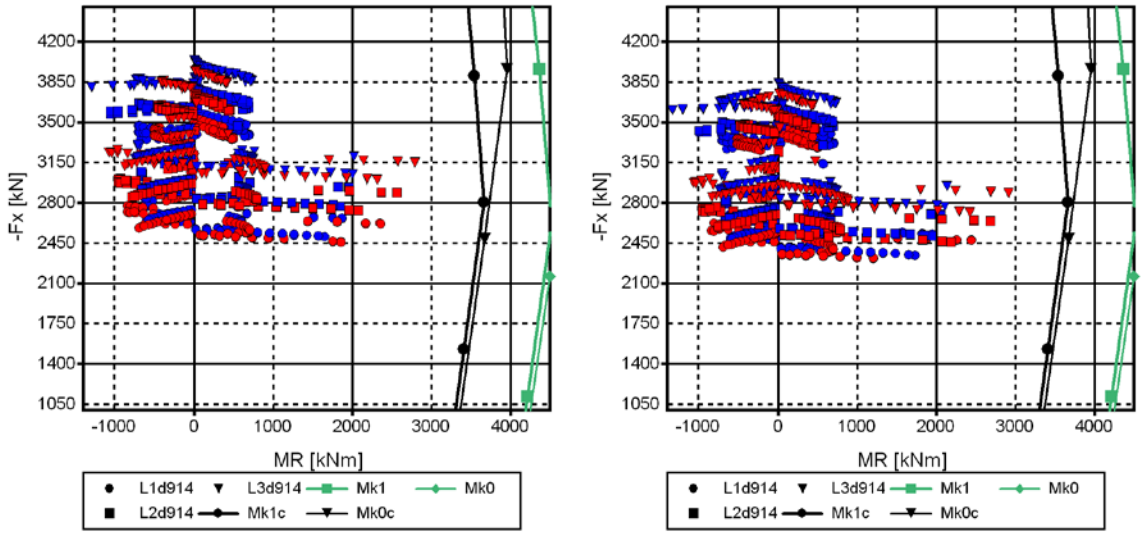

Figures 130 M_R-F_X diagrams of bridge models, left B2_T2_S1_d914, right B2_T2_S2_d914, RL2

Appendix 9.4 5(5) M_R-Z, M_R-F_X and $D_{X,end1}$-$D_{X,end2}$ diagrams of bridge models B2 257

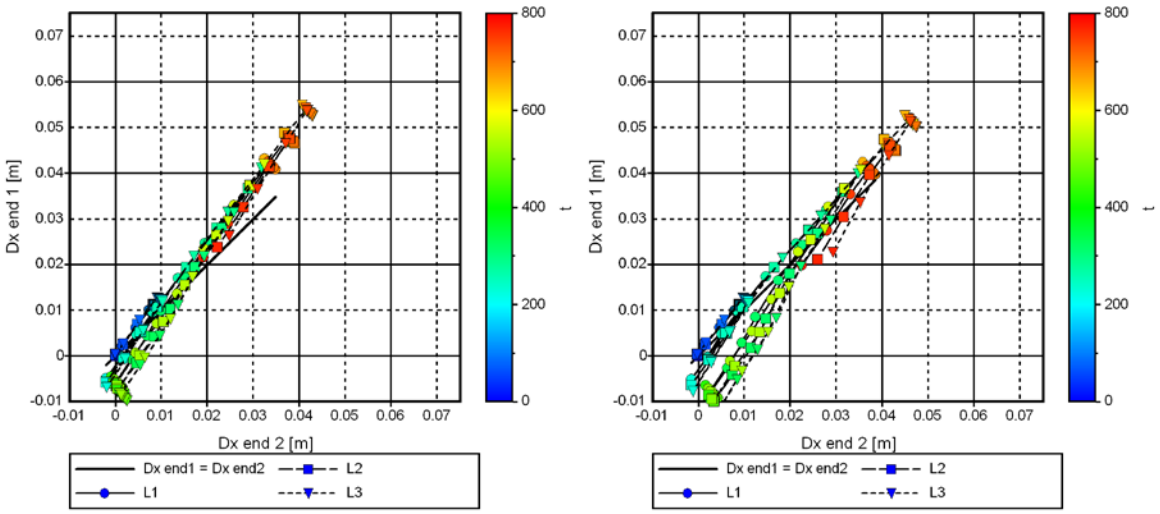

Figures 131 $D_{X,end1}$-$D_{X,end2}$ diagrams of bridge models, left B2_T1_S1_d273_SHR, right B2_T2_S1_d273_SHR, RL0

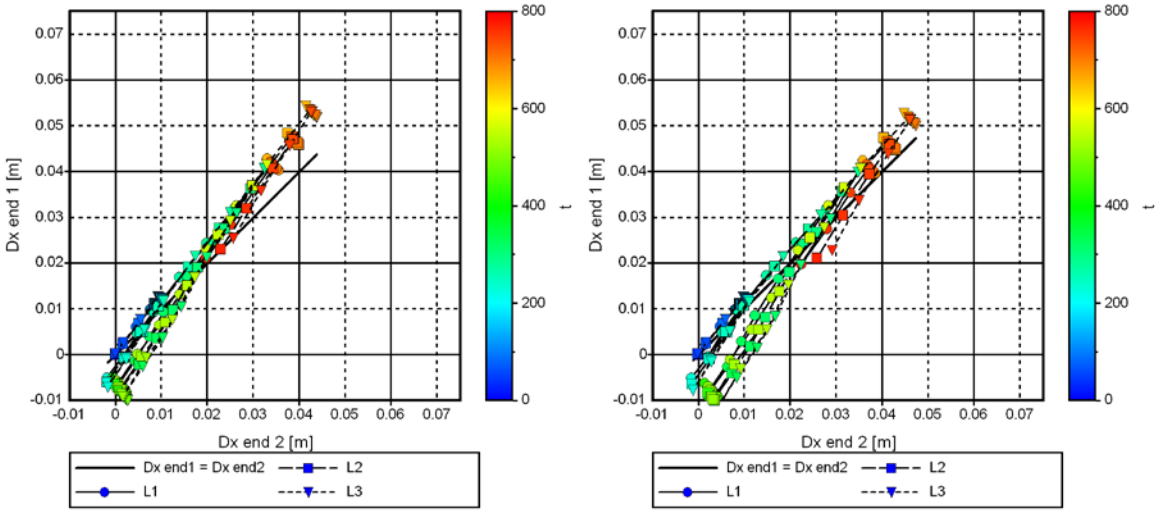

Figures 132 $D_{X,end1}$-$D_{X,end2}$ diagrams of bridge models, left B2_T1_S1_d610_SHR, right B2_T2_S1_d610_SHR, RL0

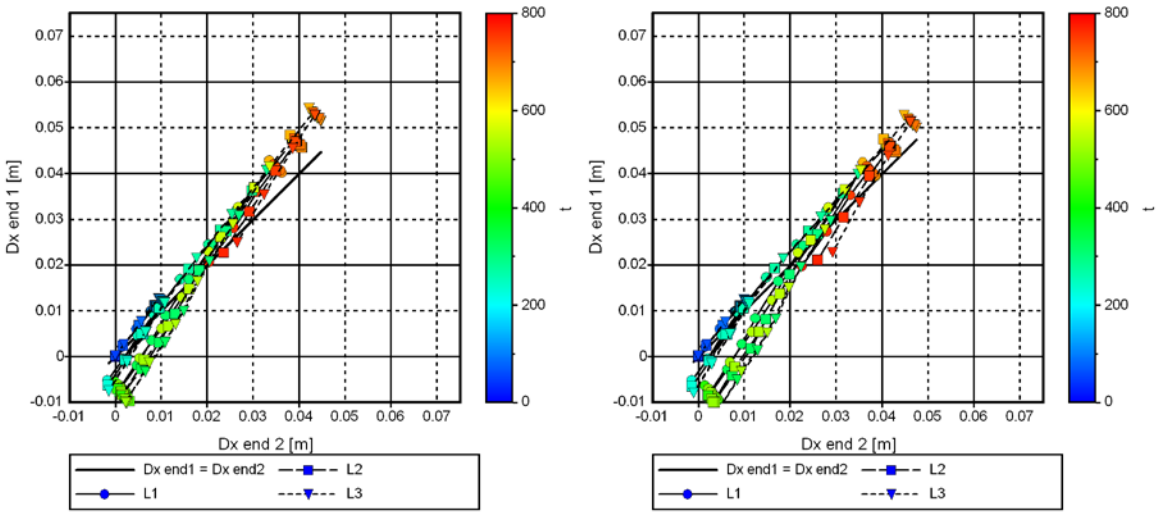

Figures 133 $D_{X,end1}$-$D_{X,end2}$ diagrams of bridge models, left B2_T1_S1_d914_SHR, right B2_T2_S1_d914_SHR, RL0

 Appendix 9.5 1(5) M_R-Z, M_R-F_X and $D_{X,end1}$-$D_{X,end2}$ diagrams of bridge models B3

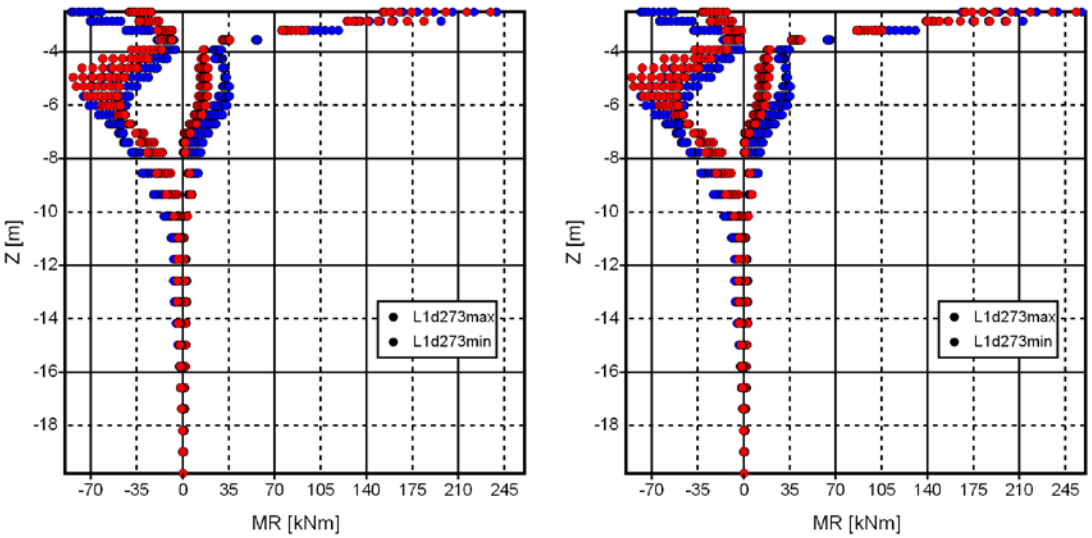

Figures 134 M_R-Z diagrams of bridge models, left B3_T1_S1_d273, right B3_T1_S2_d273, RL1

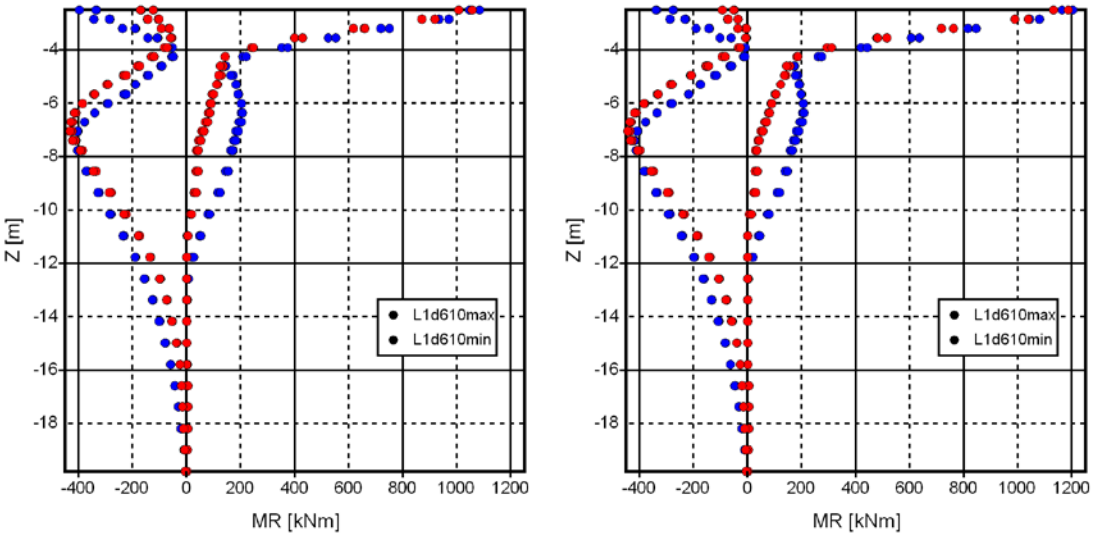

Figures 135 M_R-Z diagrams of bridge models, left B3_T1_S1_d610, right B3_T1_S2_d610, RL1

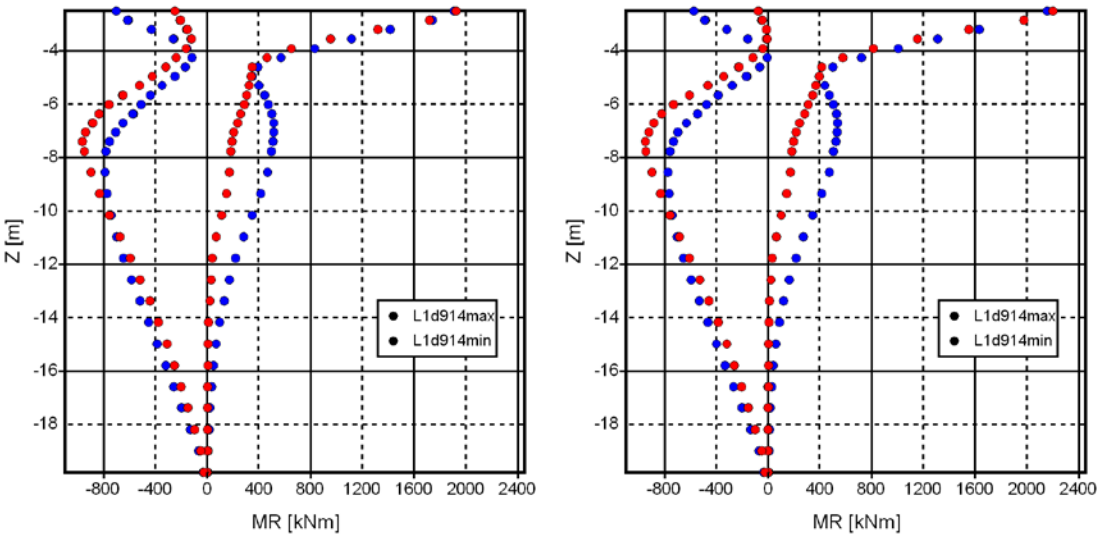

Figures 136 M_R-Z diagrams of bridge models, left B3_T1_S1_d914, right B3_T1_S2_d914, RL1

Appendix 9.5 2(5) M_R-Z, M_R-F_X and $D_{X,end1}$-$D_{X,end2}$ diagrams of bridge models B3 259

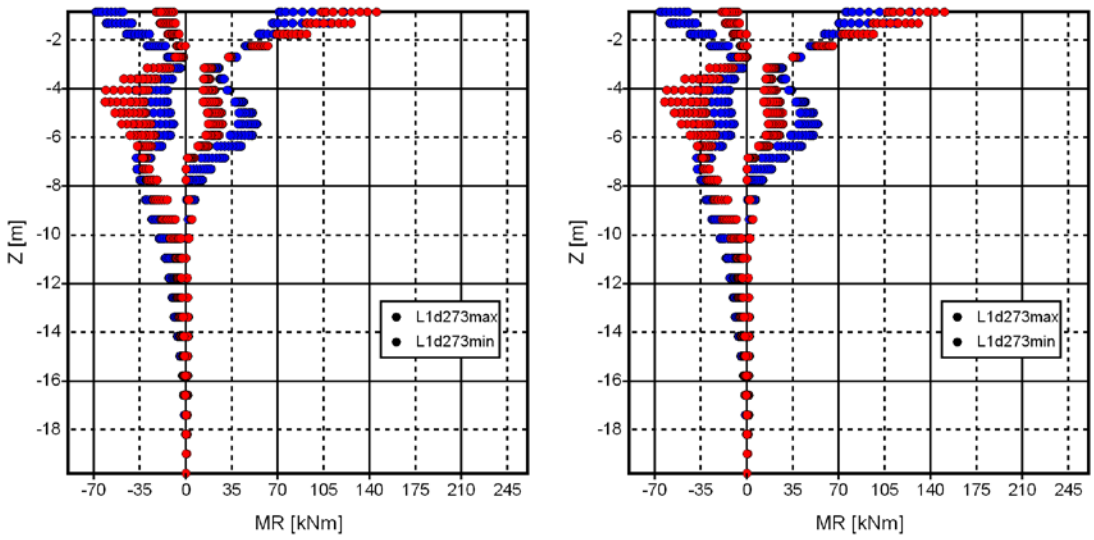

Figures 137 M_R-Z diagrams of bridge models, left B3_T2_S1_d273, right B3_T2_S2_d273, RL1

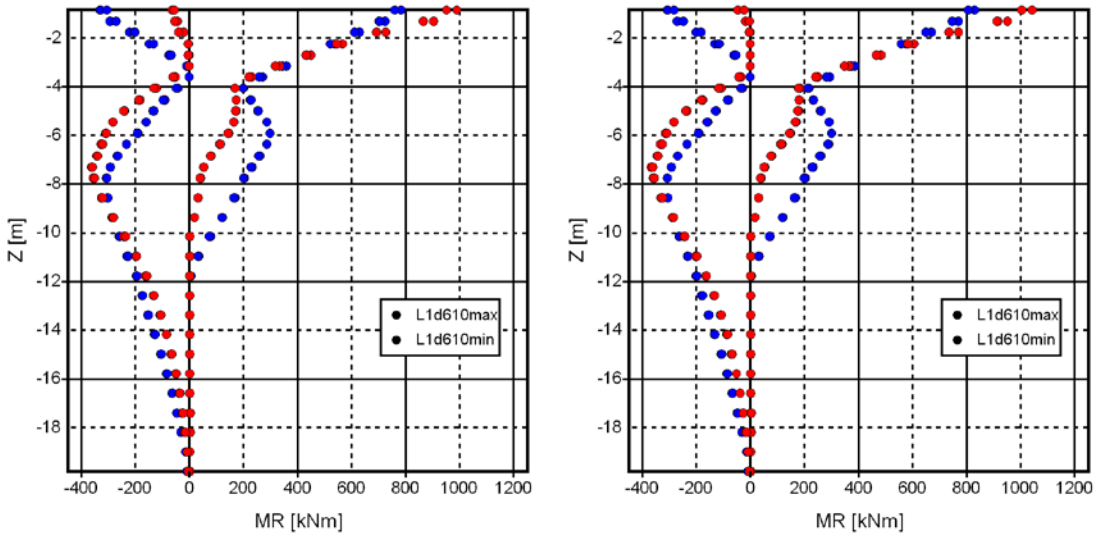

Figures 138 M_R-Z diagrams of bridge models, left B3_T2_S1_d610, right B3_T2_S2_d610, RL1

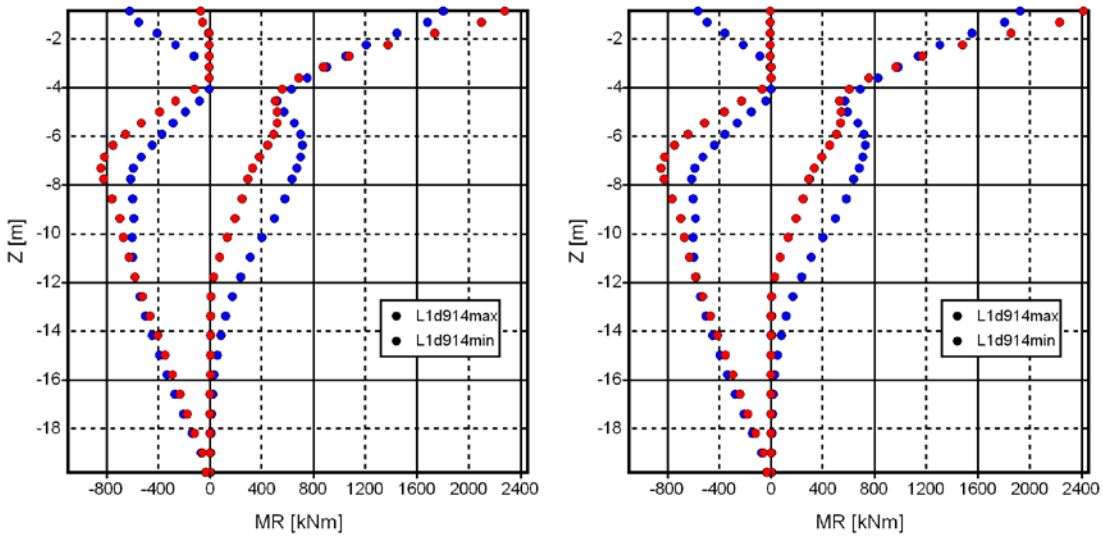

Figures 139 M_R-Z diagrams of bridge models, left B3_T2_S1_d914, right B3_T2_S2_d914, RL1

 Appendix 9.5 3(5) M_R-Z, M_R-F_X and $D_{X,end1}$-$D_{X,end2}$ diagrams of bridge models B3

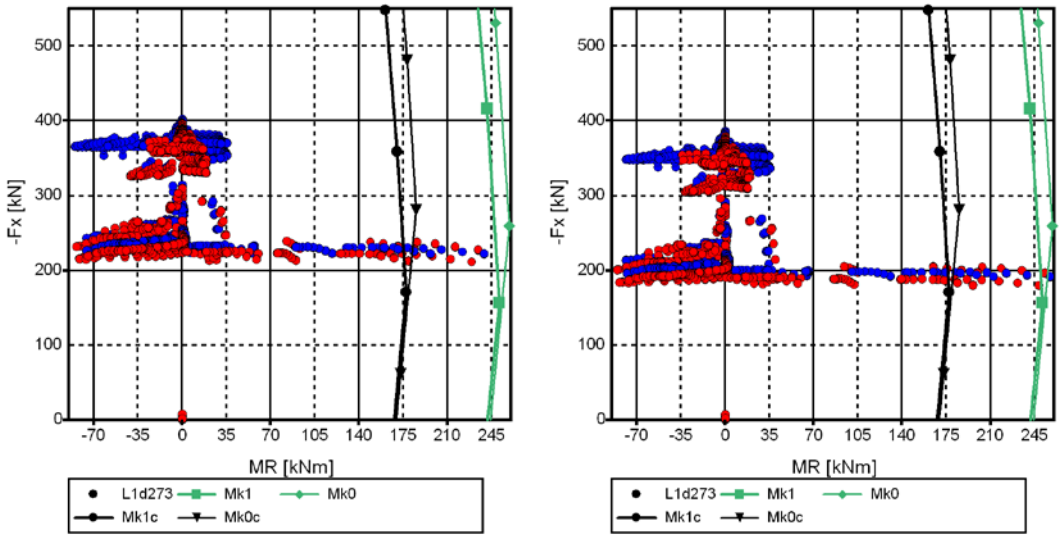

Figures 140 M_R-F_X diagrams of bridge models, left B3_T1_S1_d273, right B3_T1_S2_d273, RL2

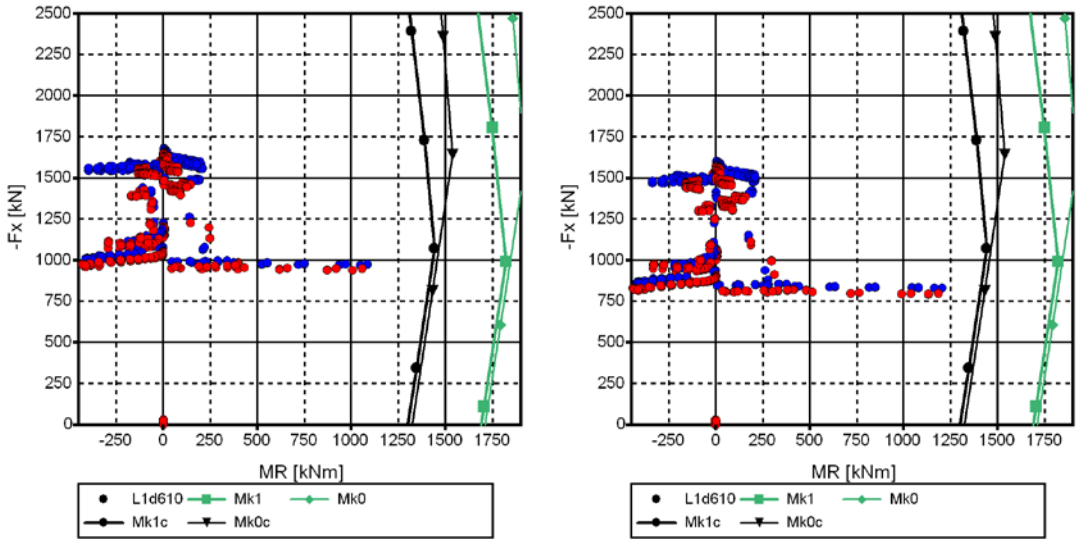

Figure 141 M_R-F_X diagrams of bridge models, left B3_T1_S1_d610, right B3_T1_S2_d610, RL2

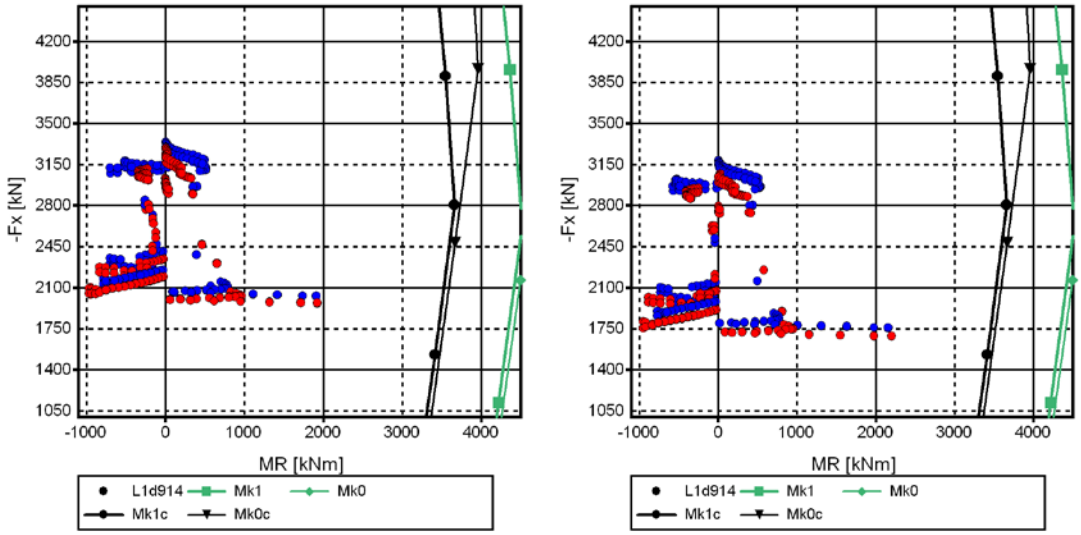

Figure 142 M_R-F_X diagrams of bridge models, left B3_T1_S1_d914, right B3_T1_S2_d914, RL2

Appendix 9.5 4(5) M_R-Z, M_R-F_X and $D_{X,end1}$-$D_{X,end2}$ diagrams of bridge models B3 261

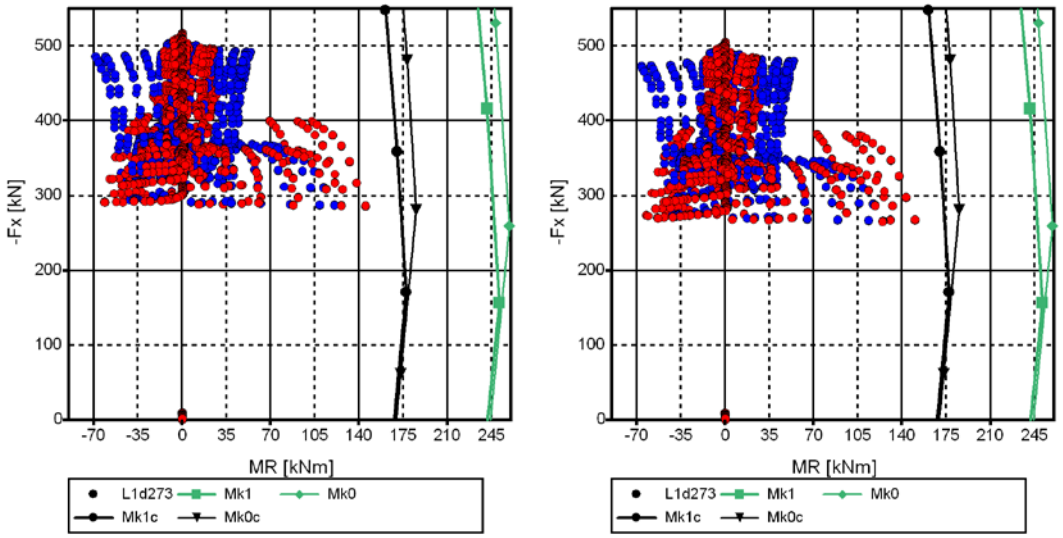

Figure 143 M_R-F_X diagrams of bridge models, left B3_T2_S1_d273, right B3_T2_S2_d273, RL2

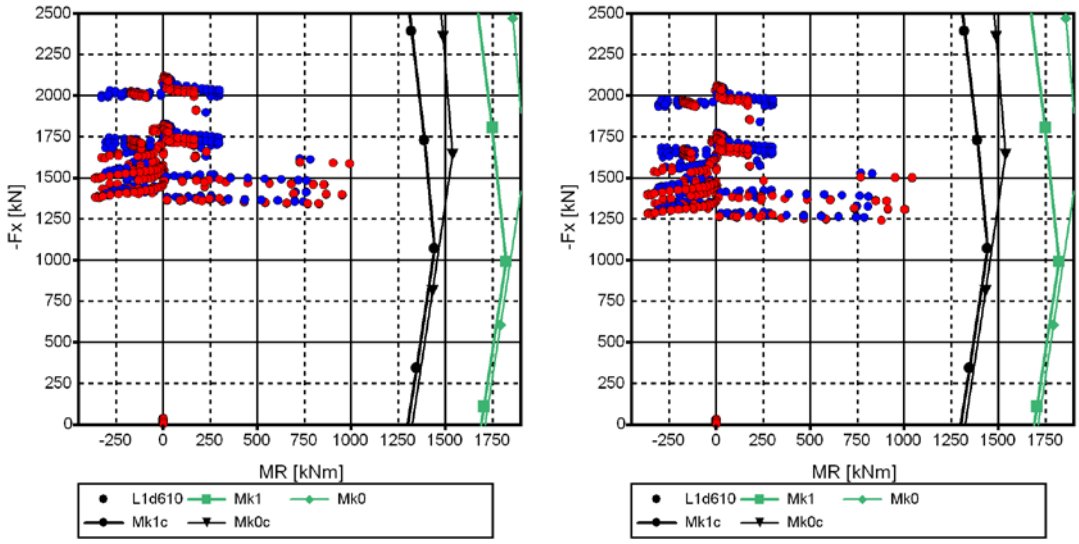

Figure 144 M_R-F_X diagrams of bridge models, left B3_T2_S1_d610, right B3_T2_S2_d610, RL2

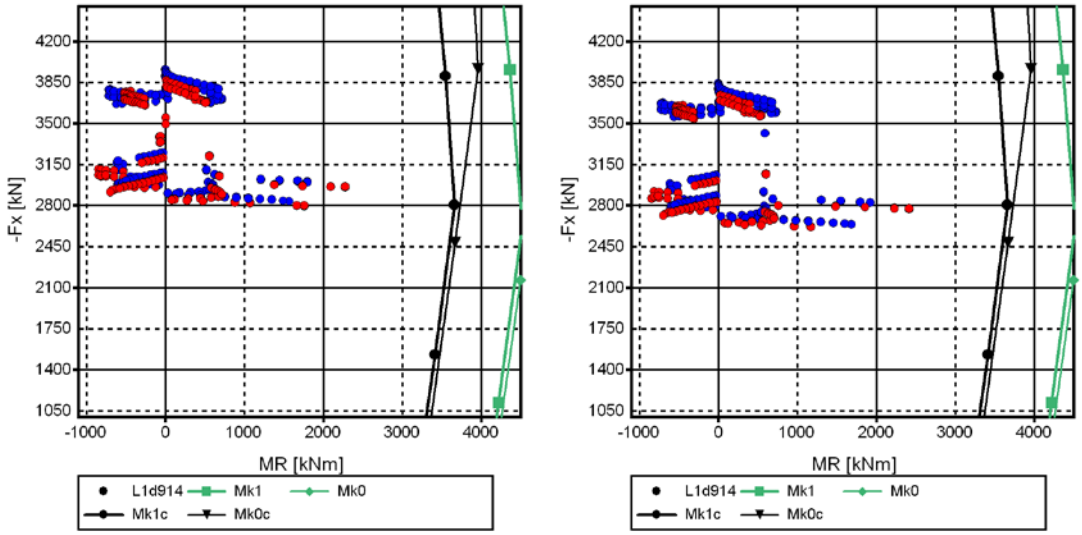

Figure 145 M_R-F_X diagrams of bridge models, left B3_T2_S1_d914, right B3_T2_S2_d914, RL2

Appendix 9.5 5(5) M_R-Z, M_R-F_X and $D_{X,end1}$-$D_{X,end2}$ diagrams of bridge models B3 262

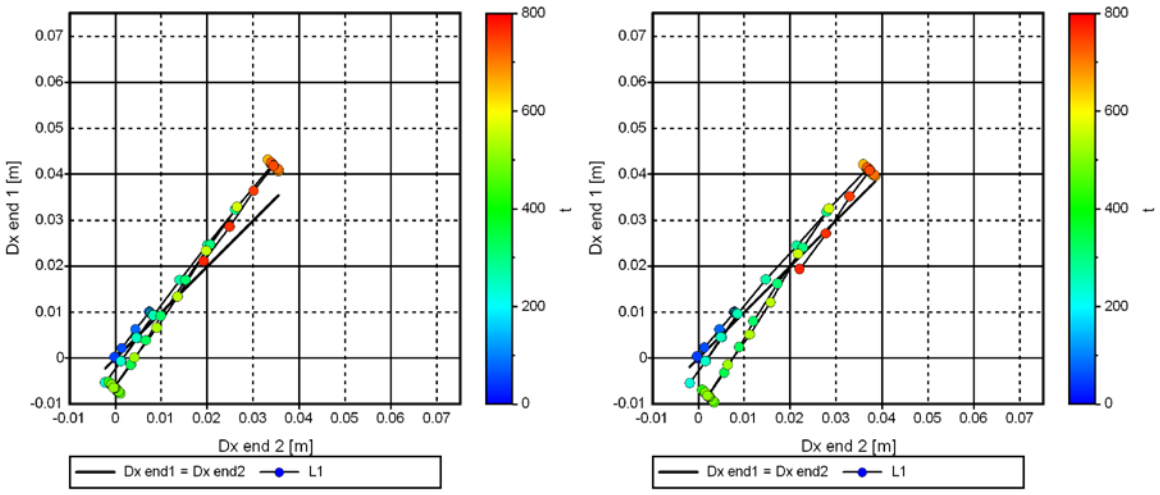

Figure 146 $D_{X,end1}$-$D_{X,end2}$ diagrams of bridge models, left B3_T1_S1_d273_SHR, right B3_T2_S1_d273_SHR, RL0

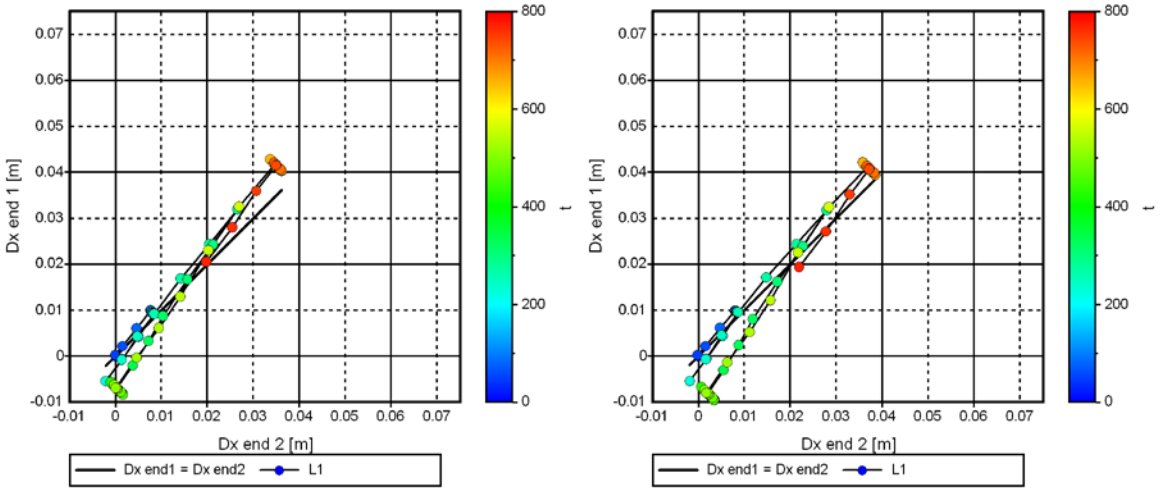

Figure 147 $D_{X,end1}$-$D_{X,end2}$ -diagrams of bridge models, left B3_T1_S1_d610_SHR, right B3_T2_S1_d610_SHR, RL0

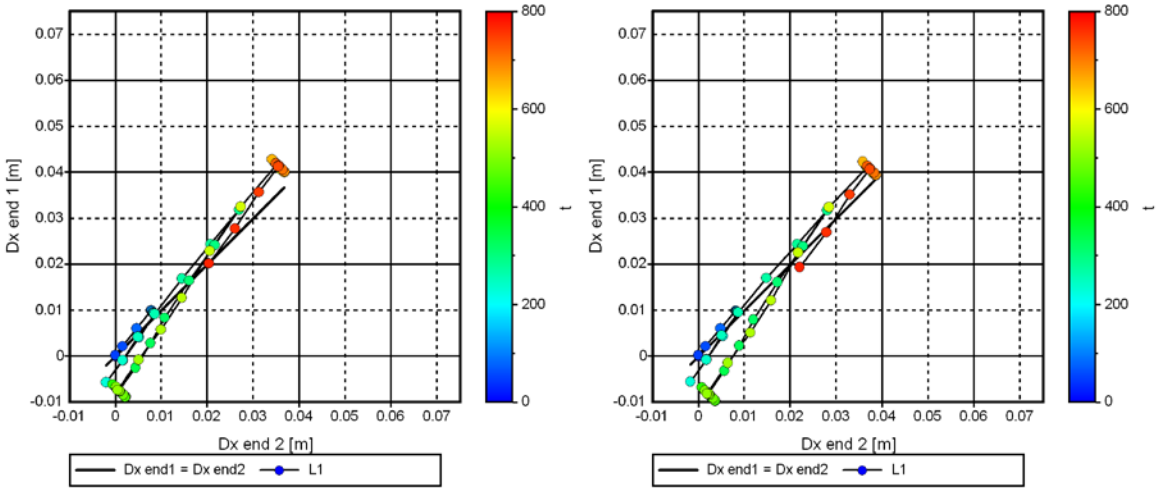

Figure 148 $D_{X,end1}$-$D_{X,end2}$ diagrams of bridge models, left B3_T1_S1_d914_SHR, right B3_T2_S1_d914_SHR, RL0

The following terms are used in this preliminary analysis:

$$d = 0.9 * h_d \tag{1}$$

$$z = \frac{7}{8} * d \tag{2}$$

$$y = 0.8 * x \tag{3}$$

The terms are also presented in the following figure:

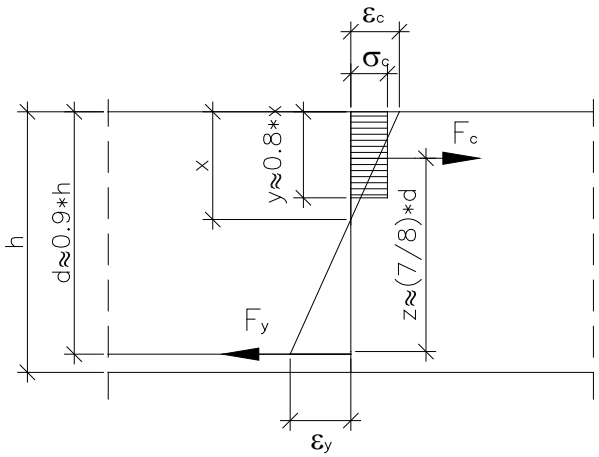

Figure 149 Behaviour of concrete cross section

The cross section is valid if the yield of reinforcement (grade A500HW ε_y = 2.5‰ [35]) occurs before the concrete reaches ultimate strain. The ultimate strain of concrete ε_{cu} is 3.5 ‰ if $f_{ck,cube} \leq 60$ MN/m^2. The relation between x and d is:

$$x \leq \frac{3.5}{3.5 + 2.5} * d \tag{4}$$

then

$$y \leq 0.8 * x = 0.467 * d \tag{5}$$

The resulting value 0.467 is called β_{max} [35]. The β_{max} is also obtained from:

$$\beta_{\max} = \frac{A_y}{b_d * d} * \frac{f_{yd}}{f_{cd}} = \rho_{y,\max} * \frac{f_{yd}}{f_{cd}} = 0.467 \quad [35] \tag{6}$$

where

$$\rho_y = \frac{A_y}{b_d * d} \tag{7}$$

Values for concrete $f_{ck,cube}$ = 40 MN/m^2 and class 1 structure partial safety factors [35], the maximum reinforcement ratio is obtained from:

$$\rho_{y,\max} = 0.467 * \frac{f_{cd}}{f_{yd}} = 0.467 * \frac{\frac{0.7 * 40}{1.35}}{\frac{500}{1.1}} = 2.13\% \tag{8}$$

264 **Appendix 9.6 2(3)** Analyses of preliminary reinforcement and bending stiffnesses of reinforced bridge superstructure

The amount of A_y is approximated with allowable stress σ_{all} = 250 MN/m^2, which leads to reasonable crack widths [45]. The formula for bending is:

$$A_y = \frac{M_y}{z * \sigma_{all}} \quad (9$$

then with Formula 7 and 9

$$\rho_y = \frac{M_y}{b_d * d * z * \sigma_{all}} = \frac{M_y}{b_d * \frac{7}{8} d^2 * \sigma_{all}} \quad (10$$

The obtained value is an estimate for reinforcement if the short-term serviceability limit state is the dimensioning case and reinforcement stress σ_{all} leads to reasonable crack widths. The bending stiffness on concrete cross section is then estimated using formula:

$$EI_{ss,eff} = \alpha_r * EI_{ce} + (1 - \alpha_r) * A_y * E_y * z * (d - x) \quad [35] \quad (11$$

where

$$\alpha_r = \left(\frac{M_{y,r}}{M_{y,k}} \right)^3 \leq 1.0 \quad [35] \quad (12$$

$$M_{y,r} = 1.7 * W_{ce} * f_{ctk} \quad [35] \quad (13$$

if the cross section is rectangular

$$W_{ce} = \frac{1}{6} * b_d * h^2 \quad (14$$

$EI_{ce,eff}$ = effective bending stiffness of bridge superstructure [MNm^2]
EI_{ce} = elastic bending stiffness of uncracked concrete cross section [MNm^2]
$M_{y,r}$ = cracking moment of cross section [MNm]
$M_{y,k}$ = moment of cross section in serviceability limit stage [MNm]
W_{ce} = elastic section modulus [m^3]
f_{ctk} = tensile strength of concrete, with $f_{ck.cube}$ = 40 f_{ctk} = 2.34 [MNm^2]

With Figure 148 and Formula 2:

$$x = (d - z) * 3 = (d - \frac{7}{8} * d) * 3 = \frac{3}{8} * d \quad (15$$

Then with Formula 2, 11 and 15:

$$EI_{ss,eff} = \alpha_r * EI_{ce} + (1 - \alpha_r) * A_y * E_y * \frac{7}{8} * \frac{5}{8} * d^2 \quad (16$$

$$= \alpha_r * EI_{ce} + (1 - \alpha_r) * A_y * E_y * \frac{35}{64} * d^2$$

Then with Formula 16 and 7:

$$EI_{ss,eff} = \alpha_r * EI_{ce} + (1 - \alpha_r) * \rho_y * E_y * b_d * \frac{35}{64} * d^3 \quad (17$$

Rough results for ρ_y and relation $EI_{ss,eff}/EI_{ce}$ (relation between estimated effective stiffness and stiffness in bridge model) in B2 bridge type with values α_r = (1/2.5)^3 = 0.064 and b_d = 2.25 m are presented in the following tables.

Table 4 Estimates for real bending stiffnesses of bridge superstructure cross section in bridge model B2_T1

B2T1		Moment from bridge models, RL1[MNm]				Reinforcement ratio ρ_y %				Relation $EI_{ss,eff}$ / EI_{ce} %			
		My end b	My end t	My mid b	My int t	ρ end b	ρ end t	ρ mid b	ρ injt t	end b	end t	mid b	int t
L1S1T1d273	1350TB	12.26	-13.63	11.04	-9.18	0.76	-0.85	0.69	-0.57	32	34	29	25
L2S1T1d273	1600TB	14.25	-15.21	14.66	-11.73	0.62	-0.66	0.64	-0.51	27	29	28	24
L3S1T1d273	1800TB	15.40	-15.92	18.45	-14.41	0.52	-0.54	0.63	-0.49	24	25	28	23
L1S1T1d610	1350TB	12.27	-12.99	11.05	-9.26	0.76	-0.81	0.69	-0.58	32	33	29	25
L2S1T1d610	1600TB	14.15	-14.68	14.62	-11.83	0.62	-0.64	0.64	-0.52	27	28	28	24
L3S1T1d610	1800TB	15.63	-15.53	18.58	-14.58	0.53	-0.53	0.63	-0.50	25	25	28	23
L1S1T1d914	1350TB	9.96	-12.82	9.95	-8.97	0.62	-0.80	0.62	-0.56	27	33	27	25
L2S1T1d914	1600TB	11.73	-14.29	13.46	-11.55	0.51	-0.62	0.59	-0.50	24	27	26	23
L3S1T1d914	1800TB	13.00	-15.07	17.30	-14.32	0.44	-0.51	0.59	-0.49	22	24	27	23
L1S2T1d273	1350TB	12.42	-13.65	8.96	-9.44	0.77	-0.85	0.56	-0.59	32	34	25	26
L2S2T1d273	1600TB	14.27	-15.26	10.80	-12.17	0.62	-0.66	0.47	-0.53	27	29	22	24
L3S2T1d273	1800TB	15.33	-15.96	13.83	-14.87	0.52	-0.54	0.47	-0.51	24	25	23	24
L1S2T1d610	1350TB	12.58	-12.94	9.03	-9.53	0.78	-0.81	0.56	-0.59	32	33	25	26
L2S2T1d610	1600TB	14.37	-14.57	10.85	-12.29	0.63	-0.63	0.47	-0.54	28	28	22	24
L3S2T1d610	1800TB	15.78	-15.40	14.06	-15.06	0.54	-0.52	0.48	-0.51	25	24	23	24
L1S2T1d914	1350TB	10.24	-12.77	7.92	-9.28	0.64	-0.80	0.49	-0.58	27	33	23	25
L2S2T1d914	1600TB	11.93	-14.15	9.66	-12.08	0.52	-0.62	0.42	-0.53	24	27	21	24
L3S2T1d914	1800TB	13.14	-14.90	12.76	-14.87	0.45	-0.51	0.43	-0.51	22	24	21	24